

# **On the Aerodynamic Performance of Automotive Vehicle Platoons Featuring Pre and Post-Critical Leading Forms**

A thesis submitted in accordance with the regulations  
for the degree of Doctor of Philosophy

By Riccardo M. Pagliarella

School of Aerospace, Mechanical and Manufacturing Engineering  
RMIT University

September 2009

# Declaration

I hereby certify that:

- Except where due acknowledgement is made, the work presented is mine alone,
- I have not plagiarised the work of others in any form, nor have I allowed or enabled others to copy from my work,
- No part of this work has been submitted previously, in whole or part, for any other academic award,
- The content of the thesis is the result of work which has been carried out since the official commencement date of the approved research program,
- Any editorial work, paid or unpaid, carried out by a third party is duly acknowledged, and,
- All relevant university ethics and guidelines procedures have been duly followed.

Riccardo M. Pagliarella



*Dedicated to the memories of Gervasio Pace and Emilio Pagliarella  
For their most enthusiastic and enduring support of my various endeavours*

# Acknowledgements

This work would not have been possible without the assistance and encouragement of others.

First and foremost, the author wishes to extend particular thanks to his supervisor, Professor Simon Watkins, and his second supervisor, Dr Angelo Tempia for their patience, support and encouragement throughout the course of this work.

Sincerest thanks are extended to Mr Gil Atkins, Mr Brett Vincent, Mr Patrick Wilkins, Mr David Goodey and Mr Don Savvides of the RMIT University School of Aerospace, Mechanical and Manufacturing Engineering for their assistance by way of support of the RMIT University Industrial Wind Tunnel and related infrastructure. The extra hands of Mr Philip Wilson in later experimental tests well into late hours were highly valued. The thoughts of Dr Jon Watmuff in understanding challenges in reliable dynamic acquisition methods were sincerely appreciated, as were those of Mr Peter Dale (RMIT University, School of Applied Sciences) and Mr Peter Mousley (Turbulent Flow Instrumentation).

“Intellectual sparring” with Mr Ben Loxton and Dr Shaun Johnson on topics related to this thesis have proved both greatly engaging and highly amusing, and will be sorely missed.

The encouragement of family throughout this period has been paramount to both the completion of this thesis and the journey preceding it. I am grateful for the constant efforts of my parents, Irene and Eraldo Pagliarella, both believers in the value of a strong education, and to both Pauline and Max Lai, for their infinite patience and understanding in its execution.

# Contents

<b>Declaration</b>	<b>II</b>
<b>Acknowledgements</b>	<b>IV</b>
<b>Contents</b>	<b>V</b>
<b>List of Figures</b>	<b>XV</b>
<b>List of Tables</b>	<b>XXV</b>
<b>Nomenclature</b>	<b>XXIX</b>
<b>Summary</b>	<b>1</b>
<b>1 Literature review</b>	<b>3</b>
1.1 General overview . . . . .	3
1.2 Characteristic passenger vehicle aerodynamics . . . . .	5
1.2.1 Classical forms: squareback, notchback, fastback . . . . .	6
1.2.2 Elementary analogous flows and relevant phenomena . . . . .	8
1.2.2.1 Quasi-two-dimensional flows . . . . .	9
1.2.2.2 Effect of freestream turbulence . . . . .	12
1.2.2.3 Three-dimensional, swirling flows . . . . .	15

1.2.2.4	Effects of ground proximity . . . . .	20
1.3	On the use of reference forms in vehicle aerodynamic testing . . . . .	20
1.3.1	Development of the Ahmed Model . . . . .	21
1.3.2	Contributions by Ahmed et al and others . . . . .	25
1.3.2.1	On the validity of the centreline symmetry plane . . . . .	31
1.3.2.2	On the use of computational sources . . . . .	31
1.3.2.3	Model forebody effects . . . . .	33
1.3.2.4	Turbulent phenomena I: the high-drag case to $\alpha_c$ . . . . .	35
1.3.2.5	Turbulent phenomena II: $\alpha > \alpha_c$ . . . . .	39
1.3.2.6	Transitional effects between about $\alpha_c$ . . . . .	40
1.3.3	Reynolds effects . . . . .	40
1.3.4	Relevance of Ahmed Model to modern vehicles . . . . .	42
1.4	Tandem arrangements . . . . .	43
1.4.1	Advantages in mean aerodynamic forces at close spacing . . . . .	43
1.4.2	Literature pertaining to tandem automotive vehicle arrangements . . . . .	44
1.4.2.1	Aerodynamic performance of platoons . . . . .	45
1.4.2.2	Upstream vehicles as a source of on-road turbulence . . . . .	50
1.4.3	Relevant tandem arrangements of fundamental bluff body forms . . . . .	51
1.4.3.1	Fundamental studies of two dimensional bluff bodies in tandem arrangements . . . . .	51
1.4.3.2	On the generation of oscillating behaviours within the gap . . . . .	53
1.4.3.3	Limitations on transferability of acoustic data in fundamental stud- ies to automotive forms . . . . .	54
1.4.3.4	Observed relationships between gap spacing and spectral properties . . . . .	55
1.5	Conclusions . . . . .	56
1.5.1	Summary of literature review . . . . .	56

1.6	Proposed scope and aims . . . . .	58
<b>2</b>	<b>Experimental methods</b>	<b>59</b>
2.1	Test models . . . . .	59
2.1.1	Physical description . . . . .	59
2.2	Instrumentation . . . . .	61
2.2.1	The RMIT Industrial Wind Tunnel (IWT) . . . . .	61
2.2.1.1	Coordinate system . . . . .	61
2.2.1.2	Flow characteristics in test section . . . . .	62
2.2.1.3	Model location in the IWT . . . . .	64
2.2.2	Force measurements/balance system . . . . .	64
2.2.2.1	JR3 Inc. 160M50A force balance system . . . . .	64
2.2.2.2	Acquisition: the TFI JR3 Test Control Panel . . . . .	65
2.2.2.3	Incorporation into Ahmed Model . . . . .	66
2.2.2.4	Acquisition procedure . . . . .	66
2.2.2.5	Error Analysis and corrections . . . . .	67
2.2.3	Dynamic pressure measuring instrumentation . . . . .	67
2.2.3.1	Digital reconstruction of dynamic pressure data . . . . .	68
2.2.3.2	Notes in processing data estimated via the ITF method . . . . .	69
2.2.3.3	Theoretical approaches in obtaining tubing transfer functions . . . .	70
2.2.3.4	Experimental approaches in obtaining tubing transfer functions . .	71
2.2.3.5	Data acquisition software . . . . .	71
2.2.4	Surface pressure measurements . . . . .	73
2.2.4.1	Tubing properties . . . . .	73
2.2.4.2	Pressure tap location . . . . .	75
2.2.4.3	Noise floor . . . . .	75

2.2.5	Flow field dynamic pressure measurement . . . . .	76
2.2.5.1	Cobra probe by Turbulent Flow Instrumentation . . . . .	76
2.2.5.2	ECA Probe by Turbulent Flow Instrumentation . . . . .	79
2.2.6	Three axis traverse . . . . .	81
2.2.7	National Instruments NI-6034E data acquisition card . . . . .	82
2.3	Spectral processing methods . . . . .	82
2.3.1	General theory . . . . .	82
2.3.2	Power spectral density . . . . .	84
2.4	Qualitative visualisation . . . . .	86
2.4.1	Smoke visualisation . . . . .	86
2.4.2	Oil and soot deposition . . . . .	87
<b>3</b>	<b>Results I: models in isolation</b>	<b>88</b>
3.1	Force data . . . . .	88
3.1.1	Reynolds similarity . . . . .	88
3.1.2	Validation of drag force trends . . . . .	90
3.2	Qualitative observations of flow phenomena . . . . .	92
3.2.1	Oil and soot depositions . . . . .	92
3.2.1.1	$\alpha = 25^\circ$ case . . . . .	92
3.2.1.2	$\alpha = 35^\circ$ case . . . . .	95
3.2.2	Flowfield smoke visualisations . . . . .	95
3.3	Quantitative investigation of mean body forces by surface pressures . . . . .	97
3.3.1	Sampling settings . . . . .	97
3.3.2	$\alpha = 25^\circ$ case . . . . .	101
3.3.3	$\alpha = 35^\circ$ case . . . . .	101
3.3.4	Model forebody . . . . .	104

3.4	Mean wake data . . . . .	104
3.4.1	Sampling settings . . . . .	104
3.4.2	Presentation of mean flow field results . . . . .	108
3.4.3	A general note on wake asymmetry . . . . .	108
3.4.4	$\alpha = 25^\circ$ case . . . . .	108
3.4.5	$\alpha = 35^\circ$ case . . . . .	111
3.4.5.1	Anomalous asymmetry and flow angularity . . . . .	111
3.4.5.2	Generalised results . . . . .	111
3.4.5.3	Conclusions . . . . .	114
3.5	Dynamic performance of models in isolation . . . . .	114
3.5.1	Generalised unsteady statistical data . . . . .	114
3.5.1.1	Surface pressure $\sigma_{C_P}$ . . . . .	114
3.5.1.2	Flow field turbulence intensity data . . . . .	116
3.5.2	Spectral performance . . . . .	117
3.5.2.1	$\alpha = 25^\circ$ case . . . . .	118
3.5.2.2	$\alpha = 35^\circ$ case . . . . .	122
3.5.2.3	Cross-spectral analysis, $\alpha = 25^\circ$ case . . . . .	124
3.5.2.4	Cross-spectral analysis, $\alpha = 35^\circ$ case . . . . .	125
3.6	Preliminary analysis of far wake characteristics . . . . .	136
3.7	Conclusions . . . . .	141
<b>4</b>	<b>Results II: two model platoons, longitudinal spacing</b>	<b>142</b>
4.1	Force data . . . . .	143
4.1.1	Limitation of spacing range . . . . .	143
4.1.2	Force data trends . . . . .	143
4.1.2.1	Specific force trends for platoon with $\alpha = 25^\circ$ leading model . . .	144

4.1.2.2	Specific force trends for platoon with $\alpha = 35^\circ$ leading model . . .	145
4.1.3	Concluding comments concerning force data . . . . .	146
4.2	Generalized trends by centreline surface pressures . . . . .	146
4.2.1	For platoons with $\alpha = 25^\circ$ leading model . . . . .	147
4.2.1.1	Upper body flows and trailing model impingement . . . . .	147
4.2.1.2	Base flows . . . . .	147
4.2.2	For platoons with $\alpha = 35^\circ$ leading model . . . . .	148
4.2.2.1	Observations for $0.125 \leq \frac{x}{L} \leq 0.5$ . . . . .	148
4.2.2.2	Observations for $\frac{x}{L} = 0.125$ . . . . .	149
4.2.2.3	Observations for $\frac{x}{L} = 1$ . . . . .	149
4.3	Generalized trends by leading and trailing model surface pressures and gap flows .	154
4.3.1	For platoons with $\alpha = 25^\circ$ leading model . . . . .	154
4.3.1.1	Trends for leading model afterbody . . . . .	154
4.3.1.2	Trends for trailing model forebody . . . . .	155
4.3.2	For platoons with $\alpha = 35^\circ$ leading model . . . . .	161
4.3.2.1	Trends for leading model afterbody . . . . .	161
4.3.2.2	Trends for trailing model forebody . . . . .	162
4.3.3	Gap flows . . . . .	167
4.3.4	General trends . . . . .	167
4.3.4.1	Trends for the $\alpha = 25^\circ$ leading model near wake . . . . .	167
4.3.4.2	Trends for the $\alpha = 35^\circ$ leading model near wake . . . . .	168
4.3.4.3	Trends upstream of the trailing model forebody . . . . .	168
4.3.5	Concluding remarks and further deconstruction of data . . . . .	172
4.4	Region I: closest spacing . . . . .	174
4.4.1	Qualitative visualisation trends for platoon with $\alpha = 25^\circ$ leading model . .	174



4.4.1.1	Leading model backlight flows . . . . .	174
4.4.1.2	Leading model base flows . . . . .	175
4.4.1.3	Trailing model forebody flows . . . . .	175
4.4.2	Generalised backlight trends for platoon with $\alpha = 35^\circ$ leading model . . . .	176
4.4.2.1	Backlight and base flows . . . . .	176
4.4.2.2	Trailing model . . . . .	177
4.5	Region II: peak trailing model drag . . . . .	183
4.5.1	Qualitative visualisation trends for platoon with $\alpha = 25^\circ$ leading model . .	183
4.5.2	Qualitative visualisation trends for platoon with $\alpha = 35^\circ$ leading model . .	183
4.6	Region III: beyond peak drag . . . . .	189
4.6.1	Qualitative visualisation trends for platoon with $\alpha = 25^\circ$ leading model . .	189
4.6.2	Qualitative visualisation trends for platoon with $\alpha = 35^\circ$ leading model . .	189
4.7	Spectral performance . . . . .	194
4.7.1	General spectral performance assessed at key shedding location . . . . .	194
4.7.2	Analysis for pre-critically led platoons . . . . .	194
4.7.2.1	Validation of key flow phenomena for leading model . . . . .	195
4.8	Trailing model afterbody performance . . . . .	202
4.8.1	Mean surface pressures . . . . .	202
4.8.2	Statistical unsteady behaviours . . . . .	202
4.8.3	Oscillating unsteady behaviours . . . . .	207
4.8.4	Confirmation of salient oscillating afterbody phenomena . . . . .	208
4.9	Conclusions . . . . .	209
<b>5</b>	<b>Conclusions and recommendations</b>	<b>217</b>
5.1	Conclusions . . . . .	217
5.1.1	Model-in-isolation performance . . . . .	218

5.1.2	Platoon performance . . . . .	218
5.1.2.1	With leading pre-critical model ( $\alpha = 25^\circ$ ) . . . . .	219
5.1.2.2	With leading post-critical model ( $\alpha = 35^\circ$ ) . . . . .	219
5.1.2.3	Effect on body force coefficients . . . . .	220
5.1.2.4	Effect on trailing model afterbody performance . . . . .	220
5.2	Recommendations . . . . .	220
<b>A</b>	<b>The RMIT University Industrial Wind Tunnel</b>	<b>222</b>
A.1	Mean flow properties . . . . .	222
A.1.1	Yaw alignment . . . . .	225
A.1.2	Effect on Ahmed model wakes . . . . .	225
A.2	Boundary layer properties . . . . .	227
A.3	Static pressure distribution . . . . .	229
A.4	Freestream velocity measurement in the IWT . . . . .	230
A.4.1	MKS Baratron <sup>TM</sup> system . . . . .	230
A.4.1.1	MKS Baratron <sup>TM</sup> system calibration notes . . . . .	231
A.4.2	System noise . . . . .	231
A.4.2.1	Baratron <sup>TM</sup> and barometer . . . . .	232
A.4.2.2	Force balances, dynamic pressure probes and surface pressure acquisition systems . . . . .	233
A.5	Dynamic flow characteristics in the IWT . . . . .	233
A.5.1	Statistical turbulence characteristics . . . . .	234
A.5.2	Low frequency pulsing . . . . .	234
A.5.3	Turbulent length scales . . . . .	236
A.5.3.1	Turbulence length scale via autocorrelation . . . . .	236
A.5.3.2	Best fit with existing theory . . . . .	238

A.5.3.3	Results . . . . .	240
A.5.3.4	Discussion . . . . .	240
<b>B</b>	<b>Further notes on pressure probes</b>	<b>244</b>
B.1	Technical differences between ECA and Cobra probes . . . . .	244
B.1.1	Notes on statistical properties obtained from Cobra and ECA probes . . . . .	245
<b>C</b>	<b>Practical challenges in accurate calibration of dynamic pressure instrumentation</b>	<b>248</b>
<b>D</b>	<b>Time alignment of acquired data</b>	<b>251</b>
D.1	Hardware particulars . . . . .	251
D.2	Challenges in multichannel, dynamic acquisition . . . . .	252
D.3	Interchannel delay . . . . .	252
D.3.1	Hardware schematic . . . . .	253
D.3.2	Timing strategies . . . . .	254
D.3.2.1	Experimental deconstruction of interchannel delay . . . . .	255
D.4	Application to devices used . . . . .	256
D.4.1	Cobra probes . . . . .	256
D.4.2	ECA probe . . . . .	258
D.4.2.1	Deconstruction of ECA probe phase response . . . . .	259
D.4.2.2	Experimental identification of phase lag . . . . .	261
D.4.2.3	Experimental results . . . . .	262
D.5	Conclusions . . . . .	265
<b>E</b>	<b><math>\alpha = 35^\circ</math> reference wake data after Lienhart et al</b>	<b>266</b>
E.1	Problem definition . . . . .	266
E.1.1	Relevance in context of the research question . . . . .	266

E.2	Key experimental setup differences . . . . .	268
E.3	Key flowfield differences . . . . .	268
E.4	Comparative limitation of acquisition methods . . . . .	272
E.5	Conclusions . . . . .	273
<b>F</b>	<b>2003 VFACTS data</b>	<b>274</b>
F.1	Data by segment and subsegment . . . . .	275

# List of Figures

1.1	Characteristic flows over a fastback-type vehicle form showing typical separations after Hucho (1998) . . . . .	6
1.2	Evolution of vehicle forms influenced by aerodynamic concerns Hucho (1978) . . .	7
1.3	Photos, flow topology and typical centreline flows of notchback, fastback and square-back forms (Barnard 1996, Hucho 1978) . . . . .	9
1.4	Revised flow topology for notchback forms with “C-pillar” greater than $15^\circ$ to the roof line after Gilhome et al. (2001) . . . . .	10
1.5	Variation in flows around a circular cylinder with $Re$ (Anderson 2001, Bearman 1997)	11
1.6	Comparison of increased turbulence on two-dimensional and three-dimensional bluff bodies . . . . .	14
1.7	Visualisation of flow past a cube in near-ground proximity at varying levels of turbulence by Nagib (Bearman 1978, in following comments)) . . . . .	15
1.8	Vortex formation over delta wing and wingtip . . . . .	16
1.9	Vortex breakdown progression and full stall visualisations over a $50^\circ$ delta wing (Ol 2003) . . . . .	17
1.10	Fluctuation in breakdown phenomena for $50^\circ$ delta wing at $\alpha = 12.5^\circ$ (Ol 2003) . .	18
1.11	Comparisons of an automotive scale model near wake (25% body length behind the vehicle) using multi-hole probes, instantaneous PIV and averaged PIV (Bearman 1997) . . . . .	19
1.12	Dimensions of Ahmed (LHS) and Morel (RHS) models (Ahmed et al. 1984, Morel 1978a) . . . . .	21
1.13	Early studies in backlight angle geometry after Janssen and Hucho (1975) . . . . .	22

1.14	Drag and lift data for Morel model in freestream condition (Morel 1978a) . . . . .	24
1.15	Pressure distribution across taps on Morel vehicle-like model (Morel 1978a, tap locations shown in figure 1.12) . . . . .	24
1.16	Comparison of pre and post-critical flow structures as observed by (Morel 1978b, LHS) and (Hucho 1978, RHS) in reference structures and full-scale vehicles alike .	25
1.17	Drag of Ahmed Model as a function of rear slant angle (Ahmed et al. 1984) ( $C_R^*$ indicates friction drag) . . . . .	26
1.18	Flow structures and on-surface flow visualisation about pre-critical/low-drag ( $12.5^\circ$ ) and critical ( $30^\circ$ ) Ahmed Model (Ahmed et al. 1984) . . . . .	27
1.19	Backlight mean surface flows for $25^\circ$ Ahmed Model after Krajnović and Davidson (2005) . . . . .	29
1.20	Triple vortex structure noted at edge of Ahmed Model “C-pillar” Krajnović and Davidson (2005) . . . . .	30
1.21	Centreline plots showing pre and post critical wake development adapted from Lienhart et al. (2000) . . . . .	31
1.22	Soot deposition over Ahmed Model forebody after Vino (2005) . . . . .	34
1.23	Visualisation and flow structure of forebody vortex formation after Spohn and Gillieron (2002) . . . . .	34
1.24	Afterbody mean flow topology by Krajnović and Davidson (2005) . . . . .	36
1.25	Proposed flow structure for high-drag Ahmed Model by Vino (2005) and Spohn and Gillieron (2002) . . . . .	37
1.26	Spectral levels in wake of pre-critical Ahmed Model for $St$ commensurate with base shedding frequency from computational results (Johnson 2005) . . . . .	38
1.27	Mean and time-dependent visualisations of $\alpha > \alpha_c$ Ahmed Model after Brunn and Nitsche (2001) . . . . .	39
1.28	Axial vortex core dynamic pressure ( $C_{DP}$ ) for Ahmed Model configurations $10 < \alpha < 30$ by Johnson (2005) . . . . .	40
1.29	Development of flow structure of $25^\circ$ Ahmed Model at low Re after Drouin in Okada (2006) . . . . .	41
1.30	Comparison of “low” and “medium” drag modes for cavity flows between a disc and cylinder normal flow flow after Koenig and Roshko (1985) . . . . .	45

1.31	Platoons in field testing (Michaelian and Browand 2000) . . . . .	45
1.32	Data for Chevrolet Lumina platoons for $0.5 \leq \frac{x}{L} \leq 3$ (Zabat et al. 1993) . . . . .	46
1.33	Chevrolet Lumina minivan as used by California PATH group in wind tunnel tests	47
1.34	Centreline flow structure deduced from surface pressure and wool tuft flow visualisations for two bus models in tandem after Fletcher and Stewart (1986) . . . . .	48
1.35	Results for two-model platoon by Ewald in Hucho (1998) . . . . .	49
1.36	Detailed data for Chevrolet Lumina platoons for $0 \leq \frac{x}{L} \leq 3$ after Zabat et al in Hong et al. (1998) . . . . .	50
1.37	Force data and trailing model downwash impingement visualisation for two 30° Ahmed Models in longitudinal convoy (Vino 2005) . . . . .	50
1.38	Pininfarina Turbulence Generation System (TGS) after Carlino and Cogotti (2006)	52
1.39	Variation in $C_D$ and $St$ for two cylinders in tandem arrangements at Okajima in Zdravkovich (1987) . . . . .	53
1.40	Variation in $St$ and downstream cylinder torque spectra with increased spacing after Shiraishi et al. (1986) . . . . .	54
1.41	Radiated acoustic spectra for a rectangular prism downstream of a blade after Leclercq and Doolan (2009) . . . . .	55
1.42	Oscillating relationship of variation in radiated acoustic spectra for various gap spacing after Bull et al. (1996) . . . . .	56
2.1	Single Ahmed Model installed in RMIT IWT . . . . .	60
2.2	Schematic depiction of RMIT Industrial Wind Tunnel . . . . .	62
2.3	JR3 160M50A force balance . . . . .	65
2.4	Ahmed Model installed in test section . . . . .	66
2.5	Real-time visualization in TFI Device Control . . . . .	72
2.6	Typical Bode plot of frequency response function of DPMS system implementation	74
2.7	Effect of likely experimental unknowns on tubing system response . . . . .	74
2.8	Typical data, noise floor and drift effects associated with DPMS system . . . . .	76
2.9	Detail of Series 100 TFI Cobra Probe . . . . .	77

2.10	Sample data set taken with Cobra probe at 6kHz, estimated using 65,536-point FFT (frequency bin size $<0.1\text{Hz}$ ), processed using Welch's method over 331 realizations	80
2.11	ECA probe detail . . . . .	80
2.12	RMIT three-axis traverse during pre-fit . . . . .	81
3.1	Re performance of $\alpha = 25^\circ$ and $\alpha = 35^\circ$ test models in isolation at various $Re$ . . .	89
3.2	Acquired drag values vs. original Ahmed et al. (1984) values . . . . .	91
3.3	Flow patterns over $\alpha = 25^\circ$ Ahmed model afterbody . . . . .	93
3.4	Flow patterns over $\alpha = 35^\circ$ Ahmed model afterbody . . . . .	94
3.5	Smoke visualisation of dominant axial vortices about $25^\circ$ Ahmed model afterbody	96
3.6	Smoke injected over backlight at centreline . . . . .	96
3.7	PSD at $y = 0$ , $z = 0$ on base of $\alpha = 25^\circ$ Ahmed model after various cumulative averaged PSD of successive data blocks . . . . .	99
3.8	All points spectra vs tubing amplitude response . . . . .	100
3.9	Development of rear surface pressure with increasing $Re$ for $\alpha = 25^\circ$ model . . . .	102
3.10	Development of rear surface pressure with increasing $Re$ for $\alpha = 35^\circ$ model . . . .	103
3.11	Pressure distribution, soot and smoke visualisations of the Ahmed model forebody (in isolation) . . . . .	106
3.12	Properties of oncoming flow $\frac{x}{L} = \frac{1}{16}$ upstream of model leading edge . . . . .	107
3.13	Normalised axial velocity component in wake of $25^\circ$ Ahmed model at various body lengths ( $x/L$ ) behind model base (all dimensions normalised) . . . . .	110
3.14	Normalised axial velocity component in wake of $35^\circ$ Ahmed model at various body lengths ( $x/L$ ) behind model base (all dimensions normalised) . . . . .	112
3.15	Vorticity plots of interest for $\alpha = 25^\circ$ and $\alpha = 35^\circ$ cases . . . . .	113
3.16	$\sigma_{C_p}$ for $\alpha = 25^\circ$ and $\alpha = 35^\circ$ models backlight and base regions at $Re = 1.8 \times 10^6$	115
3.17	Axial component of turbulence intensity ( $I_{uu}$ ) in wake of $25^\circ$ Ahmed model at various body lengths ( $x/L$ ) behind model base (all dimensions normalised) . . . .	117
3.18	Transverse component of turbulence intensity ( $I_{vv}$ ) in wake of $25^\circ$ Ahmed model at various body lengths ( $x/L$ ) behind model base (all dimensions normalised) . . . .	118



3.19	Vertical component of turbulence intensity ( $I_{ww}$ ) in wake of $25^\circ$ Ahmed model at various body lengths ( $x/L$ ) behind model base (all dimensions normalised) . . . . .	119
3.20	Axial component of turbulence intensity ( $I_{uu}$ ) in wake of $35^\circ$ Ahmed model at various body lengths ( $x/L$ ) behind model base (all dimensions normalised) . . . . .	120
3.21	Transverse component of turbulence intensity ( $I_{vv}$ ) in wake of $35^\circ$ Ahmed model at various body lengths ( $x/L$ ) behind model base (all dimensions normalised) . . . . .	121
3.22	Vertical component of turbulence intensity ( $I_{ww}$ ) in wake of $35^\circ$ Ahmed model at various body lengths ( $x/L$ ) behind model base (all dimensions normalised) . . . . .	122
3.23	PSD at various $Re$ at peak shedding location for $\alpha = 25^\circ$ Ahmed model backlight and base surfaces . . . . .	123
3.24	PSD for points of interest over $\alpha = 25^\circ$ Ahmed model backlight and base surfaces at $Re = 1.8 \times 10^6$ . . . . .	127
3.25	PSD at $St = 0.49$ for $\alpha = 25^\circ$ at $Re = 1.8 \times 10^6$ . . . . .	128
3.26	PSD for points of interest over $\alpha = 35^\circ$ Ahmed model backlight and base surfaces at $Re = 1.8 \times 10^6$ . . . . .	129
3.27	PSD for $\alpha = 35^\circ$ Ahmed model wake centreline at $Re = 1.8 \times 10^6$ . . . . .	130
3.28	Cross-spectral performance for $\alpha = 25^\circ$ Ahmed model backlight and base surfaces at $Re = 1.8 \times 10^6$ relative to bottom/base/centreline coincident (in red) . . . . .	131
3.29	Shedding at base of $\alpha = 25^\circ$ Ahmed model . . . . .	132
3.30	Periodic oscillation and bursting of axial C-pillar vortices in near wake of $\alpha = 25^\circ$ Ahmed model . . . . .	133
3.31	Cross-spectral performance for $\alpha = 35^\circ$ Ahmed model backlight and base surfaces at $Re = 1.8 \times 10^6$ relative to bottom/base/centreline coincident (in red) . . . . .	134
3.32	Shedding at base of $\alpha = 35^\circ$ Ahmed model . . . . .	135
3.33	Wake slices of $\frac{U}{U_\infty}$ in far wake of Ahmed model, $\frac{x}{L} = 1 - 6$ , $25^\circ$ and $30^\circ$ backlight angle . . . . .	138
3.34	Wake slices of $\frac{U}{U_\infty}$ in far wake of Ahmed model, $\frac{x}{L} = 1 - 6$ , $0^\circ$ and $12.5^\circ$ backlight angle . . . . .	139
3.35	Wake slices of $\frac{U}{U_\infty}$ in far wake of Ahmed model, $\frac{x}{L} = 1 - 6$ , $35^\circ$ backlight angle . . . . .	140

4.1	Normalised key force and moment data for lead and trail models in two-model, longitudinally spaced platooned with varying lead model $\alpha$ . . . . .	151
4.2	Centreline $C_P$ , $\sigma_{C_P}$ and wake flow for $\alpha = 25/25^\circ$ platoon . . . . .	152
4.3	Centreline $C_P$ , $\sigma_{C_P}$ and wake flow for $\alpha = 35/25^\circ$ platoon . . . . .	153
4.4	Comparison of surface pressures for leading model backlight and base surfaces for $\alpha = 25/25^\circ$ platoon with various longitudinal spacing . . . . .	157
4.5	Comparison of standard deviation of surface pressures for leading model backlight and base surfaces for $\alpha = 25/25^\circ$ platoon with various longitudinal spacing . . . . .	158
4.6	Comparison of surface pressures for trailing model forebody surface for $\alpha = 25/25^\circ$ platoon with various longitudinal spacing . . . . .	159
4.7	Comparison of standard deviation of surface pressures for trailing model forebody surface for $\alpha = 25/25^\circ$ platoon with various longitudinal spacing . . . . .	160
4.8	Comparison of surface pressures for leading model backlight and base surfaces for $\alpha = 35/25^\circ$ platoon with various longitudinal spacing . . . . .	163
4.9	Comparison of standard deviation of surface pressures for leading model backlight and base surfaces for $\alpha = 35/25^\circ$ platoon with various longitudinal spacing . . . . .	164
4.10	Comparison of surface pressures for trailing model forebody surface for $\alpha = 35/25^\circ$ platoon with various longitudinal spacing . . . . .	165
4.11	Comparison of standard deviation of surface pressures for trailing model forebody surface for $\alpha = 35/25^\circ$ platoon with various longitudinal spacing . . . . .	166
4.12	Comparison of $\frac{U}{U_\infty}$ in wake of $\alpha = 25^\circ$ leading model for platoon with various longitudinal spacing . . . . .	169
4.13	Comparison of $\frac{U}{U_\infty}$ in wake of $\alpha = 35^\circ$ leading model for platoon with various longitudinal spacing . . . . .	170
4.14	Comparison of $I_{ww}$ $\frac{x}{L} = 0.0625$ ahead of trailing model LE . . . . .	171
4.15	Surface flow visualisations for $\alpha = 25^\circ$ led platoon, $\frac{x}{L} = 0.125$ spacing . . . . .	178
4.16	Centreline impingement on second model in $\alpha = 25/25^\circ$ platoon, $\frac{x}{L} = 0.125$ spacing . . . . .	179
4.17	Surface flow visualisations for $\alpha = 35^\circ$ led platoon, $\frac{x}{L} = 0.125$ spacing . . . . .	180
4.18	Centreline impingement on second model in $\alpha = 35/25^\circ$ platoon, $\frac{x}{L} = 0.125$ spacing . . . . .	181
4.19	Gap behaviours in $\alpha = 35/25^\circ$ platoon, $\frac{x}{L} = 0.125$ spacing between models . . . . .	182

4.20	Surface flow visualisations for $\alpha = 25^\circ$ led platoon, $\frac{x}{L} = 0.25$ spacing . . . . .	185
4.21	Centreline impingement on second model in $\alpha = 25/25^\circ$ platoon, $\frac{x}{L} = 0.25$ spacing	186
4.22	Underbody flows about base of leading model in $\alpha = 25/25^\circ$ platoon, $\frac{x}{L} = 0.25$ spacing . . . . .	186
4.23	Surface flow visualisations for $\alpha = 35^\circ$ led platoon, $\frac{x}{L} = 0.25$ spacing . . . . .	187
4.24	Salient gap flow smoke visualisations for $\alpha = 35/25^\circ$ platoon, $\frac{x}{L} = 0.25$ spacing . .	188
4.25	Surface flow visualisations for $\alpha = 25^\circ$ led platoon, $\frac{x}{L} = 0.5$ spacing . . . . .	190
4.26	Centreline impingement on second model in $\alpha = 25/25^\circ$ platoon, $\frac{x}{L} = 0.5$ spacing .	191
4.27	Surface flow visualisations for $\alpha = 35^\circ$ led platoon, $\frac{x}{L} = 0.5$ spacing . . . . .	192
4.28	Underbody flows about base of leading model in $\alpha = 35/25^\circ$ platoon, $\frac{x}{L} = 0.5$ spacing	193
4.29	Spectra at base/bottom/centreline coincident for first model in platoon at various spacing . . . . .	197
4.30	Spectra along $y = 0$ for leading model in $\alpha = 25/25^\circ$ platoon at various spacing . .	198
4.31	Spectra on backlight side edge for leading model in $\alpha = 25/25^\circ$ platoon at various spacing . . . . .	199
4.32	Comparison of PSD in wake of $\alpha = 25^\circ$ leading model for platoon with various spacing	200
4.33	Phase plots of model afterbody for $\alpha = 25^\circ$ model in wake of $\alpha = 25^\circ$ model relative to base/bottom/centreline coincident at various spacing . . . . .	201
4.34	Comparison of surface pressures for trailing model backlight and base surfaces for $\alpha = 25/25^\circ$ platoon with various longitudinal spacing . . . . .	203
4.35	Comparison of surface pressures for trailing model backlight and base surfaces for $\alpha = 35/25^\circ$ platoon with various longitudinal spacing . . . . .	204
4.36	Comparison of standard deviation of surface pressures for trailing model backlight and base surfaces for $\alpha = 25/25^\circ$ platoon with various longitudinal spacing . . . .	205
4.37	Comparison of standard deviation of surface pressures for trailing model backlight and base surfaces for $\alpha = 35/25^\circ$ platoon with various longitudinal spacing . . . .	206
4.38	Spectra at base/bottom/centreline coincident for second model ( $\alpha = 25^\circ$ ) at various spacing . . . . .	211

4.39	Phase plots of model afterbody for $\alpha = 25^\circ$ model in wake of $\alpha = 25^\circ$ model relative to base/bottom/centreline coincident at various spacing . . . . .	212
4.40	Phase plots of model afterbody for $\alpha = 25^\circ$ model in wake of $\alpha = 35^\circ$ model relative to base/bottom/centreline coincident at various spacing . . . . .	213
4.41	PSD of base/bottom/centreline coincident and $\frac{y}{W} = 0.375$ , $\frac{z}{H} = 0.729$ surface pressure taps overlaid with cross spectral phase for $\alpha = 25^\circ$ model in wake of $\alpha = 35^\circ$ model at $\frac{x}{L} = 0.25$ spacing compared against model-in-isolation . . . . .	214
4.42	$C_P$ at $\frac{z}{H} = 0.946$ for trailing model in two-model platoon . . . . .	215
4.43	Comparative base and backlight edge spectra for trailing model in wake of $\alpha = 35^\circ$ model . . . . .	216
A.1	Angularity in IWT at $x = 2283\text{mm}$ . . . . .	223
A.2	Velocity distribution in transverse planes of IWT test section . . . . .	224
A.3	Ahmed model support base milled to support model yaw . . . . .	225
A.4	Afterbody near-wake flows in $\alpha = 25^\circ$ by Krajnović and Davidson (2005) . . . . .	226
A.5	Normalised transverse component of velocity $\frac{V}{U_\infty}$ for $\alpha = 25^\circ$ and $\alpha = 35^\circ$ cases . . . . .	227
A.6	Comparison of 95% boundary layer profile, thickness and displacement thickness along test section length . . . . .	228
A.7	Effects of boundary layer suction on two-model platoon after Zabat et al (in Chen et al. (1997)) . . . . .	229
A.8	$C_{PStatic}$ variation along test section . . . . .	230
A.9	Baratron <sup>TM</sup> system zero error . . . . .	232
A.10	Comparison of line noise influence . . . . .	233
A.11	Turbulence component profiles in IWT at $x = 2283\text{mm}$ . . . . .	234
A.12	Detailed, low-frequency spectra in IWT with empty test section (as acquired by Cobra probe) . . . . .	235
A.13	Spectra in IWT with empty test section (logarithmic axes, as acquired by Cobra probe, Kolmogorov law contrasted) . . . . .	236
A.14	A comparison of the low-frequency performance of various theorem modelling turbulence in the atmospheric boundary layer . . . . .	239

A.15 Incremental results for $L_u$ by autocorrelation method . . . . .	241
A.16 Comparison of experimental $S_u$ and best-fit Kaimal spectra . . . . .	242
A.17 Various experimental and wind tunnel data comparing turbulence intensity and turbulence length scale in various practical road contexts (Lindener et al. 2007) . .	243
B.1 % good samples 0.0625 model lengths behind rear of 25 Ahmed model at various sampling frequencies . . . . .	247
D.1 National Instruments E-series sampling engine . . . . .	254
D.2 Phase lag of four channels of a Cobra probe (as extracted from calibration data) .	257
D.3 Hypothetical effect of $5\mu s$ interchannel delay on ECA probe phase response (original "channel" phase response in red) . . . . .	258
D.4 Effect of phase lag over 13 channel input at 1Hz (left) and 800Hz (simulated us- ing unity amplitude sinusoidal input, interchannel delay of $5\mu s$ , $F_s=3kHz$ , as per supplied ECA probe calibration data) . . . . .	259
D.5 Pressure tap identification on early-generation Cobra probe after Chen et al. (2000)	260
D.6 Contour plotted relationships between independent pressure ratios and dependant, resolved variables for Cobra probe single-zone calibration surface after Chen et al. (2000) . . . . .	261
D.7 Effect of digitisation of 800Hz sine wave on channels 0 and 5 with $F_s$ of 3kHz (solid) and 15kHz (simulated interchannel delay of $5\mu s$ ) . . . . .	263
D.8 Resolved ECA probe data for 1Hz reference input signal applied simultaneously on channels 0 and 5 with $0\mu s$ (left) and $5\mu s$ phase delay in dynamic calibration . . . .	264
D.9 Resolved ECA probe data for 10Hz reference input signal applied simultaneously on channels 0 and 5 with $0\mu s$ (left) and $5\mu s$ phase delay in dynamic calibration . . . .	265
D.10 Resolved ECA probe data for 100Hz reference input signal applied simultaneously on channels 0 and 5 with $0\mu s$ (left) and $5\mu s$ phase delay in dynamic calibration . .	265
E.1 Normalised velocity contours of LDA results $35^\circ$ adapted from Lienhart et al Lien- hart et al. (2002) . . . . .	267
E.2 $C_P$ over backlight and base surfaces of $\alpha = 35^\circ$ case . . . . .	270
E.3 Axial vortex formation and impingement in $\alpha = 35^\circ$ case . . . . .	270

E.4	Transverse plane acquired at $\frac{x}{L} = 0.125$ behind $\alpha = 35^\circ$ model . . . . .	271
-----	-----------------------------------------------------------------------------------------------	-----

# List of Tables

4.1	Model-in-isolation values for $C_D$ and $M_y$ . . . . .	143
4.2	Comparison of base and backlight average pressures for $\alpha = 25^\circ$ leading model afterbody in wake of $\alpha = 25^\circ$ model . . . . .	155
D.1	Timing for interval scanning of four channels at 6kHz (first three sample sets) . . .	253
D.2	Phase lag between channels for Cobra probes at $F_s$ (as extracted from calibration data) . . . . .	257
F.1	Passenger . . . . .	275
F.2	SUV . . . . .	275
F.3	Light . . . . .	277
F.4	Small . . . . .	278
F.5	Medium . . . . .	279
F.6	Large . . . . .	279
F.7	People Movers . . . . .	280
F.8	Sports . . . . .	281
F.9	Prestige . . . . .	282
F.10	Luxury . . . . .	285
F.11	SUV Compact . . . . .	286
F.12	SUV Medium . . . . .	287

F.13 SUV Large . . . . .	287
F.14 SUV Luxury . . . . .	288



# Nomenclature

$\alpha$	C-pillar or 'backlight' angle
$\alpha_c$	Critical backlight angle ( $30^\circ$ )
$\mu$	Sample mean
$\overline{U}$	Mean component of flow
$\rho$	Density of working fluid (air)
$\rho_{xy}$	Correlation coefficient between two data sets e.g. $x(t)$ and $y(t)$
$\sigma_u$	Standard deviation of the fluctuating component of freestream velocity ( $\sigma_u = \sqrt{\overline{u^2}}$ ). Transverse and vertical components ( $\sigma_v$ and $\sigma_w$ ) are expressed similarly.
$\sigma_{xy}$	Covariance - the average product of deviation about a mean value - in two compared data sets e.g. $x(t)$ and $y(t)$
$\tau$	Time delay (seconds)
$i=u,v,w L_u$	Turbulence length scale
$A$	Reference area for force coefficient calculations, in this application frontal area
$C_D$	Coefficient of drag
$C_L$	Coefficient of lift
$C_P$	Coefficient of pressure
$D$	Tubing system diameter (metres)
$f$	Frequency (Hz)
$F_s$	Sampling frequency (e.g. as intended to satisfy the Nyquist criterion, $F_s = \frac{1}{2W}$ Hz)
$G_{xx}(f)$	Single-sided auto-spectral density of time history $x(t)$
$G_{xy}(f)$	Single-sided cross-spectral density between two time histories $x(t)$ and $y(t)$

$I_{uu}$	Freestream turbulence intensity; the level of “gustiness” in flow, expressed as the ratio of fluctuation in the axial turbulence component to the axial mean ( $I_{uu} = \frac{\sigma_u}{\bar{U}}$ ). Transverse and vertical components ( $I_{vv}$ and $I_{ww}$ ) are expressed similarly.
$L$ (1)	Characteristic length, as used in $Re$ and $St$ calculations (typically expressed in metres). For consistency with previous works using the same characteristic model, the square root of frontal area ( $L = \sqrt{A}$ ) is used as a characteristic length.
$L$ (2)	Model length (m). Allows inter-model spacing to be non-dimensionalised e.g. $\frac{x}{L}$
$P_0(t)$	Time history of pressure as measured at transducer
$P_1(t)$	Time history of pressure as estimated at measuring surface using the ITF method
$P_{x_m M}(\omega_k)$	Estimated power spectral density of a by Welch’s method using discrete Fourier transforms
$R_{xx}(\tau)$	Autocorrelation function comparing time history $x(t)$ to a time-delayed record of itself
$R_{xy}(\tau)$	Cross-correlation function between two time histories $x(t)$ and $y(t)$
$Re$	Reynolds number, dimensionless ratio of viscous to inertial forces where reference length is taken as the square root of frontal area
$S_{xy}(f)$	Double-sided cross-spectral density between two time histories $x(t)$ and $y(t)$
$St$	Strouhal number, a dimensionless number describing the oscillating property of a given flow, normalised against velocity ( $St = \frac{fL}{V}$ )
$t$	Time (seconds)
$U$	Axial flow component
$U(t)$	Time-dependent flow, composed of mean and fluctuating components ( $U(t) = \bar{U} + u(t)$ )
$u(t)$	Fluctuating component of flow
$U_\infty$	Freestream velocity
$V$	Transverse flow component
$W$	Source signal frequency (Hz)
$W$	Vertical flow component
$x$	Streamwise direction in test section (positive downstream)
$X_k(f, T)$	Fourier transform of stationary, random process $x(t)$

$y$	Transverse direction in test section
$z$	Vertical direction in test section (positive upwards)

# Summary

Reduced energy consumption represents an enduring challenge to vehicle fleets globally, more so in recent times given increasing demand and reduced supply of fossil fuel sources and increasingly in future as reduced vehicle energy consumption draws increasing attention to the importance of minimised drag force.

A considerable body of work exists concerning the aerodynamic optimisation of the vehicle form in isolation. Some valid generalised conclusions have been reached and clear definitions exist concerning optimal and sub-optimal key vehicle geometries and their relevant flow mechanics; to this end generalised test forms representing various characteristic vehicle geometries - “squareback”, “notchback” and “fastback” - have been developed and extensively studied, with critical geometries highlighted.

The study of organised vehicle convoys has similarly been researched since the early 1970’s primarily as a means to increase traffic throughput on existing road arterials, with ultimate “future-generation intelligent transport systems” envisioning scenarios where vehicles on major arterials may travel under fully automatic control, allowing possibilities in vehicle organisation not previously envisioned. Initial research simply considered reducing the spacing between vehicles travelling in localised groups to similar destinations - “platoons” - with traffic throughput scaling positively with platoon length and reduced spacing. Whilst these results have been tempered by more recent works limiting the probability of platoons with more than three members, “platooning” remains a positive concept for the future. The significant majority of research in this field is dedicated to developing concepts that increase traffic throughput; aerodynamic concerns are only recently being explored, however it is clear from relevant research concerning tandem bluff bodies that aerodynamic interaction is heightened with closer proximity. A variety of recent studies examining aerodynamic force effects in platooning confirm advantages for all vehicles in homogenous platoons of squareback and notchback geometries. The case for fastback geometries is unclear, with preliminary studies suggesting that there can be an increase in the drag force of trailing vehicles in the wake of a fastback geometry.

The work presented explores the fundamental phenomena underscoring the performance of two fastback vehicles travelling in close proximity. Vehicles are simulated using a well-known reference automotive form. A primary extension to existing works concerns effect of changing the leading

vehicles geometry to one of two different (yet practically characteristic) fastback configurations, constituting an important variable known to offer (in isolation) two markedly unique flow structures and drag force coefficients.

A series of wind-tunnel experiments were performed where rear slantback angles were varied and measurements of pressures, forces and flow visualisations were made on upstream and downstream models in addition to interrogation of the intervening gap flow field. It is demonstrated that irrespective of the upstream models form (and thus irrespective of dominant flow phenomena for such a model considered in isolation), force characteristics remain broadly similar for leading and trailing models in the platoon, primarily owing to the development of streamwise vortices originating from the C-pillar of the leading model which are shown to entrain a high-momentum flow between them, impinging on the trailing model forebody. A variety of methods - from qualitative flow visualisation to spectral methods applied to dynamic data - are employed to demonstrate that even at the closest spacing examined, salient flow phenomena of the leading and trailing models are broadly retained. A detailed investigation of gap flows and trailing model spectra effects as a function of leading model geometry and model spacing is also presented.

# Chapter 1

## Literature review

### 1.1 General overview

Reduced energy consumption represents an enduring challenge to vehicle fleets globally, more so in recent times given increasing demand and reduced supply of the fossil fuel sources used to power the majority of road vehicles.

The role of aerodynamic performance, particularly drag force, in determining the energy requirements of a road vehicle is well understood and has been an area of relatively consistent development since supply shortages in crude oil first came to prominence in the the 1970's (Hucho 1978). Research into optimisation of general vehicle forms has revealed a wealth of knowledge, pertaining not only to the reduction of drag force but also concerning how aerodynamic performance interacts with other aspects of a vehicle's more holistic performance envelope. Considering a practical road vehicle in isolation - essentially a bluff body - it is generally not possible to optimise for lowest possible drag without accepting negative implications with regard to packaging, cooling, handling and the like; in the latter case particularly some solutions are not possible on grounds of safety. Some valid generalised conclusions have been reached however; clearer definitions exist concerning optimal and sub-optimal forms leading to relevant flow mechanics, and generalised test forms representing various characteristic vehicle geometries have been developed, with critical geometries highlighted. Detailed investigations of various characteristic flow fields have revealed that while certain flow structures are macroscopically stable, considerable dynamic components also exist.

Whilst much current research is dedicated to the optimisation of interior and underbody flows, a deeper understanding of the implications of dynamic flow field components has led to a rise in interest concerning the influence of turbulence; not only as a homogeneous aspect of the freestream (as classically considered in wind-tunnel testing) but more importantly the influence of particular

sources of external turbulence. These can include sources associated with traditional environmental aerodynamic studies (e.g. winds, trees, buildings, etc), but more pertinent to the study of road vehicles is the aerodynamic influence of *other* road vehicles. Considering the practical environment, such vehicles may be located upstream or downstream of the vehicle in question, with or without lateral displacement from the vehicle evaluated. They may travel at a relative velocity which can be positive or negative (travelling in opposite crossing). The nature of each source of turbulence will change pending a variety of parameters giving a broad variety of flow fields for each vehicle sharing a given arterial in sufficiently close proximity, and this complexity in turn is compounded by the very presence of additional vehicles. This perspective is representative of present-day road vehicle aerodynamic performance, though it is clear that optimisation of vehicle arrangements on-road would yield flows leading to net drag reductions. Optimisation of these may in turn allow for reductions in net drag.

The study of organised vehicle convoys is not new, and has been researched since early pre-war times (Ioannou 1997). Recent strong growth of research in this area is attributable primarily to the growth of the global road vehicle population having exceeded growth in the road vehicle network, limiting traffic throughput and giving rise to a variety of related considerations. Considerable effort has thus been expended in researching better methods to use existing road networks, with ultimate “future-generation intelligent transport systems” envisioning scenarios where (critically) vehicles on major arterials would be under fully automatic control, allowing possibilities in vehicle organisation not previously envisioned. Initial research seeking to introduce new concepts in fleet organisation simply considered reducing the spacing between vehicles travelling in localised groups to similar destinations - “*platoons*” - with throughput scaling positively with platoon length and reduced spacing, and dates to the late 1970’s (Shladover 1978), though a significant research effort has been made by the California PATH group since 1988 (Ioannou 1997). Whilst these results have been tempered by more recent works limiting the probability of platoons with more than three members, “platooning” remains a positive concept for the future.

Alternatives exist, de-emphasising the need to group vehicles in close proximity, yet “platooning” is of greatest interest to the vehicle aerodynamics community owing to the heightened flow field interactions offered in a “closest-spacing” arrangement. Until recently, this effort has been conducted wholly independently of any implications from or for road vehicle aerodynamics. A range of studies assessing drag force and fuel consumption commissioned in the late 1990’s and early 2000’s attained positive results using practical vehicle forms. These studies did not investigate the underlying flow mechanics involved, limiting their applicability to other vehicle geometries.

The current state-of-the-art in the field therefore assesses platooning scenarios in a more fundamental context. Such research has highlighted that the aerodynamic implications of platooning are not always advantageous; in some instances the drag of trailing vehicles in platoons has been shown to exceed the model-in-isolation value (Vino 2005, also Ewald<sup>1</sup>).

---

<sup>1</sup>In Hucho (1998).

## 1.2 Characteristic passenger vehicle aerodynamics

Road vehicles are essentially bluff bodies moving in close proximity to a ground plane (Ahmed et al. 1984, Barnard 1996, Hucho 1978), characterised by significant afterbody separation, with a high degree of flow complexity about the base region. These complex flows dictate afterbody/base forces (Bearman 1984), thus being a significant factor in considering vehicle aerodynamic performance.

Aerodynamic performance is of considerable interest at highway speeds owing to the relationship between drag force and velocity being quadratic; thus whilst other losses exist (transmission, ancillary, rolling resistance), on a level road at steady-state, typical highway speeds, the majority of motive force applied needs overcome aerodynamic resistance. This proportion increases further with increased  $C_D$ .

Yet efforts to actively reduce road vehicle drag were originally of secondary design priority to market forces - aesthetic requirements - and utility demands. Whilst a variety of aerodynamic studies persisted for largely individual research or niche interest requirements, the drag of passenger vehicles remained little modified from postwar times until the oil crisis of 1973: the increased awareness regarding a more responsible use of fossil-fuel energy sources (then - and still now - the conventional energy source for road vehicles) brought efforts to reduce vehicle energy consumption to the fore. Vehicle aerodynamics thus became a key design priority, and a relatively steady decrease in vehicle  $C_D$  has been observed since (Hucho 1978). The study has since developed and expanded to encompass the relative effects on handling, cooling, noise and the like. A particularly interesting field of study concerns the effects of upstream turbulence on a vehicle form; such turbulence may be simply atmospheric; it may also be induced by the presence of other vehicles on road. New challenges exist, as does the possibility of a further decreased drag coefficient.

Practical road vehicle forms remain generally suboptimal with regard to aerodynamic performance, as concessions to design aims other than the aerodynamic ideal must be accounted for. Packaging plays a key role here; accommodating powertrain, passenger transport and luggage requirements gives rise to most modern passenger vehicle forms being styled to a three-box arrangement despite historical research into “one-volume” bodies (Barnard 1996, Hucho 1998).

If viewing vehicle aerodynamics as an avenue to reduce energy consumption, the resultant forms are generally compromised. Even the most basic forms feature flow separations (Ahmed et al. 1984) caused by unfavourably strong pressure gradients (Barnard 1996), characterising the primary mechanism by which passenger vehicle aerodynamic drag is generated (pressure drag). At best these separations are quasi-two-dimensional in nature, many are fully three-dimensional (Ahmed et al. 1984). Figure 1.1 denotes a flow structure thought characteristic of a fastback-type vehicle in 1976<sup>2</sup>; whilst salient features are captured, increasingly complex phenomena have been associated with representative geometries since.

---

<sup>2</sup>Hucho (1978) was among the first works to re-examine vehicle aerodynamic performance in the wake of the 1973 crude oil crisis.



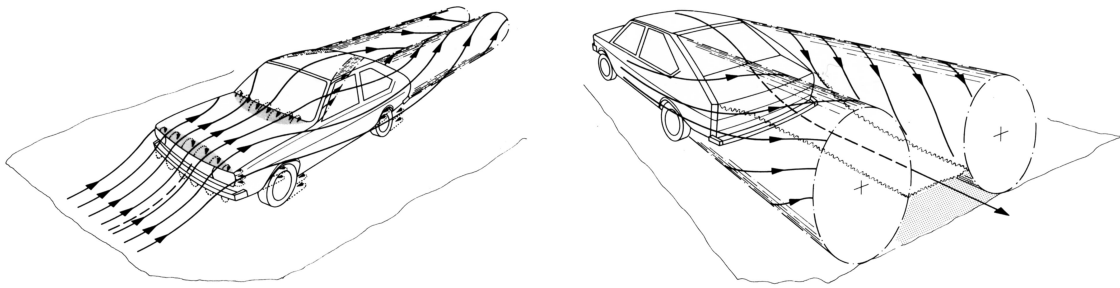


Figure 1.1: Characteristic flows over a fastback-type vehicle form showing typical separations after Hucho (1998)

Whilst form refinement can constrain many such separations (Hucho 1978) - parametric detail design has yielded significant advantages in modern vehicle aerodynamics (Buchheim and Leie 1982, Garrone and Costelli 1982, Gilhaus and Renn 1986) - afterbody separations (characteristic of bluff bodies) remain significant and typically contribute the majority of a vehicle's drag force.

### 1.2.1 Classical forms: squareback, notchback, fastback

For the purpose of generating useful, transferable research data, it is appropriate to qualify generic forms among vehicles such that characteristic flow topologies may be examined. Despite the genesis of vehicle aerodynamic studies concerning the transference of aerodynamic ideals from related domains, particularly aerospace (Barnard 1996, Hucho 1978), idealised basic bodies giving low drag differ substantially from styling models (Buchheim et al. 1981). Where originally it was thought that conventional three-body forms would need to be abandoned to achieve  $C_D < 0.3$  (Hucho 1978), it has since been proven possible with production vehicle forms developed through detail refinement (Hucho 1998). Generic automotive forms in common use thus reflect practical vehicle configurations inclusive of packaging compromises, from which relevant aerodynamic phenomena are deconstructed, as opposed to being constructions of solely aerodynamic “ideals”. It should also be appreciated that practical solutions to aerodynamic ideals have further contributed to evolve practical vehicle forms: e.g. it was originally contended that a long, tapered, “streamliner” tail was essential to achieving low drag. This was since disproved by Kamm et al; careful detail design leading to the “Kamm tail” allowed a blunt rear end to yield satisfactory aerodynamic performance, despite the resulting wake flows being particularly complicated, sufficiently so that they are still explored in the present day - as are blunt rear ends on practical automotive forms (Barnard 1996, Hucho 1978). Figure 1.2 summarises the evolution of vehicle forms where aerodynamic concerns have been applied.

Characteristic forms are typically styled (at least) after the model centreline (Barnard 1996) and projected over a width commensurate with typical aspect ratios pertaining to the vehicle's class (Ahmed et al. 1984, Johnson 2005, Morel 1978a, Okada 2006). (Hucho 1978) mentions a


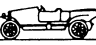













Basic shapes	1900 to 1925			
		Torpedo	Boat tail	Air ship
	1921 to 1923			
		Rumpler	Bugatti	
	1922 to 1939			
Streamlined cars		Jaray		
	1934 to 1939			
		Kamm	Schlör	
	Since 1955			
		Citroën	NSU-Ro 80	
Detail optimization	Since 1974			
		VW-Scirocco I	VW-Golf I	
Shape optimization	Since 1983			
		Audi 100 III	Ford Sierra	

Figure 1.2: Evolution of vehicle forms influenced by aerodynamic concerns Hucho (1978)

surprisingly small disparity between form and cross-sectional area between vehicles of the same class; a statistical study by the author on recent Australian sales data revealed a similar trend currently (FCAI 2003, included in Appendix F).

Three typical forms pertinent to passenger vehicles are thus presented, and described in figure 1.3:

- “*Notchback*”: characteristic to sedans, the vehicle “C-pillar” forms a “notch” against the projection of the trunk. The presence of axial vortices formed from the “C-pillars” was first observed by Carr (in Gilhome et al. (2001) and further explored by Jenkins (2000), Nouzawa et al. (1990; 1992), Vino et al. (2003). These vortices impinge on the rear window or “*backlight*” region, creating localised regions of low pressure and contributing notably to drag. Flow separating over the roof/backlight juncture forms a region of turbulent separation over the backlight/boot surfaces, bound by the “C-pillar” vortices. The deconstruction of flows within this region is important - their contribution to drag is significant - and has evolved significantly, from a simple transverse vortex (Carr<sup>3</sup>), to a more complex arch vortex (Nouzawa et al. 1990), to a complex arrangement of various-scale hairpin vortices, the smaller of which are constrained by the (more powerful) “C-pillar” vortices to realign with the axial direction

<sup>3</sup>In Gilhome et al. (2001).

prior to leaving the body (Gilhome et al. 2001). It is notable that the reappraisal of past works and the application of new tools affords a deeper understanding of the flows involved: the models deconstructed having moved considerably from those analogised along elementary two-dimensional flows to highly-turbulent, fully-three-dimensional models. Though this form is not the focus of this work, many flow topology aspects are relevant, as is the notion of evolution in relevant understanding: a comparison between figures 1.3 and 1.4 illustrates as much.

- “*Fastback*” (also known as “*hatchback*”): Characteristic of many small cars, the fastback form extends the “C-pillar” to the base region, creating a compact form. Powerful and relatively stable vortices are formed from the “C-pillars” for “C-pillar” angles of  $30^\circ$  or less to the roofline<sup>4</sup>, impinging on the backlight and contributing to markedly lower pressure in this region and heightened induced drag and lift. Beyond a *critical* angle, these vortices break down; however prior to this, the steady axial “C-pillar” vortices entrain a downwash between them (Ahmed et al. 1984, Krajnović and Davidson 2005, Vio 2005), a mean indication of which is indicated in figure 1.3. Pressures over the upper surfaces of such vehicles are generally considerably lower than those underneath; lift is therefore characteristic (Hucho 1978).
- “*Squareback*”: essentially the “fastback” type vehicle with a near-vertical C-pillar. A fully separated wake is characteristic of the form, with no impingement of large, axial vortices on the vehicle afterbody. Pressures over base surfaces show considerably less variation than for the “fastback” and “notchback” types and are generally higher.

It can be appreciated that a key criterion dictating flow structure remains the “C-pillar” angle, as it affects the generation and strength of strong, impinging “C-pillar” vortices, and the development of a separated region over the backlight.

### 1.2.2 Elementary analogous flows and relevant phenomena

Relative to traditional aerospace aerodynamics - to which the study owes its origins - vehicle aerodynamics are further complicated by relatively compact dimensions and aspect ratios, leading to considerable interaction between complex, three-dimensional flow phenomena. Flows from various geometric components cannot be successfully studied in isolation; a holistic appraisal is instead required (Hucho 1978).

Despite this, an appraisal of analogous flows is recommended in deconstructing key phenomena, being not least an approach consistent with the evolution of knowledge in the field.

---

<sup>4</sup>This has been shown to vary with aspect ratio (Johnson 2005, Morel 1978a, Okada 2006) however data from various authors indicates consistent trends with a changeover in flow structure (i.e. breakdown of the “C-pillar” vortices) occurring within close proximity of - if not, exactly at -  $30^\circ$  (Barnard 1996).

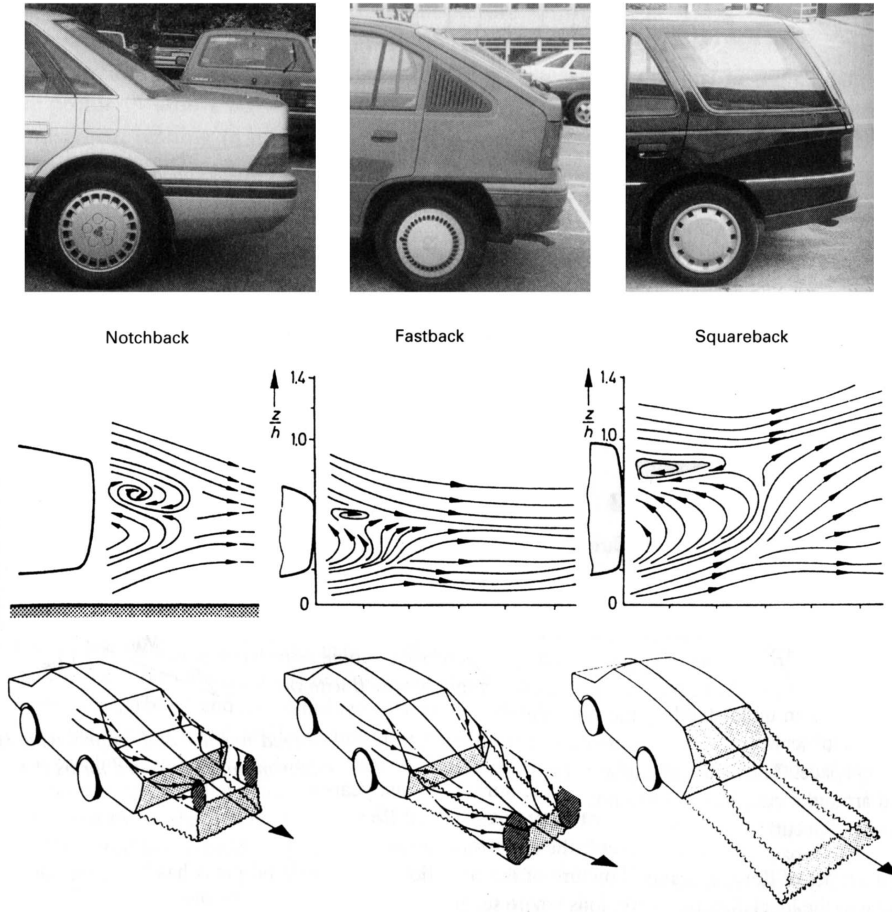


Figure 1.3: Photos, flow topology and typical centreline flows of notchback, fastback and squareback forms (Barnard 1996, Hucho 1978)

### 1.2.2.1 Quasi-two-dimensional flows

Where separations concern the span of the vehicle (e.g. leading edge of the bonnet, leading edge of the roof, trailing edge of the roof, bottom trailing edge of the base), opportunities exist for quasi-two dimensional separations to exist. Typical analogies include flows over a two-dimensional cylinder (Vino 2005) or a backwards-facing step (Okada 2006). Bluff bodies are generally sensitive to  $Re$ ; figure 1.5 presents base pressure coefficient for a range of  $Re$ , indicating a wide variation pending flow phenomena characteristic to various  $Re$ .

Whilst much is typified of the vortex shedding phenomena associated with such forms at relatively low  $Re$ , consideration is more relevant to the automotive domain at higher  $Re$  wherein *the upstream boundary layer is fully turbulent* (Cooper 1993). Of the typical modes presented in figure 1.5 for a circular cylinder, two cases are notable:

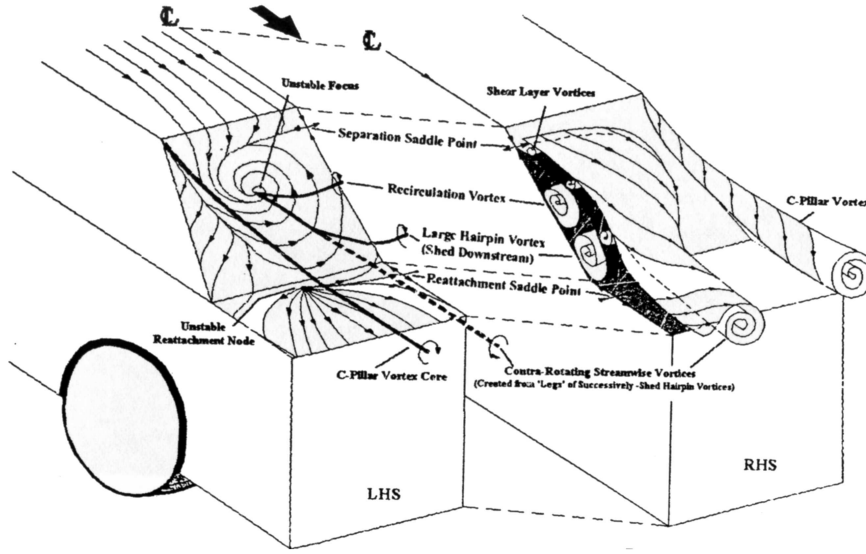


Figure 1.4: Revised flow topology for notchback forms with “C-pillar” greater than  $15^\circ$  to the roof line after Gilhorne et al. (2001)

- Between  $3 \times 10^5 < Re < 3 \times 10^6$ ; whilst the laminar boundary layer continues to separate on the forebody, a transition to turbulent flow occurs in the free shear layer. Re-energized, this boundary layer reattaches and ultimately separates some  $120^\circ$  to the stagnation point. The smaller wake (and higher base pressure) denoted in figure 1.3 not only gives rise to lower drag, but (unlike lower  $Re$  flows) the wake loses coherence; well-defined spectral peak is not observed within this  $Re$  (Anderson 2001).
- Of greater relevance are flows beyond  $Re = 3 \times 10^6$ ; the boundary layer transitions immediately to turbulence over the forebody and remain attached until separation; this initially occurs over the rear half of the form, with the separation points tending to the top and bottom of the cylinder as  $Re$  increases (a similar stable separation is observed for a backwards-facing step at turbulent  $Re$  (Eaton and Johnston 1981)). The larger wake gives rise to higher drag, increasing with  $Re$  (Anderson 2001). Periodicity is observable in the wake, as is broad-band spectral content commensurate with turbulent shedding phenomena (Roshko 1954).

For most bluff, two dimensional bodies, periodicity is *generally* observed in the wake as shear layers roll up to form and shed vortices (Bearman 1997, Houghton and Carpenter 2003). Bluff body separations are generally induced at locations where boundary layer edge velocities exceed the freestream, giving rise to a “*high rate of shedding of circulation*” (Bearman 1997).

Vortex shedding remains a two-dimensional process for two-dimensional forms at low  $Re$  only; beyond a critical  $Re$  (far below that at which upstream boundary layers are turbulent - occurring as low as  $Re = 60$  for a flat plate inclined normal to the freestream (Bearman 1997)), vortex shedding from a two dimensional form exhibits three-dimensionality (Barkley et al. 2002). Spectral peaks

## 1.2. CHARACTERISTIC PASSENGER VEHICLE AERODYNAMICS

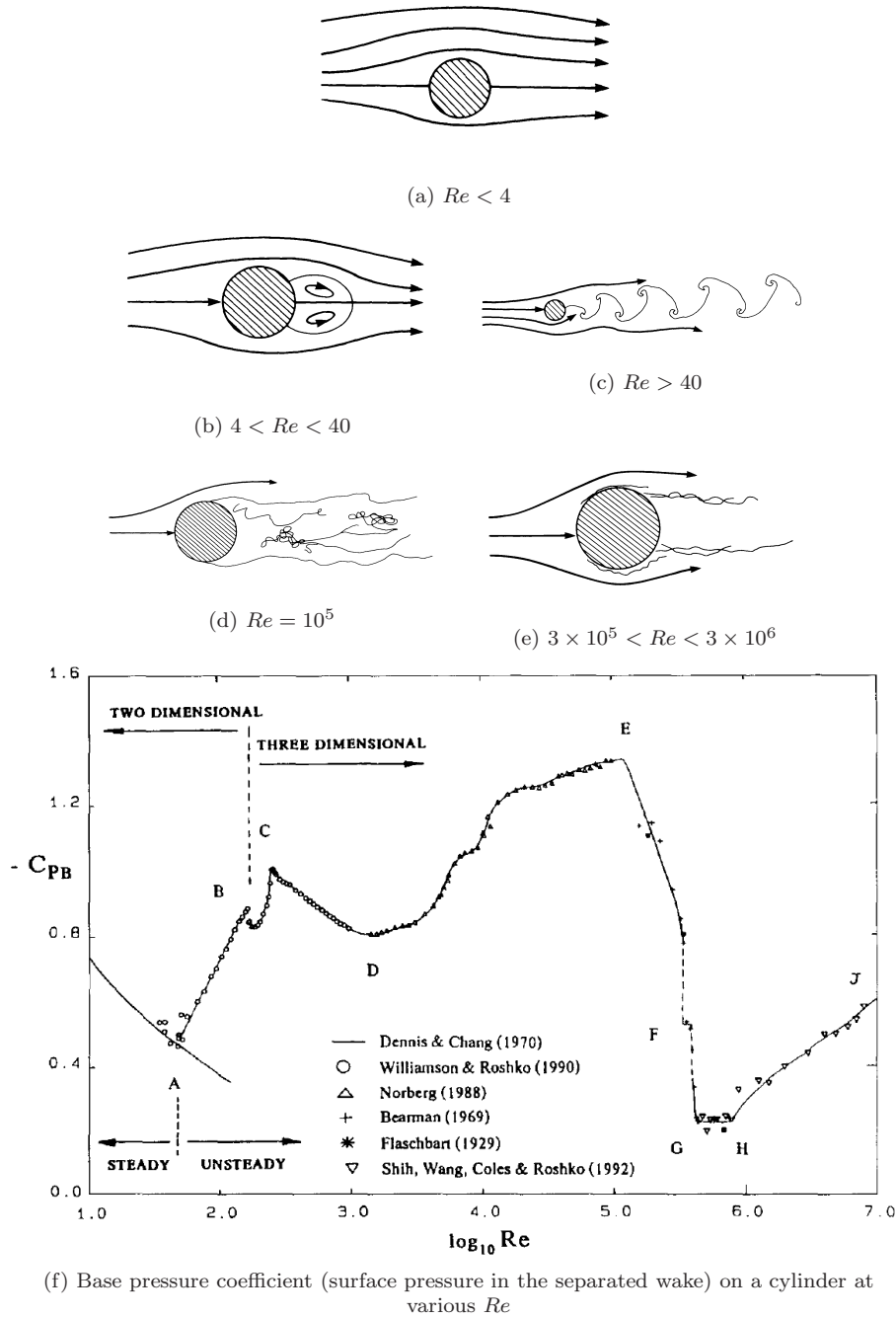


Figure 1.5: Variation in flows around a circular cylinder with  $Re$  (Anderson 2001, Bearman 1997)

are diminished in this instance; whilst the shedding process remains largely two-dimensional, phase variations may be noted along the span<sup>5</sup> The experimental visualisation of shedding phenomena is extremely difficult at high  $Re$ . Computational methods directly computing larger eddies have

<sup>5</sup>These spanwise dislocations can be controlled via designed-in geometric changes - a sinusoidal, wavy cut - to the trailing edge (Bearman and Owen 1998, Tombazis and Bearman 1997).

been used to give exceptional insight into relevant phenomena (Bearman 1997); where reference automotive forms are concerned, this method has allowed the visualisation of vortex shedding over quasi-two-dimensional regions and revealed complex, three-dimensional hairpin vortices to be characteristic (Franck et al. 2007, Krajnović and Davidson 2005).

### 1.2.2.2 Effect of freestream turbulence

Further relevant to the road vehicle practicalities, bluff body flows - quasi-two-dimensional separations and related vortex shedding included - remain sensitive to other influences e.g. surface roughness and *freestream turbulence* (Bearman 1978; 1997). Let us assume that flow over time can be represented by a mean and a fluctuating component:

$$U(t) = \overline{U} + u(t) \quad (1.1)$$

Freestream turbulence intensity ( $I$ ), a concept best described as detailing the level of “gustiness” in flow (Lindener et al. 2007) is herein defined as the ratio of fluctuation in the axial turbulence component against the axial mean:

$$\begin{aligned} I_{uu} &= \frac{\sqrt{\overline{u^2}}}{\overline{U}}, \text{ or,} \\ &= \frac{\sigma_u}{\overline{U}} \end{aligned} \quad (1.2)$$

Transverse and vertical components are similarly so:

$$I_{vv} = \frac{\sigma_v}{\overline{U}} \text{ and } I_{ww} = \frac{\sigma_w}{\overline{U}} \quad (1.3)$$

Freestream turbulence is relevant to road vehicle aerodynamics; an excellent introductory reference to bluff-body freestream turbulence effects is provided by Bearman (1978) and more specific references by Nakamura (1993) and Nakamura et al. (1988). Key points are thus:

- Increased freestream turbulence can *promote turbulent transitions* in boundary and shear layers (as per figure 1.5) at lower  $Re$  (figure 1.6a), though it should not be inferred that this “effects” a higher  $Re$ .
- *For two-dimensional forms* increased freestream turbulence - in invigorating mixing between shear layers in the near wake - causes additional entrainment, lowering the base pressure further than for smooth flows. Figure 1.6c gives a relevant example for a flat plate, relating turbulence intensity to turbulent length scale and the plate’s frontal area.



- For three-dimensional forms beyond a critical depth<sup>6</sup> and with fixed separation points, increased freestream turbulence generally *decreases* base pressure; increased turbulent mixing within separation shear layers accelerates their growth, causes them to spread out, exhibit decreased radius of curvature and thus promotes reattachment - at least intermittently so - on side faces (Gartshore, Castro and Robins<sup>7</sup>). Figure 1.6c indicates this trend for a finite-depth square cylinder in smooth and turbulent flow; where incidence to the flow is lowest (and thus the propensity for reattachment highest), a marked difference in base pressure is observed (thus leading to lower drag).

It is further suggested by Bearman that whilst a relationship between turbulence intensity and bluff-body base pressure is observable, turbulence scale is not demonstrated to relate similarly. Nakamura et al provide a revised perspective that the bluff body near wake is essentially governed by flow separation/reattachment and by vortex shedding. Both phenomena occupy unique length scale ranges: respectively, shear-layer thickness and the spacing between two shear layers<sup>8</sup>. Freestream turbulence of given length scale can exhibit considerable effect on near wake flows should it be near either of these. Thus beyond a scale at which vortex shedding is affected, the effect of larger-scale turbulence is negligible (Nakamura et al. 1988); where it is however, the variance about the spectral peak (defining shedding) increases (Hangan and Vickery 1997).

Bearman offers an important observation (citing Gartshore) relevant to road vehicles:

*“...the bluff body free shear layer development is most affected by turbulence arriving along mean stagnation streamline. It is this turbulent fluid that finds its way into the boundary layers and hence into the free stream layers.”*

Thus the flow structure about a large vehicle is rendered potentially susceptible to the turbulent wake of a smaller vehicle, should the upstream smaller vehicle be appropriately located.

A useful visualisation provided by Nagib et al (Bearman 1978, in following comments) depicts mean flows around a cuboid bluff body in near-ground proximity for low- $I_{uu}$  and various turbulence profile flows (figure 1.7a) and again for instantaneous and mean flows around the same body in the low- $I_{uu}$  configuration (figure 1.7b). The increased propensity to reattach after the top leading edge with increased  $I_{uu}$  is well depicted, as is the presence of turbulence in the stagnation region effecting the shear layer from the same leading edge (the upward movement of the stagnation point is relative to an increased velocity gradient, in the order  $\delta = 2 - 3 \times$  model height<sup>9</sup>). These visualisations further evidence that changes in vortex shedding affect the mean flow (Nakamura et al. 1988).

---

<sup>6</sup>Generally 0.6 times model height for a square flat plate in smooth flow (Nakamura et al. 1988)

<sup>7</sup>In (Bearman 1978, Nakamura et al. 1988).

<sup>8</sup>E.g. for a square cylinder with face normal to the flow, this would correspond to the body height.

<sup>9</sup> $\delta = 0.125 \times$  model height in case “A”



## 1.2. CHARACTERISTIC PASSENGER VEHICLE AERODYNAMICS

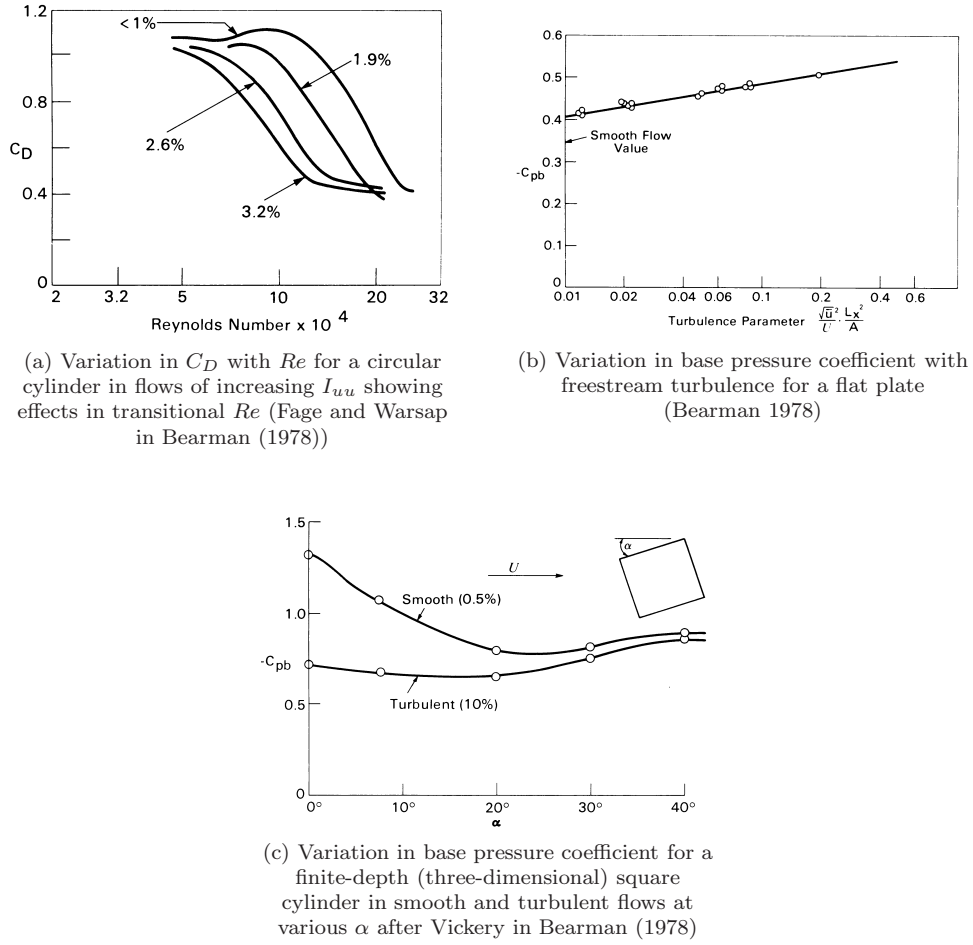
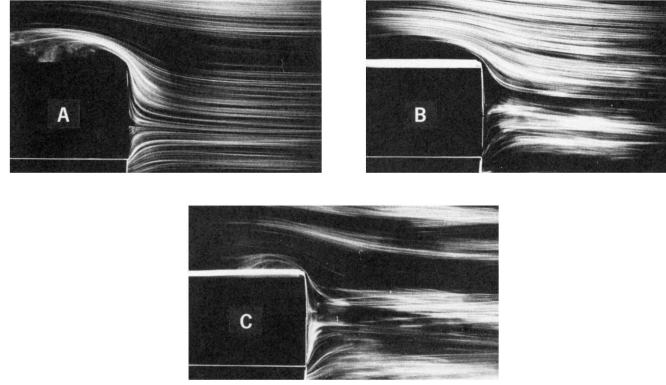
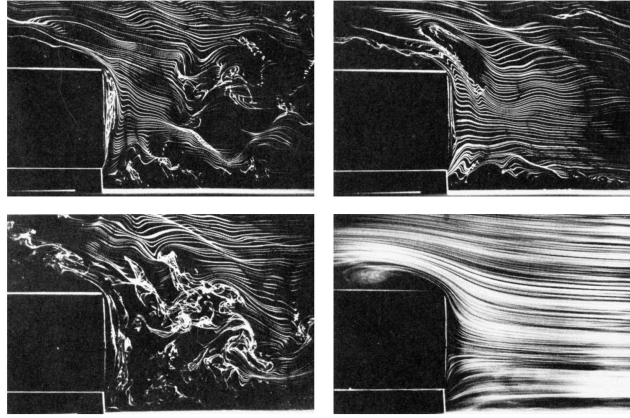


Figure 1.6: Comparison of increased turbulence on two-dimensional and three-dimensional bluff bodies

Unlike a model tested or simulated in a controlled (and characteristically low) level of freestream turbulence, a vehicle in the practical road environment experiences a wide variety of freestream turbulent characteristics (Lawson et al. 2007, Mayer et al. 2007, Morelli et al. 1981), owing to atmospheric boundary layer (ABL) effects, the presence of other vehicles, roadside obstacles and crosswinds. Cooper and Watkins (2007), Watkins and Cooper (2007) predict  $I_{uu}$  to practically vary up to 4.6% or an isolated vehicle at highway speeds, with variance difficult to predict owing to the non-isotropic nature of ABL turbulence and variances in the orientation and velocity of atmospheric winds. Relevant on-road data cites turbulence intensities between 2% and 10% (Watkins and Saunders 1998); far below the typically 30% or more experienced in wind engineering, where accurate turbulence simulation takes priority over Reynolds similarity. More recent data that despite a dearth of information quantifying the turbulent nature of practical road vehicle conditions, if testing with sharp-edged key geometry at sufficiently high Reynolds number then flow tripping is not incited by freestream turbulence effects (Cooper and Watkins 2007, Watkins and Cooper



(a) Mean visualisations in wind tunnel freestream of approximately 1%  $I_{uu}$  (A), and increasing levels of turbulence intensity and velocity gradient (B and C)



(b) Instantaneous and mean smoke-wire visualisations of 1%  $I_{uu}$  freestream

Figure 1.7: Visualisation of flow past a cube in near-ground proximity at varying levels of turbulence by Nagib (Bearman 1978, in following comments))

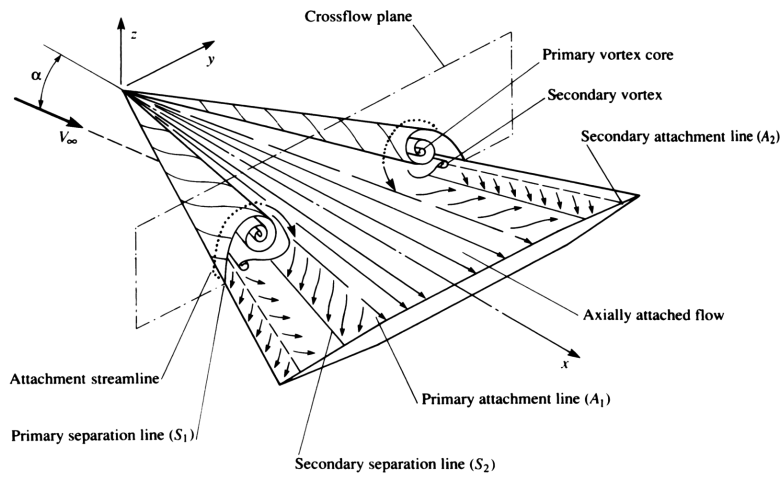
2007); as such, freestream turbulence is not envisaged to negate the salience or relevance of the experiments undertaken.

### 1.2.2.3 Three-dimensional, swirling flows

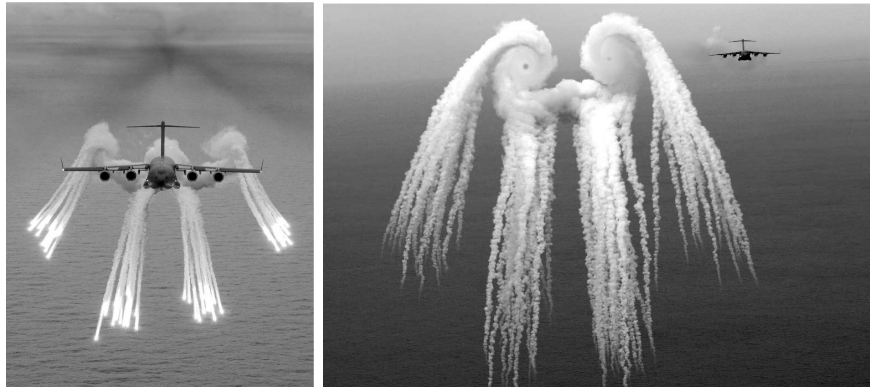
Vortex flows are simply regions of fluids swirling about a centre; essentially a spiral motion defined by closed streamlines observed in a plane normal to it's axial core. Dominant, axial vortices are commonly formed by three-dimensional forms, wherein top and side shear layers roll up to shed vortices, in turn drawn into the axial direction by the freestream<sup>10</sup> (Fröhlich and Rodi 2004).

<sup>10</sup>Where slender forms are employed, it is not uncommon for vortices to shed alternately side-to-side.

The large, axial vortices formed by shear layers off many vehicle forms’ “C-pillar” are a dominant characteristic of any relevant flow topology. Two relevant analogies often given concern vortex formation from a delta wing at given attack (Morel 1978a), and the formation of wingtip vortices in aviation (Ahmed et al. 1984). Figure 1.8 provides visualisations of both: in the case of the delta wing, both primary and secondary vortices are observable, as are effects of downstream impingement - a positive bifurcation is suggested where the shear layer of the dominant vortex first impinges, a negative bifurcation clearly marks it’s departure and the creation of the a secondary vortex of opposing sign and lesser size. Another positive bifurcation is noted further outboard, suggesting the possibility of a third vortex, smaller still but of sign commensurate with the shear layer it would be adjacent to. This is explored later in the context of the Ahmed Model (section 1.3.2, page 29).



(a) Flow topology on a slender delta wing by Stollery in Anderson (2001)



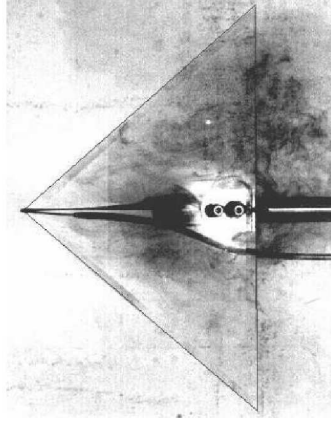
(b) Wingtip vortices on C-17 Globemaster III military aircraft (public domain media)

Figure 1.8: Vortex formation over delta wing and wingtip

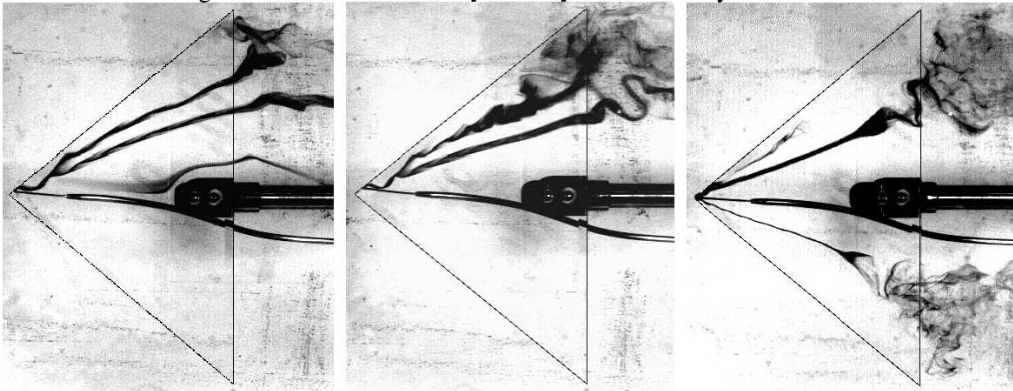
Delta wing leading edge vortices generate strong, swirling flows with a strong axial component. The strength of the phenomenon increases with increased angle of attack until vortex breakdown

occurs. The core is characterised by decreased static pressure, the impingement of which on a wing (much as it does on an automotive backlight) creates a region of localised low pressure. Lift is thus generated at the penalty of induced drag (Ahmed et al. 1984, Hucho 1978, Johnson 2004).

Vortex breakdown analogises the transition of “fastback” to “squareback” flow topologies: vortex breakdown is not an instantaneous phenomena; over affected angles of attack prior to stall it is known to be progressive, characterised by a loss (or even reversal) of axial velocity along the vortex core which fluctuates along the length of the core itself with the amplitude of length variance increasing with angle of attack. This phenomenon is often observed to commence beyond the trailing edge of the wing and to move upstream with increasing angle of attack until the vortex is definitively “burst”, with a commensurate increase in pressure on impinging surfaces and a sustained loss of lift/induced drag Johnson (2005; 2004), Ol (2003). Figure 1.9 indicates a progression to stall; figure 1.10 gives an indication of the time-dependent variance of it’s occurrence.



(a) Fully stalled



(b) Progressive breakdown of the secondary leading edge vortex core at increasing angles of attack ( $\alpha = 5^\circ, 7.5^\circ, 10^\circ$ )

Figure 1.9: Vortex breakdown progression and full stall visualisations over a  $50^\circ$  delta wing (Ol 2003)

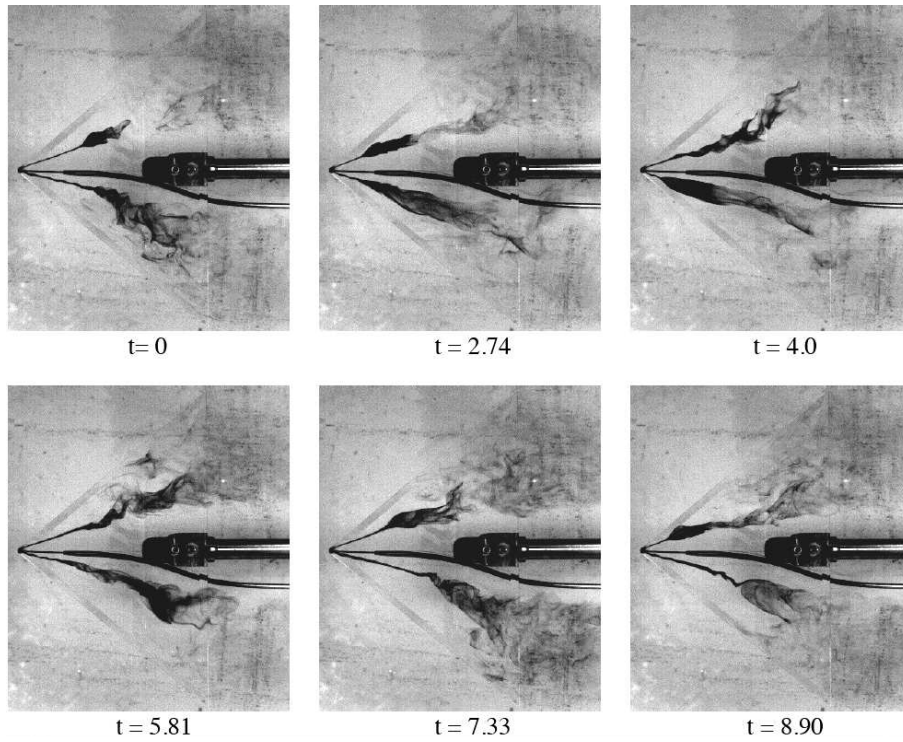


Figure 1.10: Fluctuation in breakdown phenomena for 50° delta wing at  $\alpha = 12.5^\circ$  (Ol 2003)

The exact mechanisms of vortex breakdown are not totally understood and remain a topic of ongoing research (Johnson 2005; 2004). The modes of vortex breakdown may generally be defined as axisymmetric (bubble) and non-axisymmetric (spiral, more commonly associated with the research form used throughout), though published works exist cataloguing as many as seven unique modes of vortex breakdown (Cary and Darmofal 2003). The impingement of vortex breakdown phenomena over a wing element has been observed to cause buffeting leading to premature failure (Watmuff et al. 2004) and have similar effects on parts of aircraft in the wake of vortex breakdown (Cary and Darmofal 2003). This latter fact provides an interesting analogy in an automotive context; namely that the wake of a given vehicle may be used as a source effecting (or compounding) upstream turbulence to another. This theme is explored significantly throughout this and related works.

Dominant, axial, downwash vortices causing lift are similarly common to most automotive forms, and serve to entrain flow over the backlight region (Bearman 1984, Carlino and Cogotti 2006). A key departure in relevant automotive aerodynamics from the pre-stall, slender delta wing analogy concerns the region of axially attached flow in figure 1.8; as mentioned previously, this region is highly turbulent in many automotive forms, featuring a separated region and the possibility of interaction with similarly separated base flows. Until recently, experimental resources sufficient to visualise turbulent structures in reference automotive forms were not available. Semi dynamic measurements using dynamic instrumentation capable of capturing phenomena at a single



point in space exist, and have been used to map automotive vehicle wakes, however the recent advent of particle image velocimetry (PIV) systems with sufficient response to capture dynamic flow phenomena pertinent to automotive vehicle wakes<sup>11</sup> has allowed greater insight into dynamic phenomena. Bearman (1997) presented the near wake of a scale model car acquired using a multi-hole probe by Goh (figure 1.11, contrasting instantaneous and time averaged data). The instantaneous measurements indicate that the dominant longitudinal vortex structures - as opposed to the relatively steady vortices generated in reference aerospace forms - are in fact the time-averaged sum of a number of smaller coherent vortices caused by unique vehicle geometric features. These acted broadly in a manner giving performance commensurate with time-averaged results (i.e. downwash type on a fastback vehicle model). Bearman's results cast doubt over whether dynamic data can be captured computationally using conventional turbulence models. More importantly they highlight that that reliance on time-averaged data alone does not provide a holistic interpretation of the more complex flows at play, but should be taken in a context where they may be used to usefully (if solely) deconstruct mean phenomena, i.e. mean body forces owing to pressure drag (Krajnović and Davidson 2005).

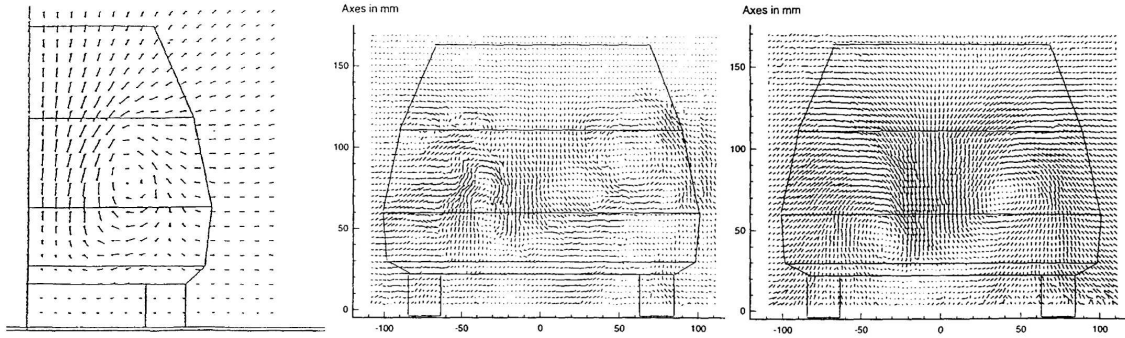


Figure 1.11: Comparisons of an automotive scale model near wake (25% body length behind the vehicle) using multi-hole probes, instantaneous PIV and averaged PIV (Bearman 1997)

As the dominant vortices grow and dissipate with increasing distance from the base they tend outwards from the model/vehicle projection and *upwards* from the initial core location. Bearman indicates that the secondary, weaker vortex pair (formed within the shear layer of the dominant vortex, as per figure 1.8) serve to both force the dominant vortex pair upwards and to contribute to their decay (given the smaller pairs' opposing sign). Peak vorticity is characteristically strong in the near wake region but diminishes rapidly thereafter, suggesting significant instability in near wake flows (Bearman 1984). This has since been observed using time-dependant methods of acquisition and computation in reference models (Hinterberger et al. 2004, Johnson 2005, Krajnović and Davidson 2004, Lienhart et al. 2000, Vio 2005).

It should be noted that not all road vehicles generate downwash vortices; a wake characterised by upwash vortices is characteristic of a downlifting vehicle form, e.g. a sports car (Carlino and Cogotti 2006).

<sup>11</sup>A predominant limitation at the time of writing concerns the availability of sufficiently fast laser lighting systems

Studies into the dynamic performance of fastback (Goh) and notchback Gilholme et al. (1998) vehicle forms indicate that “C-pillar” shedding is symmetric about the vehicle centreline and (for the notchback case at least), low frequency in nature (i.e. Gilholme et al. observed a peak at 4Hz on a full-scale vehicle).

#### 1.2.2.4 Effects of ground proximity

Near-ground proximity is an obvious characteristic of all road vehicles.

Vehicle underbody and base pressures are affected by ground clearance (Ahmed 1982). A simplest bluff-body analogy might concern a two-dimensional cylinder in cross flow in near ground proximity: in a mean sense, base pressure increases with decreased ground clearance, though the increase is more observed at the top of the base/farthest from the ground plane (Maul 1978). Relevant explanation lies in the form’s dynamic phenomena, however. Vortex formation is generally suppressed as a bluff body is brought within increased proximity of a ground plane, though a variety of parameters affect this phenomena: body width-to-height ratio,  $Re$ , blockage ratio,  $I_{uu}$ , wall boundary layer thickness and ground plane boundary layer. Periodic vortices are shed from alternating separation points on a two-dimensional body as upper and lower shear layers are effectively coupled; increased ground proximity affects the symmetry condition to a point - the *critical gap* - where mass flux under the body too low, the lower separated shear layer loses strength, the couple breaks down, and mutual, self-induced, oscillating shedding is no longer sustained. At even lower ground clearance, turbulent eddies from the turbulent boundary layer propagate through the separated shear layer, further diminishing vorticity within it and thus suppressing the propensity for vortex shedding (Kim et al. 2003).

Sensitivity to underbody mass flux, was explored by Williams et al (in a study of aspect ratio), demonstrating expectedly that the effect of near-ground proximity is heightened where rough underbodies are employed (Williams et al. 1999).

## 1.3 On the use of reference forms in vehicle aerodynamic testing

The use of reference forms in automotive aerodynamic research is commonplace. Whilst such forms may not appear immediately synonymous with a practical vehicle, their role serves to provide a “best-case” baseline from an aerodynamic perspective from which the implications (e.g. drag, fuel economy) of stylistic concessions may later be judged (Buchheim et al. 1981). They further serve to investigate flow phenomena underpinning aerodynamic force and moment characteristics in a fundamental context, allowing far deeper and more significant exploration of changes in form geometry than practical models allow (Morel 1978a, citing following comments by Hucho) and Le Good and Garry (2004). More recently reduced complexity and considerable experimental datasets concern-

ing certain reference models renders them as excellent validation cases for computational methods. Among the most commonly used and explored is the Ahmed Model (figure 1.12), a simple research body used regularly in research to recreate turbulent flow structures pertinent to road vehicles (Le Good and Garry 2004).

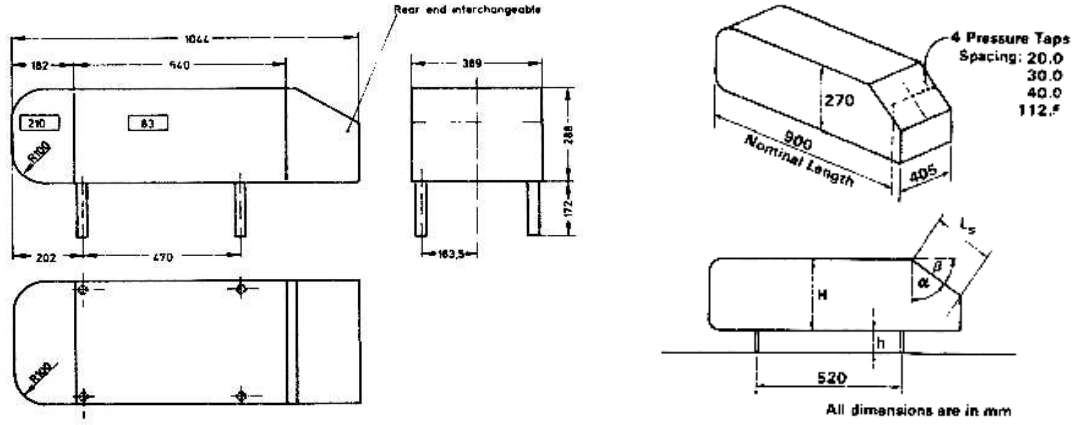


Figure 1.12: Dimensions of Ahmed (LHS) and Morel (RHS) models (Ahmed et al. 1984, Morel 1978a)

### 1.3.1 Development of the Ahmed Model

The 1970's fuel crisis placed a heightened focus on optimised vehicle aerodynamics as a method through which reduced fuel consumption would be realised (Hucho 1978, Le Good and Garry 2004).

Janssen and Hucho (1975) first studied the effect of vehicle afterbody geometry on fastback configurations in 1974, noting two distinct flow regions in which distinct near wake flow structures were noted. Figure 1.13 depicts both regions, and a further "unstable" region in which flow was observed to rapidly switch between both characterisations. The change towards higher drag was observed to coincide with strong vortices forming from side edges, giving rise to a significant induced drag component.

The work highlighted the effect of backlight angle on drag, the notion of a clearly defined maxima throughout such variance and the sensitivity of such changes: drag diminished quickly after the maxima. The significance of a slanted base was first re-examined in a more fundamental context by Morel (1978a;b). In appraising Janssen and Hucho's work, Morel correctly predicted the presence of two unique flow structures pending the base slant angle, a "quasi-axisymmetric" structure wherein pressures over the base were characteristically uniform, and a "3D" case wherein streamwise vortices rolling up from the side surfaces created a significant pressure variation across the slanted base (at the side edges of the slanted base, within close proximity to the low-pressure vortex cores). This latter mode was characterised as analogous to flow over a delta wing at attack. These streamwise vortices were later observed by Bearman (1984) as being similarly dominant in



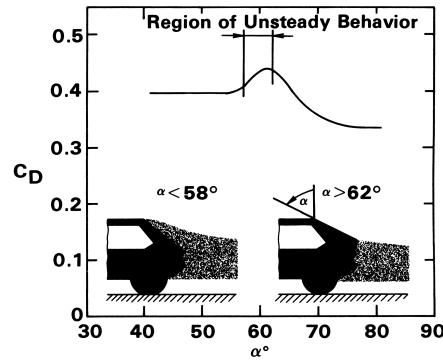


Figure 1.13: Early studies in backlight angle geometry after Janssen and Hucho (1975)

scale car models as opposed to research forms alone when contrasting phenomena observed with the Davis model<sup>12</sup> and a scale model car with rotating wheels and moving ground.

Morel began by studying an axisymmetric cylinder with a slanted base, wherein the angle of the slant relative to the horizontal axis was varied at  $Re = 9.5 \times 10^4$  (on cylinder diameter). Force and surface pressure data (from three taps distributed along one side of the base along the horizontal centreline) confirmed:

- The existence of two unique flow structures;
  - “*Regime I*,” essentially the “quasi-axisymmetric” case theorised.
  - “*Regime II*,” essentially the “3D” case theorised.
- A *sudden and abrupt changeover* between these regions in the  $47.25^\circ$  to  $48^\circ$  region characterised by:
  - A very sudden rise in drag to a maxima in Regime II with a small increase in base slant to over twice the value corresponding to the angle previous (itself the highest in Regime I).
  - A marked decrease in surface pressures near the base side edges commensurate with vortex impingement.
  - The disappearance of any well-defined spectral peak in a near-wake region located 1.33 diameters downstream and one radius below the trailing edge (e.g. directly behind the model - previously a peak existed in the range  $St = 0.2 - 0.5$  (Strouhal number with the square root of frontal area taken as reference length) present at the  $0^\circ$  configuration, rising in frequency with slant angle, peaking in amplitude at  $20^\circ$  ).

<sup>12</sup>The Davis model was so named after J. P. Davis, who devised it during the course of his Ph.D thesis “Wind Tunnel Investigation of Road Vehicle Wakes” (Le Good and Garry 2004). It similarly allowed changes in afterbody geometry, including the backlight angle.

- It was concluded from these initial tests at the flow mechanics observed in Regime II had potential to generate significant drag.

Morel thus repeated the experiment using a “vehicle like” geometry (defined in figure 1.12), again employing a variable “backlight” angle to simulate various fastback “C-pillar” geometries in the range 0-90°<sup>13</sup>. The form used a constant length backlight length (equal to the form’s height), a set cross-section aspect ratio and a nominal length able to be varied to maintain constant volume<sup>14</sup>. Variations in distance from the ground plane, yaw (for slant angles around the the regime switchover) and upper edge rounding were also examined. Initial tests at  $Re = 1.4 \times 10^6$  (i.e. a Reynolds number akin to practical road vehicles at highway speeds) with the model located in the freestream demonstrated:

- The two definitive regions in the vehicle-like form clearly existed, with a changeover between the regions at a “critical” 30° backlight angle (from 45° in the cylindrical model). This difference was initially hypothesised principally as a function of aspect ratio: as it increased the impinging vortex structures occupied a smaller portion of the net flow structure about the backlight region; as inflow from these structures gave rise to attached flow about the backlight centre, their diminished effect would have the (otherwise) attached flow break down at smaller backlight angles (Morel 1978a). This general trend was recently validated computationally by Johnson (2005), though the relationship is further complicated by changes in peak  $C_D$  with aspect ratio.
- The Regime II drag contained a significant induced component (figure 1.14). All lift values were expectedly positive for the model located in the freestream - negative pressure over the slanted backlight region generated lift force and (hypothetically) a pitch-down moment.
- The trends did not change significantly with the model in ground proximity<sup>15</sup>. (Morel commented that the change in lift was not significant as values appeared simply to shift  $C_L = 0.2$  downwards; practically this renders values in Regime I as negative lift, an important criterion in vehicle stability.)
- The drag trends corresponded well with those of Janssen and Hucho, showing a peak in drag at effectively the same backlight angle (excepting the sharp transition between flow structures with backlight angle which Janssen and Hucho did not identify).
- The pressure distribution trends across the slanted surface were consistent with those observed over the axisymmetric cylinder for Regime I and II flows (figure 1.15).

---

<sup>13</sup>This is a geometric difference from a “slanted” base, in that the base ultimately remains vertical with a slanted region above it, analogous to practical fastback vehicle configurations. Some earlier published accounts by Janssen and Hucho (1975), Morel (1978b) define the “backlight” angle as taken relative to the vertical axis; later accounts (e.g. (Morel 1978a)) define it relative to the horizontal, the same convention used by Ahmed and throughout this work.

<sup>14</sup>This was perceived a valid factor in enhancing relevance to road vehicles.

<sup>15</sup>Ground clearance was 44.8mm. No explanation is given for this value; given model dimensions it is suggested that it is of approximate scale to road vehicle characteristics

- The ability of the critical case to exhibit both flow patterns, the switch between them forced by “a very strong perturbation” (“Regime II” patterns at  $30^\circ$  were observed to be stable at yaw).
- The critical case was replicable at yaw; trends were stable at small angles of yaw, though the critical angle changed at higher angles of yaw.
- Upper edge rounding (common to practical vehicles) delayed the critical peak.

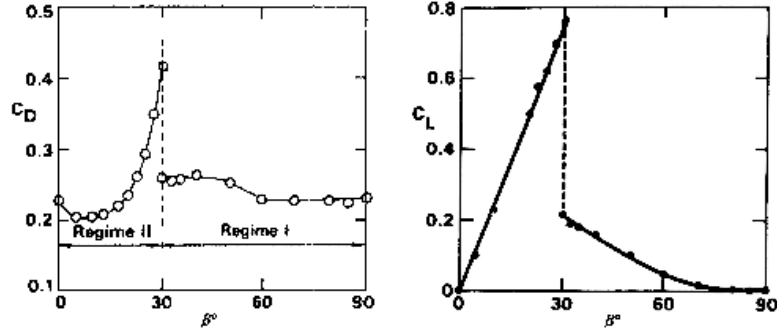


Figure 1.14: Drag and lift data for Morel model in freestream condition (Morel 1978a)

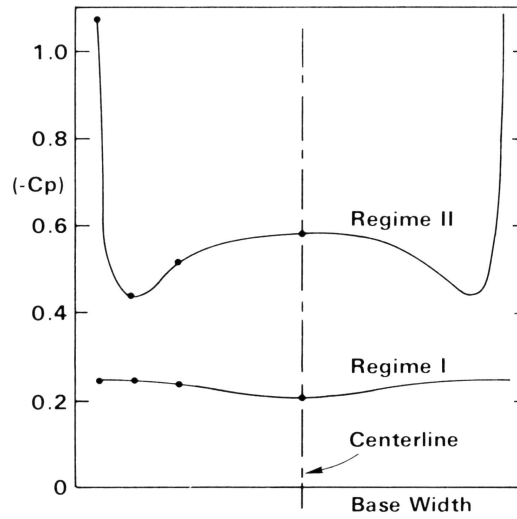


Figure 1.15: Pressure distribution across taps on Morel vehicle-like model (Morel 1978a, tap locations shown in figure 1.12)

The flow structures observed (figure 1.16 behind the vehicle-like model bore strong contrast for those observed in contemporary practical fastback research and development (e.g. by Hucho (1978)). Figure 1.16 compares the “Morel model” pre (bottom) and post-critical (top) flows Morel

(1978b) to the same phenomena observed in separate road vehicle tests (wake separation in the post-critical vehicle is artificially induced). In both cases, a downwash vortex pair serves to delay separation from the body relative to the point of smoke injection in the near wake.

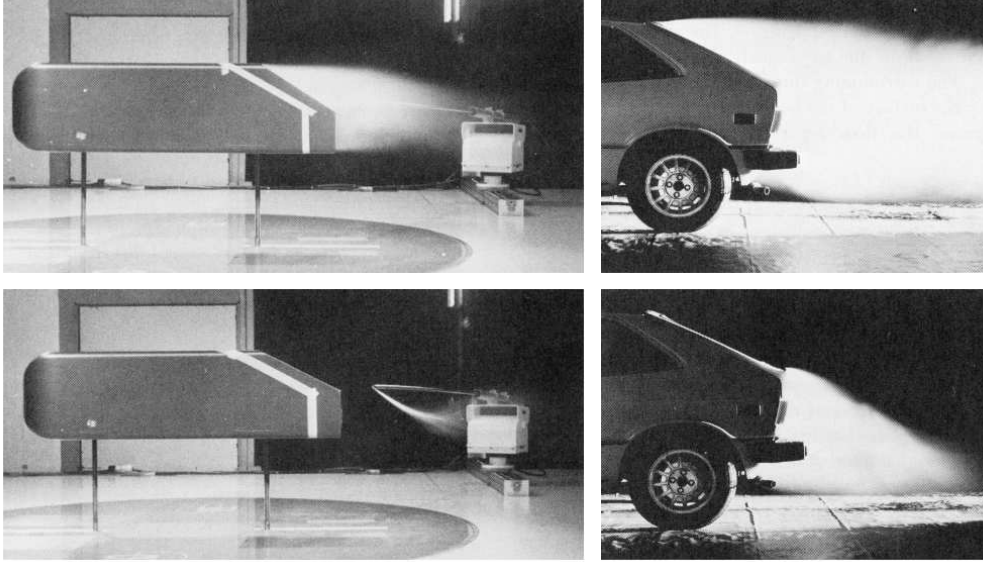


Figure 1.16: Comparison of pre and post-critical flow structures as observed by (Morel 1978b, LHS) and (Hucho 1978, RHS) in reference structures and full-scale vehicles alike

### 1.3.2 Contributions by Ahmed et al and others

The Ahmed Model was a development of that studied in detail six years prior by Morel (1978a) (a contrast is presented in figure 1.12) with minor geometric changes reflecting an intent to study proportions closer to then-current VW research vehicles. Ahmed et al's work presented a more quantitatively rigorous assessment of the effect of fastback afterbody geometry on vehicle drag, surface pressure distribution and time-averaged wake structure (Ahmed et al. 1984). Detailed surface pressure data (sufficient to form area contours) were acquired over front, rear and midsection surfaces in addition to model force data, allowing detailed drag decomposition and revealing drag trends similar to those of Morel. Detailed wake data were acquired using a multi-hole probe.

Ahmed et al's model replicated Morel's critical angle of  $30^\circ$  and provided a decomposition of the form drag components as relative to front, base or backlight regions (figure 1.17<sup>16</sup>). A rise in backlight drag component was observed with increasing backlight angle to the critical case, after which it abruptly diminished. Experimental results revealed complex, time-averaged, stable flow structures which Ahmed et al essentially defined in three categories (notations concerning basic,

<sup>16</sup>Pressure drag components over the surfaces specified were calculated by integration of the axial component of surface pressures over each surface. A significant instrumentation effort is noted; depending on configuration up to 450 pressure taps were used on half base and backlight surfaces alone in addition to midbody and nose sections.

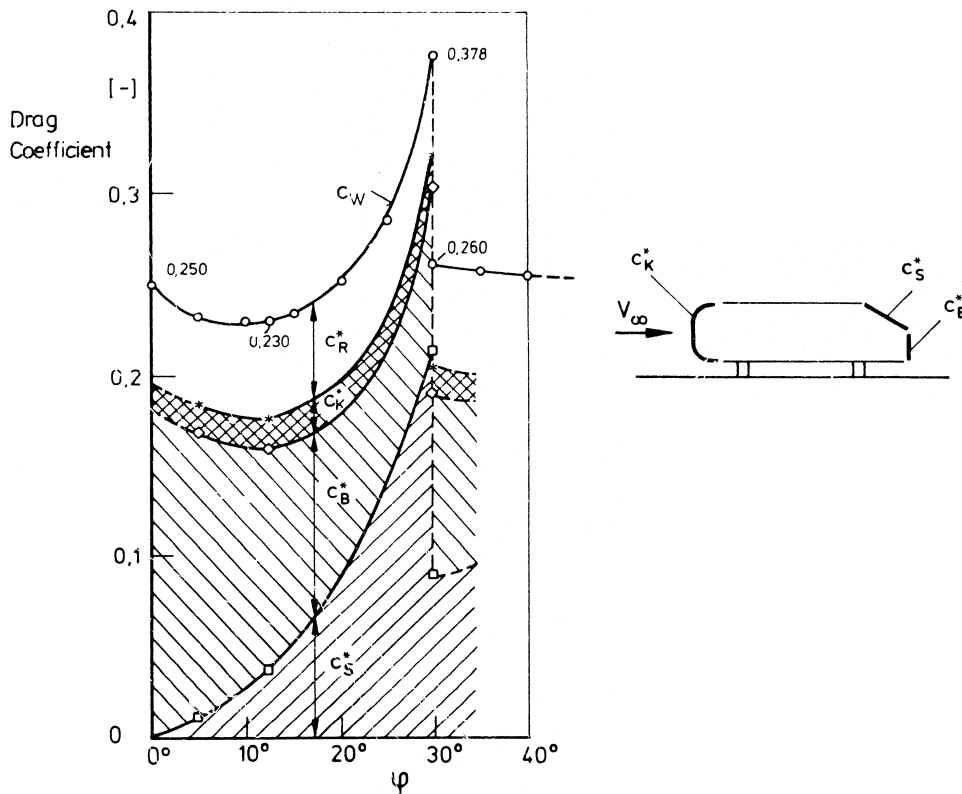


Figure 1.17: Drag of Ahmed Model as a function of rear slant angle (Ahmed et al. 1984) ( $C_R^*$  indicates friction drag)

characteristic flow structures are relevant to figure 1.18):

- Morel's "Regime II" flows in a low-drag configuration:

Flow over the backlight region was observed to be dominated by the strength of longitudinal vortex "C", rolling up from the shear layers off the model C-pillars, creating a region of low pressure on the backlight outer edges. Vortices "C" spread outwards behind the model for some considerable distance behind it, much like a pair of opposing potential vortices (Hucho 1978).

With reference to figure 1.18, a horseshoe vortex system ("A" and "B") was observed (from surface depositions) to operate on the base surface within a separated region (bounded by "D", speculated from flow-field data) pertaining to shear layers rolling up from the top and bottom base edges (in the 25° case, the wake at 0.479 body lengths was dominated by longitudinal vortex structures, i.e. "C", separated zone "D" was closed.) "A" was observed to align and merge with "C", flows pertaining to "B" were unable to be similarly traced. The strength of the dominant "C" vortices was dependent on backlight angle; the strength

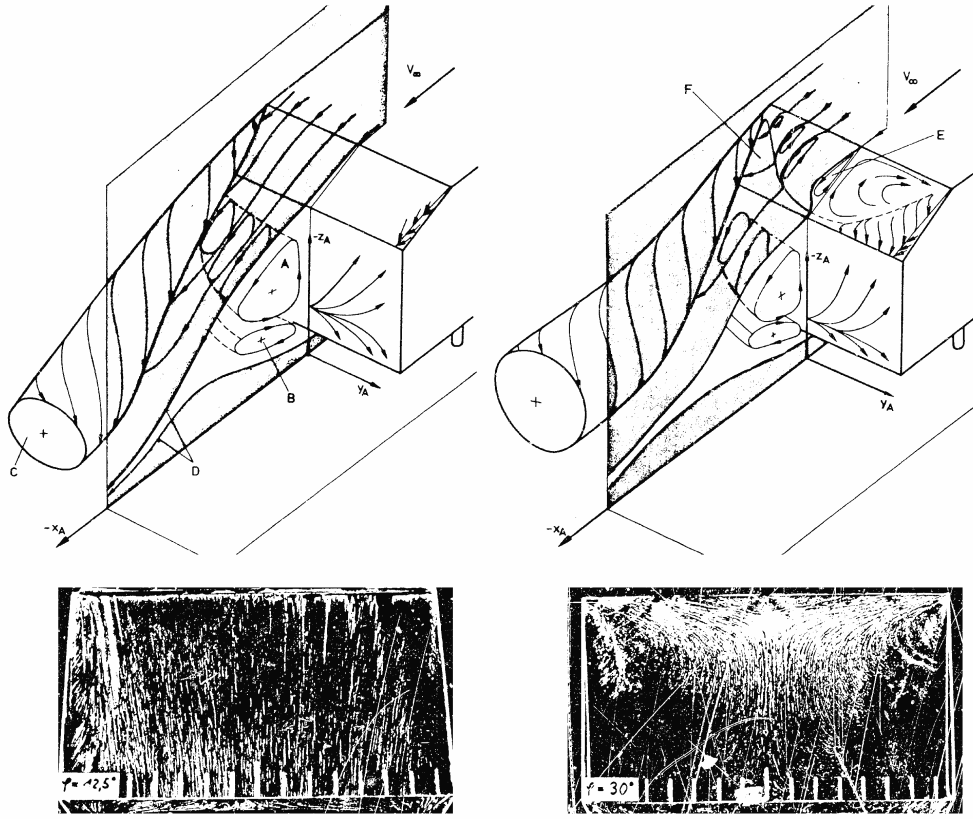


Figure 1.18: Flow structures and on-surface flow visualisation about pre-critical/low-drag ( $12.5^\circ$ ) and critical ( $30^\circ$ ) Ahmed Model (Ahmed et al. 1984)

of “A” depends on the strength of “C”, and is thus causally related to backlight angle. The strength of “B” was hypothesised to be dependent on underbody flows, but also on “A” (and thus its dependencies).

- *Morel’s “Regime II” flows in a high-drag configuration:*

This represents the most complicated case of the Ahmed Model; consequently, a significant body of literature is dedicated to it.

The increasing strength of “C” with backlight angle and the increased propensity for flow to separate off the top of the backlight region gave rise to increasingly complicated flow structures over the slanted region. An assessment of the critical ( $\alpha_c = 30^\circ$ ) revealed the flow separation “E” contained at the sides by powerful axial vortices; the separation contributing significantly to the rise in drag towards the critical case. On-surface flow visualisation for the  $25^\circ$  case confirmed this phenomenon (with lesser severity) at lower backlight angles. Attached regions “F” occupied the remaining backlight regions<sup>17</sup>. The separated region over

<sup>17</sup>Further flow structures pertaining to their generation were hypothesised but not observed, most likely due to instrumentation limitations in flow interrogation.

the backlight was constrained by vortices “C” inward towards the model centreline; their consequent impingement on the backlight sides (a phenomenon increasing with backlight angle to the critical case) created localised low pressure zones and contributed significantly to drag and (recalling analogous wingtip vortices) lift. “E” thus reattaches on the backlight region as long as vortices “C” exist; beyond  $\alpha_c$  vortex breakdown occurs, and a change of flow structure occurs.  $\alpha_c$  can be observed in both a high and low-drag state owing to small perturbations in flow (Ahmed et al. 1984). For experimental purposes, these states (and thus vortex breakdown) may be forced (Sims-Williams et al. 2001, Vio 2005). The sharp decrease in pressure over the backlight (considered as a force normal to the surface) gives rise to sharp increases in both drag and lift force.

The presence and development of separation “E” has been cited by other authors as rationale to further sub-categorize “Regime II” flows (Johnson 2005, Strachan et al. 2004). “E” is a complex area of flow, and the subject of much deconstruction in recent literature. Flow separating from the leading edge of the backlight immediately forms vortices parallel with the line of separation at the backlight centre and are then convected downstream, lifting them and creating a series of hairpin vortices, in turn distorted by vortices “C” to be pushed toward the backlight centre and change alignment (Krajnović and Davidson 2004; 2005). This mechanism, time-averaged, gives rise to the separation bubble “E” as per figure 1.18. In a time-dependent context, the entire backlight region is thus highly turbulent (particularly concerning “E”) and offers a wide variety of turbulent length scales.

Within “E”, the following structures are noted in a time-invariant sense, and are best deconstructed by Krajnović and Davidson (2005). The following notations refer to figure 1.19, using critical point theory as per Hornung and Perry (1984), Perry and Chong (1987):

- Various authors characterise the time-invariant “twisting” of the hairpin vortices via two stable foci within “E” (“F<sub>1</sub>” in figure 1.25); the separation region is bounded by a positive bifurcation line denoting the impingement of “C” (Krajnović and Davidson 2005, Spohn and Gillieron 2002, Vio 2005).
- The formation of vortices off the leading edge of the backlight gives rise to a positive bifurcation line  $PBL_{BU}$  immediately downstream of the leading edge; in the region bounded by this and the backlight leading edge, flows along the backlight surface tend upstream.
- Adjacent to the positive bifurcation line exists a downwash region bounded by  $PBL_{BU}$  and negative bifurcation  $NBL_{BM}$ . Along the centreline of the backlight and along  $NBL_{BM}$ , mean flow angularity given the influence of the stable foci mentioned above gives rise to saddle point  $S_{BCO}$ .
- A second region of net upwash impingement exists adjacent to this, bounded by positive bifurcation  $PBL_{BC}$ , formed by the initial impingement of main “C-pillar” axial vortices “C”.

It should be appreciated that the above seeks to express flows within “E” as a set of stable vortices over the backlight operating with volume and size proportionate to the mean surface



shear patterns presented. Practically, a turbulent model is more appropriate (Lienhart et al. 2000) in deconstructing practical flows and is discussed subsequently.

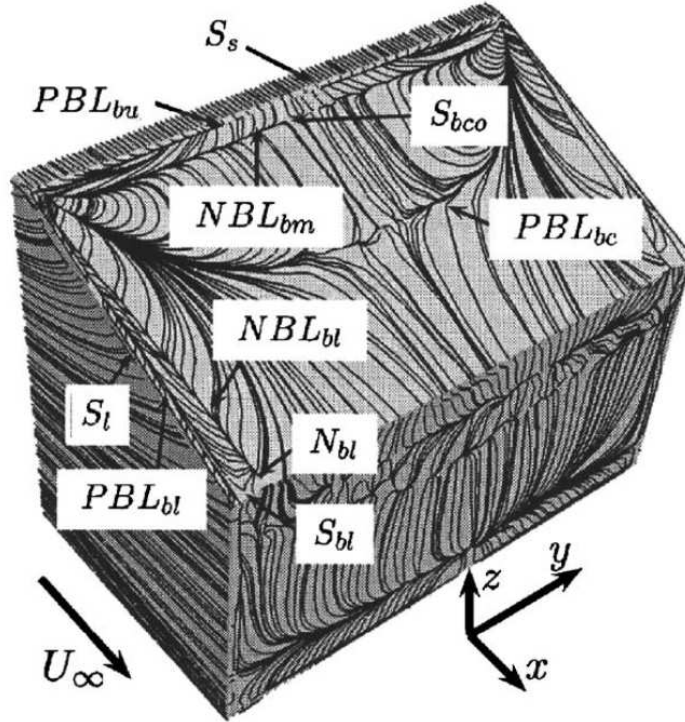


Figure 1.19: Backlight mean surface flows for 25° Ahmed Model after Krajnović and Davidson (2005)

The separation of the impingement of “C” from the backlight surface is denoted by a negative bifurcation. This has been observed to occur repeatedly at 7° to the C-pillar, and is very clearly observable in on-surface visualisation<sup>18</sup> (Ahmed et al. 1984, Krajnović and Davidson 2004; 2005, Vino 2005). A secondary vortex (weaker, and of opposing sense) bounded by “C” and the separation shear layer from the “C-pillar” has been observed (Ahmed et al. 1984, Hucho 1978, Spohn and Gillieron 2002). Later work by Krajnović and Davidson (2005) observes three vortices: the dominant axial vortex “C”, the secondary vortex noted by Spohn and Gillieron giving rise to the noted negative bifurcation line and a third, small vortex operating in the same direction as “C” further outboard against the C-pillar, with a positive bifurcation evident between it and the adjacent vortex (figure 1.20, depicting the instantaneous second invariant of the velocity gradient, showing vortices of alternate direction in black and white). Whilst not yet observed in experimental works, the presence of these three structures operating in a “gearwheel” type arrangements seems feasible given the con-

<sup>18</sup>It should be appreciated that the “observability” of the negative bifurcation line does not serve as a relative indication of it’s strength when considered against positive bifurcations on the model surface; for deposition-type visualisations the very nature of a negative bifurcation serves to collate matter locally along it’s length, where a positive bifurcation will splay it.



siderable momentum of the “C-pillar” shear layer and the noted presence of the negative bifurcation.

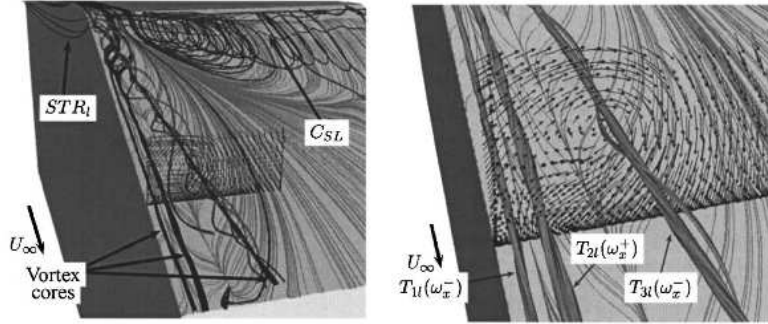


Figure 1.20: Triple vortex structure noted at edge of Ahmed Model “C-pillar” Krajnović and Davidson (2005)

A significant body of literature is further dedicated to quasi-two-dimensional horseshoe vortices “A” and “B”, being characteristic of flows about the base of a bluff body though of considerably less circulation than “C” but of roughly equal strength in the near wake (Krajnović and Davidson 2005). Ahmed et al’s original description of these as essentially free vortices with legs stretching in the streamwise direction is “*more hypothetical than actual*” (Hucho 1978), and reflects the original intention of the work to study backlight behaviour more intently.

More recently, the propensity of “A” to interact with or “bleed into” “E” at the centreline has been scrutinised: whilst a time-independent interaction has been hypothesised for  $\alpha_c$  by Vino (2005), a significant body of studies indicate otherwise (Ahmed et al. 1984, Hinterberger et al. 2004, Johnson 2005, Krajnović and Davidson 2004; 2005, Lienhart et al. 2000, Okada 2006, Sims-Williams and Duncan 2002), suggesting that any interactions are highly turbulent. This is discussed later.

- *Morel’s “Regime I” flows:*

Beyond the critical case, the separated region over the backlight “E” extended beyond the backlight trailing edge and merged with region “A”, creating a large, separated region of more uniform pressure (figure 1.21). The base/backlight region is thus concerned with vortices “A” and “B”. Vortices “C” were no longer drawn in towards the model centreline (though were noted to be visible in the wake, however with diminished strength). Pressure over the backlight region was thus more uniform and generally higher - notably so where the vortices would otherwise impinge, by consequence significantly reducing drag - validating work by Morel (1978a)).

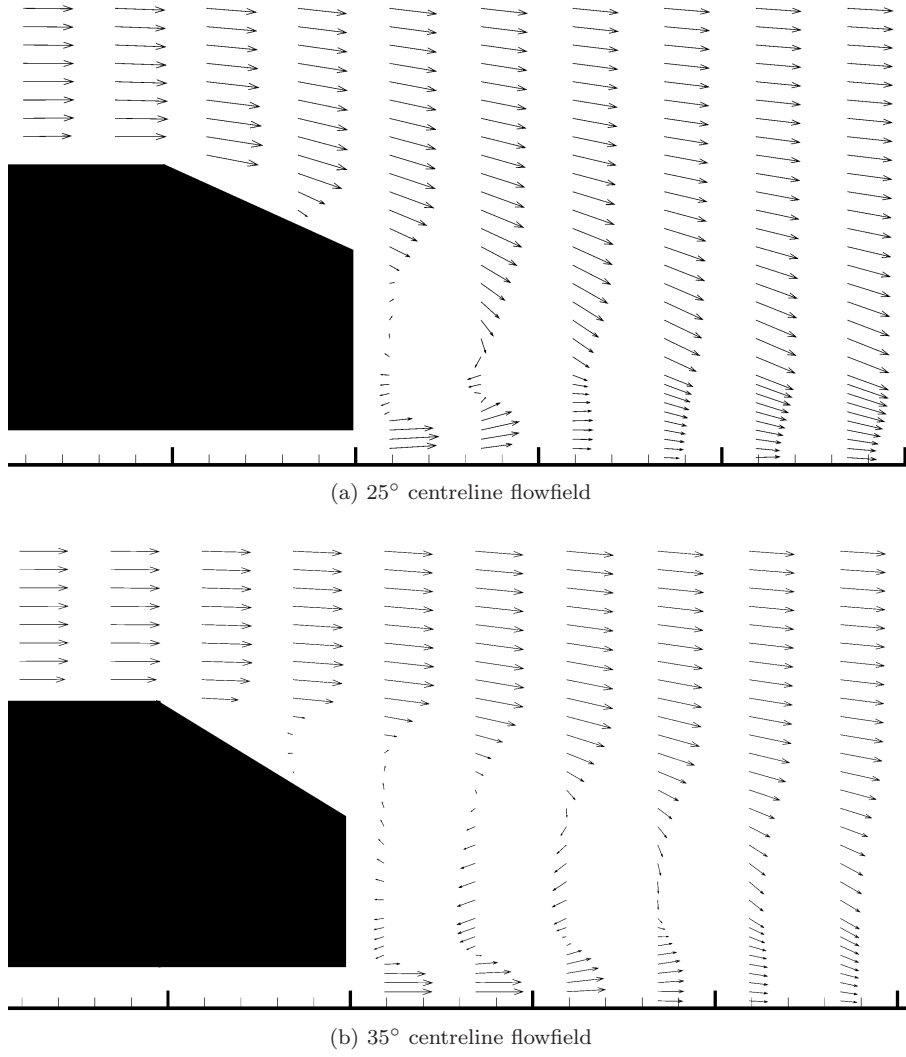


Figure 1.21: Centreline plots showing pre and post critical wake development adapted from Lienhart et al. (2000)

### 1.3.2.1 On the validity of the centreline symmetry plane

Under exacting freestream conditions, earlier notions of the centreline plane serving as a symmetry plane for mean flows (Ahmed et al. 1984, Morel 1978a) were further validated in later experiments under conditions of controlled freestream flow angularity (Lienhart et al. 2000).

### 1.3.2.2 On the use of computational sources

Though the work presented throughout is based upon experimental research, reference is made to computation works. Given the significant turbulence associated with various configurations

of the Ahmed Model, prior to exploring turbulent behaviours in greater detail is it considered appropriate that a brief prologue is given explaining the rationale for the inclusion of sources utilising computational methods.

The complexity of flow turbulent flow phenomena associated with the Ahmed Model has given rise to considerable interest in non-intrusive methods of flow visualisation. Whilst development on alternate methods are ongoing - e.g. gas dispersion (Gosse et al. 2006) and cavitation (Beaudoin et al. 2004) - recent developments in computational simulations - both in turbulence models and in computational power - have allowed relevant methods to more accurately deconstruct high-drag cases of the Ahmed Model, rendering a greater insight into relevant flow structures than possible with conventional experimental methods. This is particularly true concerning turbulent flow field aspects. Within the last ten years the MOVA (“Model for Vehicle Aerodynamics”) project sponsored a particular effort to *“develop, refine and validate the latest generation of turbulence models for selected examples encountered in vehicle aerodynamics”* (Lienhart et al. 2000), part of which involved the detailed mapping of the Ahmed Model flow field for the  $\alpha = 25^\circ$  and  $\alpha = 35^\circ$  cases using laser doppler anemometry (Lienhart and Becker 2003, Lienhart et al. 2000).

This reference set was in turn compared against a variety of turbulence models. Reynolds Averaged Navier-Stokes (RANS) approaches are incapable of simulation time-dependent, turbulent phenomena, and are thus compromised in predicting flow phenomena about the backlight region (where flows are transiently separated in the high-drag configuration) and base region (where flows are massively separated) accurately (Hinterberger et al. 2004, Howard et al. 2000, Johnson 2005, Kapadia et al. 2003, Krajnović and Davidson 2004). Contemporary computational resources (when used with performance-optimised grids) have become better capable of simulating time-dependent Ahmed Model flows. Large Eddy Simulation (LES) allows direct computation of larger turbulent structures - containing a significant proportion of the flow’s kinetic energy, and more likely to be affected by forcing and form geometry (Franck et al. 2007) - and simulation of smaller structures below the grid resolution applied. This renders LES approaches favourable to the study of bluff-body aerodynamics. Of key importance is the simulation of wall flows where turbulent structures are concerned; to ensure relevant structures are not sufficiently small as to render a problem computationally unfeasible, lower  $Re$  is preferable for LES methods (Krajnović and Davidson 2004). Assuming the  $Re$  employed allows for relevant replication of characteristic flow structures, simulation under such conditions is wholly relevant; such LES simulations have been demonstrated capable of capturing turbulence intensities relevant to experimental references over the high-drag backlight, a feat unmatched by published data for Reynolds averaged approaches (Hinterberger et al. 2004). Relevant LES simulations exist by (Sims-Williams and Duncan 2002,  $\alpha = 25$ ), (Krajnović and Davidson 2004; 2005,  $\alpha = 25$ ), (Hinterberger et al. 2004,  $\alpha = 25$ ,  $\alpha = 35$ ) and (Franck et al. 2007,  $\alpha = 12.5$ ). All show good agreement with reference experimental data sets. Sims-Williams and Duncan’s work is notable in featuring an extended runtime, with a view to exploring flow field spectral characteristics. Despite being computationally “expensive”, the LES studies cited offer extraordinary detail in results presented without any simplifications to compromise their relevance to experimental reference works.

Contemporary efforts exist where favourable elements of RANS and LES are combined. Their application to the Ahmed Model does not resolve turbulent structures in the same exacting resolution, but offers other advantages: application is less computationally expensive, mean flows and salient aspects of transient phenomena are well predicted; importantly, a higher  $Re$  is able to be simulated for contemporary computational resources, allowing simulation of a fully turbulent boundary layer approaching the backlight (Kapadia et al. 2003). Practically, a fully turbulent boundary layer is required prior to a vehicle-like form's front edges, a condition often met at lower  $Re$  than for a practical vehicle (Cooper 1993). For comparison, experiments by Vio at  $\alpha_c$  (the *critical case* of the Ahmed Model -  $\alpha = 30^\circ$  - where lift and drag force are highest),  $5 \times 10^5 < Re < 2.8 \times 10^6$  showed no discernible differences in  $C_D$  with or without boundary layer tripping applied at the model forebody (Vio 2005)<sup>19</sup>.

Given the adequate simulation of turbulent phenomena to being critical to successful simulation of the Ahmed Model and the availability of reference experimental datasets for comparison, results from carefully applied, higher-order RANS schemes can be appreciated within limitations. Decreased computational requirements also allow a broader test matrix: Johnson applied the Reynolds Stress Model (RSM) with good success, examining a variety of  $\alpha$  and aspect ratio configurations. Though a RANS approach, RSM is considered a higher-order turbulence model in which Reynolds stresses are directly computed (turbulent viscosity is not assumed isotropic), and is thus more accurate in turbulent flows. The approach was shown to offer good agreement with experimental data in literature, allowing significant exploration of the salient effects of the parameter space presented. These include time-dependent simulation of key cases (Johnson 2005). A second-order RANS model was similarly used by Liu and Moser (2003) for the  $\alpha = 35$  case, offering good agreement with reference data after Lienhart et al. (2000).

### 1.3.2.3 Model forebody effects

Limited literature exists concerning the model forebody. This is deemed relevant in the context of the experiments undertaken (where interactions between two models are studied).

Interactions between forebody and afterbody flows for the model in isolation are weak (Ahmed et al. 1984). Expectedly, flow is fully stagnated on the model forebody. Clearly defined zones of separation and reattachment on the the model sides and top sections exist prior to the model midsection (figure 1.22) characteristic of a laminar separation bubble (Sims-Williams et al. 2001). The low pressure observed in this region is commensurate with Melbourne (1993); the bluff-body leading edge separations are characterised by a subsequent region of low surface pressure, caused by the passage of the vortex formed underneath the shear layer as it convects downstream.

Thus expectedly each zone contains a stable foci at it's extremities, giving rise to vortex shedding. These were initially visualised by (Spohn and Gillieron 2002, figure 1.23), and hypothesised

---

<sup>19</sup>A variance in  $C_d$  was noted nonetheless; this was attributed to variations in the turbulent boundary layer over the model midsections with increasing  $Re$ .

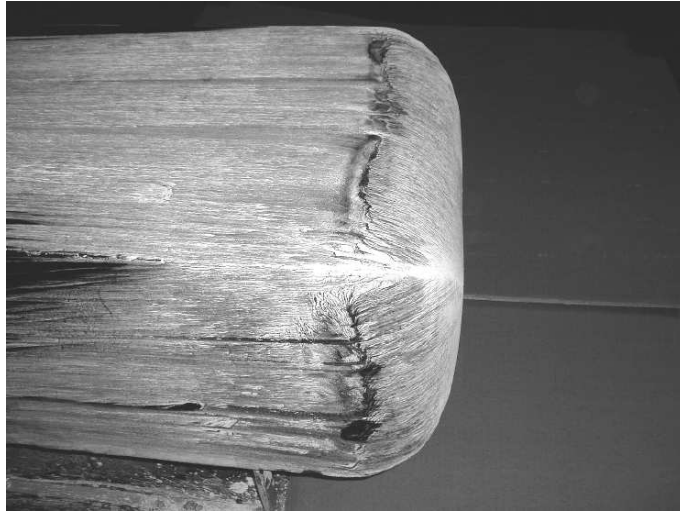


Figure 1.22: Soot deposition over Ahmed Model forebody after Vino (2005)

to be of the Kelvin-Helmholtz type. Later simulations at higher  $Re$  suggest these to quickly develop into hairpin vortices (Franck et al. 2007, Krajnović and Davidson 2005). The use of a laser light sheet in Spohn and Gillieron's work may have precluded the ability to capture three-dimensional effects succinctly. A saddle point occupies the midpoint of the positive bifurcation line bounding each separated region. Separated zones also occur towards the model underside, though relevant flow structures are complicated by the proximity of the ground plane (Krajnović and Davidson 2005).

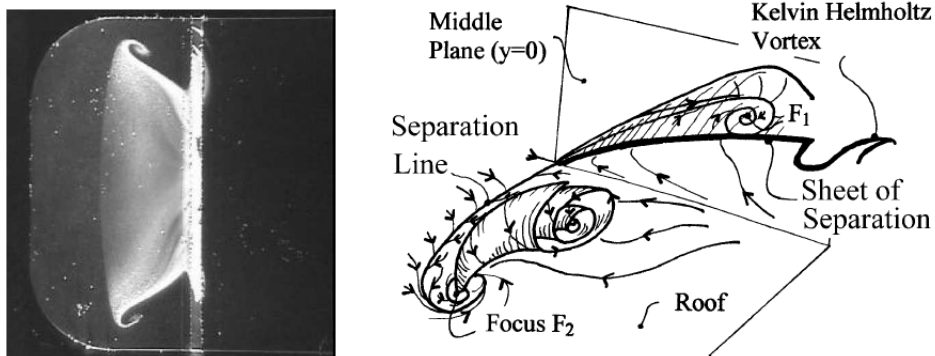


Figure 1.23: Visualisation and flow structure of forebody vortex formation after Spohn and Gillieron (2002)

1.3.2.4 Turbulent phenomena I: the high-drag case to  $\alpha_c$ 

(As with earlier assessments, the following section draws particular reference to nomenclature “A” through “F” as depicted in figure 1.18, previously presented on page 27.)

It is stressed that while the above observations regarding Morel’s “Regime II” flows are macroscopically stable (Ahmed et al. 1984), practically the flows involved contain significant turbulent phenomena. Literature contends these to be particularly observable in wake about the model mid-plane and with a sharp, singular spectral peak within the region  $St = 0.34 - 0.52$ <sup>20</sup> (Johnson 2005, Morel 1978a, Okada 2006, Sims-Williams and Duncan 2002, Vio 2005). Whilst it is not debated that dominant, axial vortices are considered broadly stable (Vio 2005), as are separations over the backlight leading edge (leading into “E”) and the mechanisms by which vortices “C” are formed (Johnson 2005), some conjecture exists in literature regarding the source of dominant turbulent phenomena.

Dynamic investigation of the “Region II” wake by Crossland et al. (2000), Sims-Williams and Dominy (1999) using an unsteady reconstruction technique showed significant *regular* unsteadiness to be concentrated in the lower central area of a transverse near-wake plane. (If so, the shedding periodicity of this region would be highly sensitive to underbody flow velocities.) It was further conjectured that “B” is created primarily by underbody flows shedding with regular periodicity at the centre/bottom of the base region, the considerable width-to-ground-clearance of the form would lend itself to a region of relative two-dimensionality at this point, appearing akin to a Von Karmann vortex street (Johnson 2005, Vio 2005). A statistical investigation of total pressure fluctuation in the axial centreline plane further suggested a weak interaction between base regions (the projection of which encapsulates the near wake of the 25° model presented) and backlight regions. Whilst on-body effects are not further explored (owing to the flow-field focus of the experiments offered), it was concluded that beyond the near wake, the dominant axial vortices “C” (or at least a component thereof relative to the conditional averaging applied) are affected by base shedding pertinent transverse vortex “B” in a similarly oscillating manner: flow packets of low total pressure convected along the ground plane preceded and succeeded by high total pressure oscillations of net upwash and downwash were observed to (respectively) weaken and strengthen the dominant axial vortices in turn (similarly observed by Johnson (2005)). The mechanism by which the axial vortex cores are pulled downwards was thus deconstructed. This effect was thus observed with identical periodicity to the causal underbody shedding “B” (Sims-Williams and Duncan 2002). This qualitatively correlates well with water-tunnel experiments by Beaudoin et al. (2004), where “C-pillar” vortices were observed to be stable initially but to oscillate behind the trailing edge. Whilst the presence or effect of “A” was not discussed, Krajnović and Davidson (2005) more recently observed in simulations that the legs of “A” indeed stretch in the streamwise direction as “A” merges with “C” beyond the near wake region. The legs of “B” were instead hypothesised to terminate at vertically higher on the base (figure 1.24), despite the strongly periodic behaviour of “A” and “B” over the base centre (Johnson 2005, Krajnović and Davidson 2005, Sims-Williams

---

<sup>20</sup>Some variance exists pending test conditions.

and Duncan 2002).

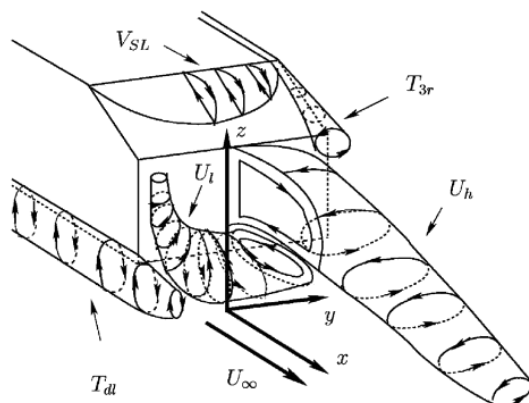


Figure 1.24: Afterbody mean flow topology by Krajnović and Davidson (2005)

Figure 1.24 offers good agreement with Okada (2006), who experimentally observed “C” to increase in turbulence and circulation whilst being advected downstream - the increased circulation attributed to the turbulent mixing of the “C-pillar” vortices with vorticity from interactions between “A” and “E”, which (as per  $U_h$  in figure 1.24 are ultimately drawn in the axial direction.

Vino (2005) indicated for the critical ( $30^\circ$ ) case that not only is the periodicity observable in the model wake, but that it exists on base and backlight surfaces. A detailed causal deconstruction citing underbody flows as the source of the periodicity is not presented, however cross-spectral phase analysis reveals the relevant phenomena observable on both backlight and base surfaces, on and off the centreline and clearly either in or out of phase relative to the signal acquired on the lower base region. “A” and “B” are expectedly shown to impinge on the base region in an alternating manner (out of phase). Critically, Vino observes two centreline pressure taps - one located on the upper base and one on the lower backlight - to be (largely<sup>21</sup>) in phase. This observation is used to surmise that regions “A” and “E” are in fact one large, continuous separated region (figure 1.25) in a time-invariant context. The use of spectral data to draw time-invariant conclusions is questionable, however. Whilst the sense of the phase lag is not presented, a general appreciation of the flow structure would suggest flow packets travelling up the base and into “E”, consistent with mean idealisations of “A” and “B” giving rise to a saddle point on the base Drouin<sup>22</sup>.

Visualisation work by Spohn and Gillieron (2002) with a  $25^\circ$  Ahmed Model suggests flow topology over the backlight region to be more complex than those originally presented in figure 1.18. It is also suggested that flows contained within recirculation zone “E” do not close as per Vino (2005). This cannot strictly be accepted as validation of “A” and “E” being merged in time-invariant context; Spohn and Gillieron used a water tunnel and very low  $Re$  ( $Re = 3 \times 10^4$ ) to explore phenomena over the backlight region. Other studies however (e.g. Drouin<sup>23</sup>, figure 1.29)

<sup>21</sup>Allowing a small delay for the flow packet to travel from one location to the other.

<sup>22</sup>in Okada (2006).

<sup>23</sup>in Okada (2006).



indicate the development of flows about the base to be highly  $Re$  sensitive at low  $Re$ , with “A” and “B” not fully developed until  $Re = 6 \times 10^5$ . Consequently, “E” is not closed below such  $Re$ . A more appropriate synthesis of VINO’s work would be to at least suggest an interaction between “A” and “E” wherein both regions are merged periodically (out of phase with “B”).

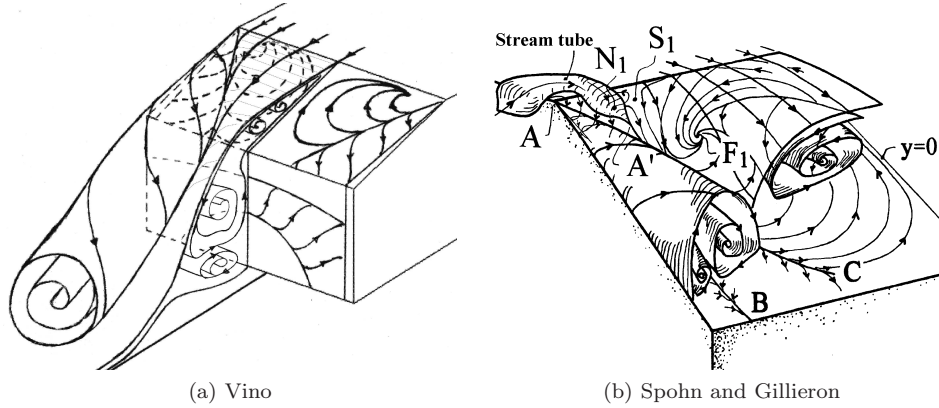


Figure 1.25: Proposed flow structure for high-drag Ahmed Model by VINO (2005) and Spohn and Gillieron (2002)

Shedding from the leading edge of the backlight is characterised as a low-amplitude, broadband (e.g. highly random) effect (Johnson 2005, Sims-Williams and Duncan 2002, VINO 2005). Simulations by Krajnović and Davidson (2005) suggest that distortion of hairpin vortices within “E” by “C” effectively severs contact of the the vortex legs and thus serves to quickly diminish any coherent structures within “E”; the bulk of coherent vortex structures within “E” therefore operate in a downstream direction, very little of which enters the downstream wake. Relevant results indicate vortex structures travelling upstream within “E” are lesser in number and of considerably lower strength. It is suggested that collisions between upstream and downstream vortex structures at the effective closure of region “E” contribute considerably to make this region particularly turbulent and it’s reattachment location particularly variable. A relationship between “A” and “E” is not explored by Krajnovic and Davidson (nor are spectral characteristics) though an extension of their conclusions renders it entirely plausible that “E” could well extend into “A” at various points in time, and that some coherent characteristic relative to “A” could develop over the backlight region.

A spectral perspective from computational works is offered by Johnson (2005), denoting spectral energy in a bandwidth commensurate with the base shedding phenomena described above is shown to decrease over the base region and increase over the backlight with increasing backlight angle to the critical case<sup>24</sup>. This would suggest that as recirculation zone “E” increases in size, it’s propensity to mix with “A” (itself operating over a smaller backlight region) is increased. Spectral energy commensurate with the base shedding peak was observed in the wake near the base/backlight (i.e. extending through regions “A” and “E”) juncture for  $22 < \alpha < 30$ , with further concentrations noted beyond the near wake just above the ground plane as per Sims-Williams and Duncan (2002)

<sup>24</sup>Data for  $10^\circ$ ,  $22^\circ$ ,  $25^\circ$ ,  $30^\circ$  and  $35^\circ$  configurations are presented.



and near the base region, where energy is highest (figure 1.26): whilst the magnitude of spectral energy at the backlight-base junction is relatively higher than for experimental results of similar test cases (Okada 2006), a periodic interaction between “A”, “E” and “B” is further suggested.

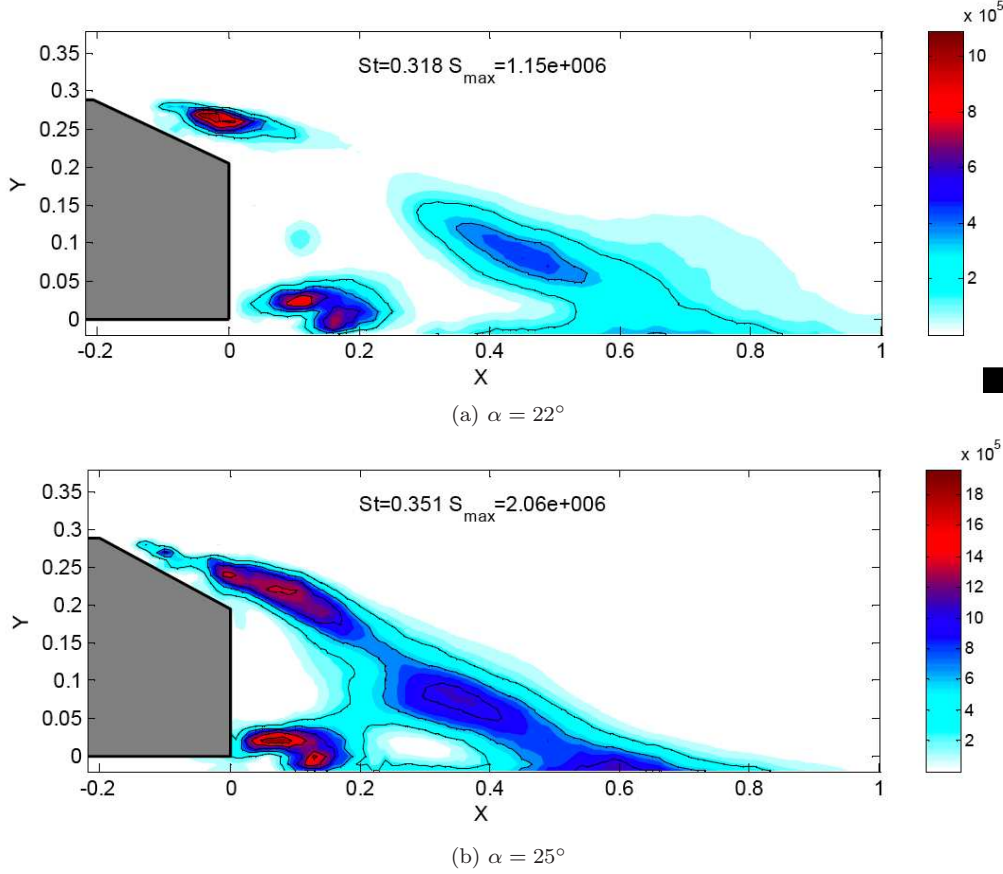


Figure 1.26: Spectral levels in wake of pre-critical Ahmed Model for  $St$  commensurate with base shedding frequency from computational results (Johnson 2005)

In addition to Sims-Williams and Duncan’s aforementioned observation of an interaction in the far wake, Vino (2005) noted pressures over a region of the backlight (at  $\alpha_c$ ) where “C-pillar” vortex (“C”) impingement was time-invariant observable<sup>25</sup> to exhibit a spectral peak commensurate with the base shedding frequency. Though far smaller in magnitude than relevant peaks observed over the base, an interaction between “A”, “E” and the breakdown of vortex “C” is given; Vino suggests that the “C” begins in a stable manner, and is then buffeted by instabilities immediately downstream. The pressure tap in question is located in a region associated with vortex breakdown by Johnson (figure 1.28), providing evidence of instability. It is possible that interactions between “A” and “E” contribute to vortex breakdown of “C” in a periodic manner.

<sup>25</sup>Using oil-and-soot deposition.

1.3.2.5 Turbulent phenomena II:  $\alpha > \alpha_c$ 

(To maintain consistency throughout the literature review, vortices “A” and “B” throughout continue to follow naming conventions depicted in figure 1.18.)

Far lesser information exists to characterise “Region I” flows in a turbulent context. Experimental data defining spectral characteristics does not exist in literature, though a regular, coherent shedding pattern has been observed: largely two-dimensional, spanwise vortices are shed from the bottom-base trailing edge and from the leading edge of the backlight in an alternating manner (Brunn and Nitsche 2001) (figure 1.27). It should be noted that this study employed an Ahmed Model of disproportionate width to give “extreme” two-dimensionality about the centreline, as such the upper vortex in figure 1.27 would likely be “pulled down” by “C-pillar” vortices to give a time-averaged flowfield akin to figure 1.21b (were the correct aspect ratio employed).

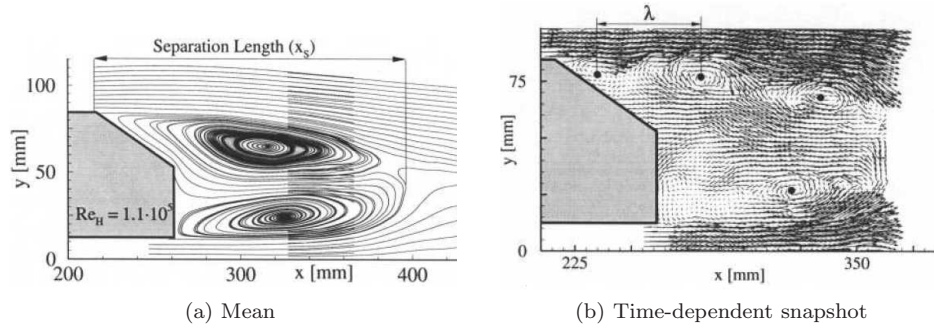


Figure 1.27: Mean and time-dependent visualisations of  $\alpha > \alpha_c$  Ahmed Model after Brunn and Nitsche (2001)

Johnson’s simulations indicate shear layers extending from the top and sides of the body, shedding at a frequency commensurate with that of “B”. The most significant oscillations are along the afterbody centreline, from which the vortices indicated in figure 1.27 are shed, albeit at a lesser frequency than for “Region II” flows. This shedding mechanism was observed to entrain the side shear layers and effectively destroy the spanwise nature of “A” and “B”, forming a two sets of vortices in the wake, being downwash or upwash in nature relative to the shedding cycle of the separation bubble (Johnson 2005). Though not explicitly mentioned, it is suggested that the size of “A” relative to “B” and the spanwise distortion of the “A” into the dominant “C-pillar” vortices contributes to the downwash vortices being stronger, leading to a mean downwash vortex pair in the far wake. It was further noted that whilst significant unsteadiness was noted in the model wake, surface flow patterns were comparatively steady. The bulk of the unsteadiness was concerned with shedding from the model top and bottom (Johnson 2005).

### 1.3.2.6 Transitional effects between about $\alpha_c$

Some conjecture exists in literature surrounding the mechanism by which flow regime transition occurs at  $\alpha_c$ . Interactions between “A” and “E” were originally cited as the rationale behind the bursting of vortices “C” at  $\alpha_c$ ; the merging of these two regions into one larger phenomena “pushing” the separation shear layers wide of the backlight and impeding the ability of the axial vortices to form (Ahmed et al. 1984). Vortex breakdown akin to delta wing phenomena was later hypothesised by Hucho (1978).

Time dependent visualisations by Johnson (2005) at various  $\alpha$  around  $\alpha_c$  give further insight into the interactions between “A” and “E”. For  $\alpha = 22$  to  $\alpha_c$ , a periodic breakdown of the dominant axial vortices was observed at an increasingly upstream location. This was characterised in a mean context by a sharp decrease in vortex core dynamic pressure (figure 1.28<sup>26</sup>, commensurate with a sharp decrease in core axial velocity) with increasing  $\alpha$  beyond  $\alpha = 25$ . This behaviour is consistent with vortex breakdown (Johnson 2004, Ol 2003).

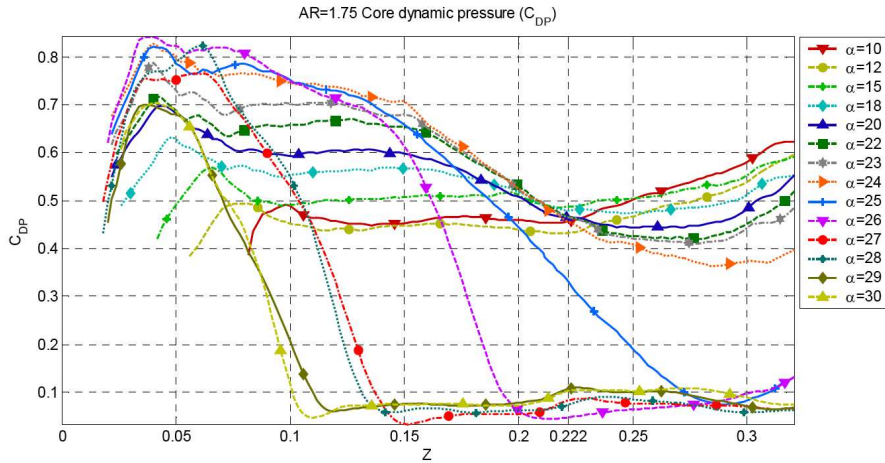


Figure 1.28: Axial vortex core dynamic pressure ( $C_{DP}$ ) for Ahmed Model configurations  $10 < \alpha < 30$  by Johnson (2005)

It is concluded that the transition about  $\alpha_c$  occurs due to vortex breakdown of the dominant, axial “C-pillar” vortices.

### 1.3.3 Reynolds effects

The Ahmed Model has been tested experimentally across a wide variety of relevant conditions. Of interest, the high Reynolds number (Re) used by Ahmed et al originally,  $4.6 \times 10^6$  has not been exceeded. Cooper suggests that for relative, relevant scale testing it is of greater importance (and

<sup>26</sup>The coordinate system employed has each plot commencing at the leading edge of the backlight angle, and the trailing edge of the model at  $Z = 0.222$ .

practicality) to not match  $Re$  but to ensure that flow over forebody edges are turbulent. Where necessary, flow tripping may be required (Cooper 1993).

The Ahmed Model has been tested in pre-critical configuration for  $Re$  as low as  $3.0 \times 10^4$  (Spohn and Gillieron 2002). Critical  $Re$  is attained when characteristic separations occur from well-defined sharp edges. Okada (2006) provides a detailed PIV analysis, concluding a critical  $Re$  of  $6.0 \times 10^4$  for the  $25^\circ$  model (figure 1.29), contrasting well with results taken by Drouin et al. (2002)<sup>27</sup> (taken similarly in a faster facility). Krajnovic and Davidson corroborate similar conclusions for large eddy simulation (LES) computational studies at  $Re = 2 \times 10^5$  for  $\alpha = 25^\circ$ <sup>28</sup> (Krajnović and Davidson 2004).

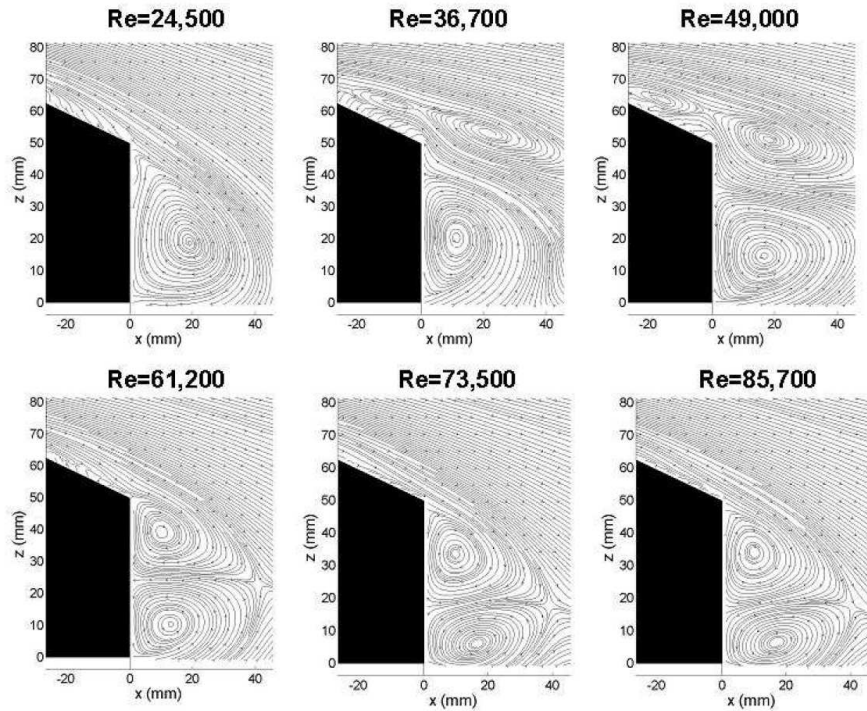


Figure 1.29: Development of flow structure of  $25^\circ$  Ahmed Model at low  $Re$  after Drouin in Okada (2006)

Relevant testing to deconstruct the relationship between drag and  $Re$  were undertaken by Vino (2005) in the same facility used throughout this work, at  $Re$  from  $0.7 \times 10^6$  to  $2.83 \times 10^6$  with turbulence intensity of 1.53% using the critical case (significantly higher than the 0.5% experienced by Ahmed et al.). Using tripwires over the forebody edges bore negligible effect on drag, confirming fully turbulent separation over the leading edges and fully turbulent boundary layers over all

<sup>27</sup>Okada's comparison was made at  $Re\ 9.8 \times 10^5$  for a 25.7% scale model; as his research involved testing unique aspect Ahmed Models and variations in backlight angle, it was arbitrarily decided to test at a higher value than the critical case observed for the "standard"  $25^\circ$  model.

<sup>28</sup>As  $Re$  effectively sets the scales of turbulent motions in the wake, and as LES directly computes larger flow structures in the wake, a lower  $Re$  was desirable in order to complete realistic simulations with acceptable grid resolutions.

surfaces. The reduction in drag with increasing Reynolds number was thus attributed to variances in the turbulent boundary layer over model midsections.

It can be surmised that no significant changes occur with increasing  $Re$ .

### 1.3.4 Relevance of Ahmed Model to modern vehicles

From a perspective concerning the direct transferability of results pertaining to the Ahmed Models to practical domains, some observations are noted:

- *Aspect ratio:* Practical road vehicles span a variety of (frontal) aspect ratios. Table 1.3.4 presents data for all vehicles sold in Australia in 2003 (FCAI 2003)<sup>29</sup>. Classes populated by a majority of fastback/squareback vehicle forms are shown in bold.

Vehicle class	Aspect ratio (H/W)	$\pm$ Ahmed Model ( $AR = \frac{H}{W}$ )
<b>Light</b>	<b>0.899</b>	<b>+17.64%</b>
<b>Small</b>	<b>0.842</b>	<b>+12.02%</b>
<b>Medium</b>	<b>0.824</b>	<b>+10.20%</b>
Large	0.786	+5.78%
People movers	0.960	+22.88%
Sports	0.781	+5.25%
Prestige	0.808	+8.32%
Luxury	0.824	+10.1%
SUV	0.965	+23.36%
<b>Compact</b>	<b>0.950</b>	<b>+22.06%</b>

Modern vehicles appear to have greater aspect ratios than the original Ahmed Model. The effect of aspect ratio variance has been studied in a fundamental context by Hoerner (1965), demonstrating that for flat plates normal to the freestream, drag remained insensitive to aspect ratio where the ratio was large, owing to a broadly two-dimensional wake. At low aspect ratios however the three-dimensionality proved sensitive to small aspect ratio changes. The complex wake interactions produced increased drag considerably. This theme is explored using Ahmed Models computationally by Johnson (2005) and experimentally by Okada (2006). The following relevant findings were observed:

- $\alpha_c$  (located by the total breakdown of the “C-pillar” vortex) increased with increasing (“taller”) aspect ratio, and decreased with decreasing (“wider”) aspect ratio. This is expected, as recirculation bubble “E” becomes increasingly difficult to close given the influence of axial vortices “C”. (For  $\alpha > \alpha_c$  at a given aspect ratio, the width of the wake simply changed.)

<sup>29</sup>The data quoted in this reference is a link to sales figures for the vehicle categories presented above. The dimensional data presented is compiled from manufacturer data for the vehicle models relevant to the sales figures within. Mean dimensions are calculated from average model dimensions appropriately weighted against sales data.

- For “taller” Ahmed Models, the flow structure (both mean and time-dependent) remained broadly identical to a “standard” Ahmed Model, as did the shedding frequencies in the centreline plane. Relevant circulatory structures exhibited slightly increased vorticity.

Flow structures surrounding the “standard” Ahmed Model are thus deemed as qualitatively relevant in the modern context as they were during Ahmed et al.’s original work.

- *Forebody effects*: the development of the Ahmed Model intended to explore afterbody geometric effects, particularly that of backlight angle and to this end offers salient data to the practical domain (Ahmed et al. 1984, Barnard 1996, Hucho 1978, Janssen and Hucho 1975, Morel 1978a). For more practically representative forms, forebody drag contributes a more significant proportion of drag force, as do flow interactions between forebody and afterbody exist (Garrone and Costelli nown).

The focus of works presented throughout is thus limited to exploring flow phenomena in the context of vehicle afterbody geometry.

## 1.4 Tandem arrangements

The aerodynamic interference between two bluff bodies separated by some longitudinal spacing is a common practical occurrence, examined in literature since at least 1910 by Eiffel in Koenig and Roshko (1985). Where proximity is sufficiently close to give rise to aerodynamic interference, the bodies in such arrangements experience a changes in aerodynamic force. This phenomena has been used to advantage in a variety of applications, and may even occur naturally: Cutts (1994) hypothesise that geese in flight likely adopt a characteristic “v-formation” (a *skein*), allowing successive, downstream geese utilising the outboard upwash of a leading geese’s wing to maximise lift and conserve energy<sup>30</sup>.

### 1.4.1 Advantages in mean aerodynamic forces at close spacing

Relevant beneficial net drag reductions are most simply illustrated by two tandem discs normal to flow: Hoerner (1965) demonstrates a significant reduction in drag of the trailing disc (at very close spacing, a net suction is experienced) yielding a net reduction in drag. Underlying flow phenomena for the configuration are presented by Koenig and Roshko (1985) (the downstream disc being the leading face of a cylinder) establishing that at very close spacing, reattachment onto the downstream shoulder occurs giving rise to a uniform, low pressure distribution on surfaces within the gap. Sakamoto and Haniu (1988), in studies of tandem rectangular prisms of height  $3W$ , observed that at relevant close spacing a notable increase in drag force on the upstream

---

<sup>30</sup>Whilst conjecture exists as to the likely power saving: theoretically as high as 60%, practically - possibly - as low as 10% owing to sub-optimal positioning within the skein.



model is observed as significant, low pressures in the gap decrease leading model base pressure; the reduction in trailing model forebody pressure similarly reduces drag of the trailing model markedly to achieve an overall net drag saving.

Though a parametric study of various spacing and leading disc diameters, Koenig and Roshko observed a common characteristic flow structure among the lowest-drag combinations; a single, stable vortical motion occupied the cavity, defining separation at the trailing edge of the leading disc and attachment on the leading edge perimeter of the trailing disc such that the free-streamline flows were approximated<sup>31</sup>. A similar “stable vortex lock-in” phenomenon is noted for square cylinder downstream of a square-ended blade in tandem (intended to limit separation to leading model afterbody effects) at close spacing by Bull et al. (1996) and Leclercq and Doolan (2009). At slightly greater spacing mean flows appeared similar, however interrogation of velocity fluctuations and Reynolds stresses within the cavity and beyond the free shear layer proved indicative of a vortex shedding-type structure in the free shear layer and a sympathetic oscillation of the entire cavity. Koenig and Roshko speculated this to be the onset of a wake mode of the leading model (i.e. when in isolation). Net drag in this instance was higher than for the former, “stable vortex” cavity mode (figure 1.30). A similar phenomena was used successfully by Saunders et al. (1993) to reduce drag of train wagons; partitions in the wagon were sized to encourage the formation of stable vortices within unladen, uncovered wagons.

### 1.4.2 Literature pertaining to tandem automotive vehicle arrangements

The exploration of relevant phenomena on automobiles has its genesis in motorsports - “*slipstreaming*” - with an original study by Romberg et al. (1971) citing individual and net convoy drag force gains for vehicles in increasingly close proximity. Whilst Hucho (1978) contended that the general effect of drag reduction on fuel consumption is overstated by a focus on steady-state driving, it is also inferred that considerable opportunity exists to reap significant reductions in energy consumption under such conditions. Synthesis with contemporaneous research into Automated Highway Systems (AHS) - envisaged to control vehicles such that reduced spacing between them may realise increased throughput on existing major road infrastructure - has led to renewed interest in tandem arrangements of automotive vehicles - “*platoons*” - as a method to reduce net drag force. The majority of relevant studies emphasise force data (rather than underlying flow phenomena); generally, substantial reductions in net platoon drag are realised where gap is spacing less than a car length (Azim and Gawad 2000, Browand and Hammache 2004, Chen 1997, Hong et al. 1998, Ioannou 1997, Marcu and Browand 1998, Noger et al. 2005, Tsuei and Savaş 2000; 2001, Zabat et al. 1993; 1994). Figure 1.31 shows three and four-car platoons undergoing field testing as part of research by the California PATH (Partners for Advanced Transit and Highways) program<sup>32</sup>. Ioannou (1997) suggests that ideally, vehicles of a common destination should be grouped into a platoons to maximise stability.

---

<sup>31</sup>The optimal combination involved a smaller diameter leading disc, allowing curvature in the separated shear layer. The degree of curvature, in turn, would be affected by freestream (or along-stagnation-streamline) turbulence.

<sup>32</sup><http://www.path.berkeley.edu/>

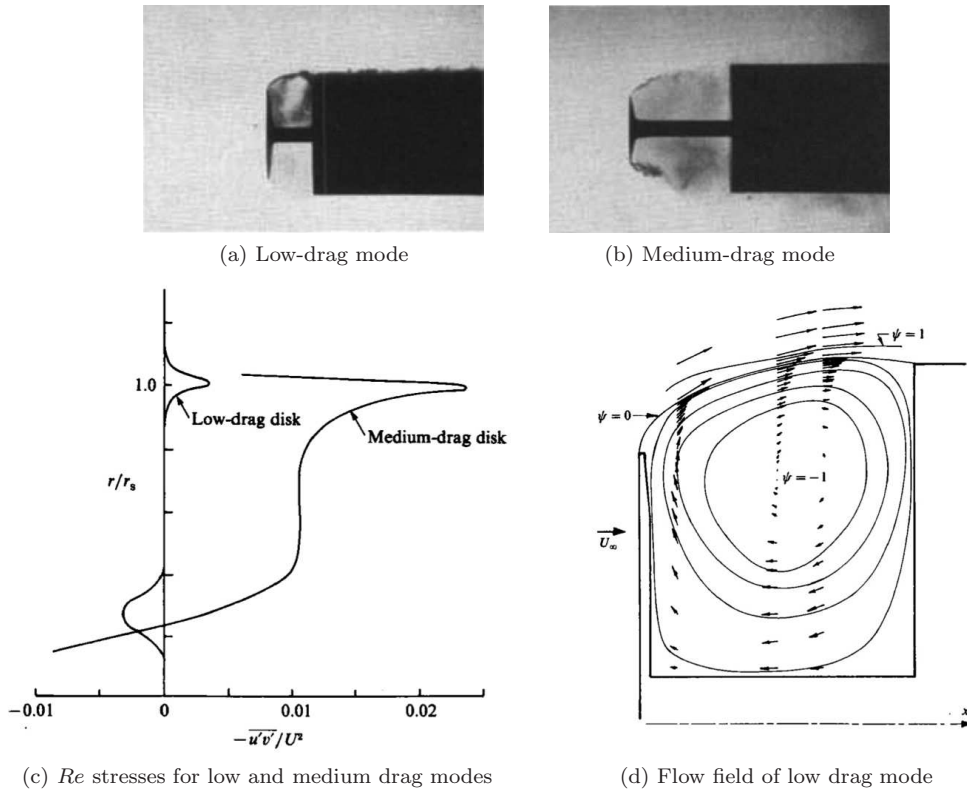


Figure 1.30: Comparison of “low” and “medium” drag modes for cavity flows between a disc and cylinder normal flow after Koenig and Roshko (1985)



Figure 1.31: Platoons in field testing (Michaelian and Browand 2000)

#### 1.4.2.1 Aerodynamic performance of platoons

The potential performance of platoons is characterised in figure 1.32 by (Zabat et al. 1993; 1994, including earlier results of Romberg et al. (1971)).

It is thus inferred that the aerodynamic advantages of platooning are (broadly) best realised



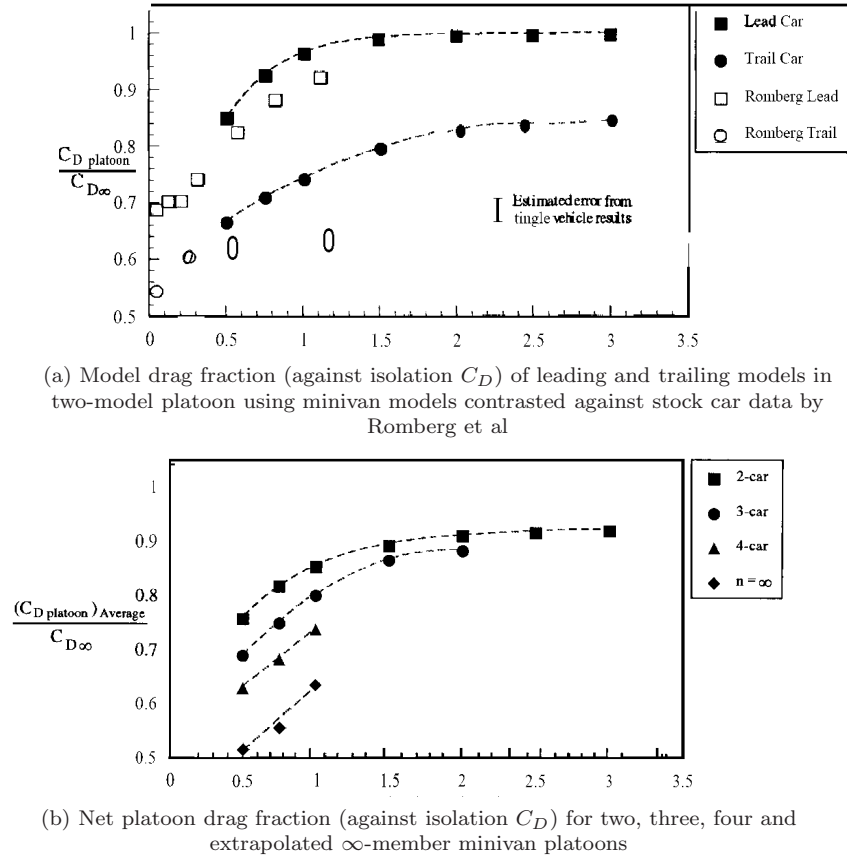


Figure 1.32: Data for Chevrolet Lumina platoons for  $0.5 \leq \frac{x}{L} \leq 3$  (Zabat et al. 1993)

where:

- *Inter-vehicle spacing is minimised*
- *Platoon length is maximised*

Practically these are difficult scenarios to realise:

- *Minimum spacing:* Sun and Ioannou (1995) cite a number of contributory variables, including but not limited to trailing vehicle reaction time, deceleration/braking performance of adjacent vehicles, road/tyre friction coefficients, lead/relative vehicle velocity. A particularly detailed study by Kanaris et al. (1996) presents a most optimistic case requiring an inter-vehicle headway of approximately 2.1m at 100km/h: considerably larger than  $\frac{x}{L} \leq 0.1$ <sup>3334</sup>,

<sup>33</sup>The mean length of new passenger cars in Australia is 4.53m, with  $\sigma = 0.4$ m, given sales data from FCAI (2003) and an independent investigation of relevant manufacturer-supplied key geometries by the author.

<sup>34</sup>Such small spacing is common to a variety of aerodynamic investigations into passenger vehicle platooning, e.g. Chen et al. (1997), Hong et al. (1998), Marcu and Browand (1998), Michaelian and Browand (2000), Vino (2005), Zabat et al. (1993).

and yet to achieve even this, a platoon would need feature co-ordinated braking and allow low-speed collisions in an emergency braking situation<sup>35</sup>. (Of interest, the study cites a significantly reduced required headway for commercial vehicles, given comparatively poorer braking performance.) Were closer spacing possible, Azim and Gawad (2000) highlight that significantly changed aerodynamic forces may present a further serious consideration to control algorithms.

- *Platoon length*: original platooning work by Shladover<sup>36</sup> predicted traffic throughput to scale with platoon length. Later works by Hall and Chin (2002) cast significant doubt upon original destination-based grouping perspectives: the probability of platoons exceeding 4 members is very small; two and three member platoons are more likely.

Some practical limits are thus placed on the effectiveness of the concept from an aerodynamic perspective.

Another important factor concerns platoon member geometry; as bluff bodies flow topology is generally form-defined, the aerodynamic performance of a platoon should also depend on the geometry of its members. Concerning passenger vehicles; works by Zabat et al. (1993; 1994) are based around models of the Chevrolet Lumina minivan (figure 1.33<sup>37</sup>), a *squareback* configuration. Later tests under the California PATH project by Hong et al. (1998), Michaelian and Browand (2000) involve models of sedan (*notchback*) configuration, as does earlier work (Romberg et al. 1971). Both configurations offer drag advantages for leading and trailing models in-platoon.



Figure 1.33: Chevrolet Lumina minivan as used by California PATH group in wind tunnel tests

The presence of a ground plane and blunt base geometries in automotive forms gives rise to high static pressure under the base and low static pressures above; an upwash is generated from the underbody giving rise to flow separation at the base/bottom/centreline coincident. A relatively square afterbody - characteristic to busses - allows such a feature to dominate the near wake. Fletcher and Stewart (1986) observed, for two-model bus convoys that such a vortex (visualised

<sup>35</sup>Minimum spacing relationships are further explored by Sun and Ioannou (1995).

<sup>36</sup>in Ioannou (1997).

<sup>37</sup>All detail features were deleted in the test models used, e.g. side mirrors, underbody and wheel details, shut lines etc.

along the centreline) could be created in a stable manner such that lead model afterbody pressures were usefully increased, reducing drag. The impingement of the same vortex on the trailing model forebody caused a local increase in surface pressure. Increased spacing allowed the vortex to grow, and - at larger still spacing - oscillate. The increased impingement increased drag of the trailing model above model-in-isolation values<sup>38</sup> (figure 1.34).

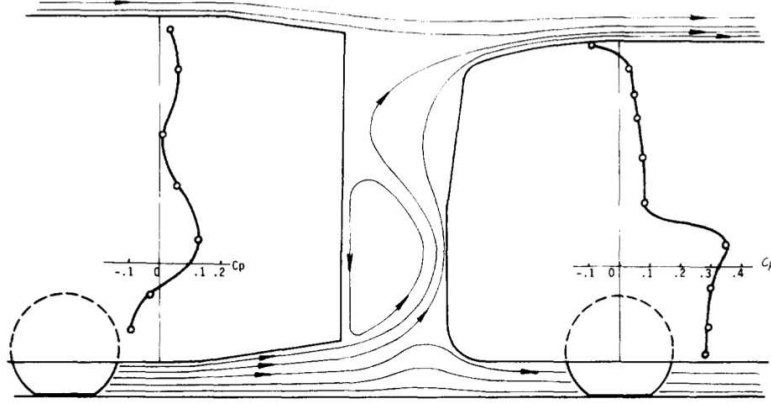


Figure 1.34: Centreline flow structure deduced from surface pressure and wool tuft flow visualisations for two bus models in tandem after Fletcher and Stewart (1986)

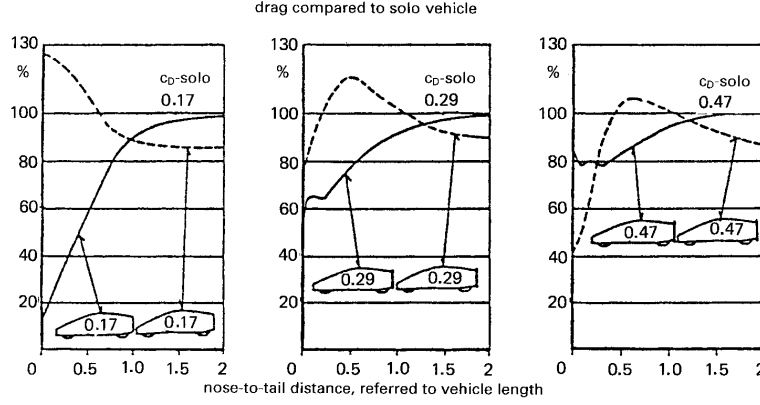
The transferability of this argument to passenger vehicles is complicated by differences in geometry - particularly C-pillars, giving rise to a delta-wing-like axial vortex pair - and resulting characteristic phenomena. The resultant low kinetic energy “cavity” in such a scenario concerning two automotive notchback scale models at ultra-close spacing was observed in a flow visualisation study by Azim and Gawad (2000), suggesting that the severely reduced flow within the gap (as per two cylinders in ultra-close proximity) would yield a lowest-possible net drag for a vehicle platoon. A slightly larger gap allowed dominant vortices to form from the C-pillars, which were observed to impinge on the trailing model forebody. Whilst Azim and Gawad alluded that this mode would still yield a net drag reduction - albeit diminished - not all studies concur.

The case for *fastback* models - representing the most extreme case of “C-pillar” vortex generation - is not as clear. Earlier work by Ewald (1984)<sup>39</sup> for low, medium and high-drag configured generic fastback models in two-model platoons confirmed increased leading model base pressure, however increased trailing model forebody pressure (figure 1.35). The net effect served to reduced net platoon drag, however for each configuration presented, at close spacing the trailing model drag force was increased. Similarly, the model used by Zabat et al. (figure 1.33) when placed in reverse orientation effectively functioned as a platoon of fastback models, despite rounded edges: the contrast in drag force trends is presented in figure 1.36 detailing increased trailing model drag

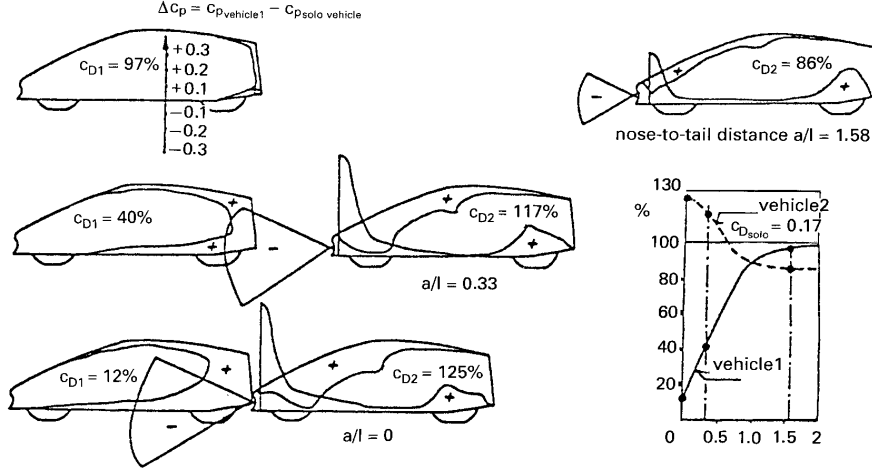
<sup>38</sup>Of interest, a second, counter-rotating vortex was able to be “trapped” from altering model geometry. The detrimental effect of this vortex’s impingement was demonstrated to be somewhat relieved by re-contouring the trailing model forebody such that it became physically distanced from this vortex.

<sup>39</sup>In Hucho (1998).

at close ( $\frac{x}{L} < 0.1$ ) spacing (Zabat et al.<sup>40</sup>); deconstruction of the underlying phenomena was not undertaken. In addition, drag force for variety of practical vehicles was observed to increase when placed in a generic downwash wake by Carlino et al. (2007), Carlino and Cogotti (2006)<sup>41</sup>.



(a) Force variation for platoons of two-model low, medium and high drag



(b) Modified pressure distribution about models in two-model platoon at various spacing

Figure 1.35: Results for two-model platoon by Ewald in Hucho (1998)

The underlying flow phenomena were explored by Vio using two  $\alpha_c$  Ahmed Models (figure 1.37); at a distance where dominant, axial, “C-pillar” vortices were free to form in a coherent manner, high-momentum flow over the model centreline to impinge on the trailing model forebody, shifting the stagnation point upwards with a sufficient increase in forebody pressure to increasing trailing model drag force markedly beyond model-in-isolation values. At closer spacing still, the formation of the upstream model’s axial vortices is constrained, as are base separations limited; the leading model’s base pressures are thus maximised (across the backlight) and trailing model drag force was minimised. The data is qualitatively similar in trend to that presented in figure

<sup>40</sup>In Hong et al. (1998).

<sup>41</sup>The “Pininfarina Turbulence Generation System (TGS), consisting of a series of retractable, adjustable vortex generators installed upstream of the test section, is best described in Cogotti (2004).

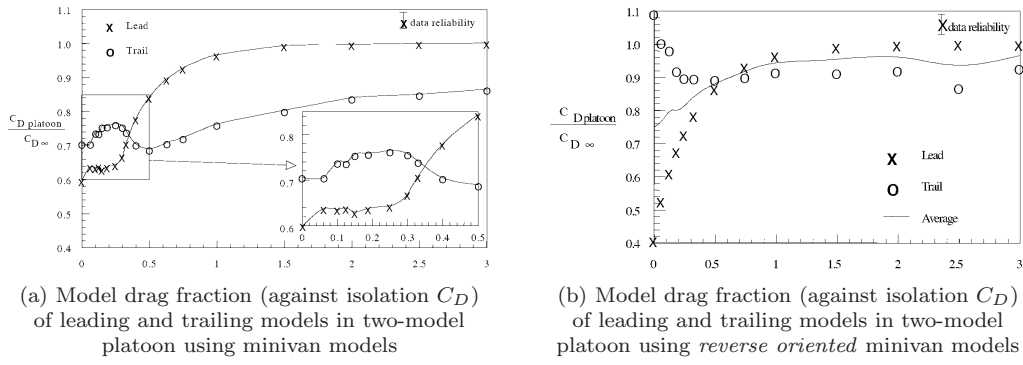


Figure 1.36: Detailed data for Chevrolet Lumina platoons for  $0 \leq \frac{x}{L} \leq 3$  after Zabat et al in Hong et al. (1998)

1.36<sup>42</sup>. These themes are similarly evidenced in experimental data by Browand and Hammache (2004) and Chen et al. (1997).

Whilst fastback structures offer essentially two unique flow fields - pre and post-critical (Ahmed et al. 1984) - studies do not presently exist examining the relative effects of either.

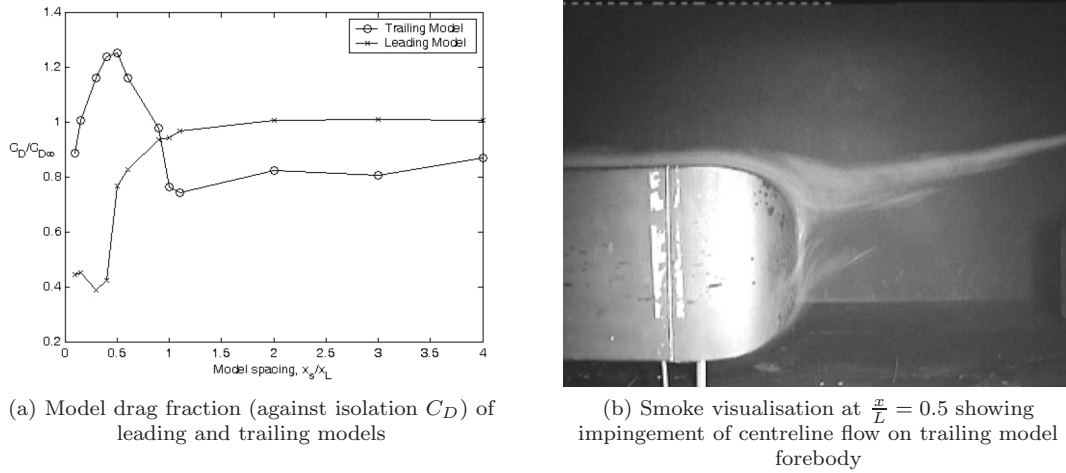


Figure 1.37: Force data and trailing model downwash impingement visualisation for two 30° Ahmed Models in longitudinal convoy (Vino 2005)

#### 1.4.2.2 Upstream vehicles as a source of on-road turbulence

If considering fastback configurations, a more generalised perspective appraises the presence of an upstream vehicle as a source of turbulence: a highly turbulent near wake beyond which a macroscopically stable, dominant axial vortex pair extending far beyond the upstream vehicle's

<sup>42</sup>A qualitative comparison of Vino's results and those of Zabat et al. contrasting data with and without boundary layer suction suggest that Vino's trends may have been further accentuated by floor boundary layer effects.

base. Recent literature addresses the influence of vehicle wakes as a significant component in the characterisation of a turbulent, practical road vehicle flow environment (Carlino and Cogotti 2006, Chen et al. 1997, Gillieron and Noger 2004, Noger et al. 2005).

For research purposes it is important to simulate turbulence parameters relevant to the practical environment; the Pininfarina Turbulence Generation System (TGS, figure 1.38) - a system of independently adjustable vortex generators to create upwash or downwash vortex structures - represents the current state-of-the art. The system is able to produce laterally misaligned wakes structures (for “adjacent lane” studies), to “flap” (and thus simulate an overtaking manoeuvre) and to replicate turbulence parameters commensurate with light-to-medium density traffic. Studies with the system indicate an increase in drag force for vehicles located within a downwash vortex wake; the trend is similar if diminished in magnitude when the vortices are translated some 0.5 body widths<sup>43</sup> (Carlino et al. 2007, Carlino and Cogotti 2006, Cogotti 2004).

### 1.4.3 Relevant tandem arrangements of fundamental bluff body forms

Platooned fastback automotive bodies represent a specific case of bluff bodies in tandem arrangements; afterbody configurations are shaped such that downwash-generating axial vortices dominate the far wake, interactions with the ground plane further complicate the flow field. Whilst few studies exist to characterise the specific case, some generalised observations are transferable from studies of generic bluff bodies in tandem arrangements. In many studies, unique flow field “modes” have been observed as a function of body geometry and (more pertinently) spacing.

The following section seeks to review statistical and spectral properties unsteady flows relative of simple cavity drag and tandem two-dimensional bluff body arrangements<sup>44</sup>. As time-dependent flows about at least the base of the pre-critical Ahmed Model have been shown to influence mean flows and thus forces (Krajnović and Davidson 2005), some consideration is given towards deconstructing spectral performance in the gap between potential tandem arrangements of such models<sup>45</sup>.

#### 1.4.3.1 Fundamental studies of two dimensional bluff bodies in tandem arrangements

A more complex aspect of bluff bodies in tandem arrangements concerns the unsteady nature of flows in the gap for gap spacing large enough for the upstream body’s separated shear layers to not reattach on the leading surface of the downstream body. Koenig and Roshko’s relatively stable

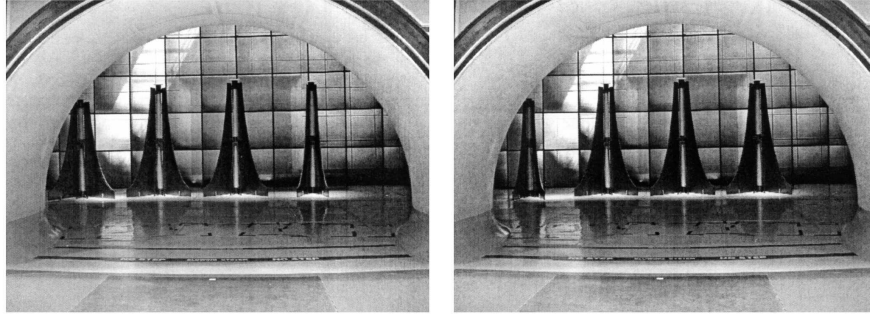
---

<sup>43</sup>Of potentially greater safety significance is severely diminished front axle downforce for vehicles in the wake of an off-axis downwash, posing a vehicle stability concern.

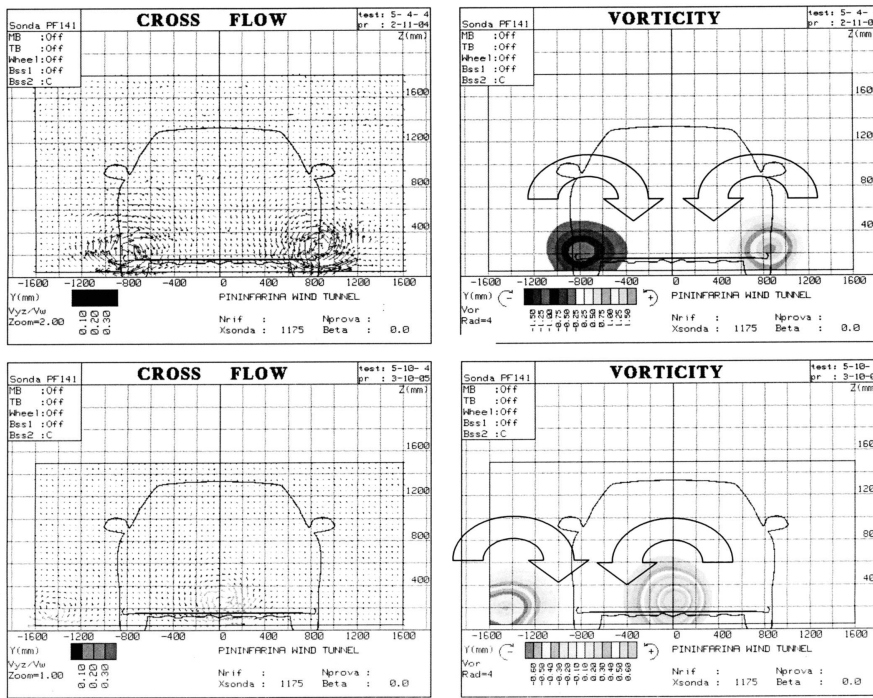
<sup>44</sup>The aerodynamic performance of slender three-dimensional forms mounted in a ground plane are also considered; excluding end effects, themes present are otherwise common to two-dimensional cylinders in tandem arrangements

<sup>45</sup>Cubic forms are not considered, as the shedding modes inherent depend strongly on interactions of flows about the top *and* sides of the leading model (Martinuzzi and Havel 2004); characteristic shedding about the Ahmed Model is instead demonstrated by Sims-Williams and Dominy (1998), Sims-Williams and Duncan (2002) to be quasi-two-dimensional.





(a) TGS system starting and final positions for generation of a downwash-type overtaking wake



(b) Vorticity contours and velocity vectors in crossplane

Figure 1.38: Pininfarina Turbulence Generation System (TGS) after Carlino and Cogotti (2006)

flow behaviour in the “stable vortex” gap is echoed in studies of tandem square two-dimensional cylinders by Takeuchi and Matsumoto (1992) and for tandem cylinders by Zdravkovich (1987). The latter also observed a flow transition at larger spacing allowing free shear layers from the upstream cylinder to roll up alternately, forming a vortex street upstream of the second cylinder (figure 1.39). The wake of the second cylinder proved a compound of shedding from both upstream and downstream cylinders, the transition between these regions being bistable and exhibiting hysteresis on modification of either velocity or gap spacing. Zhang and Melbourne<sup>46</sup> and Hangan and Vickery

<sup>46</sup>in Havel et al. (2001).

(1999) further discern the transition region by initial alternate attachment on either side of the cylinder, and at further spacing by quasi-steady attachment giving rise to irregular shedding (and thus loading; these modes are bistable).

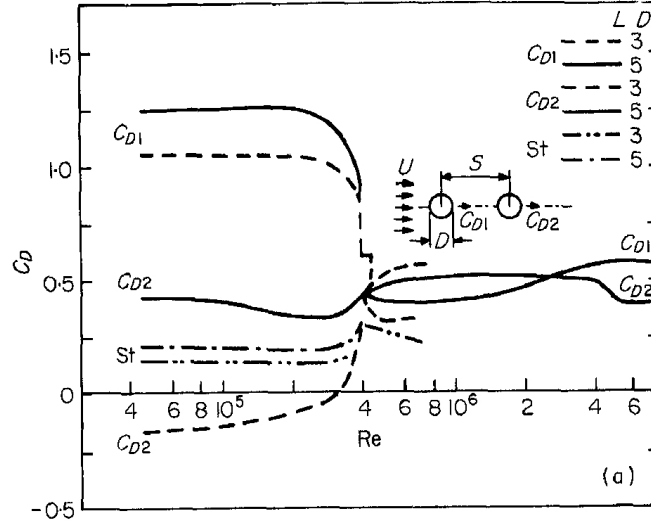


Figure 1.39: Variation in  $C_D$  and  $St$  for two cylinders in tandem arrangements at Okajima in Zdravkovich (1987)

Similar phenomena were observed in elastically-mounted square cylinders by Shiraishi et al. (1986) and Takeuchi and Matsumoto (1992) characterising a distinct change in spectral properties between two unique regimes (figure 1.40, presenting both  $St$  as a function of spacing and spectral densities of both cylinders mounted rigidly to a torque balance). Beyond a critical value; compound peaks are visible consistent with independent shedding from either cylinder, at closer spacing a unique spectral peak exists, formed at base of the trailing model: whilst the dynamics of oscillating, tandem bluff bodies are not within the scope of the this study, the observation of a flow regime at increased spacing for which *oscillating* flows are generated within the gap is of particular importance. The latter work also examined significant variations in (and relevant flow modes concerning) spectral characteristics in systems involving various degree-of-freedom cylinders, from zero to two<sup>47</sup>. Studies involving wholly-rigidly-mounted two-dimensional bluff bodies generally confirm a single spectral peak in the gap (Bull et al. 1996).

#### 1.4.3.2 On the generation of oscillating behaviours within the gap

The variance of  $St$  within the gap with spacing allowing development of oscillating vortex shedding is an important detail requiring further deconstruction. Sakamoto and Haniu, using pressure taps

<sup>47</sup>This is potentially worthy of consideration in the automotive field where response to changes in drag force for a constant load (vehicle velocity) demand are increasingly the realm of control engineering (i.e. “drive-by-wire”) technologies.



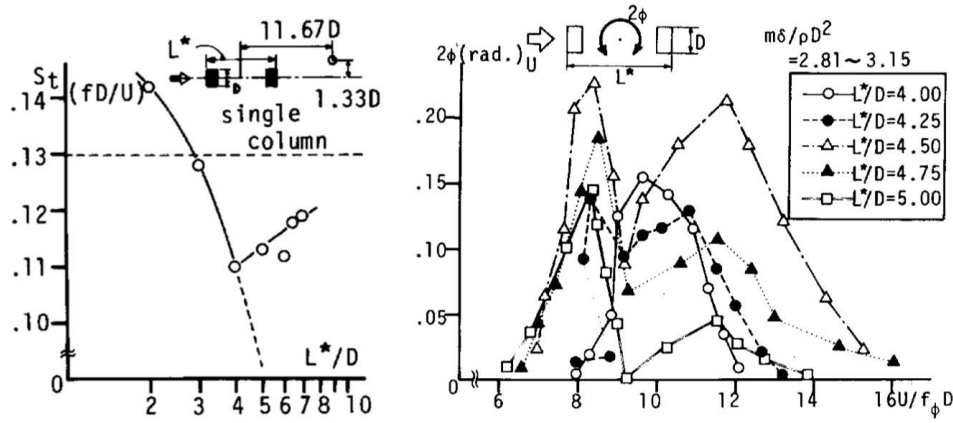


Figure 1.40: Variation in  $St$  and downstream cylinder torque spectra with increased spacing after Shiraishi et al. (1986)

on the streamwise surfaces of tandem prisms<sup>48</sup> noted no fluctuation at close spacing; as this increased, shear layers from the leading model began to flow intermittently into the gap such that mixing occurred with fluid entrained about the shear layers. Spectral peak begins to form though significant randomness existed also, however at greater spacing still, shear layers from either side of the leading model rolled up in a periodic manner and a clear spectral peak was visible in the gap.

Bull et al. (1996) presented results for a square cylinder downstream of a vortex-inducing blade (limiting significant leading body shedding to the base of the upstream body as per automotive forms); for the bluff body in isolation,  $Re$ -stable vortex shedding established a sharp spectral peak. Dominant body force fluctuations for the same body placed downstream of a two-dimensional blade were shown to be vortex (shedding) induced (allowing the authors to examine such phenomena using acoustic means) and to change with spacing, their frequency diminishing at close spacing. Relevant spectral densities were again shown to be relatively  $Re$  stable, corroborating prior observations by Shiraishi et al. in the “vortex street” regime. A similar experiment by Leclercq and Doolan (2009) corroborates a rise in radiated acoustic noise from a tandem blade/prism arrangement, with decreasing  $St$  at closer spacings (figure 1.41), with analysis against force and visualisation data confirming the near 15dB rise in peak spectral density to concern the significant pressure fluctuations in the gap.

#### 1.4.3.3 Limitations on transferability of acoustic data in fundamental studies to automotive forms

A disclaimer is prudent at this point: at relevant spacing, the short chord of the downstream bluff body causes shedding at its *leading* edges to “lock on” to oscillations in the gap. Whist

<sup>48</sup>These would experience a fluctuating variance in pressure were the adjacent streamwise edge shedding an unstable shear layer.

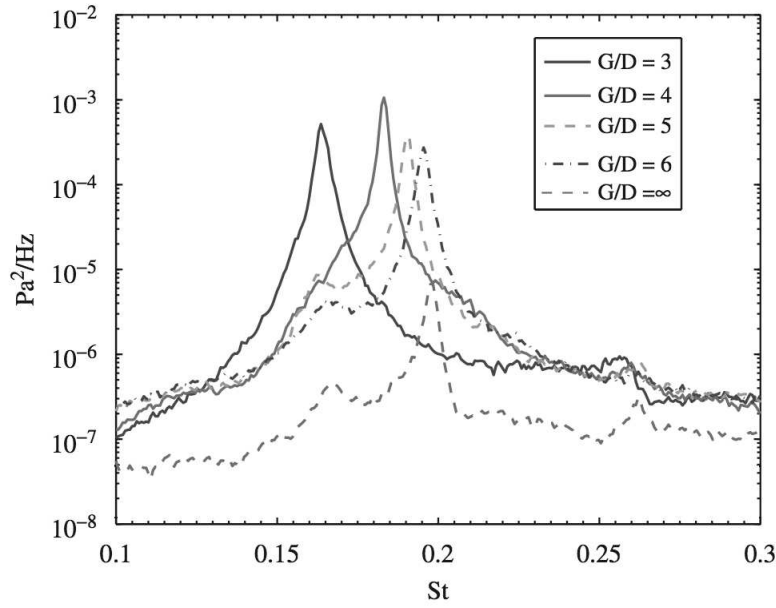


Figure 1.41: Radiated acoustic spectra for a rectangular prism downstream of a blade after Leclercq and Doolan (2009)

leading model wake vortices are stretched and weakened about the (relatively short) sides of the trailing model, a significant effect is borne on side-to-side base pressures and thus a single spectral peak is typically observed in acoustic data in vortex-street interference regimes (Leclercq and Doolan 2009)<sup>49</sup>. This is suspected of lesser relevance to automotive forms, where any separated dynamic behaviour about the base is not known to depend significantly on oscillating separations upstream but instead on developed, turbulent flows prior to a sharp geometric transition (Cooper 1993). Furthermore as oscillating shedding takes place about the bottom/base only in notchback reference forms (there being no quasi-two-dimensional “coupled” shedding about the base surface as per Sims-Williams and Dominy (1998), Sims-Williams and Duncan (2002)), the assessment of spectral phenomena using acoustic methods to assess a single oscillating frequency is envisaged not transferable to automotive forms in tandem arrangements; unique spectral peaks are instead anticipated, however the potential for upstream flows to influence oscillating separations at the base of the trailing model is not wholly negated.

#### 1.4.3.4 Observed relationships between gap spacing and spectral properties

Some additional, important insights into periodicity were suggested by Bull et al. (1996): with increasing spacing vortex formation on the upstream body occurred increasingly closer to the

<sup>49</sup>Although both Leclercq and Doolan (2009) and Sakamoto and Haniu (1988) highlight that phase differences may exist in oscillating forces between leading and trailing models as vortices shed from the leading model are accelerated and dissipated about the trailing model. The phase relation depends on spacing, convective velocity and shedding frequency. A review by Mahbub Alam and Zhou (2007) cites a relationship between phase and lift of the trailing model.

base; periodicity in both vortex formation lengths and vortex spacing relative to the number of vortices (all within the gap) suggested some form of hydrodynamic feedback from the downstream body limiting vortex formation. Peak spectral acoustic energy was observed at the transition between “vortex lock-in” and vortex shedding gap flow regimes and to decrease with increased spacing. It is postulated the the increasing limitation of vortex formation served to increase peak-to-peak pressure differences across the lead model base, giving rise to increased spectral density with diminishing  $St$  for reduced spacing.

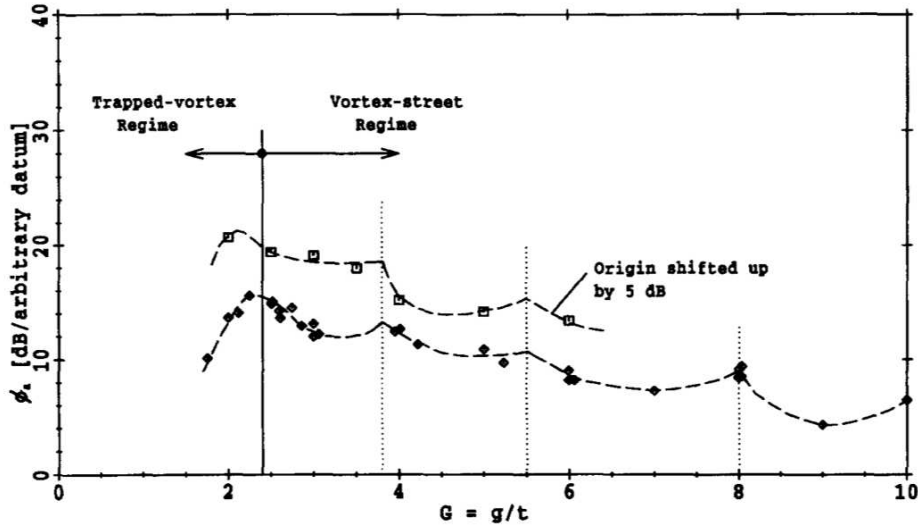


Figure 1.42: Oscillating relationship of variation in radiated acoustic spectra for various gap spacing after Bull et al. (1996)

## 1.5 Conclusions

### 1.5.1 Summary of literature review

The key aspects of this literature review are summarised thus:

- *Fleet vehicle aerodynamic performance* -  $C_DA$  particularly - bears a well-understood impact on fleet energy consumption. Beyond the aerodynamic optimisation of the vehicle-in-isolation, the use of organised vehicle convoys (particularly “*platoons*”) offers a further opportunity to reduce fleet energy consumption. A simple appreciation of the concept concerns a reduction in base pressure for leading vehicles, and a commensurate reduction in forebody pressure for trailing vehicles given reduced dynamic pressure in a leading vehicle wake. Whilst much work has been undertaken using scale models exploring mean body forces, few fundamental studies have been undertaken to deconstruct key flow phenomena.

Initial work in this area using longitudinally-spaced models indicates that platooning may not always be advantageous pending relative position in-platoon. These studies have not been expanded to account for variances in vehicle geometry. Practical platoon scenarios requiring further understanding often concern lateral misalignment of platoon members in addition to controlled longitudinal spacing.

- *Generalised vehicle aerodynamic flows* are analogous to bluff bodies in near-ground proximity, and create a far wake typically dominated (with a few exceptions) by axial downwash-generating vortices formed from separations about the C-pillar. Depending on vehicle geometry, these vortices may impinge on the vehicle backlight region in a manner analogous to flow over a delta wing at a pre-stall angle of attack; similarly, this configuration gives rise to significant body lift and drag forces. Near wake flows are driven by backlight and base geometries. Interactions between these and the dominant axial vortices give rise to highly complex, if coherent, three dimensional flows in this region. The typical automotive vehicle wake is highly unsteady.
- *The Ahmed Model* offers a useful, well-documented form with which to study typical automotive vehicle wakes, replicating key flow phenomena in cases where the dominant axial vortices impinge (the “*high drag*” case) and where they are formed off-body (the “*low drag*” case). The transition between these cases is characterised as a function of vortex breakdown, which has been demonstrated to be a function of key geometries (at “standard” aspect ratio, it is a function of “backlight angle”, as per angle of attack in the aforementioned delta wing analogy). Coherent, flat plate-type shedding is observed about the base of at least the “high-drag” case giving rise to a horseshoe vortex pair operating on the model base. Interactions between base and backlight regions are particularly complex. In addition to replicating macroscopically stable flow phenomena relevant to automotive vehicles, turbulent phenomena are similarly well replicated, allowing the model to serve in fundamental platooning studies where upstream vehicles are considered a source of upstream turbulence. The model is capable of replicating such phenomena faithfully at  $Re$  an order of magnitude below those typifying practical road vehicles.
- *Turbulence* has notable effects on bluff body forces, particularly where length scales approximate shear-layer thickness or the distance between shear layers and more so in cases where turbulence is apparent in the stagnation streamline; typically base pressure is decreased. This should be taken into consideration when comparing test data from other facilities. Relevance to practical road environment turbulence, however, concerns a wider variety of length scales given the presence or larger-scale shedding in the practical environment - particularly from other vehicles on-road. As unsteady aspects of road vehicle wakes have been demonstrated to affect mean forces, external factors which alter the aerodynamic environment in an unsteady manner are of interest in any detailed investigation of mean vehicle forces or inter-vehicle interactions.
- *Tandem arrangements* of bluff bodies in many cases offer opportunities to reduce the net drag of the bodies concerned relative to the sum of their individual drag forces. The flow

phenomena within the gap may assume one of many characteristic modes pending dominant geometric factors; for bodies of similar cross-section area, gap spacing determines gap flow phenomena and relevant body force effects. At moderate spacing, the gap is typically dominated by a vortex street shed from the leading model trailing edge(s). The nature of periodic phenomena is sensitive to gap spacing and bears effect on mean body forces.

Some care needs be taken if evaluating the above as an analogous introduction to appraising the aerodynamic mean-body-force performance of automotive passenger vehicle bluff bodies. Whilst quasi-two-dimensional shedding about the bottom/base/centreline coincident dominates the near wake, “C-pillar” geometry - where applicable - gives rise to axial vortices that entrain a net downwash into the near wake. Where this phenomena features as a dominant component of an automotive passenger vehicle wake in a location in which a trailing platoon member is placed, net platoon drag is decreased at the expense of an increase in trailing model drag force. Literature review confirms such a “strong downwash” characteristic is common to pre-critical and critical fastback geometries, though no literature exists contrasting differences in behaviour for trailing models in the wake of both pre and post-critical fastback geometries.

## 1.6 Proposed scope and aims

The research presented throughout focusses on exploring interactions between automotive forms in near proximity by exploiting two key variables in platooned convoys:

- The effect of (leading model) fastback geometry on platoon aerodynamic performance
- The effects of longitudinal spacing on platoon aerodynamic performance, subsequent to a leading model fastback geometry

To limit experimental complexity, a two-model platoon is employed. Geometric variance is explored using pre and post-critical leading Ahmed Models ( $\alpha = 25^\circ$  ,  $\alpha = 35^\circ$  respectively). Variance in flow conditions (flow yaw as generated by crosswinds, upstream turbulence variations and the like) are not explored, though relevant inherent test environment (wind tunnel test section) flow properties are acquired and examined for relevance to practical conditions.

An initial research task seeks to characterise flows pertinent to both forms: a focus is placed on validating consistency with published data and in contributing relevant knowledge to the turbulent, dynamic aspects of the forms.

A second, more significant task concerns the evaluation of two-model platoons where a upstream vehicle geometry and downstream model longitudinal spacing are varied. It is intended to broaden existing, relevant published knowledge by deconstructing flow phenomena underpinning force and moment trends.

## Chapter 2

# Experimental methods

This section details experimental equipment, methodology and post-processing techniques relevant to the research presented.

### 2.1 Test models

#### 2.1.1 Physical description

The Ahmed Models (described in section 1.3.1, page 21, also presented in figures 2.1 and 2.4) used throughout testing comprise the following:

- A single model for force data acquisition constructed in medium density fibreboard. The “nose” section was CNC machined to ensure accuracy (particularly symmetry). The force balance was located internally within a steel frame bolted rigidly to the wooden structure. A number of interchangeable “tail” sections were constructed allowing configuration of the Ahmed Model with  $0^\circ$ ,  $12.5^\circ$ ,  $25^\circ$ ,  $30^\circ$  and  $35^\circ$  backlight angles. The model was supported by four  $\frac{1}{4}$  inch diameter steel stings (from the “dead” side of the force balance) in locations commensurate with those used by Ahmed et al. (1984). These models were also used in wake interrogations.
- Two models with removable nose and tail sections for use in surface pressure measurements. The centre sections were constructed in medium density fibreboard, the nose and tail sections in fibreglass using the aforementioned force balance model sections as a master to create molds. Tail sections in  $25^\circ$  and  $35^\circ$  were constructed only.
- Two completely closed “dummy” models, one of  $25^\circ$  and one of  $35^\circ$  configuration, constructed using fibreglass (nose and tail sections, from aforementioned molds) and medium density

fibreboard (centre sections). Nose and tail sections were bonded inside-out using fibreglass-reinforced resin sections. These were used in platoon configurations where the remaining model was instrumented, and in on-surface flow visualisation.



Figure 2.1: Single Ahmed Model installed in RMIT IWT

All models were constructed to 75% scale of the linear dimensions outlined in figure 1.12. Models were sanded to a 600 grit finish with all continuous surfaces across mating edges sanded flush. Prior to testing, all gaps between model sections were taped over flush with duct tape. For testing purposes the models were secured to a 25mm thick steel plate, providing effective alignment with the floor section (discussed in section 2.2.1, page 61). An installed model is depicted in figure 2.1.

Models were supported by  $\frac{1}{4}$ " steel rod. Whilst thinner than supports utilised by originally (Ahmed et al. 1984), care was taken to locate them identically. These are thought to suppress the creation of a pair of small, counter-rotating vortices off the bottom trailing edge, observed in experiments where an overhead sting was employed (Strachan et al. 2007) and in computational work where no support structure was simulated (Kapadia et al. 2003). A likely explanation concerns the growth of boundary layers on the ground plane and the model underside; fluid is thus pushed out from under the model to the sides (consistent with continuity), causing a vortex pair to roll up against the sharp edge of the underside/side junctures (Krajnović and Davidson 2005). It is possible that the presence of the support structured introduces a disturbance sufficient to defeat these (comparatively weak) flow structures.

## 2.2 Instrumentation

### 2.2.1 The RMIT Industrial Wind Tunnel (IWT)

The RMIT University Industrial Wind Tunnel (IWT) is a closed-jet, constant cross-section, fixed-ground wind tunnel. The test section is 3m wide, 2m tall and 9m long. The tunnel features a 2:1 contraction constructed of equal radii arcs of equal arc length (owing to packaging and manufacturing constraints in the original design specification). The tunnel features a short settling chamber prior to the main contraction without straightening meshes or turbulence grids.

A fan unit with a 6-bladed impeller and 60% boss ratio is employed; some degree of flow straightening is provided by the impeller support structure consisting of 7 straightening vanes. Drive is provided by a 225kW thyristor-controlled DC motor in closed loop against a fan speed set-point (Hird 1979). This required some re-adjustment over the course of long runs, where work imparted to the working fluid would raise temperature, decrease density, thus dynamic pressure and thus freestream velocity (validated by observing spectral trends from model shedding phenomena). Maximum test velocity is limited to approximately 40m/s at 570RPM fan speed. Freestream turbulence intensity ( $I_{uu}$ ) is 1.8%<sup>1</sup>.

Dynamic pressure measurements from which velocity calculations are derived are taken with a single Pitot tube located at the start of the test section. Barometric pressure (assumed static - the test section ends with a breather slot to promote atmospheric pressure throughout) is acquired via a barometer located in the IWT control room, and test section temperature is acquired from a K-type thermocouple located mid test section. All three variables are passed as ratiometric analogue outputs, and were logged throughout all tests.

A new floor section was designed for the purposes of this work: 25mm medium density fibreboard was used to create rigidly fixed “outer floor” bounding the test section perimeter, and an interchangeable “lane simulation” section with pre-cut sections allowing the test models to be arranged in one or two vehicle lanes. Within these lanes, models could be longitudinally aligned in  $0.125\frac{x}{L}$  increments and laterally by up to 0.25 lane widths. The installation allowed quick, simple, accurate and repeatable alignment of test articles. The primary rationale for a new floor section was to address and reduce the roughness of the older section. Breakdown of vortex structures in the far wake is expected to occur at closer proximity to the model/vehicle base with a rough ground plane than over a smooth road (Bearman 1984).

#### 2.2.1.1 Coordinate system

The Cartesian coordinate system employed throughout defines the positive  $x$  direction as being downstream along the test section, with “right hand” convention consequently defining  $y$  and  $z$

---

<sup>1</sup>Earlier tests by Vino (2005) in the same facility list 1.53. The difference is potentially attributable to differences in sampling lengths/filtering techniques.%.



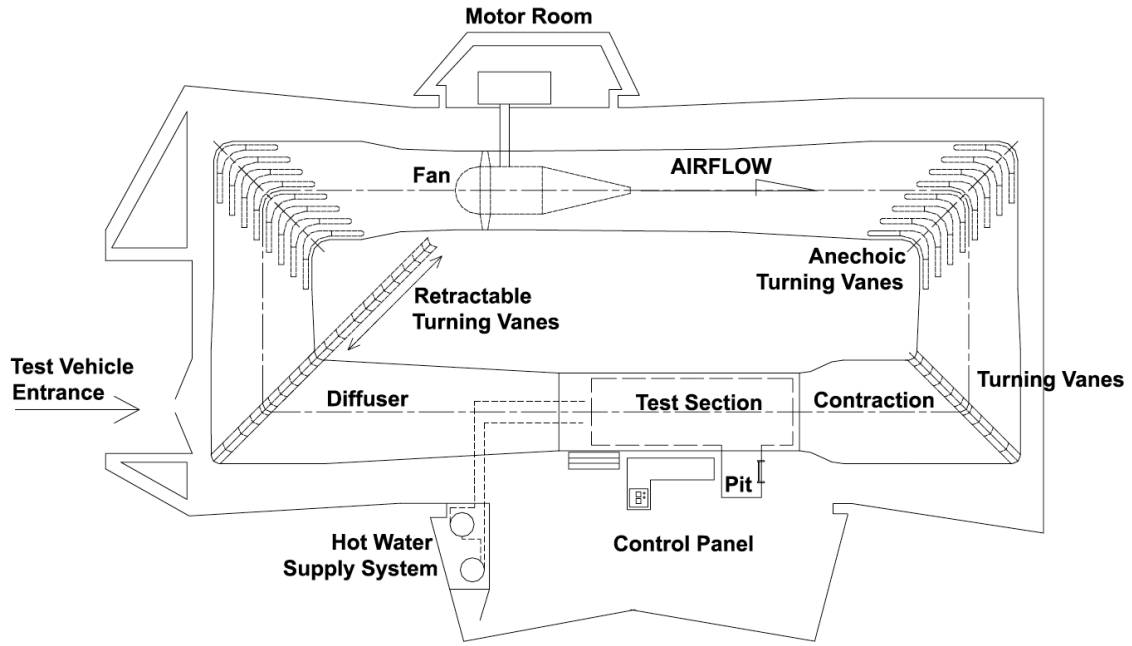


Figure 2.2: Schematic depiction of RMIT Industrial Wind Tunnel

(vertical) coordinates.

#### 2.2.1.2 Flow characteristics in test section

Particular importance was given to the characterisation of flow conditions throughout the IWT. The proposed experiments required models to be placed at various locations throughout the test section. It was deemed desirable to obtain data characterising the distribution of total pressure, static pressure and flow angularity in the volume of the test section occupied by the test models (Barlow et al. 1999). Once characterised, the effect of such conditions on the experiments proposed was able to be deconstructed with relative effects on proposed experiments determined.

This section presents a summary of the work completed in characterising IWT flows and serves as an indicator of performance (detailed deconstruction of relevant factors is given in Appendix A);

- *Flow angularity*: yaw was observed to  $\sim 3^\circ$  and pitch  $-2^\circ$  in the most upstream portion of the test section used (an exacting measurement, presented in Appendix A.1, page 222 - proved difficult given the limitations of available test equipment), as were effects of cross-plane pressure variations in known literature for the facility observable (Quirillo 1999). These effects were demonstrated not to obscure the ability of the IWT to deliver representative experimentation commensurate with known salient effects of the forms and platoon configurations

used (presented in chapters 3 and 4), however are almost an order of magnitude higher than recommended values for scale model automotive tests (Barlow et al. 1999).

- *Static pressure characteristics:* static pressure characteristics proved commensurate with expectations for a closed-jet facility with a breather slot located prior to the main diffuser (Barlow et al. 1999). Variance along the portion of test section used was considered sufficiently small ( $< 0.2C_{PStatic}$ ). As the primary works of interest concern two test articles placed in very close proximity, corrections for buoyancy are not offered throughout. A plot of static pressure variation is provided in figure A.8, page 230.
- *Freestream velocity measurement:* nominal freestream velocity was acquired via a single reference Pitot tube, installed with the total pressure tip coincident with the start of the test section. Cross-plane pressure variations throughout the test section, flow angularity and wall effects (diminishing the jet size along the length of the test section) contributed to freestream velocity being higher at the model location than at the measuring point. A Pitot-static tube was used to measure the difference, which was duly applied as a correction in post-processing.
- *Boundary layer characteristics:* The boundary layer displacement thickness (at 7.6-12.8mm) represented a significant proportion of underbody model clearance (37.5mm), a proportion higher than those commonly accepted in vehicle testing (Hucho et al. 1975, Wing 1981)<sup>2</sup>. Contemporary literature also indicated the salient features of a platoon could be replicated without boundary layer control (Zabat et al.<sup>3</sup>), but that model drag would likely be *increased* in near-ground proximity: to a “critical” ground clearance, the increase in flow velocity given a fixed separation point at the model base serves to promote stronger separation shear layers and decreased base pressure (Ahmed 1982, Bearman 1978, Wiedemann and Potthoff 2003)<sup>4</sup>. For an Ahmed model-like form,  $C_D$  is least sensitive to ground clearance at  $\alpha_c$  (Morel 1978a), about which the proposed experiments are conducted. Whilst some effect on flow phenomena vis-à-vis a (practically representative) moving ground plane are unavoidable, salient aerodynamic features of the test model were duly replicated in the installed condition (section 3, page 88). Further corrective actions are not warranted.
- *Turbulence properties:*  $I_{uu} = 1.8\%$  was observed in the test section beyond the boundary layer. The effects of this higher level of turbulence intensity than for reference experiments characterising the forms used (Ahmed et al. 1984) are difficult to quantify exactly about the backlight region, however literature discussed in section 1.2.2.2 (page 12) would indicate reduced drag through earlier reattachment of shear layers. This is tempered by the effects of turbulence length scale components matching model dimensions in model length; the effects and relevance of as much are discussed in Appendix A and found not to be significant.

---

<sup>2</sup>These values are for practical vehicles and are based on the growth and interference effects of boundary layers growing from both the test section floor and the vehicle underbody; the comparatively smooth underbody of the Ahmed Model (contrasted against that of most practical vehicles) is likely more tolerant of reduced ground clearance given relevant underbody boundary layer characteristics.

<sup>3</sup>In Chen et al. (1997).

<sup>4</sup>References to Fackrell in Ahmed (1982), Bearman (1978) are considered especially relevant.

### 2.2.1.3 Model location in the IWT

With particular respect to initial high static pressure at the trailing edge of the contraction and the possibility of higher-than-ideal freestream yaw at the test section leading edge, an initial scan was undertaken where force data was acquired from a single Ahmed with leading edge initially coincident with the test section leading edge, then moved downstream in 1 model length ( $L$ ) increments. Consistent results were achieved with the model's leading edge in the range  $3L - 8L$  from the test section leading edge. All model-in-isolation tests are therefore undertaken at the uppermost of this range. The leading model of a two-model platoon is similarly located.

## 2.2.2 Force measurements/balance system

### 2.2.2.1 JR3 Inc. 160M50A force balance system

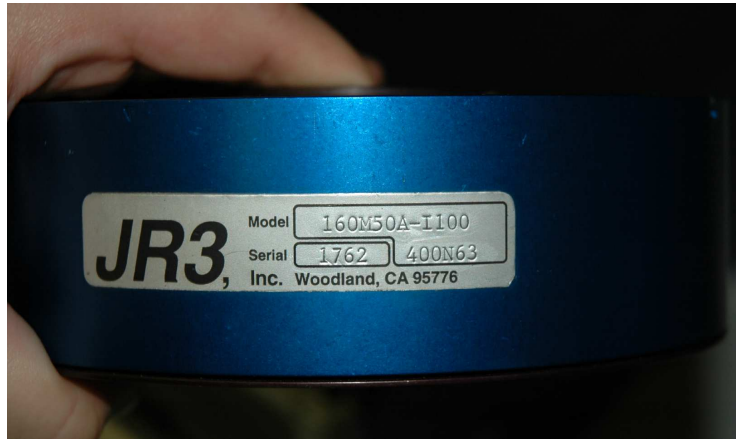
Force and moment data was acquired using a single six-axis force balance manufactured by JR3, Inc. (model 160M50A). Based about six metal-foil strain gauges mounted in a monolithic aluminium structure, the balance features internal signal conditioning electronics, incorporating requisite signal amplifiers and 16-bit analogue-to-digital converters. The balance used features 400N (giving a resolution of  $0.0122\text{N}^5$ ) load rating with accuracy 0.1N (JR3 Inc.). Though the available capacity is somewhat excessive against a maximum anticipated mean drag load of some 30N, the accuracy and resolution afforded are envisaged sufficient to provide the required discrimination in relative aerodynamic forces between test cases. The balance was last calibrated by JR3 Inc. six months prior to use; subsequent dead weight calibration checks in situ further validated this data.

The balance is interfaced via a bespoke PCI interface board. Data is streamed from the balance at 8kHz per channel. The interface board applies a six-by-six decoupling and calibration matrix (reflecting calibration data as stored in the sensor EEPROM and transferred to the interface board on acquisition - the balance is calibrated by JR3, Inc. prior to delivery). The resultant data stream is transformed in accordance with a user-assigned coordinate system, and finally passed through one of six software digital low-pass filters effected by an on-board DSP (at 500Hz and diminishing frequencies, where each frequency is a quarter of that preceding). This gives seven data streams in total (six and the original, unfiltered stream) along with force and moment vector magnitudes immediately available on the PCI bus (JR3 Inc.;I).

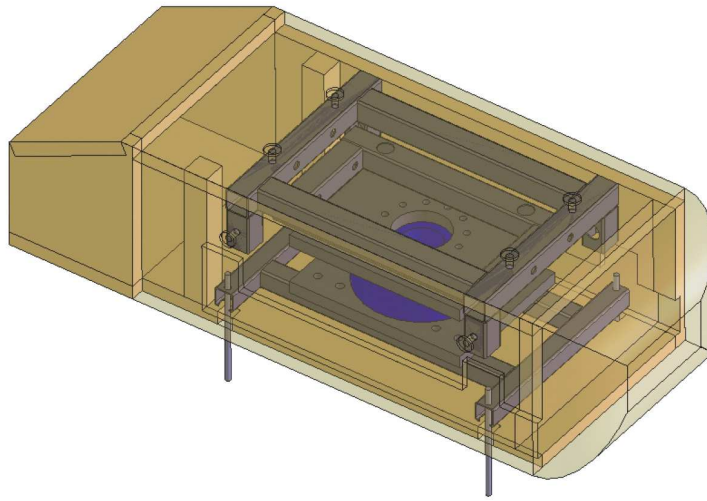
Whilst the device possess a high “mean” sampling rate, reliable timing information of discrete signals is not available. The potential performance force balance is thus not considered in a dynamic context.

---

<sup>5</sup>The reliability of the conversion is not known; no data is available on setting times for the JR3 ADC hardware. It is possible that the conversion is effectively accurate to lesser bits.



(a) JR3 160M50A force balance



(b) CAD Ahmed Model with transparent section showing force balance installation

Figure 2.3: JR3 160M50A force balance

### 2.2.2.2 Acquisition: the TFI JR3 Test Control Panel

Acquisition of mean force and moment magnitudes is accomplished using the *JR3 Test Control Panel*, a software package designed by Turbulent Flow Instrumentation to acquire data from the JR3, Inc. force balance system (as described above). The package allows zeroing, selection of sampling time, sampling rate and filter selection. The sampling rate is decimated from the force balance system's 8kHz/channel output rate. Analogue channels from installed National Instruments hardware may also be acquired, and are configured to acquire tunnel dynamic pressure and barometric pressure data. It is not possible to sample time history data in the current release<sup>6</sup>.

<sup>6</sup>Thus system noise was not able to be examined, however tests for repeatability proved acceptable using low-pass filtering as discussed in section 2.2.2.4.



Figure 2.4: Ahmed Model installed in test section

### 2.2.2.3 Incorporation into Ahmed Model

A test model was designed allowing the force balance to be incorporated internally, allowing the model in question to be moved about the tunnel test section as required with relative ease (figure 2.3b).

A steel frame bonded to the centre section of the Ahmed Model allowed a carrier frame incorporating the force balance (with requisite steel mating plates) to be bolted rigidly to the centre section. Once located, four stings as per model specification were fixed (using jig blocks to ensure correct ground clearance and zero geometric yaw) and bolted to a 55kg steel base plate. “Nose” and “rear” sections were finally attached.

### 2.2.2.4 Acquisition procedure

As the output software was, at the time of acquisition, incapable of giving a clocked output, dynamic output from the system was not suitable for spectral assessment. Care was taken to ensure that reliable statistical properties were taken. All force measurements were acquired using the supplied low-pass filter set at  $<0.2\text{Hz}$  for 30 seconds; despite low-frequency pulsing in the IWT from the near-mean peaking at  $3\text{Hz}$  (Appendix A.5.2, page 234), a 30 second interval was found to give repeatable data. Multiple such samples were taken and results averaged. Sensor offsets were removed prior to each run; test runs generating drift exceeding  $0.25\text{N}$  of the zero value on any axis

(an arbitrary limit) were discarded and repeated.

### 2.2.2.5 Error Analysis and corrections

In processing force data, the following errors from independent data are accounted for:

- Half the resolution of all measuring devices used in force coefficient calculation
- 0.1% full scale barometer accuracy (device manufacturer's specification)
- 0.1° temperature accuracy (device manufacturer's specification)
- 0.1N (Nm for moment data) force balance accuracy (device manufacturer's specification)
- 0.05% full scale dynamic pressure accuracy (device manufacturer's specification)

Results are calculated as nominal, minimum and maximum possible (with respect to error margins in calculation). Errors are presented in comparative graphs using error bars either side of the relevant nominal value (e.g. figure 4.1, 151).

As static pressure variation along the length of the test section is small and the solid blockage experienced in testing also small (<2% in all tests), force data are not corrected for buoyancy or blockage effects.

### 2.2.3 Dynamic pressure measuring instrumentation

Research work in this thesis makes extensive use of dynamic pressure measurement devices supplied by Turbulent Flow Instrumentation (TFI). Systems to acquire surface pressure and flow field are used.

These systems use sensing elements - pressure transducers - connected to measuring surfaces via tubing systems. Such approaches have traditionally required significant optimization of the tubing system (e.g. via use of restrictions and constrictions) to yield a useful frequency range of a few hundred Hertz (Bergh and Tijdeman 1965, Holmes and Lewis 1987a, Irwin et al. 1979). An ideal approach as such would typically be considered optimised were amplitude ratio to deviate not more than 5% from unity and phase response not more than  $\pm 0.1$  phase lag per Hz (Holmes and Lewis 1987a, Irwin et al. 1979). Such approaches are however limited in that the intended amplitude response is able to be maintained only over a range of a few hundred Hertz (Holmes and Lewis 1987a). Practically such methods are tedious, demanding significant iteration between setup, validation and optimisation processes. The systems used instead an automated digital method of reconstruction capable of completely correcting both amplitude and phase distortion effects.

### 2.2.3.1 Digital reconstruction of dynamic pressure data

An alternate approach first cited by Irwin, Cooper and Girard is to correct the time record at the transducer digitally using the known (theoretically or experimentally determined) transfer function of the pressure tubing system. This method is known as the Inverse Transfer Function (ITF) method (Irwin et al. 1979), and is used throughout this thesis extensively.

The method assumes that pressure at the measuring surface - that which seeks to be recreated digitally - can be represented in the frequency domain as such:

$$P_0(t) = \sum_{n=-\infty}^{\infty} A_n e^{i\omega t} \quad (2.1)$$

Thus pressure at the transducer diaphragm (representing the signal which is acquired and appropriately digitized) can be similarly represented:

$$P_1(t) = \sum_{n=-\infty}^{\infty} B_n e^{i\omega t} \quad (2.2)$$

Where both  $A_n$  and  $B_n$  are complex Fourier coefficients. There thus exists a tubing transfer function defining the characteristics of the tubing system used such that:

$$B_n = T_n A_n \quad (2.3)$$

Knowing  $B_n$  and  $T_n$ , the Fourier transform of pressure at the measuring surface can thus be obtained:

$$A_n = \frac{B_n}{T_n} \quad (2.4)$$

A time-domain record of fluctuating pressures at the measuring surface ( $P_0(t)$ ) can therefore be estimated by computing the inverse Fourier transform of  $A_n$ . Time records extending beyond the data block length used in estimation can be computed using multiple data blocks.

For digitized signals as per those acquired throughout this thesis, discrete Fourier transforms and discrete inverse Fourier transforms are computed using Discrete Fourier Transform (DFT) - implemented using Fast Fourier Transform (FFT) methods - the approach can be completed sufficiently quickly to allow near-realtime visualisation of data). Amplitude and phase distortion effects are completely corrected, conceptually allowing significantly more diverse tubing systems to be used effectively with far greater maximum useful frequency response. When combined with



near-transducer restrictions and other more traditional amplitude attenuators, frequency response can be extended further still.

Some limitations are inherent:

- The tubing transfer function must be accurate over the intended frequency response. Correct amplitude response is particularly important in computing spectral estimates of  $P_0(t)$ . As associated signal-to-noise error in  $P_0(t)$  increases with decreasing tubing transfer amplitude response, an amplitude response cutoff is typically employed: 0.4 is used throughout; the choice is arbitrary however supported in related works (Chen et al. 2000, Hooper and Musgrove 1997).
- The accurate recreation of all spectral components present in  $P_0(t)$  is dependant on the spectral resolution (e.g. particularly the frequency bin size) employed in the Fourier and inverse Fourier transforms used. Data outside such limits may be considered spurious.
- Aliasing must be avoided in the digitization process. Generally an anti-aliasing process involves:
  - Sampling with sampling frequency ( $F_s$ )  $\geq$  the lowest frequency below which all frequencies of interest are captured in the input signal ( $W$ ), such that  $F_s = \frac{1}{2W}$ , thus satisfying the Nyquist-Shannon sampling theorem (Bendat and Piersol 1993, Newland 1979, Steven 1999).
  - Applying a low-pass filter with cutoff at at a given frequency passing the highest frequency spectral energy content of interest, with a known transition band terminating in an accepted spectral noise floor by  $W$  (Steven 1999).

The latter point may be used in the absence of the former, or in conjunction with it should higher-frequency spectral content be deemed not of relevance to the results sought<sup>7</sup>. The tubing transfer function needs therefore to extend its useful range to a maximum frequency at least twice that of the highest significant energy content in the signal. Both experimentally and theoretically determined tubing transfer functions are utilised in this thesis.

### 2.2.3.2 Notes in processing data estimated via the ITF method

It is further considered important to process spectral data from estimated time histories using identical parameters to those used in estimation. As estimated data are essentially an inverse Fourier transform of select, discrete spectral content, processing parameters (particularly those involving frequency domain manipulation using Fourier methods), the “spectral resolution” of the data is essentially limited to the frequency bin sizes used in initial estimation processes. Whilst theoretically possible to reprocess estimated time records with larger length FFT blocks (e.g. for

---

<sup>7</sup>E.g. a common use is the removal of line noise and its harmonics.



the purposes of examining low-frequency content in greater detail), windowing functions used in estimation and processing complicate the contiguity of adjacent blocks in estimation; this approach can thus not be considered reliable. The variance in ensembles of spectral energy content also increases using this approach (as fewer blocks of data are processed).

Good sampling thus involved a researched combination of sampling frequency, cutoff methods, sampling time and FFT block sizes. These are duly discussed throughout where applicable.

### 2.2.3.3 Theoretical approaches in obtaining tubing transfer functions

A number of theoretical approaches to tubing response exist, including classical approaches by Helmholtz, Rayleigh et al. More modern approaches have since been developed based on theory by Iberall (1950) and further developed into the definitive form by Bergh and Tijdeman (1965). The latter is utilized in parts of this thesis, and is considered current state-of-the-art (Holmes and Lewis 1987a, Walter et al. 2007) in theorizing dynamic response in tubing systems (in lieu of recent developments in theorizing response of branched systems, which are not relevant to this work (Holmes and Lewis 1987b, Whitmore 2006)).

For a dimensionally unique section in a system of tubes and cavities, a formula theorizing the complex frequency response function (e.g. the tubing transfer function) for pressure ratio between two ends of a length of tubing with/without a cavity is applied. The frequency response function of the pressure ratio for the complete system (from measurement point to transducer diaphragm) can therefore be calculated recursively along unique, adjacent sections in the system. The approach's theoretical derivation incorporates Navier-Stokes, energy and continuity equations.

It is assumed:

- That pressure disturbances are sinusoidal in nature,
- That the working fluid behaves as an ideal gas,
- That flow within the system is laminar,
- That tubing is long with (e.g.  $L > 2D$ ) such that end effects may be negated - a number of sources (Walter et al. 2007) contrast the approach described with experimental results with short and long tubing systems,
- That sinusoidal pressure disturbances at the tube opening are small relative to mean conditions, as is cross-flow velocity small,
- That tubing used is rigid, straight (or possessing “large” radius curvature), of constant cross section a section of the tubing system, and of large thermal conductivity relative to surrounding air (such that wall temperature fluctuations are zero),

- That the sinusoidal frequency of disturbances is significantly less than  $\frac{\omega D}{c} = 1$  (this is satisfied in the work presented by at least two orders of magnitude where this theorem is used).

Response predicted using the method is particularly sensitive to tubing diameter (Behan and Watmuff 2006, Bergh and Tjeldeman 1965).

The exact nature and any apparent limitations of the method are described in further sections pertaining to the instruments that make use of it.

#### 2.2.3.4 Experimental approaches in obtaining tubing transfer functions

The experimental approach used in determining tubing transfer functions is similar to that used by Irwin et al. (1979) and since utilised by other authors using the ITF method (Hooper and Musgrove 1997). Simply, white noise in a desired frequency band is generated, amplified and reproduced using a cone driver (e.g. audio speaker). Response at the relevant pressure transducer(s) is logged, as is that of a reference microphone with known frequency response characteristics. The microphone is located from relevant measuring surfaces within a half wavelength of the highest frequency of interest. The tubing response function is generated via comparative analysis.

Some practical caveats regarding calibration exist, and are discussed in greater detail in Appendix C.

The calibration methods employed in the instruments used throughout are elaborated upon with the introduction of each instrument.

#### 2.2.3.5 Data acquisition software

All data acquisition in this thesis is completed using *Device Control* by *Turbulent Flow Instrumentation* (TFI), whose dynamic pressure instrumentation is largely used throughout (figure 2.5). In applying known calibration data, the software essentially automates the process of recreating an accurate time record (via ITF method) at the measurement surface.

It should be stressed that the exact workings of the package are unknown; Device Control is best conceptualised as a black box: raw transducer voltages as inputs, estimated time histories as outputs (this theme is further explored and to some extent deconstructed in Appendix D on page 251). Comparative analysis with published information indicates that the acquisition process evolves on those defined by (Hooper and Musgrove 1997) and Chen et al. (2000). It may be conceptualised as such:

1. A digitized time record of voltages at relevant pressure transducers is acquired for a user-configured block size (of  $2^N$ , representing a time interval of  $\frac{2^N}{F_s}$ ).

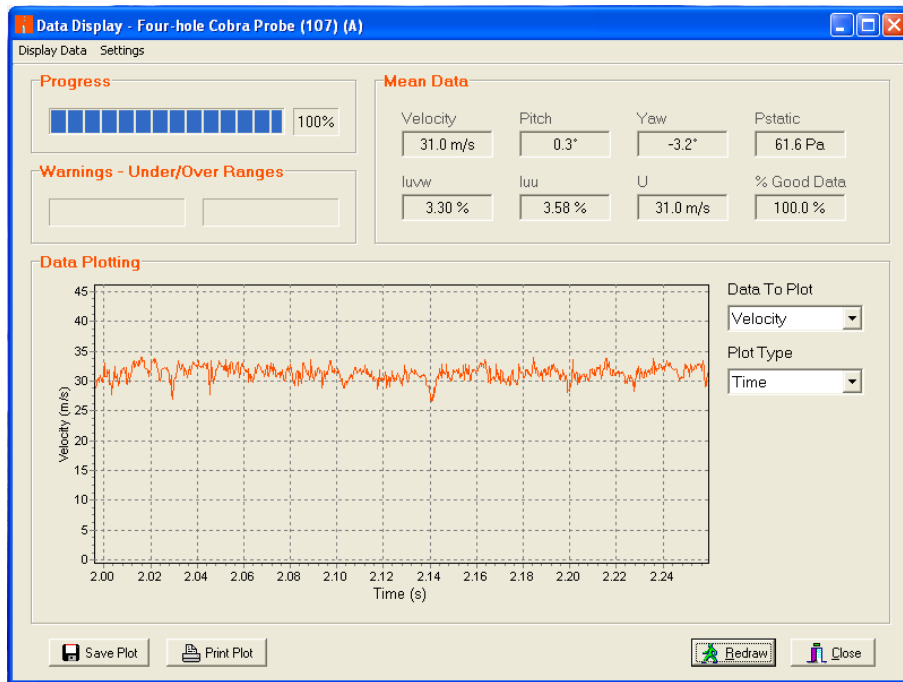


Figure 2.5: Real-time visualization in TFI Device Control

2. Voltage scaling corrections are applied reflecting individual amplifier/transducer characteristics.
3. The Fourier transform of the data block is taken, thus transforming data to the frequency domain. Digital anti-alias filtering is applied.
4. The tubing transfer function is interpolated to the block size allowing application of the ITF method as per equation 2.4<sup>8</sup>. Data pertaining to frequency components below a set amplitude ratio cutoff are truncated. A time record of block length corresponding to pressure at the measuring surface is thus estimated.
5. Where multi-hole probes are concerned, static calibration data (discussed in 2.2.5.1 on page 78) is applied to resolve pressure values from individual transducers to static pressure and velocity component data.
6. Data are written to disk at a selectable rate and block size (and are decimated where necessary).

<sup>8</sup>Though ambient conditions are configured (either by the user as constants during program operation, or reconfigured with each sampling event as the program is called externally via DLL (Dynamic Link Library) as sampling inputs, and though such conditions affect frequency response of tubing systems (Behan and Watmuff 2006, Bergh and Tijdeman 1965, Iberall 1950), it is not known whether or not these serve to affect the dynamic calibration. It is considered unlikely; decompilation of the calibration file indicates that ambient conditions during calibration are not stored.

Whilst the software supports a variety of data acquisition hardware, a software engine to correct for interchannel delay induced by multiplexing of analogue inputs is not included in the release used. Effects pertinent to the data acquisition system employed are discussed in Appendix D on page 251.

### 2.2.4 Surface pressure measurements

Whilst mean surface pressures are useful in determining generalized characteristics, dynamic measurements can give a most useful insight into periodic phenomena occurring over some surfaces, allowing better definition of relevant flow phenomena.

Time records of surface pressure data are obtained via use of the *Dynamic Pressure Measurement System* (DPMS, manufactured by TFI). The unit features four 'modules' consisting of fifteen differential pressure transducers. Within each module all transducers share a common static pressure reference<sup>9</sup>. Acquired signals are temperature compensated. Each module's electrical outputs are connected to a common box featuring a single four channel multiplexer. This box is in turn connected to the DAQ card. As each channel has its own transducer, no mechanical switching is employed. The number of channels able to be acquired in a single test is thus limited by the transducer count.

Frequency response characteristics are determined theoretically using configuration utility provided by the manufacturer. The theoretical model implemented in accompanying software is as per Bergh and Tijdeman (1965); a tubing system is thus modeled as a series of tubing sections of unique length and diameter in addition to the DPMS' own internal hardware. A 2mm<sup>3</sup> transducer volume is connected to a 20mm long, 0.6mm diameter tube section terminated in a brass fitting. The smallest diameter tubing able to be physically fitted to this tubing is of 0.8mm diameter, as utilized in this thesis (thus eliminating the need to manufacture intermediate sections and providing inherently improved frequency response in having an effective near-transducer restriction). Model tubing length was 350mm length (owing to packaging restrictions). This allowed for a small improvement in frequency range prior to the first harmonic over related work using the same system (Vino 2005). A typical bode plot is provided in figure 2.6.

A cutoff amplitude of 0.4 is applied in post-processing (in practice this is not significant; as the sampling frequency employed is far lesser than the cutoff point).

#### 2.2.4.1 Tubing properties

Various alternatives were considered; PVC tubing was chosen over teflon and silicon based alternatives as having superior resistance to crushing (over teflon) and a far more rigid tube wall (over

---

<sup>9</sup>Throughout testing, all static pressure lines are terminated exterior to the test section for convenience; static pressure is thus assumed to be equal to barometric pressure. A slight variance exists and is discussed in Appendix A.3, page 229.

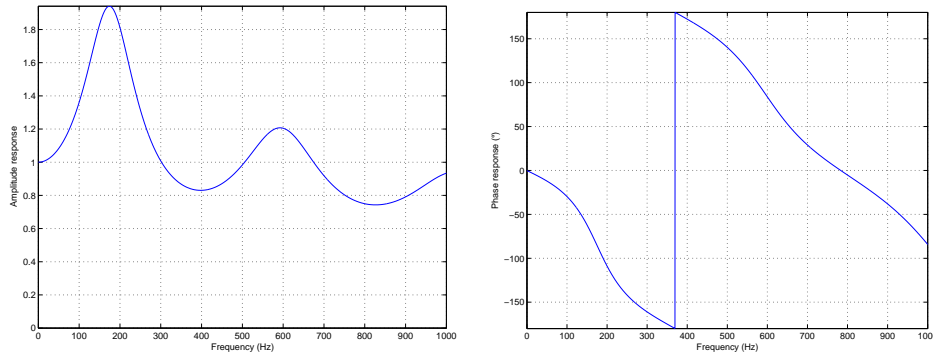


Figure 2.6: Typical Bode plot of frequency response function of DPMS system implementation

silicon).

Whilst the use of plastic tubing is not uncommon, it is also not uncommon for such tubing to exhibit some deviance from best theoretical predictions (Behan and Watmuff 2006, Holmes and Lewis 1987a). Holmes and Lewis (1987a) compared the effects of using PVC and steel tubing in controlled experimental conditions. Whilst steel offered excellent agreement with theory, PVC - with lesser rigidity and decreased thermal conductivity - presented notable error about and beyond the second resonant peak, albeit good agreement prior to it. The work cited however had good control over test temperature and tube diameter; a manufacturing tolerance of 0.1mm existed on available tubing giving rise not only to variance in mean diameter but additionally in tube diameter along a given length. Changes in air temperature and density are further unable to be accounted for in calibration over the test run. Some extremities are displayed in figure 2.7

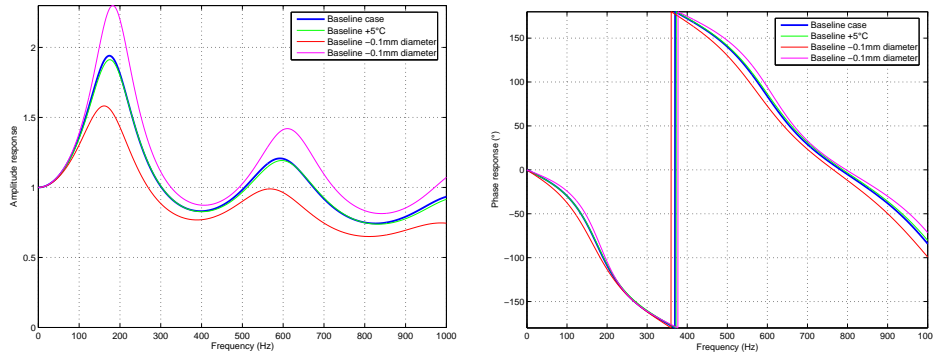


Figure 2.7: Effect of likely experimental unknowns on tubing system response

Figure 2.7 clearly indicates the significance of variance in tubing diameter on frequency response. Whilst ambient changes affect theoretical (Bergh and Tijdeman 1965) and experimentally determined (Behan and Watmuff 2006) tubing transfer functions, their effect is considered negligible relative to that of tubing diameter. It is therefore not compensated for in initial time record estimation or in post processing. It should be appreciated that that good agreement exists be-

tween the scenarios presented in figure 2.7 for frequencies less than approximately half the first resonance. It is later demonstrated that frequencies of interest pertaining to this work fall within this range, and that therefore even a 10% variance in tube diameter is acceptable for the tubing system configuration employed<sup>10</sup>.

Dynamic calibration of the pressure measurement system was therefore not undertaken.

#### 2.2.4.2 Pressure tap location

55 pressure taps shared over half the backlight and base and 39 taps over half the model nose sections were utilised. This is considerably less than those employed by Ahmed et al. (1984) originally, however the original implementation utilised a mechanically switched system to obtain time-averaged pressure data. The current system favours dynamic pressure acquisition and is hence limited by 60 available transducers<sup>11</sup>.

#### 2.2.4.3 Noise floor

No method is employed in the acquisition software to truncate data within the noise floor. A simple test series was undertaken to characterise:

- The noise floor (after a “system zero” in a “no flow” condition - taken as a maximum across all pressure taps),
- The worst-case drift (a repeated acquisition of the “no flow” condition) after 30 minutes acquisition at typical test speed (again, taken as a maximum across all pressure taps, and from an initial “cold” test section - giving rise to a significant temperature gradient relative to the conditions under which noise floor data were acquired), and,
- Typical test data at a relevant  $Re$  for both  $\alpha = 25^\circ$  and  $\alpha = 35^\circ$  models in isolation (for which the 95% confidence interval of spectra across all pressure taps is presented for each frequency bin<sup>12</sup>).

Figure 2.8 presents relevant results. Line noise is clearly evident in noise and drift data at 50Hz and harmonics thereof. Drift is shown to be very small. The lower confidence limit associated with the spectral performance of typical test data exceed the noise floor by at least two orders of magnitude in lieu of line noise. Whilst a clear spectral peak exists in the  $\alpha = 25^\circ$  case at a frequency commensurate with line noise, the magnitude of the data peak exceeds that of line noise by at least two orders of magnitude.

---

<sup>10</sup>The tubing employed had a nominal diameter of 1.0mm with a 10% manufacturing tolerance.

<sup>11</sup>55 were used to allow for some redundancy in testing

<sup>12</sup>The Null Hypothesis was rejected at the 5% confidence level in each confidence interval computation.

Noise and drift effects associated with the DPMS are not considered to significantly affect acquired data. The DPMS is deemed suitable for the experiments undertaken.

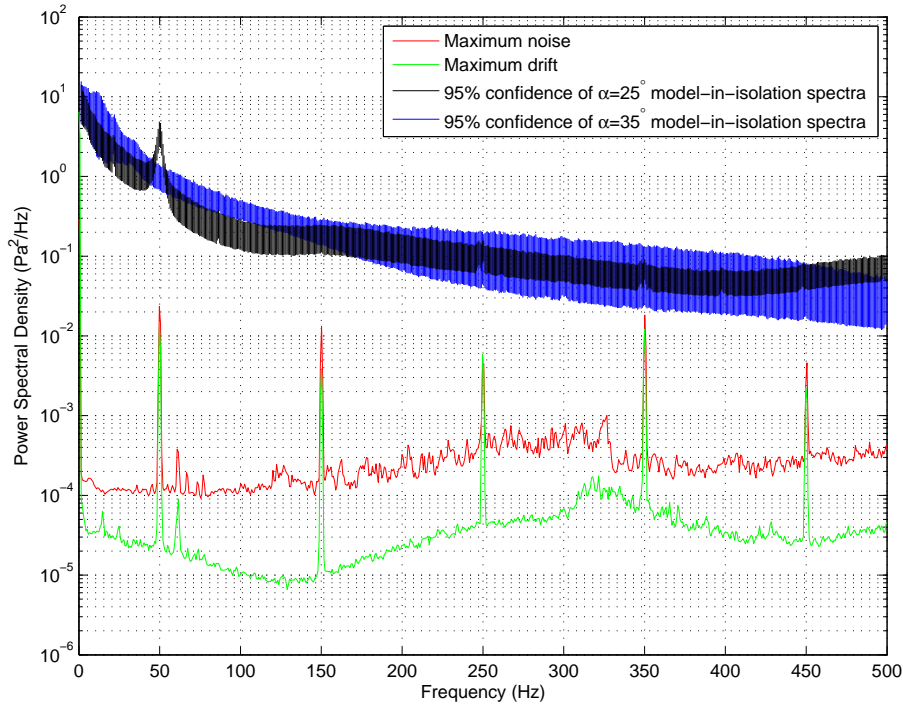


Figure 2.8: Typical data, noise floor and drift effects associated with DPMS system

## 2.2.5 Flow field dynamic pressure measurement

### 2.2.5.1 Cobra probe by Turbulent Flow Instrumentation

The Cobra probe is a four hole pressure probe capable of resolving flow pitch and yaw components in a  $\pm 45^\circ$  cone of acceptance from the freestream direction with dynamic response exceeding 2.5kHz. It has been tested, developed and validated extensively in a variety of flow conditions (Chen et al. 2000, Hooper and Musgrove 1997), and is thus deemed sufficiently validated to be used throughout this thesis. It is a useful replacement for traditional dynamic flow field instrumentation where conditions allow, being extremely robust, simple to use and configure, completely pre-calibrated and highly insensitive to external noise sources. Unlike much traditional dynamic instrumentation, local static pressure information is also provided. The Cobra probe is used only for tunnel calibration throughout this work, but is presented as a necessary prologue to the ECA probe (section 2.2.5.2), which is developed from it.

The use of multi-hole probes to resolve three dimensional flows is not new; the Cobra probe is a development of work dating to the early 1970's. Significant development from the initial



Figure 2.9: Detail of Series 100 TFI Cobra Probe

concept has incorporated advances (e.g. in calibration, in incorporation of the ITF method (Irwin et al. 1979) allowing significant extension of the dynamic performance and range, in packaging, in supporting software, etc). It takes its name from its distinctive shape, which allows rotation of the probe about its longitudinal axis without alteration of the measuring point (Hooper and Musgrove 1997). Similar multi-hole probes using identical tubing correction exist in research (Sims-Williams and Duncan 2002, Yang et al. 2006), however are not commercialised nor are yet capable of the frequency response offered by the Cobra probe.

The probe tip geometry (figure 2.9) demonstrates excellent Reynolds similarity (compared to traditional conical multi-hole probe geometries) in the range 16-110m/s, encompassing the test conditions under which it is used throughout this research (Hooper and Musgrove 1997). The probe features four holes located on a faceted head 2.6mm in diameter. To decrease head size and increase spatial resolution, four transducers are located not in the probe head but in the probe body, and connected via a system of pressure tubing consisting of four 0.5mm diameter steel tubes. The ITF method described above (Irwin et al. 1979) is used to correct for frequency distortion.

As the relationship between raw, acquired data and the final, resolved output time history is complex - and as workings relevant to the Cobra probe define key instruments used throughout the research presented - the processes defining the use of the probe are presented below.

The probe is supplied calibrated by TFI, and is composed of three parts:

- *Ratiometric scaling*: Ratiometric voltage-to-pressure scaling for each transducer is calibrated using a deadweight and reference transducer. As the transducers share a common, manifolded static pressure port, this calibration may be easily performed by the user (relevant input fields exist in software).
- *Velocity calibration*: The pressure field acquired by the probe's four transducers (duly converted to non-dimensional ratios) are related to dynamic pressure, total pressure, pitch and yaw data as obtained by orientation of the probe in a known, reference flow through various



pitch, yaw and velocity combinations<sup>13</sup>. These combinations are referred to as calibration surfaces<sup>14</sup>. These are stored as lookup tables; all raw values are converted in real time to dependent pitch, yaw, velocity magnitude and static pressure components. These calibration data lends the Cobra probe velocity and angular accuracies of  $\pm 0.3\text{m/s}$  and  $\pm 1.0^\circ$  respectively<sup>16</sup>. As calibration data are not reliable for very low speed flows, data below  $2\text{m/s}$  are truncated.

- *Dynamic calibration:* In accordance with the ITF method (Irwin et al. 1979), independent tubing transfer functions are experimentally obtained for each transducer over a  $6\text{kHz}$  range in 513 frequency bins<sup>1718</sup>. (This data attempts to incorporate multiplexing effects in acquisition, which is examined in detail in appendix D, page 251).

User alterations to static and dynamic calibrations are not supported.

In incorporating the ITF method, it should be stressed that processed data representing acquisition at the probe tip is effectively four estimates using Fourier techniques, resolved to a single point in time and space. To some degree the accuracy of as much is significantly dependent on factors pertaining to the estimation technique (e.g frequency bin size), particularly where frequency spectra of acquired data are concerned.

The probe's dynamic response is limited by the following factors:

- *Transducer noise floor:* tests with a single Cobra probe logged as four analogue channels over 16 bits input. Indicate the noise floor to be within two bits (where the velocities used in testing was acquired over 14-15 bits).
- *Amplitude response correction error:* as frequency increases, the amplitude response of the system tends towards zero. The correction thus applied by the ITF method thus introduces an increasing amount of noise into estimates; were a limit not introduced, these would increase beyond the noise floor of the system hardware in an undulating manner.

The probe's dynamic response is thus primarily limited by an amplitude ratio cutoff. This is arbitrarily set at 0.4, a value noted (albeit set similarly arbitrarily) in literature (Hooper and Musgrove 1997). As all four channels' amplitude response do not pass this threshold at the same frequency (and as subsequent resonance peaks in amplitude response may peak beyond

---

<sup>13</sup>These combinations are not disclosed, nor the interpolation method between calibration points.

<sup>14</sup>A number of methods have been documented, using one (Chen et al. 2000), three (Hooper and Musgrove 1997) and six (Shepherd, 1981<sup>15</sup>) calibration surfaces. Lesser calibration surfaces are desirable; the greater their number the greater the potential for error in interpolation along surface boundaries. Cobra Probes in service at RMIT University feature both single and multi-zone calibration data, it is cited in product literature that both methods may be used depending on the flow angularity, however the exact method by which this is effected is not disclosed.

<sup>16</sup>As stated by manufacturer data, see Mousley (2006).

<sup>17</sup>This yields a frequency bin size over  $11\text{Hz}$ ; the method of interpolation for block size is not known.

<sup>18</sup>From extracted calibration data, it is observed that the range  $\text{DC}-22\text{Hz}$  is not acquired experimentally and is instead pulled linear between hypothetical (zero) and nearest observed values by the device supplier. This is discussed further in Appendix C.

the cutoff<sup>19</sup>), it is assumed that the cutoff is effected at the frequency corresponding to that at which the amplitude ratio cutoff is first exceeded by any channel<sup>20</sup>.

- *Physical obstruction of turbulent components in flow:* commensurate with the Taylor concept of a turbulent structure advected past the probe head, the probe is capable of resolving flow structures with minimum size an order of magnitude greater than the head size (Hooper and Musgrove 1997). At 30m/s - as used throughout this research - the sampling frequency should permit acquisition of frequencies not exceeding 1.15kHz.
- *Digitization errors:* depending on sampling and estimation parameters, spectral leakage may limit the clear observation of spectral peaks. Where frequency bin sizes are especially coarse, some components may be represented with significant magnitude in two or more frequency bins. Given limitations in discretising analogue waveforms, to some small degree the reconstruction of such data using Fourier methods introduces spectral components across almost all frequency bins, raising the noise floor of the system beyond that of the base hardware alone. Where spectral content is well defined, relevant peaks are observable beyond the noise floor; at very low levels they may be indistinguishable from it.

Figure 2.10 presents a sample spectra acquired using a Cobra Probe. Aside from spectral peaks relative to the method used to restrain the device, this data is as expected, and clearly shows:

- A noise floor (taken from the  $U$  component) from approximately 1.5kHz.
- The amplitude ratio cutoff at approximately 2.75kHz.

The Cobra probe's response is thus useful where spectral energy content is of significant magnitude to exceed the above limitations; in the case of flows pertinent to the work undertaken, spectral response is limited to 1.5kHz. Frequencies of interest throughout are considerably lower; therefore whilst these limitations do not affect the operation of the Cobra probe relative to the work presented, it is noted that the Cobra probe does not replace hot-wire anemometry where more sensitive assessments of flow turbulence are required (or where greater frequency response than afforded is necessary).

### 2.2.5.2 ECA Probe by Turbulent Flow Instrumentation

The ECA probe (figure 2.11) is a 13-hole development of the same principles underlying the Cobra probe. Its key advantage is a  $\pm 135^\circ$  flow acceptance cone, improving significantly on the

<sup>19</sup>All Cobra probes used throughout this work exhibit a third resonant peak in amplitude response extending beyond 0.4 beyond 4kHz; this range is effectively low-pass filtered by anti-alias filters (effective at 3kHz) employed in acquisition software.

<sup>20</sup>Extraction of frequency response calibration data for the four probes used throughout this work shows this cutoff to be first effective (e.g. where any one of four tubing systems crosses the cutoff) at frequencies between 2,660.2-2,777.3Hz.

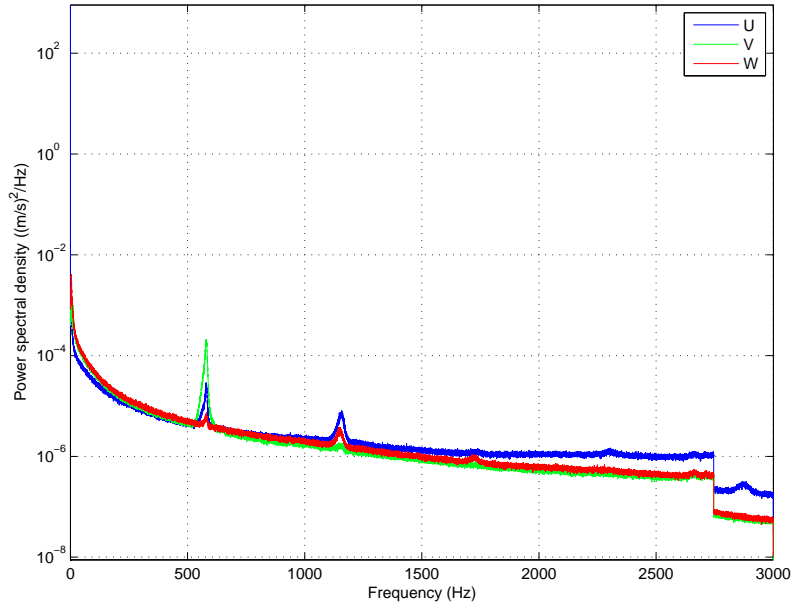


Figure 2.10: Sample data set taken with Cobra probe at 6kHz, estimated using 65,536-point FFT (frequency bin size  $<0.1\text{Hz}$ ), processed using Welch's method over 331 realizations

$\pm 45^\circ$  offered by the Cobra probe. An ability to study recirculating flows is thus afforded. As the probe body obscures possibilities outside this cone, some consideration regarding probe orientation relative to dominant flow angularity is required. Suggested orientations for a critical Ahmed Model are provided by Vino (2005); these were employed throughout with some simplifications for wake traverses of regions with flow angularity deviating little from the freestream.

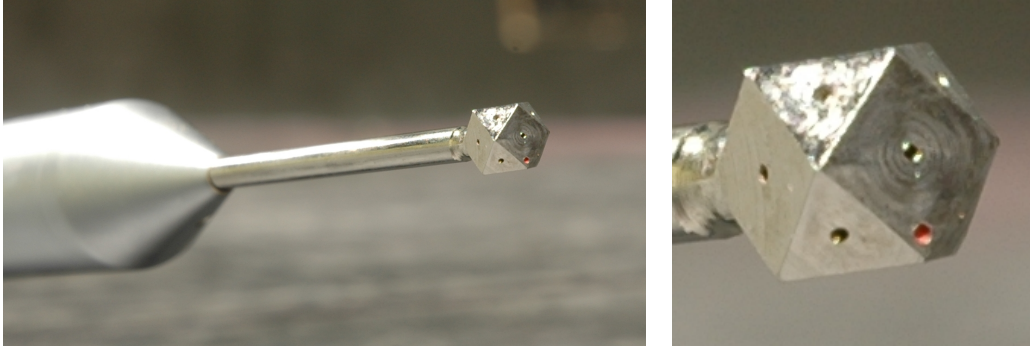


Figure 2.11: ECA probe detail

Though a relatively new instrument, validation has been undertaken against hot-wire anemometer and Cobra Probe instrumentation with favourable results (Vino 2005, Watkins et al. 2004).

Further technical details regarding ECA and Cobra probes are discussed in Appendix B. Of particular interest, the ECA probe was not supplied with an experimentally-determined dynamic

calibration. This did not prove detrimental, however modifications to calibration data to improve dynamic response are discussed further in Appendix D.4.2 (page 258).

### 2.2.6 Three axis traverse

A three axis traverse (supplied by TFI) was used to locate the Cobra and ECA probes in the flow field, shown in figure 2.12. The traverse incorporates stepper motor driven ballscrews on  $y$  and  $z$  axes, and a worm drive controlling a roll axis (along the telescopic  $y$  axis). The stepper motors are driven by an open-loop circuit.



Figure 2.12: RMIT three-axis traverse during pre-fit

Some modifications were made to the traverse. The probe was mounted on a steel section clamped to the telescopic section<sup>21</sup> (and thus cantilevered), a mechanical lockout was fashioned and implemented on the roll axis. Similarly, as the  $y$  axis system was mounted in cantilever on the main frame (a single linear slide and the relevant ballscrew provided a limited resistance to twist given incident force), a second, thin steel frame was fashioned slightly inboard of the traverse  $z$  axis frame, and bolted to both floor and ceiling. Whilst free to slide up and down along this, bulk twisting of the  $y$  axis system about the  $z$  axis frame was much reduced.

Movement in the  $x$  axis was achieved by simply moving the traverse up and downstream. A centreline painted into the tunnel floor and the adjoining floor panels provided effective alignment of the system when moved.

The limited  $y$  movement of the traverse limits acquisition to one half of the wake plane per scan (i.e.  $-y$  or  $+y$ ). The process used to calibrate and align data sets across unique  $xz$  planes is described in Appendix A.1 (page 222).

The location of the traverse in the  $-y$  section of the test section (relative to the model's location) is likely to have an effect on the wake flows observed. Whilst (in lieu of a non-invasive method of measuring data) this cannot be quantified, later work demonstrated that this did not

<sup>21</sup>Figure 2.12 shows a prototype of the probe sting. The final implementation used throughout testing had a main section twist of  $90^\circ$  (i.e. aligned with flow) to minimise bluffness.

limit the ability of experimentation undertaken with the traverse to deliver representative data with all salient flow features intact.

### 2.2.7 National Instruments NI-6034E data acquisition card

All pressure data are acquired using a National Instruments NI-6034E data acquisition (DAQ) PCI card. It is capable of acquiring 16 channels of analogue data with 16 bits resolution at an aggregate sampling rate of 200kS/s.

It features a single analogue-to-digital converter multiplexed using internal and external multiplexers to facilitate multichannel acquisition; whilst multiple samples may be timestamped identically, all are sampled at unique instants. As the work undertaken involves acquisition of highly dynamic data and resolution of multiple data channels to a single instant in time, a thorough understanding of the sampling engine is required. This is further explored in Appendix D (page 251).

In addition to analogue inputs, card features digital I/O. Where required (see section 2.2.4, page 73), these are used to switch an external multiplexer.

## 2.3 Spectral processing methods

Spectral methods are used extensively in processing to characterise time-dependent phenomena in - or between - various data sets of estimated time histories. Using Fourier methods, these time histories may be decomposed in processing on a block-by-block basis into discrete sinusoids of varying phase and amplitude<sup>22</sup> This property allows the manipulation of the original source in the frequency domain, in turn lending such manipulations to a wide variety of engineering applications. Some are utilised throughout the work presented.

References throughout this section span Bendat and Piersol (1993), Newland (1979), Smith (2002) and Steven (1999).

### 2.3.1 General theory

Whilst possible to express spectra via correlation functions (as per Appendix A.5.3.1, page 236) or via analogue filter design, the introduction given in section 2.3 lends the following theory to be expressed in terms of Fourier transforms.

Thus, for two stationary, random processes  $x(t)$  and  $y(t)$ , the relevant Fourier transforms over the  $k^{\text{th}}$  record of length  $T$  may be expressed as:

---

<sup>22</sup>(As per earlier comments) they are similarly estimated using these methods.

$$\begin{aligned} X_k(f, T) &= \int_0^T x_k(t) e^{-j2\pi f t} dt \\ Y_k(f, T) &= \int_0^T y_k(t) e^{-j2\pi f t} dt \end{aligned} \quad (2.5)$$

The spectral density function between these two time histories - the *cross-spectral density* - for  $n$  time signals may be defined as:

$$\begin{aligned} S_{xy}(f) &= X^* Y \\ &= \frac{1}{nT} \sum_{k=1}^n (X_k^*(f, T) Y_k(f, T)) \end{aligned} \quad (2.6)$$

Equation 2.6 defines a *two-sided* function (that extends into negative frequencies). The single-sided expression ( $G_{xy}$ ) and relevant single-sided autospectral density function ( $G_{xx}$ , comparing spectral density within the same time history) are thus expressed:

$$G_{xy}(f) = \frac{2}{nT} \sum_{k=1}^n (X_k^*(f, T) Y_k(f, T)) \quad f > 0 \quad (2.7)$$

$$G_{xx}(f) = \frac{2}{nT} \sum_{k=1}^n |X_k^*(f, T)|^2 \quad f > 0 \quad (2.8)$$

The above are complex functions, wherein the real and imaginary components are so defined:

$$\begin{aligned} C_{xy}(f) &= \text{Re}(G_{xy}) && \text{Coincident spectral density function} \\ Q_{xy}(f) &= \text{Im}(G_{xy}) && \text{Quadrature spectral density function} \end{aligned}$$

The complex representation of  $G_{xy}/G_{xx}$  can thus easily be manipulated to give magnitude and phase:

$$|G_{xy}(f)| = \sqrt{C_{xy}^2(f) + Q_{xy}^2(f)} \quad (2.9)$$

$$\theta_{xy}(f) = \tan^{-1} \left[ \frac{Q_{xy}}{C_{xy}} \right] \quad (2.10)$$

The above is particularly useful in comparing spectra between two points, where flow structures may be better elucidated by comparing time records taken simultaneously and allowing characterisation of whether a given flow phenomena with a defined spectral peak operates in or out of phase across multiple points. A multi-point comparison of relevant magnitudes can be characterised using a *coherence function* ( $\gamma_{xy} : 0 \leq \gamma_{xy} \leq 1$ ), which normalises cross spectral magnitude by the product of the autospectral densities of the records processed (which it cannot exceed<sup>23</sup>).

### 2.3.2 Power spectral density

Power spectral density (PSD) is a measure defining the distribution of a signal's power with frequency, allowing key periodicity to be effectively captured.

True power spectral density cannot be captured using digital acquisition and/or via use of Fourier methods in processing, as there exist inherent measures in both - thus it can only be estimated. The estimate of power spectral density is completed by means of a squared DFT, such that all elements of the resultant periodogram are real, and that the periodogram is single-sided. Inherent noise associated with digitisation and Fourier methods can be reduced via ensemble averaging. Simply put, the discretized stationary signal is divided in to equal-size, successive blocks: each has its periodogram calculated; the final result being the ensemble average of power per frequency bin. This method is known as *Bartlett's method*. Averaging reduces variance in the final result - logically, an infinite number of averaged sample sets would exhibit zero variance (at the cost of reduced estimate resolution).

An evolution of Bartlett's method used throughout this work is *Welch's method*, differing in two aspects:

- A *window function* is applied to the data blocks. Windowing essentially smooths discontinuities at the start and end of each data block, reducing *spectral leakage*: whilst averaged periodograms process finite blocks of data, the harmonic functions used to estimate spectral components represent essentially infinite processes, and “anticipate” that their application about the discontinuities remains smooth and continuous. This “wrap-around” quality rarely exists, however, rendering the estimate imperfect and having redundant energy redistributed or “leaking” through other harmonic estimates of other frequency components. In this instance, the application of a window function that smoothly tapers off gain to attain a zero or near-zero magnitude at the data block's extremities usefully diminishes this characteristic.

Spectral leakage also occurs give the discrete frequencies used to estimate spectral components; where sufficient resolution does not exist, spectral energy is represented over adjacent bins.

Various window designs exist based on form characteristics giving better narrowband or broadband dynamic performance. The Hann window is used throughout this research, being

---

<sup>23</sup>A phenomenon known as the *cross-spectrum inequality*.

commonly recognised as a moderate, all-purpose window. It is defined below for an  $N$  length window, where  $n : 0 \leq n \leq N - 1$ :

$$w(n) = \frac{1}{2} \left( 1 - \cos \frac{2\pi n}{N-1} \right) \quad (2.11)$$

It should be stressed that window application is not a substitute for frequency bin width: larger block sizes always increase signal-to-noise ratio and increase spectral resolution. Care is taken throughout to maximise block size where required.

- As windowing functions reduce discard much data at the block's extremities, these may be re-analysed by splitting the signal into overlapping segments (typically 50% overlap as used throughout). Negative effects of overlapping are effectively mitigated by the significant differences in window function amplitude for overlapping segments.
- As windowing introduces a bias error in results, gain adjustment of the output spectra is required where exacting power spectral densities are required. As this adjustment is strictly a function of the window function, gain adjustment is not undertaken throughout given consistent gain characteristics and an interest in relative - not absolute - data.

Where a “flat top” or “rectangular” window function is applied (e.g. essentially no windowing function, or a windowing function of one at all points), overlapping is not required and Welch's method functions as Bartlett's.

Equation 2.12 denotes the  $m^{\text{th}}$  block from stationary signal  $x$  with window function  $w(n)$  applied for  $K$  frames and  $R$  window size:

$$\begin{aligned} x_m(n) &\triangleq w(n)x(n+mR) \\ \text{where } n &= 0, 1, \dots, M-1 \\ m &= 0, 1, \dots, K-1 \end{aligned} \quad (2.12)$$

The periodogram for the  $m^{\text{th}}$  block is then so defined:

$$P_{x_m M}(\omega_k) = \frac{1}{M} |\text{FFT}_{N,k}(x_m)|^2 \triangleq \frac{1}{M} \left| \sum_{n=0}^{N-1} x_m(n) e^{-j \frac{2\pi n k}{N}} \right|^2 \quad (2.13)$$

The estimated power spectral density by Welch's method using the DFT is thus:

$$\hat{S}_x^W(\omega_k) \triangleq \frac{1}{K} \sum_{m=0}^{K-1} P_{x_m M}(\omega_k) \quad (2.14)$$



## 2.4 Qualitative visualisation

Qualitative visualisation of the flow field and its on-body shear effects is achieved using smoke visualisation and oil-and-soot depositions.

### 2.4.1 Smoke visualisation

White smoke - generated by pumping mineral oil through a wand and burning it at a heated tip - is injected directly into, or upstream of, coherent elements of the flow field thus allowing their visualisation.

Freestream velocity was limited to  $7\text{m/s}$  -  $Re = 4.2 \times 10^5$  - with respect to a limited frame rate in video acquisition (60 frames per second<sup>24</sup>) and practical intentions to:

- Facilitate lighting (with a limitation on flow rate, a lower freestream velocity allows for denser smoke and thus more effective contrast in visualisation), and,
- To limit the volume of smoke in the tunnel at any one time (the IWT is not equipped with a facility to readily exhaust its working fluid).

The Ahmed Model exhibits some Reynolds sensitivity (both in literature, section 1.3.3, page 40, and validated in the course of this research, section 3.1.1, page 88). However given sharp, well-defined separation lines, salient flow structures are known to remain consistent to a half order of magnitude below the  $Re$  employed in smoke visualization (Drouin<sup>25</sup>).

Coherent dynamic phenomena are known to exist over at least the base surface (discussed in section 1.3.1, page 21) in the range  $St = 0.2 - 0.5$ , where  $St$  defines the *Strouhal number* such that:

$$\begin{aligned}
 St &= \frac{fL}{v} \\
 \text{where } f &= \text{Frequency (Hz) associated with oscillation} \\
 L &= \text{Characteristic length (m)} \\
 v &= \text{Normalising velocity (m/s)}
 \end{aligned} \tag{2.15}$$

The characteristic length in equation 2.15 throughout this work refers to the square root of the model frontal area (for consistency with published data). On published literature this gives a maximum shedding frequency of approximately 14Hz. The available frame rate is thus sufficient to capture dynamic phenomena associated with the model.

---

<sup>24</sup>Using interlaced frames.

<sup>25</sup>In Okada Okada (2006).

Visualisations using this method are presented in grayscale with white levels enhanced to give more effective contrast between smoke and model outlines.

### 2.4.2 Oil and soot deposition

On-surface flow visualisation was used to reveal flow structures from an afterbody surface shear perspective and to compare with published data. On-surface shear visualisation were achieved using a mixture of China clay<sup>26</sup>, kerosene and a fluorescent pigment<sup>27</sup>. Images were acquired under florescent black (ultra violet) lights and were subsequently processed to defeat blue and green colour levels, and to raise the black point (thus eliminating reflections in the visible spectrum)<sup>28</sup>. Even application was ensured by application of the mixture using a model spraypainting gun in a regular, crosshatched series of strokes. Where low energy flows on the backlight region gave rise to excessive seepage of the mixture on the to base surface (thus contaminating the visualisation), backlight and base surface visualisations were acquired separately.

---

<sup>26</sup>China clay is a powder obtained from rocks high in kaolinite ( $\text{Al}_2\text{Si}_2\text{O}_5(\text{OH})_4$ ). Ekalite, the form used throughout this research, is a readily available, high-quality, refined China clay used where “whiteness” is important.

<sup>27</sup>By volume, 4 parts kerosene, 4 parts China clay, 1 part fluorescent pigment.

<sup>28</sup>Green and blue hues are occasionally visible in images presented throughout as (yellow) artefacts of interpolation as per resizing for typesetting.

## Chapter 3

# Results I: models in isolation

Results from detailed investigations of pre and post-critical Ahmed models ( $25^\circ$  and  $35^\circ$  respectively) are presented. These are subsequently used as a basis for deconstructing results pertaining to platooned arrangements in the following chapter.

### 3.1 Force data

#### 3.1.1 Reynolds similarity

Reynolds number,  $Re$ , is a ratio of viscous to inertial forces useful in characterising flow phenomena stability over a range of test freestream velocities (equation 3.1, where  $L$  - characteristic length - is defined herein as the model length):

$$Re = \frac{\rho V L}{\mu} \quad (3.1)$$

Drag and lift data were recorded at various test speeds. Data points presented in figure 3.1 are an ensemble of multiple test runs, with drift accounted for post each run.

The red line in figure 3.1 denotes determined similarity at  $Re = 1.8 \times 10^6$ . Whilst results are subject to acquisition error (discussed in section 2.2.2.5, page 67), some clear trends are evident:

- $C_D$  of the  $\alpha = 25^\circ$  pre-critical model does not normalise until  $Re > 1.6 \times 10^6$ . A diminishing trend exists prior to this. From  $Re > 0.6 \times 10^6$ , data compare favourably with trends by Vino (2005) for an  $\alpha_c$  model (with which flow structures are broadly similar) in the same test facility. Turbulent separations were validated by boundary layer tripping with aluminium

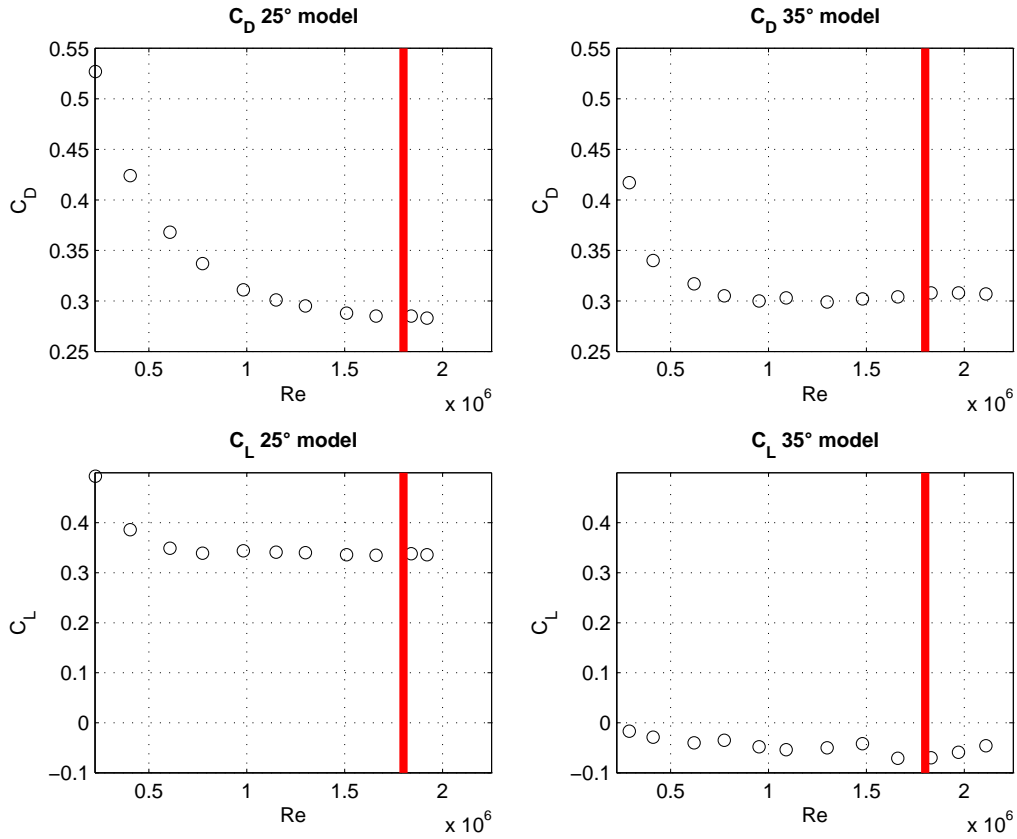


Figure 3.1: Re performance of  $\alpha = 25^\circ$  and  $\alpha = 35^\circ$  test models in isolation at various  $Re$

strips, yielding identical results. Of interest,  $C_L$  is relatively constant for  $7 \times 10^5 \leq Re \leq 1.9 \times 10^5$ .

It is known that a high proportion of drag is generated over the model midsections (Ahmed et al. 1984), being essentially flat plates aligned with the freestream). For flat plates in turbulent boundary layers, skin friction decreases with increasing  $Re$  (Schlichting 2000). As mid-body skin friction bears negligible effect on lift, the steady decrease in drag for this case for  $Re > 6 \times 10^5$  is thus attributed, in part, to relevant turbulence effects (a similar conclusion is made by Vino for  $\alpha_c$ ). More significant increases in drag for lower  $Re$  may be attributed to changes in afterbody flow structure, however relevant low  $Re$  works report the structure as stable to  $Re$  an order of magnitude lower; see figure 1.29 after Drouin<sup>1</sup>. Small changes are observed in pressure data presented in figure 3.9 (page 102), though do not offer significant changes in flow structure explaining a reduction in  $C_D$ .

- The trend is not repeated in the  $\alpha = 35^\circ$  model, which uses an identical midsection<sup>2</sup>, rendering the earlier conclusion incomplete for the  $Re$  specified. Three possibilities are considered:

<sup>1</sup>In Okada (2006).

<sup>2</sup>The “force balance” model was constructed such that the rear ends were interchangeable.

- That turbulent structures along the model midsections are affected uniquely by changes in flow structures about the backlight and base regions, or,
- That flow structures about the backlight region for  $\alpha = 25^\circ$  bear some sensitivity to  $Re$  within the range examined - e.g.  $Re$  is known to affect vortex shear layer separation and vortex location in delta wings (Crippa and Rizzi 2006) - or,
- That the phenomena observed owes to freestream flow conditions (e.g. angularity, turbulence, etc)

As these effects are small, and are not directly relevant to the work presented - the results above simply reflect an investigation towards obtaining  $Re$  similarity - further investigation is not warranted.

It should be noted that the correct trend of strong  $C_L$  in the pre-critical case (owing to impinging vortex structures over the backlight region) is replicated, as is negligible lift in the post-critical case Ahmed et al. (1984, comparing pressures over various key surfaces).

Force data at higher  $Re$  could not be acquired due to equipment limitations. Bar small force variations given bluff-body skin friction sensitivity to  $Re$ , it is deduced that forces are broadly  $Re$ -insensitive beyond  $Re = 1.8 \times 10^6$ .

### 3.1.2 Validation of drag force trends

With an appropriate  $Re$  established, a scan of forces against afterbody geometry was completed to compare trends against published data.

Figure 3.2 superimposes acquired data described previously over reference drag data acquired by Ahmed et al. (1984). Data are taken under identical conditions to  $Re$  similarity data.

Whilst higher  $C_D$  is observed than for the reference data, the general trend (increasing drag with stronger vortex impingement to the critical case followed by abrupt breakdown) is well replicated. Particularly good agreement is noted at the  $25^\circ$  and  $30^\circ$  cases. Whilst it was originally anticipated that the increased freestream turbulence in the RMIT IWT would decrease  $C_D$  (see section 1.3.1, page 21), results presented in figure 3.2 indicate otherwise. This is also contrary to data presented by Vino (2005) in the same facility using a larger scale  $\alpha_c$  Ahmed model. A possibility explanation concerning effects of relatively large turbulent length scales prevalent in the IWT is explored in Appendix A.5.3.4 (page 240).

The presence of significant flow angularity in the freestream is a more likely contributing cause<sup>3</sup>. This may not have been of issue in testing by Vino (2005), as the model in question was sting-mounted using a single, central mount allowing yaw rotation (and thus alignment with flow, not a

---

<sup>3</sup>Pressure variances leading to test section flow angularity are documented extensively in Quirillo (1999)

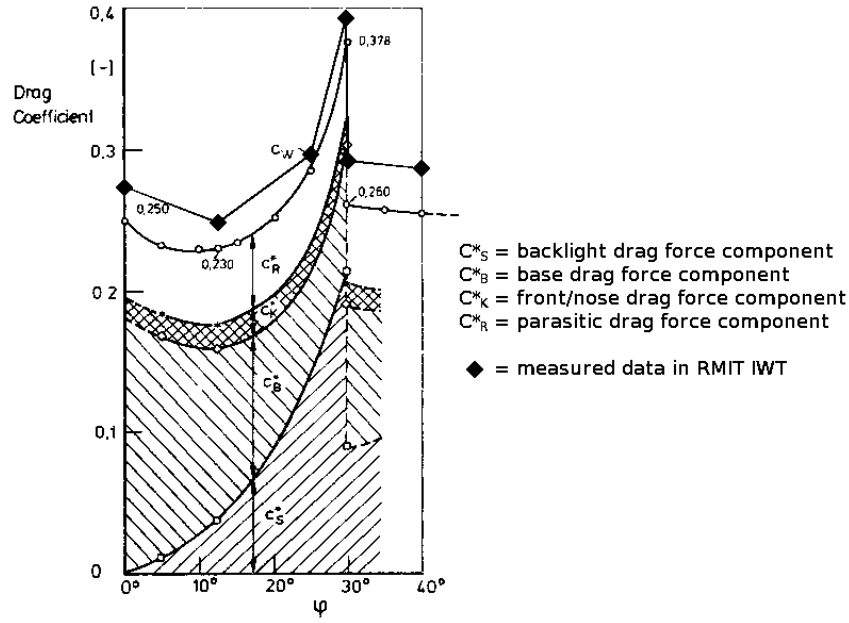


Figure 3.2: Acquired drag values vs. original Ahmed et al. (1984) values

geometric marker)<sup>4</sup>. An investigation into empty-test-section angularity is presented in Appendix A.1, page 222), confirming a detrimental effect from freestream flow angularity on force data in the installed, 0° yaw case.

Boundary layer effects (summarised in section 2.2.1.2, page 62) are also likely to affect model drag: critically, the displacement thickness under the model (taken for an empty test section) is some 20% of the ground clearance, higher than that experienced by Vio and serving to increase base drag. This is commensurate with the drag force breakdown presented by Ahmed et al. (1984) in figure 3.2 (where “ $C_B$ ” denotes base drag): a greater disparity is observed for backlight geometries where base drag is a greater contributor to overall force.

Force trends were thus deemed consistent with published data.

<sup>4</sup>When contrasted to relevant model-in-isolation wake plots (section 3.4.4 page 108) Vio’s wake plots show excellent symmetry. Despite significant effort to replicate this “baseline” trend achieved in the same facility, a suitable result was not able to be replicated throughout experiments undertaken during the course of this work. Rigorous geometric tolerances were applied in model manufacture and in the alignment of models with the test section’s geometric centreline. A possible explanation concerns Vio’s models being mounted on a sole, centre sting, and thus possibly being aligned against zero mean side force. This method was not pursued throughout as test section angularity diminishes along the test section length; identical geometric model yaw being considered more practically relevant. Of interest, some of Vio’s surface shear visualisations show distinctly asymmetric patterns. Differences in setup or possibly inherent bi-stable (or greater) flow structures may explain this discrepancy, which is not investigated in this work.

## 3.2 Qualitative observations of flow phenomena

Qualitative flow field and surface shear visualisations were used to further elucidate key flow phenomena, revealing clean separations over sharp afterbody edges at low  $Re$  ( $< 4.2 \times 10^5$ ). Smoke visualisation at this  $Re$  was thus deemed representative. Oil and soot depositions were conducted at  $Re = 1.8 \times 10^6$ .

### 3.2.1 Oil and soot depositions

#### 3.2.1.1 $\alpha = 25^\circ$ case

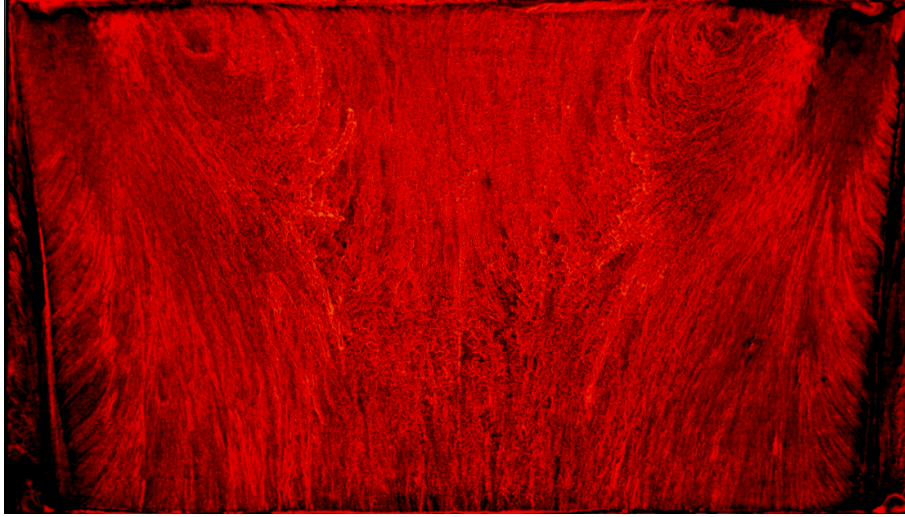
The effects of impinging, dominant C-pillar vortex structures are clearly visible in the  $\alpha = 25^\circ$  case (figure 3.3), the negative bifurcation formed by the vortex impingement at approximately  $7^\circ$  to the C-pillar being consistent with published sources (Ahmed et al. 1984, Krajnović and Davidson 2004; 2005, Vio 2005).

A recirculation zone exists over the backlight region, bounded upstream by a negative bifurcation line just downstream of the top/backlight edge. A saddle point exists at the centre of this negative bifurcation line, as do two stable foci at either side. Surface flows within this zone tend upstream and are distorted from the foci given the presence of the dominant, axial vortices operating adjacent. The downstream lower sides of the separated region are well defined, with flow tending downstream over the backlight just inboard of vortex impingement. This best echoes mean surface flows computed by Krajnović and Davidson (2004).

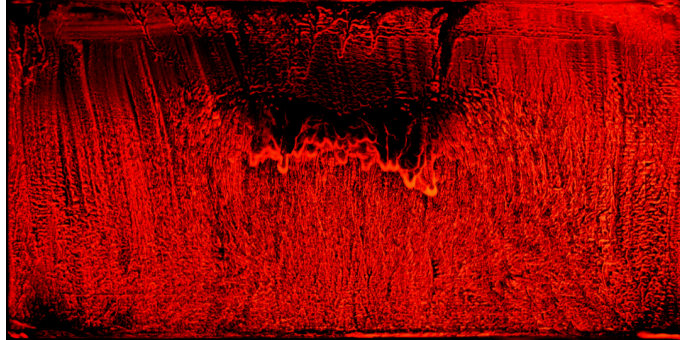
The closure of the separated zone along the model centreline (when contrasted to results from *any* time-averaged model) is less clearly defined. Figure 3.3 does not suggest (as does low- $Re$  work by Spohn and Gillieron (2002)) that the separated region does not close at all, forming a continuous region with a separated zone on the upper side of the base. The closure of the recirculation zone is ill defined in  $x$  and characterised by low-energy depositions. The location of this closure - being spread over a region from  $\frac{1}{2}x$  along the backlight extending to the base edge - contrasts poorly with time-invariant models proposed by Ahmed et al. (1984) predicting mean closure of the separated region over the backlight, instead being more consistent with Krajnović and Davidson’s turbulent computational findings discussed in section 1.3.2.4 (35): that the closure of this separated region is defined by the collision of (low-energy) upstream and downstream vortex structures within it. The lesser number and strength of upstream hairpin vortex structures - having been distorted from the presence of the dominant axial vortices - gives rise to a macroscopically stable closure of the separated region. The instantaneous closure location translates with respect to turbulent phenomena at hand. At the base/backlight edge along the model centreline, the shear in figure 3.3a tends towards downwash, though some “pocking” of the deposition indicates the possibility of the separated zone’s closure occasionally extending to base, or possibly not closing at all.

### 3.2. QUALITATIVE OBSERVATIONS OF FLOW PHENOMENA

In a way this presentation of the  $\alpha = 25^\circ$  afterbody denotes a prequel of work by Vino at  $\alpha = 30^\circ$  (flow model presented earlier in figure 1.25a, page 1.25), where soot depositions suggested that the (larger) separated zone - commensurate with stronger separation from the top/backlight edge - was not evidenced to close by the model base, and a clear interaction between base and backlight flows was observed (Vino 2005).



(a) Backlight detail



(b) Base detail, first attempt

Figure 3.3: Flow patterns over  $\alpha = 25^\circ$  Ahmed model afterbody

Depositions for the model base represent a departure from time-averaged models cited earlier: bifurcations are not clear, as such the impingement of any characteristic vortex structures are likely turbulent<sup>5</sup>). Of particular interest:

- The two vertical artefacts shown by Vino (figure 1.25a) are not related to flow effects, and simply represent overrun from accumulated visualisation material on the backlight (specifically material along the negative bifurcations caused by C-pillar vortex impingement).

---

<sup>5</sup>Figure 3.3b is also unique in being the only result presented for which the mixture was painted on, as opposed to being sprayed, hence the difference in uniformity to other oil and soot depositions presented throughout.



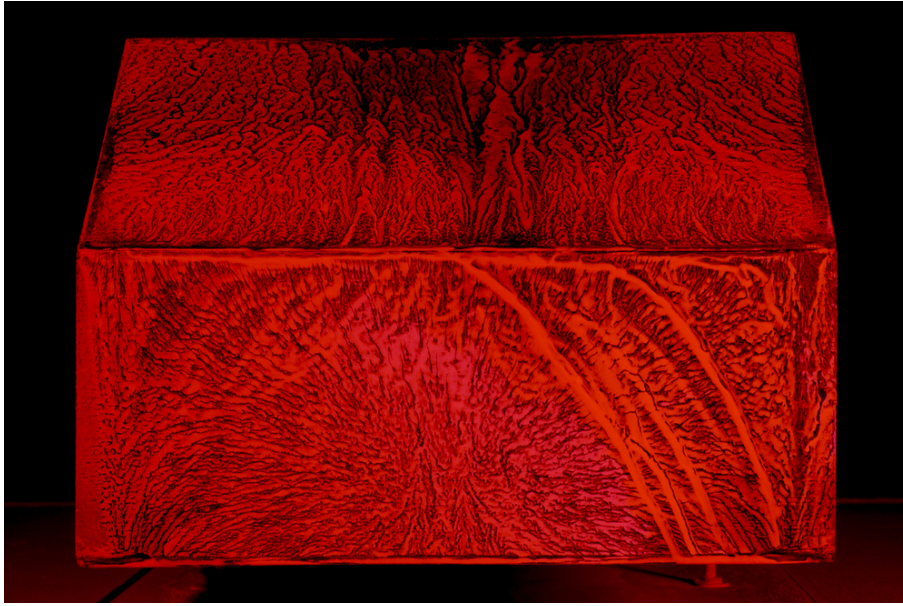


Figure 3.4: Flow patterns over  $\alpha = 35^\circ$  Ahmed model afterbody

- Flow about the centre of the base is clearly unsteady, requiring understanding beyond previously reviewed time-averaged models (1.18, 1.19, 1.24, 1.25a). Clear impingement on the horseshoe vortex pair operating on the model base is consistent with Ahmed et al. (1984), Franck et al. (2007), Hinterberger et al. (2004), Howard et al. (2000), Johnson (2005), Krajnović and Davidson (2004; 2005), Lienhart et al. (2000), Okada (2006), Sims-Williams and Dominy (1998), Sims-Williams et al. (2001), Sims-Williams and Duncan (2002), Vino (2005), forming an unstable node at approximately  $0.17 \frac{z}{H}$ <sup>6</sup>. Contrary to models by Ahmed et al. (1984) and Vino (2005), the positive bifurcations either side of the node appear to tend slightly upwards (in addition to a “bending” of surface shear patterns away from the centreline) corroborating more recent work by Krajnović and Davidson (2005) suggesting the upper base vortex is distorted upwards and away from the base.
- Shear forces are insufficient to visibly disturb the visualisation mixture about the side of the base. This confirms speculations by Ahmed et al. (1984) that the horseshoe vortex pair operating about the base are drawn into the axial direction by the dominant axial vortices, merging with them and serving as an additional source of vorticity. (It was later verified computationally by Krajnović and Davidson (2005) and experimentally by Okada (2006) that only the upper of the vortex pair contributes to the far wake. The fate of the smaller, lower vortex is unknown).
- A double-arch-like line defines the upper bound of the impingement of the upper vortex, above which a region of exceptionally low shear energy exists. This region would appear to be a low-energy separated region bounded by separation from the backlight/base edge and

<sup>6</sup>For reference, the base concerns approximately  $0.67 \frac{z}{H}$  for the  $\alpha = 25^\circ$  case

by the upper vortex operating over the base region, as suggested by Ahmed et al. (1984) and Vio (2005), with the “double arch” pattern presented being more consistent with the aforementioned upward “bending” of the upper base vortex. No further evidence exists to suggest a surface-impinging interaction with separated backlight flows.

#### 3.2.1.2 $\alpha = 35^\circ$ case

A quasi-two-dimensional behaviour is evident in the post-critical case (figure 3.4). Energy associated with surface flows appears to be lower and broadly consistent across backlight and base surfaces, indicative of “clean” separation at upper, lower and side edges giving rise to a large separated volume enveloping the entire base/backlight region.

The base depositions again feature an unstable node at the bottom centre. This is entirely consistent with time-averaged data presented by Lienhart et al. (2000) (depicted previously in figure 1.21b); separations from the top/backlight edge and the base/bottom edge create a pair of counter-rotating (likely horseshoe) vortices as suggested by Johnson (2005) and Brunn and Nitsche (2001).

### 3.2.2 Flowfield smoke visualisations

Key aspects of the flows observed in oil and soot depositions were then further explored off-body using smoke in figures 3.5 and 3.6. The dominant, axial downwash vortices impinging on the backlight region in the  $\alpha = 25^\circ$  case are clearly visible: figure 3.5d in particular shows a notable expansion of the vortex core beyond the model base indicative of a loss in core  $C_{DP}$ . This is commensurate with near-wake computational studies (Johnson 2005, detailed previously in figure 1.28) wherein  $C_{DP}$  of 0.1 was observed commensurate to (spiral) vortex breakdown, computed to occur shortly beyond the model base in the  $\alpha = 25^\circ$  case (Johnson’s studies did not examine the coherence of these structures in the far wake however).

Important differences between pre and post-critical wakes are observed in figure 3.6 visualising streamlines over the afterbody centreline. Flow in both cases clearly separates over the top/backlight edge (a key criteria for  $Re$  stability). Entrained flows over the backlight are clearly affected by the dominant axial vortices in the pre-critical case (figure 3.6a). As the streamtube spreads wide over the (turbulent) region defining the backlight recirculation zone closure, a long exposure photo reveals a region of reattachment consistent with figure 3.3. Whilst figure 3.6a evidences a small separated zone at the backlight/base edge and extending over much of the base; it is important to note that the distribution of smoke impinging on the downstream backlight surface extends to the base edge. This thus does not serve as a definitive proof that the separation over the backlight *always* closes prior to the base edge, but supports the notion that it closes the *majority* of the time.

### 3.2. QUALITATIVE OBSERVATIONS OF FLOW PHENOMENA

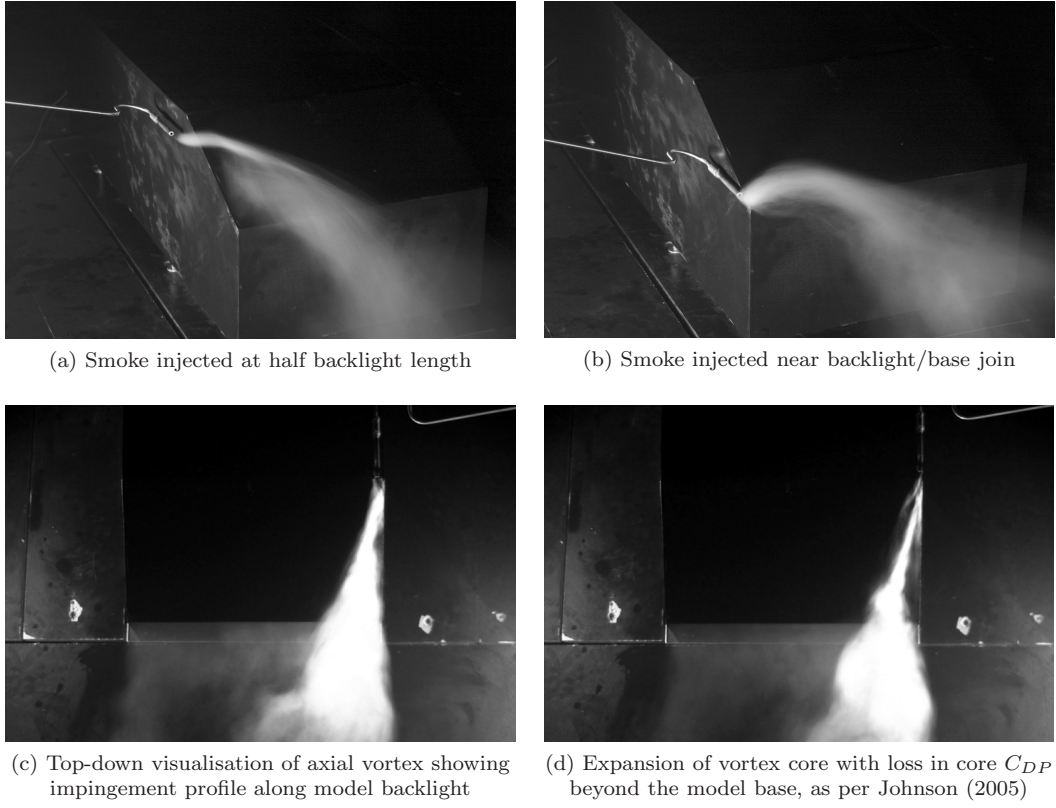


Figure 3.5: Smoke visualisation of dominant axial vortices about  $25^\circ$  Ahmed model afterbody



Figure 3.6: Smoke injected over backlight at centreline

The spread of the smoke streamtube in figure 3.6a owing to turbulent activity is consistent with key regions of unsteadiness associated with known interactions with the spanwise upper-base-horseshoe vortex and the backlight separated region, previously visualised computationally by (Johnson 2005, figure 1.26, page 38).

The relevant spectral peaks Johnson attributed to these unsteady regions were consistent

with base separations (strongest about the base/bottom/centreline coincident) observed by Sims-Williams and Dominy (1998), Sims-Williams et al. (2001), Sims-Williams and Duncan (2002) and Vino (2005); Vino noted significant spectral energy in this region. Prior work by the Sims-Williams and Duncan (2002) observed quasi-two-dimensional flat-plate-type shedding base bottom edge. Ahmed et al's initial study indicated two discrete vortices to operate over the base atop each other Ahmed et al. (1984); cross-spectral phase analysis of surface pressure data by Vino (2005) suggests an out-of-phase relationship at certain points (explored quantitatively in subsequent analysis.)

Interactions between base flows and incomplete closure of the backlight separated region has been speculated by various authors (Ahmed et al. 1984, Hinterberger et al. 2004, Johnson 2005, Krajnović and Davidson 2004; 2005, Lienhart et al. 2000, Okada 2006, Sims-Williams and Duncan 2002). The turbulent dispersion of the smoke stream in figure 3.6a about the trailing edge of the backlight and the downstream projection of the base - in regions known to exhibit relevant oscillations - suggests the vortex operating on the upper base region distorts adjacent flow structures in an oscillating manner. The particularly low energy associated with the closure of the backlight separation (described by Krajnović and Davidson (2004; 2005) and elaborated upon in section 3.2.1.1, page 92) renders it especially susceptible to local pressure fluctuations.

The post-critical case is considerably simpler; the wake at the model centreline is dominated by a large, separated region extending well beyond the model base, with shedding from the top edge commensurate with observations by Brunn and Nitsche (2001) and Lienhart et al. (2000) and consistent with the quasi-two-dimensional soot depositions in figure 3.4.

### 3.3 Quantitative investigation of mean body forces by surface pressures

A quantitative investigation of mean body forces with relevance to salient flow phenomena was subsequently undertaken. One half of the model afterbody for either case was outfitted with 55 pressure taps, 35 of which were concentrated over the backlight. Taps were evenly spaced over both surfaces. Data are sampled as fully dynamic sample sets encompassing all notable spectral energies of interest, from which statistical data are computed.

For visualisation purposes, data are mirrored about the centreline.

#### 3.3.1 Sampling settings

The following settings were applied when sampling dynamic pressure data:

- *Sampling rate:* to minimise inter-channel delay a sampling frequency of 3kHz (giving an

aggregate sampling rate close to the maximum possible 200kHz - see section 2.2.7, page 82)<sup>7</sup>. A description of inter-channel delay, multiplexing and correction methods applied can be found in Appendix D.3 (page 252).

- *Truncation:* spectra for all points sampled over both model configurations are contrasted with the amplitude response for the tubing system employed throughout in figure 3.8. In both cases the bulk of spectral energies concern 0-500Hz. In the  $\alpha = 25^\circ$  case, spectra clearly begins to increase for some channels in an undulating manner sympathetic to the diminishing amplitude response of the tubing system. As these energies are unrelated to flow phenomena they are excluded from further analysis. Data presented herein is thus truncated to 500Hz.
- *Time history estimation parameters:* Excluding noise and drift data, time histories were estimated from 439 realisations of 4096-point FFT's at 50% overlap (approximately five minutes sampling), giving a frequency bin size (or "spectral resolution") of 0.73Hz. Given a "lower" key frequency of interest of approximately 50Hz (figure 3.8a), the number of realisations far exceeds that required to calculate meaningful confidence intervals and gives usefully low variance: figure 3.7, showing cumulative averages of PSD's taken over increasing numbers of successive data blocks, suggests the central limit theorem to be satisfied by averaged the averaged PSD of as few as 10 realisations. Averaged spectral estimates are generated using Welch's method with the same parameters used in acquisition.

---

<sup>7</sup>As the DPMS has a "live" noise floor as opposed to the "truncated" floor in the Cobra and ECA probe acquisition routines, issues encountered in Appendix 3 (page 245) were not encountered.

### 3.3. QUANTITATIVE INVESTIGATION OF MEAN BODY FORCES BY SURFACE PRESSURES

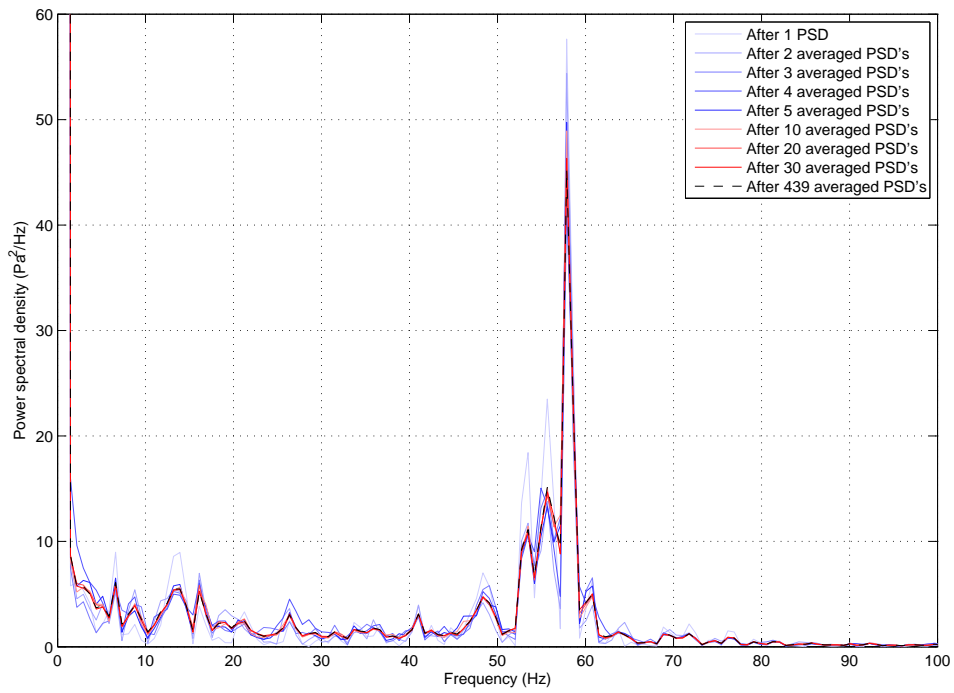
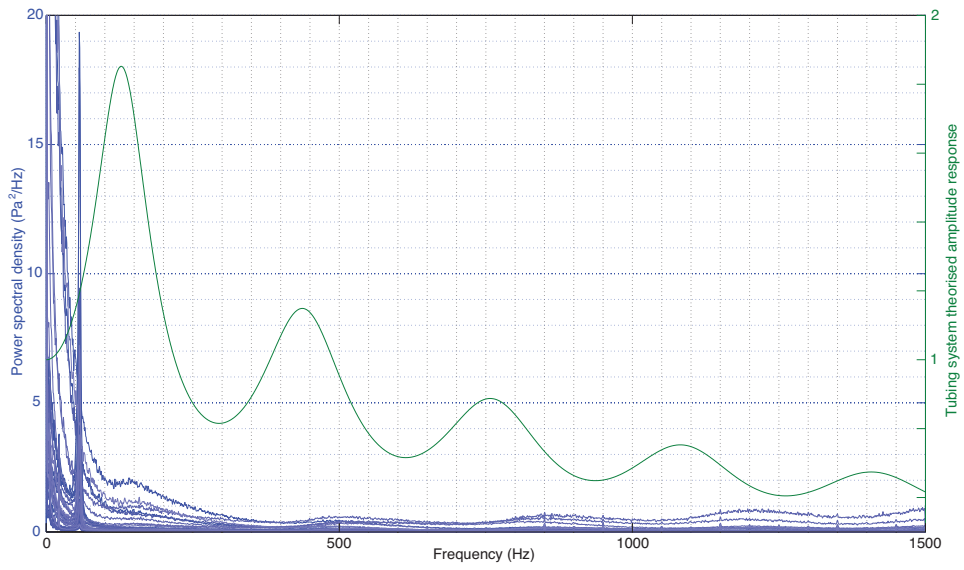
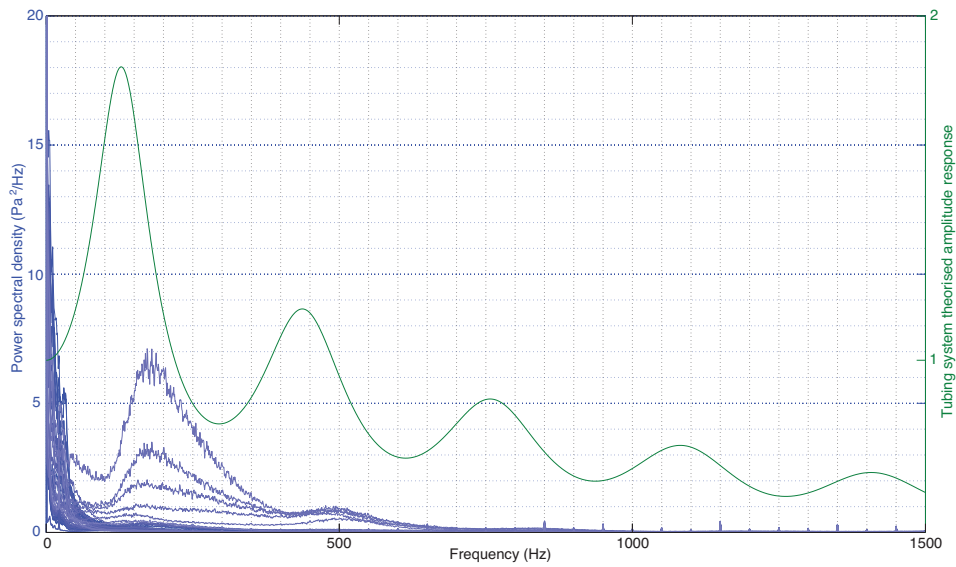


Figure 3.7: PSD at  $y = 0$ ,  $z = 0$  on base of  $\alpha = 25^\circ$  Ahmed model after various cumulative averaged PSD of successive data blocks

### 3.3. QUANTITATIVE INVESTIGATION OF MEAN BODY FORCES BY SURFACE PRESSURES



(a)  $\alpha = 25^\circ$



(b)  $\alpha = 35^\circ$

Figure 3.8: All points spectra vs tubing amplitude response



### 3.3.2 $\alpha = 25^\circ$ case

Figure 3.9 presents mean surface pressures about the  $\alpha = 25^\circ$  afterbody, corresponding broadly to the  $Re$  range presented in figure 3.1.

The “ $Re$ -stable” case (figure 3.9a) presents significant pressure gradients over the backlight. Low pressure over the top/backlight edge indicates flow is initially attached, accelerating over this edge (though this is not elucidated at low  $Re$ ). A sharp positive pressure gradient shortly downstream indicates separation takes place commensurate with the sudden geometric expansion of momentum from the model roof. This separation appears to be spanwise. Pressures at the top/side corners of the backlight remain notably low downstream of the top/backlight edge; a positive pressure gradient exists along the backlight sides. This coincides with the developing separation shear layer along this edge, and impingement and expansion of the main axial vortices on the adjacent backlight surface (an observation first noted by Morel (1978b), figure 1.15).

The development of the flow structure with increasing  $Re$  is demonstrably consistent with earlier work by Drouin<sup>8</sup> (see 1.3.3, page 40) and consistent with force data presented in section 3.1.1, page (page 88); Essentially the increasing strength of the axial C-pillar vortices with increasing  $Re$  increases vortex impingement and draws centreline flows “tighter” over the backlight region, delaying bulk separation. This is further evidenced by a region of (relatively) lower pressure ( $C_P \sim 0.6$ ) developing over the backlight from  $Re > 1.4 \times 10^6$ : though figure 3.9 is constructed of data taken over a spatially coarse resolution, this region is broadly commensurate with the backlight recirculation zone identified in soot depositions (figure 3.3a).

Pressure over the base region is largely uniform.

### 3.3.3 $\alpha = 35^\circ$ case

Surface pressures over the  $35^\circ$  model backlight and base covering a broad  $Re$  range are presented in figure 3.10. Compared to similar data for the  $25^\circ$  case in figure 3.9, the same contour scale in figure 3.10 depicts a smaller pressure range. Excluding relatively low pressure at “ $Re$ -stable”  $Re$  at the top corners of the backlight, pressures for the  $35^\circ$  case are, compared to the  $25^\circ$  case, relatively constant across backlight and base regions indicative of full separation at border edges (consistent with Ahmed et al.’s original studies and with qualitative visualisations presented in figure 3.4 - oil and soot - and the smoke visualisation presented in figure 3.6b).

The low pressure at the top corner is not fully explained. Localised attachment is not observed in qualitative visualisation. The possibility of a misaligned pressure tap (i.e. with the top surface instead of the intended edge) is negated by figure 3.10b, showing clean separation at lower  $Re$ . A more likely possibility concerns the interaction between the top/backlight and side/backlight shear layers; whilst the former interacts along the wake centreline with the bottom/base edge shear layer,

---

<sup>8</sup>in Okada (2006).



### 3.3. QUANTITATIVE INVESTIGATION OF MEAN BODY FORCES BY SURFACE PRESSURES

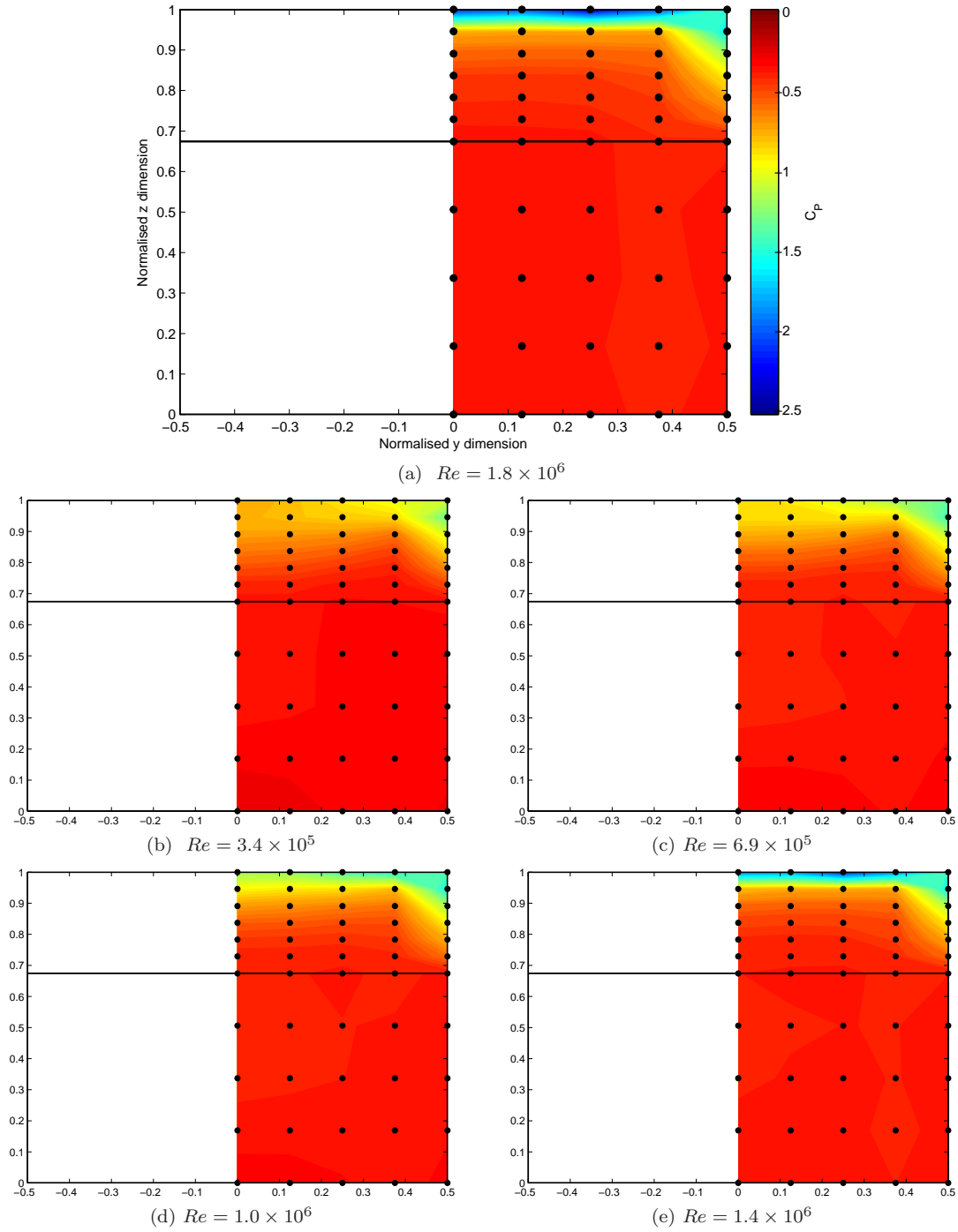


Figure 3.9: Development of rear surface pressure with increasing  $Re$  for  $\alpha = 25^\circ$  model

forming a broadly two-dimensional counter-rotating vortex pair (figure 1.21 observed by Brunn and Nitsche (2001), Lienhart and Becker (2003), Lienhart et al. (2000)), the C-pillar shear layer rolls up forming dominant axial vortices. Flow inertia associated with the vortex formation likely promotes

initial local attachment, insufficient to promote closure of the separated region over the backlight, nor to have the vortices impinge on it. The localised low pressure at the backlight top corner is thus considered legitimate.

This should not be considered analogous to flow phenomena giving low pressure for the  $\alpha = 25^\circ$  case, as pressures in the latter are approximately two times lower. It is possible that the crude spatial resolution employed exaggerates the size of the low-pressure region presented in figure 3.10<sup>9</sup>.

A third observation pertains to pressures over the  $35^\circ$  base; a region of relatively lower pressure is observed at  $\frac{z}{H} = 0.4$  between  $-0.25 \leq \frac{x}{W} \leq 0.25$ , with pressures notably higher just below this region. With reference to figures 3.4 and 1.21, this is conjectured to be a localised upwash above the time-averaged impingement of the counter-rotating centreline vortex pair (mentioned in the prior paragraph).

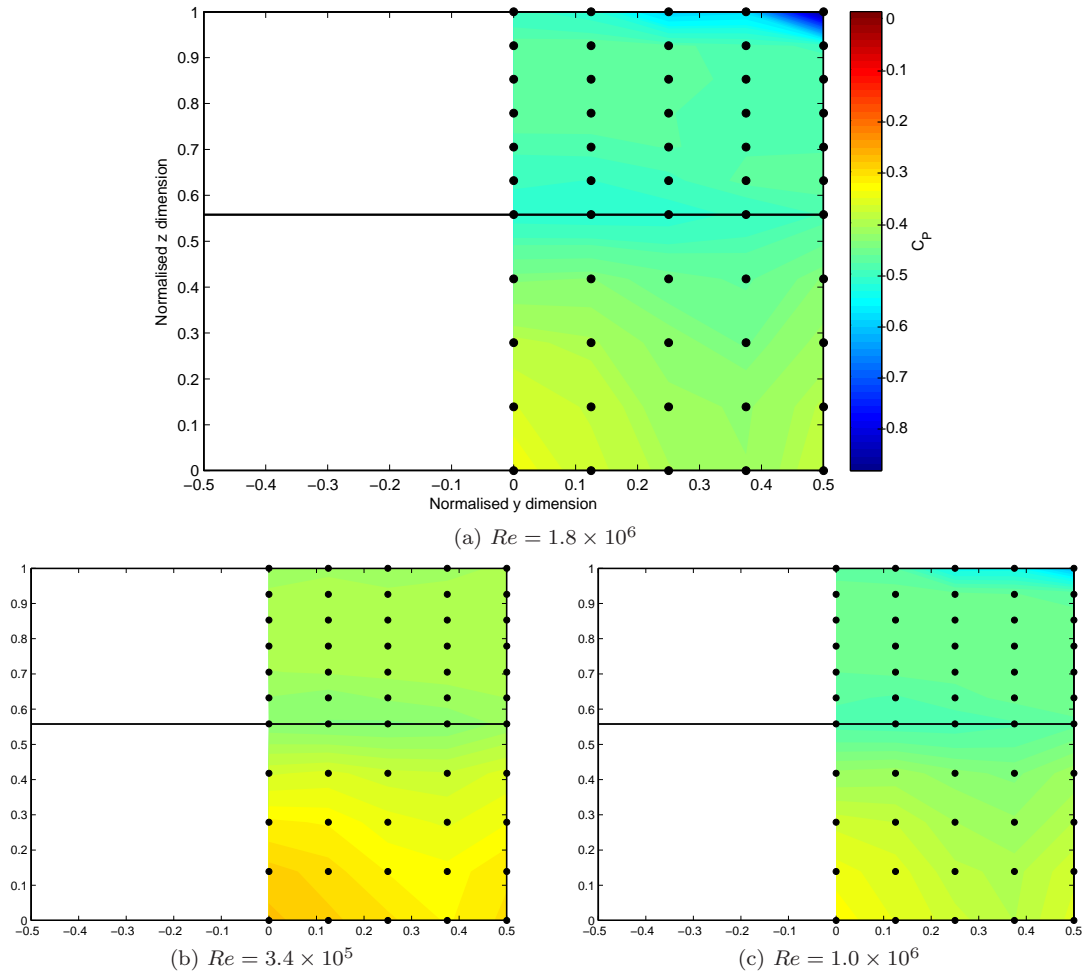


Figure 3.10: Development of rear surface pressure with increasing  $Re$  for  $\alpha = 35^\circ$  model

<sup>9</sup>A comparison against a reference data set at higher spatial resolution is provided in Appendix E (page 266).

### 3.3.4 Model forebody

Forebody surface pressure characteristics and soot depositions for a model in isolation in figure 3.11 indicate a stagnation point just above the centre of the front projection. Whilst  $C_P = 1$  - indicating stagnation - was not captured in acquisition (the scale in figure 3.11 indicates a maximum  $C_P \sim 0.75$ ), this is likely due to insufficient spatial resolution (a notion corroborated by flow phenomena observed in 3.11b-d correlating well with pressures observed in 3.11a, and the slight translation of the stagnation point from the cross-section centre, as evidenced in figures 3.11b and 3.12). Of interest, the range of pressures acquired correlates well with Vio (2005)<sup>10</sup>.

Separation of flows after accelerating downstream above and to the side of the stagnation point, as discussed in section 1.3.2.3 (page 33) are presented in figures 3.11b-e (a similar but not identical separation towards the forebody underside exists however is not presented).

The slight top-to-bottom asymmetry observed in soot depositions (particularly figure 3.11b) reflects the effect of the ground plane. This and basic statistical data are explored in figure 3.12, which presents mean  $U$  and  $I_{UU}$  at  $\frac{x}{L} = \frac{1}{16}$  upstream of the model leading edge<sup>11</sup>. Flow component magnitudes (from which superimposed cross-flow vectors are generated, i.e. composed of  $V$  and  $W$  components) indicate a slight lateral asymmetry in upstream conditions (giving rise to a likely slight  $+y$  translation of the stagnation point), however salient flow effects are duly observed. The intended low-turbulence nature of the upstream flow is confirmed, with an expected rise in  $I_{UU}$  owing to ground effects clearly visible.

No differences are observed in the model-in-isolation forebody for pre or post-critical afterbody geometries.

## 3.4 Mean wake data

A quantitative wake interrogation of the model wake was undertaken to identify and confirm key flow structures alluded to from surface and force data. The wake was interrogated using the ECA probe (described earlier in section 2.2.5.2, page 79) affixed to a three axis traverse (described earlier in section 2.2.6, page 81).

### 3.4.1 Sampling settings

The following settings were applied when sampling dynamic flow field data:

- $Re$ : All flow field interrogations were conducted at  $Re = 1.8 \times 10^6$ .

---

<sup>10</sup>Both maximum and minimum  $C_P$ .

<sup>11</sup>Data are acquired using pressure-based flow field instrumentation described in section 2.2.5.2, page 79. Unlike the surface pressure data, the flow field sets presented in figure 3.12 are not mirrored.

- *Sampling rate:* given the propensity of the near wake to contain regions of near-zero velocity flows (essentially, flows near the probe cut-off) and limitations in data reconstruction arising from this (detailed in appendix 5, page 246), sampling rates are strictly limited to the highest frequency of interest, twice over (to satisfy the Nyquist criterion). As preliminary scanning of the near wake did not find frequencies of interest exceeding approximately 310Hz, data were thus sampled at 625Hz<sup>12</sup>, falling desirably below 800Hz with respect to the tubing response of the ECA probe<sup>13</sup> and usefully limiting sample set size.
- *Sampling time and time history estimation parameters:* wake data are estimated from 27 realisations of 1024-element blocks at 50% overlap (effectively 22.9 seconds sampling time per point<sup>14</sup>). Mean results are averaged from estimated time histories.
- *Spatial resolution and range:* samples are taken at 20mm  $y$  and  $z$  intervals (effectively  $\frac{y}{W} = 0.0686$ ,  $\frac{z}{H} = 0.0926$ ). Samples are taken over  $-1.03 \leq \frac{y}{W} \leq 1.03$  and  $-0.08 \leq \frac{z}{H} \leq 1.49$ . The traverse was manually translated in  $x$  over a range  $0.0625 \leq \frac{x}{L} \leq 1$ <sup>15</sup>.
- *Device limitations:* velocities less than 2m/s are truncated by the sampling hardware (section 2.2.5.2, page 79), corresponding to velocities under  $\frac{U,V,W}{U_\infty} \sim 0.07$  being truncated. This is relevant when considering near wake flows, particularly in near proximity of the base.

As the model is known to produce a symmetric wake in lieu of upstream effects, only half-planes ( $-y$ ) are acquired for the model-in-isolation case. An effective “symmetry check” is performed by acquiring both sides for the  $\frac{x}{L} = 1$  case.

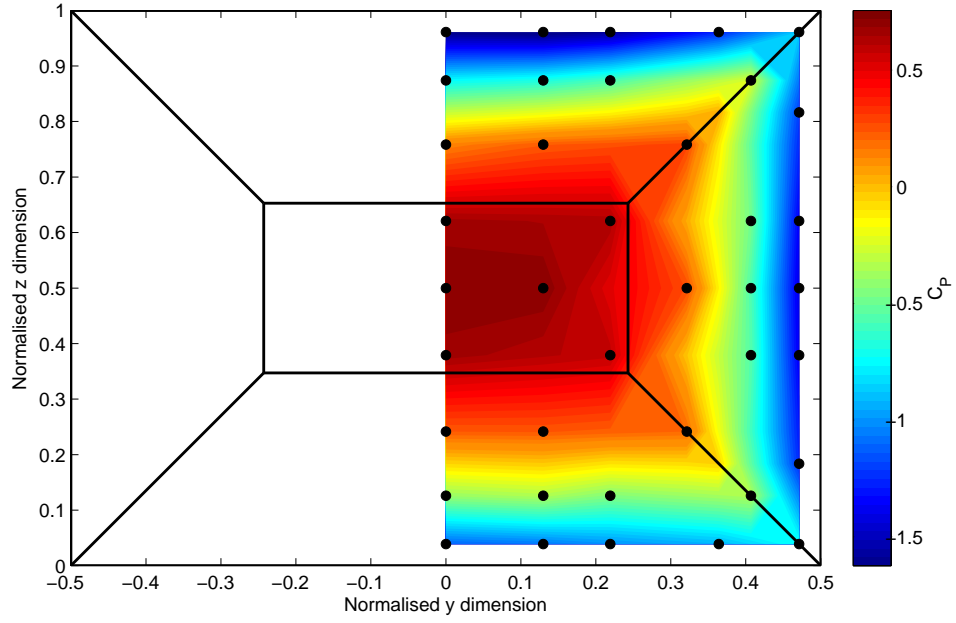
---

<sup>12</sup>The nearest “multiple” in the acquisition software.

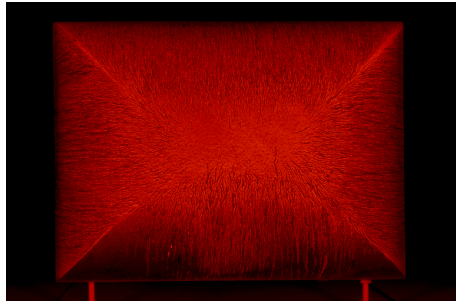
<sup>13</sup>As detailed in section 2.2.5.2 (page 79), the ECA probe tubing system is estimated to fall outside a useful amplitude response range at just over 800Hz.

<sup>14</sup>Whilst an unusually long time for mean measurements, this allowed for relatively good averaging of spectral data across blocks with <1Hz bin size. Relevant results are presented later.

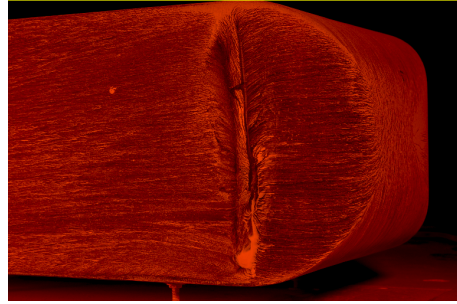
<sup>15</sup>In the model-in-isolation wake interrogations,  $\frac{x}{L} = 1$  is not exceeded being deemed sufficient to illustrate salient wake effects.



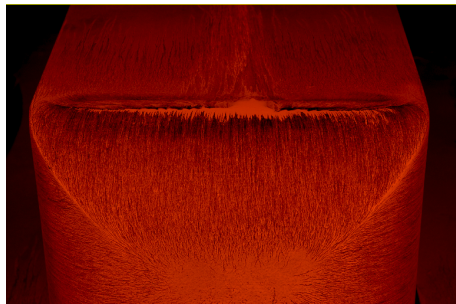
(a) Surface pressure distribution



(b) Front view



(c) Side view



(d) Top view



(e) Smoke visualisation of separation over top

Figure 3.11: Pressure distribution, soot and smoke visualisations of the Ahmed model forebody (in isolation)

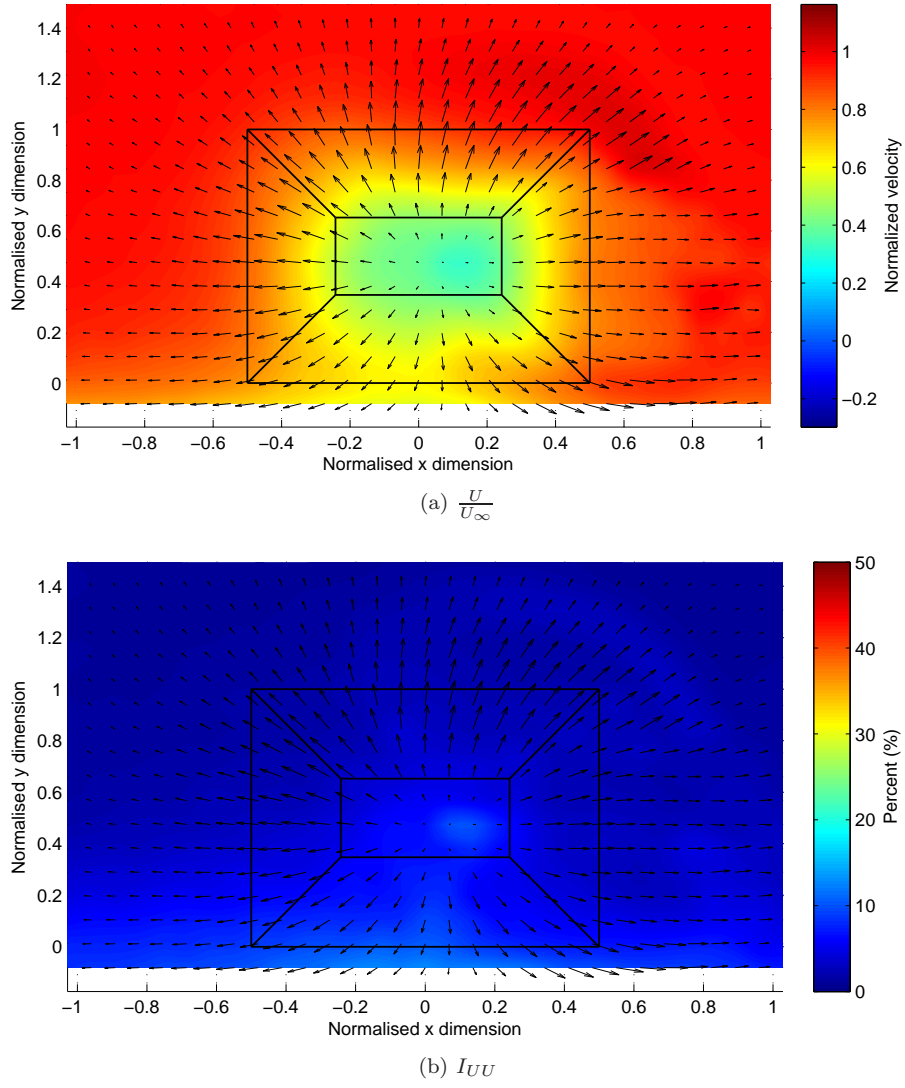


Figure 3.12: Properties of oncoming flow  $\frac{x}{L} = \frac{1}{16}$  upstream of model leading edge

### 3.4.2 Presentation of mean flow field results

Contours of the in-plane component, normalised ( $\frac{U}{U_\infty}$ ) with vectors indicating transverse and vertical components ( $V$  and  $W$ ) overlaid (the “centreline” plot also presents contours of  $\frac{U}{U_\infty}$ , however vectors are generated by  $U$  and  $W$  components).

Vorticity is calculated as the curl of the vector field ( $\vec{v}$  where the field is composed of the cross-plane components presented; transverse and vertical):

$$\vec{\zeta} = \vec{\nabla} \times \vec{v} \quad (3.2)$$

Contours in all plot groups are scaled identically unless otherwise indicated.

### 3.4.3 A general note on wake asymmetry

A general trend is observable in all wake plots where the model wake is skewed in the  $-y$  direction.

Geometric misalignment is considered unlikely. A high level of accuracy was employed in model construction and in ensuring model alignment with the geometric centreline of the test section (refer sections 2.1.1 and 2.2.1, pages 59 and 61 respectively). This trend in wake properties was similarly observed by Vino (2005) for Ahmed model experiments in the same facility.

An investigation was undertaken confirming sufficiently high pressure in-plane variances in the test section, substantiating earlier tunnel calibration results (Quirillo 1999). Relevant results and discussion are found in appendix A.1 (page 222). Particular effects on the Ahmed model near wake are discussed in Appendix A.1.2 (page 225).

The following sections demonstrate, in discussing flow effects arising from results as presented, that the test section flow anomalies do not limit the ability of the experiment as conducted to replicate the salient effects of the Ahmed model.

### 3.4.4 $\alpha = 25^\circ$ case

Figure 3.13 presents mean flow components for the  $\alpha = 25^\circ$  model. A separation projected from the model base is immediately evident, extending outwards to  $\frac{x}{L} \sim 0.25$ . The centreline plot for vorticity, figure 3.15a, confirms this separation to contain two counter-rotating recirculatory regions. Both regions extend over the base projection in a manner consistent with soot depositions presented in figure 3.3b (explored in section 3.2.1.1, page 92) and smoke visualisations presented in figure 3.6: the upper vortex is larger, whilst highest levels of reversed flow concentrated about the lower portion of the base (e.g. at  $\frac{x}{L} = 0.125$  flow reversal is evident between  $0.1 \leq \frac{z}{H} \leq 0.35$ ).

An unstable node just below  $\frac{z}{H} = 0.2$  is similarly suggested - indicating both components of the horseshoe vortex pair shown in the centreline plot impinge on the model base, with the upper vortex operating over the majority of the surface.

As much of the flow about the base is of extremely low, near-zero velocity, owing to probe limitations some truncation of velocity data is evident. It is otherwise expected that relatively stronger negative vorticity exist near the base region in figure 3.15a at  $\frac{z}{H} \sim 0.3$  (commensurate with the formation of the unstable node) than that observed. The salient effects of the wake are however captured, with strongest vorticity exhibited in the centreline plane along the bottom/base and backlight/base edge shear layers that constrain the separated region. The lower of these shear layers exhibits a stronger vorticity magnitude (commensurate with aforementioned highest levels of flow reversal); an important consideration elaborated upon later.

The quasi-two-dimensionality alluded by the centreline plot is clearly not maintained across the model span, with traverse planes indicating a highly three-dimensional wake. As suggested in the soot deposition discussion, further evidence of the upper of the horseshoe vortex pair being drawn upwards, towards the dominant axial vortex pair, bent in the axial vortex direction and contributing vorticity to them (as per figure 1.24 suggested by Krajnović and Davidson (2005) and also Okada (2006)) is noted at  $\frac{x}{L} \sim 0.25$  (3.15b), where both the separated region is observed to close and a source of vorticity is clearly seen to extend below the axial vortex core. This contrasts well with the progression of the axial vortices' cores: initially strongly concentrated near the model width extremity along the projection of the base/backlight edge, the core initially moves inwards ( $\frac{x}{L} = 0.125$ ), further inwards and downwards as the core weakens and interaction with the upper of the horseshoe vortices occurs ( $\frac{x}{L} = 0.25$ , distorting the vortex to an ellipsoidal cross-section, "long" vertically). Further downstream the vortices continue to weaken ( $\frac{x}{L} = 0.5$ ), by which point the wake is dominated solely by the axial vortices) and finally, further weakening, pushed again outwards, further downwards and further distorted by interaction with the ground plane by  $\frac{x}{L} = 1$ .

The high strength of the axial vortices serves to entrain a significant downwash between them along the model centreline. This feature is well developed by  $\frac{x}{L} = 0.125$  and continues downstream proportionate to the strength and proximity of the axial vortices (i.e. tending downwards and dissipating in strength).

The separated region, as alluded previously for mean-averaged behaviours, does not project onto the backlight region. Whilst confined to the width of the model just beyond the base at  $\frac{x}{L} = 0.0625$ , it quickly tends inwards, suggesting closure with the mixing of the upper horseshoe vortex with the axial vortices beyond  $\frac{x}{L} = 0.25$ . The separated region thus diminishes in cross-section downstream of the model base. The axial vortex cores similarly exhibit their highest levels of axial velocity deficit at this point as they mix with the upper horseshoe vortex, entraining reversed flow towards the axial direction (a similar phenomenon was observed by Vino for the  $\alpha_c$  case, however the "mixing" phenomena was observed to take place further upstream; possibly the decreased base area of the  $\alpha_c$  configuration, in offering decreased proximity to base separations and axial vortices, was more conducive to this). Beyond this point the vortex cores weaken; in



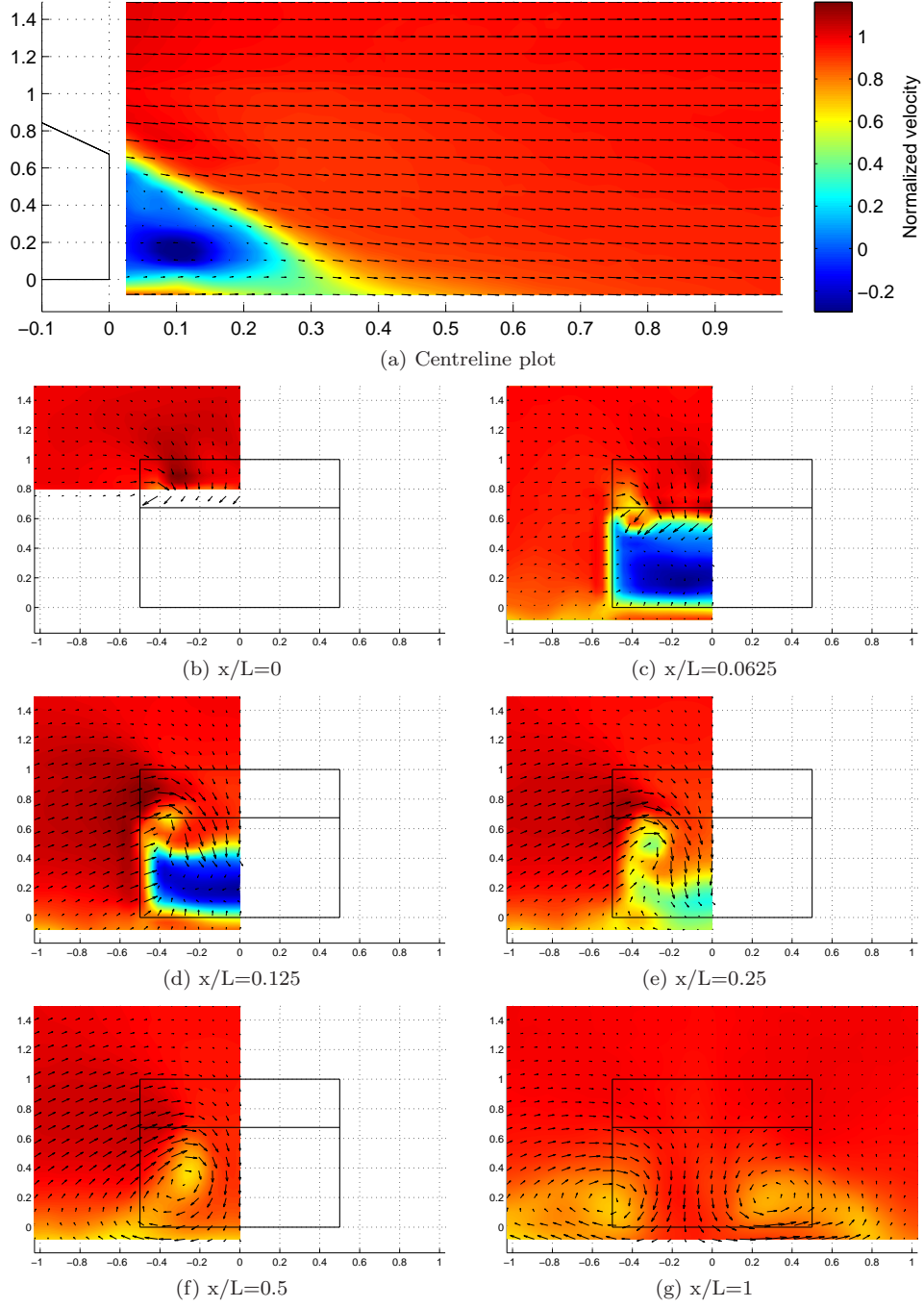


Figure 3.13: Normalised axial velocity component in wake of 25° Ahmed model at various body lengths ( $x/L$ ) behind model base (all dimensions normalised)

ceding energy to the freestream the axial velocity deficit is recovered.

### 3.4.5 $\alpha = 35^\circ$ case

Anomalous results presented in this section warrant further discussion, which is presented prior to a more generalised discussion of the results.

#### 3.4.5.1 Anomalous asymmetry and flow angularity

Despite force and surface pressure data, smoke visualisation, soot depositions and far field wake interrogations corroborating well with known data after Ahmed et al. (1984), Lienhart et al. (2000) and Brunn and Nitsche (2001), asymmetry in near wake plots particularly for  $0 \leq \frac{x}{L} \leq 0.125$  is apparent. Results proved repeatable over multiple runs.

Wake data adapted from results of experiments by Lienhart et al. (2000; 2002) for the  $\alpha = 35^\circ$  case taken using non-intrusive methods are presented in Appendix E (page 266) is used as a reference by which to better deconstruct results presented throughout. It should be stressed that, whilst owing to flow conditions, some differences in transverse plane data are observed, the characteristic feature of the post-critical wake - a “fully separated” near wake - is duly replicated.

#### 3.4.5.2 Generalised results

Immediately notable in the  $\alpha = 35^\circ$  case is the presence of a large separated region projected over the backlight and base centreline (figure 3.14a); some flow reversal is evident immediately downstream of the base region between  $\frac{z}{H} \leq 0.5$ . Together with the relevant centreline vorticity plot (figure 3.15c) indicating strong separating shear layers from the top/backlight (as per smoke visualisation, figure 3.6b) and bottom/base edges from which flows “turn in” to the base, the base flow impingement evidenced soot depositions (figure 3.4) is well supported. This observation is in excellent agreement with published data by Lienhart et al. (2000) in suggesting a horseshoe vortex pair giving rise to impingement in the form of an unstable node on the model base. The magnitude of vorticity observed in the centreline plane compares similarly with that for the pre-critical case at the base/bottom edge consistent with shear formation along a geometrically similar surface. Vorticity magnitude from the top/backlight edge is weaker, however, suggesting a weaker interaction for the horseshoe pair.

Spanwise behaviours are clearly not two-dimensional in nature, with relative strengths of top, side and bottom shear layers giving rise to circulation, culminating in a far wake that, similar to the pre-critical case, is dominated by a counter-rotating axial vortex pair. Expectedly, these vortices are weaker than for the pre-critical case, though their distortion of the separated region is particularly prominent at  $\frac{x}{L} = 0.125$ .

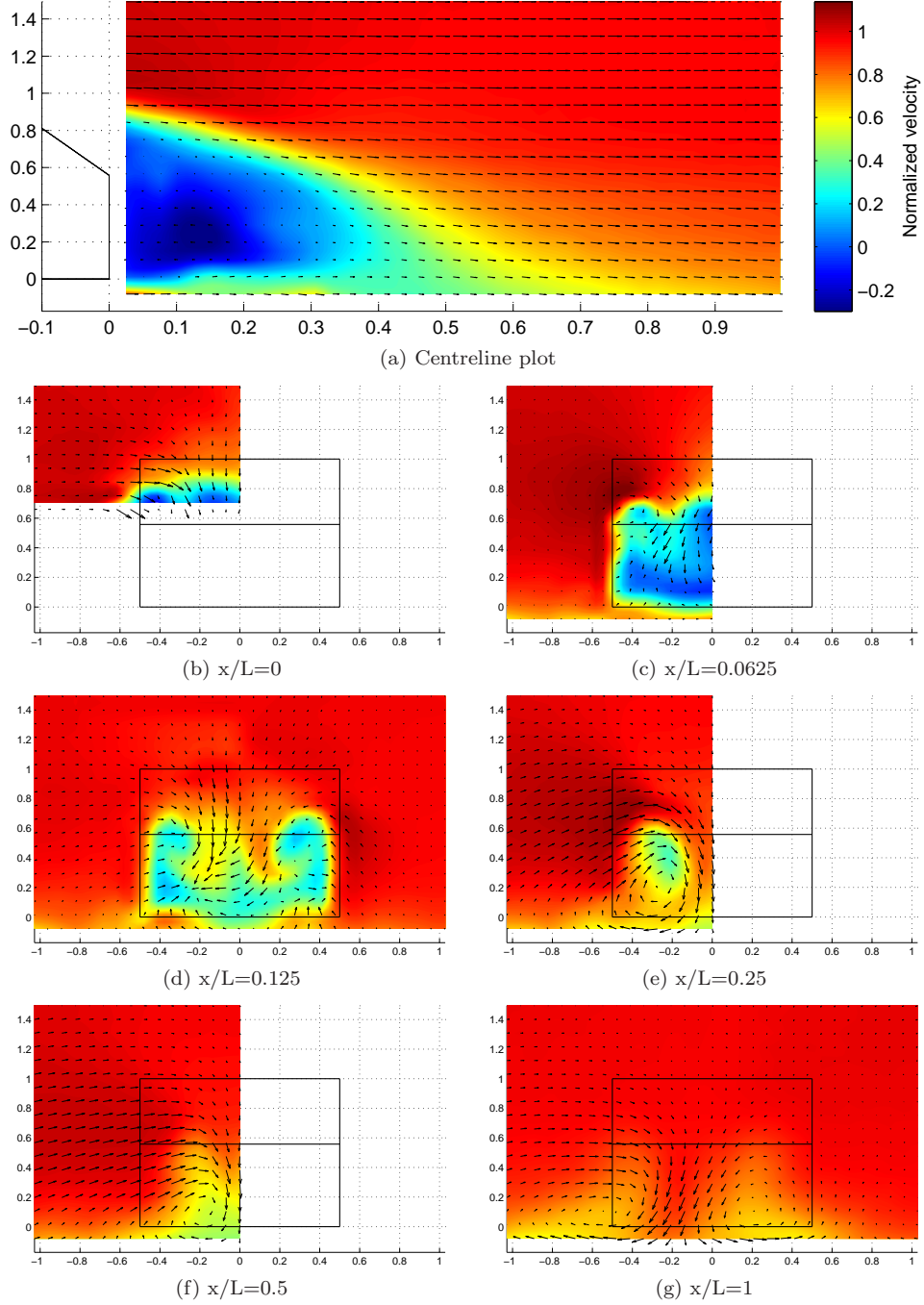
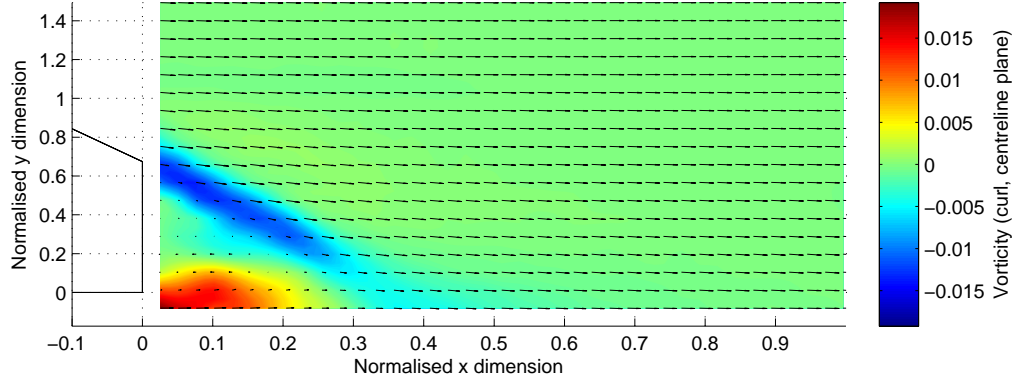
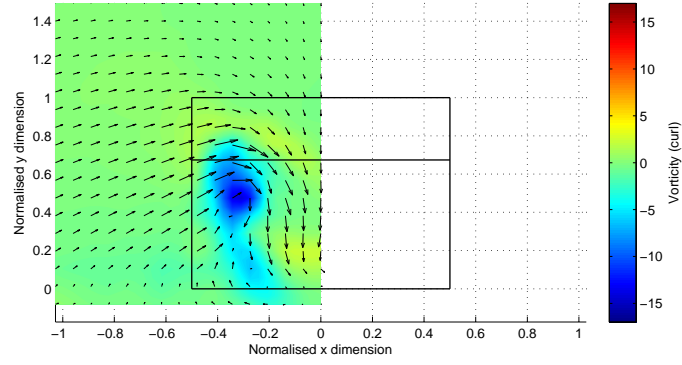


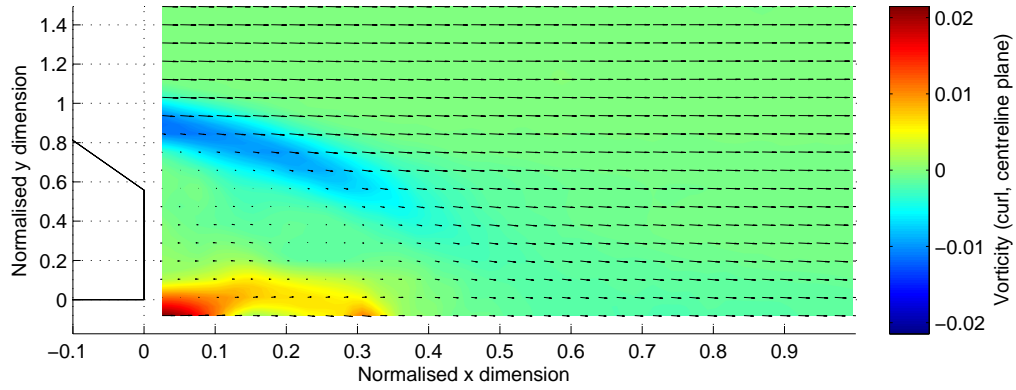
Figure 3.14: Normalised axial velocity component in wake of 35° Ahmed model at various body lengths ( $x/L$ ) behind model base (all dimensions normalised)



(a)  $\alpha = 25^\circ$  case, centreline plot



(b)  $\alpha = 25^\circ$  case,  $\frac{x}{L} = 0.25$



(c)  $\alpha = 35^\circ$  case, centreline plot

Figure 3.15: Vorticity plots of interest for  $\alpha = 25^\circ$  and  $\alpha = 35^\circ$  cases

### 3.4.5.3 Conclusions

The 75% scale Ahmed models as installed in the IWT demonstrated flow structures commensurate with relevant literature defining the aerodynamic characteristics of their form. Related salient phenomena (e.g. force trends) are duly captured.

They are thus deemed suitable as forms able to examine phenomena between pre and post-critical vehicle forms in organised convoys.

## 3.5 Dynamic performance of models in isolation

Flows about both pre and post-critical Ahmed model configurations were observed to contain significant unsteady components. Unsteady flows may display either *random* or *coherent, oscillatory* flows. These are analysed separately.

### 3.5.1 Generalised unsteady statistical data

Turbulence intensity (as defined in equation 1.3, page 12 - essentially the standard deviation divided by the mean of the axial/freestream component) is a useful statistical property able to assess unsteadiness in flow. Turbulence intensities exceeding 50% are capped to 50%<sup>16</sup>.

A relevant analogous statistic for surface pressures is the standard deviation of  $C_P$ <sup>17</sup>.

#### 3.5.1.1 Surface pressure $\sigma_{C_P}$

Standard deviation of surface pressures are presented in figure 3.16 for  $\alpha = 25^\circ$  and  $\alpha = 35^\circ$  cases. To better elucidate properties over base and backlight regions, each are presented separately with each contour plot scaled individually.

Backlight pressure distributions follow assertions in Melbourne (1993); though not leading-edge attachment, regions of intermittent flow attachment (and thus low mean pressure) are characterised by highly variant surface pressures as unsteady flow structures created under the fluctuating separation stream line are convected downstream. The region of highest uncertainty in the  $\alpha = 25^\circ$  case coincides neatly with the span of the separated region operating over it at this point; Saathoff's<sup>18</sup>

<sup>16</sup>An arbitrary value; whilst Watkins et al. (2004) present successful use of the probe in high-velocity flows to 32% turbulence, success at higher still levels remain unproven. Whilst theoretically possible (limited only by the dynamic response of the unit, angular acceptance of flows and selection of appropriate sampling rates), the practical constraints of highly-turbulent, low velocity flows (the probe software truncates values below 2m/s to zero) bears potential to render erroneously high turbulence levels. The qualitative salience of the results is not lost however.

<sup>17</sup>Related works have alternately presented  $C_{P_{RMS}}$  (Vino 2005) which is considered analogous, being the standard deviation added to the mean.

<sup>18</sup>in Melbourne (1993).

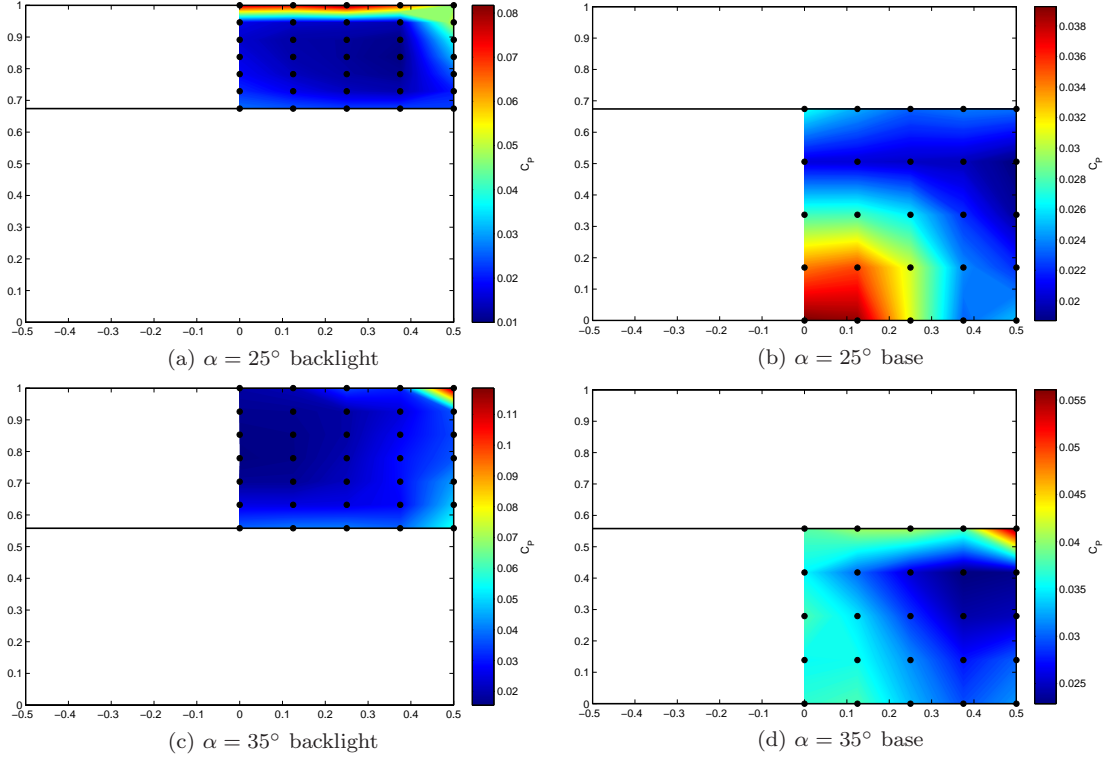


Figure 3.16:  $\sigma_{C_P}$  for  $\alpha = 25^\circ$  and  $\alpha = 35^\circ$  models backlight and base regions at  $Re = 1.8 \times 10^6$

assertion of vortices created under the shear layer being convected downstream coincides neatly with the observation of such structures within the separated region by Krajnović and Davidson (2005) (discussed further in section 3.2.1.1, page 92). The axial C-pillar vortex (formed of a separation shear layer from the backlight/side edge) appears a more stable process, as evidenced by lower  $\sigma_{C_P}$  over the region it impinges (figure 3.3a).

A region of high pressure in the upper outboard corner of the backlight in the  $\alpha = 35^\circ$  case is commensurate with local flow attachment first highlighted in section 3.3.3 (page 101), and further discussed (and visualised) in Appendix E (page E).

Base pressure for both cases present with similar  $\sigma_{C_P}$  magnitudes at the centre of the bottom/base edge. This region is best characterised by Sims-Williams and Duncan (2002) - in experimental and computational investigations of the  $\alpha = 25^\circ$  case - as a region in which the large width-to-ground clearance ratio defining the case produces a region in which an essentially two-dimensional vortex shedding phenomena was observed at  $St = 0.5$ <sup>19</sup> at a range of  $Re$ <sup>20</sup>. Nouzawa et al. (1992) noted a similar phenomena for a reference model generating analogous flows, with os-

<sup>19</sup>Morel (1978a), Morelli et al. (1981) had observed this in a similar body in the range  $St = 0.2 - 0.5$  for pre-critical afterbody geometries. The peak was not observable beyond the effective  $\alpha_c$ .

<sup>20</sup>Vino (2005) noted a similar phenomena in subsequent experiments with an Ahmed model configured at  $\alpha_c$  at approx  $St = 0.42$ , however unlike Sims-Williams and Duncan (2002), Vino's results would appear to scale slightly with  $Re$ . No rationale is given.

cillating phenomena in the range  $St = 0.37 - 0.55$ . As the shedding mode would appear analogous to two-dimensional flat plate shedding, it is not unreasonable to expect as much of the  $\alpha = 35^\circ$  case: Brunn and Nitsche (2001)) observed a similar phenomena in water tank experiments of a span-increased (to  $4H$ )  $\alpha = 35^\circ$  model.

### 3.5.1.2 Flow field turbulence intensity data

The progression of flows originating from the backlight/base edge shear layer in the wake differs pending model geometry.  $I_{uu}$  of the pre-critical case (figure 3.17) presents with significant intensity along the centreline extending from the lower base edge to approximately  $\frac{x}{L} = 0.3$ ; indeed the transverse wake plot (figure 3.17c) suggests this region to interact with the dominant axial C-pillar vortices in good agreement with Sims-Williams and Duncan (2002) in suggesting that low-pressure packets - shed from the base/bottom edge and convected downstream - cause a “pumping” of the far wake, in turn causing the position and strength of the C-pillar vortices to oscillate. Beyond this region the separation closes, and axial turbulence intensity is limited to the C-pillar vortex cores. Figures 3.17a and 3.17b indicate turbulence associated with vortex shedding from the upper base separation streamline to be equally strong in magnitude however limited to approximately  $\frac{x}{L} = 0.15$  behind the base; agreeing well with assertions by Ahmed et al. (1984) and the work of Krajnović and Davidson (2005) that the upper horseshoe vortex is distorted upwards and then backwards in the axial direction, merging with the C-pillar vortices. This is further highlighted by high  $I_{vv}$  in the relevant transverse plane ( $\frac{x}{L} = 0.125$ , figure 3.18).

High  $I_{ww}$  (figure 3.19) - particularly visible in the centreline plot - supports earlier notions that the base shedding process operates in a region of effective two-dimensionality (i.e. crossplane in the centreline plane).

At  $\frac{x}{L} = 0.125$  (figures 3.17b, 3.18b, 3.19b) the core of the C-pillar vortices are clearly visible in superimposed cross-plane vector components, however turbulence levels are low: until mixing with the base separated region occurs, the dominant axial vortices are thus stable phenomena, supporting soot deposition of figure 3.3.

The post-critical case (figures 3.20, 3.21 and 3.22) presents with similar turbulence intensities for shedding about the base/bottom edge (figures), operating over a larger range (to  $\frac{x}{L} = 0.5$ ) commensurate with the size of the separated region. Centreline plots denote a similar level of unsteadiness concerning flows from the top/backlight edge, suggesting shedding from this location also. A notable difference concerns unsteadiness associated with the C-pillar vortices; a higher level of turbulence about the vortex cores is noted relative to the pre-critical case particularly at  $\frac{x}{L} = 0.125$ , suggesting (possibly) greater interaction - commencing further upstream - with oscillations in the separated region.

In both pre and post-critical cases, highest levels of turbulence are expectedly associated with separated regions and their mixing with otherwise stable phenomena. Downstream of this, turbu-

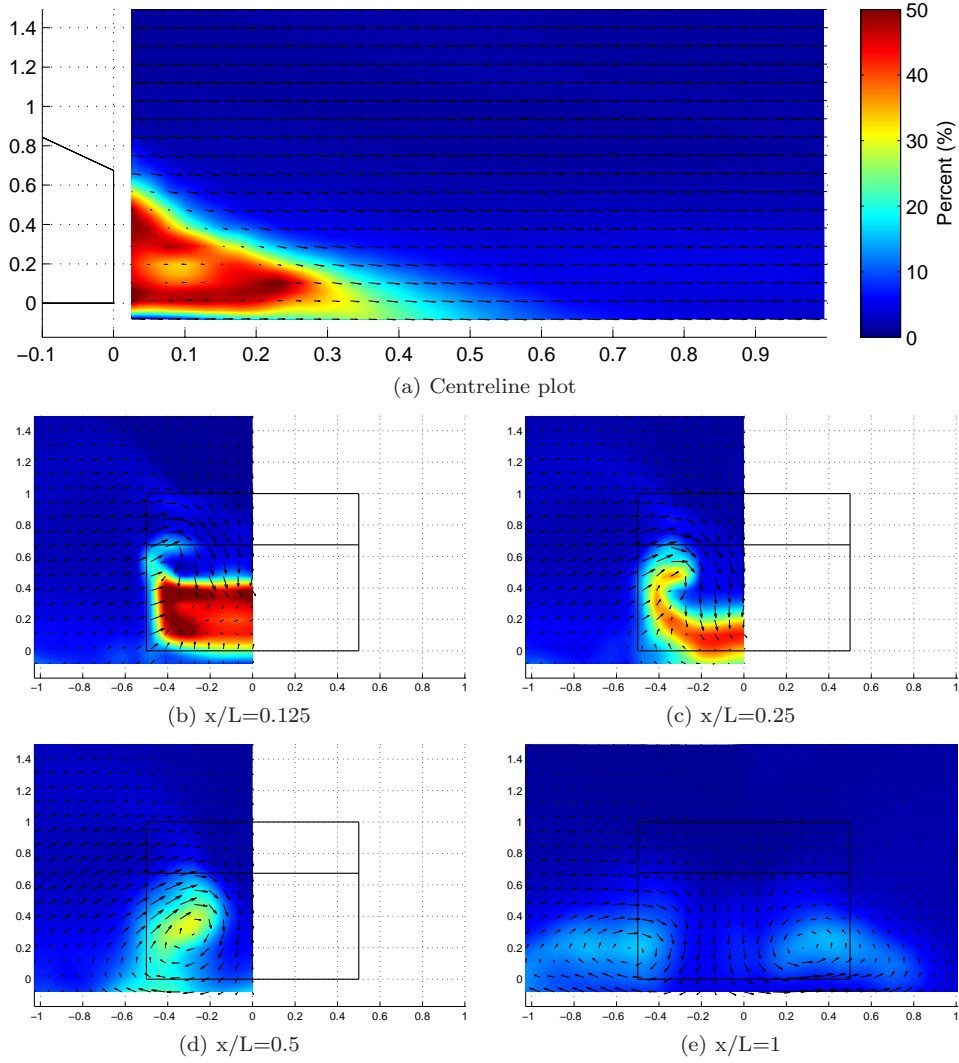


Figure 3.17: Axial component of turbulence intensity ( $I_{uu}$ ) in wake of 25° Ahmed model at various body lengths ( $x/L$ ) behind model base (all dimensions normalised)

lence levels return to low levels (visible in all plots at  $\frac{x}{L} = 1$ ). The far wake is thus dominated by relatively steady flow structures.

### 3.5.2 Spectral performance

Further elucidation of unsteady phenomena is achieved using spectral methods.

Time histories of surface pressure data are processed for spectral content, with the resulting power spectral density (PSD) by Welch's method (equation 2.14, page 85). As the time histories used acquired in both surface pressure and flow field data are estimated using spectral methods, spectral processing parameters (block size, FFT) used to calculate PSD are set identical to those



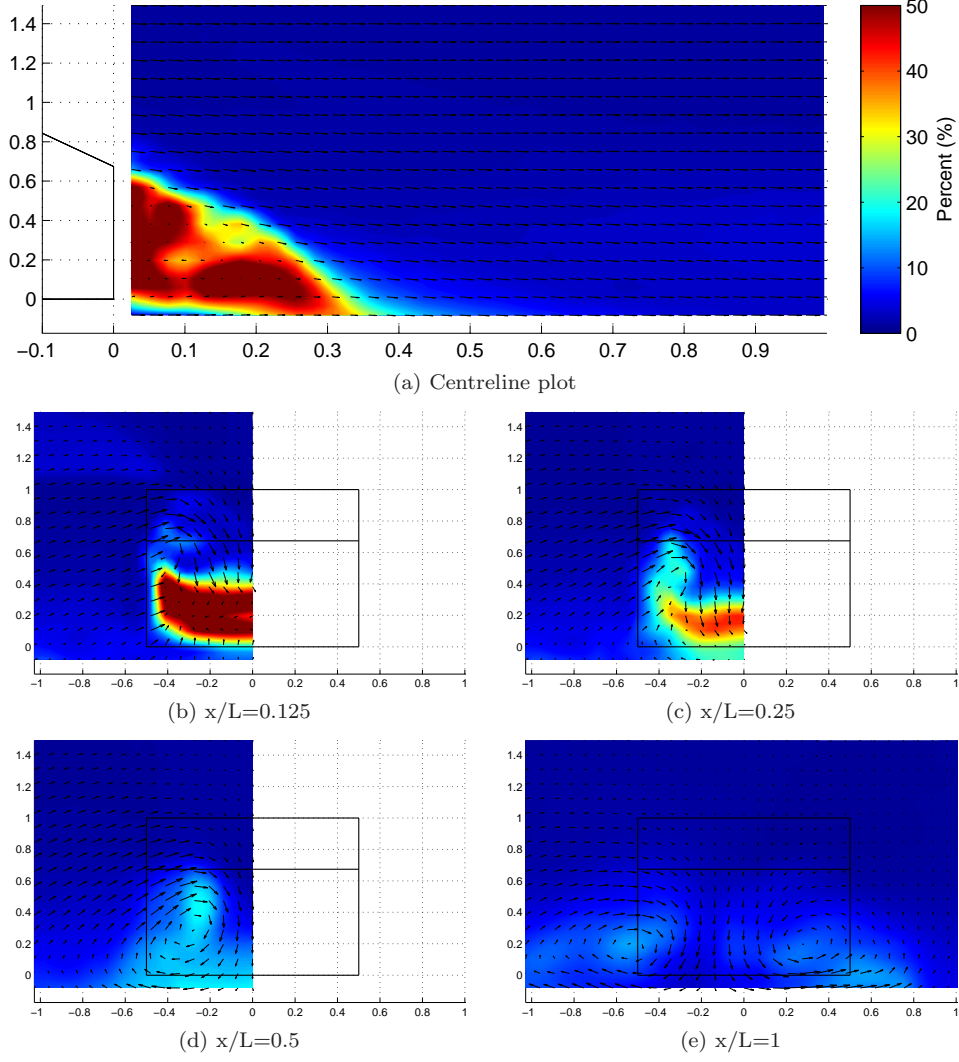


Figure 3.18: Transverse component of turbulence intensity ( $I_{vv}$ ) in wake of  $25^\circ$  Ahmed model at various body lengths ( $x/L$ ) behind model base (all dimensions normalised)

used in time history estimation to maintain identical frequency bin sizes<sup>21</sup>.

### 3.5.2.1 $\alpha = 25^\circ$ case

Flows are clearly shed about the bottom/base edge in an oscillating manner at approximately  $St = 0.49$ . Spectral densities are strongest at this point. As attested in figure 3.23; a minor trend towards lower  $St$  with lower  $Re$  is noted though this sensitivity is not nearly as marked as in Vino (2005) for  $\alpha_c$ , and considered to be more consistent with observations by Sims-Williams and Duncan (2002) where the phenomena appears  $Re$ -stable.

<sup>21</sup>Thus limiting the propensity for spectral energy to “bleed” into adjacent bins.

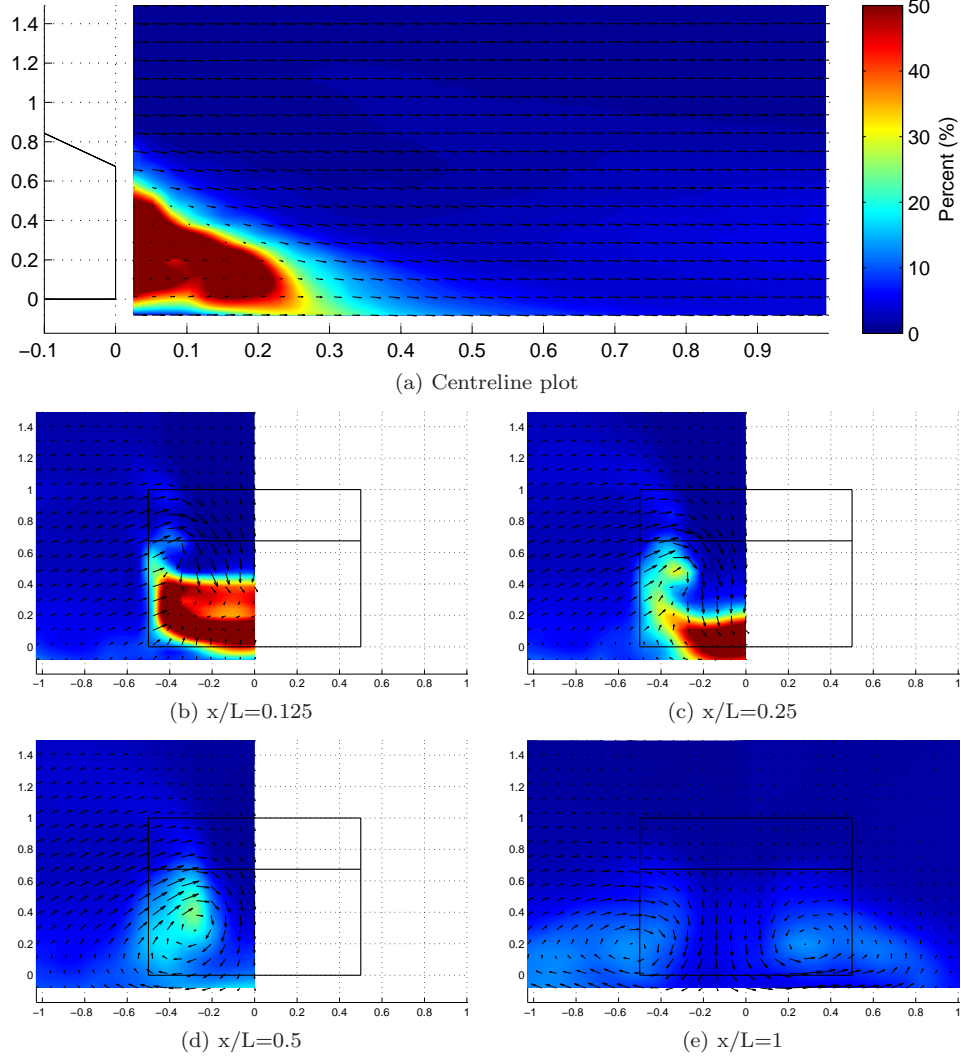


Figure 3.19: Vertical component of turbulence intensity ( $I_{ww}$ ) in wake of 25° Ahmed model at various body lengths ( $x/L$ ) behind model base (all dimensions normalised)

Figure 3.24a presents spectra for select points along the intersection of the base/backlight and model centreline. The same dominant spectral peak is present at various distances away from the main point of shedding, with energy decreasing with proximity. No clear spectral peaks are seen at the base/backlight edge, correlating well with mean pressures indicating intermittent flow attachment in this region, denoted by a broad dispersal of spectral energies about the mean.

Figure 3.24b (with ordinate scale reduced for clarity) presents pressures along the outboard backlight edge, and serves to indicate the progression of the axial vortices formed along this edge. Close to the backlight leading edge, the lack of any unique spectral peak indicates random detachment about a mean pressure, corroborating earlier statistical data. Spectra computed from pressure taps having increasing proximity to the base (commencing at  $\frac{z}{H} = 0.783$ , highlighted in

### 3.5. DYNAMIC PERFORMANCE OF MODELS IN ISOLATION

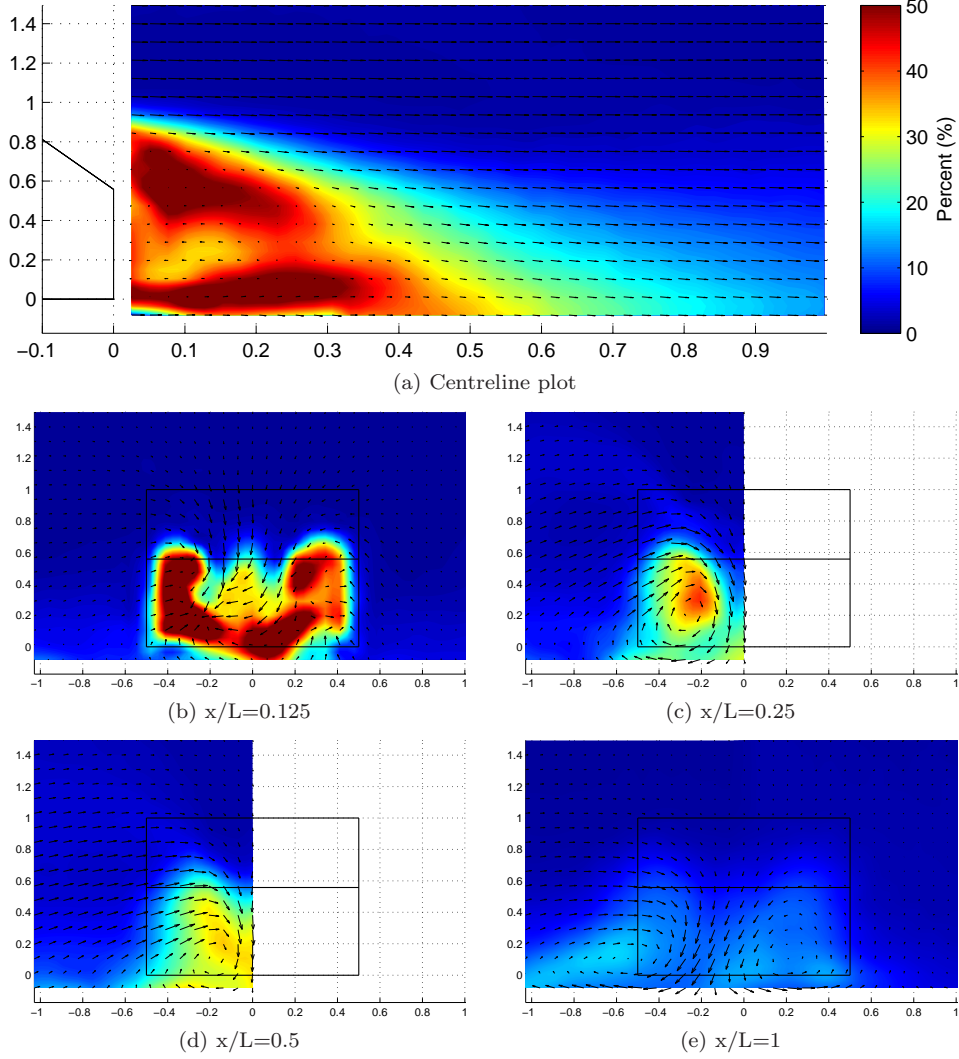


Figure 3.20: Axial component of turbulence intensity ( $I_{uu}$ ) in wake of  $35^\circ$  Ahmed model at various body lengths ( $x/L$ ) behind model base (all dimensions normalised)

red) denote a small spectral peak commensurate with base shedding, suggesting the vortices are formed in steady process and that as per Sims-Williams and Duncan (2002), they begin to oscillate in space as they interact with pumping of base flows in the near wake.

A small spectral peak is observed at most points at approximately  $St = 0.19$ , and is not mentioned in previous studies of this form. As this is evident in all spectra regardless of location (for both model configurations), it is assumed to be spurious<sup>22</sup> and is ignored.

With a single, key spectral peak dominating the  $\alpha = 25^\circ$  case, the findings of figure 3.24 are possibly better visualised as contours of spectral energy; these are presented in figure 3.27, showing contours of energy pertaining to frequencies within a  $\frac{1}{6}^{\text{th}}$  octave band about the frequency

<sup>22</sup>Likely sampling system noise; the commensurate frequency (22.5Hz) does not correspond with line noise.

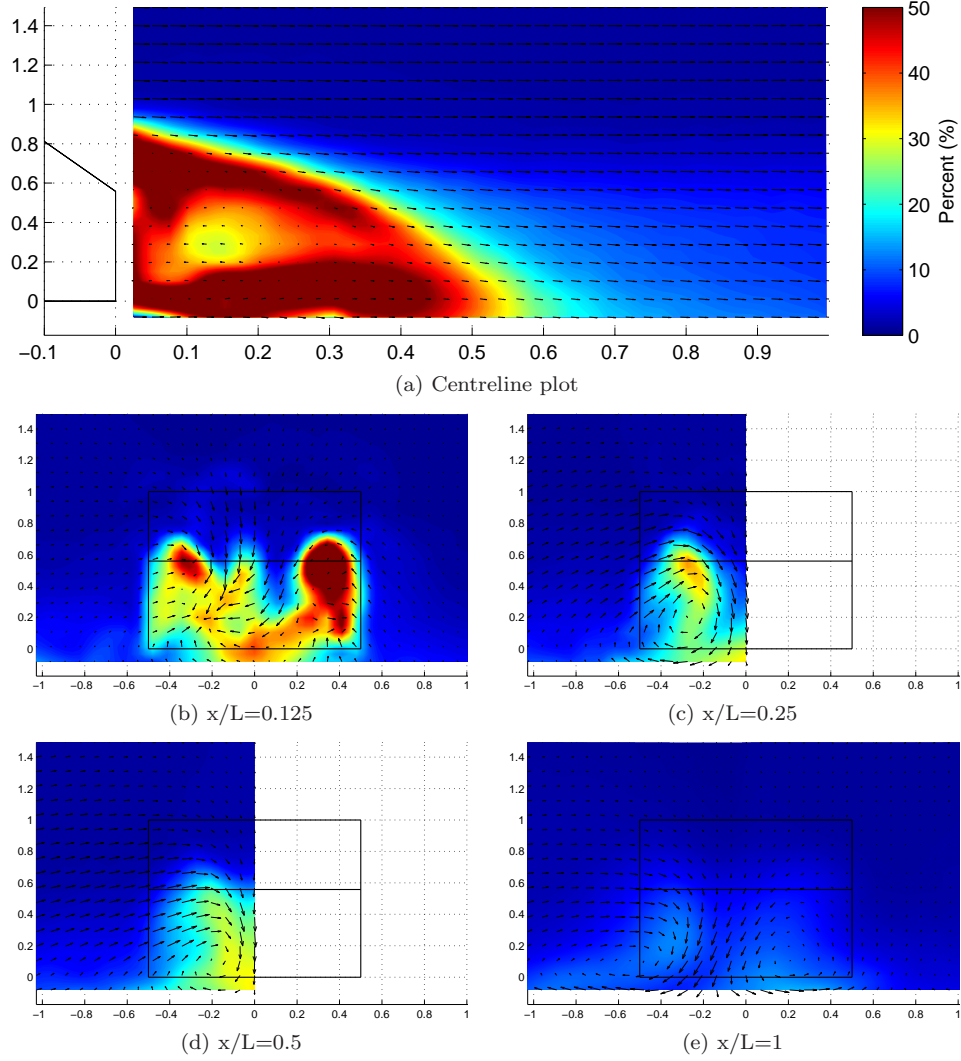


Figure 3.21: Transverse component of turbulence intensity ( $I_{vv}$ ) in wake of 35° Ahmed model at various body lengths ( $x/L$ ) behind model base (all dimensions normalised)

of interest<sup>23</sup>. The origin of the shedding frequency of interest can be clearly seen, corroborating Sims-Williams and Duncan (2002) in that oscillating features of the pre-critical wake are indeed a function of shedding at the bottom/base/centreline coincident. Figure 3.27b shows contours of relevant spectral energy in the wake centreline for velocity magnitude; oscillations of greatest strength are clearly concentrated at the mean closure of the base separated region, with flapping rollup of the shear layer pertaining to the lower of the base horseshoe vortex pair (expectedly) especially dominant in spectral energy.

<sup>23</sup>To allow for variances in tunnel speed, small perturbations in regular oscillations, etc.

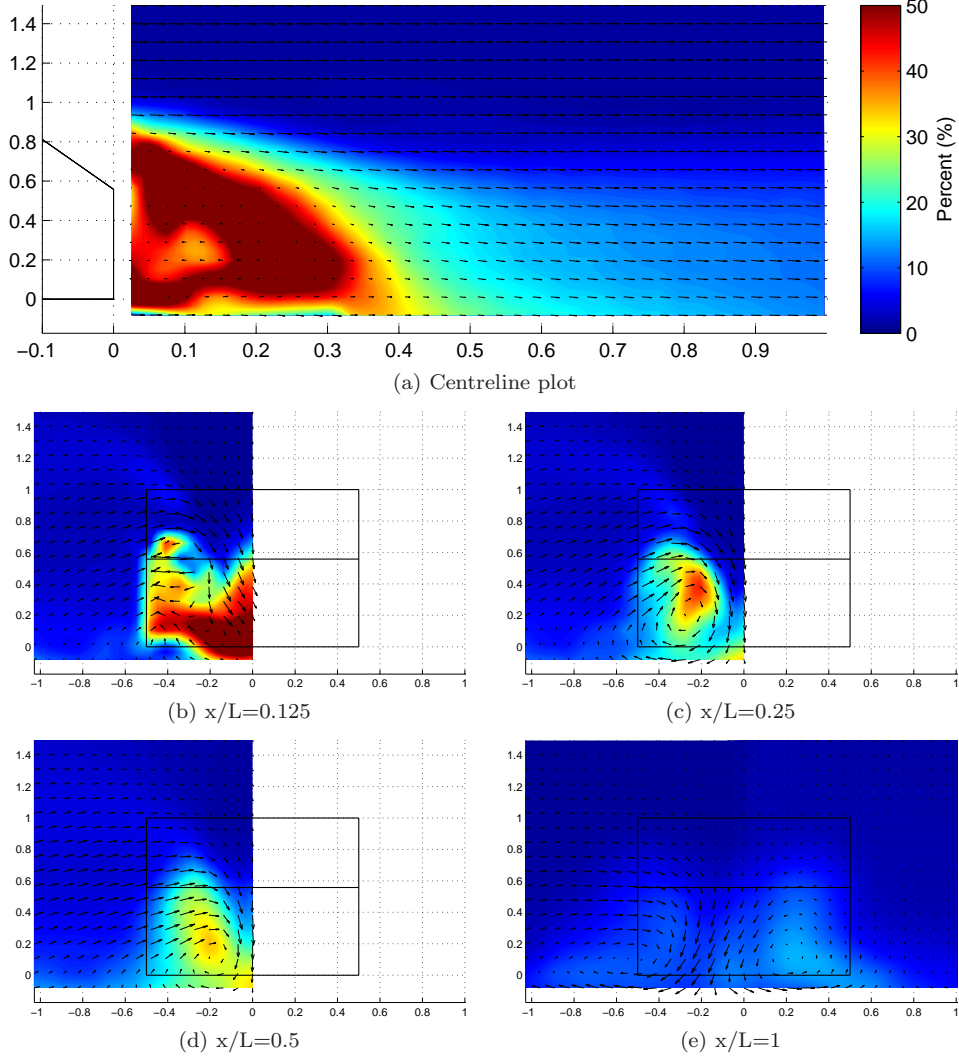


Figure 3.22: Vertical component of turbulence intensity ( $I_{ww}$ ) in wake of  $35^\circ$  Ahmed model at various body lengths ( $x/L$ ) behind model base (all dimensions normalised)

### 3.5.2.2 $\alpha = 35^\circ$ case

Clear oscillations are not observed in nearly as prominently in the  $\alpha = 35^\circ$  case. A peak at  $St = 0.28$  is observed (figure 3.26a), though energies are 30% of those observed for the pre-critical case, and the spectral peak is not quite as clearly defined. Lower frequency oscillations at frequencies closer to DC are noted at  $St = 0.035 - 0.04$  at points lying on edges corresponding to upper and lower shear layers. Energies are some 200% of the previous peak, though again the peak is not as clearly defined as per that in the pre-critical case. A nearest reference is offered by Brunn and Nitsche (2001) observed  $St = 0.17^{24}$ , though the prominence of the spectral peak is

<sup>24</sup>Expressed as  $St_H = 0.2$  on model height, as opposed to the square root of frontal area; duly converted this gives  $St = 0.2$ .

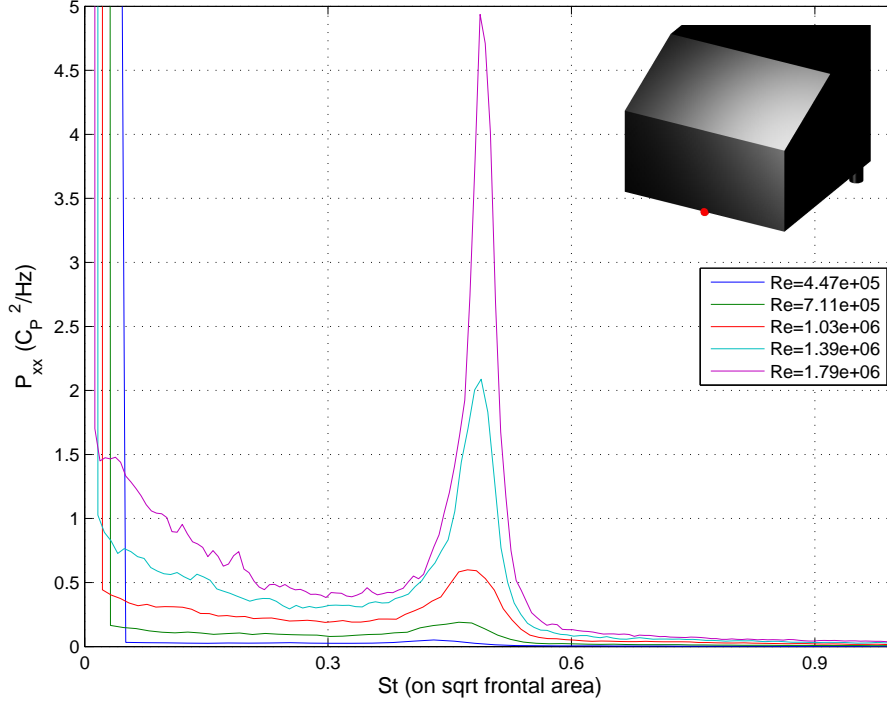


Figure 3.23: PSD at various  $Re$  at peak shedding location for  $\alpha = 25^\circ$  Ahmed model backlight and base surfaces

not characterised, and this concerns a model of stretched aspect ratio where  $W = 4H$ , the width of which occupied the test section, giving rise to an effectively two-dimensional form.

Figure 3.26b shows energies for a selection of pertinent pressure taps over the afterbody along the centreline plane. The tap just above the base/bottom/centreline coincident exhibits similar spectra, suggesting that the same flow structure may impinge on it. Earlier studies by Lienhart et al. (2000) (explored in Appendix E, page 266) indicate unique the responsible transverse vortices operate over to be unique. Spectral energies over the base support the surface soot deposition of figure 3.4; the vortex shed from the top impinges on the base; little coherent oscillation outside of the mean exists over the backlight.

Further elucidation of surface pressure spectra are provided in figures 3.27a and 3.27b; contours of spectral energy are presented for  $\frac{1}{6}^{\text{th}}$  octave bands about  $St = 0.037$  and  $St = 0.28$  respectively. The lower frequency oscillations are clearly weakly represented in the wake<sup>25</sup>, whilst spectral energies about  $St = 0.28$  feature prominently. Whilst the “flapping” of the bottom shear layer is constrained to between  $0.15 \leq \frac{x}{L} \leq 0.35$ , the shear layer atop the model extends further, exhibiting a comparatively long region over which shear layer rollup occurs in a manner not unlike flows over a backwards-facing step, where the degree of rollup is proportionate to the strength of

<sup>25</sup>Possibly, in being present on the model surfaces only in locations coincident with separation shear layer creation or the impingement of relevant flow phenomena, these low-frequency spectral energies concern a noted low-frequency pulsing in the IWT (see Appendix A.5.2, page 234).

the shear layer and the pressure difference either side of it at a given location downstream of the step (Simpson<sup>26</sup>). This phenomena is visible in the earlier centreline smoke visualisation of figure 3.6b, and is commensurate with the mean flows along the centreline (figure 3.14a, also figure E.1, page 267).

### 3.5.2.3 Cross-spectral analysis, $\alpha = 25^\circ$ case

Cross-spectral analysis (equation 2.10, page 83) allows further analysis by assessing phase relationships between various points. Using the bottom/base/centreline coincident as a reference point, figure 3.28a shows phase relationship to the tap above, which expectedly is only slightly phase forward given the propagation of pressure fluctuations from the shedding point. At the backlight/base/centreline coincident, however - figure 3.28b - though spectral peaks coincide in frequency, pressure fluctuations are clearly out of phase. Previous visualisations confirm a span-wise horseshoe vortex pair operating over the base region; these results agree with those of Vino (2005) for the  $\alpha_c$  case in that these vortices appear to operate out of phase. The significantly lower spectral energy at the compared point suggest that the upper vortex is formed as a function of the lower vortex; as low pressure packets “pump” the base region and continue downstream, the pressure difference vacated at the upper base region forms a “reactionary” vortex. This sequence is duly captured in smoke flow visualisation in figure 3.29.

Figure 3.28c presents a contour plot of the cross-spectral phase magnitude for all points over the afterbody surface, taken against the bottom/base/centreline coincident and at the key frequency of interest. Oscillating flow structures clearly operate over the lower half of the base in phase with the key point, and are out of phase over the upper half. Of greater interest is that flows over the backlight surface are similarly out of phase (to  $-150^\circ$  for pressure taps at  $\frac{z}{H} = 0.946$ ). Flows over the backlight are therefore affected by those about the base, distorted by relevant oscillations in time. It remains important to consider phase relations in light of the energies of the spectral content concerned: figure 3.28c should be taken in the context of figure 3.27. Figures 3.28d and 3.28e provide the relevant comparison; whilst the phase relations are clear, spectral energy at the frequency of interest clearly diminishes with reduced proximity to the key shedding location.

It should be stressed that this infers distortion in time of backlight flows owing to relatively powerful base flow oscillations; it does not infer that backlight and base flow structures bleed into each other. The latter conclusion requires synthesis with earlier surface and smoke flow visualisation (figures 3.3a and 3.6a); it is known that the downstream closure of the separated region over the backlight is essentially turbulent in nature. Results of cross-spectral phase analysis suggest that backlight flows are not only buffeted by the upper base horseshoe vortex, but that the backlight separated region may at times be drawn into blending with it. This presents a precursor to work by Vino (2005) for the  $\alpha_c$  case, which is correct (as the high-drag  $\alpha_c$  case features similar flows to the pre-critical  $\alpha = 25^\circ$  case with stronger dominant axial vortices).

---

<sup>26</sup>In Okada (2006)



Figure 3.28c also provides a unique perspective from which to confirm suspicions of Ahmed et al. (1984) and simulations of Krajnović and Davidson (2005); vortex impingement over the backlight appears to oscillate in phase with the upper of the base horseshoe vortex - which is drawn into the axial direction having legs with the same sense as the dominant axial vortex - and thus (as suspected) blends with it. It may thus be possible to extend earlier findings shown in figure 3.24b, where it is revealed that the impingement of the C-pillar axial vortices is initially steady, then begins to oscillate with increasing proximity to the base. This could infer that the location of vortex breakdown may not only translate with base pressure oscillations - suggested in computational analysis by Johnson (2005) - but may further coincide with mixture of the backlight separated region and the upper base horseshoe vortex as one complete, eddying motion. This is duly captured using smoke visualisation in figure 3.30<sup>27</sup> The upstream portion of the axial vortex that remains steady is clearly visible, corroborating spectra in figure 3.28c.

#### 3.5.2.4 Cross-spectral analysis, $\alpha = 35^\circ$ case

The isolation of clear relationships between coherent oscillations in the  $\alpha = 35^\circ$  flow field is more difficult to discern, given the lesser definition of any spectral peaks over the model backlight and/or base surfaces.

Earlier suggestions that flows just above the bottom/base/centreline coincident concern impingement of phenomena owing to separation from the bottom/base edge are proved correct in figure 3.31a, showing similar spectral energies which remain in phase for all spectra below approximately  $St = 0.375$  (above this point there is a sharp drop in spectral energy towards the noise floor, rendering cross-spectral phase data irrelevant). Further up the base at  $\frac{z}{H} = 0.418$ , weaker spectral energy exhibits a clear out-of-phase relationship with shedding phenomena at the lower edge (figure 3.31b). This is continued at the base/backlight edge (figure 3.31c) and further still up the backlight at  $\frac{z}{H} = 0.779$  (figure 3.31d), where although weak, notable spectral energies above the noise floor exist.

Analysis of upper and lower afterbody trailing edges - figure 3.31e - is comparatively inconclusive; oscillations are in phase at the the peak of interest for the bottom/base/centerline coincident, however the location reveals it's own unique spectral peak at slightly lower frequency. This is not surprising; whilst upper and lower shear layers govern the nature of the post-critical wake, the nature of flows and surrounding geometries that drive them are unique. Whilst this does not suggest that the upper and lower shear layers shed low pressure packets in an out-of-phase manner, the impingement of both vortices over the base in an unstable node is likely an oscillating phenomenon driven by stronger oscillations of underbody flows shedding at the bottom trailing edge, creating strong pressure variations within the afterbody separated wake region, driving recirculation of flows pertaining to the upper shear layer. As the distance between both shear layers is farther than

---

<sup>27</sup>The influence of the smoke probe is not ignored. Every precaution was taken to ensure the presence of the probe did not cause the eddying motions observed in the downstream portion of the impinging vortex. The probe was rigidly mounted on a fixed retort. Care was taken to ensure the oscillations observed matched those observed in surface pressure spectra presented in figure 3.24b.



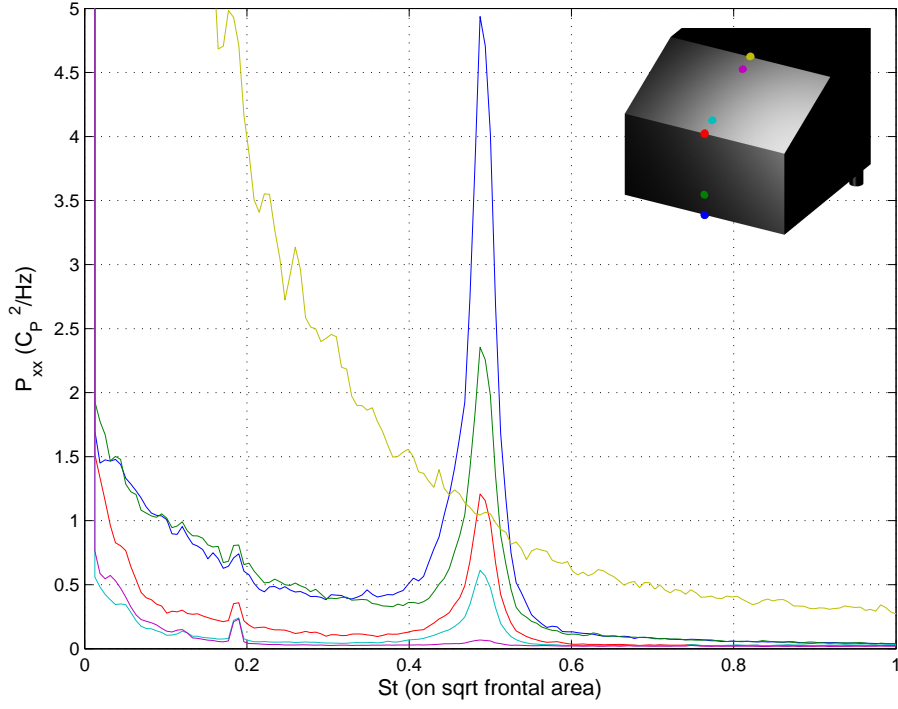
for the  $\alpha = 25^\circ$  case (the energy of oscillations driven by resultant eddying flows being smaller) - with the upper likely more significantly affected by a moderate level of freestream turbulence in the IWT than in reference experiments<sup>28</sup> - some degree of randomness in key spectral levels are anticipated, and duly observed in lesser-defined spectral peaks. Cross-spectral phase assessments (particularly when viewed against  $\alpha = 25^\circ$  results) need be taken in this context.

Certainly results in figure 3.31 suggest the lower vortex is isolated to the lower half of the base region's projection. This is captured in smoke visualisation in figure 3.32, which also captures the extent of impingement on the base region, corroborating well with the spectral analysis presented.

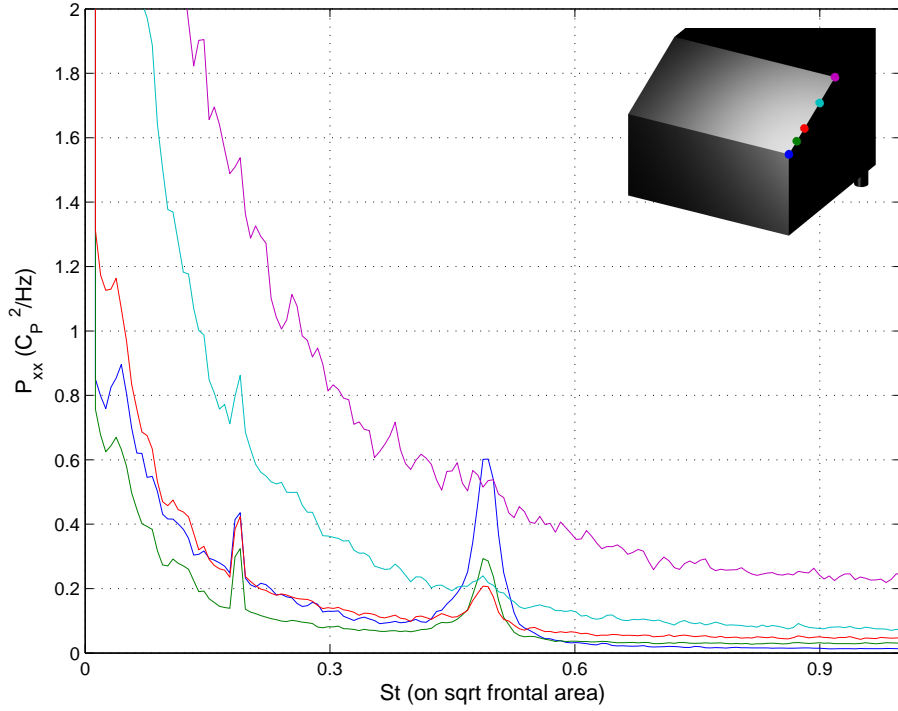
---

<sup>28</sup>Brunn et al. (2007), Lienhart et al. (2000)

### 3.5. DYNAMIC PERFORMANCE OF MODELS IN ISOLATION



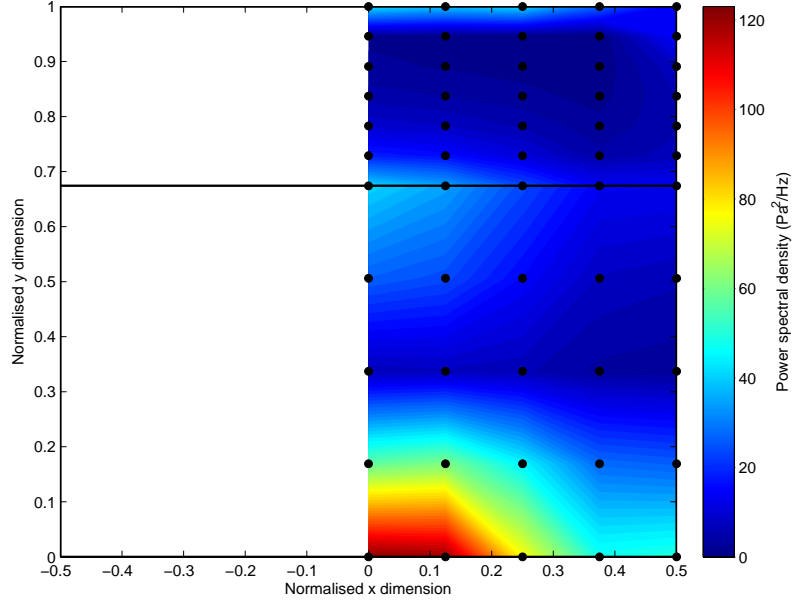
(a) Along afterbody centreline



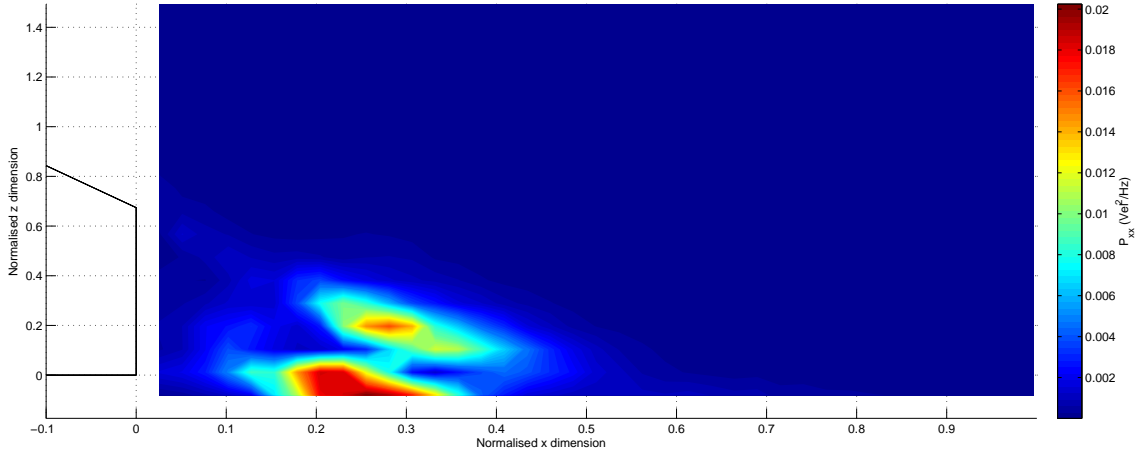
(b) Along backlight side edge

Figure 3.24: PSD for points of interest over  $\alpha = 25^\circ$  Ahmed model backlight and base surfaces at  $Re = 1.8 \times 10^6$

### 3.5. DYNAMIC PERFORMANCE OF MODELS IN ISOLATION



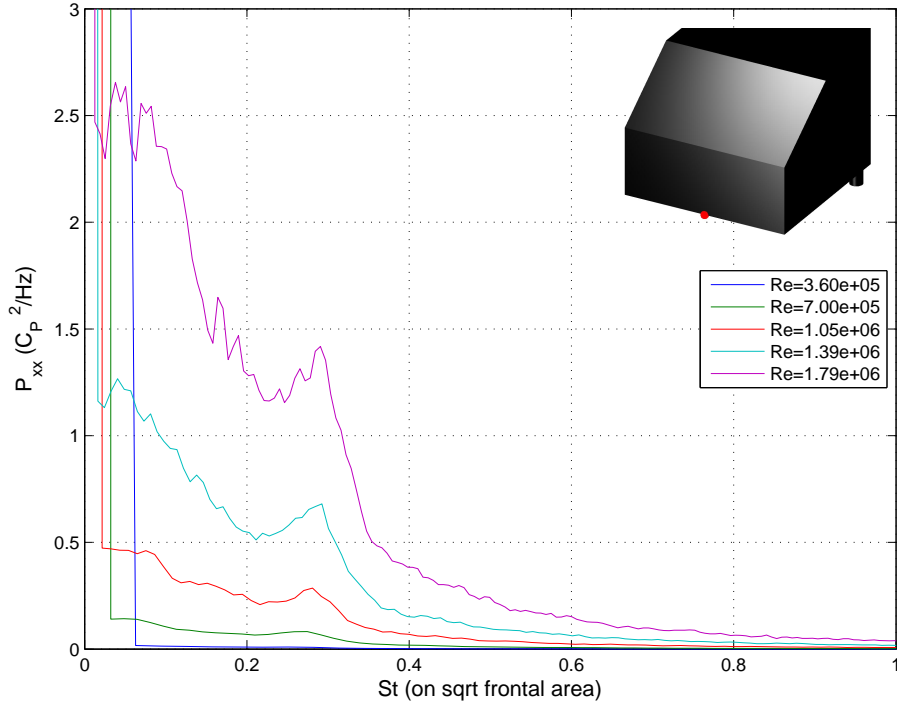
(a) Over backlight and base surfaces



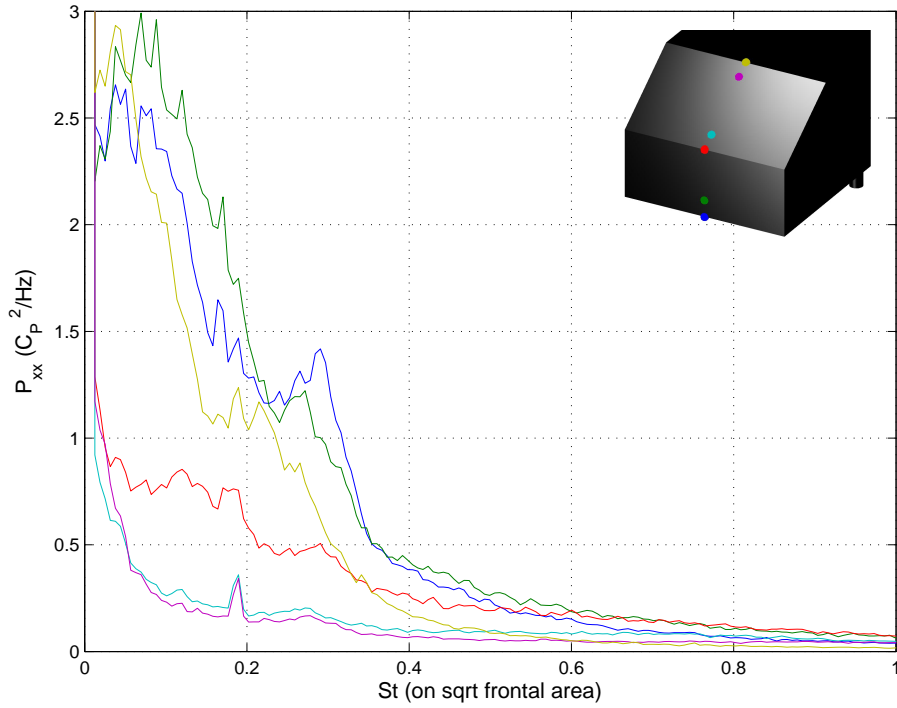
(b) Along centreline plane within  $\frac{1}{6}^{\text{th}}$  octave of  $St = 0.49$

Figure 3.25: PSD at  $St = 0.49$  for  $\alpha = 25^\circ$  at  $Re = 1.8 \times 10^6$

### 3.5. DYNAMIC PERFORMANCE OF MODELS IN ISOLATION



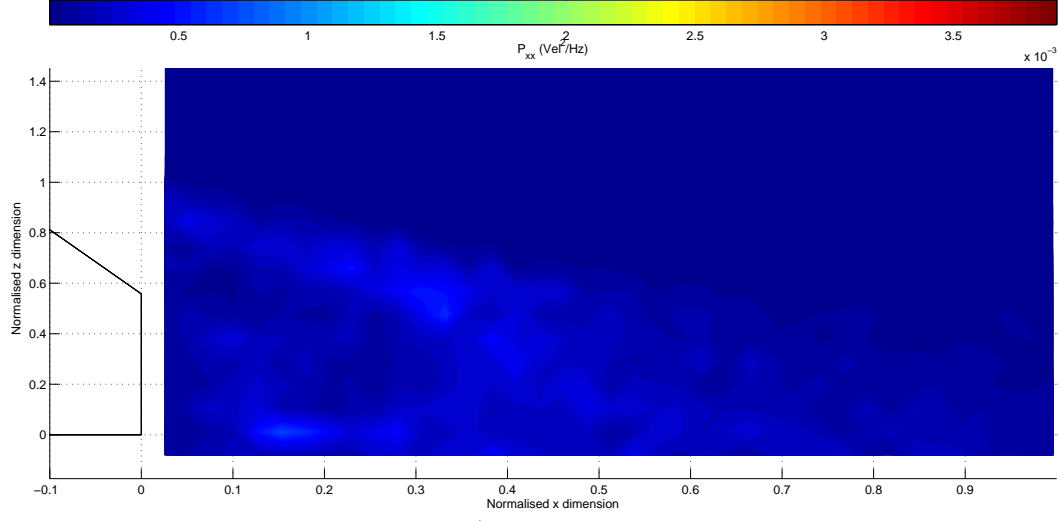
(a) Power spectral density at various  $Re$  at peak shedding location for  $\alpha = 35^\circ$  Ahmed model backlight and base surfaces



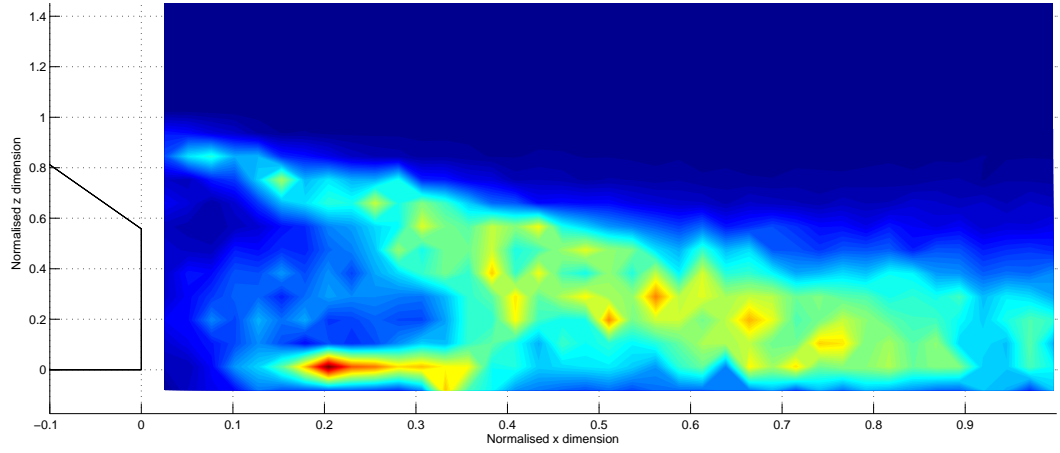
(b) Along afterbody centreline

Figure 3.26: PSD for points of interest over  $\alpha = 35^\circ$  Ahmed model backlight and base surfaces at  $Re = 1.8 \times 10^6$

### 3.5. DYNAMIC PERFORMANCE OF MODELS IN ISOLATION



(a) For  $\frac{1}{6}$ th octave about  $St = 0.037$



(b) For  $\frac{1}{6}$ th octave about  $St = 0.28$

Figure 3.27: PSD for  $\alpha = 35^\circ$  Ahmed model wake centreline at  $Re = 1.8 \times 10^6$

### 3.5. DYNAMIC PERFORMANCE OF MODELS IN ISOLATION

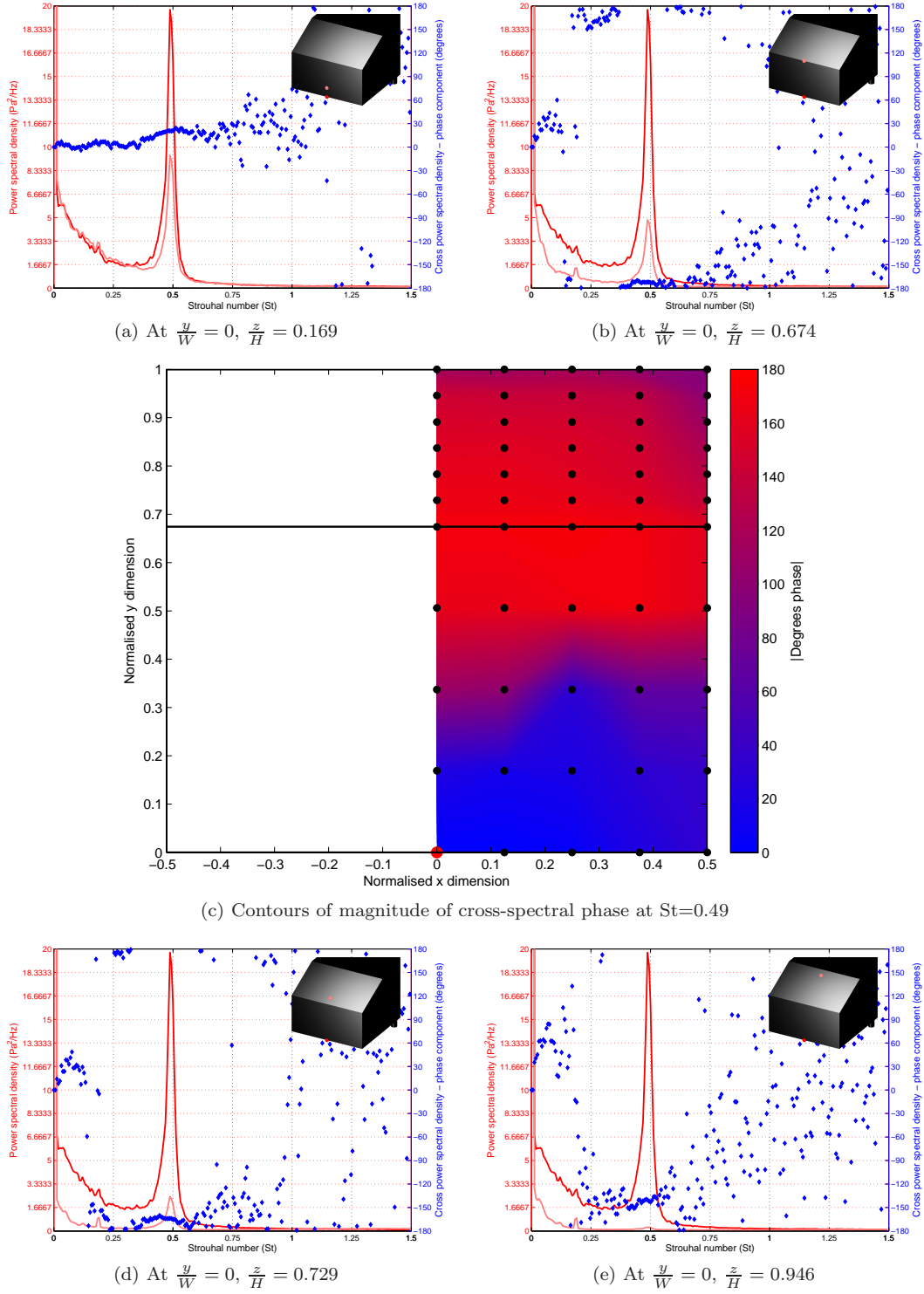


Figure 3.28: Cross-spectral performance for  $\alpha = 25^\circ$  Ahmed model backlight and base surfaces at  $Re = 1.8 \times 10^6$  relative to bottom/base/centreline coincident (in red)



Figure 3.29: Shedding at base of  $\alpha = 25^\circ$  Ahmed model

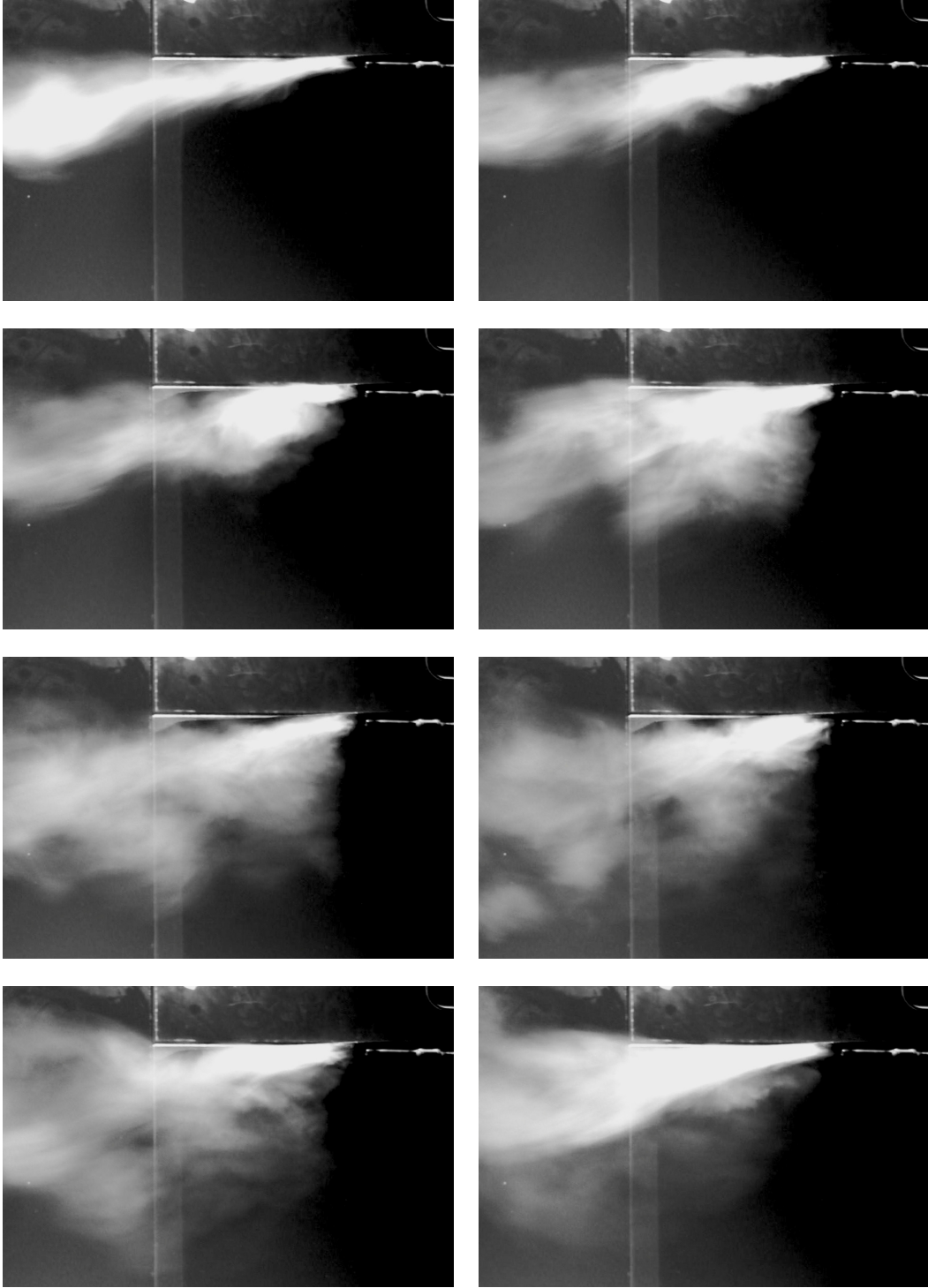


Figure 3.30: Periodic oscillation and bursting of axial C-pillar vortices in near wake of  $\alpha = 25^\circ$  Ahmed model



### 3.5. DYNAMIC PERFORMANCE OF MODELS IN ISOLATION

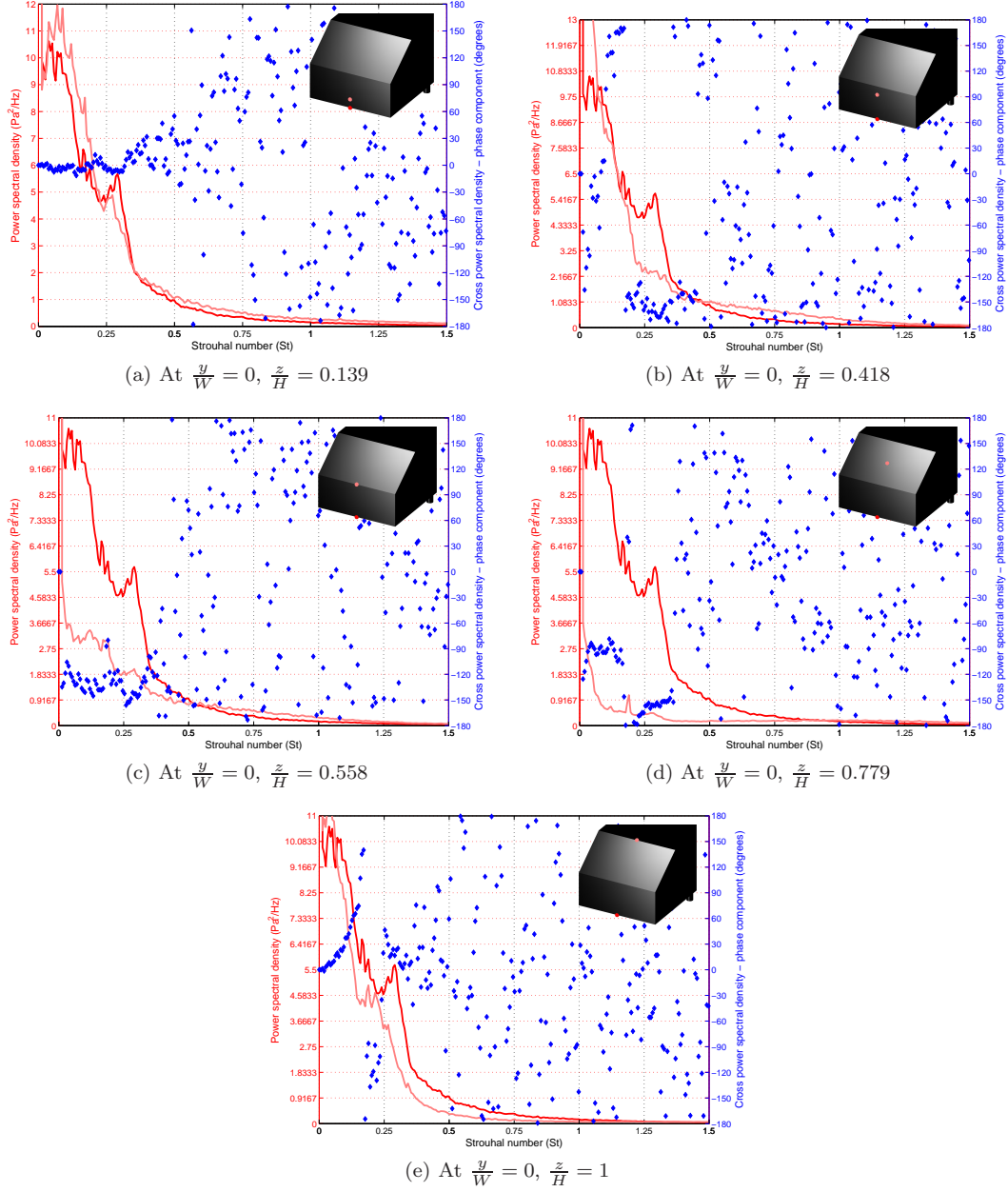


Figure 3.31: Cross-spectral performance for  $\alpha = 35^\circ$  Ahmed model backlight and base surfaces at  $Re = 1.8 \times 10^6$  relative to bottom/base/centreline coincident (in red)



Figure 3.32: Shedding at base of  $\alpha = 35^\circ$  Ahmed model

### 3.6 Preliminary analysis of far wake characteristics

The prior analyses are primarily concerned with the near wake of the pre and post-critical cases. Whilst the following chapter observes and deconstructs force phenomena in two-model platoons with a particular emphasis on the (more complicated) near-wake interactions concerning closer inter-model spacing, the following analysis of axial velocity deficit and flowfield angularity in the far wake is provided to examine the potential ultimate limit (in  $\frac{x}{L}$ ). It is logical that a reduction in axial velocity relative to the freestream - and thus a reduction in dynamic pressure - should yield a consequent reduction in pressure over the trailing model forebody, and thus a reduction in drag force. However it has been shown by Vano (2005) that high-momentum entrained flows between dominant axial vortices formed about leading model “C-pillars” can serve to increase trailing model forebody pressure significantly.

Figures 3.33-3.35 provide normalised axial velocity deficit contours and in-plane vectors composed of  $V$  and  $W$  components for far wakes ( $\frac{x}{L} = 1 - 6$  in increments of  $\frac{x}{L} = 1$ ) behind Ahmed models of  $\alpha = 0^\circ$ ,  $\alpha = 12.5^\circ$ ,  $\alpha = 25^\circ$ ,  $\alpha = 30^\circ$  and  $\alpha = 35^\circ$  backlight configurations<sup>29</sup>. A projection of key model afterbody geometry is also presented in each plane. Data were acquired using the Cobra probe<sup>30</sup>. As the spectral performance of the  $\alpha = 0^\circ$  and  $\alpha = 12.5^\circ$  samples were not quantified and as the dynamic performance of the Cobra probe allows a significantly faster sampling, a 1kHz sampling rate was used. Data were acquired over 13 realisations (at 50% overlap) of 1024-element blocks<sup>31</sup>. Mean results were averaged from estimated time histories. The spatial resolution applied was slightly cruder than for prior wake plots (increasing from 20mm to 25mm). The spatial range evaluated in the  $yz$  plane concerned  $-1.03 \leq \frac{y}{W} \leq 1.03$  and  $-0.05 \leq \frac{z}{H} \leq 1.29$ .

The following themes were observed:

- In all cases the most significant flow angularity - always a downwash - was observed at  $\frac{x}{L} = 1$ . The magnitude of this phenomena significantly reduced by  $\frac{x}{L} = 2$ .
- (Flow asymmetry affects aside) only in the  $0^\circ$  case - where, effectively, no backlight angle exists and axial vortices have no “C-pillar” to roll up from - were axial vortices not observed. The velocity deficit instead was instead observed largely within the model projection, with a tangible reduction observed even at  $\frac{x}{L} = 6$ . This may explain the positive drag reductions observed in platoons of forms with similar afterbody geometries (Hammache et al. 2001, Zabat et al. 1993).
- Axial vortices clearly form in the  $\alpha = 12.5^\circ$  case and increase in strength to the  $\alpha = 30^\circ$  case. In the  $\alpha = 25^\circ$  and  $\alpha = 30^\circ$  cases, the axial velocity deficit comprising the dominant axial vortex cores has already translated largely outside of the model projection at  $\frac{x}{L} = 2$ ,

<sup>29</sup>For ease of visualisation, the  $x$  axis is not presented to scale.

<sup>30</sup>As reversion was not observed in prior analyses for  $\frac{x}{L} \geq 1$ , the greater angular acceptance of the ECA probe was not required.

<sup>31</sup>A greater number of realisations were deemed unnecessary; the change in the mean values observed fell within device error in back-to-back testing, furthermore, as the spectral properties of this data were not of interest, a significant number of realisations were not required for heightened statistical confidence in relevant spectral calculations.

### 3.6. PRELIMINARY ANALYSIS OF FAR WAKE CHARACTERISTICS

and the recovery of any velocity deficit in the projection is very nearly complete. Given this and the negligible downwash at this location, it is unlikely that a trailing model in such a wake would experience significant (if any) drag force reductions if located with leading edge at or beyond this location and with no lateral misalignment.

- A clearly unique flow mode is observed for the  $\alpha = 35^\circ$  case, consistent with previously observed phenomena relevant to the configuration. A weaker pair of axial vortices is formed off-body which similarly expand and translate away from the model projection with increasing distance from the model base, however a more substantial, lower proportion of the projection is observed to contain a velocity deficit at  $\frac{x}{L} = 2$ , as is a slight - but more prominent (compared to the  $\alpha = 25^\circ$  wake) - downwash observed at this location. These two factors have opposing effects on drag force and are slight nonetheless. It is anticipated, for a trailing model with leading edge located at this location and no lateral misalignment, that any deviation in drag force from isolation values would be slight at best. The further diminishment of these features at  $\frac{x}{L} = 3$  suggest a more definitive return to isolation values at and beyond this spacing.

The data acquired suggests that for the pre and post-critical forms evaluated throughout, little if any change in drag force vis-à-vis isolation values should be observed beyond  $\frac{x}{L} = 2$ .

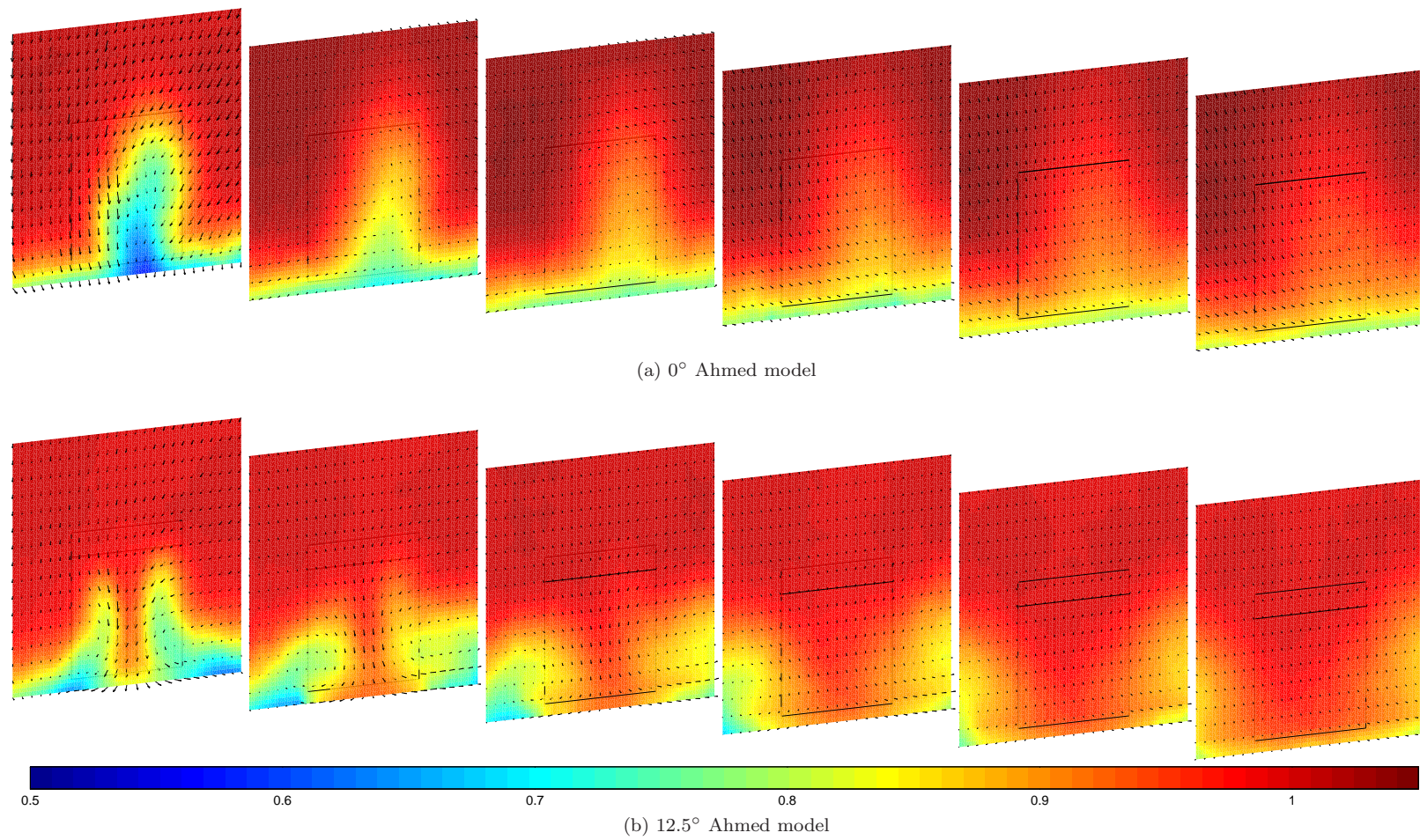


Figure 3.33: Wake slices of  $\frac{U}{U_\infty}$  in far wake of Ahmed model,  $\frac{x}{L} = 1 - 6$ ,  $25^\circ$  and  $30^\circ$  backlight angle



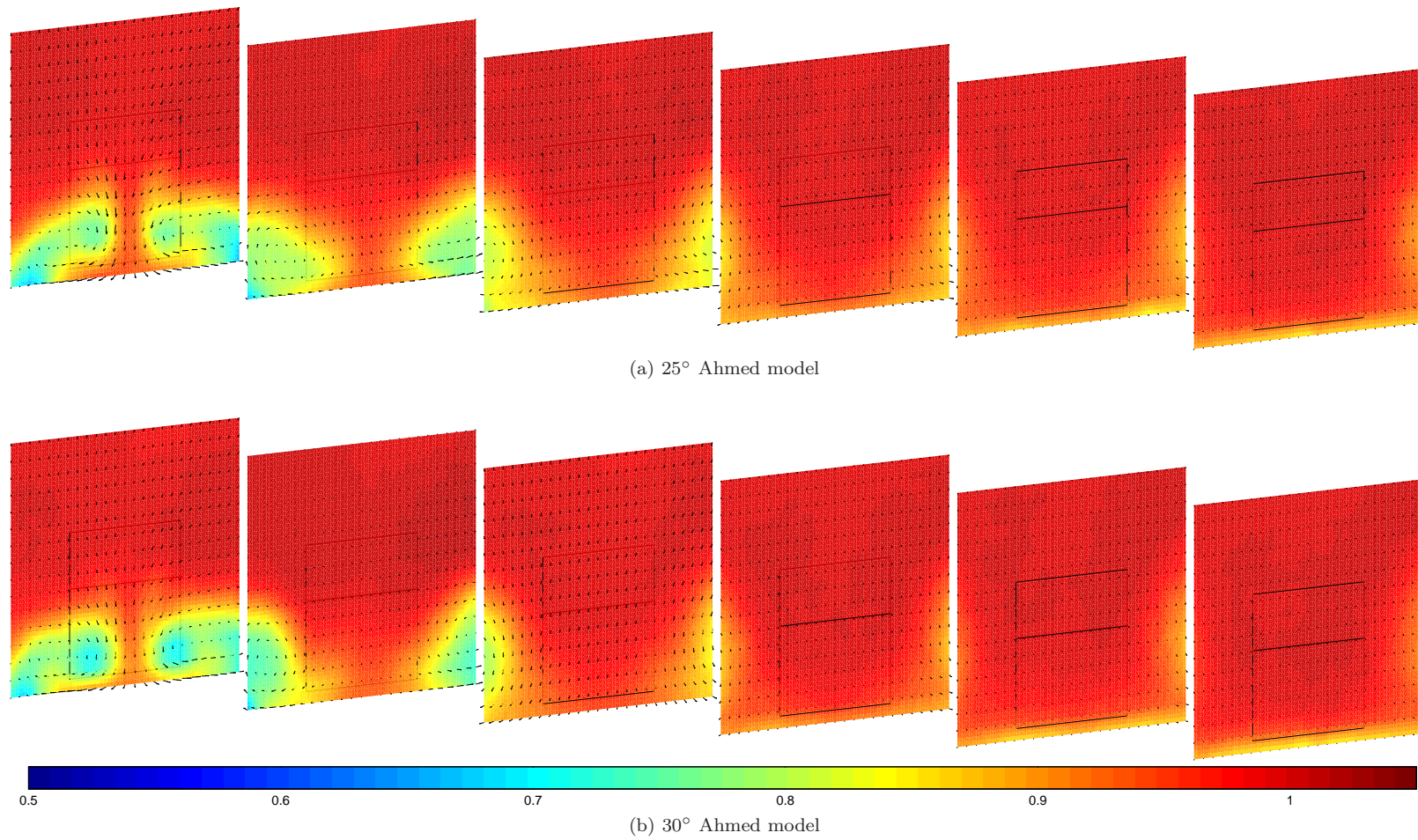


Figure 3.34: Wake slices of  $\frac{U}{U_\infty}$  in far wake of Ahmed model,  $\frac{x}{L} = 1 - 6$ ,  $0^\circ$  and  $12.5^\circ$  backlight angle

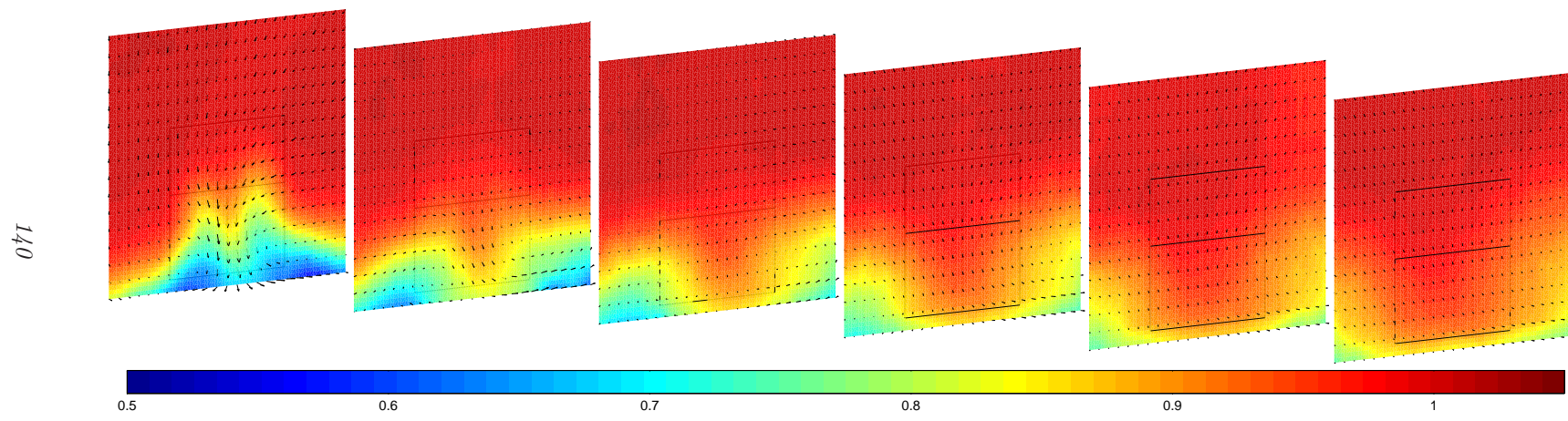


Figure 3.35: Wake slices of  $\frac{U}{U_\infty}$  in far wake of Ahmed model,  $\frac{x}{L} = 1 - 6$ ,  $35^\circ$  backlight angle

## 3.7 Conclusions

The salient steady and unsteady features of flows about the  $\alpha = 25^\circ$  and  $\alpha = 35^\circ$  models were successfully deconstructed.

The models presented for analysis in the RMIT IWT performed successfully, reconciling well with results of prior research in light of the freestream flow characteristics of the IWT.

Spectral methods were used to good effect in both cases, allowing both an extension of knowledge presented in prior works and the reconciling of unique aspects of flow phenomena observed in data acquired via a variety of qualitative and quantitative means.



## Chapter 4

# Results II: two model platoons, longitudinal spacing

This chapter presents results pertaining to organised convoys of two models with close inter-vehicle longitudinal spacing, referred to as “two-model *platoons*”.

Whilst a number of studies exist documenting mean body forces on models of various specific vehicle geometries in tandem arrangements (Browand and Hammache 2004, Hammache et al. 2001, Hong et al. 1998, Marcu and Browand 1998, Michaelian and Browand 2000, Romberg et al. 1971, Zabat et al. 1993; 1994), few deconstructions of relevant flow phenomena have been undertaken. In particular there have been no generalised vehicles studied where the influence of backlight angle is varied (i.e. around  $\alpha_c$ , allowing contrast between unique afterbody flow structures). An initial study of a platooned arrangement is presented by Vino (2005), wherein forces relevant to a platoon of two  $\alpha_c$  Ahmed models are deconstructed using primarily time-averaged and statistical data, showing that contrary to available data for homogeneous platoons of squareback and notchback vehicles, detrimental drag force is experienced by a model trailing a fastback form, at least at  $\alpha_c$ .

The work presented in this chapter extends on the above body of knowledge by examining key phenomena - largely concerning flows in the gap and on adjacent surfaces - for a two-body platoon led by a model with pre-critical ( $\alpha = 25^\circ$ ) afterbody geometry using mean, statistical and spectral data. Data concerning the suitability of leading fastback forms is further expanded by contrasting the above with results for a similar two-model platoon employing a leading post-critical ( $\alpha = 35^\circ$ ) model.

Deconstruction of relevant phenomena is first presented using two dimensional surface and flow field data along  $y = 0$ , then further expanded into a three-dimensional analysis across  $\pm y$ . Qualitative methods are used to investigate elements of flow phenomena encountered beyond the limitations of the quantitative methods employed.

The chapter concludes with an analysis of spectral properties of gap flows and an examination of trailing model afterbody phenomena.

All experiments are conducted at  $Re = 1.8 \times 10^6$ .

## 4.1 Force data

Force data are presented as normalised force coefficients (e.g.  $\frac{C_D}{C_{D\infty}}$ ) in figure 4.1, i.e. being normalised by  $C_D$  or  $C_L$  for a model-in-isolation at the relevant  $x$  location in the test section. Pitch forward moment ( $-M_y$ , taken about the model geometric centre) is similarly presented, being indicative of lift characteristics, unique (backlight particularly) flow structures in the pre and post-critical cases and in being pertinent in assessing aerodynamic stability<sup>1</sup>.

Relevant force and moment coefficients for the model-in-isolation at the most forward location utilised in testing are presented in table 4.1.

Force/moment coefficient	$\alpha = 25^\circ$	$\alpha = 35^\circ$
$C_D$	0.30	0.27
$M_y$	-1.10	-0.01

Table 4.1: Model-in-isolation values for  $C_D$  and  $M_y$

### 4.1.1 Limitation of spacing range

After initial experimentation at significant separation (to  $6L$ ) no difference in model forces exceeding the error margins of the methods and equipment employed could be found at spacing greater than  $1.5L$ . For all cases bar that of a trailing model in the wake of a pre-critical model, pitch moment data (figure 4.1b) indicates a return to isolation values at  $\frac{x}{L} \leq 2L$ . The spacing range evaluated is thus limited to  $\frac{x}{L} \leq 2L$ .

The relevance of the closest spacing evaluated  $\frac{x}{L} = 0.125$  is questionable considering any practical relevance (see section 1.4.2.1, page 46). It is included to allow comparison with related studies (Chen et al. 1997, Hammache et al. 2001, Hong et al. 1998, Marcu and Browand 1998, Michaelian and Browand 2000, Vino 2005, Zabat et al. 1993) and to explore unique aerodynamic phenomena observed at ultra-close spacing.

### 4.1.2 Force data trends

The following trends are evident in drag force data to  $\frac{x}{L} < 2$  as presented in figure 4.1a:

---

<sup>1</sup>In particular, rear axle lift.

- *Leading model* drag force is *always decreased* relative to model-in-isolation values.
- *Trailing model* drag force is *always increased* relative to model-in-isolation values.
- The *net drag* of the platoon is *always reduced*.
- The magnitudes of both the *leading model drag reduction* and *trailing model drag increase* are *greater for the pre-critical lead model* at close ( $0.125 \leq \frac{x}{L} \leq 0.25$ ) spacing.
- Both *maximum trailing model drag increase* and *maximum leading model drag reduction* occur at larger spacing for the post-critical model ( $\frac{x}{L} = 0.375$  vs  $\frac{x}{L} = 0.25$  for the pre-critical case).

Whilst drag force trends appear to be broadly similar, closer investigation reveals significant differences pending the leading model geometry.

#### 4.1.2.1 Specific force trends for platoon with $\alpha = 25^\circ$ leading model

The increase in drag on the trailing model (to  $1.38 \frac{C_D}{C_{D\infty}}$ ) coincides with a decrease in leading model drag to  $0.36 \frac{C_D}{C_{D\infty}}$  at  $\frac{x}{L} = 0.25$  spacing between models. The rise in leading model drag to  $0.63 \frac{C_D}{C_{D\infty}}$  at  $\frac{x}{L} = 0.5$  spacing is pronounced, though not nearly as sharp as that observed by Vino for a leading  $\alpha_c$  model (figure 1.37a, page 50). A significant change in flow structure is suggested by an increase in pitch-down moment (to  $0.8 \frac{C_{My}}{C_{My\infty}}$ , evidenced in figure 4.1b) suggesting maximum lift about the lead model rear at this spacing.

In assessing  $M_y$  for the rear model: a maximum  $1.62 \frac{C_{My}}{C_{My\infty}}$  is observed at  $\frac{x}{L} = 0.125$ , indicating a pitch-down moment consistent with flow impingement on the model forebody as per Vino's results for the  $\alpha_c$  case. This decreases rapidly to  $1.30 \frac{C_{My}}{C_{My\infty}}$  at  $\frac{x}{L} = 0.375$ . Between  $0.5 \leq \frac{x}{L} \leq 2$  spacing, pitch moment appears to gradually decline towards the model-in-isolation value, however remains nearly 20% above this at  $2L$  spacing. This suggests downwash from the leading model wake to still be prevalent, however sufficiently diminished (or operating in conjunction with other flow phenomena) to not increase model drag beyond model-in-isolation values.

It is suggested that the initial flow mode at close spacing broadly concerns Azim and Gawad (2000)'s vortex impingement mode: spacing is too close for a low-pressure cavity to form between the models, thus the dominant axial vortices still appear to form at  $\frac{x}{L} = 0.125$  spacing. Similarly, leading model drag is likely reduced by reductions in strength of the horseshoe vortex pair operating over the pre-critical base, giving rise to higher base pressures:  $0.80 \frac{C_{My}}{C_{My\infty}}$  at  $\frac{x}{L} = 0.25$ , rising to model-in-isolation  $M_y$  at  $2L$  spacing is consistent with this suggestion. The formation of the affected vortex pair is known to be "driven" by the separating shear layer about the base/bottom/centreline coincident (Sims-Williams and Dominy 1998, Sims-Williams and Duncan 2002). It is also likely that the presence of the trailing model in near proximity gives rise to feedback along relevant leading model separating shear layers (Bull et al. 1996), affecting vortex formation

in the region  $0.25 \leq \frac{x}{L} \leq 2$ . Consequently the frequency of shedding in this region should diminish with decreased spacing (Bull et al. 1996, Leclercq and Doolan 2009, Sakamoto and Haniu 1988, Shiraishi et al. 1986, Takeuchi and Matsumoto 1992, discussed further in section 1.4.3.2, page 53).

A clear change occurs at very close spacing ( $\frac{x}{L} = 0.125, 1.06 \frac{C_{My}}{C_{My\infty}}$ ) not consistent with the above theory. Additional data are required for deconstruction.

#### 4.1.2.2 Specific force trends for platoon with $\alpha = 35^\circ$ leading model

Peak drag reduction (to  $0.44 \frac{C_D}{C_{D\infty}}$ ) for the  $\alpha = 35^\circ$  leading model was observed at both  $\frac{x}{L} = 0.25, 0.375$  spacing<sup>2</sup>. This is little changed ( $0.47 \frac{C_D}{C_{D\infty}}$ ) at  $\frac{x}{L} = 0.5$ , then rising to  $0.68 \frac{C_D}{C_{D\infty}}$  by  $\frac{x}{L} = 0.75$ .

Broadly speaking, the trailing model exhibits broadly similar drag force trends to those experienced with a leading pre-critical model effectively “shifted” by an additional  $\frac{x}{L} = 0.25$  (peak trailing model drag of  $1.36 \frac{C_D}{C_{D\infty}}$  at  $\frac{x}{L} = 0.375$ . At closest spacing the trail model exhibits significantly less drag than it does when incremented slightly further ( $1.12 \frac{C_D}{C_{D\infty}}$  at  $\frac{x}{L} = 0.125$  against  $1.29 \frac{C_D}{C_{D\infty}}$  at  $\frac{x}{L} = 0.25$ ).

Consideration of  $M_y$  suggests the underlying flow phenomena to be completely different. For clarity of presentation, figure 4.1b is presented with two ordinates allowing unique scales for pre and post-critical leading model platoons<sup>3</sup>, however the reader should bear in mind that the model-in-isolation  $M_y$  for the post critical model is  $< 1\%$  of that for the pre-critical model. It is thus immediately apparent that leading model afterbody flow structures are completely unique from the pre-critical case, despite comparable drag force trends at close proximity. The leading model pitch moment is broadly at model-in-isolation levels for  $\frac{x}{L} \geq 1$ . Two unique phases exist otherwise: a *rise* in pitch moment for  $\frac{x}{L} < 0.375$ , and a *recovery* in pitch moment to isolation values for  $\frac{x}{L} < 0.375$ . It is suspected that a unique flow structure exists over the leading model backlight at very close ( $\frac{x}{L} = 0.125$ ) spacing; moderately lower backlight surface pressure is consistent with increased pitch moment and slightly increased drag relative to  $\frac{x}{L} = 0.25$ . Both  $C_D$  and  $C_{My}$  for  $\frac{x}{L} \geq 0.375$  are consistent with broadly consistent surface pressure over backlight and base regions as per the model-in-isolation: feedback along both upper and lower separating shear layers limits vortex formation with increased trailing model proximity, raising base pressure. The initial decrease in  $C_{My}$  may be explained by the nearer proximity of the lower (base/bottom edge) separating shear layer to the trailing model; a relatively (slightly) higher increase in base pressure (than backlight pressure) giving rise to the small moment change.

Pitch moment for the trailing model is similar to the pre-critically-led model, decreasing from  $1.34 \frac{C_{My}}{C_{My\infty}} = 1$  to  $> 10\%$  above model-in-isolation values. The increase at close spacing is not

<sup>2</sup>A lack of mounting hardware limited testing at intermediate resolutions. It is possible that a minima exists between these points, however the general trend - when considering adjacent data - suggests any difference to be small.

<sup>3</sup>Model-in-isolation,  $\frac{C_{My}}{C_{My\infty}} = 1$ , is located identically on either to further facilitate interpretation.

as significant, nor is the rate of decrease in  $C_{M_y}$  with increased spacing. Flow impingement over the upper half of the model forebody is suspected, however the characteristic flows involved would appear to differ from those prevalent in the  $\alpha = 25^\circ$  platoon despite comparable drag force data. Further investigation is required.

### 4.1.3 Concluding comments concerning force data

Whilst the force data does not elucidate underlying flow phenomena, the notions established by Carlino et al. (2007), Carlino and Cogotti (2006), Vio (2005) and Zabat et al in Hong et al. (1998) - broadly, that a leading fastback model, in creating a downwash-type wake, serves to increase the drag force experienced by a trailing model in a two-car platoon - would appear to hold true irrespective of the leading model being of critical or post-critical configuration<sup>4</sup>. However, in contrasting drag force and pitch moment data it is shown that despite similar drag force trends, the underlying gap flow phenomena is unique to leading model geometry.

The effect of the employing Ahmed model geometry to study platooning effects - rather than a scale (practical) model - needs be considered when appraising the severity of force data results. The intent of the Ahmed model is to generate pronounced axial vortices in pre-critical configurations and a distinct, quasi-two-dimensional wake in post-critical configurations. Whilst this allows salient automotive-type flow phenomena to be explored, it is not representative of modern efforts to reduce road vehicle aerodynamic drag (Hucho 1978). Though exaggerated relevant to practical implementations, the downstream and transverse propagation of the axial vortices dominating the Ahmed model wake - representing the far wake velocity deficit and entraining a downwash along the projected model centreline plane - significantly limits the possibility of drag reduction for trailing vehicles.

## 4.2 Generalized trends by centreline surface pressures

A further preliminary investigation of platooning effects is undertaken by assessing centreline mean surface pressures and statistical unsteadiness. Figures 4.2 and 4.3 provide mean  $C_P$  and  $\sigma_{C_P}$  for both the leading model afterbody and trailing model forebody superimposed over a scale representation of the test arrangement concerned for  $0.125 \leq \frac{x}{L} \leq 1$ . A dashed yellow line indicates  $C_P = 0$ . Centreline flowfield data is also presented; the magnitude of  $U$  and  $W$  components being denoted by vector length, the unsteadiness (expressed as  $\sigma \frac{\sqrt{u^2+v^2+w^2}}{U_\infty}$ ) represented by vector colour. A similar representation (without unsteadiness) is provided by Fletcher and Stewart (1986) in expressing gap effects of a two-bus platoon.

---

<sup>4</sup>A notable difference exists; Vio presents near-constant drag of  $0.8 \frac{C_D}{C_{D_\infty}}$  for the trailing model in the range  $2 \leq \frac{x}{L} \leq 4$ . This is discounted. The velocity deficit known to propagate away from the trailing model forebody, and as larger turbulent structures dissipate back into the freestream, any velocity deficit (which would give rise to a reduced drag force experienced by the trailing model) would reduce also.

For reference, relevant model-in-isolation  $C_P$  and  $\sigma_{C_P}$  are shown in dashed lines.

### 4.2.1 For platoons with $\alpha = 25^\circ$ leading model

#### 4.2.1.1 Upper body flows and trailing model impingement

The most immediately notable variation with spacing for the pre-critically-led platoon concerns the movement of the trailing model stagnation point.

Figure 4.2 clearly shows the stagnation point of the trailing model being highest (at almost  $\frac{z}{H} = 0.8$ ) for  $\frac{x}{L} = 0.125$  spacing, gradually decreasing in  $z$  with increased spacing. This is commensurate with downwash impingement along the leading model centreline entrained by dominant axial vortices in the leading model wake. Standard deviations of flow field data and trailing model forebody surface pressures indicate this impingement to be relatively steady, commensurate with earlier observations of steady axial vortex formation for the model-in-isolation. A slight increase in unsteadiness for the trailing model forebody at the stagnation point for the  $\frac{x}{L} = 0.125$  and  $\frac{x}{L} = 0.25$  cases possibly suggests the impinging flows to be in relatively close proximity to the oscillating upper horseshoe vortex (over the base; in the model-in-isolation these are known to mix off-body). This is supported to some extent by a greater degree of unsteadiness in the  $\frac{x}{L} = 0.25$  case (for which the upper horseshoe vortex is stronger). This point is elaborated upon later in this section.

Significant unsteadiness is noted on the uppermost pressure tap of the leading model after-body. These fluctuations were previously attributed to intermittent flow attachment along the top/backlight edge. In all cases, flow field data suggests peak unsteadiness to occur in the wake of the base/bottom/centreline coincident. This is an expected observation given model-in-isolation behaviour.

At close spacing, (particularly  $0.125 \leq \frac{x}{L} \leq 0.25$ ), flow field data suggests a clear velocity deficit within the gap, diminishing with increased spacing.

#### 4.2.1.2 Base flows

Evidence of mean flow recirculation is prevalent at all spacings, diminishing with decreased spacing as feedback along the base/bottom separating shear layer modifies shedding characteristics. Average  $C_P$  decreases with increased spacing towards the lower base, consistent with greater base vortex formation from separating flows, in turn lowering surface pressure. Lower base pressure begins to increase notably at  $\frac{x}{L} = 0.25$  with a marked increase just exceeding mean  $C_P = 0$  at the base/bottom/centreline coincident for  $\frac{x}{L} = 0.125$ .  $\sigma_{C_P}$  is significantly increased also, commensurate with the oscillating impingement of low-pressure packets convected from the leading model bottom/base separating shear layer. The flow field vectors remain commensurate with a

counter-rotating horseshoe vortex pair operating over the model base: behaviours akin to the model-in-isolation case are observed at  $\frac{x}{L} \geq 0.25$ .

At  $\frac{x}{L} = 0.125$ , flow field vectors in the gap do not confirm a recirculating region or a low-pressure cavity (formed by steady reattachment of leading model separating shear layers onto the trailing model forebody) operating at  $\frac{x}{L} = 0.0625$  behind the leading model base. Lower base pressures are higher, commensurate with the inhibition of spanwise base vortices by the near presence of the trailing model, however significantly more unsteady. It is speculated that characteristic base shedding phenomena may exist at  $\frac{x}{L} = 0.125$ , albeit compressed upstream of data acquired at  $\frac{x}{L} = 0.0625$ , though further investigation is warranted.

#### 4.2.2 For platoons with $\alpha = 35^\circ$ leading model

Figure 4.3 clearly shows gap flows for the platoon with  $\alpha = 35^\circ$  model to be unique from those in figure 4.2, despite similar force trends.

##### 4.2.2.1 Observations for $0.125 \leq \frac{x}{L} \leq 0.5$

Immediately obvious is the relatively high level of unsteadiness associated with centreline impinging flows on the trailing model forebody and in the preceding gap flow. This suggests the impingement to be composed of both the leading model's separating shear layer from the top/backlight edge and of entrained downwash flows between the "C-pillar" axial vortices (of lower strength than for the  $\alpha = 25^\circ$  leading model). A significant level of unsteadiness in the backlight projection is observable for  $0.125 \leq \frac{x}{L} \leq 0.5$  spacing but not at  $\frac{x}{L} = 1$ . Base flows from the bottom/base separating shear layer show similar levels of unsteadiness in the flow field and again, between  $0.125 \leq \frac{x}{L} \leq 0.5$  impinge on the trailing model lower forebody with a relatively high level of unsteadiness.  $C_P$  is expectedly low given a the lack of entrained flows, relevant angularity and lower momentum relative to impinging flows over the trailing model upper forebody, but remains higher than for the model-in-isolation case where flows smoothly accelerate towards the underbody with a relatively low level of upstream turbulence (similar behaviour is observed at  $\frac{x}{L} = 1$ ).

It can be surmised that between  $0.125 \leq \frac{x}{L} \leq 0.5$ , separating shear layers from the leading model impinge on the trailing model sufficiently to increase local unsteadiness on the surface. Not only do the separating shear layers - owing to pressure differences on either side - bend "into" the separated wake, but the entrained flows, their relative momentum (there being a greater momentum entrained by the upper separating shear layer) and amenable trailing model forebody geometry appear to create a (relatively stable, evidenced by low trailing model forebody  $\sigma_{C_P}$ ) counter-rotating vortex pair within the gap. A significant downwash exists over the trailing model forebody below the stagnation point in the  $xz$  plane (particularly visible in the flow field visualisation in figure 4.3c). It should be further stressed that this flow phenomena is greatly aided by the Ahmed model forebody geometry; recirculation of flows concerning the upper shear layer would likely be weaker

if at all present for models with typical passenger vehicle forebody geometry. Whilst outside the intent of the Ahmed model, this provides a useful recommendation for further study.

#### 4.2.2.2 Observations for $\frac{x}{L} = 0.125$

Unsteadiness over the trailing model lower forebody peaks at  $\frac{x}{L} = 0.25$  in contrast to that over the upper forebody peaking at closer trailing model proximity ( $\frac{x}{L} = 0.125$ ): an important observation, highlighting the effect of trailing model proximity on the development of leading model flow field phenomena. The lower separating shear layer is given less space to develop at closer spacing with peak unsteadiness occurring further down the model forebody. The preceding flow field vector at  $\frac{x}{L} = 0.125$  relevant to the lower shear layer is less unsteady than for  $\frac{x}{L} = 0.25$ , although the closer proximity and lack of an apparent “low-pressure cavity” (Azim and Gawad 2000) between both models suggests that coherent oscillations within the gap should occur with increased amplitude at closer spacing, if with reduced frequency (Bull et al. 1996) given the presence of the trailing model serving to limit vortex formation (this explains the heightened levels of unsteadiness over the leading model base with decreased spacing). This also raises leading model base pressure (especially near the shedding location i.e. the base/bottom edge in the  $xz$  plane).

$C_P$  and  $\sigma_{C_P}$  distributions for the leading model backlight are unique from other cases. The gap flow field suggests the vortex pair is “squashed upwards”, giving rise to an unstable impingement node acting not only over the base (as suggested for  $0.25 \leq \frac{x}{L} \leq 0.5$ ), but partially over the backlight, potentially giving rise to comparatively turbulent upwash over the lower surface. This suggestion is corroborated by locally higher  $C_P$  and  $\sigma_{C_P}$ . This upwash is not expected to act over the entire backlight region given a strong separating shear layer from the top/backlight edge of the leading model.

#### 4.2.2.3 Observations for $\frac{x}{L} = 1$

The flow modes observed at  $\frac{x}{L} = 1$  spacing are clearly unique from those observed at closer spacing. The  $C_P$  distribution over the trailing model forebody is broadly similar to the model-in-isolation, with a higher degree of unsteadiness over the upper half commensurate with shedding from the leading model’s upper separated shear layer. This contrasts with the closed separated leading model wake at the same spacing for the pre-critically-led platoon (figure 4.3d), where  $\sigma_{C_P}$  is relatively constant on the trailing model forebody in the  $xz$  plane.

Whilst surface pressure data for the leading model afterbody is as anticipated (being a continuation of trends observed for  $\frac{x}{L} = 0.5$ ), the flow field data taken  $\frac{x}{L} = 0.125$  behind the leading model base was not, being similar to that behind the model-in-isolation at  $\frac{x}{L} = 0.25$  behind the base<sup>5</sup>. Mean reversion (of flows entrained by upper and lower shear layers) towards the model base - present at closer spacing for the same location - is not observed. As some reversion (although

---

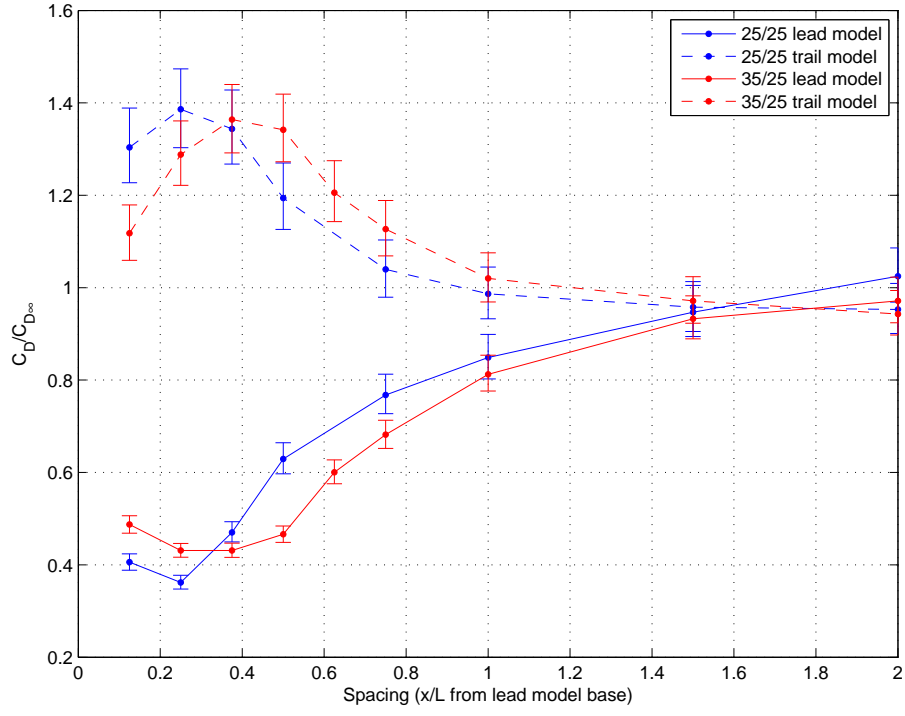
<sup>5</sup>This was repeated with a similar result.



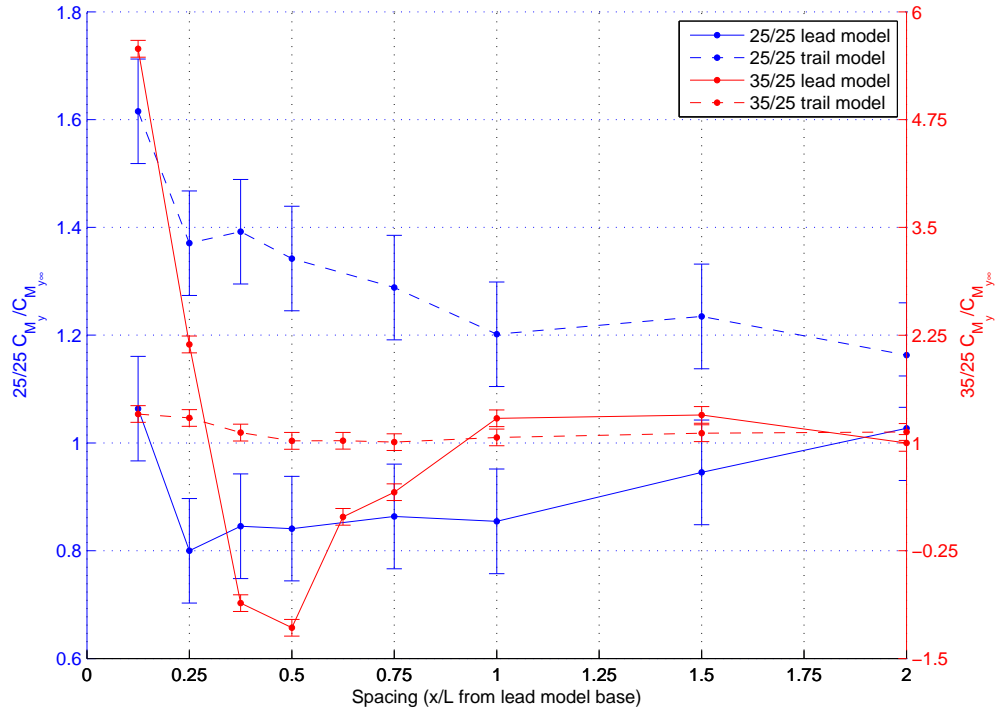
#### 4.2. GENERALIZED TRENDS BY CENTRELINE SURFACE PRESSURES

weaker) is observed for the model-in-isolation's wake at this location, it is contended that feedback along the separating shear layers (evidenced by higher  $\sigma_{C_P}$  and an upwards-shifted stagnation point on the trailing model forebody) “compresses” characteristic wake flows upstream towards the leading model base. This hypothesis is not definitively proved with data in figure 4.3d, however; further investigation is required (explored subsequently).

#### 4.2. GENERALIZED TRENDS BY CENTRELINE SURFACE PRESSURES



(a) Normalised  $C_D$  comparison



(b) Normalised  $M_y$  (pitch moment) comparison

Figure 4.1: Normalised key force and moment data for lead and trail models in two-model, longitudinally spaced platooned with varying lead model  $\alpha$

#### 4.2. GENERALIZED TRENDS BY CENTRELINE SURFACE PRESSURES

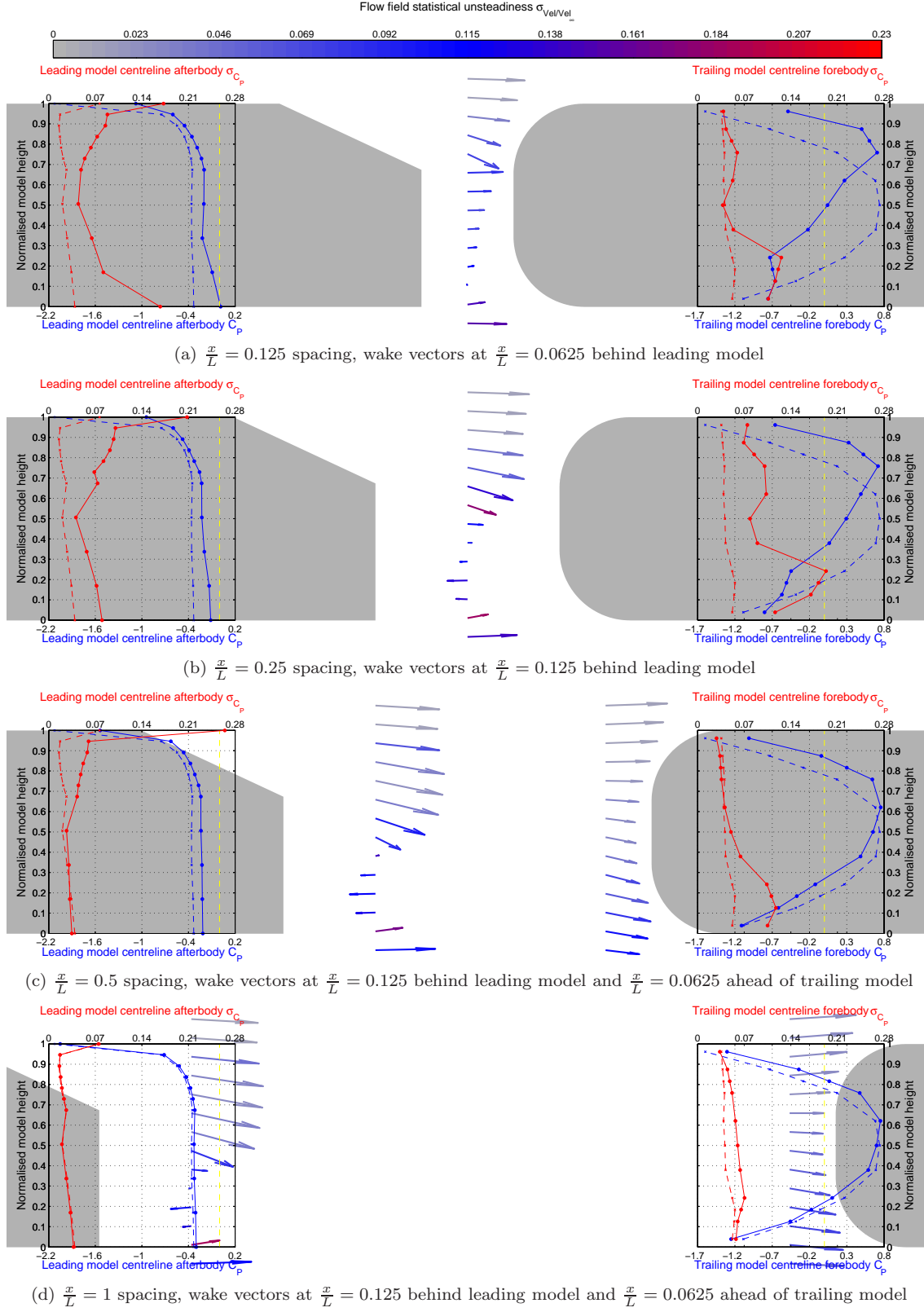


Figure 4.2: Centreline  $C_P$  (in blue),  $\sigma_{C_P}$  (in red) and wake flow (coloured by  $\sigma_{Vel/Vel_\infty}$ ) for  $\alpha = 25/25^\circ$  platoon. Model-in-isolation pressure data values shown dashed.

#### 4.2. GENERALIZED TRENDS BY CENTRELINE SURFACE PRESSURES

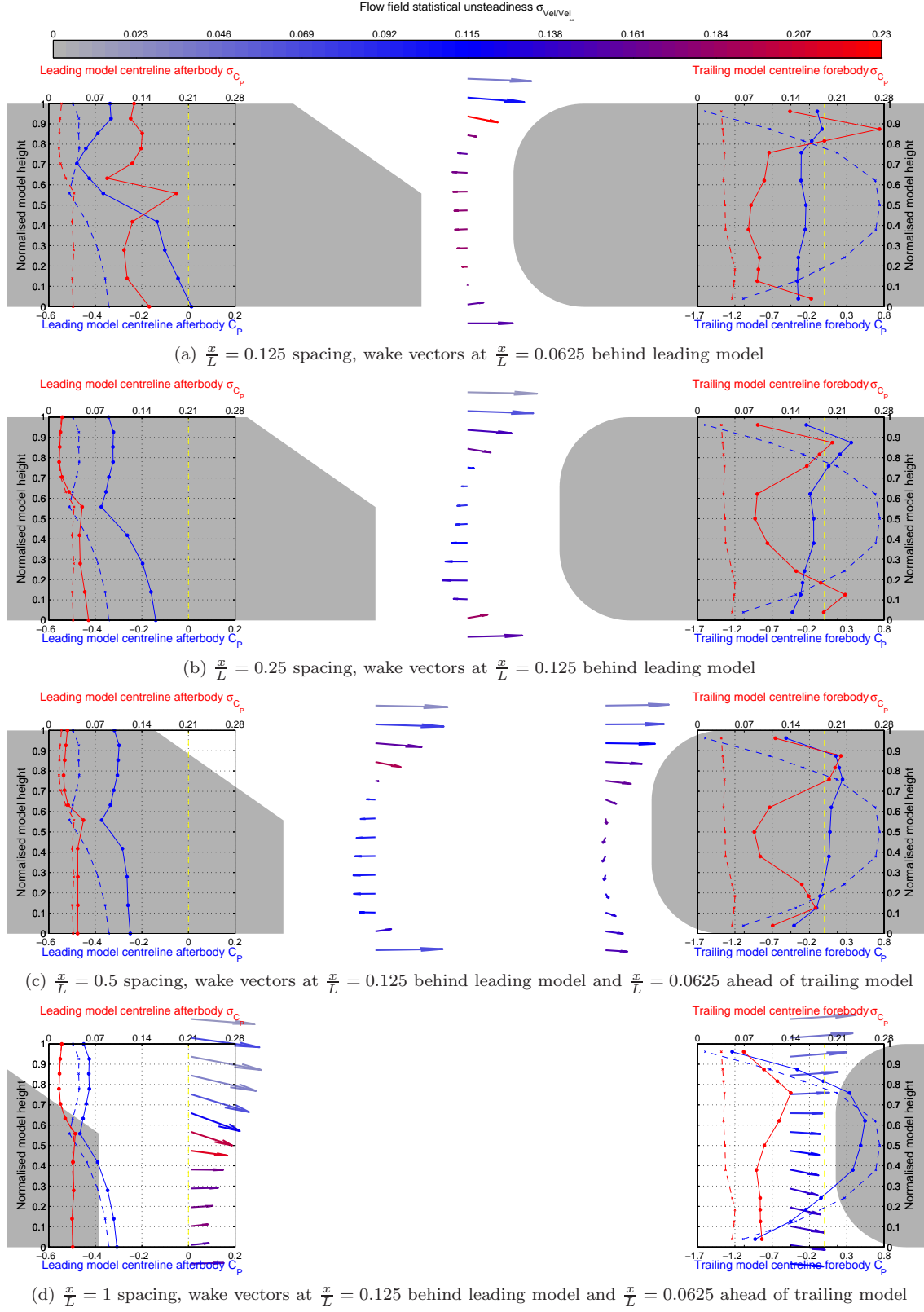


Figure 4.3: Centreline  $C_P$  (in blue),  $\sigma_{C_P}$  (in red) and wake flow (coloured by  $\sigma_{Vel/Vel_\infty}$ ) for  $\alpha = 35/25^\circ$  platoon. Model-in-isolation pressure data values shown dashed.

### 4.3 Generalized trends by leading and trailing model surface pressures and gap flows

A further insight into general trends is obtained by examining mean pressures and statistical unsteadiness across leading model afterbody and trailing model forebody surfaces. This section aims to expand prior observations in a fully three-dimensional context. Given the limited spatial resolution afforded by the hardware employed, these results broadly summarise general trends only; a detailed investigation of flow phenomena at various key spacing follows.

A further examination of flow angularity, velocity deficit and turbulence properties of gap flows is provided, confirming phenomena alluded to in surface pressure analysis.

This section confirms gap flows to concern two unique of phenomena pending pre or post-critical leading model geometry.

#### 4.3.1 For platoons with $\alpha = 25^\circ$ leading model

Figures 4.4 to 4.7 present mean  $C_P$  and  $\sigma_{C_P}$  for for the pre-critically led platoon at various spacing.

##### 4.3.1.1 Trends for leading model afterbody

Figure 4.4 confirms pressure distributions at all spacings to broadly approximate the model-in-isolation. Some key differences are evident:

- *“C-pillar” vortices are weakened* at close spacing. The presence of the trailing model clearly inhibits the formation of the dominant axial vortices to an increasing degree with decreased spacing, however it remains clear that “C-pillar” vortices are formed by the rollup of the separating shear layers at the backlight sides and that these impinge on the backlight surface even at the closest spacing evaluated.
- *Low velocity flows immediately downstream of the top/backlight edge* are impeded at close spacing, particularly at  $0.125 \leq \frac{x}{L} \leq 0.5$ . This is likely a function of the (presence of the) trailing model giving rise to feedback along the separating shear layer off the top/backlight edge.
- *Base pressure are increased and non-uniform* at  $0.125 \leq \frac{x}{L} \leq 0.5$ . Feedback along the separating shear layer from the bottom/base edge owing to the presence of the trailing model appears to inhibit vortex shedding at it’s key location (the bottom/base/edge coincident), raising pressure across the base surfaces (whose impinging phenomena are driven by this shedding) and especially (at close spacing) at the shedding location itself.

#### 4.3. GENERALIZED TRENDS BY LEADING AND TRAILING MODEL SURFACE PRESSURES AND GAP FLOWS

Table 4.2 corroborates the above findings, which are consistent with force data trends bar  $C_D$  at  $\frac{x}{L} = 0.125$ ; the pressure data suggests a minima at closest spacing, the force data at  $\frac{x}{L} = 0.25$ . This discrepancy proved repeatable in both force and pressure testing. It should be stressed that these discrepancies concern small magnitudes, and that compared to reference data (Ahmed et al. 1984, Lienhart et al. 2000) the pressure tap spatial resolution used throughout (owing to equipment limitations) is quite coarse about significant mean pressure gradients<sup>6</sup>. The force data is thus regarded as the more conclusive.

Spacing $\frac{x}{L}$	Base $\overline{C_P}$	% MII base $\overline{C_P}$	Backlight $\overline{C_P}$	% MII backlight $\overline{C_P}$	$\frac{\text{Base } \overline{C_P}}{\text{Backlight } \overline{C_P}}$
Model-in-isolation	-0.36	-	-0.77	-	0.46
0.125	-0.16	46	-0.51	67	0.32
0.250	-0.18	49	-0.52	67	0.34
0.375	-0.20	57	-0.56	73	0.36
0.500	-0.23	66	-0.61	80	0.38
1.000	-0.32	91	-0.73	95	0.44

Table 4.2: Comparison of base and backlight average pressures for  $\alpha = 25^\circ$  leading model afterbody in wake of  $\alpha = 25^\circ$  model

##### 4.3.1.2 Trends for trailing model forebody

Figure 4.6 confirms pressure distributions at all spacings to broadly approximate the model-in-isolation, in that forebody surface pressures are dominated by a clear stagnation point along the  $xz$  plane caused by impingement of flows entrained between the dominant axial vortices in the wake of the pre-critical leading model. Negative pressures under the stagnation point suggest that flows diverge from the stagnation region, with especially low-pressure/high-velocity flows occurring as a neat downwash/along the  $xz$  plane.

Significant levels of unsteadiness -  $\sigma_{C_P}$  as presented in figure 4.7 - are associated with two unique locations owing to two separate phenomena:

- *Upper outboard corner unsteadiness owing to leading model axial vortex impingement:* as predicted from centreline data, unsteadiness concerning leading model axial vortex impingement is weak at  $\frac{x}{L} = 0.125$  spacing. Mean and statistical unsteadiness data do not elucidate the presence or otherwise of base vortex flows; it remains suspected that the phenomena do exist - albeit “compressed” against the leading model base. It is confirmed, however, that any such phenomena do not interact with the leading model axial vortices sufficiently to induce significant unsteadiness. As such, they impinge only moderately on the trailing model forebody. Again commensurate with centreline data, the clear development of model-in-isolation type base flows in the gap region for  $0.25 \leq \frac{x}{L} \leq 1$  sees significant unsteadiness at  $\frac{x}{L} = 0.25$ , diminishing with increased spacing as eddying motions dissipate into the freestream. The lo-

<sup>6</sup>The pressure taps were instead located to facilitate studying distributions of dynamic surface pressure properties.

cation of peak  $\sigma_{C_P}$  does not change significantly between  $0.25 \leq \frac{x}{L} \leq 0.5$ , possibly given the presence of the trailing model progressively limiting axial vortex development with increased spacing.

A moderate level of unsteadiness is noted on the forebody side associated with axial vortex impingement (not prominent at  $\frac{x}{L} = 0.125$  and associated with the axial vortex unsteadiness only at  $\frac{x}{L} = 0.5$ ); this likely concerns interactions between downwash flows away from the stagnation point and the unsteady axial vortex.

- *Lower section unsteadiness owing to leading model base shedding impingement:* unsteadiness associated with impingement on the lower forebody concerns either vortices shed from the leading model base/bottom edge, or the impingement of the separating shear layer itself - there is insufficient information to corroborate coherent shedding at  $\frac{x}{L} = 0.125$  spacing. Expectedly, unsteadiness of impinging flows diminishes with increased distance from the leading model.

An interesting note concerns unsteadiness on the lower forebody along the  $xz$  plane: low  $\sigma_{C_P}$  is observed. This region corresponds with flows accelerating towards the model underbody. As shedding at the leading model base/bottom/centreline coincident is known to be quasi-two-dimensional (Sims-Williams and Duncan 2002), it is possible that relatively low degree of distortion of essentially transverse vortex phenomena from this region gives rise to more coherent oscillations than the potentially more random turbulence inherent at  $\pm y$  away from the  $xz$  plane (an exploration of periodicity is subsequently presented).

4.3. GENERALIZED TRENDS BY LEADING AND TRAILING MODEL SURFACE PRESSURES AND GAP FLOWS

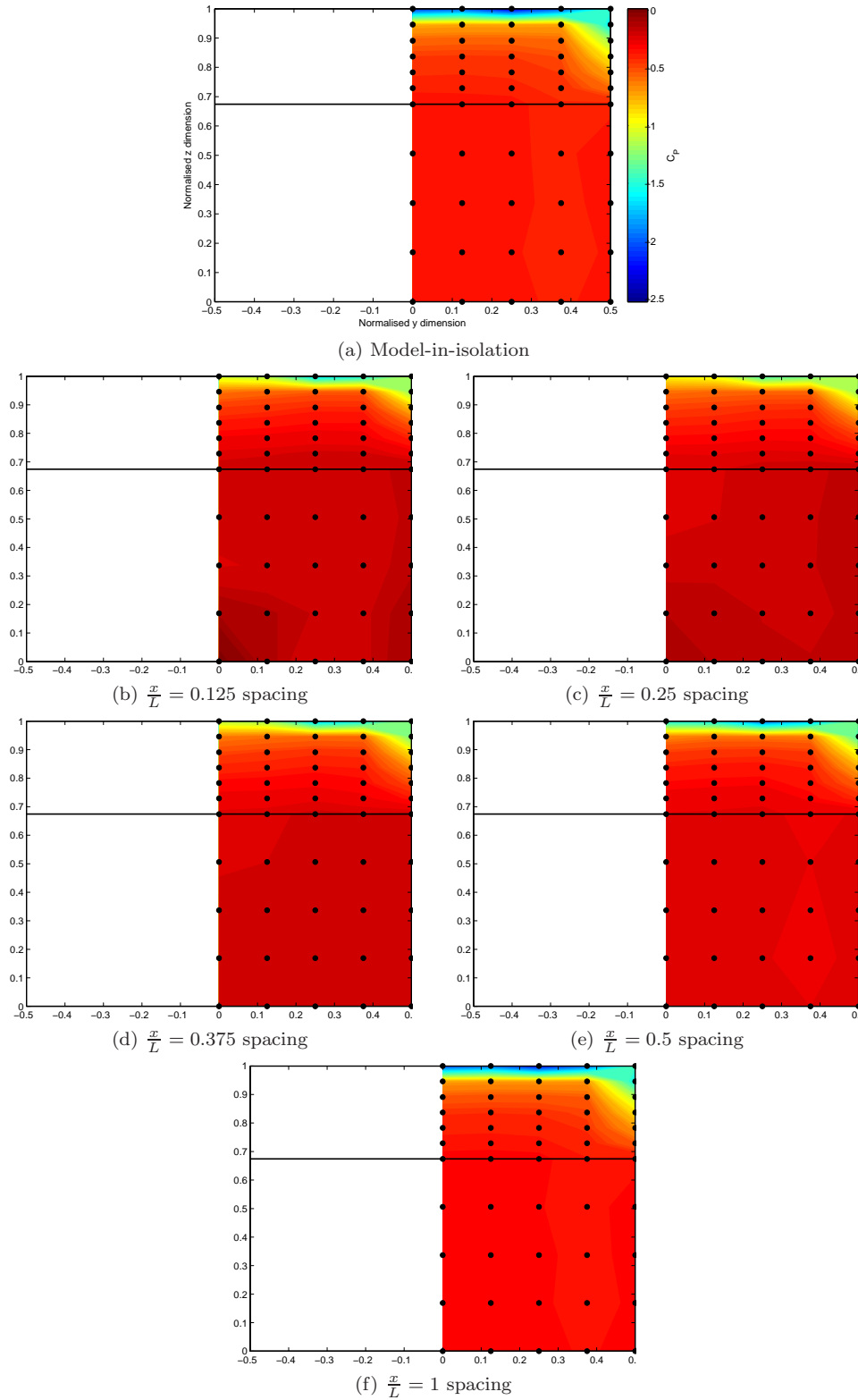


Figure 4.4: Comparison of surface pressures for leading model backlight and base surfaces for  $\alpha = 25/25^\circ$  platoon with various longitudinal spacing



#### 4.3. GENERALIZED TRENDS BY LEADING AND TRAILING MODEL SURFACE PRESSURES AND GAP FLOWS

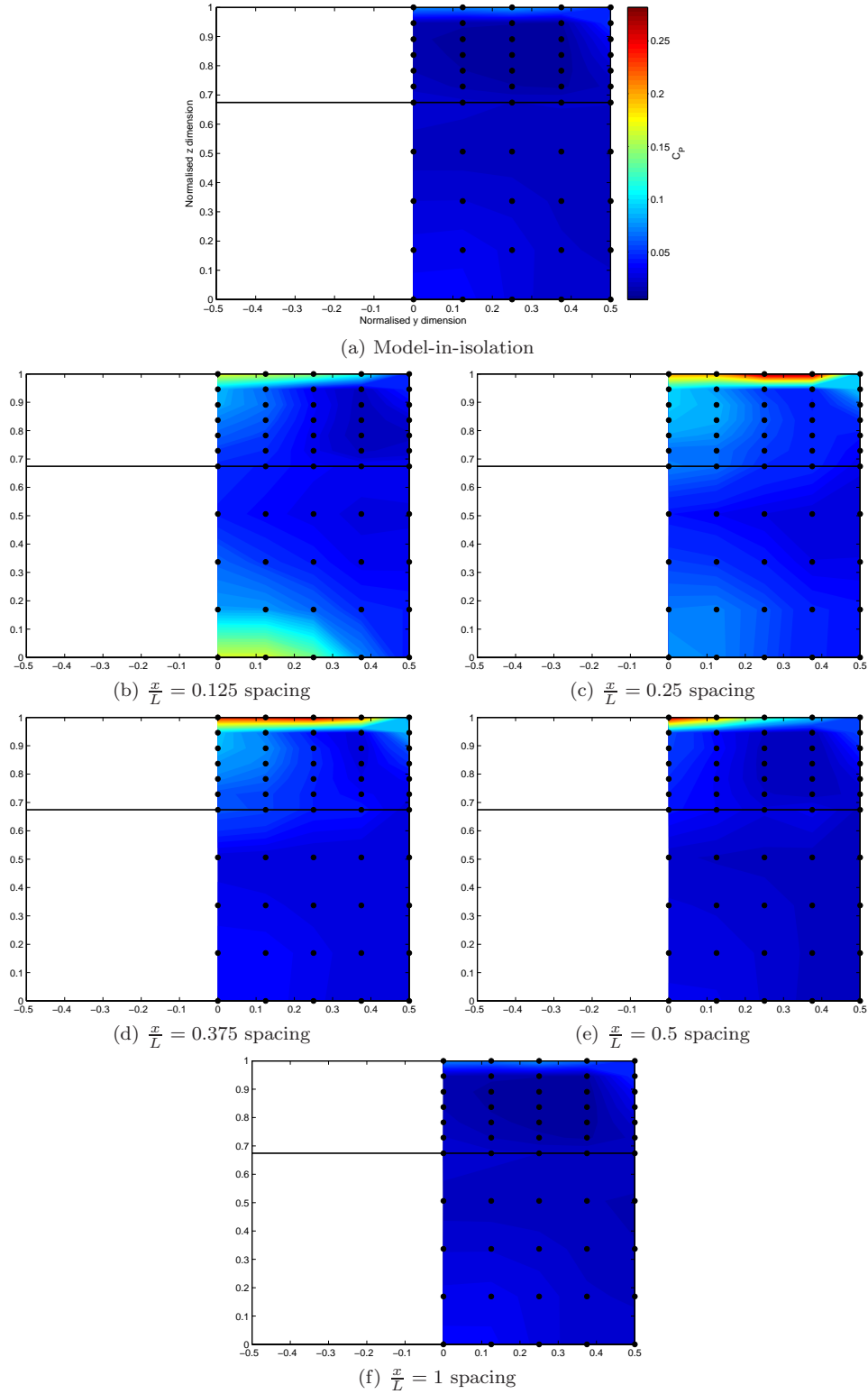


Figure 4.5: Comparison of standard deviation of surface pressures for leading model backlight and base surfaces for  $\alpha = 25/25^\circ$  platoon with various longitudinal spacing

4.3. GENERALIZED TRENDS BY LEADING AND TRAILING MODEL SURFACE  
PRESSURES AND GAP FLOWS

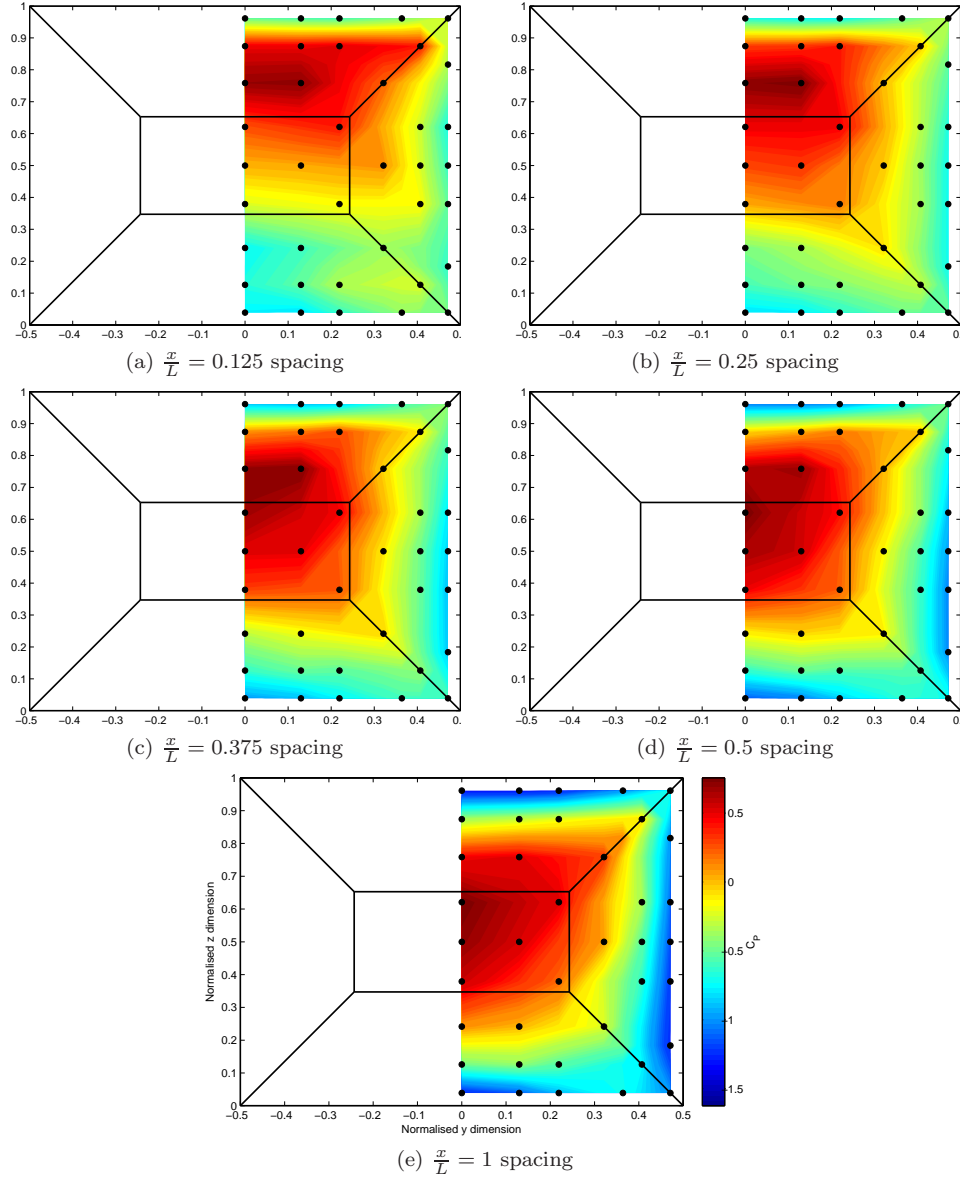


Figure 4.6: Comparison of surface pressures for trailing model forebody surface for  $\alpha = 25/25^\circ$  platoon with various longitudinal spacing

4.3. GENERALIZED TRENDS BY LEADING AND TRAILING MODEL SURFACE PRESSURES AND GAP FLOWS

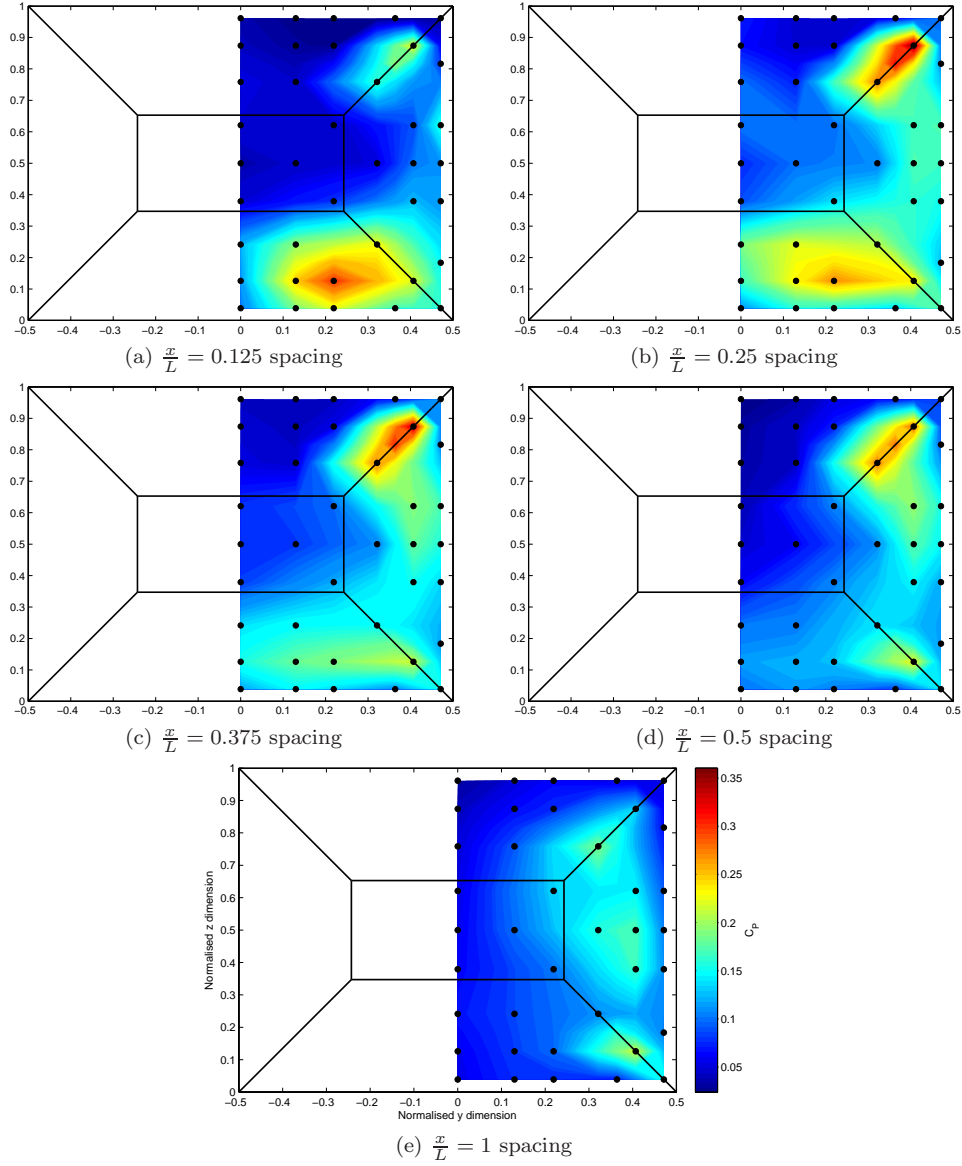


Figure 4.7: Comparison of standard deviation of surface pressures for trailing model forebody surface for  $\alpha = 25/25^\circ$  platoon with various longitudinal spacing

### 4.3.2 For platoons with $\alpha = 35^\circ$ leading model

Figures 4.8 to 4.11 present mean  $C_P$  and  $\sigma_{C_P}$  for the pre-critically led platoon at various spacing.

#### 4.3.2.1 Trends for leading model afterbody

Trends for the leading  $\alpha = 35^\circ$  model afterbody are broadly unique from those experienced by the leading pre-critical mode for the same spacing. The suggestion in force and centreline pressure/flow field data that the leading model behaves similarly at  $\frac{x}{L} = 1$  spacing is duly validated. Surface pressures are shown to be broadly quasi-two-dimensional as per the model-in-isolation, rendering conclusions observed about the centreline (figure 4.3) of particular relevance. Two clear changes in phenomena are observable at the intervening spacing ( $0.125 \leq \frac{x}{L} \leq 1$ ):

- *Base pressures are increased*, markedly so at  $0.125 \leq \frac{x}{L} \leq 0.25$ , diminishing with increasing spacing.
- *Backlight pressures are increased* between  $0.25 \leq \frac{x}{L} \leq 0.5$ . Curiously, aside from a peak at the centreline/backlight/top coincident, backlight pressures are relatively lower at  $\frac{x}{L} = 0.125$ .

Both phenomena concern the presence of the trailing model giving rise to feedback along the separating shear layer, modifying shedding conditions such that vortex shedding is impeded, in turn raising pressure on the surfaces over which the relevant vortex phenomena act.

Base pressures and unsteadiness are raised most significantly at  $\frac{x}{L} = 0.125$  spacing, with  $C_P$  highest at the base/bottom/centreline coincident (where shedding is strongest and, owing to trailing mode phenomena discussed in the following section, most inhibited).  $C_P$  diminishes with increased spacing.

Backlight pressures develop uniquely; being relatively low at  $\frac{x}{L} = 0.125$  spacing commensurate with the surface upwash owing to a likely “squashing upwards” of gap recirculating flows discussed in section 4.2.2.2 (page 149). A slight increase at the top/backlight/centreline coincident is observed, likely owing to impeded vortex shedding from a relevant shear layer at this location.  $\frac{x}{L} = 0.25$  presents similarly, with base separations impeded to a lesser degree. At  $0.375 \leq \frac{x}{L} \leq 0.5$  backlight and base pressures are broadly equal, suggesting that the recirculating phenomena developed in the gap are broadly stable in this region despite significant turbulence in the relevant shear layers (corroborating flow field data presented in figure 4.3, page 153), corroborating the stable leading model force coefficients in this spacing range (figure 4.1, page 151). Though relevant surface pressure is not acquired, force data suggests this “region of stability” to not extend to  $\frac{x}{L} = 0.625$  (as  $C_D$  rises sharply from  $\frac{x}{L} = 0.5$ ).

A relatively low level of unsteadiness is observed for  $0.25 \leq \frac{x}{L} \leq 1$ , with a slight rise at the bottom/base/centreline coincident where shedding flows are known to occur. Unsteadiness is

significantly increased at  $\frac{x}{L} = 0.125$ , reflecting significantly higher levels of unsteadiness in gap flows (figure 4.3a).

#### 4.3.2.2 Trends for trailing model forebody

Figure 4.10 provides an interesting insight into flows impinging on the trailing model forebody, and corroborates data in figure 4.1a indicating peak trailing model drag force at  $\frac{x}{L} = 0.375$ . The surface pressure distributions presented for  $0.125 \leq \frac{x}{L} \leq 0.5$  indicate markedly unique flow phenomena in the gap from those experienced at  $\frac{x}{L} = 1$  (where model-in-isolation-type behaviours are observed), corroborating observations made in figure 4.3: the stagnation regions appear to be formed of impinging separating shear layers from the model top and sides. The lack of similar high-pressure impingement on the trailing forebody underside along the  $xz$  plane suggests flow accelerate *inwards* from the stagnation regions and *under* the model at this location.

$\frac{x}{L} = 0.125$  serves as a precursor to higher-drag cases ( $\frac{x}{L} = 0.25, 0.375$ ) in that the separating shear layers from the leading model top, sides and bottom edges do not have sufficient spacing in which to curve inwards towards the model projection. Their impingement is thus confined to the model outer extremities, and the centre region bounded by their impingement is concerned with negative pressures of flows accelerating from them. Observations from 4.3a are further corroborated: whilst a counter-rotating vortex pair exists in the wake, the lower vortex is clearly “pushed” forward of the trailing model along the centreline (trailing model forebody  $C_P$  at this spacing lacks a bounding lower region of high pressure, and thus does not corroborate the requisite negative bifurcation). At  $y = 0$  therefore, downwash dominates impinging flows. Between approximately  $0.2 \leq \frac{y}{W} \leq 0.4$  impingement of the lower separating shear layer suggests vortices formed off the lower separating shear layer are “squashed outwards” by the presence of the trailing model, impinging only in this region. Figure 4.11a confirms this to be a region of significant unsteadiness, with the forebody  $\sigma_{C_P}$  distribution generally higher than for the same model in the wake of the pre-critical model at the same spacing. The mean pressure effect is weaker however, suggesting that surface flows experience a net downwash to the underbody at  $y = 0$ .

Increased spacing allows shear layers to develop further, entraining high-momentum flows from outside the shear layer (Sakamoto and Haniu 1988) as they curve and spread (Bearman 1978, Nakamura et al. 1988, see section 1.2.2.2, page 12). Between  $0.25 \leq \frac{x}{L} \leq 0.5$  the strength and spread of side impingement regions are seen to grow, as is (with increased spacing) the prominence of impingement from flows of the leading model’s lower separating shear layer. The “medium-drag mode” of Koenig and Roshko (1985) (figure 1.30, page 45) provides a good analogy, however increased freestream turbulence and spacing in this instance likely contributes to accelerated growth of the impinging shear layers and external flow mixing. These processes are characteristically unstable. Figures 4.11b-d corroborate this well, with the bounding top, side and bottom regions presenting with significant unsteadiness commensurate with their increasing  $C_P$ .

4.3. GENERALIZED TRENDS BY LEADING AND TRAILING MODEL SURFACE PRESSURES AND GAP FLOWS

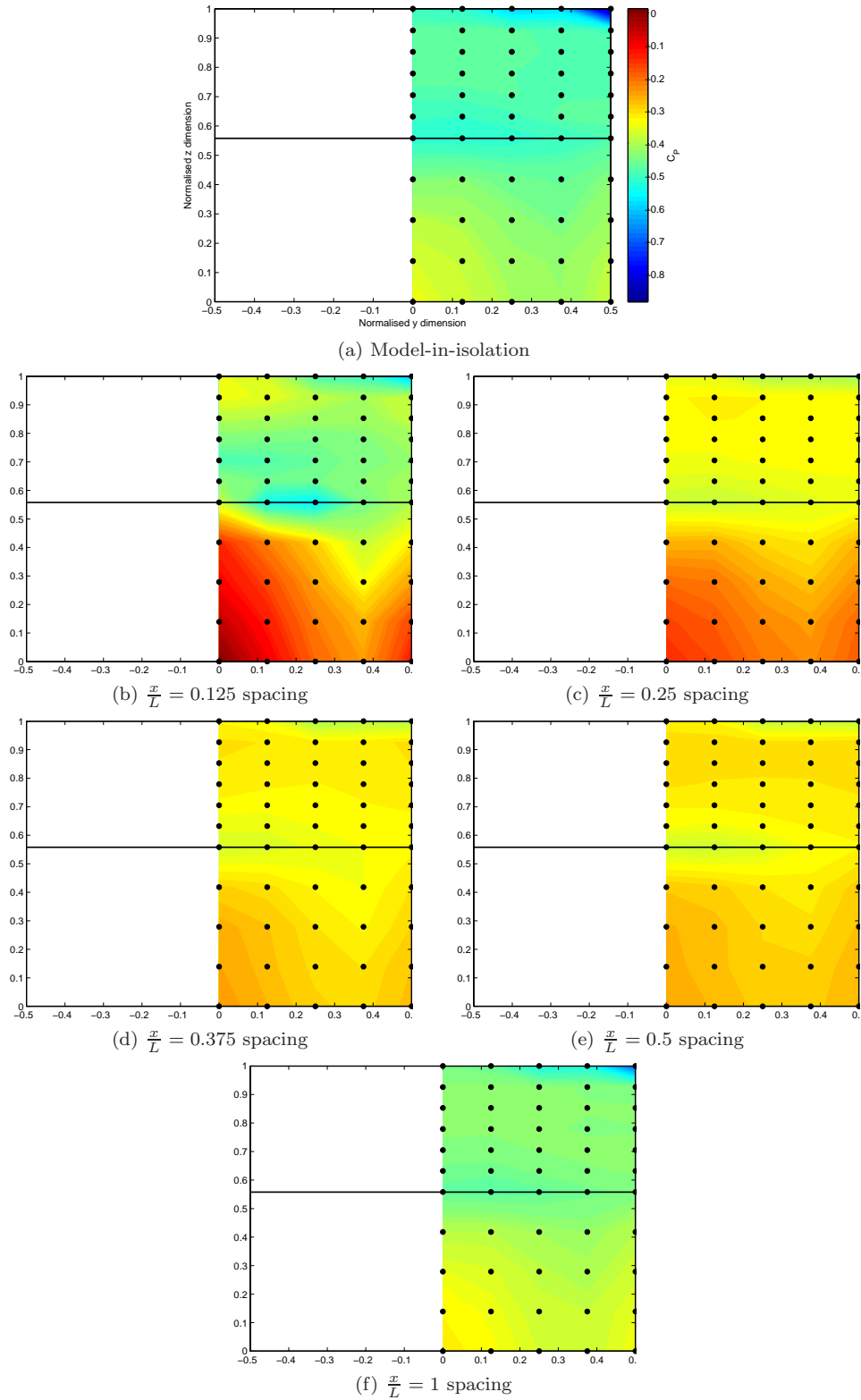


Figure 4.8: Comparison of surface pressures for leading model backlight and base surfaces for  $\alpha = 35/25^\circ$  platoon with various longitudinal spacing

4.3. GENERALIZED TRENDS BY LEADING AND TRAILING MODEL SURFACE PRESSURES AND GAP FLOWS

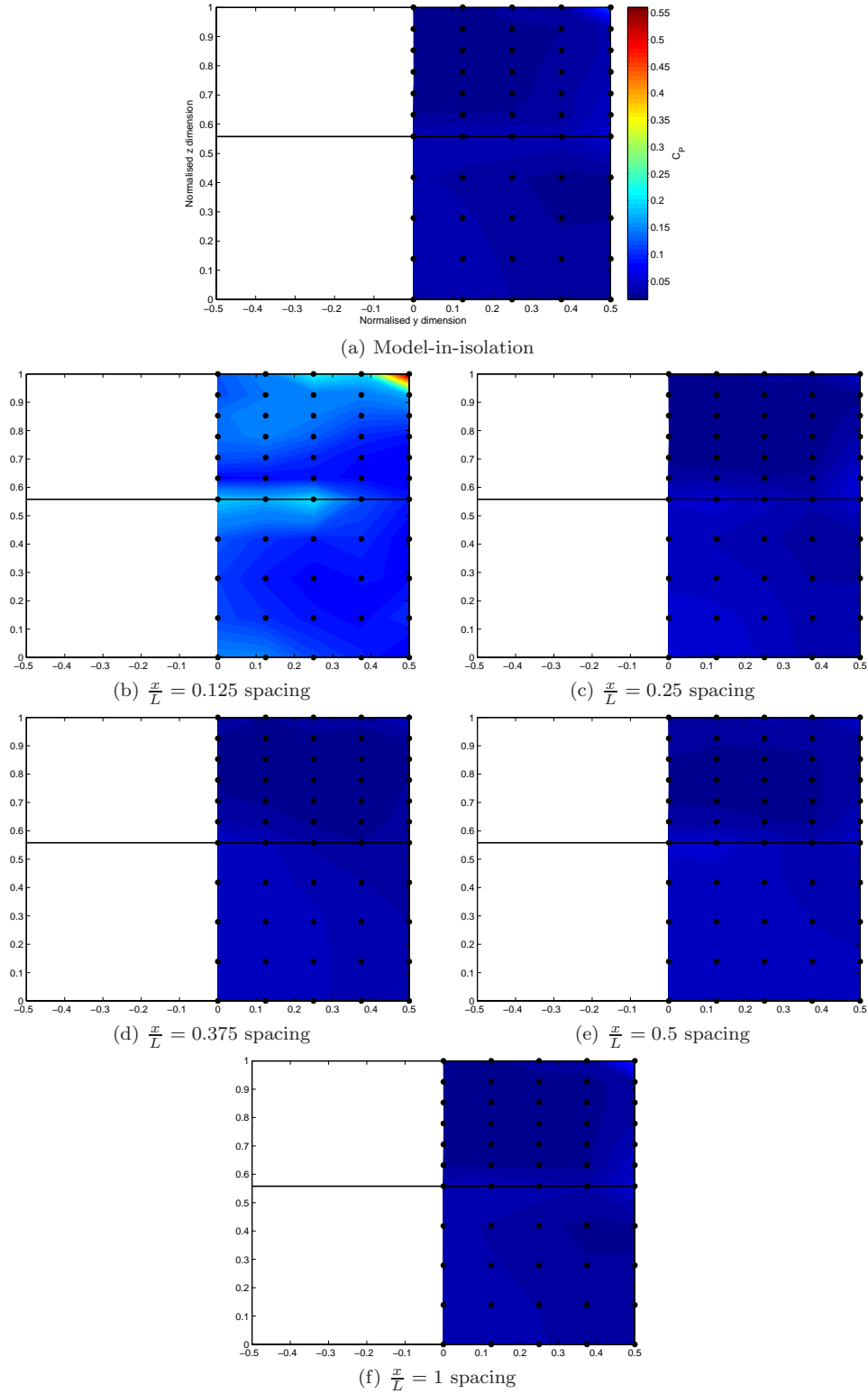


Figure 4.9: Comparison of standard deviation of surface pressures for leading model backlight and base surfaces for  $\alpha = 35/25^\circ$  platoon with various longitudinal spacing

#### 4.3. GENERALIZED TRENDS BY LEADING AND TRAILING MODEL SURFACE PRESSURES AND GAP FLOWS

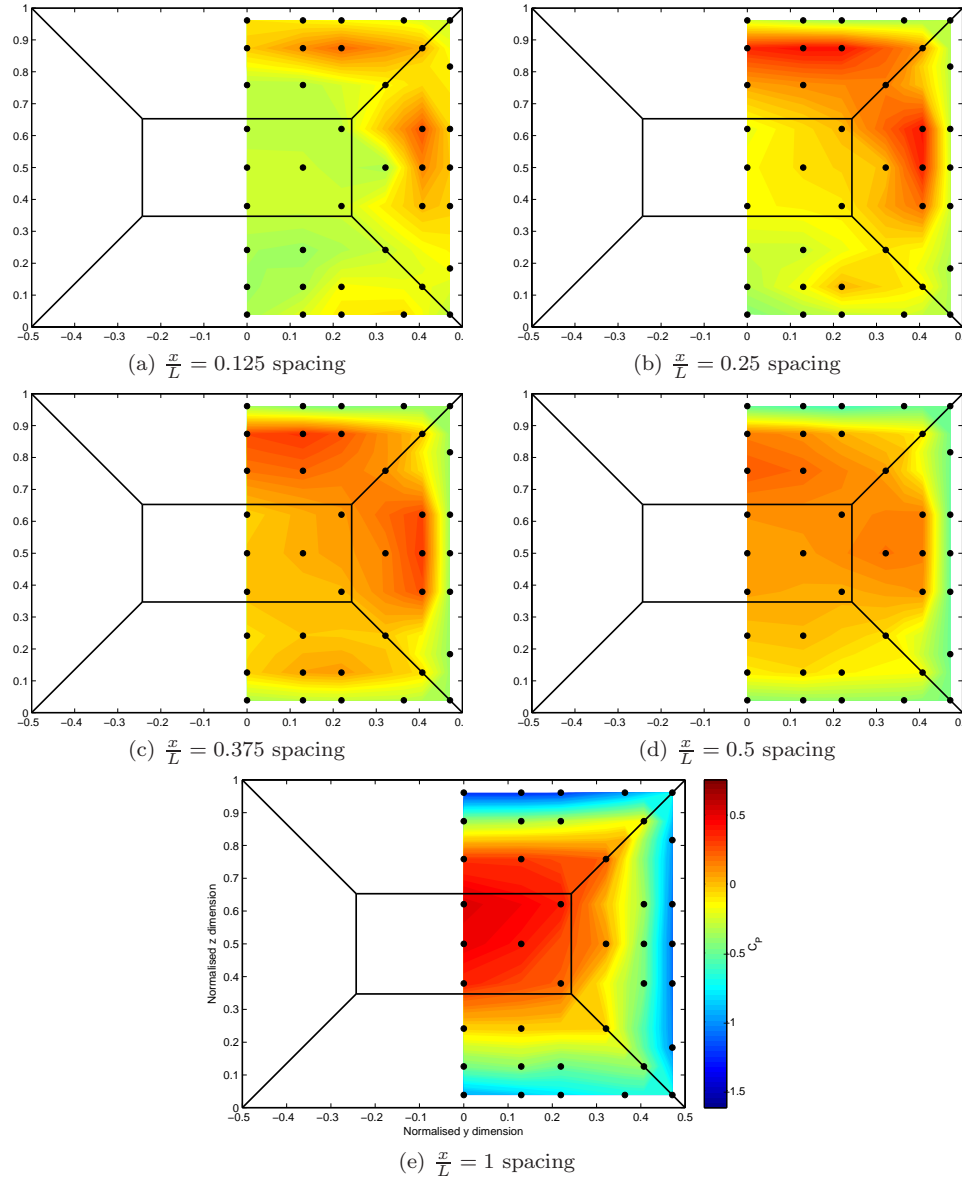


Figure 4.10: Comparison of surface pressures for trailing model forebody surface for  $\alpha = 35/25^\circ$  platoon with various longitudinal spacing



4.3. GENERALIZED TRENDS BY LEADING AND TRAILING MODEL SURFACE PRESSURES AND GAP FLOWS

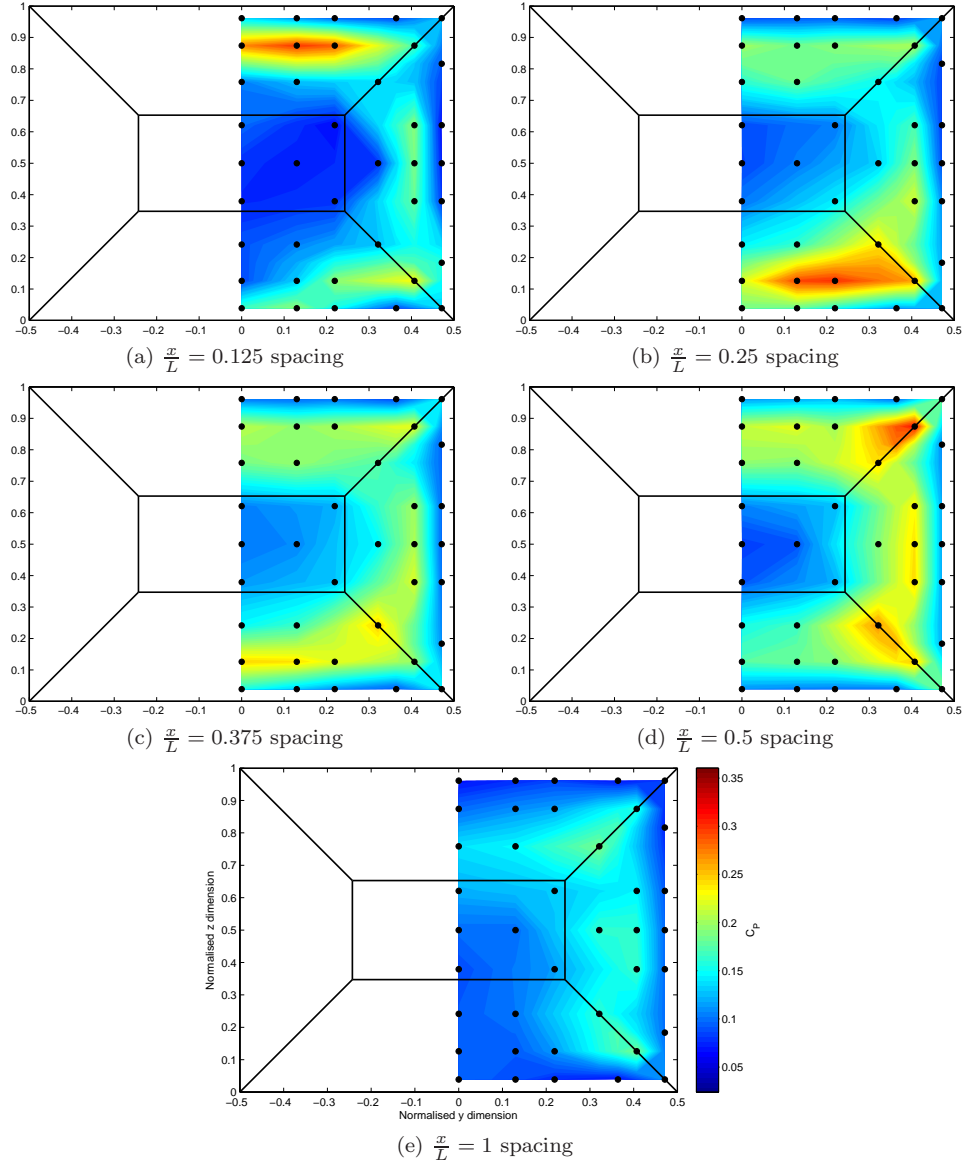


Figure 4.11: Comparison of standard deviation of surface pressures for trailing model forebody surface for  $\alpha = 35/25^\circ$  platoon with various longitudinal spacing

### 4.3.3 Gap flows

Gap flows were acquired using the ECA probe (described in section 2.2.5.2, page 79).

Figures 4.12 and 4.13 present axial velocity deficit ( $\frac{U}{U_\infty}$ ) and flow angularity data for gap flow concerning both pre and post-critically led platoons. Wake traverses are acquired mid-gap for  $\frac{x}{L} = 0.125$  and  $\frac{x}{L} = 0.25$  spacing, and  $\frac{x}{L} = 0.125$  downstream of the leading model trailing edge and  $\frac{x}{L} = 0.0625$  upstream of the trailing model leading edge for  $\frac{x}{L} = 0.5$  and  $\frac{x}{L} = 1$  spacing. Figure 4.14 presents a comparison of vertical turbulence intensity component for flows just upstream of the trailing model at the two larger spacings relevant to both leading model configurations, thus offering a comparison of gap flows in a region where mean flows are similar however turbulence phenomena differ significantly, reflecting unique elements of gap flow phenomena.

Generally, a clear shift towards  $-y$  within the recirculating region is immediately observed, as alluded to in subsequent surface shear visualisations (discussed later). A similar trend is observed for the separated region of the model-in-isolation wake, the rationale for which discussed further in Appendix E (page 266). To capture salient effects in light of this known asymmetry, wake traverses were acquired for  $\pm y$  and “joined” in post-processing for visualisation purposes.

### 4.3.4 General trends

Irrespective of the leading model afterbody geometry, flow field data further corroborates the notion that at  $\frac{x}{L} = 1$  spacing, near wake flows about the leading model base are broadly returned to model-in-isolation conditions.

#### 4.3.4.1 Trends for the $\alpha = 25^\circ$ leading model near wake

The effect of the dominant axial vortices is impaired somewhat, however are still clearly formed mid-gap for  $\frac{x}{L} = 0.125$  spacing<sup>7</sup>. The recirculating flow region - bounded by  $\frac{U}{U_\infty} = 0$  - is smaller at closer spacing, suggesting the transverse, spanwise, counter-rotating pair operating over the base to be “pushed upstream” up against the leading model base by the presence of the trailing model.

Recirculation appears prevalent in the  $\frac{x}{L} = 0.125$  case for  $+y$ ; angularity in the flow field about  $y = 0$  may have obscured the potential to observe characteristic flows in centreline data.

---

<sup>7</sup>Vorticity is relatively constant in the flow field data (not presented here) being computed curl over discrete spatial resolution; small movements in the vortex cores relative to the measuring location render this method unreliable for calculating exacting differences in vorticity. Surface pressures presented in figure 4.4 are a more exacting indicator, indicating that model-in-isolation vortex strength is reached at  $\frac{x}{L} = 1$  spacing.

#### 4.3.4.2 Trends for the $\alpha = 35^\circ$ leading model near wake

Without a trailing model, relative strengths of separating shear layers are known to cause axial vortices to form off-body and to dominate the wake (section 3.4.5, page 111). Relevant behaviour is only seen for  $\frac{x}{L} = 1$  spacing, corroborating observations from surface pressure data.

At  $\frac{x}{L} = 0.0625$  behind the leading model base for  $\frac{x}{L} = 0.125$  spacing, turbulence intensities in the region bounded by  $\frac{U}{U_\infty} < 0.6$  (including the separated region) are significant, exceeding 50%<sup>8</sup>. Whilst figure 4.13b shows the effect of the axial vortices generated by upper and side shear layers, such is the effect of the trailing model that their effect is diminished relative to that shown for the model-in-isolation at the same spacing (figure 3.14c, page 112). Despite close proximity to the trailing model, at this location the flow field angularity is yet to align itself with the trailing model's forebody geometry<sup>9</sup>. Shear stresses in flow are thus likely higher. Significant energy is thus contained in gap flows for this configuration.

Between  $0.25 \leq \frac{x}{L} \leq 0.5$ , a large recirculating region is formed in the gap, consistent with upper and side separating shear layers impinging on the trailing model forebody extremities. Commensurate with little changed force coefficients for the leading model in this configuration, velocity deficit distribution and magnitudes are broadly similar.

#### 4.3.4.3 Trends upstream of the trailing model forebody

Flows just ( $\frac{x}{L} = 0.0625$ ) upstream of the trailing model forebody for  $\frac{x}{L} = 0.5$  spaced platoons reflect the nature of flows within the gap for either leading model case, despite assuming angularity consistent with the bluff body immediately downstream (as is common for subsonic flows). For the pre-critically led platoon, the velocity deficit is concentrated about the impingement of the axial vortices formed off the leading model "C-pillars". High levels of unsteadiness exist in the vortex cores, dissipating outwards and extending down to the ground plane. At  $\frac{x}{L} = 1$  the effect is similar, however the vortices are logically weakened with increased distance from shear layers forming them. Unsteadiness is similarly diminished.

The vertical component of turbulence intensity  $I_{ww}$  is chosen to elucidate effects relevant to the post-critically led platoon, where gap flows appear quasi-two-dimensional. A clear downwash is observed across the face of the trailing model in the  $\frac{x}{L} = 0.5$  case as is high  $I_{ww}$ , suggesting that flows in this region both recirculate into the gap *and* are directed underbody, the processes determining which being highly turbulent.

Commensurate with a return to model-in-isolation type flows within the gap, the flow field just upstream of the trailing model for the  $\frac{x}{L} = 1$  spaced platoon is broadly similar to the pre-critically led case at the same spacing.

---

<sup>8</sup>The probe is reliably calibrated to 30% turbulence intensity. As a qualitative measure, it is sufficient to understand that the region is extremely turbulent.

<sup>9</sup>As per a subsonic flow field upstream of a bluff body.

### 4.3. GENERALIZED TRENDS BY LEADING AND TRAILING MODEL SURFACE PRESSURES AND GAP FLOWS

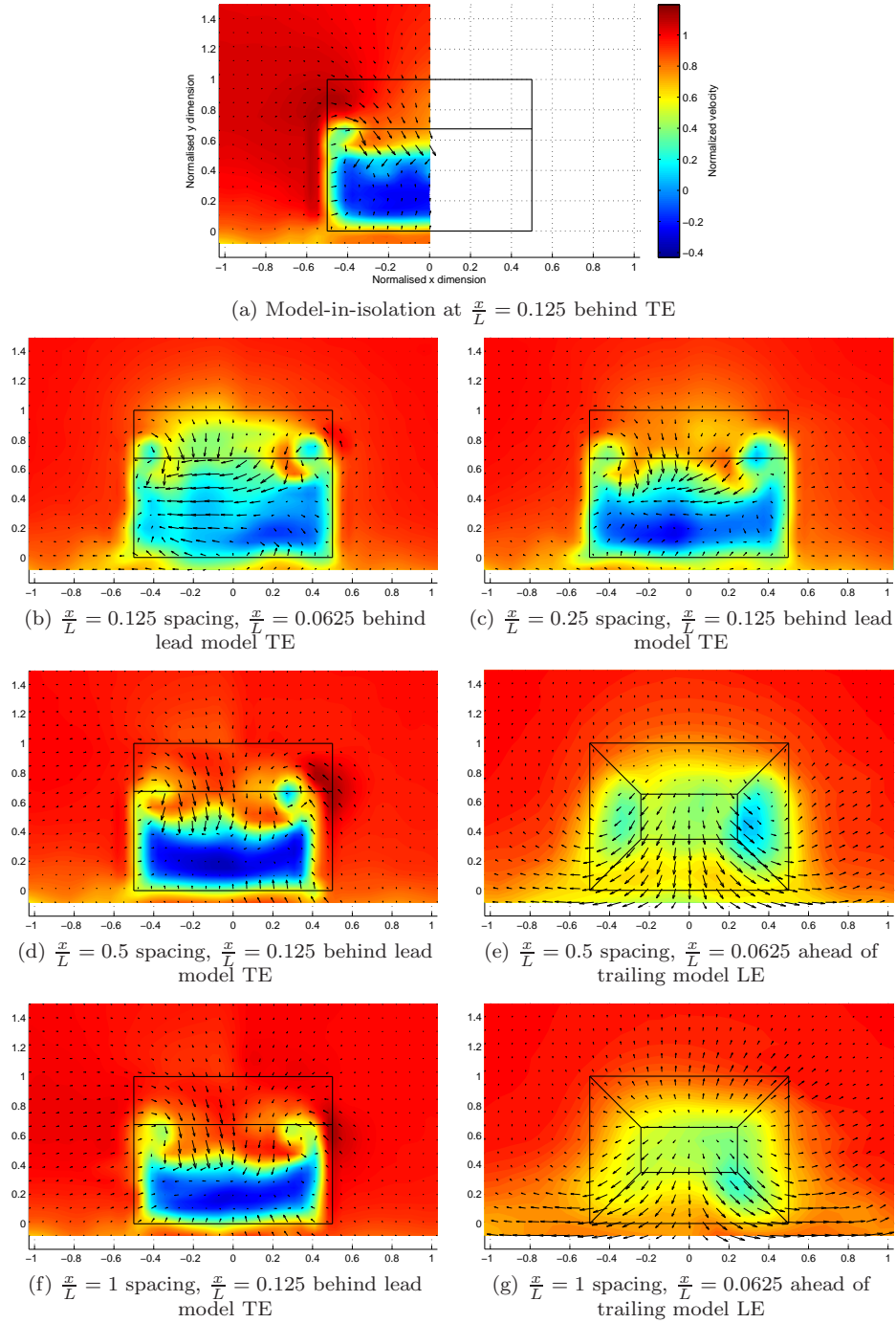


Figure 4.12: Comparison of  $\frac{U}{U_\infty}$  in wake of  $\alpha = 25^\circ$  leading model for platoon with various longitudinal spacing

#### 4.3. GENERALIZED TRENDS BY LEADING AND TRAILING MODEL SURFACE PRESSURES AND GAP FLOWS

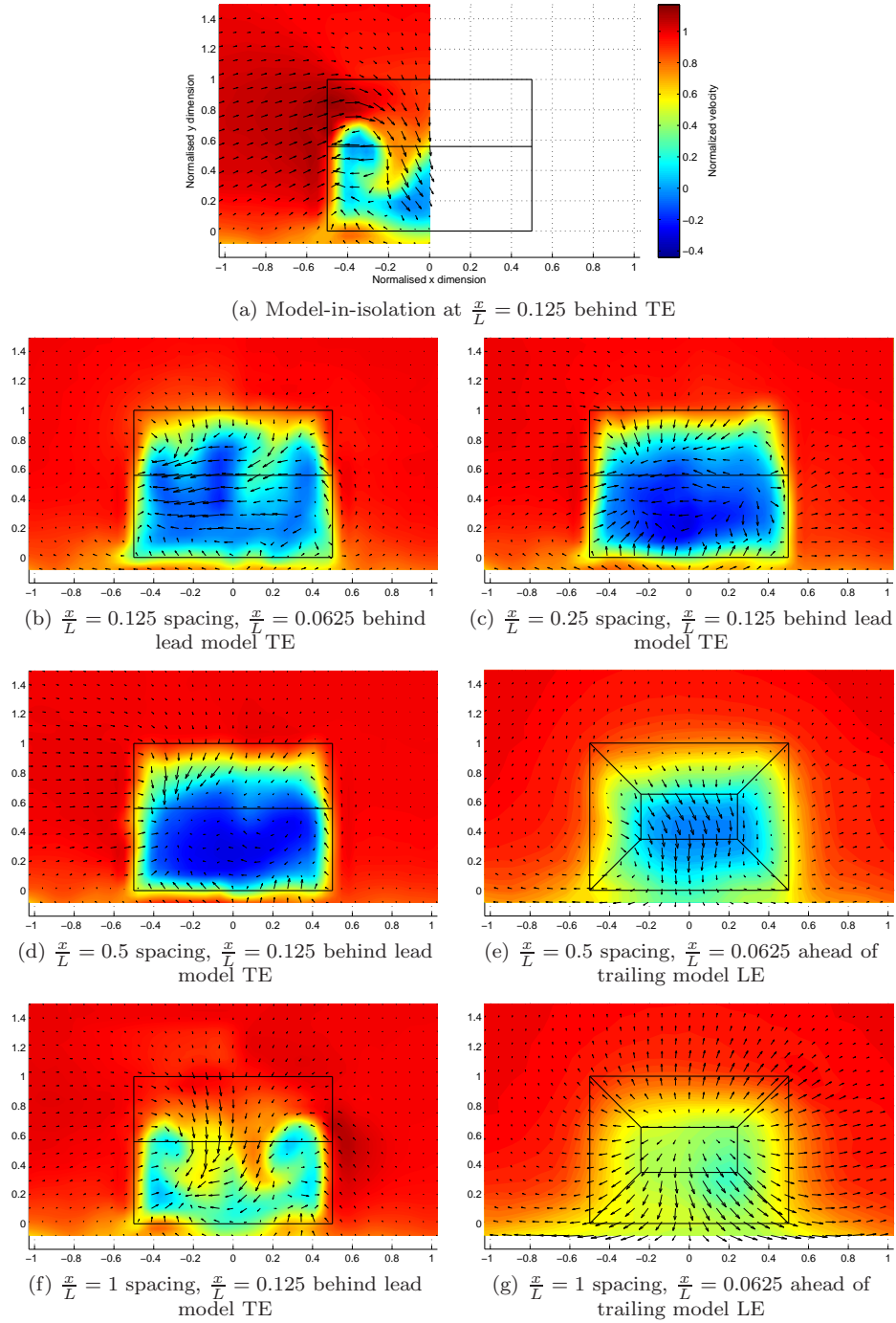
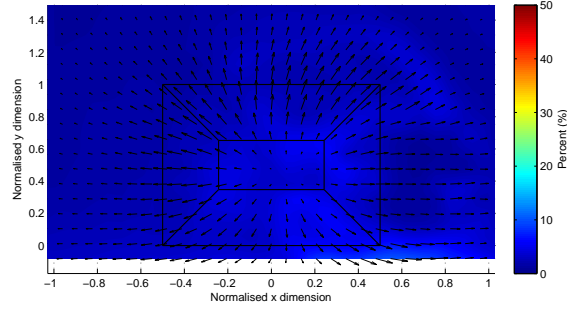
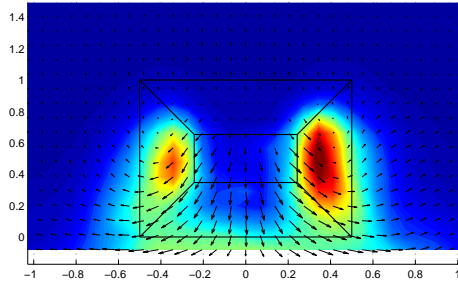


Figure 4.13: Comparison of  $\frac{U}{U_\infty}$  in wake of  $\alpha = 35^\circ$  leading model for platoon with various longitudinal spacing

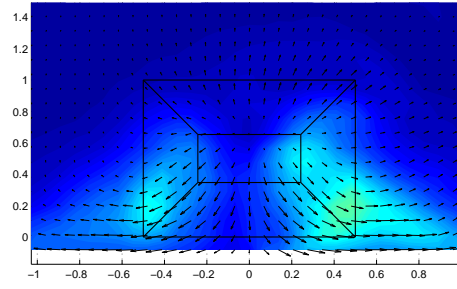
4.3. GENERALIZED TRENDS BY LEADING AND TRAILING MODEL SURFACE PRESSURES AND GAP FLOWS



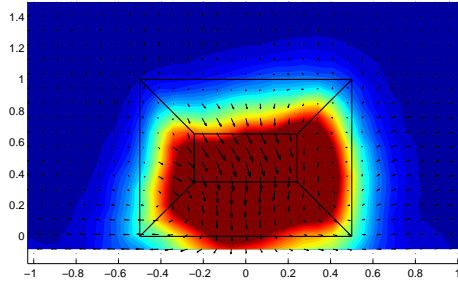
(a) Model-in-isolation



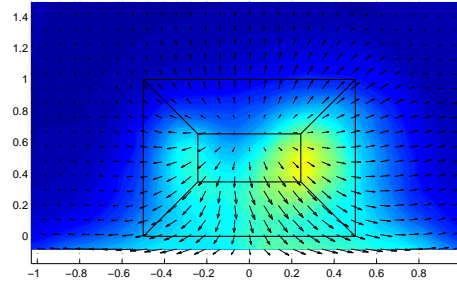
(b)  $\alpha = 25^\circ$  leading model,  $\frac{x}{L} = 0.5$  spacing



(c)  $\alpha = 25^\circ$  leading model,  $\frac{x}{L} = 1$  spacing



(d)  $\alpha = 35^\circ$  leading model,  $\frac{x}{L} = 0.5$  spacing



(e)  $\alpha = 35^\circ$  leading model,  $\frac{x}{L} = 1$  spacing

Figure 4.14: Comparison of  $I_{ww}$   $\frac{x}{L} = 0.0625$  ahead of trailing model LE

### 4.3.5 Concluding remarks and further deconstruction of data

Evidence of two unique “families” of gap flow phenomena are suggested by leading model afterbody and trailing model forebody surface pressure. Some key flow phenomena are maintained throughout:

- *The leading pre-critical model* has the formation of characteristic, impinging axial vortices impeded at close spacing, with vorticity increasing with model spacing. Quasi-two-dimensional shedding at the base/bottom/centreline coincident appears similarly maintained (evidence of characteristic counter-rotating, horseshoe base vortices is evidenced at all spacing bar  $\frac{x}{L} = 0.125$  thus far), with the presence of the trailing model impeding vortex shedding and raising base pressure with closer proximity.
- *The leading post-critical model* is still dominated by quasi-two-dimensional shedding from upper and lower separating shear layers.

The observation of two unique flow phenomena pending leading model geometry is important. Previous observations by Vano (2005) for a two-model platoon with leading and trailing  $\alpha_c$  models noted behaviour at closest spacing ( $\frac{x}{L} = 0.15$ ) similar to the leading pre-critical case, however leading model afterbody trends at  $\frac{x}{L} = 0.3, 0.5$  behaved similar to post-critical behaviours observed throughout the current research at relevant spacing - this would appear a function of the bistable nature of the  $\alpha_c$  Ahmed model. As modern practical forms are not likely to exhibit high-drag  $\alpha_c$  flows, the notion of two separate flow regimes pending leading model geometry is considered especially useful.

For either leading model configuration, three key spacing of interest require further deconstruction:

- *Closest spacing:* unique flow behaviours exist for pre and post-critically led platoons at closest spacing. Whilst such close spacing is of questionable practical relevance (section 1.4.2.1, page 46), the flow phenomena observed gives a useful insight into key phenomena at peak trailing model drag spacing. Leading model base unsteadiness is significantly increased in both platoons.
- *Peak trailing model drag:* whilst force trends are broadly similar for the pre and post-critically-led platoons, the phenomena determining these forces appear unique in each case. Whilst the pre-critically-led platoon’s increase in trailing model drag clearly owes much to steady impingement of entrained flows on the trailing model forebody along  $y = 0$ , the same model forebody in the wake of a post-critical model experiences significantly reduced pressure along  $y = 0$  for  $0.125 \leq \frac{x}{L} \leq 0.5$ . The similar drag force experienced likely owe to impingement away from the centreline.

- *Beyond peak drag:* whilst both platoons experience a near-return to model-in-isolation by  $\frac{x}{L} = 1$ , the flow mechanisms at shorter spacing differ considerably: the leading  $\alpha = 25^\circ$  model appears to retain characteristic afterbody flow phenomena at most (if not all) spacing, however the leading  $\alpha = 35^\circ$  model “traps” a counter-rotating vortex pair formed by separating shear layers from the afterbody top and bottom edges, in turn bounded by the trailing model forebody. A unique flow “regime” thus exists between  $0.125 \leq \frac{x}{L} \leq 0.5$ . Leading model afterbody and trailing model forebody pressure distributions at  $\frac{x}{L} = 1$  appear similar to the model-in-isolation, however higher trailing model forebody unsteadiness is observed relative to  $\alpha = 25^\circ$  led platoon at the same spacing.

The following sections examine aerodynamic performance using qualitative surface shear and flow field smoke visualisations and quantitative surface pressure and flow field data. Whilst qualitative in nature, surface shear visualisations offer spatial resolution beyond that offered by the surface pressure acquisition employed, if not offering a comparable indication of relative magnitudes of mean and unsteady pressure components. Data from qualitative surface methods are thus considered complimentary to the quantitative methods applied.



## 4.4 Region I: closest spacing

Both platoons evaluated exhibited lower trailing model drag prior to demonstrating a trend towards a maxima at larger spacing; similarly, leading model drag increased prior to trending towards a minima at larger spacing (whilst the exact maxima/minima were not investigated, sufficient data was acquired to establish salient trends). A significant pitch down moment in both trailing models was observed, suggesting flow impingement on the upper forebody.

### 4.4.1 Qualitative visualisation trends for platoon with $\alpha = 25^\circ$ leading model

Data presented thus far suggests that closest spacing -  $\frac{x}{L} = 0.125$  - is not sufficient to impede the formation of dominant axial vortices, but that however their position may not be buffeted about by base flows as per the model-in-isolation.

#### 4.4.1.1 Leading model backlight flows

Figure 4.15 provides key oil-and-soot visualisations of surface shear patterns. Immediately confirmed in figure 4.15a is the presence of impinging axial vortices in a surface shear distribution bearing much in common with that pertaining to the model-in-isolation (figure 3.3a, page 93). The shear patterns appear broadly symmetric, suggesting the relative circulation of the “C-pillar” vortices to be approximately equal, thus that the models are well aligned both with each other and the freestream.

The dimensions of the separated region differ from the model-in-isolation. Closure occurs further upstream over the backlight as is the separated region wider, commensurate with weakening of the dominant axial vortex pair caused by the presence of the trailing model inhibiting their development. The positive bifurcation defining closure of the region is conspicuously broad (i.e. consistent with moving impingement), indicating a heightened level of unsteadiness with this phenomena compared to the model-in-isolation. This is consistent with a higher magnitude of oscillation caused by feedback along the top/backlight edge separating shear layer owing to the presence of the trailing model (Bull et al. 1996), and thus corroborates well with data in figure 4.2a.

Foci at the upper side extremities of the backlight separation are poorly defined compared to the model-in-isolation, as do flows within the separation appear to have a more clearly defined upwash. Both observations suggest the effect of the “C-pillar” vortices is diminished at this spacing (typically the model-in-isolation “C-pillar” vortices serve to manifest their presence in the separated region as relatively powerful foci (Spohn and Gillieron 2002)). The bulk of upstream hairpin vortex structures within this region - distorted by the foci - typically have their legs severed with

the surface, compromising their coherency in the region (this phenomena was elaborated upon in section 1.3.2.4, page 37). At  $\frac{x}{L} = 0.125$  it would appear that this is not the case; as the collision of upstream and downstream vortex structures within the separated region determine closure (Krajnović and Davidson 2005), the relatively increased strength of the upstream component within this region may, in part, explain the movement of the closure point upstream. It remains significantly unsteady; entrained flows above the separating shear layer do not appear to flow onto the model backlight downstream of the recirculating region's closure (some “scrubbing” either side of the centreline indicates this to be the case between the impinging “C-pillar” vortices and the separated zone). It is possible that about the backlight/base/centreline coincident, some interaction with base flows occurs; figure 4.15a solely clarifies that this region is more unsteady and closer to zero  $C_P$  than for the model-in-isolation.

A slight reduction in  $C_P$  is anticipated over the backlight, highest over the region dominated by now-weakened “C-pillar” vortex impingement. Figure 4.2a suggests the modified shedding conditions at the backlight/base edge to limit attached flows giving rise to an even greater local delta, though figure 4.15a does not elucidate the relevant phenomena in sufficient detail for the effect to be visible; this is however confirmed in prior  $C_P$  plots relative to model-in-isolation values (figure 4.4, page 157).

#### 4.4.1.2 Leading model base flows

The low energy in the gap region made base surface flows particularly difficult to acquire using this method. Surface pressures must instead be used to elucidate base flows and confirm the presence of the characteristic spanwise vortex pair (this is further explored later).

#### 4.4.1.3 Trailing model forebody flows

Figures 4.15b-c capture salient effects of the trailing model forebody. Though the point of impingement is not well elucidated, it is clear nevertheless that the stagnation point is shifted upwards. A clearer visualisation using smoke is captured in figure 4.16, suggesting a location agreeing with prior surface pressure data.

Surface visualisations suggest a net downwash below the stagnation point, under which flow accelerates towards the model underside and around the sides. Comparison with the model-in-isolation forebody visualisation (figure 3.11, page 106, discussed further in section 1.3.2.3, page 33) reveals the laminar separations present on the model-in-isolation forebody sides to be contained to their uppermost region - the upper foci still present - with the rest of the region dominated by downwash-type flows, a likely compound of flows away from the stagnation region and impingement of axial vortices from the leading model “C-pillars”.

The spanwise laminar separation just upstream of the the horizontal section on top of the

model forebody suggests flows in this region to be accelerated beyond the stagnation point and of particularly high momentum. Overall this component is in good agreement for the  $\alpha_c$ -led platoon at  $\frac{x}{L} = 0.15$  by Vino (2005), save for the forebody separation and downwash phenomena being more pronounced.

#### 4.4.2 Generalised backlight trends for platoon with $\alpha = 35^\circ$ leading model

The presence of the trailing model at closest proximity gives rise to flows unique from those observed for the pre-critically led platoon at the same spacing, despite similar force trends. Observations made previously in force and centreline analysis are well corroborated.

##### 4.4.2.1 Backlight and base flows

Figure 4.17a presents backlight flows for the leading  $\alpha = 35^\circ$  model ahead of a  $\alpha = 25^\circ$  model at  $\frac{x}{L} = 0.125$  spacing.

Prior observations from centreline data and surface pressure trends suggested a mean transverse vortex pair formed by separating shear layers from leading model top/backlight and bottom/base edges operating in the gap for  $0.125 \leq \frac{x}{L} \leq 0.5$ , with the nearest proximity case causing the vortex pair to “squash upwards”, moving impingement upwards and over the backlight. Whilst this quasi-two-dimensional phenomena is validated, the surface visualisation data reveals further detail at closest spacing.

- *Impingement* occurs at approximately  $\frac{3}{4}z$  on the base (figure 4.18b) as a stagnation point from which flows spread out laterally (figure 4.19b - a positive bifurcation line is not observed). This occurs at slightly  $-y$ , commensurate with asymmetric flows observed in the gap.
- *Base shedding effects* at the bottom/base/centreline coincident indicate downwash below the stagnated impinging flows is diverted around immediately impinging, counter-rotating base shedding flows near the bottom edge. Shear patterns confirm these effects to be significantly turbulent and to operate within a very limited  $z$ . The impinging downwash raises base pressure and limits base shedding, further raising pressure local to the shedding location.
- *Backlight upwash* is visible above the base stagnation point. Along the centreline this appears to terminate in a saddle point, the exact location of which is poorly defined. Along  $y = 0$  towards the backlight/top edge it would appear some turbulent, impinging vortex shedding occurs as part of the separation process at the backlight/top edge giving rise to a local increase in pressure. These vortices are the same sense as the dominant upwash forming a counter-rotating flow of low energy, explaining the local rise in pressure observed between approximately  $0.9 \leq \frac{z}{H} \leq 1.0$  (figures 4.3a, 4.8b).

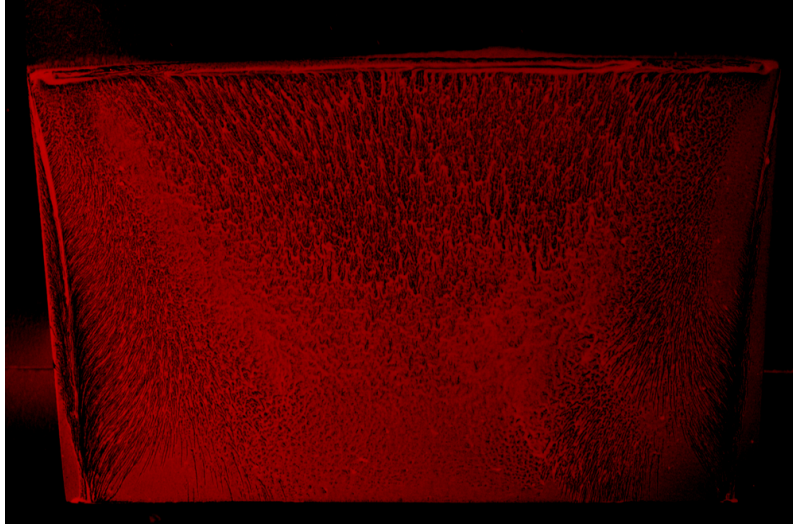
Clearly this phenomena operates quasi-two-dimensionally at  $y = 0$ . Flow otherwise spreads out towards the lower-pressure side regions, ultimately bounded by separating side edge shear layers. The transverse vortex pair model thus is valid primarily about  $y = 0$ .

#### 4.4.2.2 Trailing model

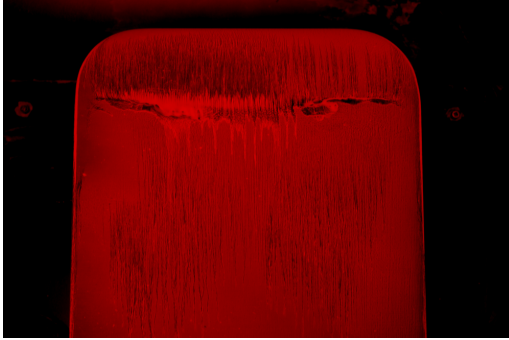
Figures 4.6 and 4.10) confirm the nature of impinging trailing model flows to differ significantly in the wake of a pre or post-critical model; clearly unique surface shear patterns are observed in figures 4.17d and 4.19a.

Impingement from top and side shear layers is immediately obvious, the trailing model being in sufficiently close proximity that top and side shear layer impingement - on account of being located near the extremities of the model projection - do not cause the laminar separation bubbles seen on the model-in-isolation.

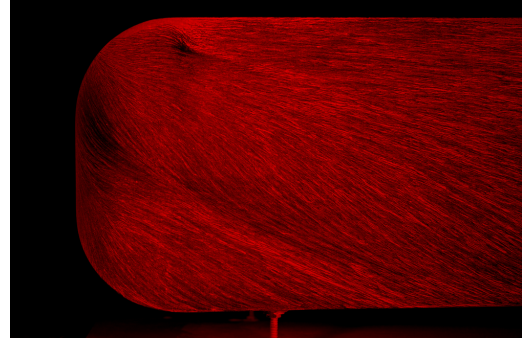
Downwash towards the model underside dominates the trailing model forebody. Clearly, much of these flows are directed under the model along  $y = 0$  (some asymmetry is noted as per leading model base shear patterns), though centreline flow field analysis indicates a portion of these flows to be recirculated in the gap (a clearly turbulent process validating the high levels of flowfield turbulence observed in figure 4.3a, page 153). As suggested by surface pressures, recirculating flows owing to the leading model bottom shear layer do not impinge at  $y = 0$  but *away* from the centreline. Limited impingement is observed at the lower spanwise extremities, inboard of which vortex roll-up of the leading model lower shear layer appears to commence. Figure 4.19a suggests the bottom transverse vortex develops sufficiently within the gap to displace the downwash away from  $y = 0$  in a manner consistent with its circulation. The momentum of the downwash over the trailing model face is consequently concentrated along  $y = 0$  (ideally; being displaced in the visualisation acquired).



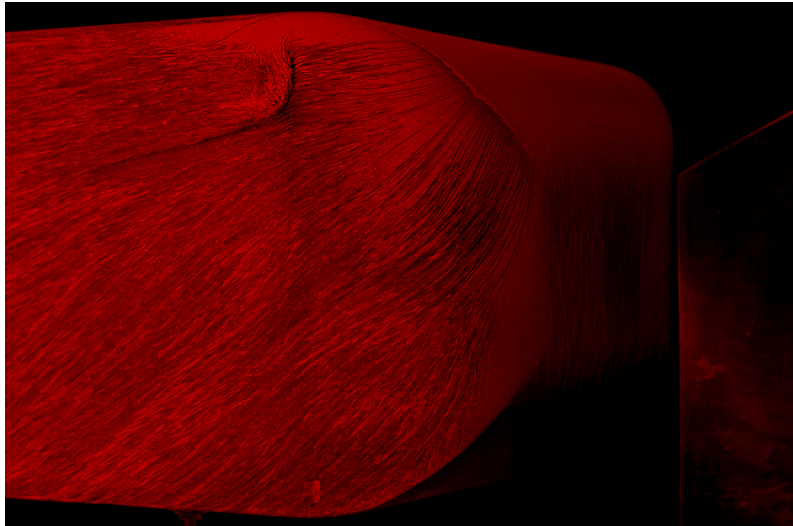
(a) Leading model afterbody, top view



(b) Trailing model forebody, top view



(c) Trailing model forebody, side view



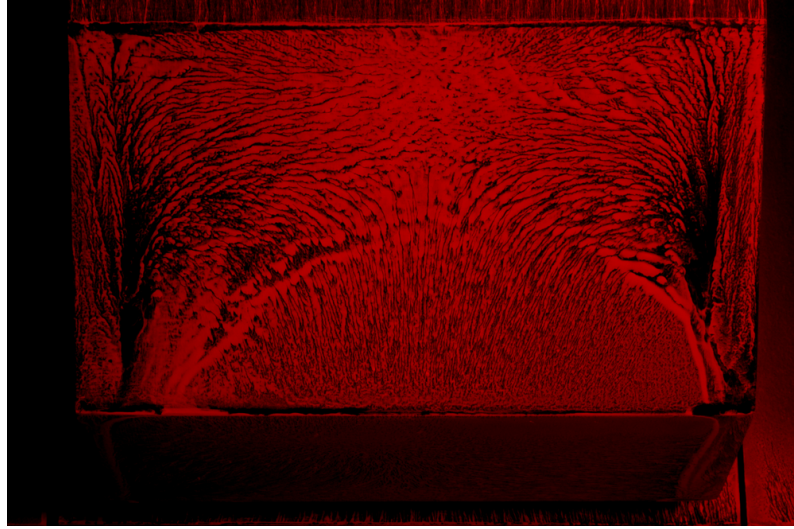
(d) Trailing model forebody quarter view

Figure 4.15: Surface flow visualisations for  $\alpha = 25^\circ$  led platoon,  $\frac{x}{L} = 0.125$  spacing

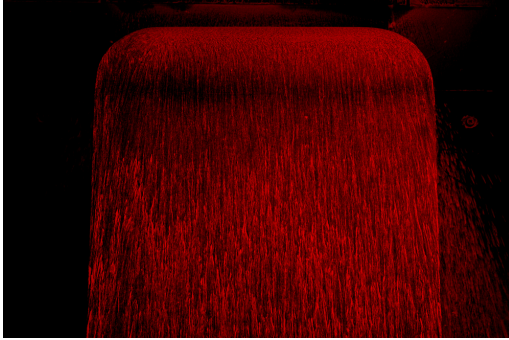


Figure 4.16: Centreline impingement on second model in  $\alpha = 25/25^\circ$  platoon,  $\frac{x}{L} = 0.125$  spacing

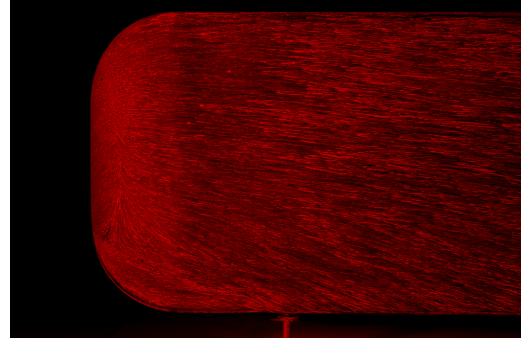




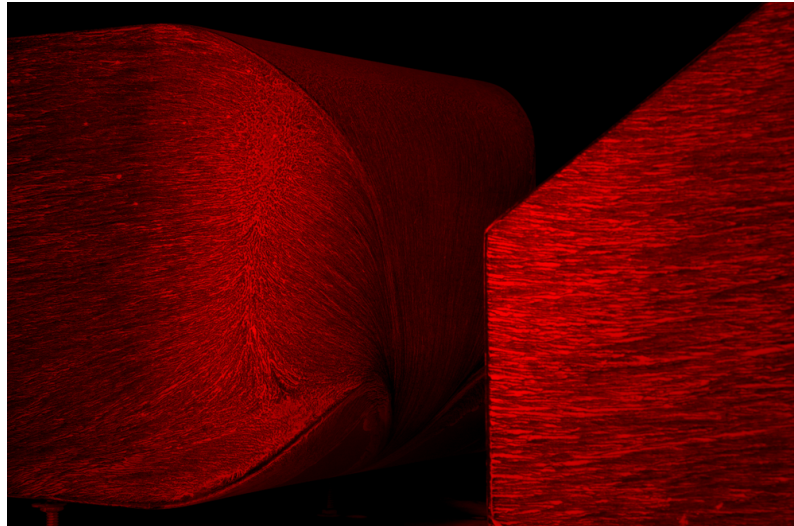
(a) Leading model afterbody, top view



(b) Trailing model forebody, top view



(c) Trailing model forebody, side view



(d) Trailing model forebody quarter view

Figure 4.17: Surface flow visualisations for  $\alpha = 35^\circ$  led platoon,  $\frac{x}{L} = 0.125$  spacing

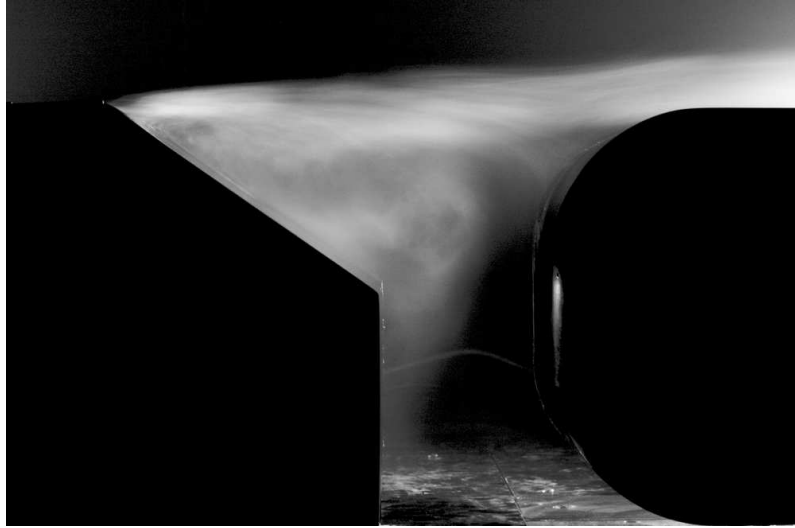
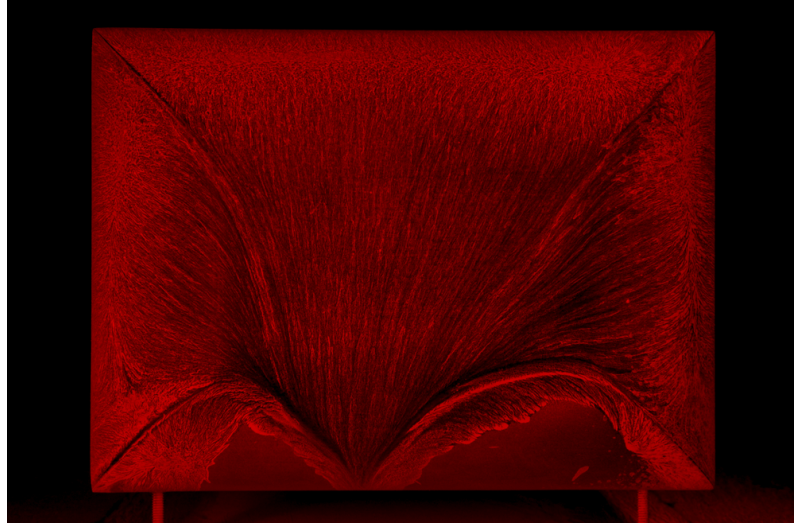
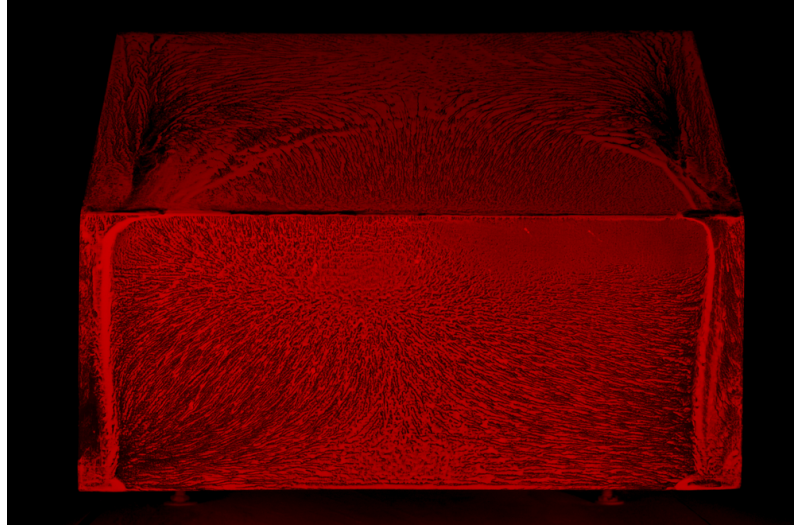


Figure 4.18: Centreline impingement on second model in  $\alpha = 35/25^\circ$  platoon,  $\frac{x}{L} = 0.125$  spacing





(a) Trailing model front surfaces



(b) Leading model rear surfaces

Figure 4.19: Gap behaviours in  $\alpha = 35/25^\circ$  platoon,  $\frac{x}{L} = 0.125$  spacing between models

## 4.5 Region II: peak trailing model drag

Trends at relevant spacing are shown to be logical evolutions of flow modes associated with closer spacing evaluated prior ( $\frac{x}{L} = 0.125$ ).

Peak trailing model drag occurs for the pre-critically led platoon at  $\frac{x}{L} = 0.25$  spacing, coinciding with the peak leading model drag reduction. Both peaks are pronounced. The post-critically led platoon experiences peak trailing model drag at  $\frac{x}{L} = 0.375$ , though this is little changed at  $\frac{x}{L} = 0.5$ . Greatest reductions in leading model drag are observed at similar spacing, if similar in the range  $0.25 \leq \frac{x}{L} \leq 0.5$  (figure 4.1a, page 151).

### 4.5.1 Qualitative visualisation trends for platoon with $\alpha = 25^\circ$ leading model

Figures 4.20b-d and 4.21 confirm the trailing model stagnation point to be similar to that observed at  $\frac{x}{L} = 0.125$ . Strong scrubbing on the downstream portion of the backlight leading inboard to the positive bifurcation line bounding the separated region (figure 4.20) - not present in the  $\frac{x}{L} = 0.125$  case - confirm stronger axial vortices formed from the backlight side edges.

The stagnation point, indeed all flows on the trailing model forebody, appear little changed from the  $\frac{x}{L} = 0.125$  case, though the stronger leading model vortices entrain a greater momentum, raising trailing model drag to peak values. In addition to the translation of the stagnation point compared to the model-in-isolation case, pressures over the entire forebody section are increased (figure 4.6, page 165).

Figure 4.21 indicates a strong net downwash in the gap from flows along the top of the leading model entrained by the “C-pillar” vortices. Figure 4.22 suggests that downwash below the trailing model stagnation point does not enter the leading model base recirculation, which instead appears to form in a manner identical to the model-in-isolation base and, corroborating surface shear data, does not appear to flow into the backlight region. Thus beyond the mean closure of the base separated zone stagnation flows are diverted underbody, although some periodicity is anticipated as low pressure packets arising from oscillating base/bottom edge separation are convected downstream.

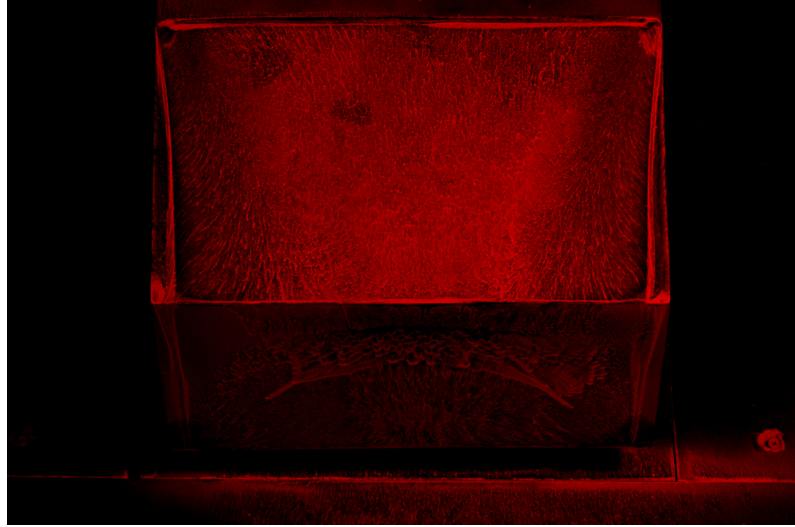
### 4.5.2 Qualitative visualisation trends for platoon with $\alpha = 35^\circ$ leading model

Surface shear for the leading model in the the wake of a post-critical geometry towards peak drag offers significant visual departures from the  $\frac{x}{L} = 0.125$  case. The actual peak drag case ( $\frac{x}{L} = 0.375$ ) is not presented, as the bounding cases ( $\frac{x}{L} = 0.375$  is presented subsequently) sufficiently explain transitional phenomena. In any case, force coefficients are little changed within this range.

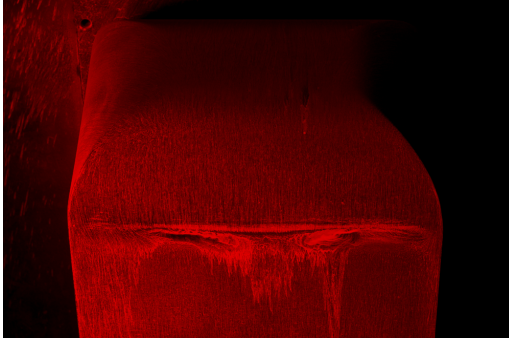
Whilst base surface shear (not shown) remains broadly identical to that observed at closer spacing, the relevant backlight visualisation shows quasi-two-dimensional flow patterns commensurate with separation at the top/backlight edge of relatively uniform pressure and low unsteadiness, corroborating surface pressure data (figure 4.23a). Figures 4.23b-d show broadly similar trailing model forebody shear, however the regions “pushed up” by the lower transverse vortices are larger in size, indicating their increased relative size and strength in the gap as increased spacing impedes their formation to a lesser degree, consistent with previously observed lower surface pressures on the leading model base.

Flows along the trailing model forebody are well captured in figure 4.24a, capturing a net downwash below the stagnation point across the face of the model, a component of which - just upstream - is seen to recirculate. Shedding at the base/bottom edge appears to exhibit an oscillating component, impinging on the model base with an upper, counter-rotating transverse vortex doing similarly at the same location (figure 4.24b). The trend for relevant flows within trailing model forebody stagnation lines to tend towards the trailing model underbody at  $y = 0$  is captured in figure 4.24d, similarly confirming leading model afterbody flows to be fully separated over the model backlight and base as per the model-in-isolation.

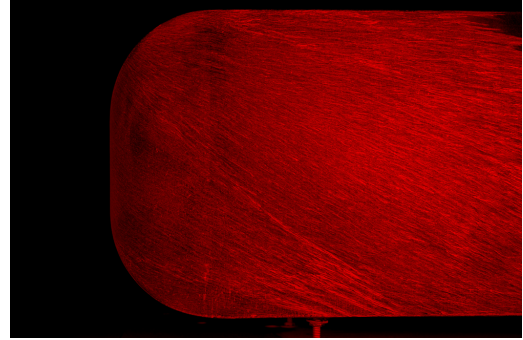
4.5. REGION II: PEAK TRAILING MODEL DRAG



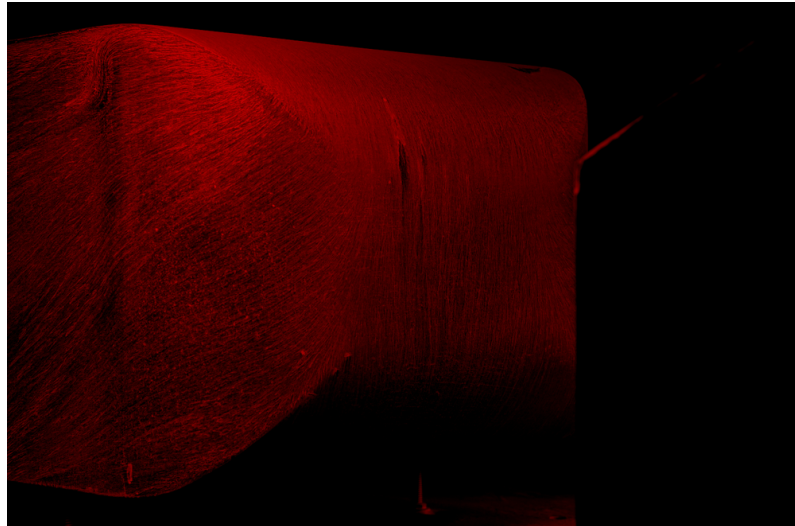
(a) Leading model afterbody, top view



(b) Trailing model forebody, top view



(c) Trailing model forebody, side view



(d) Trailing model forebody quarter view

Figure 4.20: Surface flow visualisations for  $\alpha = 25^\circ$  led platoon,  $\frac{x}{L} = 0.25$  spacing

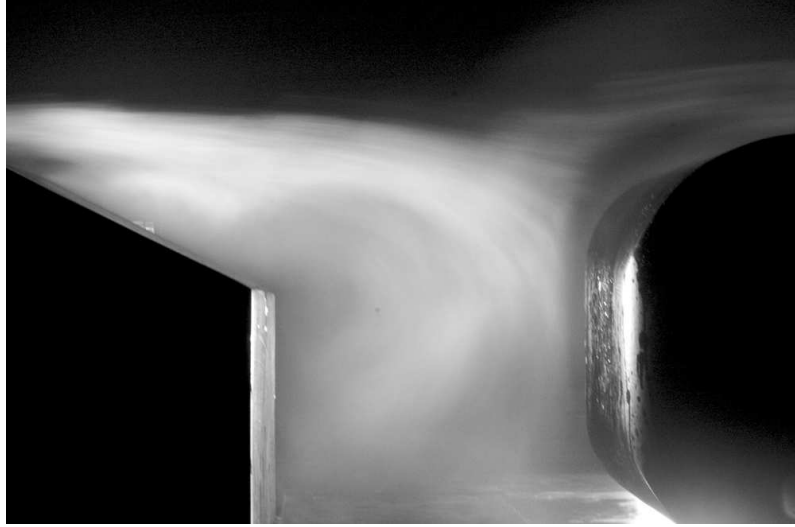
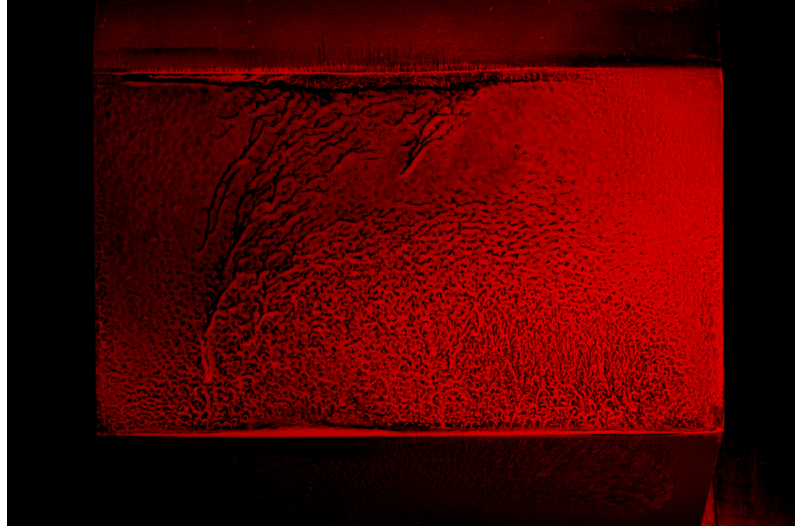


Figure 4.21: Centreline impingement on second model in  $\alpha = 25/25^\circ$  platoon,  $\frac{x}{L} = 0.25$  spacing

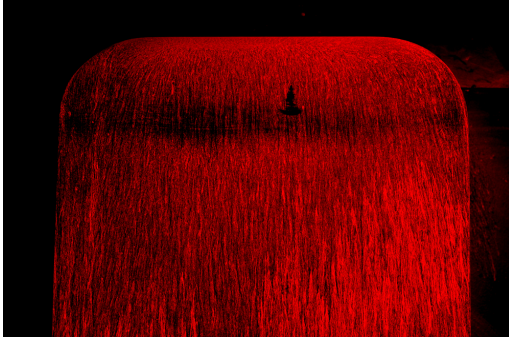


Figure 4.22: Underbody flows about base of leading model in  $\alpha = 25/25^\circ$  platoon,  $\frac{x}{L} = 0.25$  spacing

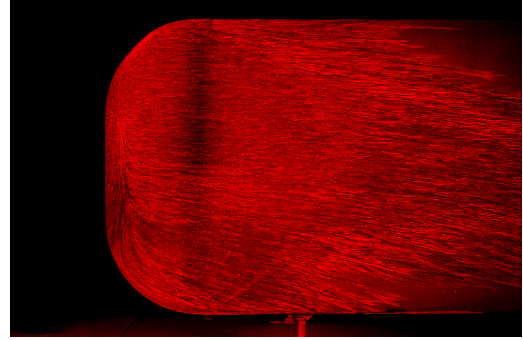
#### 4.5. REGION II: PEAK TRAILING MODEL DRAG



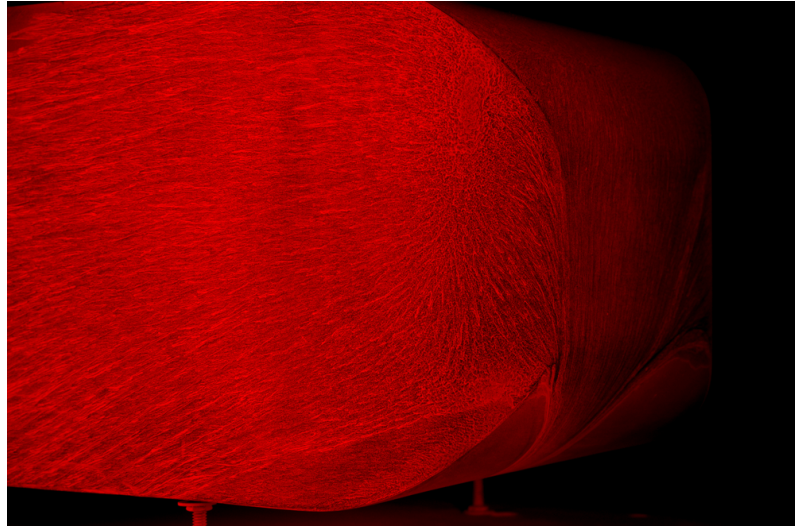
(a) Leading model afterbody, top view



(b) Trailing model forebody, top view



(c) Trailing model forebody, side view

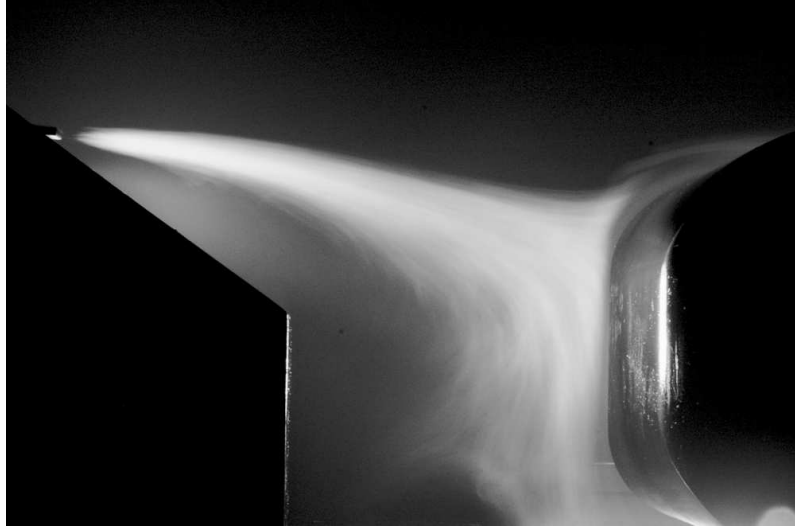


(d) Trailing model forebody quarter view

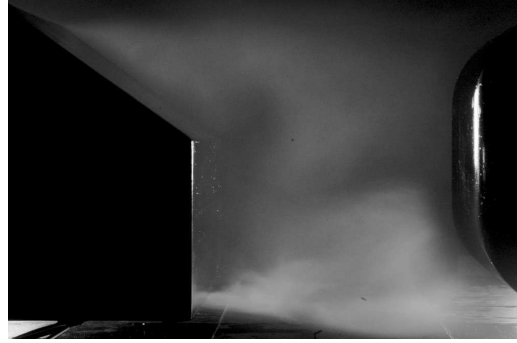
Figure 4.23: Surface flow visualisations for  $\alpha = 35^\circ$  led platoon,  $\frac{x}{L} = 0.25$  spacing



4.5. REGION II: PEAK TRAILING MODEL DRAG



(a) Centreline impingement on second model



(b) Underbody flows about base of leading model



(c) Backlight flows for leading model

Figure 4.24: Salient gap flow smoke visualisations for  $\alpha = 35/25^\circ$  platoon,  $\frac{x}{L} = 0.25$  spacing

## 4.6 Region III: beyond peak drag

### 4.6.1 Qualitative visualisation trends for platoon with $\alpha = 25^\circ$ leading model

Figure 4.27 shows trends for leading and trailing models are little changed, corroborating surface pressure data. Commensurate with increased model spacing, the stagnation point on the trailing model forebody moves downwards, although the effect of the axial axial vortices in creating a downwash towards  $y = 0$  remains prominent (figure 4.26).

### 4.6.2 Qualitative visualisation trends for platoon with $\alpha = 35^\circ$ leading model

Whilst the surface shear visualisation of figure 4.27a concerns impinging leading model afterbody flow phenomena consistent with those observed for  $\frac{x}{L} = 0.25$  spacing, figure 4.28 confirms longer vortex formation lengths<sup>10</sup>, indicative of stronger vortex shedding typical of increased spacing to a downstream bluff body giving feedback along a separating shear layer (Bull et al. 1996). Leading model base pressure is thus further reduced, giving rise to an increase in drag. Examination of video footage suggested the formation lengths to vary somewhat, suggesting broadband pressure spectra along this edge (i.e. a lack of a clearly defined spectral peak).

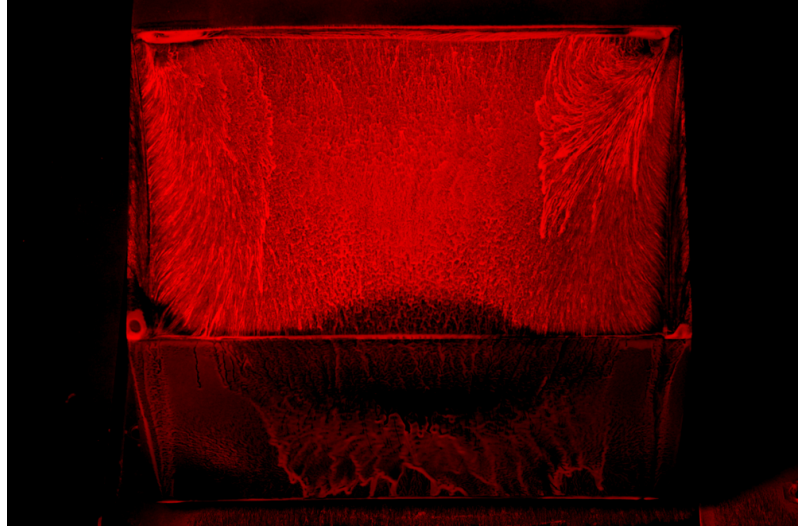
Trailing model impingement of leading model upper and side separating shear layers occurs further inboard of the model top and sides and presents with poorer definition. Angularity of trailing model side flows beyond the stagnation regions is reduced. All are features consistent with the separating shear layers increased curvature and spread in the increased gap.

As the lower vortices roll up at increasing upstream proximity from the trailing model forebody their impact on surface flows is diminished, the “double hump” either side of  $y = 0$  (contrasting figures 4.23d and 4.27d) indicative of the upwards and inwards distortion of downwash flows being no longer visible.

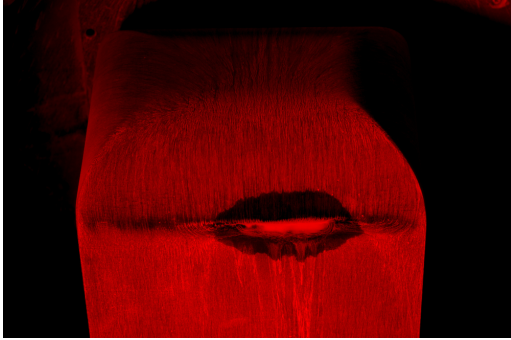
---

<sup>10</sup>The distance behind a shedding edge before flow takes up a position normal to the freestream.

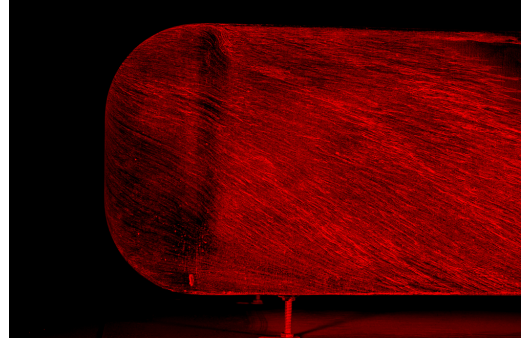




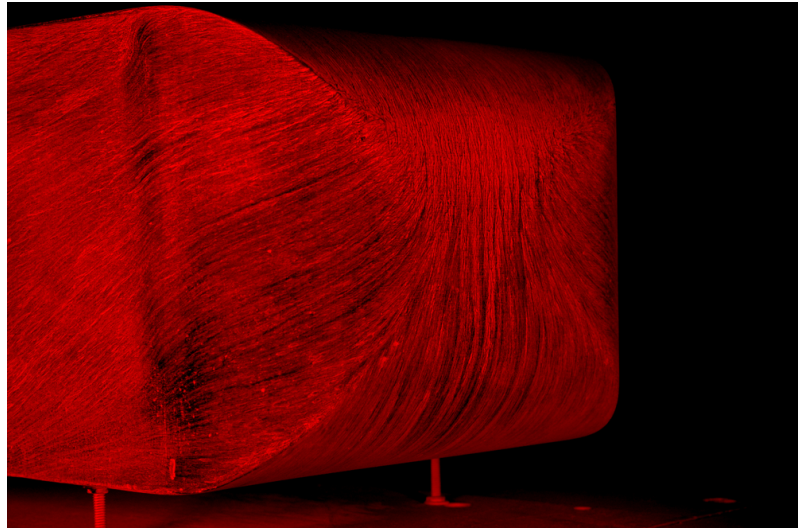
(a) Leading model afterbody, top view



(b) Trailing model forebody, top view



(c) Trailing model forebody, side view



(d) Trailing model forebody quarter view

Figure 4.25: Surface flow visualisations for  $\alpha = 25^\circ$  led platoon,  $\frac{x}{L} = 0.5$  spacing

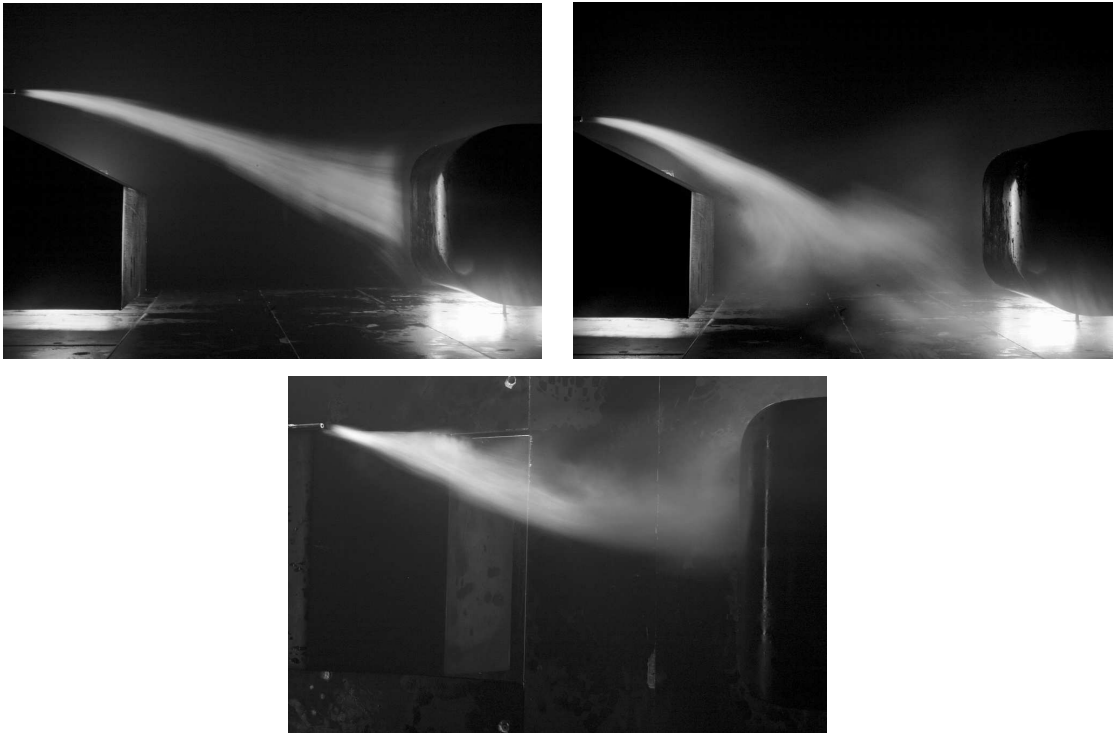
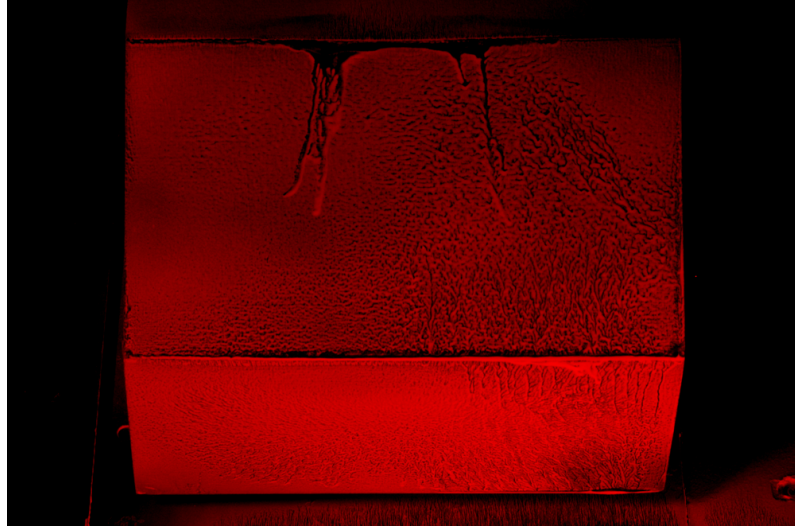
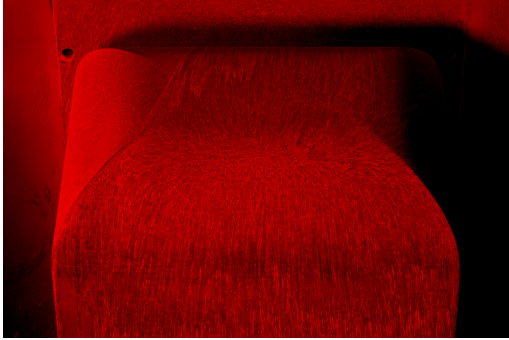


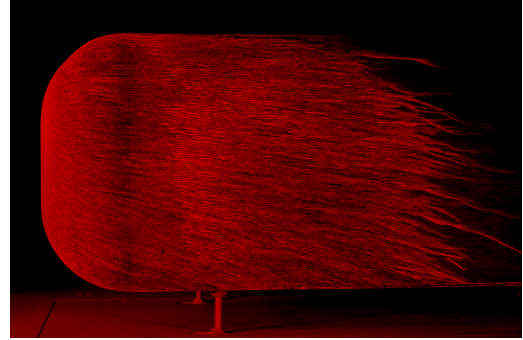
Figure 4.26: Centreline impingement on second model in  $\alpha = 25/25^\circ$  platoon,  $\frac{x}{L} = 0.5$  spacing



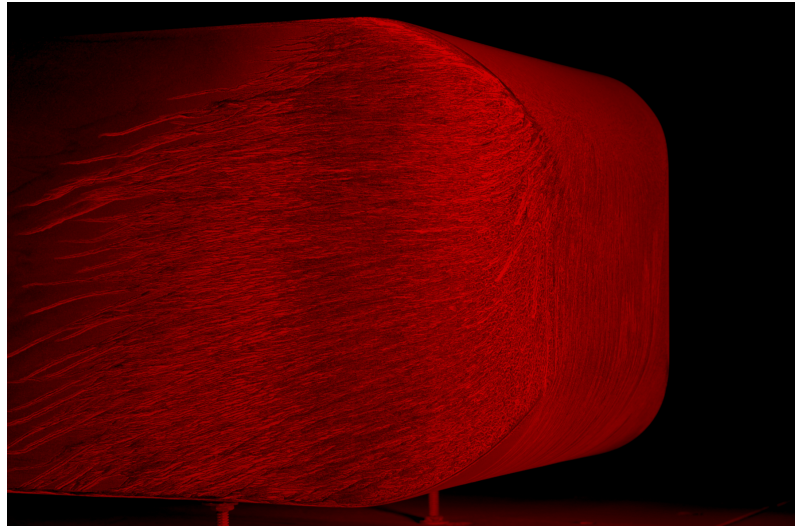
(a) Leading model afterbody, top view



(b) Trailing model forebody, top view



(c) Trailing model forebody, side view



(d) Trailing model forebody quarter view

Figure 4.27: Surface flow visualisations for  $\alpha = 35^\circ$  led platoon,  $\frac{x}{L} = 0.5$  spacing



Figure 4.28: Underbody flows about base of leading model in  $\alpha = 35/25^\circ$  platoon,  $\frac{x}{L} = 0.5$  spacing

## 4.7 Spectral performance

A final assessment of mean and dynamic performance in the gap is undertaken using spectral methods.

### 4.7.1 General spectral performance assessed at key shedding location

Prior examination of the model-in-isolation confirmed spectral trends observed in prior literature; that the Ahmed model exhibits periodicity, particularly in pre-critical configuration, driven by shedding about the model base/bottom/centreline coincident.

Figure 4.29 re-examines shedding at this location on the leading model afterbody for each of the platoon configurations evaluated:

- For either leading model configuration, spectral performance at  $\frac{x}{L} = 1$  is almost identical to the model-in-isolation.
- Between  $0.25 \leq \frac{x}{L} \leq 1$  spacing, the  $\alpha = 25^\circ$  leading model exhibits expected performance for a shear layer incurring feedback from a downstream bluff body at increasing proximity; the frequency of oscillation decreases and amplitude increases commensurate with impeded vortex shedding (Bull et al. 1996, Leclercq and Doolan 2009, Sakamoto and Haniu 1988, Shiraishi et al. 1986, Takeuchi and Matsumoto 1992). Behaviour at  $\frac{x}{L} = 0.125$ , however, is unique: spectral energy increases markedly and the peak returns to approximately  $St > 0.4$ , albeit with slightly poorer definition.
- Spectra for the  $\alpha = 35^\circ$  model is typically broadband in nature, with energies increasing with decreased spacing. A small “hump” in spectra is observed at  $St = 0.28$  for  $\frac{x}{L} = 1$  as per the model-in-isolation. A slightly larger “hump” appears at  $St = 0.19$  for  $\frac{x}{L} = 0.375$ , growing in magnitude to  $\frac{x}{L} = 0.125$  whilst the frequency associated with the peak first rises to approximately  $St = 0.28$  at  $\frac{x}{L} = 0.25$ , and diminishing to  $St = 0.15$  at double the energy for  $\frac{x}{L} = 0.125$ . These phenomena indicate some coherent periodicity among what appears to be a significantly random shedding processes.

As significant gap periodicity exists only for the platoon  $\alpha = 25^\circ$  leading model, the following work is relevant solely to the pre-critically led platoon.

### 4.7.2 Analysis for pre-critically led platoons

A key characteristic of base pumping in the model-in-isolation concerns the interaction between the upper horseshoe base vortex and the downstream portion of the axial “C-pillar” vortices, giving rise

to pressure oscillations in the axial vortices and the surfaces they impinge upon, with consequent oscillations in adjacent flow structures (with lesser spectral magnitude).

It was suggested earlier that the presence of the trailing model not only limited vortex shedding, but distorted the base horseshoe vortex pair upstream and downwards towards the base, limiting interaction with flow phenomena  $+z$  of their mean location (specifically, any interaction with backlight flows). Figure 4.30 presents spectra along key  $y = 0$  locations for the leading  $\alpha = 25^\circ$  model at a variety of spacing (a similar plot for the model-in-isolation is provided in figure 3.24a, page 127). Whilst at  $0.375 \leq \frac{x}{L} \leq 1$  the strength of the base oscillations are sufficient to cause backlight flows to oscillate sympathetically, the ability appears impaired at  $\frac{x}{L} = 0.25$  (a very weak “hump” is observed at the backlight/base edge), and is visibly defeated for  $\frac{x}{L} = 0.125$ . Figure 4.31 contrasts the same “main” shedding location with spectra along the backlight side edge from which the “C-pillar” vortices are shed (the relevant model-in-isolation comparison provided in figure 3.24b); clearly, the impinging vortex oscillates with identical frequency at  $\frac{x}{L} \geq 0.375$  only.

The effect in the flow field is visualised in figure 4.32. The relative magnitudes of base oscillations corroborate well with corresponding surface pressure spectra presented in figure 4.29a. Clearly for  $0.125 \leq \frac{x}{L} \leq 0.25$  strong oscillations are observed in the flow field in a location corresponding to key base shedding. The relative magnitude of the oscillations concerned relative to that about the axial vortex cores shows a considerable disparity, which is not visualised at larger spacing. Surface pressure data are this well corroborated.

The effects of asymmetry in gap flows are also visible in figure 4.32; the relative strength of oscillations in vortex cores both immediately behind the leading model and just upstream of impingement in the  $\frac{x}{L} = 0.5, 1$  cases suggests shedding owing to the base vortex is distorted in an asymmetric manner immediately downstream of the leading model trailing edges, such that oscillating interactions favour one of the axial vortices ( $+y$ ) more than the other.

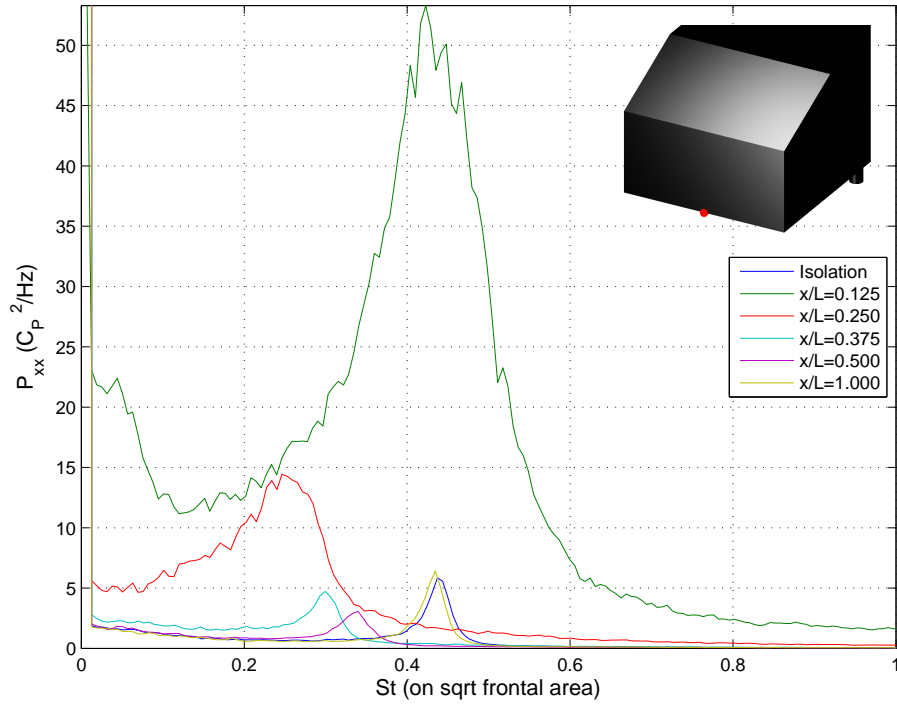
#### 4.7.2.1 Validation of key flow phenomena for leading model

The previous analysis gives good insight into the relative strengths of shedding phenomena for key locations on the model afterbody surface at various spacing, though does not prove that characteristic model-in-isolation type base shedding occurs for the pre-critical leading model at closest spacing.

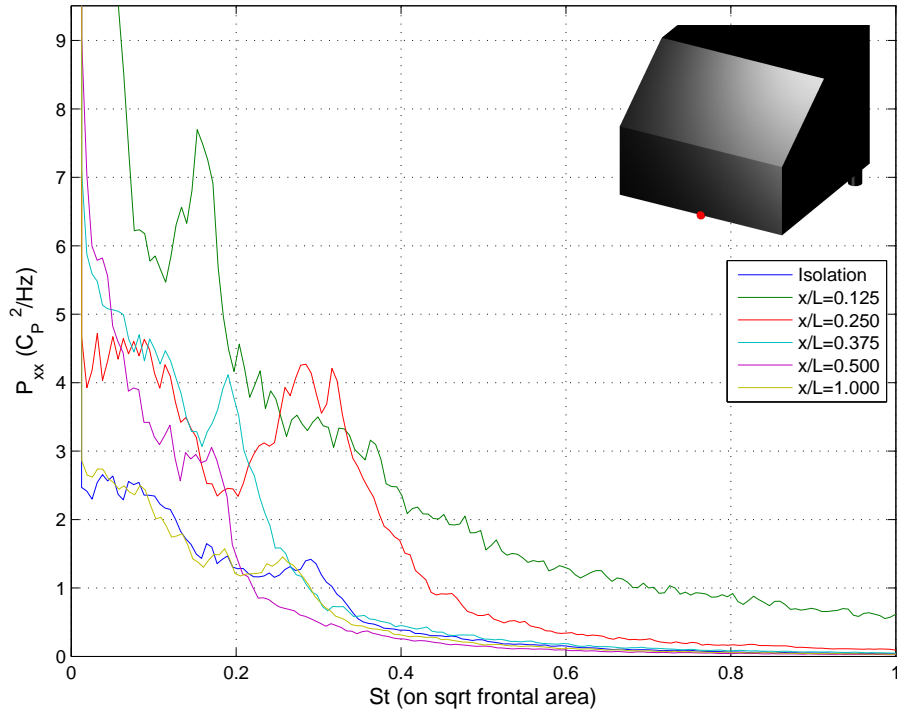
The relevant cross-spectral phase magnitude for the  $\alpha = 25^\circ$  leading model is presented in figure 4.39. Despite the significantly reduced spectral densities previously observed over the model backlight and base away from the shedding location, what weak periodicity exists at the relevant base shedding frequency forms coherent, out-of-phase structures operating over the backlight and base in a manner consistent with model-in-isolation characteristics. Figure 4.39a suggests the lower base vortex to be considerably smaller in  $z$  than for larger spacing, suggesting a shorter vortex formation length in relevant shedding. For given underbody momentum, this facilitates a higher

frequency of oscillation, consistent with diminished gap spacing little more than that sufficiently close for the leading model separating shear layers to reattach directly onto the trailing model leading surfaces (Bull et al. 1996, Leclercq and Doolan 2009, Shiraishi et al. 1986). This represents a clear departure from relevant work by Vano (2005) for a leading  $\alpha_c$  model, having observed negligible spectral energy at the same location for similarly close spacing.

Very low surface pressures on the relevant trailing model forebody surface suggests the leading model lower separating shear layer does not intermittently attach directly onto the trailing model leading edge (figure 4.8, page 163).



(a) For platoon with leading  $\alpha = 25^\circ$  model



(b) For platoon with leading  $\alpha = 35^\circ$  model

Figure 4.29: Spectra at base/bottom/centreline coincident for first model in platoon at various spacing



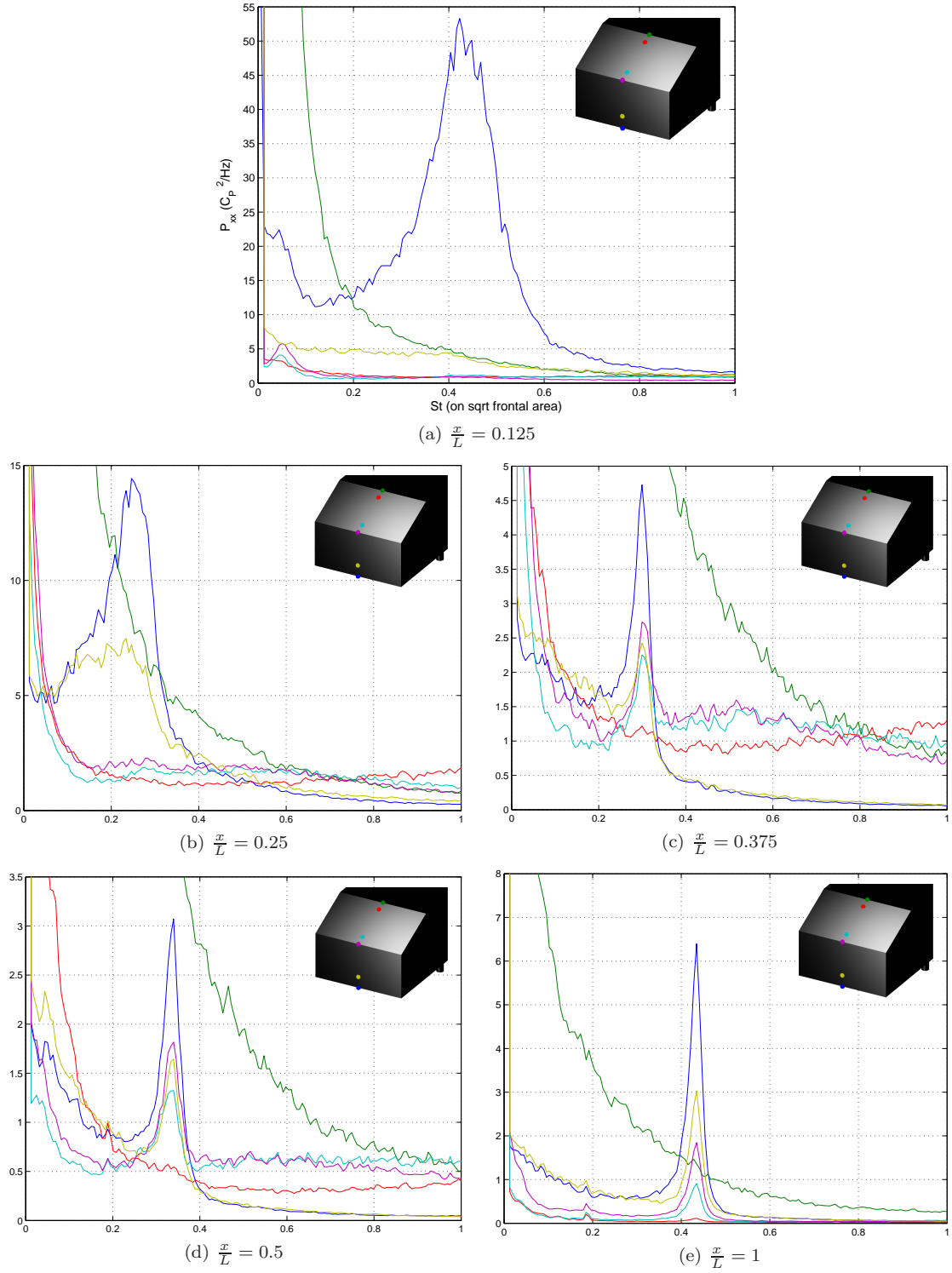


Figure 4.30: Spectra along  $y = 0$  for leading model in  $\alpha = 25/25^\circ$  platoon at various spacing

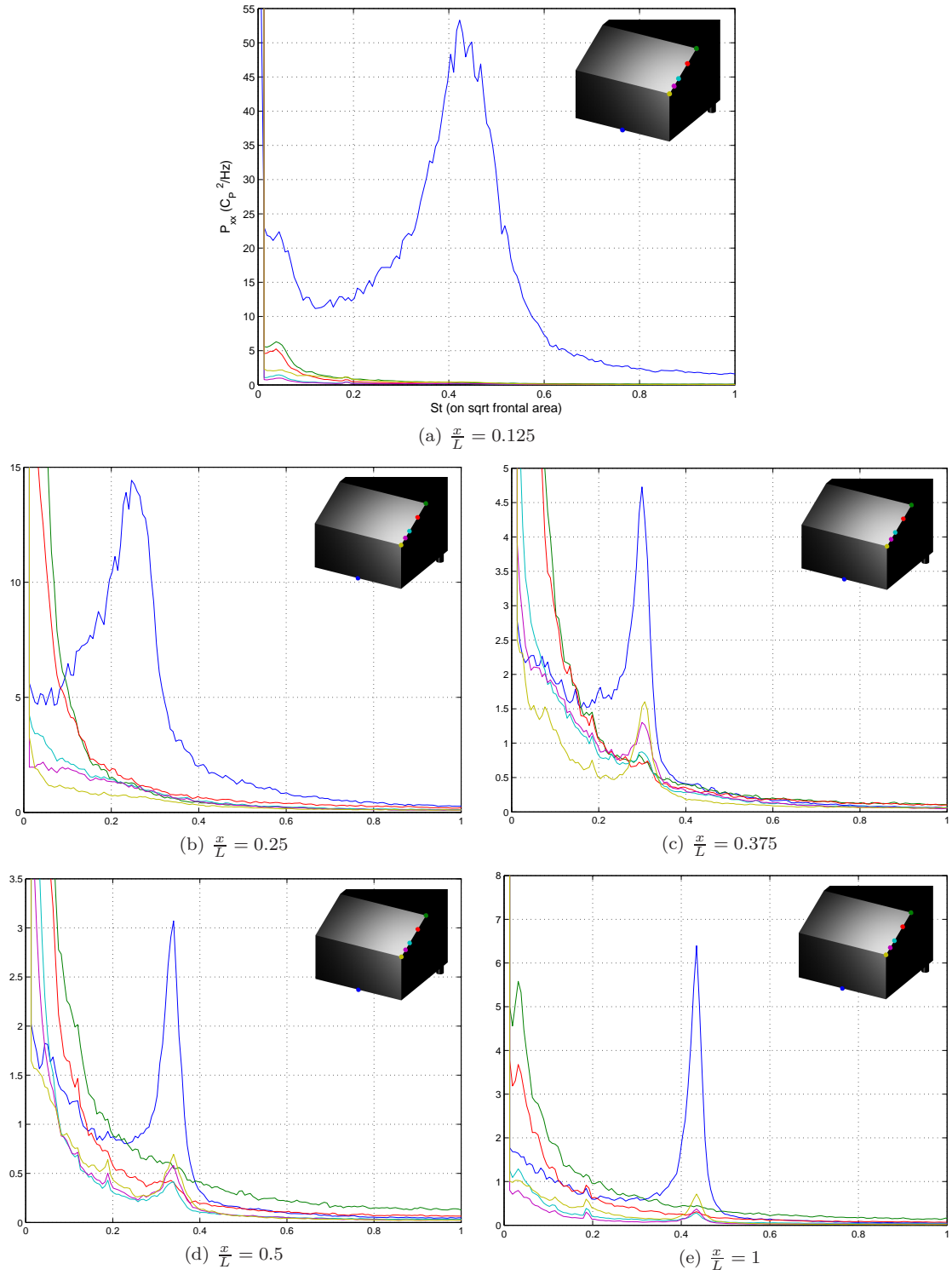


Figure 4.31: Spectra on backlight side edge for leading model in  $\alpha = 25/25^\circ$  platoon at various spacing

#### 4.7. SPECTRAL PERFORMANCE

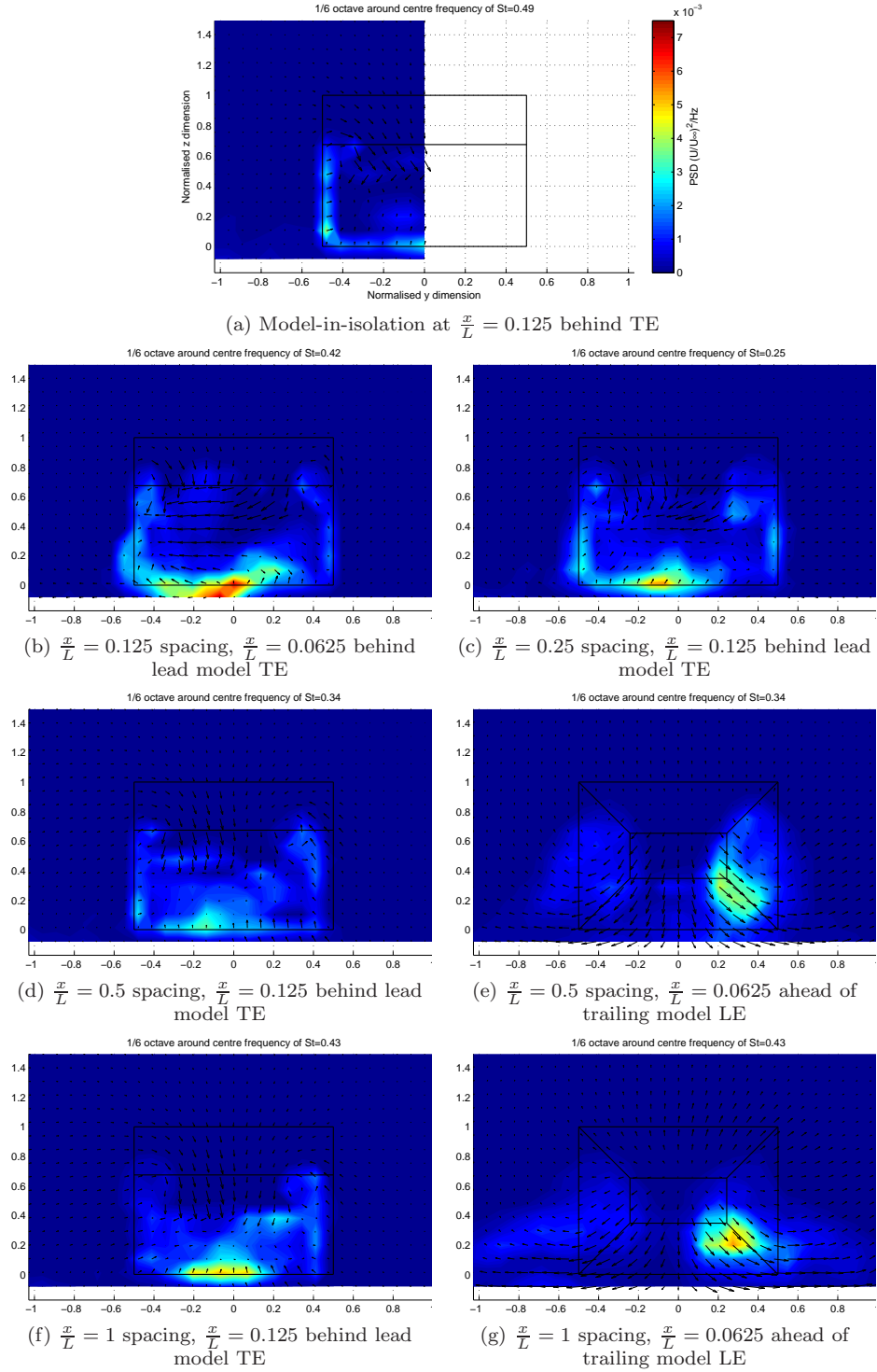


Figure 4.32: Comparison of PSD in wake of  $\alpha = 25^\circ$  leading model for platoon with various spacing

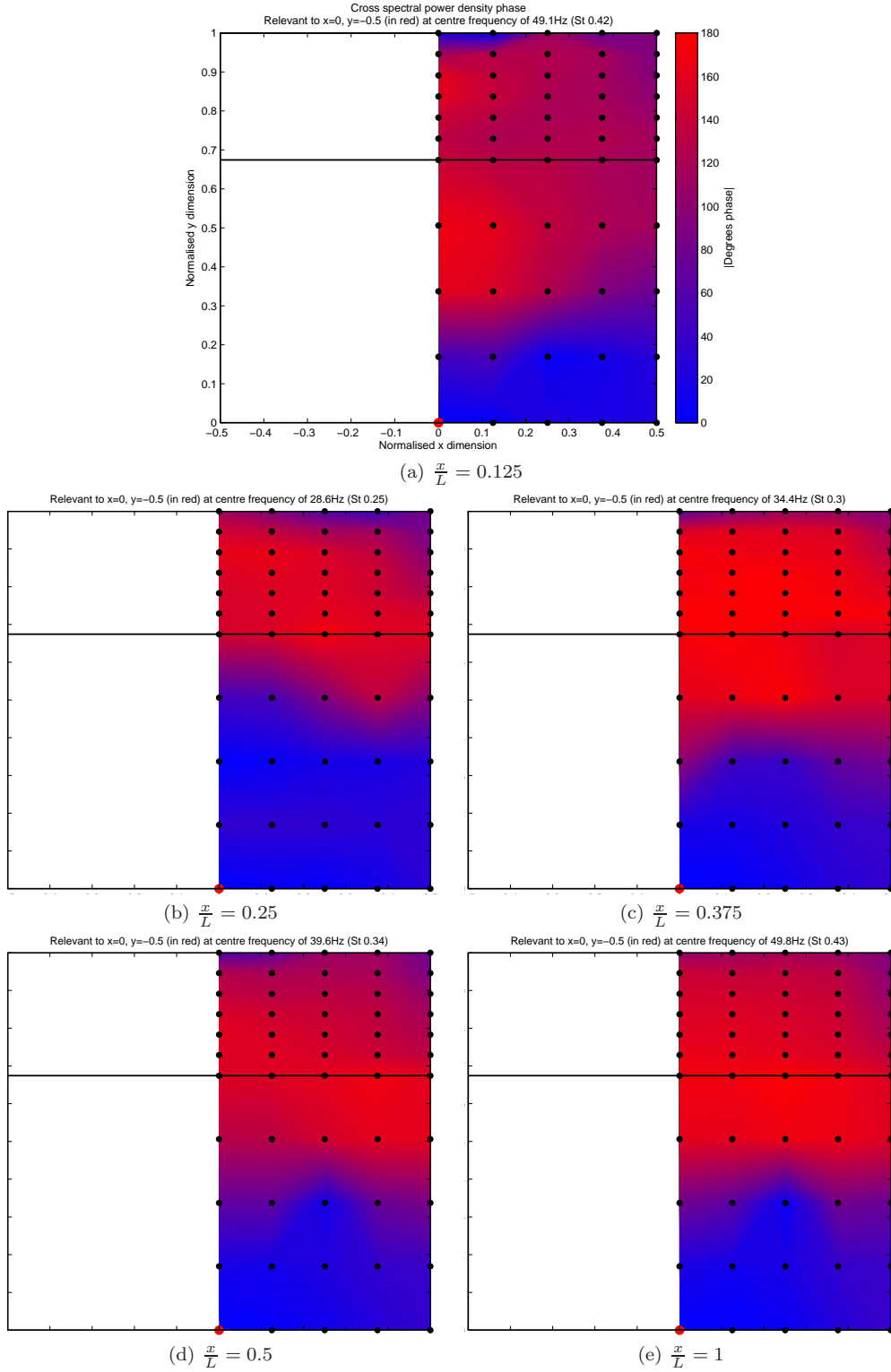


Figure 4.33: Phase plots of model afterbody for  $\alpha = 25^\circ$  model in wake of  $\alpha = 25^\circ$  model relative to base/bottom/centreline coincident at various spacing

## 4.8 Trailing model afterbody performance

This section is included for completeness in the context of deconstructing aerodynamic effects associated with two automotive models in a tandem arrangement. Whilst relevant, it is of secondary importance to the investigation and analysis of gap flows - practically, automotive forms differ considerably in glasshouse form, being proportionately shorter, appropriately contoured and featuring a generally “notched” forebody<sup>11</sup>. The increase proximity to the forebody alone is likely giving rise to more substantial aerodynamic interactions between forebody and afterbody flows in the practical domain. Misalignment is known to cause force variations in platooned forms (Marcu and Browand 1998, Tsuei and Savaş 2001). Potential disparities between cross sectional area of leading and trailing vehicles in a practical platoon would further complicate trailing model afterbody flow behaviours.

As such, investigations of trailing model aerodynamic performance are limited to surface pressure data only. Analysis of relevant results is presented in contrast with model-in-isolation contrast and upstream inter-model gap aerodynamic performance.

Simultaneous acquisition of leading and trailing model afterbodies was not undertaken owing to equipment limitations<sup>12</sup>. An exacting deconstruction of phase relations on surfaces adjacent to the gap was therefore not explored.

### 4.8.1 Mean surface pressures

The performance of the trailing model afterbody ( $\alpha = 25^\circ$  in all cases) contrasts favourably with conclusions drawn in earlier analysis. Figures 4.34 and 4.35 primarily confirm that afterbody surface pressure distributions are little changed irrespective of model spacing and upstream model configuration. All salient mean effects for the pre-critical afterbody pressure distribution are present.

### 4.8.2 Statistical unsteady behaviours

The performance of time-dependent behaviours were observed to differ slightly those experienced by the model-in-isolation. Comparisons of statistical unsteadiness (standard deviation of  $C_P$ ) are provided in figures 4.36 and 4.37 (for the same cases presented in figures 4.34 and 4.35).

For the  $\alpha = 25^\circ$  model in the wake of an identical, pre-critical model, surface pressure unsteadiness is similar to the model in isolation for spacing  $\frac{x}{L} \geq 0.5$ . The unsteady region associated with base shedding is smaller in the closest spacing evaluated  $\frac{x}{L} = 0.125$ , being concentrated in a region

<sup>11</sup>Aspect ratios are also unique model-to-model, see Appendix F, page 274.

<sup>12</sup>The limited channel count would not have allowed “whole surface” acquisition, a separate study involving surface acquisition at key locations would have been required. This was deemed beyond the scope of the research question, however is recommended as a further study.

#### 4.8. TRAILING MODEL AFTERBODY PERFORMANCE

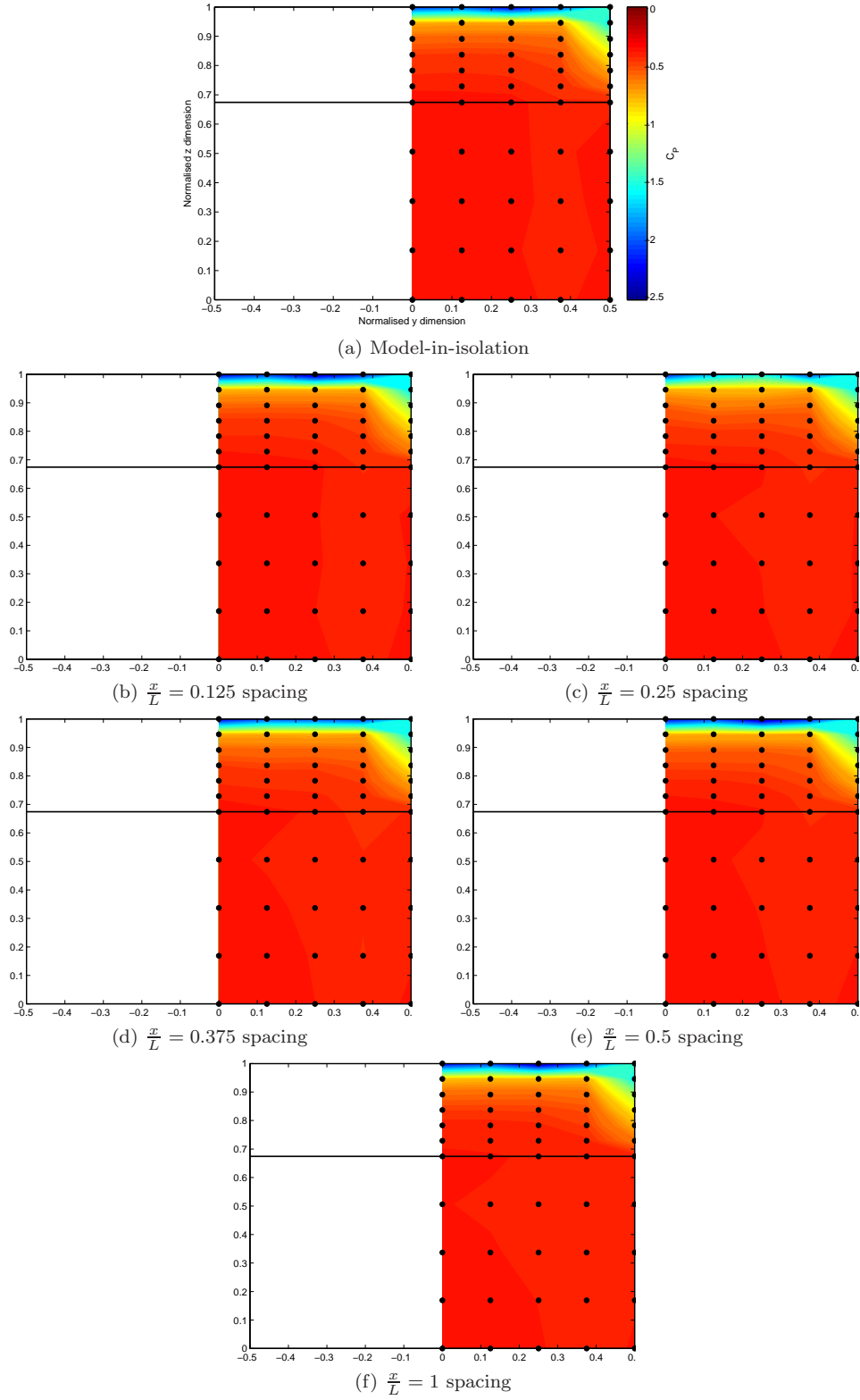


Figure 4.34: Comparison of surface pressures for trailing model backlight and base surfaces for  $\alpha = 25/25^\circ$  platoon with various longitudinal spacing

#### 4.8. TRAILING MODEL AFTERBODY PERFORMANCE

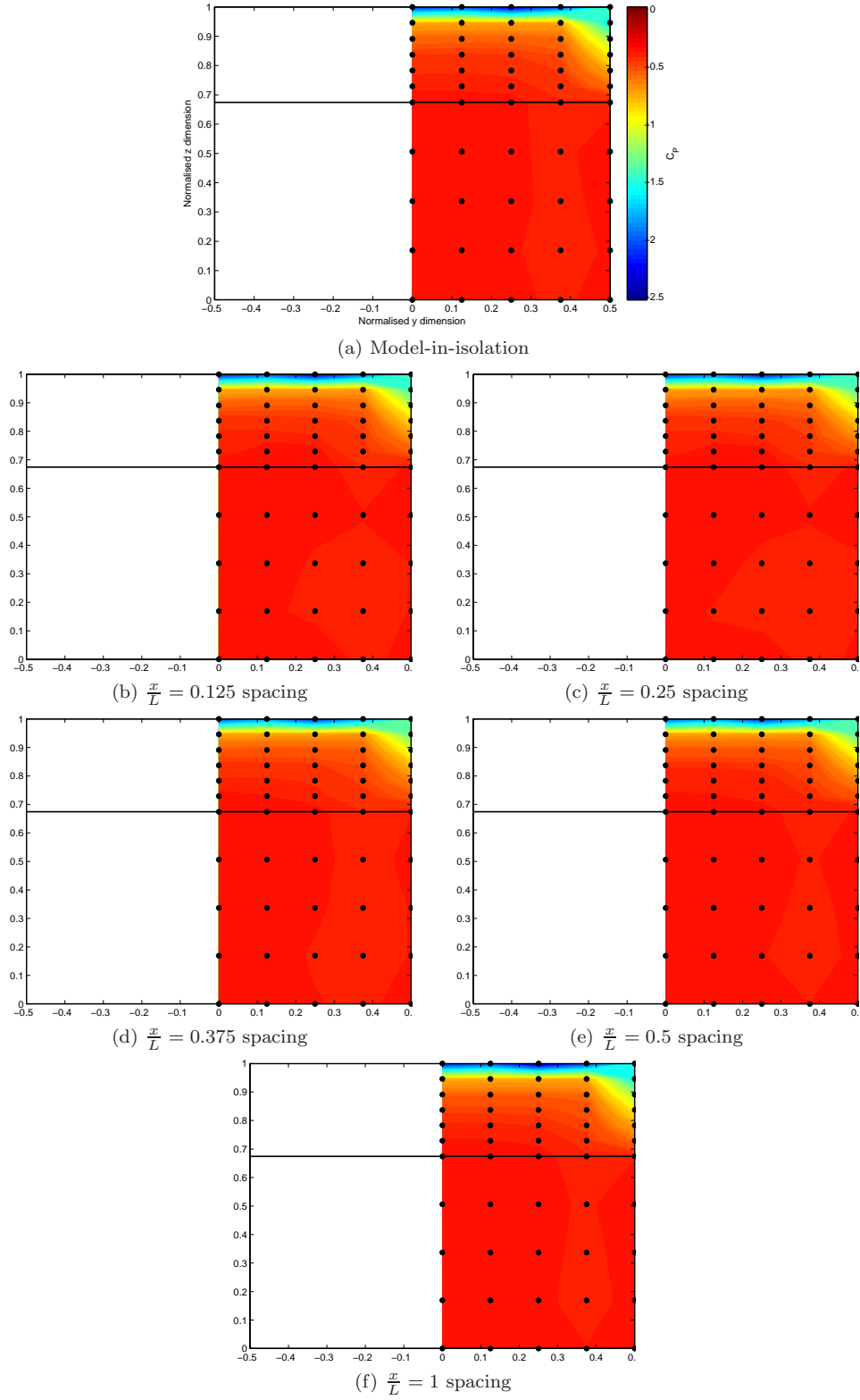


Figure 4.35: Comparison of surface pressures for trailing model backlight and base surfaces for  $\alpha = 35/25^\circ$  platoon with various longitudinal spacing

#### 4.8. TRAILING MODEL AFTERBODY PERFORMANCE

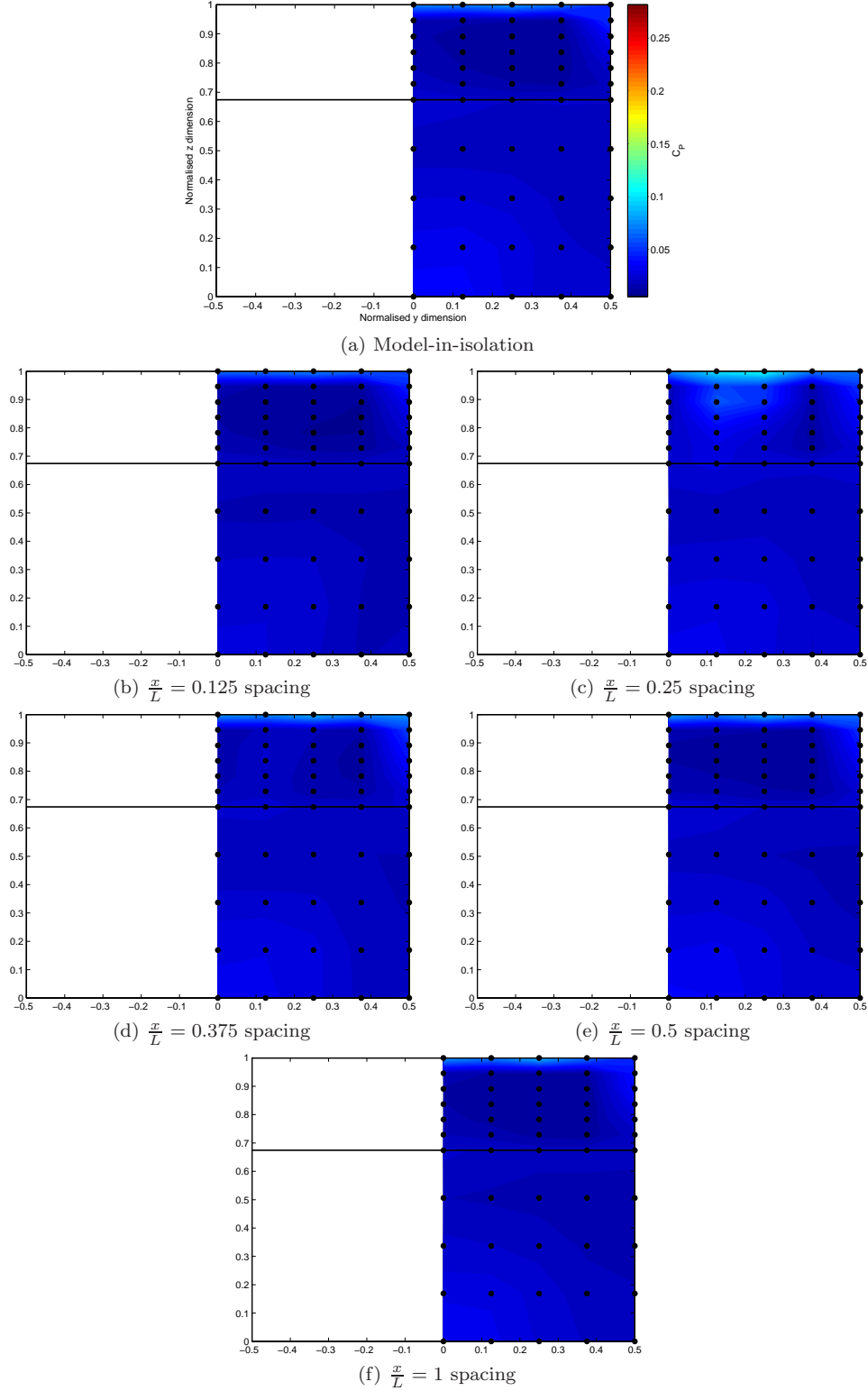


Figure 4.36: Comparison of standard deviation of surface pressures for trailing model backlight and base surfaces for  $\alpha = 25/25^\circ$  platoon with various longitudinal spacing



#### 4.8. TRAILING MODEL AFTERBODY PERFORMANCE

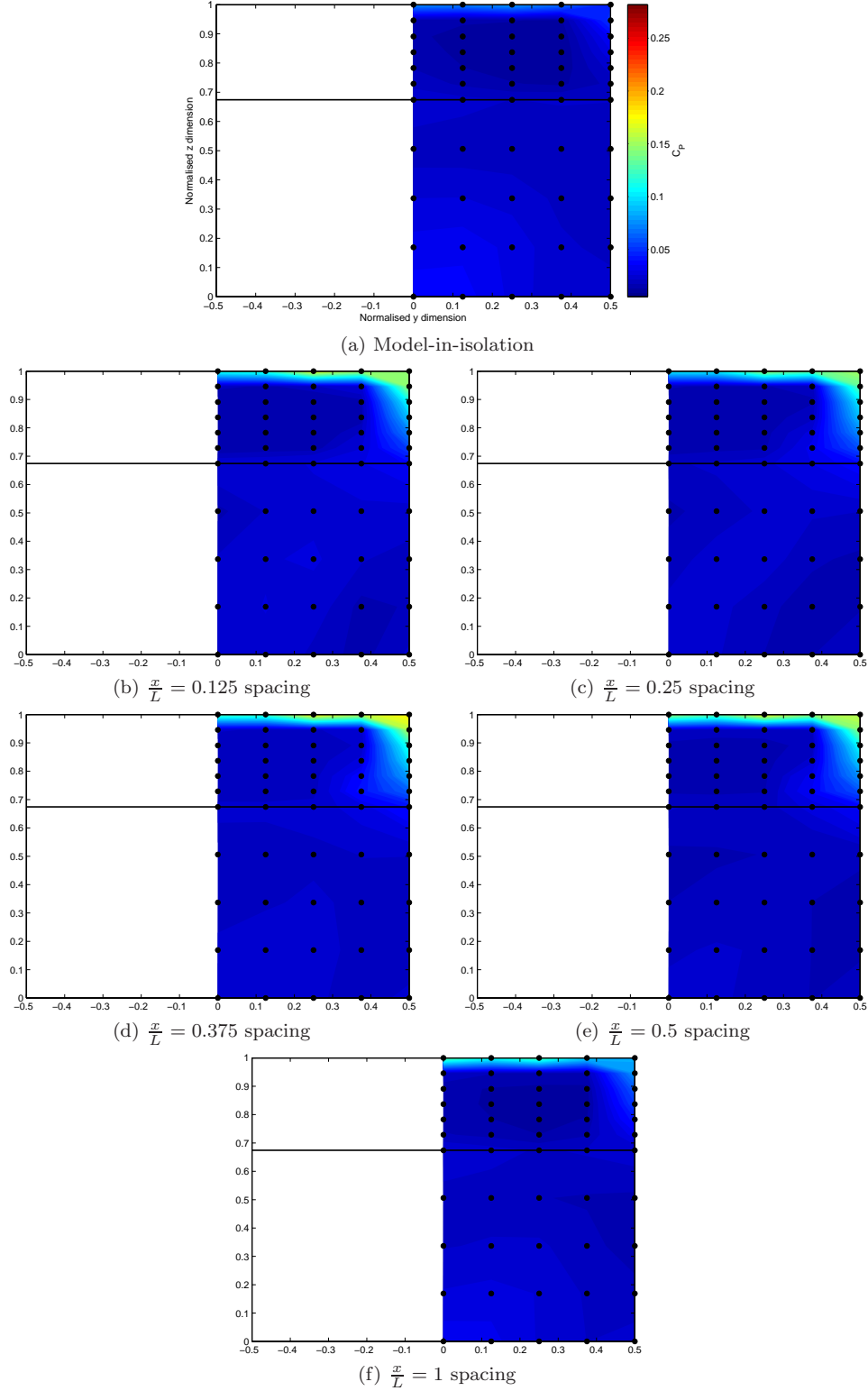


Figure 4.37: Comparison of standard deviation of surface pressures for trailing model backlight and base surfaces for  $\alpha = 35/25^\circ$  platoon with various longitudinal spacing

$-0.2 \leq \frac{y}{L} \leq 0.2$ . The interim spacings ( $\frac{x}{L} = 0.25$  particularly) are clearly unique: base unsteadiness remains similar, however the backlight region presents with a considerably more unsteady region bounded by the  $xz$  plane and the approximate width of the backlight separated region (the region just outboard of this owes low levels of unsteadiness to the adjacent, steady impingement of the side-backlight “C-pillar” vortex). The  $z$ -height of the unsteady region about the top/backlight edge is clearly increased for  $0.125 \leq \frac{x}{L} \leq 0.5$ .

The same model in the wake of a post-critical model presents with higher levels of unsteadiness about the backlight/top and backlight/side edges for  $0.125 \leq \frac{x}{L} \leq 0.5$  than for the model-in-isolation by a factor of (approximately) three. This location is consistent with the location of impingement over the model forebody at the same spacings (figure 4.10, page 165) - which is itself relatively unsteady (figure 4.11, page 166) - suggesting the possibility that relevant variations in velocity are advected downstream, giving rise to similarly relevant unsteadiness in the formation of the C-pillar vortex. *This cannot be definitively proven* in lieu of comparative flowfield interrogation of flows about the trailing model side. The known yaw in the RMIT IWT may similarly contribute to the observed phenomena (section A.1, page 222), a possibility not explored in detail, however a qualitative corroboration exists in that unsteady backlight edge flows towards  $\frac{x}{L} = 1$  diminish with the movement of the stagnation point to one similar to that of the model-in-isolation<sup>13</sup> (an elementary confirmation was provided by acquiring data sets for both sides of the model. These were subsequently merged and presented in figures 4.35f and 4.37f; no clear yaw effects are observed). The potential effects of this phenomena are elaborated upon in section 4.8.4.

### 4.8.3 Oscillating unsteady behaviours

A relatively simple approach to validate salient oscillating features of the trailing  $\alpha = 25^\circ$  model is to assess oscillations about the base/bottom/centreline coincident - shedding from which is known to cause periodic oscillations in the pre-critical model wake - and to examine cross-spectral phase magnitude against between this point and base/backlight surfaces. As per the model-in-isolation (section 3.5.2.3, page 124), a clearly defined oscillation is anticipated.

For the pre-critically led platoon, base oscillations are shown to increase in normalised frequency between  $0.25 \leq \frac{x}{L} \leq 1$  (figure 4.38a), consistent with the order of increasing frequency of impinging oscillating phenomena on the model forebody alluded to in figure 4.32. The acceleration of flows under the forebody stagnation point and under the model is speculated to be a plausible contributor in explaining a general shift towards slightly higher oscillating frequencies in each case. As surface pressures are not representative of impinging flows, overall levels are broadly consistent for the same location in the model-in-isolation.

An interesting observation concerns an increase in shedding frequency beyond the model-in-isolation value for  $\frac{x}{L} \geq 0.5$ , presenting with a higher-energy spectral peak at  $\frac{x}{L} = 0.5$  than at  $\frac{x}{L} = 1$ .

---

<sup>13</sup>This suggestion is presented with caution in that yaw present in the IWT freestream is known to diminish along the test section's length (Quirillo 1999).

A plausible explanation concerns the mean nature of gap flows; the pre-critical wake is known to produce a pronounced downwash with strength relative to that of the dominant axial vortices entraining it (figure 3.13a, page 110). Consequently, the stagnation point of the trailing model in such a wake moves progressively downwards (figure 4.6, page 159). Thus the relative strength of the downwash and increased diversion of oncoming flows towards the trailing model underbody may contribute to underbody momentum exceeding that of the model-in-isolation, giving rise to larger pressure differences incurred in shedding phenomena. At  $\frac{x}{L} = 1$  there is insufficient information to suggest whether or not pressure fluctuations in the gap play a significant part in determining the frequency of trailing model base shedding, as spectra for the leading model show little change between  $\frac{x}{L} = 1$  and the model-in-isolation (figure 4.29a, page 197). It is thus possible that any increased underbody momentum gives rise to the increase in periodicity, whereas for intermediate spacing ( $\frac{x}{L} < 1$ ), normalised frequencies of trailing model base shedding phenomena reflect those of relevant upstream flows impinging on the model forebody as oscillating pressure packets from the lead model base are convected downstream. This theory is supported by data for the post-critically led platoon, where model-in-isolation spectral energy is exceeded at  $\frac{x}{L} = 1$  (figure 4.38b); figure 3.14a (page 112, a similar comparison is provided by data of Lienhart et al. in figure 1.21, page 31) confirms downwash in the  $\alpha = 35^\circ$  wake, however it is more prominent at larger spacing, consistent with the larger separated wake bounded by the top and bottom afterbody edges. Similarly, a clear stagnation region on the model “nose” is not developed until  $\frac{x}{L} = 1$  spacing (figure 4.10, page 165). The phenomena suggested in the pre-critically led platoon would thus logically occur at larger spacing.

*It should be stressed that the above hypothesis is entirely speculative; experimental resources did not permit simultaneous acquisition of both leading and trailing model base flows, nor were comparative interrogation of the relevant flow fields undertaken. As oscillating base behaviours affect the mean flow field, it is recommended that this be considered a topic of further study.*

The closest spacing cases ( $\frac{x}{L} = 0.125$  for the pre-critically led platoon,  $\frac{x}{L} = 0.125, 0.25$  for the post-critically led platoon) present with comparatively muted spectral peaks commensurate with gap flow phenomena.

#### 4.8.4 Confirmation of salient oscillating afterbody phenomena

As per the  $\alpha = 25^\circ$  model-in-isolation, confirmation of salient oscillating flow phenomena on model afterbody surfaces is undertaken by analysis cross-spectral phase magnitude over backlight and base surfaces relevant to the base/bottom/centreline coincident. Both figures 4.39 and 4.40, for the pre-critically and post-critically led platoons, confirm the lower portion of the base to be in phase with this location at the shedding frequencies presented in figures 4.38a and 4.38b, with the rest of the model neatly out of phase. This is consistent with model-in-isolation behaviour presented in figure 3.28c (page 131), and is thus consistent with the presence of an out-of-phase, spanwise horseshoe vortex pair operating over the model base, with the upper vortex causing weak

oscillations in backlight flows.

A point of interest concerns the trailing model backlight in the wake of the post-critical model; an out-of-phase region is noted on the backlight, being most prevalent for  $0.125 \leq \frac{x}{L} \leq 0.5$ . A suitable spectral evaluation is presented in figure 4.41 for  $\frac{x}{L} = 0.25$ ; compared to the model-in-isolation, spectra for the point of interest is highly random in nature with no clear peak present. Spectral density associated with shedding is considerably weaker, thus the absence of any clear oscillating phenomena at the point of interest may be attributed, in part, to weaker oscillations about the base: oscillations over the upper base were shown earlier to bleed into the backlight separation (Vino 2005, proved similarly for the  $\alpha_c$  model), the merging of the upper horseshoe vortex was similarly shown to cause oscillations in the dominant axial vortices off-body, affecting the vortex sufficiently upstream for the downstream half of the backlight side edges to present with sympathetic oscillations (figure 3.24b, page 127). The portion of the backlight surface so bounded - in which lies the point of interest - typically exhibits weak periodicity (figure 3.27, page 130).

A further contributor concerns the diminished influence of potentially weaker axial vortices. This slightly weaker axial vortex is broadly consistent with greater velocity fluctuations in the forebody projection discussed in section 4.8.2. Figure 4.42 (presenting  $C_P$  across first row of pressure taps below the backlight/top edge) suggests for the trailing model in the wake of a post-critical model, backlight pressures are generally higher in the range  $0.125 \leq \frac{x}{L} \leq 0.5$ , with the difference greatest at the backlight edge. This in turn suggests a weaker axial vortex formed from the relevant separating shear layer.

As the base shedding is weakened, the vortex also experiences weakened periodicity, captured in figure 4.43 which contrasts spectra along the backlight edge, upper backlight and base/bottom/centreline coincident for  $\frac{x}{L} = 0.25$  and  $\frac{x}{L} = 1$ . Scaled identically, the backlight edge is considerably more unsteady at the closer spacing over the upstream half and less likely to be influenced by a considerably weaker shedding peak at  $St = 0.35$  (that associated with the upper base vortex is barely visible above the noise floor). Conversely at  $\frac{x}{L} = 1$ , the energy associated with the base shedding - and that with the out-of-phase upper vortex - dominates spectral energies associated with axial vortex formation, invoking periodicity in proximity to the base.

## 4.9 Conclusions

Two-model platoons led by either pre-critical ( $\alpha = 25^\circ$ ) and post-critical ( $\alpha = 35^\circ$ ) models yield unique, three-dimensional gap flow structures, however maximum drag force characteristics for either model in either platoon are similar.

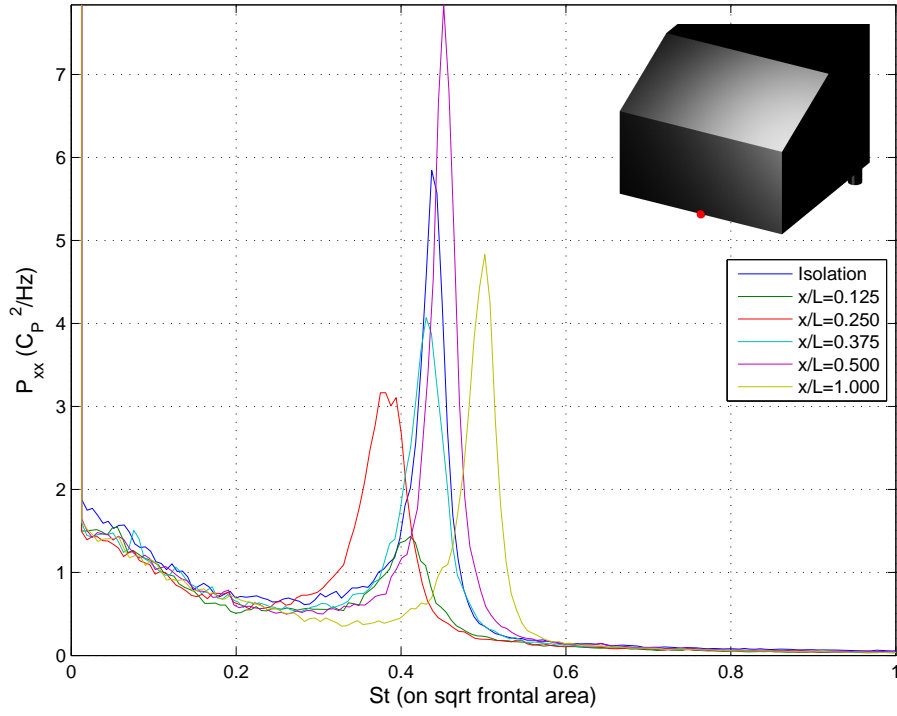
Trailing model drag force is always increased in the range  $0.125 \leq \frac{x}{L} \leq 1$ , as is leading model drag always decreased. The drag force of both models returns to isolation values in either platoon by  $\frac{x}{L} = 2$  (having returned to model-in-isolation values within error by  $\frac{x}{L} = 1.5$ ). Maximum trailing

model drag force occurs at spacing consistent with minimum leading model drag force, observed at  $\frac{x}{L} = 0.25$  for the pre-critically led platoon and  $\frac{x}{L} = 0.375$  for the post-critically led platoon, however the magnitude of the drag force trends are unique in either case pending the nature of gap flows. A net platoon drag reduction is always achieved. The overriding flow mechanisms involved are increased leading model base pressure and increased trailing model forebody pressures.

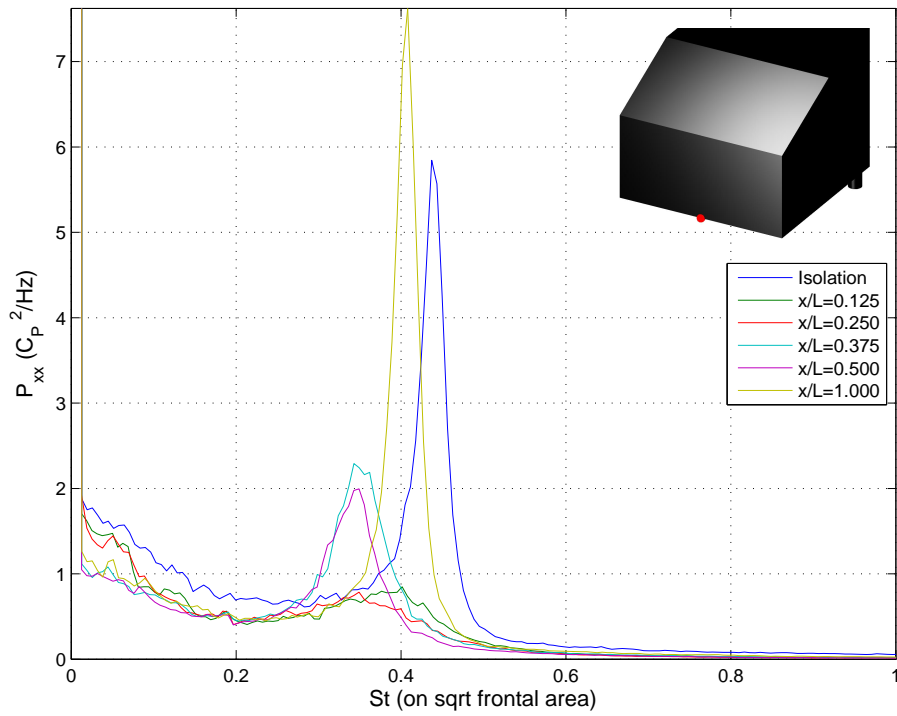
Whilst pre-critical leading model base vortices are distorted downwards ( $-z$ ) at closest spacing (essentially limiting sympathetic oscillations of the dominant axial vortices by base shedding flows), all key model-in-isolation spectral behaviours are essentially preserved for leading and trailing models. The presence of the trailing model at close spacing gives rise to modified leading model base shedding behaviours consistent with feedback along the base/backlight edge separating shear layer as discussed in reviewed literature.

Mean flows about the (always pre-critical) trailing model afterbody are consistent with model-in-isolation behaviours regardless of spacing or leading model geometry (thus regardless of gap flows). A slight weakening of the dominant “C-pillar” axial vortices is observed when led by a post-critical model.

The spectral characteristics of gap flows are shown to affect base oscillations about the trailing model, being sympathetic to those observed at the base of the leading model. The ability of the relevant trailing model base flows to oscillate the dominant “C-pillar” axial vortices is consequently compromised.



(a) In wake of  $\alpha = 25^\circ$  model



(b) In wake of  $\alpha = 35^\circ$  model

Figure 4.38: Spectra at base/bottom/centreline coincident for second model ( $\alpha = 25^\circ$ ) at various spacing

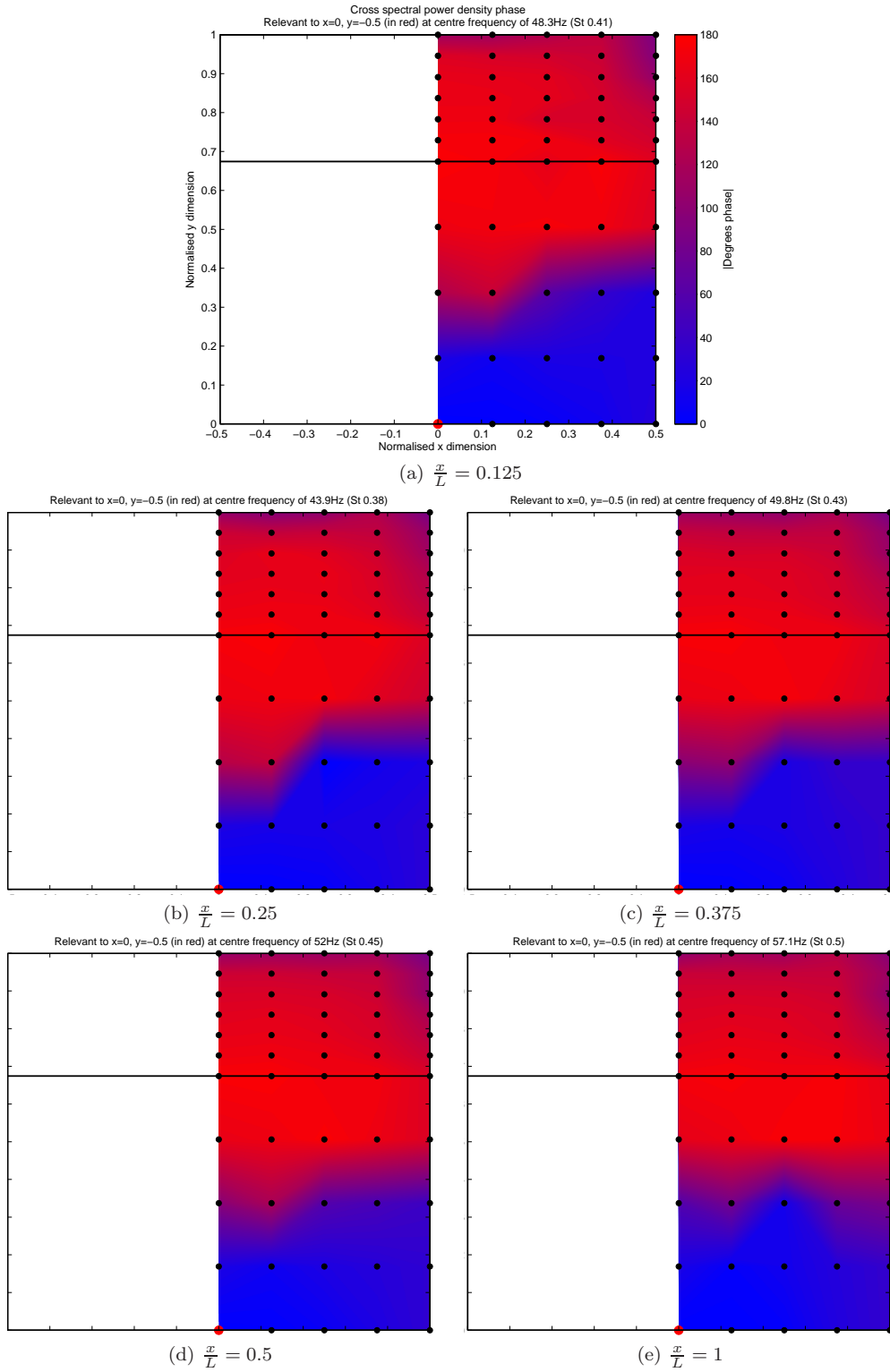


Figure 4.39: Phase plots of model afterbody for  $\alpha = 25^\circ$  model in wake of  $\alpha = 25^\circ$  model relative to base/bottom/centreline coincident at various spacing

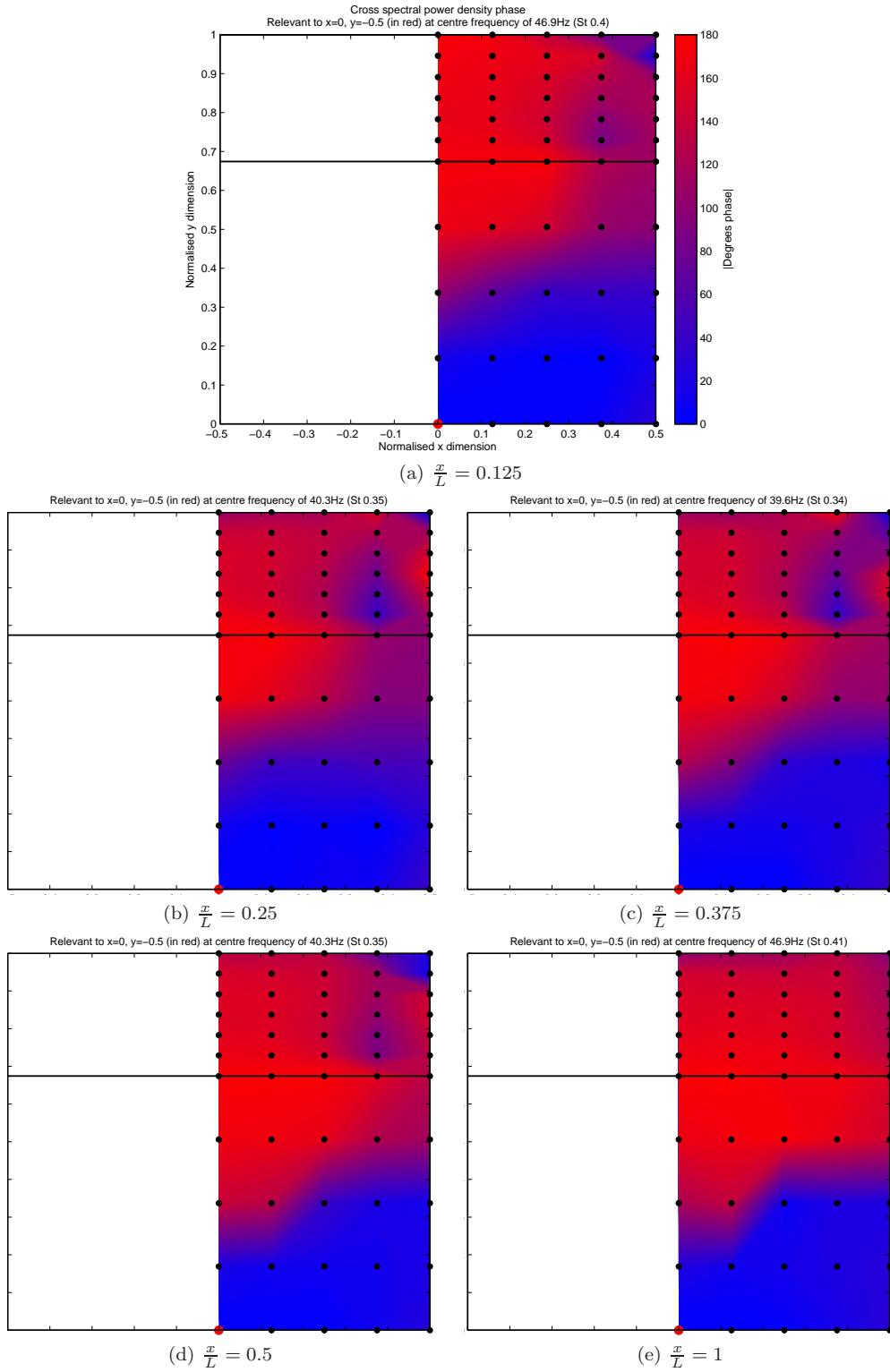
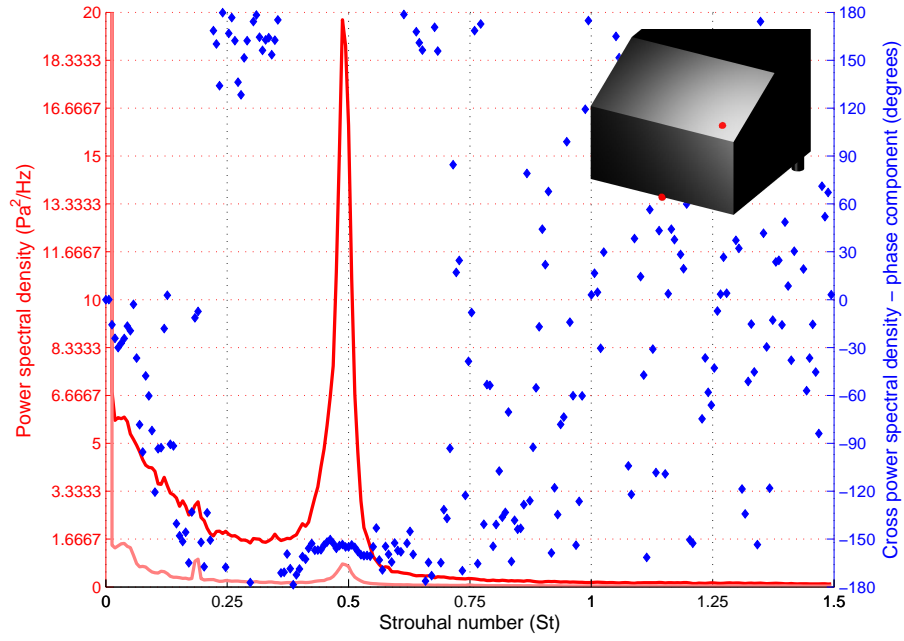


Figure 4.40: Phase plots of model afterbody for  $\alpha = 25^\circ$  model in wake of  $\alpha = 35^\circ$  model relative to base/bottom/centreline coincident at various spacing





(a) Model-in-isolation

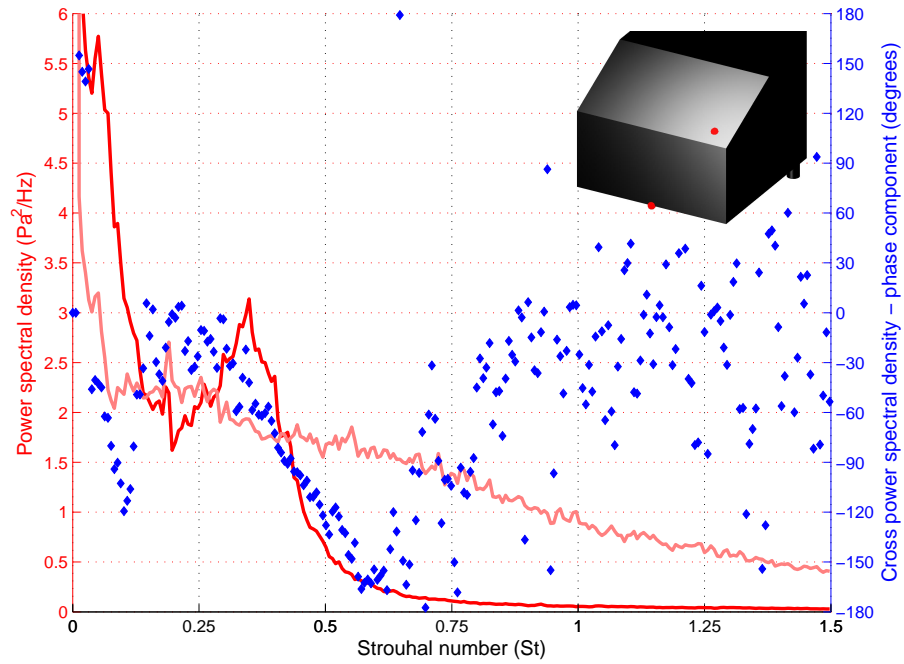
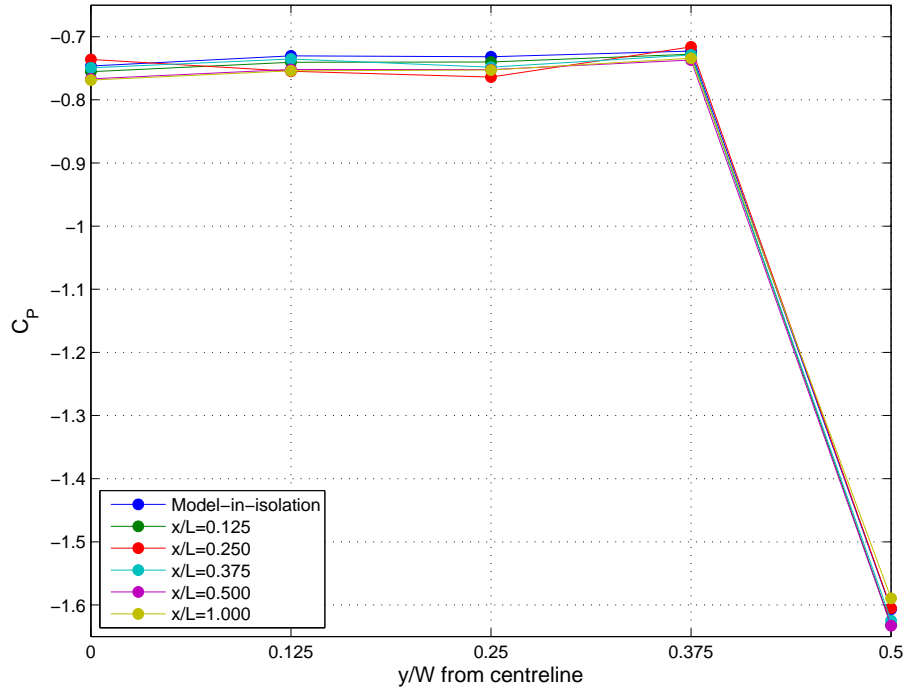
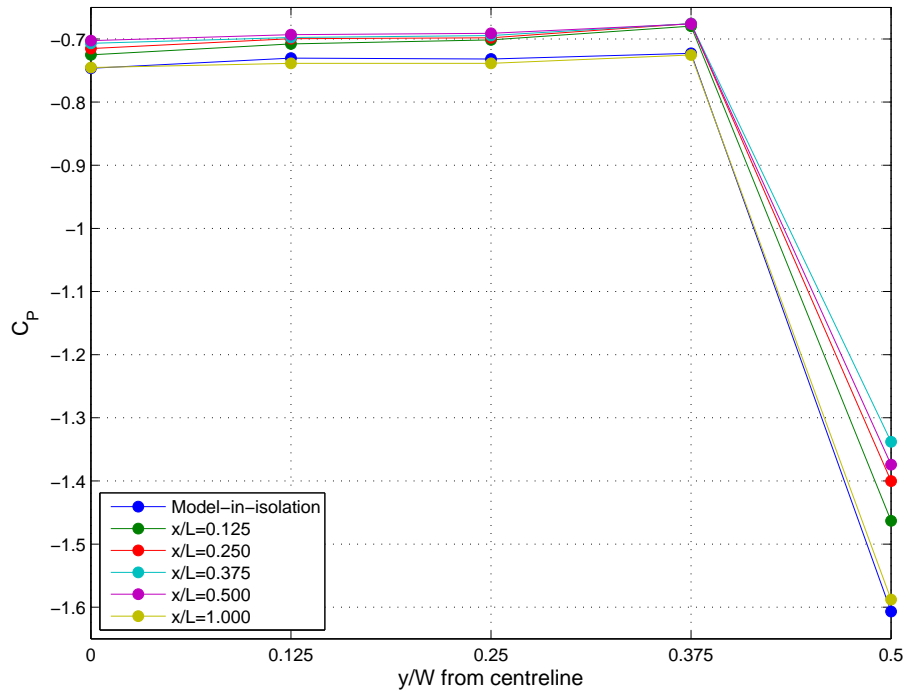
(b) Model in wake of  $\alpha = 35^\circ$  model at  $\frac{x}{L} = 0.375$  spacing

Figure 4.41: PSD of base/bottom/centreline coincident and  $\frac{y}{W} = 0.375$ ,  $\frac{z}{H} = 0.729$  surface pressure taps overlaid with cross spectral phase for  $\alpha = 25^\circ$  model in wake of  $\alpha = 35^\circ$  model at  $\frac{x}{L} = 0.25$  spacing compared against model-in-isolation

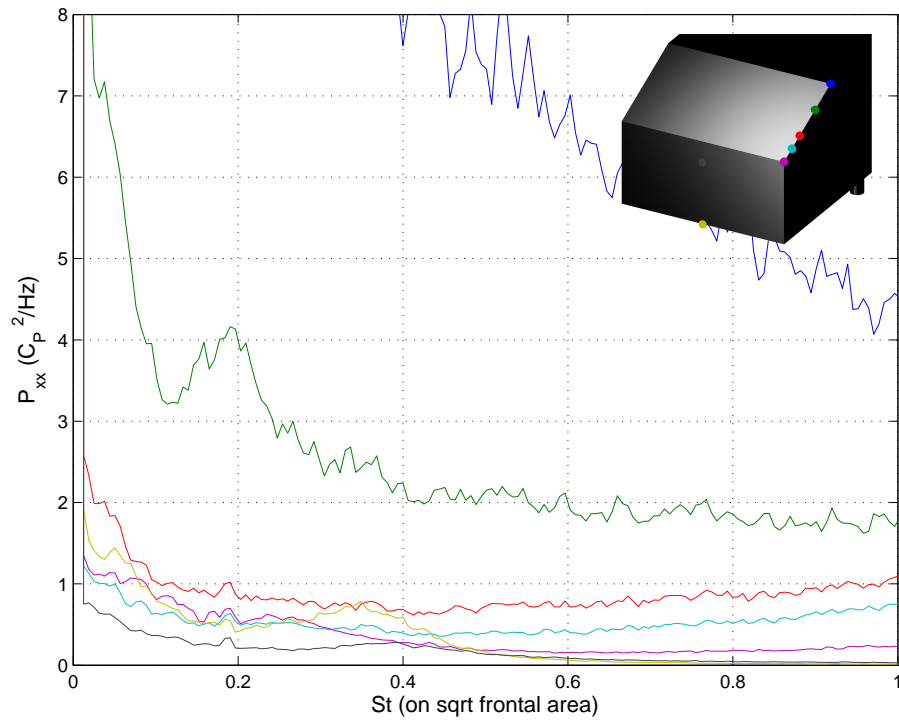


(a) In wake of pre-critical model

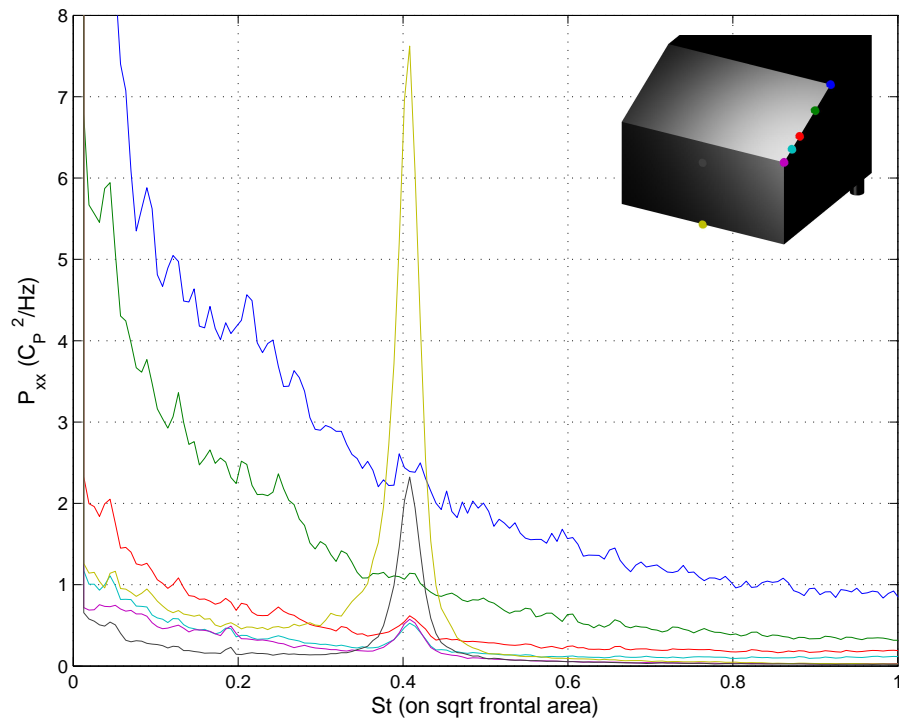


(b) In wake of post-critical model

Figure 4.42:  $C_P$  at  $\frac{z}{H} = 0.946$  for trailing model in two-model platoon



(a)  $\frac{x}{L} = 0.25$



(b)  $\frac{x}{L} = 1$

Figure 4.43: Comparative base and backlight edge spectra for trailing model in wake of  $\alpha = 35^\circ$  model

## Chapter 5

# Conclusions and recommendations

### 5.1 Conclusions

A detailed investigation of aerodynamic platooning for ground vehicle pre and post-critically led fastback platoons was undertaken using  $\alpha = 25^\circ$  and  $\alpha = 35^\circ$  Ahmed model.

The core objectives of the research concerned:

- An exploration of differences in body force coefficient trends for members of a two-model fastback platoon as a function of pre or post-critical leading model fastback geometry
- (As a function of the above) to explore platoon aerodynamic performance as a function of gap spacing

The Ahmed Model was chosen as a suitable experimental model, being able to recreate key features of pre and post-critical fastback geometries. A two-model platoon consisting of trailing a pre-critical ( $\alpha = 25^\circ$  backlight) and either pre or post-critical ( $\alpha = 35^\circ$  backlight) leading model was utilised to examine platoon phenomena.

Investigations of the above were preceded by an experimental deconstruction of salient afterbody flow phenomena for the models-in-isolation, and abetted by both mean and dynamic acquisition methods allowing elucidation of relevant bluff-body flow phenomena pertinent to the force trends observed.

### 5.1.1 Model-in-isolation performance

All salient features of the Ahmed model for  $\alpha = 25^\circ$  and  $\alpha = 35^\circ$  configurations were replicated in the RMIT IWT, despite a higher level of freestream turbulence and a moderate freestream angularity relative to contemporary facilities utilised in reference works.

$Re$  stability was reached at  $Re = 1.8 \times 10^6$  (on model length). Characteristic drag force trends were realised across five unique afterbody configurations, with differences in drag to reference data after Ahmed et al. (1984) accounted for by differences in test conditions.

Qualitative and qualitative data corroborated observations in literature. Of particular interest, separations over the base and backlight of the pre-critical model were shown to be unique flow phenomena influencing each other weakly in an oscillating manner, with the spectral characteristics of the entire backlight and base surface dominated by regions oscillating out-of-phase. The post-critical model featured bulk, quasi-two-dimensional separation of the entire afterbody about the perimeter edges with comparatively weak periodicity observed in separating shear layers. A weaker recirculation of flows from upper and lower shear layers gave rise to unsteady impingement on the base surface. Some comparatively weak periodicity was observed, presenting with clear phase relations at  $St = 0.28$ . Shear layers rolled up off-body to form a unique downwash-type far wake.

### 5.1.2 Platoon performance

Significant variations in drag force were observed in two-model platoons for both leading model geometric configurations.

Spacing range was limited to an eighth model length and did not exceed two model lengths ( $0.125 \leq \frac{x}{L} \leq 1$ ). Literature for relevant platoon control systems architecture indicated smaller spacing to be unfeasible given safety concerns. Contrary to related contemporary studies exploring platooning for aerodynamic benefit, drag force results (once corrected for all relevant test effects) for two-model fastback platoons indicated that both leading and trailing model drag force returned to model-in-isolation values by  $\frac{x}{L} = 2$  spacing. This observation was corroborated by qualitative surface shear and quantitative surface pressure data for the leading and trailing model afterbody and the trailing model forebody.

In both cases the trailing model exhibited a rise in drag force above model-in-isolation values, whilst the leading model exhibited a drag reduction. Net platoon drag was lower than for model-in-isolation values. Two distinct gap flow phenomena “regimes” were observed in the intervening spacing examined, based about either leading model geometry.

**5.1.2.1 With leading pre-critical model ( $\alpha = 25^\circ$ )**

For the leading model, a progressive impeding of the leading model base/bottom edge shear layer - given the presence of the trailing model - limited vortex formation in a manner consistent with feedback along the separating shear layer (a theme explored in reviewed literature). Diminished shedding gave rise to a consequent increase in base pressure. The dominant “C-pillar” vortices were formed at lower strength with close gap spacing, yet still impinged on the model backlight. All salient phenomena relevant to the leading model-in-isolation were found on the same model when leading a second model at close proximity. Mean pressure distributions proved similar. The base vortex pair was distorted upstream against the model base at closer spacing, with modified shedding conditions giving rise to decreased shedding periodicity and progressively increasing amplitude with decreasing model spacing. At the closest spacing evaluated, vortex formation length proved exceptionally short, giving rise to high-frequency, high-amplitude oscillations at the key base shedding location and a consequently limited height for the base vortex. Despite this significant distortion and consequent weakening of periodic interaction with upper wake flows, characteristic phase relations over the model surface were retained. A minima in drag force (based on surface pressure data) was observed at  $\frac{x}{L} = 0.125$ .

The trailing model in this configuration inherited a shifted stagnation point relative to the impingement of flows entrained by dominant axial vortices in the leading models wake. The relative drag increase was shown to be a function of model proximity and leading model axial vortex strength. Flow field periodicity in the gap confirmed oscillation in the impinging axial vortices where sufficient spacing existed to allow leading model base shedding and vortex flow to interact. A drag force maxima was observed at  $\frac{x}{L} = 0.25$ .

**5.1.2.2 With leading post-critical model ( $\alpha = 35^\circ$ )**

For  $\frac{x}{L} = 0.125 \leq \frac{x}{L} \leq 0.5$ , impingement of separating shear layers from the leading model gave rise to stagnation regions on the trailing model top and sides inboard of the horizontal surfaces and a net inboard downwash across the forebody surface. The gap was dominated by a counter-rotating transverse vortex pair created by recirculating flows inboard of the upper and lower separating shear layer impingement. The upper vortex, rotating such to yield downwash over the trailing model, dominated the majority of the gap region along the centreline, with the lower vortex distorted outboard. Limited impingement by the lower vortex caused a local distortion upwards and inwards of the local flow field about the trailing model forebody. The net downwash thus flowed under the trailing model in a pronounced manner about the centreline.

Unsteadiness in the flow field upstream of the trailing models was concerned with the reversion of flows within the downwash region back towards the leading models base, and was thus concentrated in the centre of the trailing model forebody projection.

The impingement of these vortices occurred on the leading model base in a relatively steady

manner, bar at closest spacing where the presence of the trailing model impeded this possibility, and a significantly turbulent upwash impinging on the leading model backlight giving rise to unique surface shear phenomena in this instance. Leading model backlight flows proved otherwise quasi-two-dimensional as per the model-in-isolation.

Behaviour consistent with feedback along the leading model afterbody upper and lower separating shear layers impeded relevant vortex formation as a function of spacing. Unique flow phenomena over the leading model backlight at  $\frac{x}{L} = 0.125$  yielded exceptionally low backlight pressure for this configuration. A minima in leading model drag force was observed between  $0.25 \leq \frac{x}{L} \leq 0.375$ , however the net effect of counter-rotating transverse vortices in the gap (the characteristic gap phenomena) served to maintain relatively stable leading model drag force to  $\frac{x}{L} = 0.5$  spacing.

As the effect of the transverse gap vortices diminished with increased spacing, the relative strength and curvatures of leading model separating shear layers gave rise to characteristic model-in-isolation type downwash axial vortices in the wake and a more uniform pressure distribution over the leading model forebody. A compound of both modes gave rise to a maxima in trailing model drag force at  $\frac{x}{L} = 0.375$ .

#### 5.1.2.3 Effect on body force coefficients

Despite significant differences in gap flow phenomena, force coefficients were not found to vary significantly pending leading model geometric configuration. Neither pre nor post-critical fast-back geometries as evaluated were observed to offer significant advantages in platoon aerodynamic performance in the range  $0.125 \leq \frac{x}{L} \leq 2$ .

#### 5.1.2.4 Effect on trailing model afterbody performance

Mean pressures for the trailing model afterbody were little changed in spite of significant changes in gap behaviour.

It was demonstrated that oscillating leading model base phenomena, convected under the model, was able to significantly influence the spectral performance of base shedding phenomena about the trailing model base, albeit not in a sufficiently significant manner to disrupt characteristic afterbody surface phase relations.

## 5.2 Recommendations

The following recommendations are suggested for further research based on observations and conclusions arising from the research undertaken.

- *Modified ground plane conditions:* base shedding was demonstrated to be an important determinant of mean flows and instrumental in characterising the spectral characteristics over both backlight and base surfaces. The research conducted evaluated a sole ground clearance over a stationary ground plane. Whilst salient phenomena were proved able to be evaluated for this ground plane condition employed, a useful extension of the work may involve experimentation with a moving ground plane to more appropriately simulate underbody momentum typical of a practical road vehicle.
- *Relevant forebody geometries:* the gap phenomena observed - particularly impingement phenomena on the trailing model forebody giving rise to significant increases in drag force - would likely be muted were forebody geometry representative of a practical passenger vehicle forebody applied. Whilst downwash-based impingement phenomena would likely be little changed, the scope for transverse recirculation in the gap (observed for the post-critically led platoon for  $0.125 \leq \frac{x}{L} \leq 0.5$  - a phenomena afforded by, and bounded by an upper impingement on a near-normal-to-flow surface) may be diminished. Scope for a unique - and potentially more advantageous regarding trailing model drag - gap flow regime may be afforded, giving rise to new opportunities for fastback model arrangements in-platoon. The influence of the “A-pillar” vortex is similarly potentially significant (being able to influence afterbody flows, and in turn being able to be influenced by upstream turbulence).
- *Simulation of salient freestream conditions:* the work presented was undertaken in a relatively high-turbulence freestream (relative to those employed in reference works for the model used throughout), however more recent literature reviewed concluded these freestream conditions to be of useful relevance to the practical ground vehicle domain. A salient addition to the simulation of the freestream conditions would include vehicle yaw, giving rise to asymmetric distortion of gap flows and modified upstream shedding conditions. Given the low mean speeds alluded to in platooning control system literature (for safety and traffic throughput concerns), likely wind effects would render the inclusion of yaw effects in future related studies as a highly relevant concern. The propensity of yawed flows to alter the gap flow field and affect mean forces and stability parameters may similarly bear relevance to contemporary research into misaligned platoons, which share similar concerns.
- *Consideration of other aspects of vehicle systems:* the variation of gap spacing was observed to modify shedding conditions in both frequency and amplitude about leading and trailing model afterbody separating shear layers, however secondary modes arising from excitation of the models were not explored. Compound spectral phenomena may alter the flow field further and affect ride and aeroacoustic noise parameters, which are of significant practical relevance to modern automotive aerodynamic performance.

The impact on a vehicle cooling system of travelling in a velocity deficit for prolonged time periods (consistent with highway driving on “ITS-enabled” road networks) - particularly at close proximity - requires further consideration with respect to the nature of upstream vehicle geometries.



## Appendix A

# The RMIT University Industrial Wind Tunnel

A general introduction and summary of the Industrial Wind Tunnel (IWT) is provided in section 2.2.1 (page 61). The purpose of this appendix is to detail (and where necessary, deconstruct) various flow phenomena characteristic of the IWT and to quantify their relevance to the experiments completed.

### A.1 Mean flow properties

Flow velocity and angularity variations in the IWT test section are difficult to quantify exactly (the former particularly), as:

- The traversing mechanism is not aligned to any geometric plane of reference, allowing some yaw error in mounting. It is installed on one side ( $-y$ ) of the tunnel and has no fairing to reduce bluff elements of the frame; the effect of the traverse's presence on freestream conditions is difficult to quantify. Furthermore as the  $y$ -axis arm and telescopic extension are cantilevered about the main frame, some deflection about it under aerodynamic load is anticipated<sup>1</sup>.
- The telescopic arm of the traverse is of round section, and offers no reference edges for alignment. A degree of rotation is offered to any mounted hardware, restrained only by friction.
- The devices used to obtain angular measurements (the Cobra probe and ECA probe) possess

---

<sup>1</sup>As the arm extends outwards, the magnitude of the the deflection is further anticipated to change.

a cylindrical body with no on-body reference markings or edges for alignment. A degree of rotation is thus offered about the probe's length.

- No reference data exists defining flow angularity in the IWT to calibrate such devices against.

A "best case" approach involved:

- Acquiring a plane of data.
- Acquiring a "*calibration reference*" point in-plane located centrally along the test section's width and height with the test section otherwise empty.
- Applying Eulerian transformations to  $U$ ,  $V$  and  $W$  flow components to reset pitch and yaw to zero, and to then apply the same degree of correction to all other points in-plane, rendering them effectively rotated against an assumed zero-angularity condition mid-plane.

A further test was conducted to account for variances in flow angularity along the test section's length at the calibration reference. The traverse was moved along the length of test section used ( $2283 \leq x \leq 4632\text{mm}$ , or  $3L \leq x \leq 6L$ ) at  $783\text{mm}$  ( $L$ ) increments without changing the installed condition of the probe<sup>2</sup>. The maximum pitch/yaw variance point-to-point observed was within the angular accuracy of the probes. It is thus not corrected for.

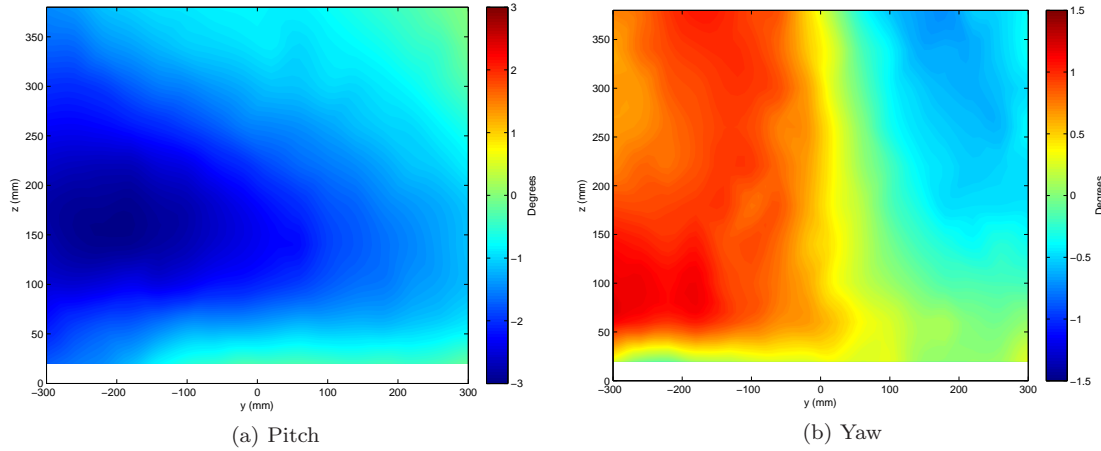


Figure A.1: Angularity in IWT at  $x = 2283\text{mm}$

Figure A.1 indicates pitch and yaw at  $x = 2283\text{mm}$ , though expectedly trends towards  $0^\circ$  pitch and yaw at the calibration point are observed. Though a similar trend is shown by Vino (2005) for the same facility and instrumentation, it is difficult to discern the yaw trend shown from cantilevering of the traverse assembly. A better approach examines net velocity variation in the IWT. A sheared flow in the test section has been characteristic of the IWT since it's inception;

<sup>2</sup> $\pm 1^\circ$  Mousley (2006).

causes cited by various authors persisting in the current configuration include extensive separation off the fan nacelle<sup>3</sup> and off the inner wall of the fan diffuser section (Quirillo 1999, Watkins 1984) and separation along the outer wall of the main diffuser, giving rise to a separation around turn one owing to corner geometry (Quirillo 1999): these all rank as important considerations in determining test section flow quality (Barlow et al. 1999). The net effects of these factors were observed most prominently upstream in the test section (Gadd<sup>4</sup>).

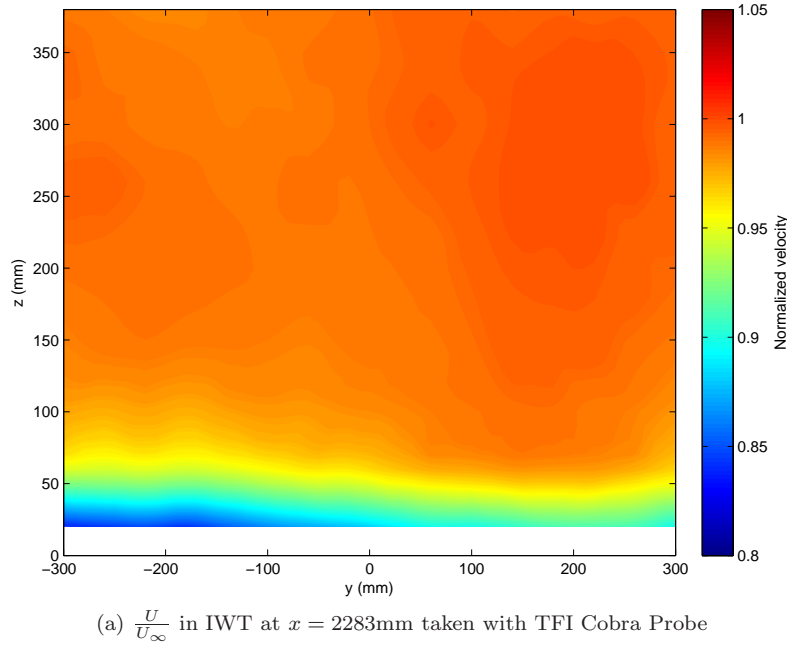


Figure A.2: Velocity distribution in transverse planes of IWT test section

Whilst figure A.2 does not provide for a direct measure of angularity, synthesis of the flow phenomena involved supports the practical experience in testing wherein a net cross-plane yawing of model flow phenomena was experienced.

A qualitative observation was made using a tuft grid revealing observable yaw towards the outside wall. The author furthermore noted misalignment in installation of the inner turning vanes of turn four<sup>5</sup>; this - and poor velocity distribution prior to turn three - are characteristic causes of test section flow angularity (Barlow et al. 1999).

<sup>3</sup>The nacelle wake in fact does not close prior to upstream turning vanes (Quirillo 1999).

<sup>4</sup>In Quirillo (1999).

<sup>5</sup>The reader should appreciate that the facility was moved from its original location to the current installation in 1996; some misalignment of various sections ensued.

### A.1.1 Yaw alignment

A second approach involved creating a model mount with a limited yaw capacity (shown in figure A.3). A scan of model drag force across various angles of yaw achieved lowest drag at  $0.55^\circ$  yaw at  $\alpha_c$ . As it would be impractical to align models as such in platooned configuration (possibly further compounded by a likely variance in yaw along the length of the test section), models are aligned with the test section's geometric centreline and intrinsic yaw is accepted in test results.

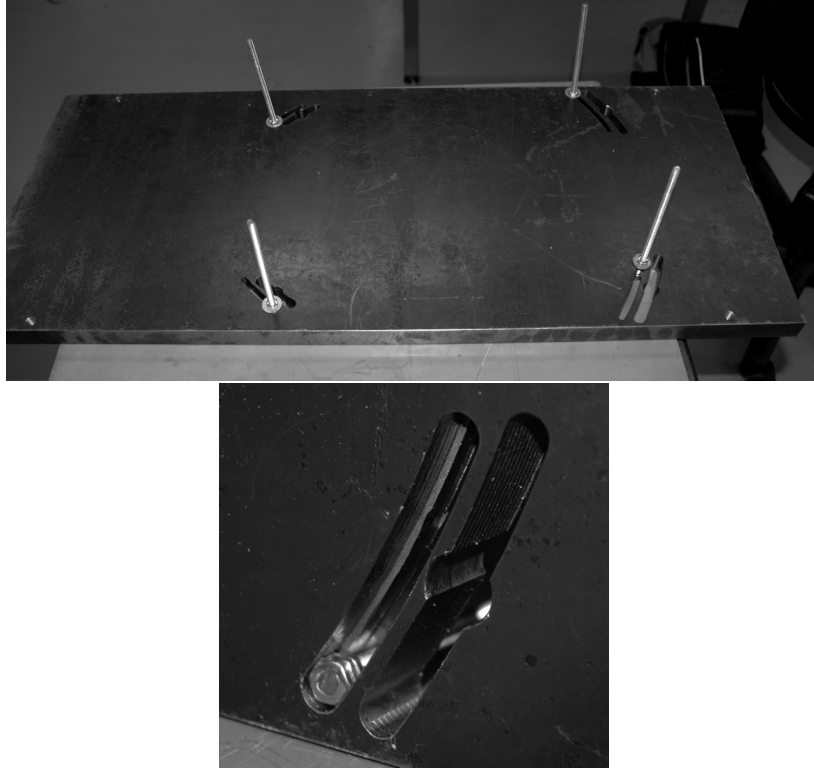


Figure A.3: Ahmed model support base milled to support model yaw

### A.1.2 Effect on Ahmed model wakes

Ahmed et al. (1984) originally proposed that the upper of the horseshoe vortices operating over the base region in the pre-critical case had legs extending in the axial direction, such that they merged with the axial “C-pillar” vortices. This was further visualised at low  $Re$  by Okada (2006) and in greater detail by Krajnović and Davidson (2005), who proposed in their LES study of the (in their study of the  $\alpha = 25^\circ$  case) that this merger occurred downstream of  $\frac{x}{L} = 0.15$  as per figure A.4<sup>6</sup>.

---

<sup>6</sup>This study normalised distance beyond the trailing edge by model height. It is converted to length normalisation for consistency here.

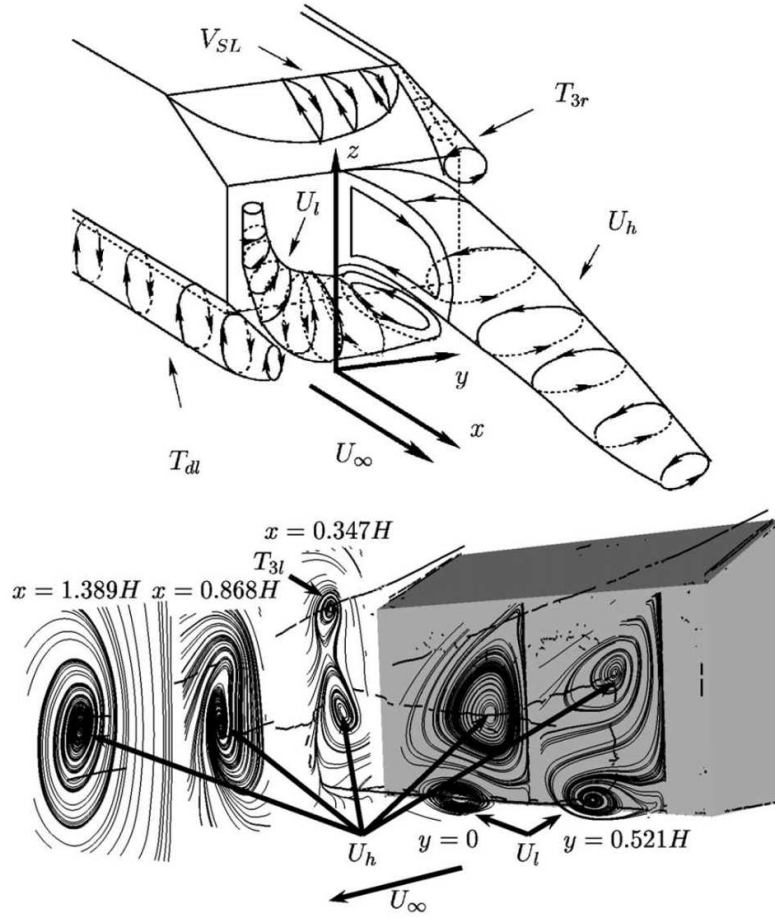


Figure A.4: Afterbody near-wake flows in  $\alpha = 25^\circ$  by Krajnović and Davidson (2005)

Therefore an effect of flow angularity in this region - by changing relative side separation shear layer strengths, and thus the axial vortices formed with serve to draw the legs of  $U_h$  (figure A.4) in the axial direction - is to create an asymmetry at along the centreline by means of relative pressure differences between the axial C-pillar vortices. A net flow towards the stronger of these vortices (inner test section wall side,  $-y$ ) is anticipated towards the rear of separated flows about the base. This is visible in transverse plots for the  $\alpha = 25^\circ$  model in the near wake (figure 3.13, page 110) and validated for the transverse flow component along the centreline (figure A.5a).

It is not unreasonable to suggest a similar phenomenon should occur in the  $\alpha = 35^\circ$  case given the relative strength of the C-pillar vortex pair and their influence on a comparatively weaker, larger upper horseshoe vortex defining a larger separated region (vis-à-vis the  $\alpha = 25^\circ$  case). A weaker transverse net flow spread over a larger region, further downstream with respect to the size of the separated region is anticipated, and duly captured in centreline plane data (figure A.5b).

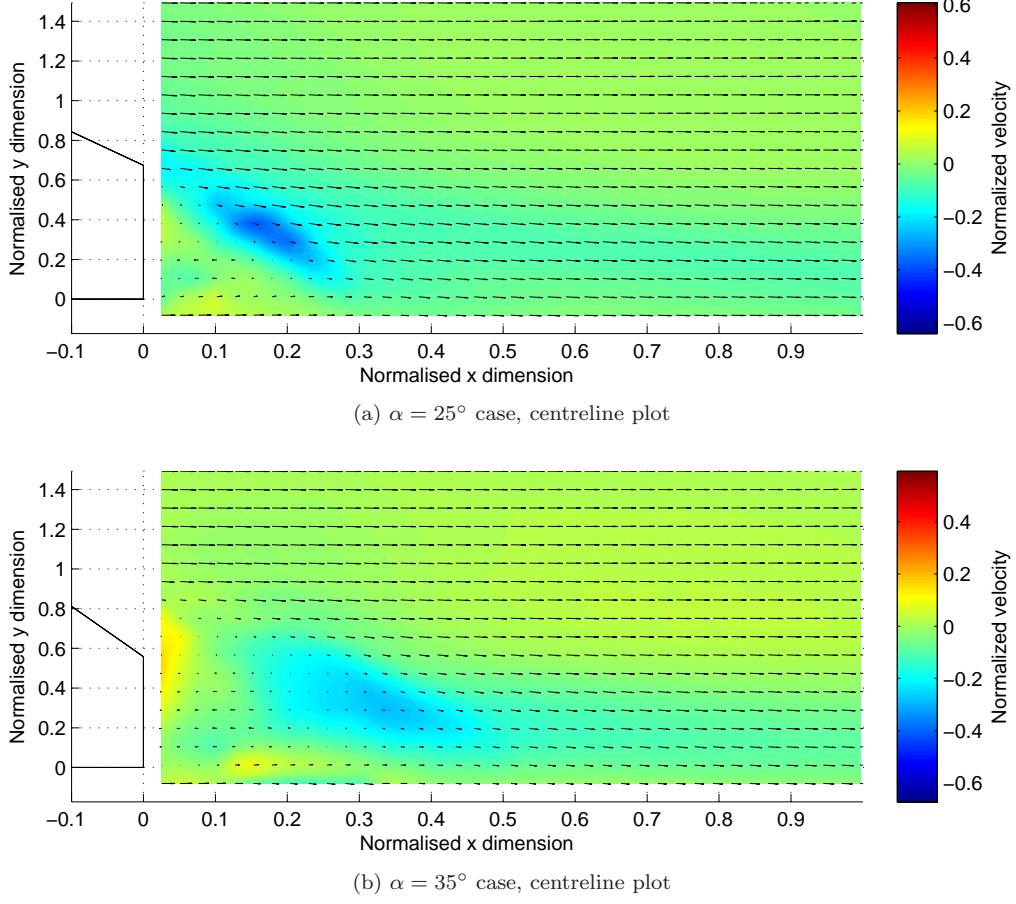


Figure A.5: Normalised transverse component of velocity  $\frac{V}{U_\infty}$  for  $\alpha = 25^\circ$  and  $\alpha = 35^\circ$  cases

## A.2 Boundary layer properties

As the IWT is not equipped with any form of boundary layer control and as experiments are completed in ground proximity (with the intention of simulating a vehicle against an effectively moving ground plane), it was deemed important to characterise the IWT's boundary layer properties. Measurements presented in figure A.6 were taken with a Cobra probe at 2kHz over 10 seconds at 2mm intervals; velocity of 0m/s at the floor is assumed (law of the wall).

The displacement thickness - a measure of the deflection of a streamline from the ground plane given the presence of the boundary layer (thus a particularly important parameter in characterising the effect of a ground plane on a bluff body in near proximity) - is defined as such:

$$\delta^* = \int_0^\infty \left(1 - \frac{u}{U_\infty}\right) dz \quad (\text{A.1})$$

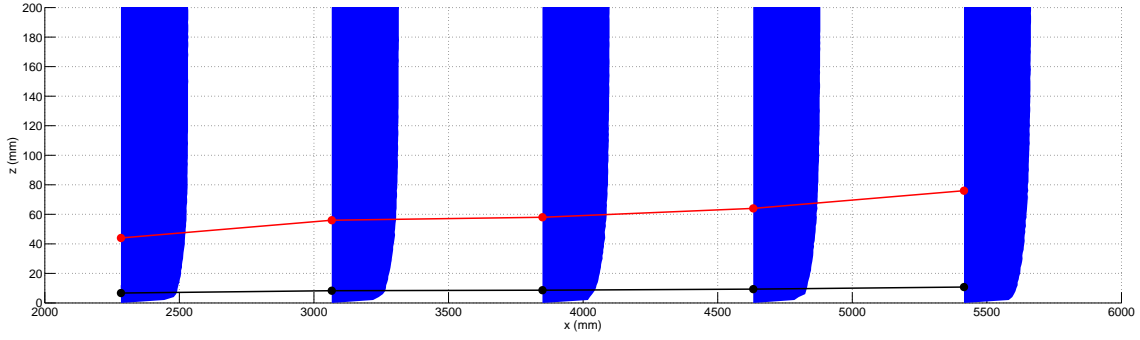


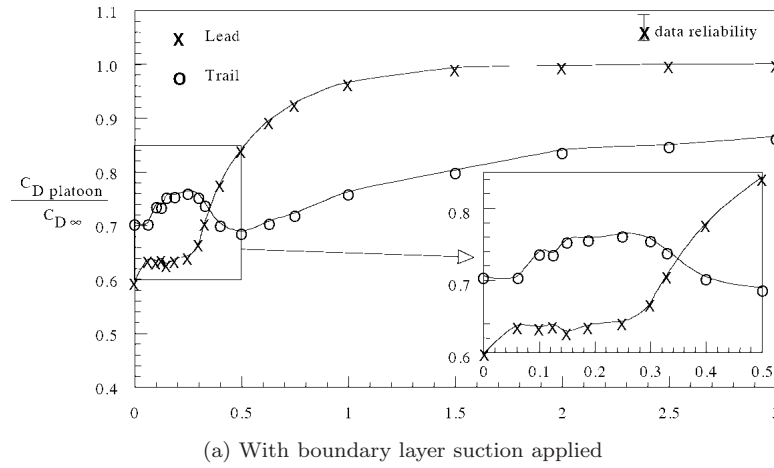
Figure A.6: Comparison of 95% boundary layer profile, thickness and displacement thickness along test section length

In the range  $2283 \leq x \leq 5415\text{mm}$ , the 95% boundary layer thickness ( $\delta$ , in red) increased from 44mm to 76mm; the corresponding displacement thickness ( $\delta^*$ , in black) increased from 6.7mm to 10.8mm. Hucho and Sovran<sup>7</sup> state that use of a fixed ground plane to simulate road conditions in testing is only possible where  $\delta^*$  is a tenth of the test article's ground clearance (Wing 1981) (contemporary 1970's data places typical  $\delta^*$  at 0.085 of ground clearance (Hucho et al. 1975)), a condition clearly not met here (with ground clearance of 37.5mm). The process of raising ground clearance to accommodate for displacement thickness effects (Beauvais et al. 1968) was not considered, as not only does suitable reference data for an Ahmed model on a moving ground not exist, but the results presented in section 3 (page 88) indicated that the salient features of the form were duly captured in the installed configuration (including those dependent on underbody flows). Further considerations exist relative to the experiments at hand: the amount raised would need change depending on position in the tunnel and would be further complicated by effects of an upstream model: Hucho et al indicate the presence of a vehicle to severely reduce the boundary layer between the ground plane and underbody (Hucho et al. 1975).

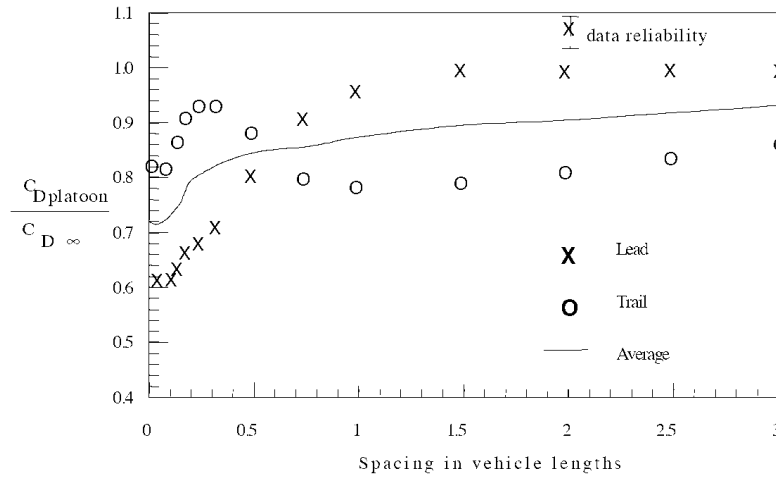
A qualitative observation by Zabat et al. (1993) in considering boundary layer implications for scale model platooning experiments reiterates the intention of the experiment being to examine relative changes between platoon configurations, which are less sensitive to ground plane conditions than absolute  $C_D$  values. Figure A.7 evidences as much; the plot without boundary layer control yields broadly similar and continuous trends; expectedly the second model's drag values are more affected in an individual sense as the suction applied effects a greater change in ground plane conditions where the boundary layer would have been greater.

It should further be appreciated that bar implementation of a moving ground plane - being impractical to implement within the scope of these works - many other methods of reducing displacement thickness (tangential blowing, boundary layer suction, etc) effect changes at the boundary layer not representative of the road environment, the complications of which in the low ground-clearance environment experienced herein are not examined.

<sup>7</sup>In Zabat et al. (1993).



(a) With boundary layer suction applied



(b) Without boundary layer suction applied

Figure A.7: Effects of boundary layer suction on two-model platoon after Zabat et al (in Chen et al. (1997))

### A.3 Static pressure distribution

In a return tunnel static pressure is typically least throughout the test section, and constant throughout the length of the test section used in experimentation. The static pressure distribution along the length of the IWT (taken with a Pitot-static tube and inclined manometer) is shown in figure A.8. Originally the IWT was designed with a perforated roof intended to promote atmospheric static pressure conditions throughout (Watkins 1984). A drop in static pressure is anticipated given constant cross sectional area along the test section with consequent increasing boundary layer growth (Barlow et al. 1999), and is illustrated in figure A.8.

Figure A.8 also displays expected effects of proximity to the settling chamber at the test section leading edge (i.e. raised static pressure), and that static pressure remains broadly constant



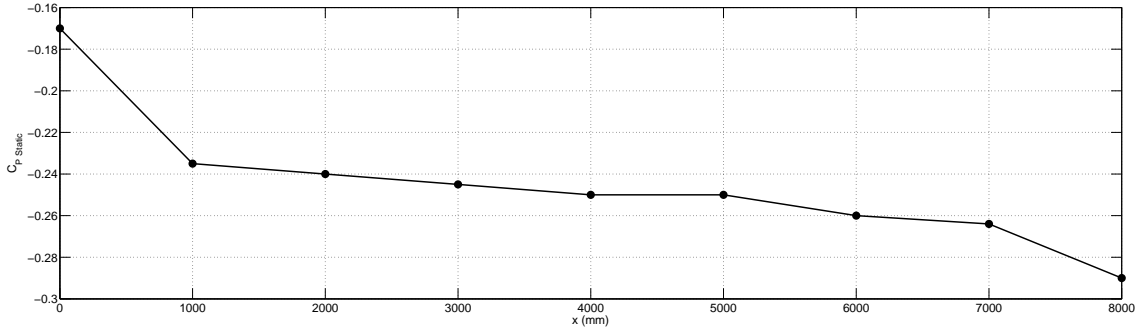


Figure A.8:  $C_{P\text{Static}}$  variation along test section

throughout the length of the test section used ( $2283 \leq x \leq 5415\text{mm}$ , within  $< 0.03C_P$ ). Buoyancy corrections are therefore not considered.

## A.4 Freestream velocity measurement in the IWT

Velocity measurement in the RMIT IWT is achieved primarily via a Pitot tube located in the upper-outside corner of the test section. Its opening is located coincident to the leading edge plane of the test section, a location offering static pressure (ideally) equal to that throughout the test section (Nijhof and Wickern 2003) however the total pressure variances observed in section A.1 and the (typically) decreasing size of the jet's cross-section along the test section's length contributed to measurements obtained slightly underestimating tunnel velocity. Reference tests were completed and corrections made in post-processing.

### A.4.1 MKS Baratron<sup>TM</sup> system

An MKS Baratron<sup>TM</sup> system is used to acquire relevant dynamic pressure data. Static (atmospheric) and total pressures are connected to a MKS Instruments type 398 high-accuracy differential pressure transducer<sup>8</sup>, featuring a temperature-controlled aluminium housing intended to negate the effects of changeable ambient temperatures on the sensor's zero point accuracy and repeatability. Outside of the temperature-controlled environment there is an "electronics unit" (a PCB) featuring circuitry to control sensor environmental conditions and to provide an analogue ratiometric output (to 10V) proportional to pressure. Full-scale (10mmHg) accuracy is 0.05%, guaranteed in ambient environments to the sensor's conditioning temperature (45°C). Resolution is 1ppm; temperature effects on span and zero are at most less than half the full scale accuracy.

Relevant output signal conditioning and transducer configuration is completed with a MKS Instruments type 270D signal conditioner. This allows selectable instrument response of 165, 4

<sup>8</sup>Functionally identical to the current 698A unit (Pagliarella 2006)

and 0.4Hz. The latter was then used throughout; it should be stressed that the instrument is not used as a dynamic device; though theoretically capable of low-frequency performance, the length of tubing used - some 10m - would yield poor amplitude response even at low frequencies (Bergh and Tijdeman 1965). The conditioned output signal is in turn acquired by the National Instruments E-series data acquisition card.

##### A.4.1.1 MKS Baratron™ system calibration notes

The Baratron™ system allows for zero and span adjustments to be made on the sensor unit. A second zero adjustment facility is provided on the conditioning unit. The sensor electronics unit can also be calibrated for linearity and range.

Necessary equipment to calibrate system span and to calibrate the electronics unit appropriately was not available for the duration of this research<sup>9</sup>. The last calibration date for the system is unknown. It is assumed that all relevant pressure data acquired using the system are thus relative to each other.

The temperature conditioning facility in the sensor head was nonfunctional for the duration of the research work, requiring consideration when collecting set results over variable ambient and tunnel fluid conditions as temperature stability in the sensor head could not be achieved: the manufacturer quotes a minimum four hours temperature stabilisation prior to reliable instrument use (MKS Instruments Inc.). The resulting error was most obvious at zero differential pressure, where errors exceeding 2% of full scale were observed (far exceeding the delivered accuracy of the device). Figure A.9 presents system zero error against test section temperature for all force tests. Whilst not an exacting comparison<sup>10</sup>, a consistent trend is shown commensurate with the expectation of higher error at lower test temperatures. The zero error far exceeds the manufacturer's stipulated 0.05% of full scale.

Whilst possible to continually adjust the zero of the conditioned output, this would also effectively change the range of the instrument. It was therefore decided to simply offset acquired data against the pressure data zero condition. Relative accuracy between thermal conditions is thus afforded.

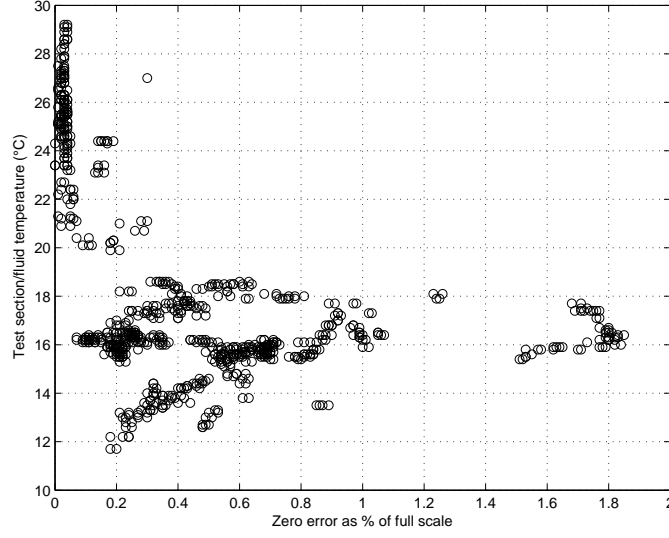
##### A.4.2 System noise

The DC drive of the IWT created a significant current draw during testing (up to 250A DC) on the mains power rail shared with other devices in the IWT, including instrumentation power. A power conditioner is fitted to the test facility, though its effectiveness was unknown. No mains-specific

---

<sup>9</sup>The system is usually supplied with a deadweight pressure test set.

<sup>10</sup>Test section temperature could only be considered in thermal equilibrium at the start of day; once running, work applied to the working fluid created a temperature differential between the balance housing and the working fluid. Scatter is thus present in zero and drift check data relative to temperature.



(a) Zero error as % of full scale

Figure A.9: Baratron<sup>TM</sup> system zero error

lowpass or notch filters were placed on instrumentation DC power stages or output signals. Given the propensity of the Ahmed model to exhibit periodic shedding about the base region, a short investigation was thus conducted to ascertain any possible effect of related noise on test/acquisition equipment.

#### A.4.2.1 Baratron<sup>TM</sup> and barometer

Whilst the MKS Baratron<sup>TM</sup> system was installed (in a common cabinet with the IWT's barometer) with due diligence to manufacturer's procedures regarding appropriate isolation, line noise is clearly observable at 50Hz and harmonics thereof. For a maximum possible sampling frequency of 32kHz, spectral densities significantly above the data acquisition card's noise floor were notable to frequencies exceeding 6kHz.

Similar artifacts can be seen in the barometer data. Figure A.10 compares spectra from Baratron<sup>TM</sup> and barometer sources at various speeds from zero to the test velocity (the data is processed over 173 realisations with bin size of 1.9Hz). As the barometer is not exposed to the freestream it can be assumed that artifacts present in both spectra are not flow artifacts. There is some significant data present in the Baratron<sup>TM</sup> signal at approximately 6kHz; as this is significantly beyond the response of the Baratron<sup>TM</sup> it can be assumed this noise is instrument-specific. As other devices required much of the data acquisition card's aggregate sampling rate, digital filtering of the signal was not possible.

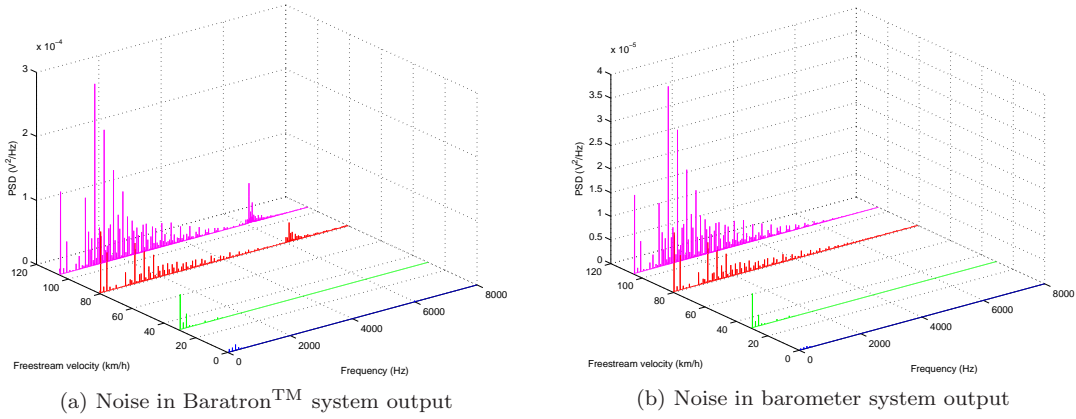


Figure A.10: Comparison of line noise influence

It should be stressed that the noise present concerns practically very low amplitudes; whilst a RMIT IWT employs a DC motor, a line filter is used. Repeated comparisons between acquisition of the Baratron™ signal at lower frequencies (commensurate with those used in experimentation) and again at higher frequencies - capturing the full spectra observed in figure A.10 - revealed a maximum disparity of 0.7%; an acceptably small error<sup>11</sup>.

#### A.4.2.2 Force balances, dynamic pressure probes and surface pressure acquisition systems

Power for these devices is sourced from DC power rails on either the force balance DSP or data acquisition cards. These sources are not only well regulated, but in turn draw their power supply from the power supply of the computer that houses them, which in turn is heavily regulated. The JR3 force balances additionally interface their DSP board via a digital serial protocol; the analogue-to-digital conversion is completed inside the test section (a significant distance from any power sources).

Line noise observed in the Baratron system data was observed to affect expected trends from probe data.

## A.5 Dynamic flow characteristics in the IWT

No obvious spectral peaks in empty-tunnel spectra pertaining to organ pipe resonance, Kelvin-Helmholtz separations of the test-section leading-edge shear layer or otherwise. Figure A.13 shows good agreement with the Kolmogorov law (wherein spectral energy asymptotes to  $n^{-\frac{5}{3}}$ , where

<sup>11</sup>One needs also consider the test section velocity control being essentially open loop against fan speed; in turn, the accuracy any repeatability metric is thus compromised.

$n$  = frequency), indicating the effective decay of turbulent eddies to increasingly higher frequencies as turbulent energy dissipates to heat energy (Burton et al. 2001). Similarly shown are low spectral levels for the axial component of spectral energies, indicative of relatively low  $I_{UU}$ .

### A.5.1 Statistical turbulence characteristics

Plots of turbulence intensity are presented in figure A.11. Whilst significant variation exists in the axial component in proximity of the boundary layer (to a maximum of 8.8%), midplane at  $x = 2283\text{mm}$   $I_{uu} = 1.8\%$ , remaining constant downstream (within the length of test section used) within 0.2%.

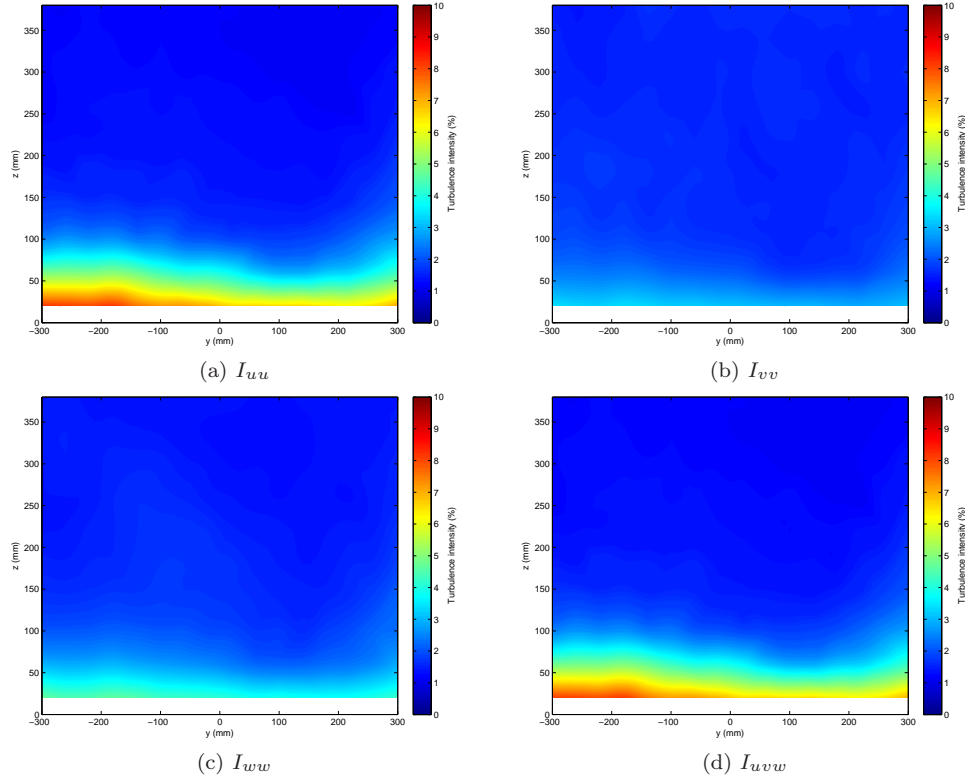


Figure A.11: Turbulence component profiles in IWT at  $x = 2283\text{mm}$

### A.5.2 Low frequency pulsing

A low-frequency, high-amplitude oscillation was also noted in testing. This was previously observed by Quirillo in the IWT's present configuration (acquired crudely from a cadence of acoustic references and a stopwatch); whilst the amplitude of the commensurate acoustic phenomena was qualitatively felt to diminish with improvements to corner one flow, it could not be eliminated

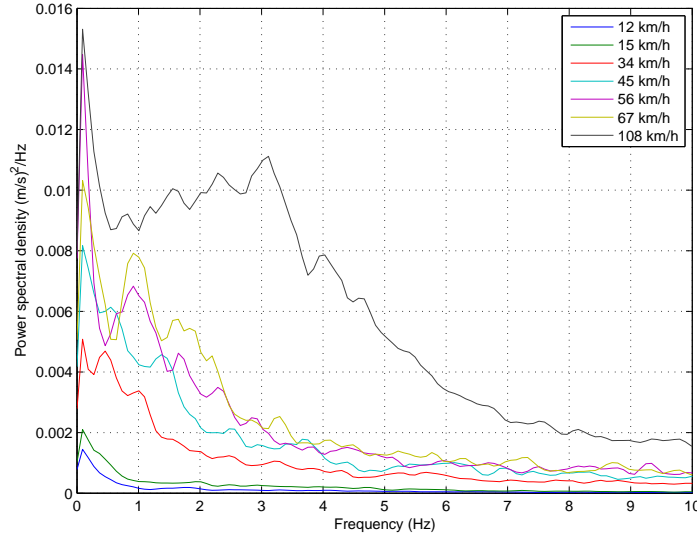


Figure A.12: Detailed, low-frequency spectra in IWT with empty test section (as acquired by Cobra probe)

completely (Quirillo 1999). This author noted a low-frequency fluctuation in motor drive power; as the drive PID controller employs a fan speed set-point, the notion of sub-optimal PID tuning is not excluded.

The ready availability of the Cobra probe and the ease with which dynamic measurements could be taken invited an investigation using an unusually long sampling time (30 minutes) and bin sizes (65,536) which, even at a relatively generous sampling frequency of 6kHz<sup>12</sup> gave a usefully small bin size of  $9.2 \times 10^{-2}$  Hz. Results were averaged over 248 realisations, the first 10 Hz of which (for net velocity records) are de-trended and presented in figure A.12.

A broad-band peak increasing in frequency with speed (peaking at 3 Hz for at 108 km/h, commensurate with typical test speeds) is clearly evident (the initial “spike” at the first bin is likely spectral leakage about the mean).

As this spectral characteristics do not obscure characteristic shedding of the forms studied, this data is treated as being characteristic of hysteresis in the IWT’s ability to maintain consistent velocity. This “tolerance” is duly accounted for in the examination of spectral content in experimental results (commensurately, best results in conditional averaging were obtained with such a tolerance applied).

Further causes are not investigated.

<sup>12</sup>The probe’s response extends to approximately 2.7 kHz,  $F_s = 6$  kHz was employed to allow simultaneous study the probe’s software’s handling of data beyond the the response cut-off.

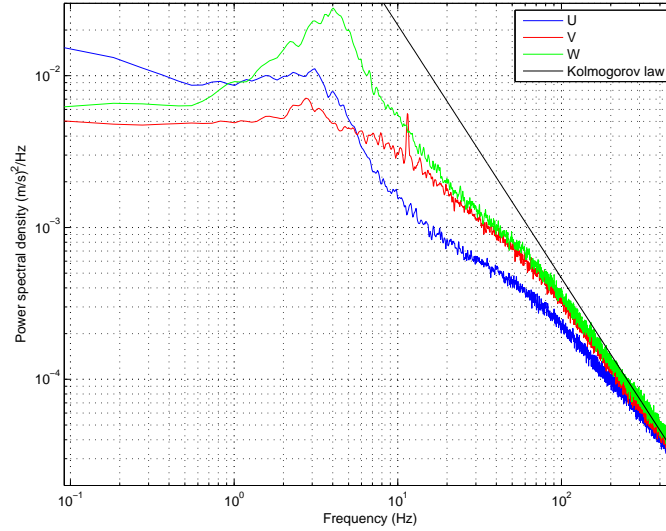


Figure A.13: Spectra in IWT with empty test section (logarithmic axes, as acquired by Cobra probe, Kolmogorov law contrasted)

### A.5.3 Turbulent length scales

Whilst a general description of statistical turbulence parameters and effects is given in section 1.2.2.2 (page 12), turbulence intensity alone does not fully characterise freestream dynamic characteristics. Spectral densities (described above and detailed in figures A.12 and A.13) serve to characterise the distribution of relative energy per frequency bin pertaining to turbulent phenomena about the flow's mean velocity; the nature of these distributions are in turn defined by nature of large eddying motions in flow. The measure of their characteristic size is defined as the turbulence length scale,  $L_u$ .

As with methods seeking to simulate atmospheric turbulence (Baran and Infield 1995), a variety of approaches exist to characterise turbulence length scale depending on the flow conditions involved (Burton et al. 2001, Lungu and van Gelder 1997, Moraes et al. 2008, Oetl et al. 2005). Two examples are presented herein: the freestream characterisation of  $L_u$  is achieved by either *autocorrelation* or via *best-fit comparison* with one of two dominant models characterising freestream turbulence ( $L_u$  in non-freestream conditions is otherwise calculated via autocorrelation.)

#### A.5.3.1 Turbulence length scale via autocorrelation

(Mathematical references throughout the following are drawn from Bendat and Piersol (1993), Newland (1979), Steven (1999). Relevant fluid mechanics theory is drawn from ESDU (1974; 1985) and Lindener et al. (2007)).

Covariance - sometimes termed a indicator of “linear dependence” between data sets - seeks to characterise analytical relationships between multiple sets of data. Covariance is thus defined as the average product of deviation about a mean value ( $\mu$ ) in compared data sets:

$$\sigma_{xy} = \lim_{N \rightarrow \infty} \frac{1}{N} \sum_{i=1}^N (x_i - \mu_x)(y_i - \mu_y) \quad (\text{A.2})$$

Where two sets are perfectly, linearly correlated (i.e.  $y = x$ ),  $x_i - \mu_x$  and  $y_i - \mu_y$  are equal in magnitude and sense. This strongest degree of correlation yields an average product of:

$$\sigma_{xy} = \sigma_x \sigma_y \quad (\text{A.3})$$

Thus equation A.3 defines the maximum covariance possible between two random variables. Rather than let correlation be scaled according to the deviation of the data sets involved, for convenience  $\sigma_x \sigma_y$  can thus be used to normalise covariance. The *correlation coefficient* is thus defined:

$$\rho_{xy} = \frac{\sigma_{xy}}{\sigma_x \sigma_y} \quad -1 \leq \rho_{xy} \leq 1 \quad (\text{A.4})$$

Thus a complete positive correlation is indicated by  $\rho_{xy} = 1$ , an inverse complete correlation by  $\rho_{xy} = -1$  and two unrelated sets by  $\rho_{xy} = 0$ . The above concepts may be extended to the *time domain*, where  $x(t)$  and  $y(t)$  represent time records of two random, assumed stationary processes, and  $\tau$  the time delay between them. The relevant covariance function is thus defined:

$$\begin{aligned} C_{xy}(\tau) &= \lim_{T \rightarrow \infty} \frac{1}{T} \int_0^T \{x(t) - \mu_x\} \{y(t + \tau) - \mu_y\} dt \\ &= R_{xy}(\tau) - \mu_x \mu_y \end{aligned} \quad (\text{A.5})$$

$R_{xy}(\tau)$  - the *cross-correlation function* - is thus:

$$R_{xy}(\tau) = \lim_{T \rightarrow \infty} \frac{1}{T} \int_0^T x(t)y(t + \tau)dt \quad (\text{A.6})$$

The relevant *autocorrelation function* of  $x(t)$  - used to compare  $x(t)$  to a time-delayed record of itself - is therefore:



$$R_{xx}(\tau) = \lim_{T \rightarrow \infty} \int_0^T x(t)x(t+\tau)dt \quad (\text{A.7})$$

Autocorrelation essentially allows the comparison of a signal with itself, such that periodic phenomena may be clearly isolated from noise contained within the signal. For detrended data (mean negated) - as processed throughout this section - the covariance function and the cross-correlation function are equal ( $C_{xy} = R_{xy}$ ,  $C_{xx} = R_{xx}$ ). Where, again, these are normalised by the variances in the record an *autocorrelation coefficient* function is derived. Expressed as along Cartesian axes relevant to axial, transverse and vertical flow components, the following correlation coefficient functions are revealed:

$$\rho_{uu} = \frac{R_{uu}}{\sigma_u^2} \quad \rho_{vv} = \frac{R_{vv}}{\sigma_v^2} \quad \rho_{ww} = \frac{R_{ww}}{\sigma_w^2} \quad (\text{A.8})$$

Equations A.8 and related (above) theory may be considered relevant in a context pertinent to turbulence length scale by the assumption of Taylor's frozen turbulence approximation - that flows are statistically stationary, of large mean velocity and possessing eddies of consistent shape passing a given measurement point. Initially, the autocorrelation is integrated between  $\tau = 0$  (where correlation is complete) and the first zero crossing of the function (at  $t_0$ ), wherein the records are completely de-correlated - effectively, the time taken for one complete eddy to (on statistical average) pass the measuring point:

$$T_i = \int_0^{\tau_0} \rho_{ii}(\tau)d\tau \quad \text{where } i = u, v, w \quad (\text{A.9})$$

Given the assumption of the Taylor's hypothesis,  $\tau$  can thus be easily manipulated to provide necessary spatial information - turbulence length scale:

$$^iL_u = \overline{U}T_i \quad \text{where } i = x, y, z \quad (\text{A.10})$$

As Taylor's hypothesis best holds true for large  $\overline{U}$  and highly regular periodicity in the time record considered, equation A.10 is generally most effective in the freestream direction where mean velocity is large and/or behind bluff bodies offering strongly periodic shedding phenomena. The use of the autocorrelation method in less favourable situations demands significantly longer time records with which to calculate statistically viable trends giving rise to a well-defined de-correlation.

### A.5.3.2 Best fit with existing theory

Another approach in characterising length scale is simply to fit (generally via regression) an existing theory to atmospheric turbulence to experimentally obtained spectra (an excellent reference to this

end is Burton et al. (2001)). Whilst a variety of relevant theory exists, two are notable: that by Von Karman<sup>13</sup> (equation A.11, a commonly used reference in literature) and Kaimal<sup>14</sup> (equation A.12) spectra:

$$\frac{nS_u(n)}{\sigma_u^2} = \frac{4n_u}{(1 + 70.8n_u^2)^{\frac{5}{6}}}, \quad \text{where } n_u = \frac{L_{1u}n}{\bar{U}} \quad (\text{A.11})$$

$$\frac{nS_u(n)}{\sigma_u^2} = \frac{4n_u}{(1 + 6n_u)^{\frac{5}{3}}}, \quad \text{where } n_u = \frac{L_{2u}n}{\bar{U}} \quad (\text{A.12})$$

$n$  = frequency

$S_u$  = spectral density at  $n$

$\sigma_u$  = standard deviation of  $U$

$\bar{U}$  = mean velocity of  $U$

$L_{1u}, L_{2u}$  = model-relevant turbulence length scales

An emphasis in either theorem is given to the suitable replication of low-frequency wind gusts (figure A.14); at high frequencies the models are intended to asymptote with Kolmogorov law. It should be stressed that these methods are intended to simulate atmospheric turbulence; Von Karman spectra has been demonstrated to give good agreement with flows obtained in some wind tunnel environments, it is not an intended use.

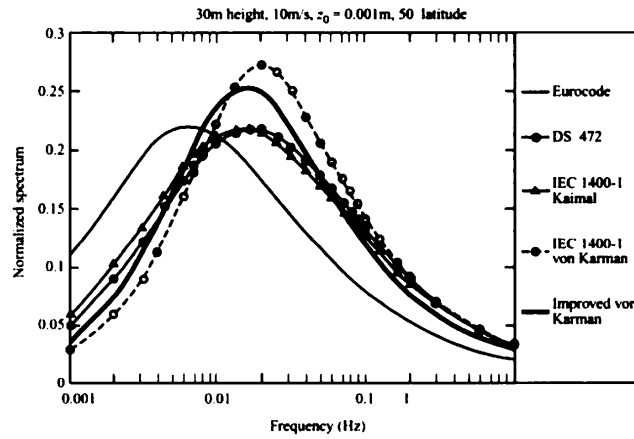


Figure A.14: A comparison of the low-frequency performance of various theorem modelling turbulence in the atmospheric boundary layer

<sup>13</sup> A modified form exists giving improved performance at altitudes  $\geq 150\text{m}$ .

<sup>14</sup> Uniquely, the Kaimal spectra also takes identical form for orthogonal flow components.

### A.5.3.3 Results

The same dataset as section A.5.2 was used. The Taylor model of a frozen turbulent structure advected past the probe head was used to effect a frequency cutoff; frequencies commensurate with structures less than ten times the size of the probe's head were not considered (due to the propensity of the probe to influence them). Encompassing this dynamic range at speed was not possible with the ECA probe; the larger head would limit acquired range further still, and accurate dynamic calibration data was unavailable (refer section D.4.2, page 258): the Cobra probe is thus regarded a superior instrument for this application.

The autocorrelation method gave  $^xL_u = 0.791\text{m}$  for the 30 minute sample with a strong cutoff observed indicative of clear de-correlation at a single turbulence length scale. As de-correlation had not been observed by Vino in the same facility using a one-minute sample, the sample was reprocessed in minute increments (figure A.15). It is probable that additional sampling time would give a zero crossing with minima on the  $x$ -axis, however area with the second zero crossing considered sufficiently small to suggest the  $^xL_u$  would equal the median case (e.g.  $0.79\text{m}$ ). Transverse and vertical turbulence length scale components did not readily de-correlate despite an exceptionally long sample time, producing correlation coefficient functions with effectively zero gradient in the vicinity of the  $x$ -axis. These results indicate weaker periodicity and a higher degree of randomness for these components (possibly expected given the lack of turbulence control hardware and low contraction ratio in the IWT).

When using comparison, a better fit (using least-squares regression) to the IWT's turbulent spectral characteristics was found using Kaimal spectra, giving  $^xL_u = 0.52\text{m}$ <sup>15</sup>. Whilst  $^yL_u = 0.5\text{m}$  and  $^zL_u = 0.23\text{m}$  were also estimated, poor results observed in autocorrelation renders the strength of the relevant, estimated, periodic phenomena questionable. Broadly consistent turbulence length scales were obtained for all test speeds presented in section A.5.2.

It should be stressed that neither the Von Karman or Kaimal spectra matched the low-frequency behaviour described in section A.5.2 successfully (particularly at higher velocities). Thus the length scales obtained are envisaged more representative of the limitations of the model's used than an accurate indication of those characteristic to the flow. It is thus suspected that  $L_u$  as measured by autocorrelation to be a more accurate estimate.

Expressed as a function of model length ( $L$ ),  $^xL_u = 1.01L$ ,  $^yL_u = 0.58L$  and  $^zL_u = 0.94$ .

### A.5.3.4 Discussion

The mean flows about three-dimensional bluff bodies have been shown to exhibit sensitivity (albeit at high turbulence intensities) to turbulence length scales approaching body dimensions, as eddies of such size serve to distort key vortex shedding phenomena leading to a decrease in base pressures

---

<sup>15</sup>Von Karman spectra gave  $^xL_u = 0.44\text{m}$ .

## A.5. DYNAMIC FLOW CHARACTERISTICS IN THE IWT

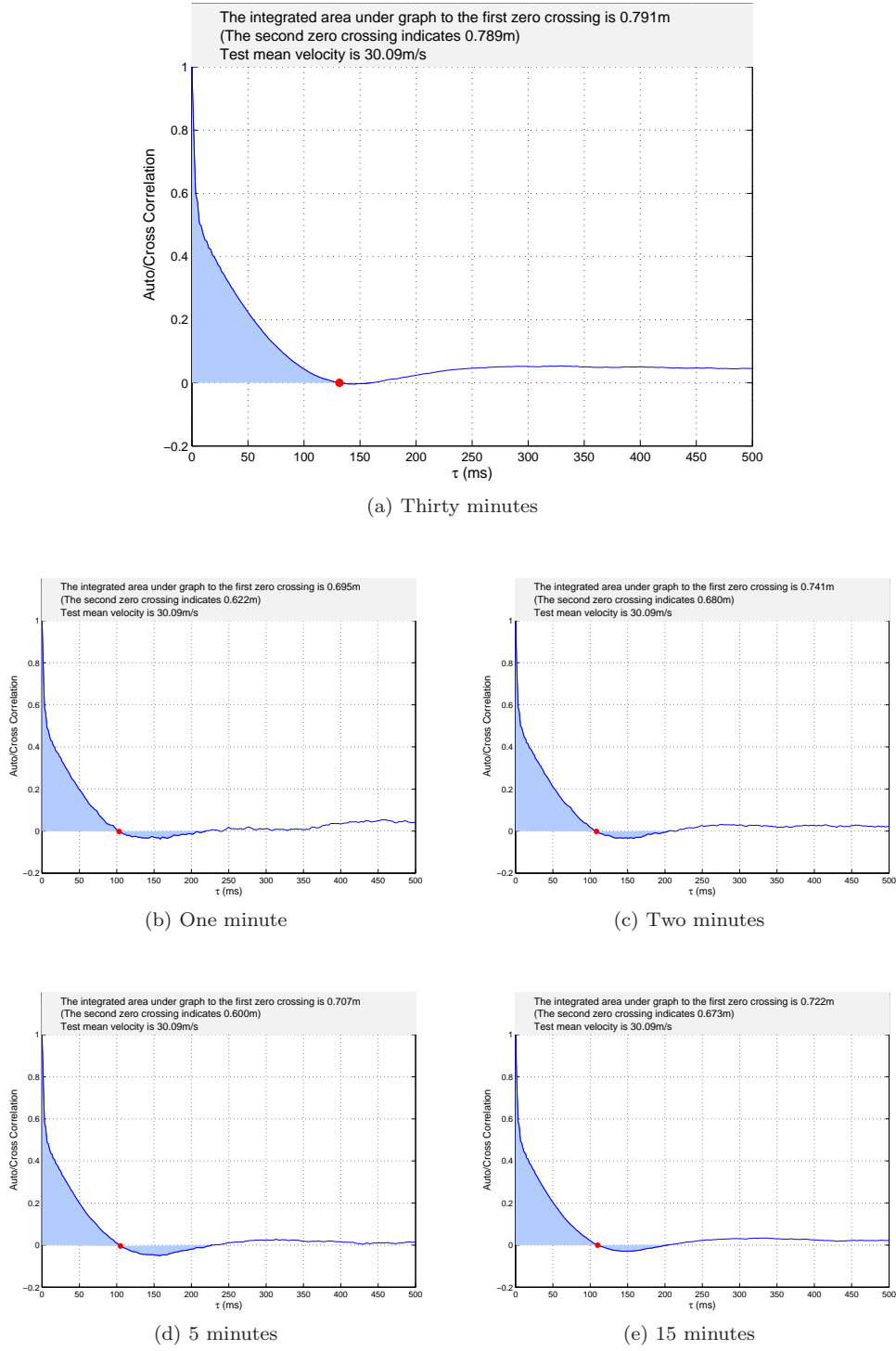


Figure A.15: Incremental results for  $L_u$  by autocorrelation method

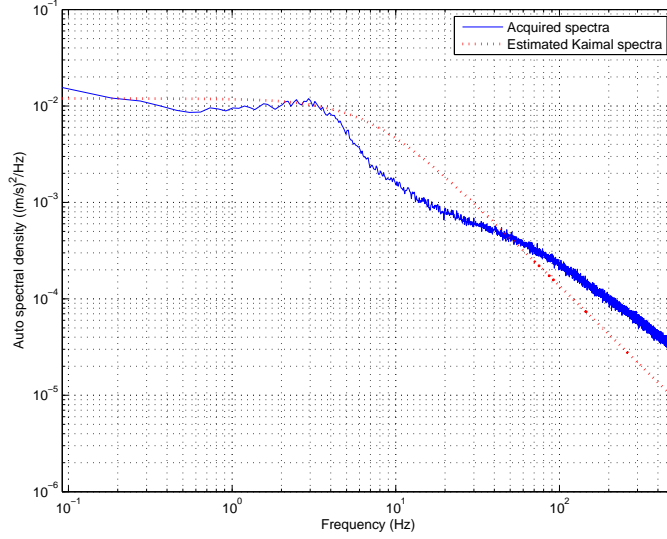


Figure A.16: Comparison of experimental  $S_u$  and best-fit Kaimal spectra

(Nakamura 1993, Nakamura et al. 1988); e.g.: the effects of  $^z L_u$  particularly would serve to disrupt (largely two-dimensional) shedding from the leading edge of the Ahmed model backlight and the bottom trailing edge of the base (salient effects are captured nonetheless and evidenced in section 3, page 88). This would be most notable at configurations away from the  $\alpha_c$  (i.e. where C-pillar vortex impingement would be relatively weaker). Larger scales (i.e.  $^x L_u$ ) serve to increase variance in shedding spectra (Nakamura et al. 1988).

Whilst the turbulence length scales and intensities observed in the IWT are higher than for other automotive test facilities (Lindener et al. 2007), relevant concerns must be considered in the contexts of:

- *Their relative importance in the context of wind tunnel performance:* the overall turbulence intensity remains relatively low (1.8%) in the developed freestream. Other flow parameters exert an arguably greater influence over results obtained in testing; e.g. the effects of net flow angularity and according pressure variations throughout the test section introduce a notable shift in the symmetry of wake flows. It should, furthermore, be noted that a variety of turbulent length scales exist in the IWT's freestream; the methods provided serve to *estimate* only the most prevalent.

Whilst the replication of primary turbulent characteristics represents a current leading edge in experimental turbulent automotive research (Carlino et al. 2007, Carlino and Cogotti 2006, Cogotti 2004, Lindener et al. 2007), it should be further highlighted that the relative strengths of other turbulent length scales and their statistical distribution as obtained in any automotive wind tunnel would fail to replicate the practical environment, where turbulence is derived from a range of stationary and moving sources of various size and geometry operating

in a time-dependant manner.

- *Their relevance in the context of practical road vehicle flows:* vehicle aerodynamic performance is historically assessed in environments of low turbulence intensity and with characteristic length scales far smaller than key body dimensions. The presence of atmospheric winds, roadside objects and traffic generates higher turbulence intensities with typically longer length scales, though a wide variety of combinations exist (figure A.17): data pertaining to the practical road environment in “light traffic” (with a moderate level of road side obstacles/RSO as per figure A.17) demonstrates turbulence length scales commensurate with a vehicle length, with turbulence intensities *greater* than those experienced in the IWT for relevant conditions (Lindener et al. 2007). The length scales presented in figure A.17 pertain to the flow axial component only - it should be further appreciated that under certain conditions, the effects of transverse components of turbulent phenomena may bear a more salient effect on vehicle aerodynamic performance; a condition not easily characterised or acquired in on-road tests.

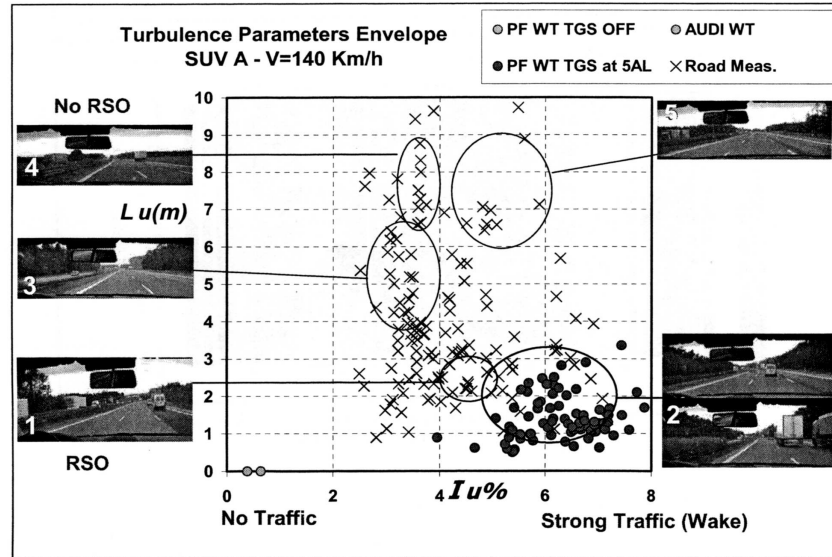


Figure A.17: Various experimental and wind tunnel data comparing turbulence intensity and turbulence length scale in various practical road contexts (Lindener et al. 2007)

The effects of turbulence length scales commensurate with body dimensions are thus not deemed to detrimentally affect the results provided.

In any case, practically, other freestream conditions may bear greater significance (e.g. yaw).

## Appendix B

# Further notes on pressure probes

### B.1 Technical differences between ECA and Cobra probes

The ECA Probe is essentially a 13-hole evolution of the four-hole Cobra probe, the latter of which is detailed in the Experimental Methods chapter.

Some further key differences vis-à-vis the Cobra probe include:

- A head size of 6mm, compromising spatial resolution somewhat and limiting the applicability of the probe in regions with large local pressure gradients beyond that of the Cobra probe (this is still considerably smaller than other probes with similar time-invariant functionality, e.g. Cogotti's 14-hole probe Cogotti (1987)),
- A moderately larger 4mm stem diameter,
- Tubing diameter (from head to transducer) reduced to 0.3mm, limiting the dynamic response of the device to some 800Hz<sup>1</sup>; thus the smallest length turbulent structure (60mm) the probe can measure is duly captured by the probe at 30m/s ( $W = 500\text{Hz}$ ),
- A unique static calibration method based on those used with the Cobra Probe; the number of dimensionless calibration coefficients used in calibration rises from four to nine (given 13 instead of 4 probe holes/transducers - see page 260, equations D.4 and D.5 for a more complete definition of probe static calibration methods). The calibration is completed in 5° increments at multiple flow velocities (from 2-40m/s), with turbulence varying from 0.5-1.5% pending on calibration flow velocity. The device accuracy is reported to be  $\pm 2^\circ$  in pitch and yaw, and  $\pm 0.7\%$  turbulence intensity, with velocity accurate to at worst  $\pm 2\%$  at the

---

<sup>1</sup>Extracted from supplied calibration data.

extremities of the devices' angular acceptance Vino (2005)<sup>2</sup>.

- The dynamic calibration is comparatively incomplete (being completed theoretically for a single tap only)<sup>3</sup>. Whilst much development work with the Cobra Probe by Hooper and Musgrove (1997) utilised a single tap approximation also, unique aspects in the manufacture of each pressure tube - from more extreme corner geometry in the probe head (particularly for rear facing holes) and exacerbated by the smaller diameters involved - it is envisaged that dynamic response of the ECA Probe would, relative to a Cobra Probe and in a qualitative sense at least, be further compromised (though dominant frequency response characteristics would be duly captured). The incorporation of multiplexer effects was initially unknown; it is explored in greater detail in Appendix D (page 251).

### B.1.1 Notes on statistical properties obtained from Cobra and ECA probes

Probe data as processed by TFI Device Control includes (in addition to aforementioned dependent variables) all six Reynolds shear stresses, turbulence intensities and various statistic properties. Whilst all data used throughout this work (on basis of thoroughness) uses statistical properties calculated from sampled time histories, some concessions are made due to the nature of the devices used.

1. *Calculation of angular acceptance of flows:* due to the limited angular acceptance of the devices - despite the ECA probe offering significantly enhanced angular acceptance over the Cobra probe at  $\pm 135^\circ$  ( $\pm 45^\circ$  for the Cobra probe) - it is not improbable (particularly in highly turbulent flows) that flows experienced during sampling are not able to be resolved in part or whole over the calibrated probe head surfaces at all time instants during acquisition. In cases where no flow is resolved over the calibration surface, the sample is regarded as a “zero sample”, the sum of which (i.e.  $U = V = W = 0$ ) over a set is deducted from a perfect score to give a “% good” statistic. Whilst this is not able to indicate the proportion of pressure distribution over the calibrated surfaces where relevant flows can only be resolved partly over them, sufficient information is provided with which to optimise probe orientation relevant to the task at hand. This data are used as such throughout.
2. *Angular acceptance and highly turbulent flows:* the above suggests that highly turbulent flows may (considering the time-averaged “% good” statistic) result in low acceptance over the probe calibration surface.
3. *Noise floor:* use of the ITF method and consideration of the practical noise floor associated with probe pressure transducers, amplifiers and relevant data acquisition hardware limits

---

<sup>2</sup>This information is cited from Vino (2005); discussions from the developer indicate that the probes calibration is divided into “zones” based on relative flow angularity, and that no more than five channels of data are used to resolve data at any one time. Pagliarella (2007).

<sup>3</sup>Experimental calibration data utilised by Vino (2005) was not available during the course of this work.



accurate acquisition to flows above 2m/s (see section 2.2.5.1, page 78). This is employed as a cutoff in software; time histories thus record speeds below this threshold as zero samples<sup>4</sup>.

4. *A practical limitation on turbulence intensity data:* given (2) and (3) above - and considering the definition of turbulence intensity used throughout this work:

$$I_{ii} = \frac{\sigma_i}{\overline{U}} \quad (\text{B.1})$$

It is possible - with a significant number of zero samples characteristic of highly turbulent, low velocity flows relevant to an automotive vehicle near wake - to obtain large standard deviations over a sample set and very small average velocity. The computed turbulence intensities would thus be erroneously large. A compromise is to calculate such statistics using a modified time history of only “good” values (i.e. those above the velocity cutoff). The reader is thus advised to treat values of turbulence intensity presenting throughout exceeding 30% with caution<sup>5</sup>. All values presented in contour plots are arbitrarily clipped at 50%.

5. *Effect of proper sampling rate in low-speed flows:* assuming sampling speed were sufficiently in excess of that required to capture all spectral activity, a single “zero sample” acquired under such circumstances would be acquired as a succession of zeros at higher sampling rates. The use of discrete Fourier methods to estimate a fluctuating signal (as per the ITF method) become compromised where significant sequences in a time history equal their mean - in this case, zero - which the estimated signal “clamps down” to. A short experiment was run to deduce potential effects, with results presented in figure B.1; the test case is characterised by a low-speed, highly turbulent near wake with spectral energy limited to 312Hz.  $F_s = 625\text{Hz}$  employed to meet the Shannon-Nyquist criterion. As it would appear the cutoff in (3) is effected after linearisation, the percentage of good samples decreases markedly with sampling rates above the minimum sampling rate necessary.

Sampling rates are thus set to the minimum required to capture all salient spectral effects for the test cases used. Errors relating to multiplexing are handled in post processing, with methods described in Appendix D (page 251).

---

<sup>4</sup>Assuming that the acquisition and export sampling rates are set identically, as they are throughout this work. The digital cutoff appears to be effective from the acquisition stage only; any reprocessing involving filtering of data (e.g. upsampling/decimation) may introduce samples with values below the cutoff into the exported time history. Careful consideration may be warranted when working with filtered data.

<sup>5</sup>30% corresponds to the rounded minimum value of  $I_{uu}$  calculated in the work presented.

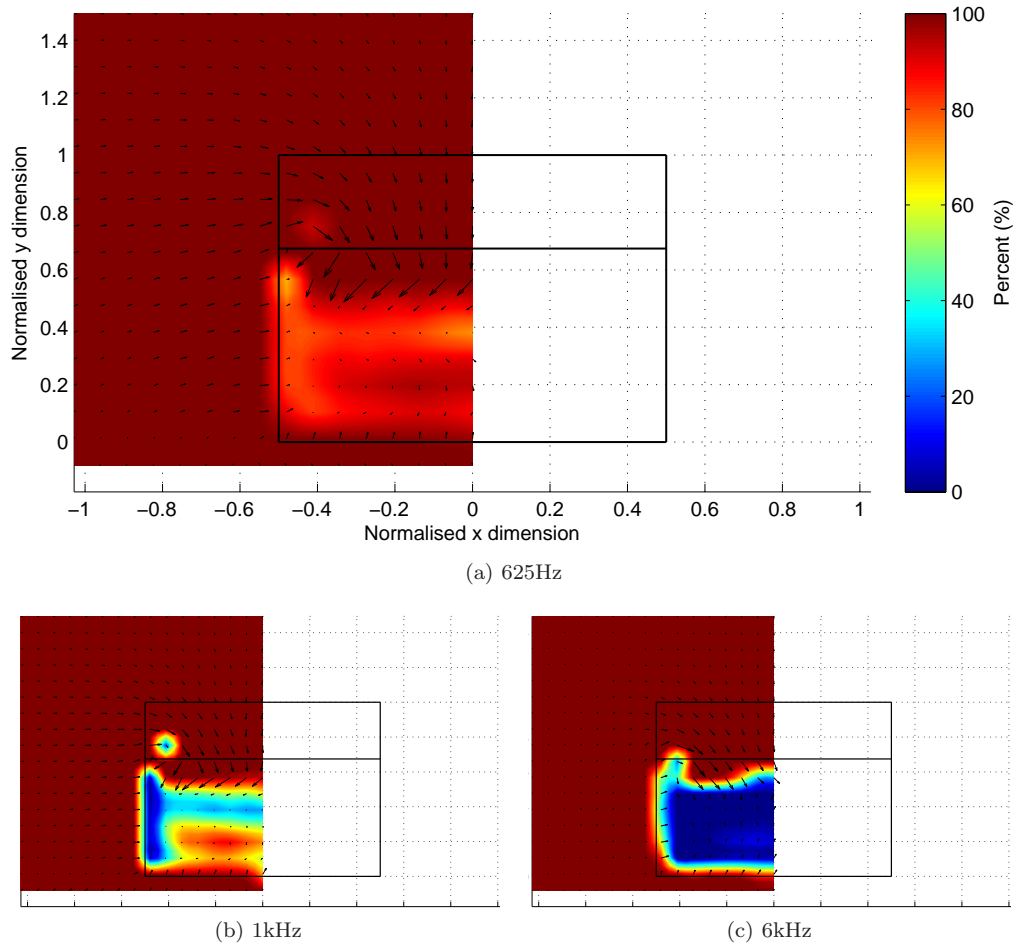


Figure B.1: % good samples 0.0625 model lengths behind rear of 25 Ahmed model at various sampling frequencies

## Appendix C

# Practical challenges in accurate calibration of dynamic pressure instrumentation

Instruments used throughout this work featuring manufacturer-supplied dynamic calibrations (ECA Probe, Cobra Probe) are completed using a method first used in this context by Irwin et al. (1979); essentially, a white noise source is applied to the tubing system and the downstream sensor response is compared to that of a reference microphone located within a suitable distance of pressure system's measuring surface.

Whilst the digital corrections for amplitude and phase distortion are powerful, the method is highly reliant on the validity of the calibration data applied. Some practical caveats researched from various sources are thus presented and contrasted in light of the contexts in which both calibration and instrument use have taken place.

- The generation of sound pressure levels relevant to test conditions requires a sound source and transmission path specifically engineered to attain very high pressures ( $C_{PRMS} = 1$  at 105km/h corresponds to 148dB). Some common methods to increase gain at the calibration surface involve focussing sound using funnels, parabolic dishes (akin to a parabolic microphone) with the output focussed onto the calibration surface<sup>1</sup> (Hooper and Musgrove 1997, Irwin et al. 1979). Even higher gain can be achieved focussing acoustic pressure into an individual pressure tap (Behan and Watmuff 2006), offering excellent repeatability.

It should be appreciated that any method that imposes a change in geometry on a propagating

---

<sup>1</sup>“Calibration surface” in this context implies a surface having one (or more) hole(s) connected to a transducer(s) via tubing. This is a different context to that concerning static calibration of Cobra and ECA probes, mentioned in 2.2.5.1 on page 78.

sound wave introduces some degree of reflection and thus attenuation that is inconsistent throughout the frequency range; a parabolic dish (unless impossibly large) exhibits poor response at low frequencies (of key interest throughout this thesis) and produces focussing errors similar to optical coma aberration (therefore giving markedly different response on and around the focussing point); tubes exhibit well-known tube resonance phenomena.

Whilst a use of white noise in calibration may give rise to a source with flat amplitude characteristics, introduction of attenuation and resonance across various frequencies may net significant differences in pressure level at different frequencies, with a proportionate variance in pressure-related error.

- Cone driver-based systems typically have limited frequency response characteristics in a range relevant to work presented in this thesis; the largest such drivers have useful response extending not below  $18\text{Hz}^2$  though struggle to give useable response to (let alone beyond)  $1\text{kHz}$  (e.g. within  $\pm 3\text{dB}$  response throughout). Some consideration needs to be given to use of multiple drivers (or use of a single driver with significantly diminished amplitude response at low frequencies).

The low frequency region is of particular interest to the forms studied Vano (2005); ultra-low frequencies are of significant interest in assessing underlying periodic phenomena common to wind tunnel calibration. Where the ability to calibrate experimentally is limited, an attempt to reconcile and blend theoretical and experimental approaches is required.

Reverse-engineering of the Cobra Probe dynamic calibration by the author revealed both amplitude and phase response to be pulled linear in the range  $0\text{--}22\text{Hz}$  (i.e. correct at the former, experimentally-determined at the latter and estimated in between). A suitable theoretical calibration using theory developed by Bergh and Tijdeman (1965) was generated and applied throughout the “missing” range. These revised dynamic calibration datasets were used throughout.

- The accurate creation of white noise pressure forms is similarly challenging, demanding multifrequency cone excitation. A cone driver does not allow for decoupling of frequency and amplitude sources in operation, white noise replication inevitably compromises both and limits the ability of the driver to create composites of pure sinusoidal wave forms. A stepped frequency sweep can be used as an alternative procedure (one that also allows higher sound pressures to be generated<sup>3</sup>) however time resources are compromised.

It is often more practical to observe response to the point that the desired white noise output is at least stable, and then to begin instrument calibration. Non-stable output may yield spurious frequency spectra data as intended periodic phenomena are not faithfully recreated in the pressure field.

---

<sup>2</sup>Devices able to create high amplitude, low frequency pressure waves (as low as  $0.1\text{Hz}$  at suitable SPL) do exist. These are known as rotary woofers. Currently these are not cost feasible nor nearly as practical in size (as cone drivers, once enclosure/baffle requirements are considered).

<sup>3</sup>As the superposition of two or more frequencies each of identical amplitude demands a proportionate amount of cone excursion - which is inevitably limited - a single frequency (or lesser frequencies) will use a lesser proportion of maximum excursion at the same amplitude, or be able to make use of maximum excursion at higher amplitude (and thus higher sound pressure level).

- Pressure field amplitude may further affect instrument calibration where tubing used is not sufficiently rigid; additionally there exists the potential for harmonic distortion within tubes at very high amplitudes (unlikely with very short tubes as used in Cobra and ECA probes).

## Appendix D

# Time alignment of acquired data

The following section details the process used to obtain time-accurate data from the data acquisition board used throughout.

It is important to appreciate that the TFI packages (comprising hardware and software solutions) used throughout testing are essentially black boxes, in that whilst inputs are known and outputs acquired, the exact nature of the systems' working is not publicly disclosed. It is furthermore important to appreciate that the whilst software solution supplied (*“Device Control”*) supports a wide variety of data acquisition hardware, comments regarding software functionality are limited within the context of the hardware DAQ solution used.

The following work details, in a context relevant to signal time alignment:

- What information is openly available concerning various system components,
- What information can be readily deconstructed from available resources, and,
- What remains unknown concerning system operation.

The resulting synthesis details the procedures utilised throughout this thesis.

### D.1 Hardware particulars

The DAQ hardware used throughout the research presented is a National Instruments NI-6034E (E series) data acquisition board. It features 16 analogue inputs, 16-bit analogue-to-digital conversion and a 200kS/s aggregate sampling rate (National Instruments Corp. 2007).

To allow an appropriate channel count at moderate cost, the NI-6034E employs a single 16-bit analogue-to-digital converter (ADC) which is multiplexed on-card to give 16 analogue inputs (an additional four channel external multiplexer is employed on the DPMS to yield 60 available channels; each DPMS module features 15 useable pressure inputs).

Device Control calls the device driver supplied by National Instruments Corporation, “NI-DAQ”, in sampling. Default values in acquisition for the version of NI-DAQ employed throughout are known, however any customisations as called by the version of TFI Device Control used throughout are unknown. Attention is drawn where appropriate.

## D.2 Challenges in multichannel, dynamic acquisition

The use of a single ADC presents a challenge when acquiring dynamic pressure data from multiple channels; whilst the acquisition software timestamps the full channel complement of data as being acquired at a given instant, each conversion actually takes place at a unique time instant.

For the accurate reconstruction of multichannel data, these unique time instruments must be deconstructed and applied to acquired data - or at least be accounted for within calibration procedures - such that phase lag between channels does not adversely affect reconstruction (via ITF method), time-resolution (of multi-hole devices) or cross-correlation of acquired data.

## D.3 Interchannel delay

A key concept in the successful use of DAQ devices using multiplexing to increase channel count is that of *interchannel delay*; whilst a data sequence may show a number of channels being sample at the same time instant, practically there exists a small *time lag* between successive samples. This is represented as a *phase lag* (e.g. thus affecting phase response) in the frequency domain.

Phase lag is calculated as follows:

$$p(^{\circ}) = \Delta t \times f \times 360 \quad (\text{D.1})$$

(In equation D.1,  $f$  is the frequency of interest. It can be appreciated from later sections that two successive sampling events where the frequency of interest equals  $F_s$  - the sampling frequency - are  $360^{\circ}$ , or in phase, as expected).

Table D.1 illustrates the concept; four channels are scanned at 6kHz; the *sample clock* provides timing for the group acquired, the *convert clock* provides timing for the actual conversion of each channel as multiplexed though the single ADC (National Instruments Corp. 2009). The convert

clock rate always equals (for single channel sampling) or exceeds (for multichannel sampling) the sample clock. The time at which each individual conversion in a sample set is initiated is separated by interchannel delay  $x$ <sup>1</sup>.

Sample clock	Convert clock	Time (nearest $\mu$ s)
0	0	0
0	1	$0+x$
0	2	$0+2x$
0	3	$0+3x$
1	0	167.67
1	1	$167.67+x$
1	2	$167.67+2x$
1	3	$167.67+3x$
2	0	333.34
2	1	$333.34+x$
2	2	$333.34+2x$
2	3	$333.34+3x$

Table D.1: Timing for interval scanning of four channels at 6kHz (first three sample sets)

Various strategies exist in calculating and/or modeling this phase lag; it is crucial in this application to appreciate the relevant implementation and what limitations it imposes on correct dynamic functionality of the devices at hand.

### D.3.1 Hardware schematic

An understanding of the E series sampling engine is paramount; figure D.1 presents a basic schematic:

- *AI+*, *AI-*: Input analogue channel data which can be single ended, as is used in this thesis, or differential).
- *Mux*: 16 channel multiplexer used to route analogue signals through the instrumentation amplifier (NI-PGIA).
- *NI-PGIA*: The programmable (for range and polarity per channel) gain instrumentation amplifier. Essentially, this component is designed to minimise settling time such that maximum resolution digitization can take place prior to the next sampling event taking place.

<sup>1</sup>Practically, a further small delay exists between the sample clock event and the first convert clock event it initiates. The device driver defaults this to two ticks of the convert clock timebase, however this is configurable. Its present configuration as called by TFI Device Control is unknown. In any configuration it could not be set to less than 50ns; effectively  $0.5^\circ$  phase lag at the highest frequency a Cobra probe could observe, and almost an order of magnitude greater than frequencies of interest throughout this thesis. The effect is potentially larger, but unable to be quantified and certainly, relatively small at frequencies of interest.



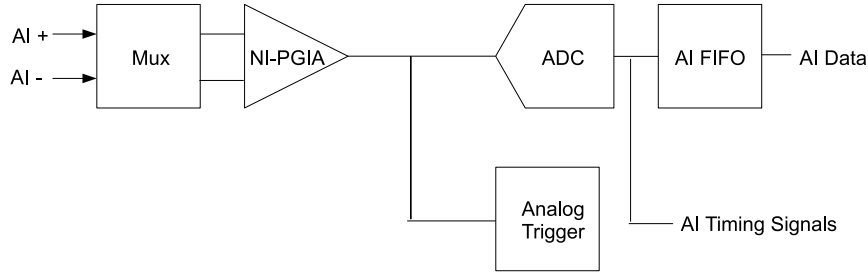


Figure D.1: National Instruments E-series sampling engine

- *ADC*: Analogue to digital converter; conversion is resolved over 16 bits.
- *AI FIFO*: A first-in first-out sample buffer.
- *Analog trigger*: A hardware or software trigger used to initiate sampling.
- *AI Timing Signals*: A series of timing signals provided by the on-board timing engine to coordinate individual sampling events.
- *AI Data*: Final, digitized output data.

Simultaneous sampling, a multichannel sample-and-hold buffer or other similar strategies are not employed. Every reading corresponds to a unique time period.

### D.3.2 Timing strategies

The exact timing strategy employed is set at device driver level. This can be set/called by a user or front-end program; the defaults reflect the intention to maximise conversion accuracy by allowing the instrumentation amplifier appropriate settling time to realise a “truly”<sup>2</sup> 16-bit accurate conversion and to reduce effects of phenomena that increase setting time e.g. charge injection<sup>3</sup>. It is thus not generally desirable to sample at maximum speed.

Three timing strategies are available:

- *Interval scanning*: This method attempts to reconcile the fastest performance the DAQ card allows whilst allowing adequate settling time for conversion accuracy. It is simply the fastest

<sup>2</sup>Conversion always takes place over 16 bits; however should conversion take place when instrument amplifier output has not yet settled to a value beyond the resolution of the digitization to take place, the result is effectively rendered accurate to the last significant bit.

<sup>3</sup>A key limitation herein may concern the (unknown) impedance of the sensors used; high impedance sensors coupled with the switched capacitor bank used in the multiplexer can have voltages pertaining to a prior channel leaking back through the reading a subsequent channel; giving rise to crosstalk (e.g. where the value of one channel is reflected on another). This phenomenon is exacerbated at high sampling rates, and can be alleviated by increasing the interchannel delay.

sampling rate allowed plus  $10\mu\text{s}$ : in the case of the available hardware, the interchannel delay via interval scanning is:

$$\begin{aligned} &= \frac{1}{200000} + 10 \\ &= 5 + 10 \\ &= 15\mu\text{s} \end{aligned} \tag{D.2}$$

- *Round robin scanning:* The interchannel delay is simply obtained by dividing the time between scans by the number of channels being sampled. e.g. for the scenario presented in table D.1, the interchannel delay using round robin sampling is:

$$\begin{aligned} &= \frac{\frac{1}{6000}}{4} \\ &= 41.67\mu\text{s} \end{aligned} \tag{D.3}$$

- *Customised interchannel delay:* Software may alternately force the hardware to use a predetermined interchannel delay.<sup>4</sup> This delay is identical across all channels.

The device driver default is to use interval scanning for all sampling conditions where the sampling rate is slow enough to complete all conversions in a sample set prior to the next sample clock event; beyond this point, the driver implements round robin scanning (though conversion accuracy may be compromised). A relevant example considers a Cobra probe; 4 channels at 6kHz: the sample clock (6kHz) allows  $166.67\mu\text{s}$  between rising edges; clearly, interval scanning is possible (4 conversions delayed at  $15\mu\text{s}$  each).

#### D.3.2.1 Experimental deconstruction of interchannel delay

A simple experiment was conducted to ascertain the interchannel delay employed by TFI Device Control, thus allowing its effects to be put in the appropriate context on a device-by-device basis.

A signal generator set to output a 1kHz sine wave was connected to three channels of the DAQ card using a breakout board. A sampling rate of 3kHz was employed<sup>5</sup>. The test waveform was optimised for sampling headroom within the limits of the DAQ card using a cathode ray oscilloscope. Device Control was configured to sample a Cobra probe in addition to the analogue channels in question; two were adjacent channels and one spaced three channels apart (to note clearly a relevant difference in phase). A 4096-point FFT was taken of the acquired analogue time history. Amplitude response data was used to identify the frequency peak. Phase at the same

<sup>4</sup>Customisation also gives rise to the possibility of mismatched sample and convert clocks, in which instance events on either clock are gated e.g. effectively ignored (National Instruments Corp. 2007).

<sup>5</sup>The maximum calibrated sampling rate of the ECA probe.

point was recorded for the channels of interest. Using equation D.1 an interchannel delay of  $5\mu\text{s}$  was noted<sup>6</sup>.

This interchannel delay corresponds to the fastest possible using the data acquisition card in use (e.g. an aggregate sampling rate of 200kS/s). 16-bit resolution is not possible using this method, however the interchannel delay will neither scale with the aggregate scanning rate (e.g. this would otherwise change when the total scanning requirement demanded round robin scanning).

## D.4 Application to devices used

it is essential to correctly account for phase lag in sampling in scenarios where multiple channels are used to resolve the same point in space and time (e.g. as per Cobra and ECA probes) or where phase-based comparisons of time records taken at unique points are sought (e.g. concerning cross-correlation of dynamic data from unique surface pressure taps).

### D.4.1 Cobra probes

It was confirmed by the supplier that the phase lag between the four channels of the Cobra probe is accounted for in the calibration process (Pagliarella 2007). Comments herein are dependant on this assumption.

As the four holes of the probe are used to provide data that resolves - dynamically - a single point in space, it is crucial that the phase lag due to multiplexing is accounted for. This is achieved simply by using the same sampling configuration in calibration as is used in acquisition; a source provides an oscillating pressure signal which is assumed to reach each measuring surface at the same instant<sup>7</sup>. The resulting acquired tubing transfer functions therefore include phase lag owing to both tubing response and multiplexed input characteristics.

The phase lag between adjacent channels at  $F_s$  for all available probes (at time of writing) is shown in table D.2<sup>8</sup>.

Figure D.2 denotes typical calibration data from a four hole Cobra probe (specifically the phase lag of each channel over the 6kHz calibration range).

---

<sup>6</sup>The exact delay noted was  $4.9973\mu\text{s}$ , however this is a product of the discrete FFT implemented. It would not be possible to note the exact interchannel delay using discrete Fourier methods.

<sup>7</sup>There is practically a very small delay between the centre hole and the three surrounding holes (the former is located slightly further upstream). There is also the potential for small phase error and amplitude disparity between the four measuring surfaces in calibration (output from the pressure source is focussed to a point to facilitate significant attenuation; deviation from the foci would give an error best characterised as similar to coma aberration in an optical telescope). Data concerning the former error with the calibration device used is not available, the latter cannot be quantified with the reference microphone used (owing to poorer spatial resolution than that the probe allows).

<sup>8</sup>As phase lag increases with frequency (of interest),  $F_s$  is chosen to characterise the phenomena. Practically  $F_s$  is of no relevance as a "frequency of interest".

Probe ID	Phase lag ch. 1-2	Phase lag ch. 2-3	Phase lag ch. 3-4
Cobra 107	21.12°	0.42°	6.46°
Cobra 109	33.59°	-5.08°	8.96°
Cobra 133	25.76°	10.85°	13.40°
Cobra 137	38.86°	33.45°	-11.05°

Table D.2: Phase lag between channels for Cobra probes at  $F_s$  (as extracted from calibration data)

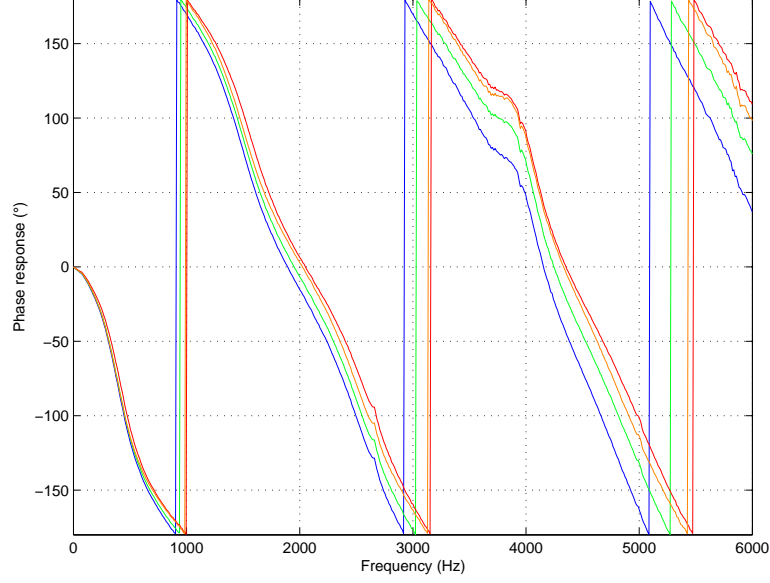


Figure D.2: Phase lag of four channels of a Cobra probe (as extracted from calibration data)

It should be noted that a number of unknowns contribute to phase lag, most notably the geometric characteristics of the tubing systems involved - exact length is unknown in each instance, as is there significant possibility for variance in production in what are essentially hand-made specialty instruments. Phase lag owing to multiplexing contributes in addition to the above. As long as these these differences are appropriately captured in the calibration process, the instrument will function correctly in a dynamic context.

Whilst it is known that the calibration method generally replicates that cited in Hooper and Musgrove (1997), it is not known whether the reference microphone is acquired in phase with the with the first probe channel. The calibration data in figure D.2 indicates phase lag relative channel-to-channel; if the same (multiplexed) DAQ device is used to sample the reference microphone without a correction for incurred (multiplexer-induced) phase lag (relative to the channel the reference microphone occupies), then the dynamic calibration is still relevant - the resulting estimated time history (Irwin et al. 1979, ITF method) will incur a slight time lag. This is practically small enough to be considered negligible; it could not exceed the applicable interchannel delay.

More critically, it is assumed that the interchannel delay used in testing is identical to that employed in calibration.

The dynamic calibrations provided for the Cobra probe are thus considered relevant assuming the sampling engine configuration used in acquisition replicates that used in calibration. This is duly replicated in the research presented.

#### D.4.2 ECA probe

An increase in channel count increases any inter-channel delays significantly - the 13 channels of the ECA probe thus warrant additional consideration.

The calibration file currently supplied by TFI contains a transfer function for a single tube, theoretically derived using theory by Bergh and Tijdeman (1965). This response function is applied to data acquired from all 13 tubes in the device. Phase lag due to multiplexing is thus not incorporated in a calibration procedure as per the Cobra probes. It is not known if the software support for the device includes compensation for this much.

The effect of the difference is hypothesised for a  $5\mu\text{s}$  interchannel delay on the phase response of the theoretically determined, single tube calibration supplied is shown in figure D.3. The original calibration is in red, and the plot is limited to the practical response of the device (e.g. frequencies where the tubing system exhibits amplitude response over 0.4, corresponding to 800Hz).

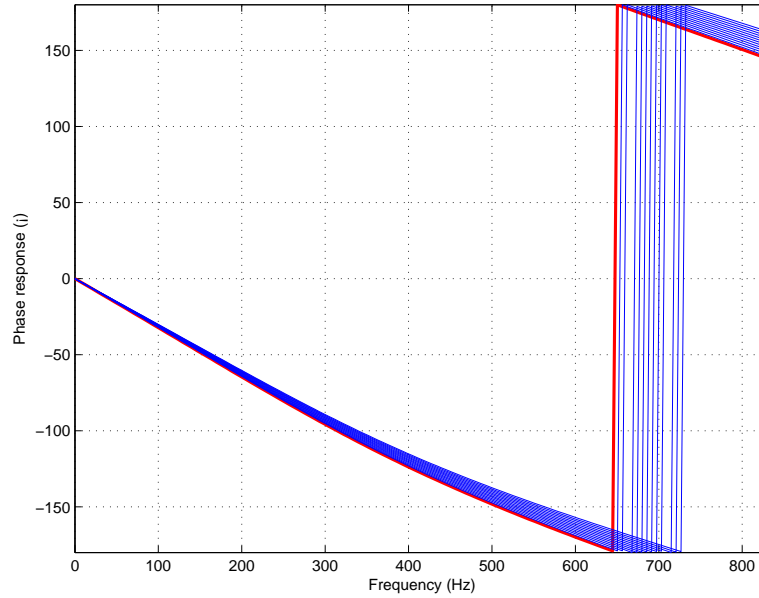


Figure D.3: Hypothetical effect of  $5\mu\text{s}$  interchannel delay on ECA probe phase response (original "channel" phase response in red)

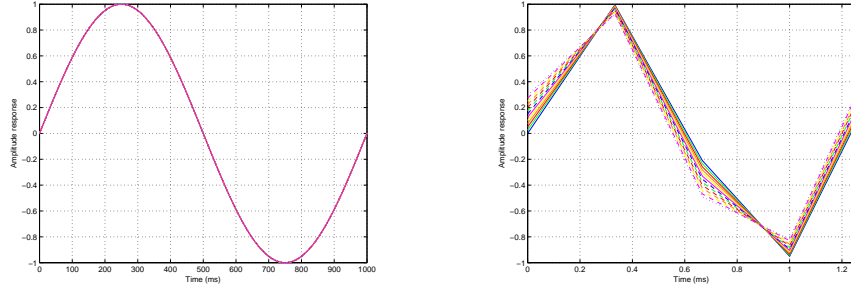


Figure D.4: Effect of phase lag over 13 channel input at 1Hz (left) and 800Hz (simulated using unity amplitude sinusoidal input, interchannel delay of  $5\mu\text{s}$ ,  $F_s=3\text{kHz}$ , as per supplied ECA probe calibration data)

Figure D.4 further demonstrates the potential effect of multiplexer induced phase lag; essentially the phase lag increases linearly with frequency.

Vino (2005) presents a data supplied by the device manufacturer denoting excellent agreement between an estimated time record for a single hole on the device and a reference transducer attached to the probe head for all flow artefacts under 800Hz; whilst an excellent testament to the validity of the ITF method, it is pertinent to ensure that all data from the device (e.g. from all transducers) may be resolved accurately for a unique point and at a unique instant in time.

#### D.4.2.1 Deconstruction of ECA probe phase response

An experimental investigation was undertaken to explore whether or not the ECA probe system (comprising both hardware and software aspects) compensated for multiplexer-induced phase lag. It must be reinstated that the system is effectively a black box; when configured to acquire data from the ECA probe the data output is resolved to U, V, W and static pressure coefficients. Raw transducer data cannot be observed; conclusions must be drawn from resolved data. It was not known whether software support for the ECA probe includes compensation for multiplexing-induced phase lag<sup>9</sup>.

A method was derived from available resources. It is known from published sources (Chen et al. 2000, Hooper and Musgrove 1997) that the resolution process (from raw transducer outputs to velocity components) equates non-dimensionalized pressure ratios (obtained from individual probe transducer measurements) to relevant ratios obtained in static calibration under known orientations relative to a freestream jet (the process is facilitated via lookup table). A relevant calibration method for the Cobra probe is presented below (Chen et al. 2000); the calibration method employed for the ECA probe is known to be an extension of this method<sup>10</sup>:

<sup>9</sup>Information was not available from the device manufacturer.

<sup>10</sup>It is reported in TFI Device Control that the calibration employed is a single-zone calibration.

$$\begin{aligned}
 C_{P-pitch} &= (P_2 - 0.5(P_1 + P_3))/(P_0 - \bar{P}) \\
 C_{P-yaw} &= (P_1 - P_3)/(P_0 - \bar{P}) \\
 C_{P-static} &= (\bar{P} - P_s)/(P_0 - \bar{P}) \\
 C_{P-total} &= (P_0 - P_t)/(P_0 - \bar{P})
 \end{aligned}
 \tag{D.4}$$

In equation D.4,  $P_0$  though  $P_3$  are pressures at each individual measuring surface as per figure D.5,  $P_t$  and  $P_s$  are total and static pressures, and  $\bar{P} = (P_1 + P_2 + P_3)/3$ .

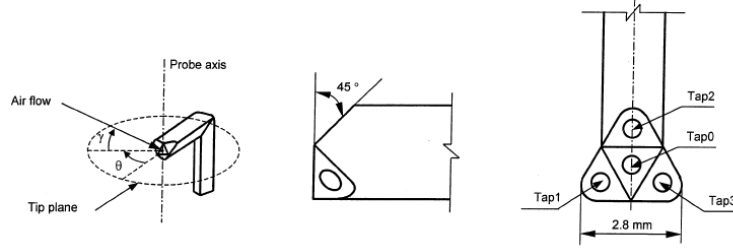


Figure D.5: Pressure tap identification on early-generation Cobra probe after Chen et al. (2000)

Alternately, if the probe were instead calibrated using multi-zone approaches as alluded by Viono (2005), then a relevant set of constants as per the Cobra probe would be as such:

$$\begin{aligned}
 X_1 &= (P_i - P_j)/(P_0 - P_k) \\
 X_2 &= (P_j - P_k)/(P_0 - P_k) \\
 X_d &= P_d/(P_0 - P_k) \\
 X_t &= (P_t - P_0)/(P_0 - P_k)
 \end{aligned}
 \tag{D.5}$$

Where in equation D.5  $P_0$  is the centre hole pressure,  $P_k$  is the minimum of the outer hole pressures,  $P_i$  and  $P_j$  are determined cyclically from the remaining outer hole pressures.  $P_d$  is the dynamic pressure and  $P_t$  the total pressure.

A sample set of data relating dependent and independent variables is provided in figure D.6 Whilst the exact implementation utilised in the ECA probe is unknown - and would need to account for 13 unique pressure values - the theory within Cobra probe implementations is assumed relevant.

Alternately, the multizone approach adopted by Hooper and Musgrove presents alternate characteristic data for a zone (Chen et al. 2000); essentially all values (pitch, yaw,  $X_t$  and  $X_d$ ) remain similarly dependent on  $X_1$  and  $X_2$ .

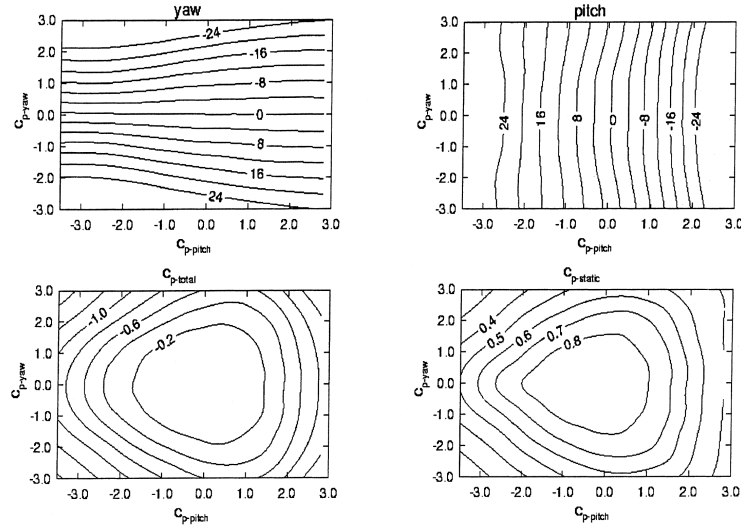


Figure D.6: Contour plotted relationships between independent pressure ratios and dependant, resolved variables for Cobra probe single-zone calibration surface after Chen et al. (2000)

#### D.4.2.2 Experimental identification of phase lag

It is therefore theoretically possible to simply identify the presence or absence of compensation for multiplexer-induced phase lag via use of a known dynamic input in place of relevant pressure data obtained from the ECA probe. The ECA probe is substituted for an oscillating, analogue voltage source of known frequency:

- If the source were connected in parallel to all channels, in accordance with D.4 or D.5 all numerators and denominators will equal zero, giving rise to a "divide by zero" error should multiplexer induced phase lag compensation exist.
- A more elegant approach requiring less experimental overhead would be to connect the source to two channels only and thus simulate a pitch or yaw condition. If one assumes a pressure variable with time  $x$  applied to the centre hole and the hole located in line with the pitch axis only (e.g. from D.5, tap 2), then:

For the single zone method:

$$\begin{aligned} C_{P-pitch} &= 3/2 \\ C_{P-yaw} &= 0 \end{aligned} \tag{D.6}$$



Similarly, for the multi-zone method (assuming  $P_i$  to be tap 2):

$$\begin{aligned} X_1 &= 1 \\ X_2 &= 0 \end{aligned} \tag{D.7}$$

(For the above to hold in the multizone case, the source would need to be above zero at all times e.g. a DC offset greater than the amplitude). Both solutions (refer D.6 and Chen et al for calibration surface plots for singlezone and multizone surfaces respectively) yield solutions with zero yaw, constant pitch and positive dynamic pressure, irrespective of the magnitude of  $x$ . Resolved velocity should vary in time with proportion to  $x$  (appropriately scaled to a pressure value); a spectral peak should be noted at the source frequency.

The absence of such compensation would reveal a difference in magnitude between  $P_0$  and  $P_2$  (or  $P_i$ ) varying in time, with resultant oscillations pitch and resolved pressures.

Relevant ratio definitions in equations D.4 and D.5 are relevant to the Cobra probe only. It is not unreasonable to assume that similar logic is applied in deriving appropriate ratios for the ECA probe<sup>11</sup>. Whilst static calibration would reveal four or five pressure taps with positive pressure for any flow angularity with the practical range of acceptance, the method used to resolve pressure and angularity remains a ratio of surface pressure<sup>12</sup>. Thus application of the above source to two or more pressure taps should yield oscillating velocity with a constant flow angularity.

#### D.4.2.3 Experimental results

This experiment was duly implemented using a signal generator, connected to a breakout board interfacing the data acquisition card, with Device Control configured to accept the ECA probe as an input device.

The ECA probe was connected with acquisition set to acquire individual analogue channels (e.g. the probe was not configured in software). Selectively changing pressures on each individual pressure tap allowed deconstruction of the channel map.

The probe was then connected with all channels pulled to the DAQ card ground source bar channels 0 and 5 (simulating a pitch-up orientation). A source waveform of 3V amplitude with offset above 3V+DC (without exceeding 10V peak) was verified using an oscilloscope. Initial testing revealed the following items apparent:

- Device Control supported and demonstrated sensitivity to the use of calibration files with

---

<sup>11</sup>These remain undisclosed in open literature.

<sup>12</sup>This reveals another possibility in the calibration method; the ratios employed may focus on ratios between four or five unique taps only. The exact taps used could be determined by the tap with highest instantaneous pressure, as it would be that best oriented to (e.g. closest to perpendicular) to the net flow direction.

unique frequency response characteristics per tube; testing with (supplied)  $0\mu\text{s}$ ,  $5\mu\text{s}$ , and others to  $100\mu\text{s}$  interchannel delay revealed differences in resolved results.

- The amplitude ratio cutoff of 0.4 (effective from some 823Hz) was ineffective in Device Control's ECA probe support. Data sets pertinent to this thesis therefore necessitated post-processing to remove higher frequency components.
- Use of the Nyquist theorem to determine sampling frequency proved insufficient; whilst adherence allowed identification of the presence of relevant frequency content, it did not allow for accurate digitisation at higher frequencies.

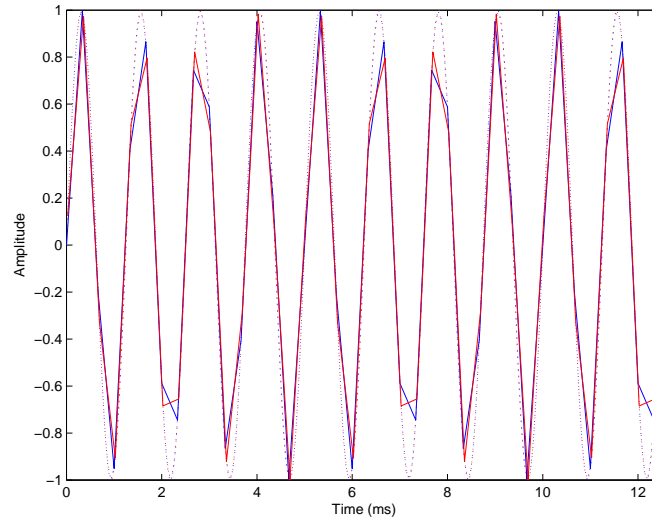


Figure D.7: Effect of digitisation of 800Hz sine wave on channels 0 and 5 with  $F_s$  of 3kHz (solid) and 15kHz (simulated interchannel delay of  $5\mu\text{s}$ )

Figure D.7 compares simulations of an 800Hz sine wave input digitised at 3kHz (the maximum frequency of the supplied calibration data) and 15kHz (close to the DAQ card's maximum aggregate sampling rate). The lower sampling rate is poorer at capturing the full amplitude of the waveform being digitised and allows for significant error particularly near maximum amplitude between past-shifted input channels; these errors are expectedly periodic. Phase shifting of input data cannot correct as much (nor can amplitude response adjustment correct such periodic phenomena); were such data used to resolve the input waveforms to a series of points in time and space, the resolved, dependent output would not fully reflect its input. This is thus alleviated (but not eliminated) by sampling at higher frequency. 15kHz sampling is thus used herein (it should be noted that the interchannel delay remains unchanged despite the higher sampling frequency, thus any effects pertinent to the delay remain unchanged).

Errors relevant to digitisation (e.g. noise, resolution, etc) are immediately apparent with a 1Hz input waveform (figure D.8). Whilst pitch is relatively constant and the velocity well resolved,

noise in the resolved signal increases. Slightly better performance with  $5\mu\text{s}$  included phase delay just observable in the general trend of the resolved pitch output.

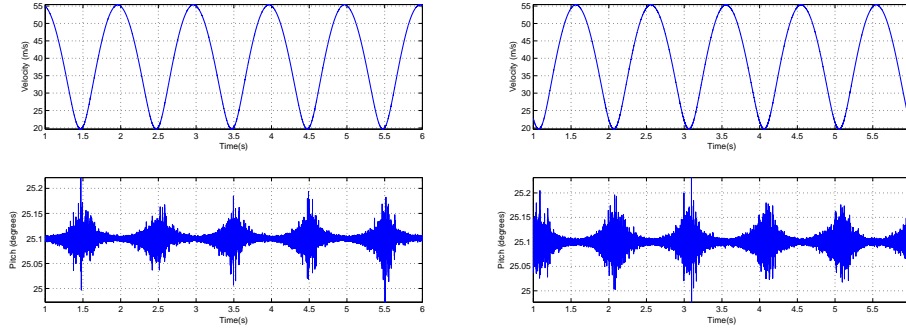


Figure D.8: Resolved ECA probe data for 1Hz reference input signal applied simultaneously on channels 0 and 5 with  $0\mu\text{s}$  (left) and  $5\mu\text{s}$  phase delay in dynamic calibration

System performance with included phase delay is better defined with an order-of-magnitude increase in source frequency (figure D.9) to 10Hz. Whilst similar noise behaviour is identifiable in the  $5\mu\text{s}$  inclusive plot,. Changing pressure ratios in time resolve similarly oscillating pitch values; where the phase lag is not compensated for, the pitch gradient is positive about the minima and otherwise negative. With  $5\mu\text{s}$  delay some noise is noted about the minima. It can be surmised that:

- It is clearly evident that no phase lag compensation is evident in the supplied configuration.
- Whilst mean trends appear identical, the addition of  $5\mu\text{s}$  phase lag between channels in calibration data gives definitively more favourable dynamic characteristics. Accuracy is also improved.
- There is behaviour of interest at low source amplitudes; the estimated and resolved pitch time history with phase lag compensation shows increased noise towards the input signal minima (resolved in D.9 as net velocity). The phase lag uncompensated signal however undergoes a regular reversal of gradient in the same region, giving rise to pitch time history oscillating in time with the source frequency. The nature of this phenomenon - a direct result of differences in estimated pressure magnitudes between channels - is speculated to be a function of:
  - The unknown nature of the dimensionless ratios used to ascertain flow pressure and angularity components,
  - Their evident interaction with phase lag effects (in the uncompensated case), and,
  - The inability of the IFT method (when working with digitised cosine sums, refer figure D.4) to exactly, definitively compensate for phase lag effects, resulting in amplitude discrepancies between channels. These are expected to increase with increasing frequency.

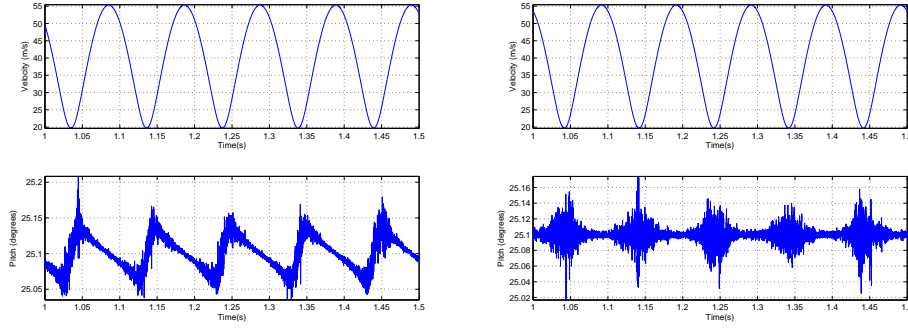


Figure D.9: Resolved ECA probe data for 10Hz reference input signal applied simultaneously on channels 0 and 5 with  $0\mu\text{s}$  (left) and  $5\mu\text{s}$  phase delay in dynamic calibration

The above trends are similarly noted at frequencies an order of magnitude greater again e.g. 100Hz (figure D.10). As frequency increased, the difference between adjacent samples values without phase lag compensation yielded a predictable increase in pitch variance.

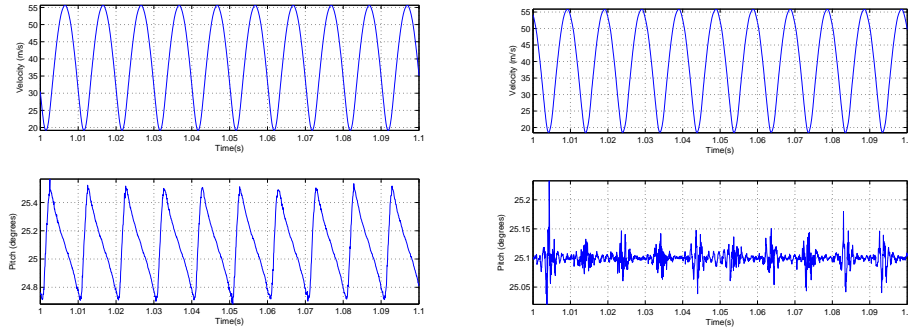


Figure D.10: Resolved ECA probe data for 100Hz reference input signal applied simultaneously on channels 0 and 5 with  $0\mu\text{s}$  (left) and  $5\mu\text{s}$  phase delay in dynamic calibration

## D.5 Conclusions

Cobra probe calibrations were accepted on basis of their being the possibility to apply sampling settings to replicate the calibration conditions, giving favourable results using the supplier multi-hole calibration.

The ECA probe single-point calibration was reverse engineered and a script written to include a programmable phase lag between channels reflecting the sampling conditions employed. Whilst a lack of in-situ dynamic calibration tools prevented verification of the amplitude response employed being suitable for all channels, theoretical time-dependent angularity associated with the single-point calibration supplied was successfully eliminated.

## Appendix E

# $\alpha = 35^\circ$ reference wake data after Lienhart et al

### E.1 Problem definition

Figure E.1 presents flow field data adapted from reference experiments undertaken by Lienhart et al. (2000; 2002) (a set of results were taken for both  $\alpha = 25^\circ$  and  $\alpha = 35^\circ$  cases) using non-intrusive LDA methods. In lieu of a significant body of research using the post-critical form (relative to that available for the pre-critical), these data are presented as a reference for model-in-isolation experiments conducted as part of this research.

The data are presented in a manner consistent with that used for experiments conducted throughout. Figure 3.14 (page 112) provides the relevant comparison.

#### E.1.1 Relevance in context of the research question

It should be stressed that an exacting replication of reference flow field data is not essential to the research questions proposed (essentially, to investigate the aerodynamic performance of platoons in longitudinal and laterally spaced arrangements, and how this changes with respect to pre and post-critical leading model afterbody geometries).

It is only essential that the post-critical ( $\alpha = 35^\circ$ ) model is capable of replicating post-critical behaviours. Experiments undertaken throughout substantiate this ability by force data, qualitative surface shear and flow field visualisations and surface pressure data. This section is simply presented to better deconstruct flow field data in the context of a given, prominent reference set, for comparatively little research exists detailing the aerodynamic performance - particularly

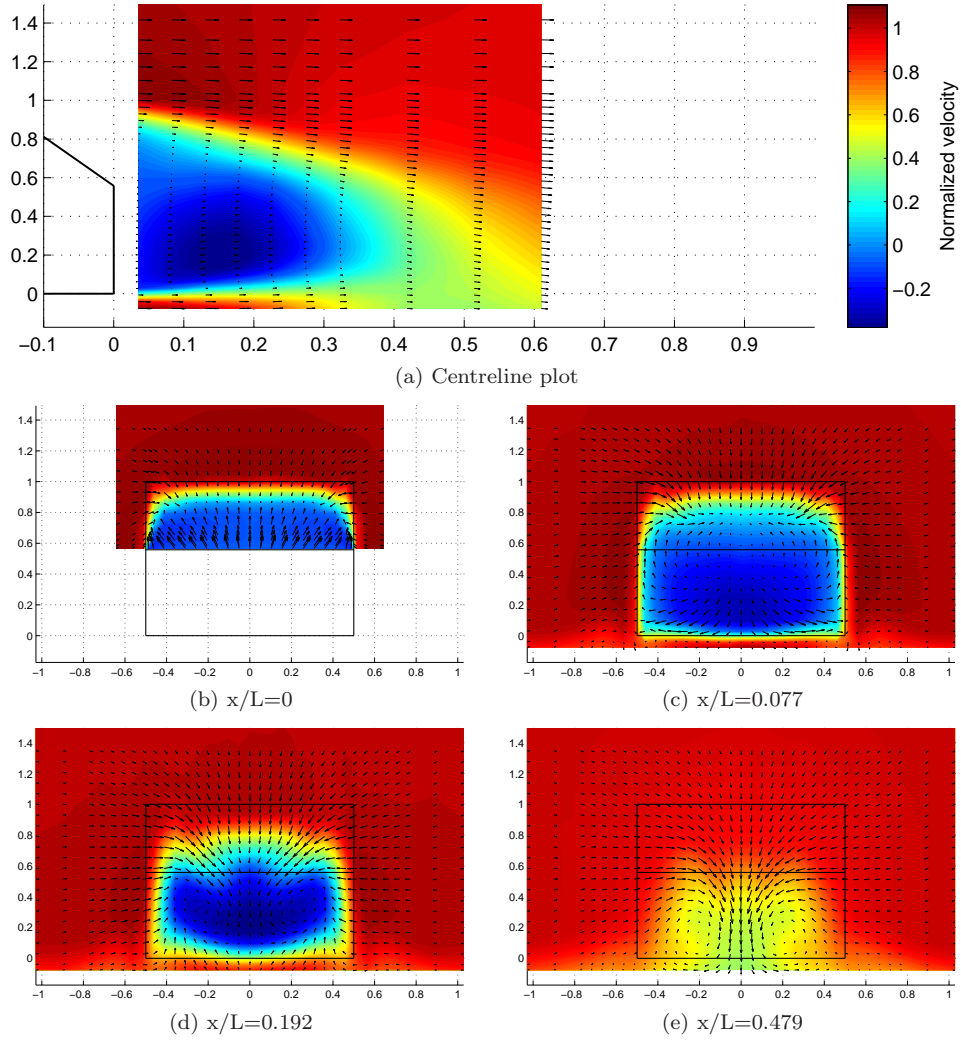


Figure E.1: Normalised velocity contours of LDA results 35° adapted from Lienhart et al  
Lienhart et al. (2002)

the flow field - of the post-critical  $\alpha = 35^\circ$  case.

## E.2 Key experimental setup differences

Key differences between Lienhart et al's experiments and those undertaken in this research include:

- *Model scale:* the model employed by Lienhart et al was 33% larger, with commensurately larger ground clearance.
- *Higher  $Re$ :* a  $Re$  of  $3.2 \times 10^6$  was used (as opposed to  $1.8 \times 10^6$  used throughout).
- *Smaller boundary layer:*  $\delta_{99} = 30\text{mm}$ , 80% of ground clearance, at  $\frac{x}{L} = -0.38$  upstream of the model leading edge (as opposed to  $\delta_{99} = 100\text{mm}$  - some 267% of ground clearance - for the test section used throughout at the same location).
- *Lower freestream turbulence intensity:* an  $I_{uu} = 0.25\%$  was characteristic to the test section used (as opposed to  $I_{uu} = 1.8\%$  throughout)
- *Flow angularity/cross-plane pressure variances:* significant variances exist in the IWT, and are discussed in appendix A.1 (page 222).
- *Intrusiveness of flow field interrogation method:* a two-component LDA system was employed, being completely non-intrusive (as opposed to the pressure-based probe used throughout). The intrusiveness of the method used in research presented here cannot be quantified, and may bear significant effect on low-energy flows characteristic to the post-critical near wake.
- *Relative limitations of the measuring instrument employed:* the methods used by the ECA probe to discern highly turbulent flows close to it's noise floor - as are those in the near wake of the  $\alpha = 35^\circ$  case - are unknown. The manufacturer does not guarantee accuracy of data in highly turbulent ( $I_{uu,vv,ww} > 30\%$ ) flows (Pagliarella 2007); flows below 2m/s are truncated (see section 2.2.5.1, page 76). The traverse employed is based in the test section at  $x$  commensurate with the transverse plane acquired, and possesses bluff elements in construction (section 2.2.6, page 81).

## E.3 Key flowfield differences

Acquired data for the centreline plot compares favourably with that of the reference set, indicating the quasi-two-dimensional behaviours associated with shear layers from top/backlight and bottom/base edges are replicated faithfully. A unique separated region operating solely over the backlight - as per the pre-critical case and as would "grow" with increasing backlight angle - is not acquired. This indicates that axial vortices formed by the interaction of top and side shear

layers are not sufficiently strong to constrain flows over the top of the body and force reattachment over the backlight, which the correct, definitive behaviour for the post-critical case. This is further validated by surface pressure and qualitative surface and flow field visualisations presented throughout.

The far wake is dominated by a pair of counter-rotating axial vortices with cores at the projection of the base at approximately  $\frac{x}{L} = 0.5$ ; again, in good agreement with the reference data and within expectations.

Significant differences exist in transverse plane data within the near wake, however, which warrant further deconstruction, notably:

- The separated region closes further upstream away from the centreline
- The separated region does not appear to extend to the full extremities of the model projection, particularly at the base bottom edges
- The axial “C-pillar” vortices are more prominent further upstream, and influence the near wake to a greater degree away from the centreline
- The lower vortex pair formed at the the spanwise extremities of the bottom/base edge - present in the reference data - is not replicated
- The wake is affected by flow angularity

The most prevalent effect concerns the influence of the upper axial vortex pair. Despite lower  $Re$  potentially contributing to comparatively weaker separation shear layers and a commensurately smaller separated region, the presence of low pressure at the upper spanwise corners of the model surface (figure E.2b) indicates some form of local flow attachment in this region, commensurate with the influence of a local vortex. The base/backlight pressure distribution otherwise agrees favourably with that of Lienhart et al (figure E.2a), though the reference set does not include a similarly-located pressure tap at the backlight’s upper spanwise extremity<sup>1</sup>.

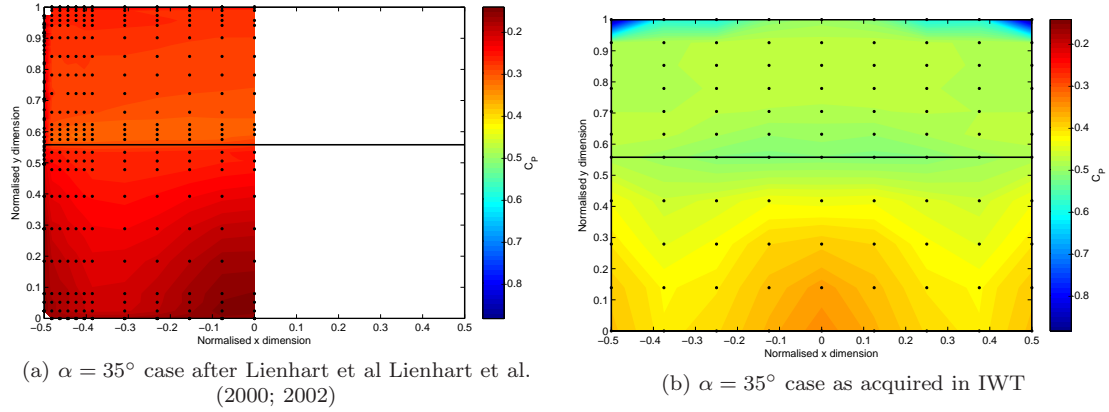
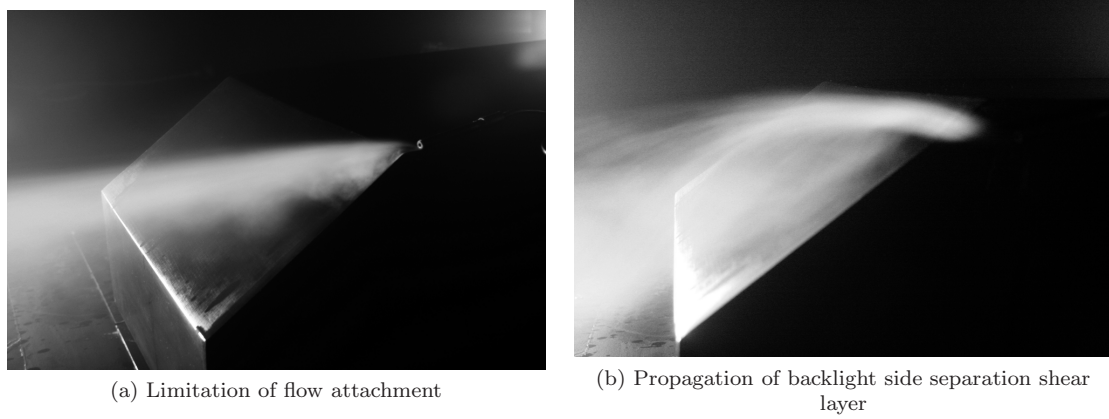
The presence of some form of flow attachment is substantiated by figure E.3, showing a limited local attachment and strong roll-up of the C-pillar separation shear layer.

A possibility existed whereby asymmetry in the IWT freestream were sufficiently severe to change the relative strengths of the top and side separation shear layers such that a stronger C-pillar axial vortex could be formed from one side, exacerbating flow asymmetry in the wake. To explore this further, the flow field in  $+y$  was interrogated at  $\frac{x}{L} = 0.125$ . The acquired half planes from either side were combined into a single data set, the result of which is presented in figure E.4,

---

<sup>1</sup>Whilst the distributions are agreeable - the key feature denoting favourable comparison - exact magnitudes are not. Methods used to calculate  $C_P$  in Lienhart et al’s data are unknown (a difference in reference static pressure is suggested). A small decrease in  $C_P$  is known for increased levels of turbulence intensity (Nakamura 1993), insufficient to justify the difference in magnitudes observed.



Figure E.2:  $C_P$  over backlight and base surfaces of  $\alpha = 35^\circ$  caseFigure E.3: Axial vortex formation and impingement in  $\alpha = 35^\circ$  case

where good agreement side-to-side is shown. The lack of significant flow angularity in Lienhart et al's data is obvious; though this does not impair the ability of the results presented to demonstrate flow characteristics relevant to the  $\alpha = 35^\circ$  case, the symmetry the model intends of time-averaged data cannot be replicated.

With the comparative high influence of the axial vortices confirmed on both sides, other aspects of the flow quality need to be examined. Turbulence properties, particularly, vary considerably:  $\leq 0.25\%$  intensity, scale unknown for Lienhart et al's experiments,  $1.8\%$  with length scale approximating model length<sup>2</sup> in the IWT. Two contributing factors to the unique wakes observed in research undertaken are identified:

- *Increased turbulence intensity:* The effect of increased turbulence intensity on sharp bluff-body leading edges is well known (discussed in section 1.2.2.2, page 12): increased turbulence

---

<sup>2</sup>See Appendix A.5.3, page 236

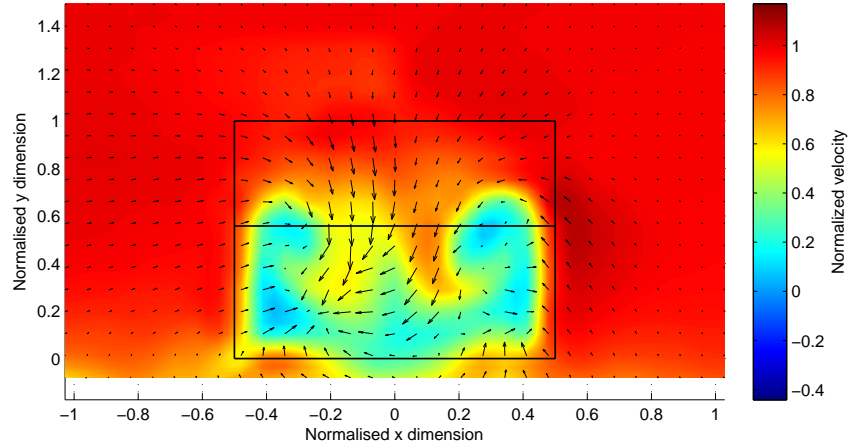


Figure E.4: Transverse plane acquired at  $\frac{x}{L} = 0.125$  behind  $\alpha = 35^\circ$  model

intensity associated with fine scale turbulence increases separation shear layer growth on bluff body leading edges, reducing the radius of curvature and promoting reattachment on streamwise surfaces (Gartshore in Bearman (1978) and Melbourne (1993)). Whilst relevant to the Ahmed model forebody, the effects of such behaviours at trailing edges is not as well explored and are possibly more difficult to quantify speculatively given already turbulent boundary layers approaching model afterbody edges<sup>3,4</sup>. Increased small-scale freestream turbulence, despite distortion by salient effects of the flow field, serves to increase mixing and entrainment of the shear layers in which it operates (Gartshore in Melbourne (1993)).

Certainly, where rear separation shear layers for the acquired data vis-à-vis those of Lienhart et al's reference set are concerned, the acquired data evidences decreased curvature of upper and side separation shear layers, essentially shifting axial vortex core location inboard, thus increasing their prominence in the near wake.

It is similarly not unreasonable to suggest that the unsteady flow attachment “bubble” witnessed in figure E.3a (corroborating the backlight upper corner low pressure region presented in figure E.2b) is a function of increased turbulence intensity: inertial forces being least for flows over the backlight upper corner extremities, the propensity to reattach over a short distance may be exacerbated by a higher level of turbulence in relevant shear layers causing sufficiently increased entrainment to give rise to local re-attachment.

Saathoff in Melbourne (1993) suggests the exceptionally low pressures observed underneath such bubbles to be caused by small vortices, created in the unsteady re-attachment process and convecting downstream. Whilst likely sufficiently small to be incapable of being

<sup>3</sup>See Vio (2005), proven during  $Re$  sensitivity tests for the  $\alpha_c$  case.

<sup>4</sup>It should also be appreciated that Gartshore's work - as presented in Melbourne (1993) - demonstrated that freestream turbulence effects on leading edge separation could be effectively triggered by turbulence applied along the stagnation streamline, negating the need for a large grid to generate homogenous, higher turbulence in the test section. Subsequent evolutions on this experiment explored similar themes of limited-depth forms. Flow field effects of increased small-scale freestream turbulence on afterbody separation are thus not commonly explored.

accurately measured by the pressure probe employed, such vortices may combine with the dominant C-pillar axial vortex, further strengthening it in the near wake.

- *The effect of large turbulence length scale:* length scales approximating key bluff body dimensions are known to interact with flow field in a manner affecting mean flows (Bearman and Morel in Watkins (1990), also Nakamura et al. (1988) and Melbourne (1993)) though the phenomena is limited to length scales approximating the distance between alternating shear layers, wherein turbulence length scales either promote resonant interaction (increasing vortex shedding) or can weaken two-dimensional shedding by weakening spanwise correlation<sup>5</sup>. Whilst shedding from upper and lower afterbody separation shear layers has been observed to operate in a quasi-two-dimensional manner by Ahmed et al. (1984) and Brunn and Nitsche (2001), the length scale in the IWT is considerably longer than model height (instead approximating model length). Therefore length scale is thought not to be a contributing factor.

In addition to the above factors, lower mass flow under the model - arising from reduced ground clearance and a larger boundary layer - is anticipated to give rise to a weaker separation shear layer, particularly also a “less defined” wake at the span extremities where the model supports limit flow and along the projection of which underbody momentum escapes through the side, rolling up to form small axial vortices from the bottom edge at the span extremities, demonstrated computationally by Krajnović and Davidson (2005). These effects are known to be even more prevalent with further underbody mass flow as afforded by the presence of a moving ground plane in Strachan et al. (2007). Experimental conditions throughout represent the other extreme; thus expectedly the separated region does not follow the projection of the base/bottom edge as “squarely” as for Lienhart’s reference data. The lower axial vortices observable in the reference data in figures E.1c and E.1d - despite a similar measurement resolution - are not observed in the experiments undertaken.

## E.4 Comparative limitation of acquisition methods

The limitations of the measurement device in the  $\alpha = 35^\circ$  case are notable given the especially bluff nature of the form (i.e. with a region of “dead” flow just downstream of the trailing edge). The especially low velocities in this region do not lend themselves to a device that truncates data below 2m/s ( $\frac{U}{U_\infty} = 0.067$ ). The minimum percentage of samples in the time record for a given data point for which, though legitimate measurement or truncation, zero-velocity (e.g.  $U = V = W = 0\text{m/s}$ ) samples were not recorded are:

- $\frac{x}{L} = 0$ : 85%
- $\frac{x}{L} = 0.0625$ : 74%

---

<sup>5</sup>These observations by Nakamura et al. (1988) are based on experiments where freestream turbulence was generated using large grids, which not only increased length scale, but increased  $I_{uu}$  well beyond the 1.8% observed in the IWT.

- $\frac{x}{L} = 0.125$ : 86%

A significant proportion of samples in the time records concerned are thus effectively “missing”, effectively skewing the time records calculated from them. These affected regions also feature high ( $> 30\%$ ) turbulence intensity. The ability of the ECA probe to acquire faithful data under such conditions - let alone to consider the effects of its own intrusive nature in the flow field - render near-wake acquisition for the  $\alpha = 35^\circ$  case to be compromised.

The effect of the traverse (constructed partially of bluff elements) being located in the test section, whilst not able to be quantified, cannot be negated. Most likely a compounding of flow angularity is anticipated. Given the limited range of the device, transverse planes exploring  $\pm y$  ranges required the traverse to be reinstalled on the other side of the test section; given existing angularity in the freestream a compound yawing effect on acquired data is anticipated.

## E.5 Conclusions

Differences in relevant freestream and test section characteristics are discussed, with known rationale agreeing favourably with the smaller wake and increased prominence of the dominant, axial vortices observed in transverse planes of the acquired data. Changes in ground clearance and boundary layer conditions similarly/expectedly limited exacting replication of flow conditions about the lower model base.

The far wake compares favorably. The effects of freestream angularity are noted.

The validity of near wake data in regions of high turbulence and/or low velocity are questionable owing to limitations of the device used to interrogate the flow field.

The key salient effect of the post-critical Ahmed model - a large, single separated region formed along the centreline and between upper and lower separation shear layers - is duly replicated. Data acquired for the  $\alpha = 35^\circ$  model therefore indicates the installation suitable for further experimentation in platooned configurations.

## Appendix F

### 2003 VFACTS data

During November 2004, the Federal Chamber of Automotive Industries (FCAI Australia) made available “VFACTS ’03” (FCAI 2003), containing vehicle sales data containing year to date (YTD) sale volumes per segment for the preceding year. The data in this document was contrasted by the author with available vehicle dimensional and mass data as made available on regional (Australian) vehicle manufacturer/distributor websites primarily to investigate the currency of the Ahmed model’s aspect ratio. These websites are referenced though can be considered current for the period 10-12 November, 2004.

The vehicle data pertains to the model cited in relevant sales volumes within the following limitations:

- Ground clearance data is not available.
- Where multiple variants of the same model exist, data were acquired for the “base model”.
- Where sales data cites an extremely low-volume make of vehicle (e.g. “Ferrari”, “Maserati”, “Morgan”, “Rolls-Royce”, etc), the most data were acquired for the most common model in consultation with local distributors.
- Where the vehicle model in question were superseded at the time of research, data for the applicable replacement model is used in lieu of any reliable references.
- Commercial vehicles are not represented, as very little width variance exists and height is generally limited by industry (load carrying) and legislative (maximum height) requirements.

As the data presented is a month short of an entire year’s data, data are reinterpreted into relevant portions (by percentage) of segments and into weighted averages of mass and dimensional properties. Data are split primarily into “Passenger vehicle” and “Sport Utility Vehicle (SUV)”

## F.1. DATA BY SEGMENT AND SUBSEGMENT

segments, each having a range of sub-segments. Tables F.1 and F.2 present the two major segment summaries, whilst tables F.3 through F.14 explore each sub-segment in greater detail.

It was concluded that within the passenger vehicle segment, the Ahmed model is wider than the majority of contemporary vehicles in all segments, particularly in smaller vehicle classes more traditionally associated with fastback geometries. The average is 20% lesser in width-to-height aspect ratio than the Ahmed model in “Light” and “People mover” sub-segments, otherwise <10% lesser. SUV’s proved notably more upright in aspect ratio, averaging less than 20% lesser in aspect ratio.

Contemporary, extensive research into Ahmed model aspect ratio sensitivity by Johnson (2005) revealed that within a wider range of aspect ratios than those encountered in the above research, Ahmed model mean and dynamic behaviours are generally preserved, with the critical geometry ( $\alpha_c$ ) shifting within  $5^\circ$  of the “original” model’s  $30^\circ$ . The interested reader is encouraged to review Johnson’s work in greater detail.

29.5% of all passenger vehicles sold in the YTD period cited were “hatchbacks” (fastbacks) of unknown backlight angle.

### F.1 Data by segment and subsegment

Subgroup	Sales YTD		Dimensions (mm) and mass (kg)					$\frac{W}{H}$ % Ahmed
	Total	%	Mass	Height	Width	Length	-	
Light	76716	13.04	1006	1495	1663	3820	1.11	79
Small	175651	29.85	1179	1450	1723	4325	1.19	88
Medium	47164	8.01	1398	1475	1789	4723	1.21	90
Large	203524	34.58	1616	1445	1839	4884	1.27	94
People Movers	11852	2.01	1692	1752	1825	4802	1.04	78
Sports	10175	1.73	1393	1369	1752	4363	1.28	93
Prestige	29167	4.96	1457	1448	1793	4636	1.24	92
Luxury	34262	5.82	1502	1409	1788	4599	1.27	89
<b>Totals and averages</b>	<b>588511</b>	<b>100</b>	<b>1372</b>	<b>1458</b>	<b>1770</b>	<b>4526</b>	<b>1.22</b>	<b>89</b>

Table F.1: Passenger

Subgroup	Sales YTD		Dimensions (mm) and mass (kg)					$\frac{W}{H}$ % Ahmed
	Total	%	Mass	Height	Width	Length	-	
SUV Compact	75062	49.85	1413	1669	1757	4343	1.05	76
SUV Medium	38220	25.38	2048	1838	1828	4745	1.00	73
SUV Large	25375	16.85	2460	1873	1936	4947	1.03	76
SUV Luxury	11921	7.92	2056	1745	1892	4713	1.09	80
<b>Totals and averages</b>	<b>150578</b>	<b>100</b>	<b>1802</b>	<b>1752</b>	<b>1816</b>	<b>4576</b>	<b>1.04</b>	<b>76</b>

Table F.2: SUV

Model	Form					Dimensions (mm) and mass (kg)				$\frac{W}{H}$	
	Sedan	Wagon	Hatch	Total	% segment	Mass	Height	Width	Length	-	% Ahmed
Citroen C3	0	0	908	908	1.18	1147	1520	1667	3850	1.10	81
Daewoo Kalos	1622	0	1740	3362	4.38	1030	1495	1670	3880	1.12	83
Daewoo Lanos	80	0	1205	1285	1.68	1109	1433	1679	4074	1.17	87
Daewoo Matiz	0	0	942	942	1.23	786	1485	1495	3497	1.01	75
Daihatsu Charade	0	0	450	450	0.59	720	1500	1475	3410	0.98	73
Daihatsu Cuore	0	0	177	177	0.23	735	1420	1475	3410	1.04	77
Daihatsu Sirion	0	0	2128	2128	2.77	965	1550	1665	3630	1.07	80
Daihatsu YRV	0	125	0	125	0.16	880	1550	1620	3765	1.05	77
Ford Ka	0	0	634	634	0.83	955	1400	1640	3660	1.17	87
Holden Barina	0	0	4764	4764	6.21	1041	1440	1646	3839	1.14	85
Honda Insight	0	0	6	6	0.01	827	1355	1695	3955	1.25	93
Honda Jazz	0	0	8501	8501	11.08	1026	1525	1675	3845	1.10	81
Hyundai Accent	1	0	9	10	0.01	1047	1395	1680	4215	1.20	89
Hyundai Getz	0	0	11141	11141	14.52	990	1495	1665	3810	1.11	82
Kia Rio	1866	0	5355	7221	9.41	1035	1420	1700	4240	1.20	89
Mazda 121	0	0	13	13	0.02	969	1500	1670	3800	1.11	82
Mazda2	0	0	4016	4016	5.23	1081	1540	1680	3926	1.09	81
Mitsubishi Mirage	0	0	6661	6661	8.68	1090	1550	1680	3870	1.08	80
Peugeot 206	0	0	1978	1978	2.58	1025	1428	1652	3835	1.16	86
Proton Satria	0	0	311	311	0.41	930	1360	1680	3990	1.24	91
Renault Clio	0	0	1228	1228	1.60	1035	1410	1640	3810	1.16	86
Smart City	226	0	0	226	0.29	990	1549	1515	2500	0.98	72
Suzuki Ignis	0	0	2115	2115	2.76	880	1540	1595	3615	1.04	77
Toyota Echo	3739	0	13247	16986	22.14	950	1510	1660	3640	1.10	81
Toyota Prius	155	0	137	292	0.38	1310	1490	1725	4445	1.16	86
Volkswagen Polo	0	0	1236	1236	1.61	1060	1465	1650	3897	1.13	83

Totals and averages	7689	125	68902	76716	100.00	1006	1495	1663	3820	1.11	79
---------------------	------	-----	-------	-------	--------	------	------	------	------	------	----

Table F.3: Light



Model	Form					Dimensions (mm) and mass (kg)					$\frac{W}{H}$ % Ahmed
	Sedan	Wagon	Hatch	Total	% segment	Mass	Height	Width	Length	-	
Citroen Xsara	0	0	175	175	0.10	1141	1405	1705	4188	1.21	90
Daewoo Lacetti	749	0	0	749	0.43	1223	1445	1725	4500	1.19	88
Daewoo Nubira	1028	451	0	1479	0.84	1189	1430	1700	4495	1.19	88
Ford Focus	4972	0	7530	12502	7.12	1295	1443	1840	4341	1.28	94
Ford Laser	119	0	250	369	0.21	1164	1410	1705	4250	1.21	90
Holden Astra	8035	0	18104	26139	14.88	1175	1425	1709	4252	1.20	89
Honda Civic	2811	0	940	3751	2.14	1208	1495	1695	4295	1.13	84
Hyundai Accent 1.6	0	0	4087	4087	2.33	1047	1395	1680	4215	1.20	89
Hyundai Elantra	4705	480	5443	10628	6.05	1233	1425	1720	4520	1.21	89
Kia Spectra	0	0	1779	1779	1.01	1145	1415	1720	4525	1.22	90
Mazda 323	8548	0	12445	20993	11.95	1205	1465	1755	4480	1.20	89
Mazda Premacy	0	0	332	332	0.19	1330	1600	1705	4295	1.07	79
Mitsubishi Lancer	17502	429	0	17931	10.21	1215	1430	1695	4595	1.19	88
Nissan Pulsar	16718	0	2254	18972	10.80	1190	1448	1706	4197	1.18	87
Peugeot 307	0	255	3607	3862	2.20	1216	1510	1746	4202	1.16	86
Proton Persona	0	0	147	147	0.08	995	1382	1690	4270	1.22	91
Proton Waja	167	0	0	167	0.10	1160	1420	1740	4465	1.23	91
Renault Megane	0	0	74	74	0.04	1265	1457	1777	4209	1.22	90
Subaru Impreza	4596	0	3055	7651	4.36	1295	1440	1740	4415	1.21	89
Suzuki Baleno	0	0	1	1	0.00	890	1395	1680	3900	1.20	89
Suzuki Liana	722	0	556	1278	0.73	1180	1550	1720	4230	1.11	82
Toyota Corolla	12902	3565	19661	36128	20.57	1060	1470	1695	4175	1.15	85
Volkswagen Golf	0	0	6457	6457	3.68	1240	1485	1759	4204	1.18	88
<b>Totals and averages</b>	<b>83574</b>	<b>5180</b>	<b>86897</b>	<b>175651</b>	<b>100.00</b>	<b>1179</b>	<b>1450</b>	<b>1723</b>	<b>4325</b>	<b>1.19</b>	<b>88</b>

Table F.4: Small

Model	Form					Dimensions (mm) and mass (kg)					$\frac{W}{H}$ % Ahmed
	Sedan	Wagon	Hatch	Total	% segment	Mass	Height	Width	Length	-	
Chrysler PT Cruiser	0	0	876	876	1.86	1412	1600	1704	4288	1.06	79
Daewoo Leganza	75	0	0	75	0.16	1407	1438	1778	4671	1.24	92
Daewoo Tacuma	0	0	251	251	0.53	1349	1580	1755	4305	1.11	82
Holden Vectra (4 cyl)	807	0	616	1423	3.02	1406	1460	1798	4596	1.23	91
Hyundai Sonata (4 cyl)	568	0	0	568	1.20	1474	1475	1832	4800	1.24	92
Mazda 626 (4 Cyl)	1	0	0	1	0.00	1251	1430	1710	4590	1.20	89
Mazda6	5262	746	6700	12708	26.94	1407	1435	1780	4670	1.24	92
Renault Scenic	0	990	0	990	2.10	1415	1620	2087	4259	1.29	95
Subaru Liberty	3582	1429	0	5011	10.62	1375	1425	1730	4665	1.21	90
Toyota Camry (4 cyl)	25251	10	0	25261	53.56	1395	1495	1795	4805	1.20	89
<b>Totals and averages</b>	<b>35546</b>	<b>3175</b>	<b>8443</b>	<b>47164</b>	<b>100.00</b>	<b>1398</b>	<b>1475</b>	<b>1789</b>	<b>4723</b>	<b>1.21</b>	<b>90</b>

Table F.5: Medium

Model	Form					Dimensions (mm) and mass (kg)					$\frac{W}{H}$ % Ahmed
	Sedan	Wagon	Hatch	Total	% segment	Mass	Height	Width	Length	-	
Ford Falcon	60397	12823	0	73220	35.98	1694	1444	1864	4916	1.29	96
Holden Commodore	68280	18273	0	86553	42.53	1568	1440	1842	4876	1.28	95
Holden Vectra V6	1	0	13	14	0.01	1521	1460	1798	4596	1.23	91
Hyundai Grandeur	75	0	0	75	0.04	1599	1420	1825	4865	1.29	95
Hyundai Sonata V6	653	0	0	653	0.32	1595	1475	1832	4800	1.24	92
Mitsubishi Magna V6	17621	3920	0	21541	10.58	1648	1435	1785	4860	1.24	92
Mitsubishi Verada	1955	170	0	2125	1.04	1586	1435	1785	4978	1.24	92
Toyota Avalon	6064	0	0	6064	2.98	1515	1455	1790	4855	1.23	91
Toyota Camry V6	13276	3	0	13279	6.52	1500	1495	1795	4805	1.20	89
<b>Totals and averages</b>	<b>168322</b>	<b>35189</b>	<b>13</b>	<b>203524</b>	<b>100.00</b>	<b>1616</b>	<b>1445</b>	<b>1839</b>	<b>4884</b>	<b>1.27</b>	<b>94</b>

Table F.6: Large

Model	Form					Dimensions (mm) and mass (kg)				-	$\frac{W}{H}$ % Ahmed
	Sedan	Wagon	Hatch	Total	% segment	Mass	Height	Width	Length		
Chrysler Voyager	0	1127	0	1127	9.51	1862	1804	1997	5094	1.11	82
Holden Zafira	0	0	1494	1494	12.61	1460	1634	1742	4317	1.07	79
Honda Odyssey	0	649	0	649	5.48	1610	1550	1800	4780	1.16	86
Hyundai Trajet	0	292	0	292	2.46	1741	1710	1840	4695	1.08	80
Kia Carnival	0	2634	0	2634	22.22	1888	1805	1900	4925	1.05	78
Mazda MPV	0	580	0	580	4.89	1753	1830	1785	4807	0.98	72
Mitsubishi Nimbus	0	233	0	233	1.97	1525	1650	1775	4950	1.08	80
Mitsubishi Starwagon 4x2	0	411	0	411	3.47	1640	1855	1695	4665	0.91	68
Toyota Avensis	0	1253	0	1253	10.57	1500	1675	1760	4960	1.05	78
Toyota Tarago	0	2736	0	2736	23.08	1655	1780	1790	4780	1.01	74
Volkswagen Caravelle	0	325	0	325	2.74	1820	1920	1840	4789	0.96	71
Volkswagen Kombi	0	118	0	118	1.00	1670	1940	1840	4789	0.95	70
<b>Totals and averages</b>	<b>0</b>	<b>10358</b>	<b>1494</b>	<b>11852</b>	<b>100.00</b>	<b>1692</b>	<b>1752</b>	<b>1825</b>	<b>4802</b>	<b>1.04</b>	<b>78</b>

Table F.7: People Movers

Model	Form					Dimensions (mm) and mass (kg)				$\frac{W}{H}$	
	Sedan	Wagon	Hatch	Total	% segment	Mass	Height	Width	Length	-	% Ahmed
Alfa Romeo GTV 2.0	23	0	0	23	0.23	1370	1318	1780	4285	1.35	100
Alfa Romeo Spider	199	0	0	199	1.96	1370	1315	1776	4299	1.35	100
Citroen Xsara Coupe	154	0	0	154	1.51	1134	1405	1705	4188	1.21	90
Daihatsu Copen	144	0	0	144	1.42	830	1260	1475	3395	1.17	87
Ford Cougar	83	0	0	83	0.82	1441	1325	1780	4699	1.34	99
Ford Mustang	135	0	0	135	1.33	1617	1359	1965	4661	1.45	107
Holden Astra Convertible	2470	0	0	2470	24.28	1393	1390	1709	4266	1.23	91
Holden Monaro	2889	0	0	2889	28.39	1696	1397	1841	4798	1.32	98
Honda Integra	0	0	922	922	9.06	1230	1395	1725	4400	1.24	92
Honda Prelude	3	0	0	3	0.03	1379	1316	1753	4521	1.33	99
Hyundai Tiburon	410	0	0	410	4.03	1375	1330	1760	4395	1.32	98
Mazda MX5	540	0	0	540	5.31	1102	1225	1680	3975	1.37	102
MG MGF	5	0	0	5	0.05	1060	1270	1780	3910	1.40	104
MG TF	216	0	0	216	2.12	1165	1263	1807	3943	1.43	106
Nissan 200SX	73	0	0	73	0.72	1284	1285	1695	4445	1.32	98
Peugeot 206 Convertible	859	0	0	859	8.44	1159	1373	1673	3835	1.22	90
Peugeot 306 Convertible	49	0	0	49	0.48	1474	1424	1759	4347	1.24	91
Renault Megane	155	0	0	155	1.52	1265	1457	1777	4209	1.22	90
Smart Roadster	29	0	0	29	0.29	790	1192	1615	3427	1.35	100
Toyota Celica	0	0	445	445	4.37	1173	1315	1735	4335	1.32	98
Toyota MR2	161	0	0	161	1.58	1028	1240	1695	3895	1.37	101
VW Beetle Cabrio	201	0	0	201	1.98	1324	1502	1724	4081	1.15	85
VW Golf Cabriolet	10	0	0	10	0.10	1225	1422	1694	4074	1.19	88
<b>Totals and averages</b>	<b>8808</b>	<b>0</b>	<b>1367</b>	<b>10175</b>	<b>100.00</b>	<b>1393</b>	<b>1369</b>	<b>1752</b>	<b>4363</b>	<b>1.28</b>	<b>93</b>

Table F.8: Sports

Model	Form					Dimensions (mm) and mass (kg)				$\frac{W}{H}$	
	Sedan	Wagon	Hatch	Total	% segment	Mass	Height	Width	Length	-	% Ahmed
Alfa Romeo 147	0	0	942	942	3.23	1360	1412	1764	4213	1.25	92
Alfa Romeo 156 2.0	568	52	0	620	2.13	1285	1430	1743	4435	1.22	90
Audi A3	0	0	643	643	2.20	1370	1421	1765	4203	1.24	92
Audi A4 2.0	1069	202	0	1271	4.36	1400	1428	1772	4586	1.24	92
BMW Compact	0	0	820	820	2.81	1320	1421	1817	4520	1.28	95
Citroen C5	660	116	0	776	2.66	1419	1476	1770	4617	1.20	89
Ford Fairlane	2389	0	0	2389	8.19	1808	1444	1862	5153	1.29	95
Holden Statesman	4363	0	0	4363	14.96	1707	1444	1847	5193	1.28	95
Holden Vectra CDX	0	0	1390	1390	4.77	1527	1460	1798	4596	1.23	91
Honda Accord	6204	0	0	6204	21.27	1360	1445	1760	4675	1.22	90
Lexus IS200	1016	0	0	1016	3.48	1425	1420	1725	4400	1.21	90
Mercedes-Benz A-Class	0	0	919	919	3.15	1270	1595	1764	3838	1.11	82
MINI Cooper	0	0	1633	1633	5.60	1150	1408	1925	3635	1.37	101
Nissan Maxima	1283	0	0	1283	4.40	1475	1475	1765	4890	1.20	89
Peugeot 406	348	73	0	421	1.44	1573	1455	1811	4676	1.24	92
Renault Laguna	326	140	0	466	1.60	1431	1429	1783	4576	1.25	92
Saab 93	952	0	0	952	3.26	1505	1466	1762	4635	1.20	89
Volkswagen Bora	1050	0	0	1050	3.60	1249	1446	1735	4376	1.20	89
Volkswagen New Beetle	540	0	0	540	1.85	1231	1498	1724	4081	1.15	85
Volkswagen Passat	845	129	0	974	3.34	1476	1462	1746	4703	1.19	88
Volvo S40	298	0	0	298	1.02	1425	1452	1770	4468	1.22	90
Volvo V40	0	197	0	197	0.68	1340	1413	1720	4483	1.22	90
<b>Totals and averages</b>	<b>21911</b>	<b>909</b>	<b>6347</b>	<b>29167</b>	<b>100.00</b>	<b>1457</b>	<b>1448</b>	<b>1793</b>	<b>4636</b>	<b>1.24</b>	<b>92</b>

Table F.9: Prestige

Model	Form					Dimensions (mm) and mass (kg)				$\frac{W}{H}$	
	Sedan	Wagon	Hatch	Total	% segment	Mass	Height	Width	Length	-	% Ahmed
Alfa Romeo 156	181	0	0	181	0.53	1320	1430	1743	4435	1.22	90
Alfa Romeo 166 3.0	28	0	0	28	0.08	1550	1416	1800	4720	1.27	94
Alfa Romeo GTV 3.0	13	0	0	13	0.04	1415	1318	1780	4285	1.35	100
Audi A4	1158	4	0	1162	3.39	1400	1428	1772	4586	1.24	92
Audi A6	298	6	0	304	0.89	1555	1459	1855	4916	1.27	94
Audi A8	66	0	0	66	0.19	1790	1438	1880	5194	1.31	97
Audi Convertible	325	0	0	325	0.95	1560	1391	1777	4573	1.28	95
Audi S3	0	0	75	75	0.22	1420	1415	1763	4159	1.25	92
Audi TT	395	0	0	395	1.15	1475	1348	1764	4041	1.31	97
Bentley	31	0	0	31	0.09	2655	1515	1932	5640	1.28	94
BMW 3-Series	4942	222	0	5164	15.07	1320	1421	1817	4520	1.28	95
BMW 3-Series Convertible	678	0	0	678	1.98	1575	1372	1757	4488	1.28	95
BMW 3-Series Coupe	1717	0	0	1717	5.01	1408	1369	1757	4488	1.28	95
BMW 5-Series	1201	34	0	1235	3.60	1565	1468	1846	4841	1.26	93
BMW 7-Series	392	0	0	392	1.14	2038	1491	1902	5039	1.28	94
BMW Z4	461	0	0	461	1.35	1275	1299	1781	4091	1.37	102
Chrysler Viper	6	0	0	6	0.02	1560	1118	1923	4475	1.72	127
Ferrari	73	0	0	73	0.21	1450	1214	1923	4512	1.58	117
Ford LTD	146	0	0	146	0.43	1808	1444	1862	5153	1.29	95
Holden Caprice	1061	0	0	1061	3.10	1750	1444	1847	5193	1.28	95
Honda Legend	15	0	0	15	0.04	1645	1435	1810	4980	1.26	93
Honda NSX	2	0	0	2	0.01	1420	1170	1810	4430	1.55	115
Honda S2000	79	0	0	79	0.23	1255	1285	1750	4145	1.36	101
Jaguar S-Type	314	0	0	314	0.92	1620	1444	1819	4861	1.26	93
Jaguar XJ SERIES	142	0	0	142	0.41	1545	1448	1860	5090	1.28	95
Jaguar XK8	47	0	0	47	0.14	1735	1296	2015	4760	1.55	115

Jaguar X-Type	930	0	0	930	2.71	1485	1392	1782	4672	1.28	95
Lamborghini	8	0	0	8	0.02	1650	1135	2045	4580	1.80	133
Lexus ES300	496	0	0	496	1.45	1570	1455	1810	4855	1.24	92
Lexus GS300	135	0	0	135	0.39	1620	1430	1820	4825	1.27	94
Lexus IS300	391	0	0	391	1.14	1528	1420	1725	4400	1.21	90
Lexus LS	185	0	0	185	0.54	1870	1490	1830	5025	1.23	91
Lexus SC430	118	0	0	118	0.34	1755	1370	1825	4515	1.33	99
Lotus Elise	50	0	0	50	0.15	812	1143	1719	3785	1.50	111
Maserati	60	0	0	60	0.18	1660	1305	1820	4510	1.39	103
Mazda RX8	949	0	0	949	2.77	1359	1340	1770	4435	1.32	98
M-Benz C-Class Sports Coupe	1235	0	0	1235	3.60	1480	1406	1728	4343	1.23	91
Mercedes-Benz C-Class	4544	164	0	4708	13.74	1400	1426	1728	4526	1.21	90
Mercedes-Benz CL-Class	53	0	0	53	0.15	2179	1407	1857	4989	1.32	98
Mercedes-Benz CLK-Class	1952	0	0	1952	5.70	1665	1413	1740	4643	1.23	91
Mercedes-Benz E-Class	2702	85	0	2787	8.13	1680	1449	1822	4818	1.26	93
Mercedes-Benz S-Class	427	0	0	427	1.25	1770	1444	1855	5038	1.28	95
Mercedes-Benz SL-Class	367	0	0	367	1.07	1845	1298	1815	4535	1.40	104
Mercedes-Benz SLK-Class	184	0	0	184	0.54	1465	1298	1788	4082	1.38	102
MG ZT	147	21	0	168	0.49	1520	1410	1780	4740	1.26	93
Morgan	3	0	0	3	0.01	868	1290	1500	3890	1.16	86
Nissan 350Z	1662	0	0	1662	4.85	1466	1320	1815	4314	1.38	102
Peugeot 406 Coupe	51	0	0	51	0.15	1455	1354	1780	4615	1.31	97
Peugeot 607	89	0	0	89	0.26	1644	1460	1826	4871	1.25	93
Porsche 911	417	0	0	417	1.22	1395	1310	1808	4427	1.38	102
Porsche 986	328	0	0	328	0.96	1295	1295	1801	4329	1.39	103
Rolls-Royce	1	0	0	1	0.00	2350	1515	1930	5390	1.27	94
Rover 75	240	36	0	276	0.81	1465	1427	1778	4745	1.25	92
Saab 93 Convertible	803	0	0	803	2.34	1630	1434	1762	4635	1.23	91

Saab 95	292	105	0	397	1.16	1643	1475	1792	4827	1.21	90
Volkswagen Passat W8	28	0	0	28	0.08	1787	1461	1746	4703	1.20	88
Volvo C70 Convertible	72	0	0	72	0.21	1510	1429	1817	4716	1.27	94
Volvo C70 Coupe	2	0	0	2	0.01	1464	1410	1820	4720	1.29	96
Volvo S60	559	0	0	559	1.63	1574	1428	1804	4576	1.26	94
Volvo S80	60	0	0	60	0.18	1675	1434	1832	4822	1.28	95
Volvo V70	0	199	0	199	0.58	1528	1488	1804	4710	1.21	90
Totals and averages	33311	876	75	34262	100.00	1502	1409	1788	4599	1.27	89

Table F.10: Luxury



Model	YTD	% segment	Dimensions (mm) and mass (kg)				-	$\frac{W}{H}$ % Ahmed
			Mass	Height	Width	Length		
Daihatsu Terios	1557	2.07	1000	1695	1555	3845	0.92	68
Ford Escape	3238	4.31	1527	1775	1825	4415	1.03	76
Holden Cruze	3371	4.49	993	1605	1640	3625	1.02	76
Honda CR-V	9736	12.97	1485	1710	1785	4610	1.04	77
Honda HR-V	0	0.00	1160	1590	1695	3995	1.07	79
Hyundai Santa Fe	2105	2.80	1664	1730	1845	4500	1.07	79
Kia Sportage	784	1.04	1688	1695	1800	4350	1.06	79
Land Rover Freelander	496	0.66	1598	1708	1809	4423	1.06	78
Mazda Tribute	6394	8.52	1585	1770	1800	4395	1.02	75
Mitsubishi Outlander	3011	4.01	1580	1680	1780	4550	1.06	78
Mitsubishi Pajero iO	175	0.23	1310	1700	1680	4010	0.99	73
Nissan X-Trail	12675	16.89	1445	1675	1765	4510	1.05	78
Renault Scenic 4X4	265	0.35	1465	1720	1775	4424	1.03	76
Subaru Forester	11780	15.69	1405	1590	1735	4485	1.09	81
Subaru Outback	5387	7.18	1430	1545	1770	4730	1.15	85
Suzuki Grand Vitara	1547	2.06	1280	1740	1780	3935	1.02	76
Suzuki Jimny	515	0.69	1050	1705	1600	3625	0.94	69
Toyota RAV4	12026	16.02	1295	1665	1735	3860	1.04	77
<b>Totals and averages</b>	<b>75062</b>	<b>100.00</b>	<b>1413</b>	<b>1669</b>	<b>1757</b>	<b>4343</b>	<b>1.05</b>	<b>76</b>

Table F.11: SUV Compact

Model	YTD	% segment	Dimensions (mm) and mass (kg)				-	$\frac{W}{H}$ % Ahmed
			Mass	Height	Width	Length		
Daewoo Korando	0	0.00	1860	1840	1841	4330	1.00	74
Daewoo Musso	0	0.00	1900	1735	1864	4656	1.07	80
Holden Adventra	78	0.20	1940	1654	1934	5047	1.17	87
Holden Frontera	137	0.36	1700	1765	1815	4670	1.03	76
Holden Jackaroo	1641	4.29	2190	1840	1845	4775	1.00	74
Hyundai Terracan	952	2.49	2109	1840	1860	4700	1.01	75
Jeep Cherokee	1888	4.94	1956	1817	1819	4496	1.00	74
Jeep Wrangler	723	1.89	1630	1748	1740	3883	1.00	74
Kia Sorento	1114	2.91	2027	1810	1863	4567	1.03	76
Land Rover Defender S/Wgn	334	0.87	2039	2035	1790	5152	0.88	65
Land Rover Discovery	2271	5.94	2017	1940	1895	4705	0.98	72
Mitsubishi Challenger	1590	4.16	1850	1735	1775	4610	1.02	76
Mitsubishi Pajero	7580	19.83	2220	1885	1895	4830	1.01	74
Nissan Pathfinder	2505	6.55	2191	1783	1850	4740	1.04	77
Suzuki XL-7	1388	3.63	1625	1740	1780	4700	1.02	76
Toyota Kluger	1380	3.61	2250	1680	1825	4690	1.09	80
Toyota Prado	14639	38.30	2000	1850	1790	4810	0.97	72
<b>Totals and averages</b>	<b>38220</b>	<b>100.00</b>	<b>2048</b>	<b>1838</b>	<b>1828</b>	<b>4745</b>	<b>1.00</b>	<b>73</b>

Table F.12: SUV Medium

Model	YTD	% segment	Dimensions (mm) and mass (kg)				-	$\frac{W}{H}$ % Ahmed
			Mass	Height	Width	Length		
Ford Explorer	1467	5.78	2139	1822	1871	4835	1.03	76
Nissan Patrol Wagon	9483	37.37	2450	1855	1940	5050	1.05	77
Toyota Landcruiser Wagon	14425	56.85	2500	1890	1940	4890	1.03	76
<b>Totals and averages</b>	<b>25375</b>	<b>100.00</b>	<b>2460</b>	<b>1873</b>	<b>1936</b>	<b>4947</b>	<b>1.03</b>	<b>76</b>

Table F.13: SUV Large

Model	YTD	% segment	Dimensions (mm) and mass (kg)				-	$\frac{W}{H}$ % Ahmed
			Mass	Height	Width	Length		
Audi Allroad	209	1.75	1810	1551	1852	4810	1.19	88
BMW X5	2506	21.02	2200	1707	1925	4667	1.13	83
Honda MDX	949	7.96	1980	1770	1955	4800	1.10	82
Jeep Grand Cherokee	1778	14.91	1854	1805	1858	4611	1.03	76
Land Rover Range Rover	644	5.40	2440	1863	2009	4950	1.08	80
Lexus LX470	478	4.01	2525	1850	1940	4890	1.05	78
Lexus RX330	1671	14.02	1875	1720	1845	4740	1.07	79
Mercedes-Benz M-Class	1628	13.66	2090	1807	1833	4587	1.01	75
Porsche Cayenne	442	3.71	2355	1699	1928	4786	1.13	84
Volkswagen Touareg	311	2.61	2235	1726	1925	4754	1.12	83
Volvo XC70	683	5.73	1655	1488	1860	4733	1.25	93
Volvo XC90	622	5.22	2037	1784	1898	4798	1.06	79
<b>Totals and averages</b>	<b>11921</b>	<b>100.00</b>	<b>2056</b>	<b>1745</b>	<b>1892</b>	<b>4713</b>	<b>1.09</b>	<b>80</b>

Table F.14: SUV Luxury

# Bibliography

- Abdel Gawad, A. (2001). Aerodynamics of vehicles driving through tunnels - experimental study of interference and drag reduction. Technical Report 2001-01-1044, Society of Automotive Engineers, Warrendale, PA.
- Ahmed, S. R. (1982). Influence of ground clearance on the aerodynamic characteristics of wake structure of a vehicle type body. Technical report, Institut für Entwurfsaerodynamik DFVLR (West Germany).
- Ahmed, S. R., Ramm, G., and Faltin, G. (1984). Some salient features of the time averaged ground vehicle wake. Technical Report 840300, Society of Automotive Engineers, Warrendale, PA.
- Al-Garni, A., Bernal, L., and Khalighi, B. (2004). Experimental investigation of the flow around a generic suv. Technical Report 2004-01-0228, Society of Automotive Engineers, Warrendale, PA.
- Anderson, J. (2001). *Fundamentals of Aerodynamics*. McGraw-Hill, New York.
- Azim, A. F. A. and Gawad, A. F. A. (2000). A flow visualization study of the aerodynamic interference between passenger cars. Technical Report 2000-10-0335, Society of Automotive Engineers, Warrendale, PA.
- Baker, C. J. (2001). Flow and dispersion in ground vehicle wakes. *Journal of Fluids and Structures*, 15:1031–1060.
- Baran, A. J. and Infield, D. G. (1995). Simulating atmospheric turbulence by synthetic realization of time series in relation to power spectra. *Journal of Sound and Vibration*, 180(4):627–635.
- Barkley, D., Gomes, M. G. M., and Henderson, R. (2002). Three-dimensional instability in flow over a backward-facing step. *Journal of Fluid Mechanics*, 473:167–190.
- Barlow, J. B., Rae, W. H., and Pope, A. (1999). *Low-Speed Wind Tunnel Testing*. John Wiley and Sons, Inc., third edition.
- Barnard, R. H. (1996). *Road Vehicle Aerodynamic Design: An Introduction*. Longman Publishing Group.
- Bearman, P. (1971). An investigation of the forces on flat plates normal to a turbulent flow. *Journal of Fluid Mechanics*, 46(1):177–198.

- Bearman, P. (1978). Some effects of free-stream turbulence and the presence of the ground on the flow around bluff bodies. *Aerodynamic drag mechanisms of bluff bodies and road vehicles*. Plenum, New York.
- Bearman, P. (1984). Some observations on road vehicle wakes. Technical Report 840301, Society of Automotive Engineers, Warrendale, PA.
- Bearman, P. (1997). Near wake flows behind two- and three- dimensional bluff bodies. *Journal of Wind Engineering and Industrial Aerodynamics*, 69-71:33–54.
- Bearman, P. and Owen, J. C. (1998). Reduction of bluff-body drag and suppression of vortex shedding by the introduction of wavy separation lines. *Journal of Fluids and Structures*, 12(1):123–130.
- Beaudoin, J. F., Cadot, O., Aider, J. L., Gosse, K., Paranthoën, P., Hamelin, B., Tissier, M., Allano, D., Mutabazi, I., Gonzales, M., et al. (2004). Cavitation as a complementary tool for automotive aerodynamics. *Experiments in Fluids*, 37(5):763–768.
- Beauvais, F. N., Tignor, S. C., and Turner, T. R. (1968). Problems of ground simulation in automotive aerodynamics. *SAE Papers 680*, 121.
- Behan, R. and Watmuff, J. (2006). Direct acoustic calibration of dynamic pressure measurement systems. Technical Report AL-2006-03, RMIT University (Centre of Expertise in Aerodynamic Loading).
- Bendat, J. S. and Piersol, A. G. (1993). *Engineering Applications of Correlation and Spectral Analysis*. Wiley-Interscience, 2nd edition.
- Bergh, H. and Tijdeman, H. (1965). Theoretical and experimental results for the dynamic response of pressure measuring systems. Technical Report NLR-TR F238, National Aerospace Laboratories (Netherlands).
- Blazewicz, A. M. (2008). *On the relation between fluid flow over bluff bodies and accompanying acoustic radiation*. PhD thesis, The University of Adelaide.
- Browand, F. and Hammache, M. (2004). The limits of drag behavior for two bluff bodies in tandem. Technical Report 2004-01-1145, Society of Automotive Engineers, Warrendale, PA.
- Brunn, A. and Nitsche, W. (2001). Drag reduction of an Ahmed car model by means of active separation control at the rear vehicle slant. *Numerical Flow Simulation II: Cnrs-Dfg Collaborative Research Programme, Results 1998-2000*.
- Brunn, A., Wassen, E., Sperber, D., Nitsche, W., and Thiele, F. (2007). Active drag control for a generic car model. *Notes on Numerical Fluids and Multidisciplinary Design*, 95:247–259.
- Buchheim, R., Deutenbach, K. R., and Luckoff, H. J. (1981). Necessity and premises for reducing the aerodynamic drag of future passenger car. Technical Report 810185, Society of Automotive Engineers, Warrendale, Pa.

- Buchheim, R. and Leie, B. (1982). The development of the Audi 100 - a new approach in aerodynamic passenger car design. In *Symposium Vehicle Aerodynamics*. Volkswagenwerk AG.
- Bull, M. K., Blazewicz, A. M., Pickles, J. M., and Bies, D. A. (1996). Interaction between a vortex wake and an immersed rectangular plate. *Experimental Thermal and Fluid Science*, 12:209–220.
- Burton, T., Sharpe, D., Jenkins, N., and Bossanyi, E. (2001). *Wind Energy Handbook*. John Wiley and Sons.
- Carlino, G., Cardano, D., and Cogotti, A. (2007). A new technique to measure the aerodynamic response of passenger cars by a continuous flow yawing. In *SAE 2007 Transactions Journal of Passenger Cars: Mechanical Systems*, number 2007-01-0902 in SAE special paper collections. Society of Automotive Engineers, Warrendale, PA.
- Carlino, G. and Cogotti, A. (2006). Simulation of transient phenomena with the turbulence generation system in the pininfarina wind tunnel. In *SAE 2006 Transactions Journal of Passenger Cars: Mechanical Systems*, number 2006-01-1031 in SAE special paper collections. Society of Automotive Engineers, Warrendale, PA.
- Cary, A. W. and Darmofal, D. L. (2003). Axisymmetric and non-axisymmetric initiation of vortex breakdown. In *RTO AVT Symposium on “Advanced Flow Management: Part A – Vortex Flows and High Angle of Attack for Military Vehicles”*.
- Chen, A. (1997). *Experimental investigation of transient aerodynamics in vehicle interactions*. PhD thesis, University of California, Berkeley.
- Chen, A. L., Hedrick, K., and Savas, O. (1997). Transient aerodynamics in vehicle interactions. Technical Report PATH research report UCB-ITS-PRR-97-50, Institute of Transportation Studies, California PATH, Berkeley CA.
- Chen, J., Haynes, B. S., and Fletcher, D. (2000). Cobra probe measurements of mean velocities, reynolds stresses and higher-order velocity correlations in pipe flow. *Experimental Thermal and Fluid Science*, 21:206–217.
- Cogotti, A. (1987). Flow-field surveys behind three squareback models using a new fourteen hole probe. Technical Report 870243, Society of Automotive Engineers, Warrendale, PA.
- Cogotti, A. (2004). Update on the Pininfarina “Turbulence Generation System” and its effects on the car aerodynamics and aeroacoustics. Technical Report 2004-01-0807, Society of Automotive Engineers, Warrendale, PA.
- Cooper, K. (1993). Bluff-body aerodynamics as applied to vehicles. *Journal of Wind Engineering and Industrial Aerodynamics*, 49:1–22.
- Cooper, K. R. and Watkins, S. (2007). The unsteady wind environment of road vehicles, part one: A review of the on-road turbulent wind environment. In *SAE 2007 Transactions Journal of Passenger Cars: Mechanical Systems*, number 2007-01-1236 in SAE special paper collections. Society of Automotive Engineers, Warrendale, PA.

- Crippa, S. and Rizzi, A. (2006). Numerical investigation of Reynolds number effects on a blunt leading-edge delta wing. *24th AIAA Applied Aerodynamics Conference*.
- Crossland, S. C., Sims-Williams, D. B., and Dominy, R. G. (2000). The reconstruction of bluff-body unsteady flow fields. *9th International Symposium on Flow Visualisation*.
- Cutts, C. (1994). Energy savings in formation flight of pink-footed geese. *Journal of Experimental Biology*, 189(1):251–261.
- Drouin, V., Giovannini, A., and Gillieron, P. (2002). Topology and characterization of the vortical near-wake flow over a simplified car model. *Proceedings of the bluff body wakes and vortex induced vibrations (BBVIV3) conference, Port-Douglas, Australia*.
- Eaton, J. and Johnston, J. (1981). A review of research on subsonic turbulent flow reattachment. *AIAA J*, 19(9):1093–1100.
- ESDU (1974). Characteristics of atmospheric turbulence bear the ground part I: Definitions and general information. Technical Report 74030, Engineering Science Data Unit (ESDU).
- ESDU (1985). Characteristics of atmospheric turbulence bear the ground part II: Single point data for strong winds (neutral atmosphere). Technical Report 85020, Engineering Science Data Unit (ESDU).
- FCAI (2003). VFACTS sales data, 2003 fiscal year, Federal Chamber of Automotive Industries (Australia). Spreadsheet.
- Fletcher, C. A. J. and Stewart, G. D. H. (1986). Bus drag reduction by the trapped vortex concept for a single bus and two busses in tandem. *Journal of Wind Engineering & Industrial Aerodynamics*, 24:143–168.
- Franck, G., Nigro, N., Storti, M., and D’Elia, J. (2007). Numerical simulation of the Ahmed vehicle model near-wake. *Int. J. Num. Meth. Fluids*.
- Fröhlich, J. and Rodi, W. (2004). LES of the flow around a circular cylinder of finite height. *International Journal of Heat and Fluid Flow*, 25(3):537–548.
- Garrone, A. and Costelli, A. (Year unknown). Contribution of car forebody and afterbody to drag resistance methodology and measurement technique in wind-tunnel. Technical report, Fiat Auto S.p.A.
- Gilhaus, A. M. and Renn, V. E. (1986). Drag and driving-stability-related aerodynamic forces and their interdependence—results of measurements on 3/8-scale basic car shapes. Technical Report 860211, Society of Automotive Engineers, Warrendale, PA.
- Gilholme, B. R., Saunders, J. W., and Mansour, R. (1998). The fluctuating pressure on the rear of a passenger vehicle. In *The Proceedings of the 13th Australasian Fluid Mechanics Conference*.
- Gilhome, B., Saunders, J., and Sheridan, J. (2001). Time averaged and unsteady near-wake analysis of cars. Technical Report 2001-01-1040, Society of Automotive Engineers, Warrendale, PA.

- Gillieron, P. and Chometon, F. (1999). Modelling of stationary three-dimensional detached airflows around an Ahmed reference body. *Third International Workshop on Vortex, ESAIM, Proceedings*, 7:173–182.
- Gillieron, P. and Noger, C. (2004). Contribution to the analysis of transient aerodynamic effects acting on vehicles. *SAE Transactions*, 113(6):893–900.
- Gosse, K., Patte-Rouland, B., Gonzalez, M., and Paranthoën, P. (2006). Scalar dispersion in the near wake of a simplified model car. *Experiments in Fluids*, 40(1):135–140.
- Guilmineau, E. and Chometon, F. (2007). Experimental and numerical analysis of the effect of side wind on a simplified car model. Technical Report 2007-01-0108, Society of Automotive Engineers, Warrendale, PA.
- Hall, R. and Chin, C. (2002). Vehicle sorting for platoon formation: Impacts on highway entry and throughput. Technical Report UCB-ITS-PRR-2002-7, Institute of Transportation Studies, California PATH, Berkeley CA.
- Hammache, M., Michaelian, M., and Browand, F. (2001). Aerodynamic forces on truck models, including two trucks in tandem. Technical Report UCB-ITS-PRR-2001-27, Institute of Transportation Studies, California PATH, Berkeley CA.
- Hangan, H. and Vickery, B. (1999). Buffeting of two-dimensional bluff bodies. *Journal of Wind Engineering & Industrial Aerodynamics*, 82(1-3):173–187.
- Hangan, H. and Vickery, B. J. (1997). A wake model for two-dimensional (sharp-edged) bluff bodies. *Journal of Wind Engineering & Industrial Aerodynamics*, 72:47–60.
- Havel, B., Hangan, H., and Martinuzzi, R. (2001). Buffeting for 2D and 3D sharp-edged bluff bodies. *Journal of Wind Engineering & Industrial Aerodynamics*, 89(14-15):1369–1381.
- Hinterberger, C., Garcia-Villalba, M., and Rodi, W. (2004). Large eddy simulation of flow around the Ahmed body. *The Aerodynamics of Heavy Vehicles: Trucks, Buses and Trains, Lecture Notes in Applied and Computational Mechanics*, 19.
- Hird, T. G. (1979). The design and construction of an industrial wind tunnel. Technical Report ECO/902, Royal Melbourne Institute of Technology.
- Hoerner, S. (1965). *Fluid-Dynamic Drag: Practical Information on Aerodynamic Drag and Hydrodynamic Resistance*. Hoerner, S. F.
- Holmes, J. D. and Lewis, R. E. (1987a). Optimisation of dynamic-pressure-measurement system, I: Single point measurements. *Journal of Wind Engineering and Industrial Aerodynamics*, 25:249–273.
- Holmes, J. D. and Lewis, R. E. (1987b). Optimisation of dynamic-pressure-measurement systems, II: Parallel tube-manifold systems. *Journal of Wind Engineering and Industrial Aerodynamics*, 25:275–290.



- Hong, P., Marcu, B., Browand, F., and Tucker, A. (1998). Drag forces experienced by two, full-scale vehicles at close spacing. Technical Report UCB-ITS-PRR-98-5, Institute of Transportation Studies, California PATH, Berkeley CA.
- Hooper, J. D. and Musgrove, A. R. (1997). Reynolds stress, mean velocity, and dynamic static pressure measurement by a four-hole pressure probe. *Experimental Thermal and Fluid Science*, 15:375–383.
- Hornung, H. and Perry, A. (1984). Some aspects of three-dimensional separation. 1-streamsurface bifurcations. *Zeitschrift fuer Flugwissenschaften und Weltraumforschung*, 8:77–87.
- Houghton, E. L. and Carpenter, P. W. (2003). *Aerodynamics for Engineering Students*. Butterworth-Heinemann.
- Howard, R. J. A., Lesieur, M., and Bieder, U. (2000). Structured and non-structured large eddy simulations of the Ahmed reference model. In *EUROMECH Colloquium 412 on LES of complex transitional and turbulent flows*.
- Hucho, W. H. (1978). The aerodynamic drag of cars - current understanding, unresolved problems, and future prospects. In Sovran, G., Morel, T., and Mason, W. T. J., editors, *Aerodynamic Drag Mechanisms of Bluff Bodies and Road Vehicles (proceedings of Symposium held at General Motors Research Laboratories, Warren, MI, 1976)*, pages 7–44. Plenum Press.
- Hucho, W. H. (1998). *Aerodynamics of Road Vehicles: from Fluid Mechanics to Vehicle Engineering*. Society of Automotive Engineers.
- Hucho, W. H., Janssen, L. J., and Schwartz, G. (1975). The wind tunnel’s ground plane boundary layer: Its interference with the flow underneath cars. Technical Report 750066, Society of Automotive Engineers, Warrendale, PA.
- Hummel, D. and Redeker, G. (2003). A new vortex flow experiment for computer code validation. Technical report, NATO research and technology angecy CEDEX, (France).
- Iberall, A. S. (1950). Attenuation of oscillatory pressures in instrument lines. *Journal of Research, National Bureau of Standards*, 45(RP2115):85–108.
- Ioannou, P. A. (1997). *Automated highway systems*. Springer.
- Irwin, H. P. A. H., Cooper, K., and Girard, R. (1979). Correction of distortion effects caused by tubing systems in measurements of fluctuating pressures. *Journal of Wind Engineering and Industrial Aerodynamics*, 5(1-2):93–107.
- Janssen, L. J. and Hucho, W. H. (1975). Aerodynamische Entwicklung von VW Golf und Scirocco. *ATZ*, 77:1–5.
- Jenkins, L. (2000). An experimental investigation of the flow over the rear end of a notchback automobile configuration. Technical Report 2000-01-0489, Society of Automotive Engineers, Warrendale, PA.

- Johnson, S. (2005). *Wake structures of simplified automotive geometries using numerical methods*. PhD thesis, Monash University.
- Johnson, W. F. (2004). A comprehensive study of vortex breakdown flow mechanisms: Computational investigation and preliminary control. Master's thesis, University of Washington Graduate School.
- JR3, Inc. (1994). *DSP-based force sensor receivers - Software and installation manual*. JR3 Inc., Woodland, CA.
- JR3, Inc. (last accessed 2007a). *160M50A force balance overview*. JR3 Inc., Woodland, CA.
- JR3, Inc. (last accessed 2007b). *PCI-bus receiver overview*. JR3 Inc., Woodland, CA.
- Kanaris, A., Ioannou, P. A., and Ho, F.-S. (1996). Spacing and capacity evaluations for different AHS concepts. Technical Report Report UCB-ITS-PRR-96-30, Institute of Transportation Studies, California PATH, Berkeley CA.
- Kapadia, S., Roy, S., and Wurtzler, K. (2003). Detached eddy simulation over a reference Ahmed car model. *AIAA Paper*, 857:2003.
- Keser, H. I. and Ünal, M. F. (2003). Flow around a circular cylinder downstream of a blunt-based flat plate in tandem and staggered arrangements. *Journal of Fluids and Structures*, 17(6):783–791.
- Kim, T. Y., Lee, B. S., Lee, D. H., and Hwang, J. H. Lee, D. H. (2003). A study on vortex shedding around a bluff body near the ground. Technical Report 2003-01-0652, Society of Automotive Engineers, Warrendale, PA.
- Koenig, K. and Roshko, A. (1985). An experimental study of geometrical effects on the drag and flow field of two bluff bodies separated by a gap. *Journal of Fluid Mechanics*, 156:167–204.
- Krajnović, S. and Davidson, L. (2004). Large-eddy simulation of the flow around simplified car model. *SAE paper*.
- Krajnović, S. and Davidson, L. (2005). Flow around a simplified car, part 2: Understanding the flow. *Journal of Fluids Engineering*, 127:919–928.
- Lawson, A. A., Dominy, R. G., Sims-Williams, D. B., and Mears, P. (2007). A comparison between on-road and wind tunnel surface pressure measurements on a mid-sized hatchback. In *SAE 2007 Transactions Journal of Passenger Cars: Mechanical Systems*, number 2007-01-0898 in SAE special paper collections. Society of Automotive Engineers, Warrendale, PA.
- Le Good, G. M. and Garry, K. P. (2004). On the use of reference models in automotive aerodynamics. Technical Report 2004-01-1308, Society of Automotive Engineers, Warrendale, PA.
- Leclercq, D. J. J. and Doolan, C. J. (2009). The interaction of a bluff body with a vortex wake. *Journal of Fluids and Structures*, 25(5):867–888.

- Lienhart, H. and Becker, S. (2003). Flow and turbulence structures in the wake of a simplified car model. Technical Report 2003-01-0656, Society of Automotive Engineers, Warrendale, PA.
- Lienhart, H., Stoots, C., and Becker, S. (2000). Flow and turbulence structures in the wake of a simplified car model (Ahmed model). *DGLR Fach Symp. der AG STAB*, 15.
- Lienhart, H., Stoots, C., and Becker, S. (2002). Case 9.4 (data sets for the 10th joint ERCOFTAC (SIG-15) -IAHR-QNET/CFD workshop on refined turbulence modelling).
- Lindener, N., Miehl, H., Cogotti, A., Cogotti, F., and Maffei, M. (2007). Aeroacoustic measurements in turbulent flow on the road and in the wind tunnel. Technical Report 2007-01-1551, Society of Automotive Engineers, Warrendale, PA.
- Liu, X., Levitan, M., and Nikitopoulos, D. (2007). Wind tunnel tests for mean drag and lift coefficients on multiple circular cylinders arranged in-line. *Journal of Wind Engineering and Industrial Aerodynamics*, 96:831–839.
- Liu, Y. and Moser, A. (2003). Numerical modeling of airflow over the Ahmed body. In *Proceedings of the 11th Annual Conference of the CFD Society of Canada*.
- Lungu, D. and van Gelder, P. (1997). Characteristics of wind turbulence with applications to wind codes. *Proceedings of the 2nd European & African Conference on Wind Engineering*, pages 1271–1277.
- Mahbub Alam, M. and Zhou, Y. (2007). Phase lag between vortex shedding from two tandem bluff bodies. *Journal of Fluids and Structures*, 23:339–347.
- Marcu, B. and Browand, F. (1998). The aerodynamic forces of misaligned platoons. Technical Report UCB-ITS-PRR-98-4, Institute of Transportation Studies, California PATH, Berkeley CA.
- Martinuzzi, R. J. and Havel, B. (2004). Vortex shedding from two surface-mounted cubes in tandem. *International Journal of Heat and Fluid Flow*, 25(3):364–372.
- Maull, D. J. (1978). Mechanisms of two and three-dimensional base drag. *Aerodynamic Drag Mechanisms of Bluff Bodies and Road Vehicles*.
- Mayer, J., Schrefl, M., and Demuth, R. (2007). On various aspects of the unsteady aerodynamic effects on cars under crosswind conditions. In *SAE 2007 Transactions Journal of Passenger Cars: Mechanical Systems*, number 2007-01-1548 in SAE special paper collections. Society of Automotive Engineers, Warrendale, PA.
- Melbourne, W. H. (1993). Turbulence and the leading edge phenomenon. *Journal of Wind Engineering and Industrial Aerodynamics*, 49:45–64.
- Merrill, B. R. (1993). Vortex shedding by blunt/bluff bodies at high reynolds numbers. volume 1: Data analysis. Technical Report 93-09622, Phillips Laboratory, Air Force Materiel Command.

- Michaelian, M. and Browand, F. (2000). Field experiments demonstrate fuel savings for close following. Technical Report PATH research report UCB-ITS-PRR-2000-14, Institute of Transportation Studies, California PATH, Berkeley CA.
- Milbank, J. (2004). *Investigation of fluid-dynamic cavity oscillations and the effects of flow angle in an automotive context using an open-jet wind tunnel*. PhD thesis, RMIT University.
- MKS Instruments, Inc. (1997). *Manual for MKS Type 690A Absolute / MKS Type 698A Differential High Accuracy Pressure Transducers*. MKS Instruments, Inc., e edition.
- Moraes, O. L. L., Fitzjarrald, D. R., Acevedo, O. C., Sakai, R. K., Czikowsky, M. J., and Degrazia, G. A. (2008). Comparing spectra and cospectra of turbulence over different surface boundary conditions. *Physica A: Statistical Mechanics and its Applications*, 387(19-20):4927–4939.
- Morel, T. (1978a). Aerodynamic drag of bluff body shapes characteristic of hatch-back cars. Technical Report 780267, The Society of Automotive Engineers.
- Morel, T. (1978b). The effect of base slant on the flow pattern and drag of three-dimensional bodies with blunt ends. In Sovran, G., Morel, T., and Mason, W. T. J., editors, *Aerodynamic Drag Mechanisms of Bluff Bodies and Road Vehicles (proceedings of Symposium held at General Motors Research Laboratories, Warren, MI, 1976)*, pages 191–226. Plenum Press.
- Morelli, A., Nuccio, P., and Visconti, A. (1981). Automobile aerodynamic drag on the road compared with wind tunnel tests. Technical Report 810186, Society of Automotive Engineers, Warrendale, PA.
- Mousley, P. (2006). Cobra probe catalogue - Turbulent Flow Instrumentation.
- Mousley, P. D., Watkins, S., and Hooper, J. D. (1998). Use of a hot-wire anemometer to examining the pressure signal of a high-frequency pressure probe. In *13th Australasian Fluid Mechanics Conference*.
- Nakamura, Y. (1993). Bluff-body aerodynamics and turbulence. *J. Wind Eng. Ind. Aerodyn*, 49:65–78.
- Nakamura, Y., Ohya, Y., and Ozono, S. (1988). The effects of turbulence on bluff-body mean flow. *Journal of Wind Engineering and Industrial Aerodynamics*, 28:251–259.
- National Instruments Corp. (2007). *DAQ E Series - E Series user manual*. National Instruments Corporation.
- National Instruments Corp. (2009). National Instruments KnowledgeBase article 1DAIG7W3: What is the difference between interval scanning and round robin scanning? Online article.
- Newland, D. E. (1979). *An Introduction to Random Vibrations and Spectral Analysis*. Longman Group Limited, first edition.
- Nijhof, B. C. and Wickern, G. (2003). Reference static and dynamic pressures in automotive wind tunnels. Technical Report 2003-01-0428, Society of Automotive Engineers, Warrendale, PA.

- Noger, C., Regardin, C., and Széchényi, E. (2005). Investigation of the transient aerodynamic phenomena associated with passing manoeuvres. *Journal of Fluids and Structures*, 21(3):231–241.
- Nouzawa, T., Haruna, S., Hiasa, K., Nakamura, T., and Sato, H. (1990). Analysis of wake pattern for reducing aerodynamic drag of notchback model. Technical Report 900318, Society of Automotive Engineers, Warrendale, PA.
- Nouzawa, T., Hiasa, K., Nakamura, T., Kawamoto, A., and Sato, H. (1992). Unsteady-wake analysis of the aerodynamic drag of a notchback model with critical afterbody. Technical Report 920202, Society of Automotive Engineers, Warrendale, PA.
- Oetl, D., Goulart, A., Degrazia, G., and Anfossi, D. (2005). A new hypothesis on meandering atmospheric flows in low wind speed conditions. *Atmospheric Environment*, 39(9):1739–1748.
- Okada, M. (2006). *Experimental investigations of wake flow structures behind simplified automotive geometries*. PhD thesis, Monash University.
- Ol, M. V. (2003). An experimental investigation of leading edge vortices and passage to stall of non-slender delta wings. Technical report, Air Vehicles Directorate, Air Force Research Laboratory, USA.
- Pagliarella, R. M. (2006). Conversation with MKS Instruments inc. technical support staff (on performance of non-conditioned baratron systems).
- Pagliarella, R. M. (2007). Conversation with Peter Mousley, software engineer, Turbulent Flow Instrumentation.
- Pagliarella, R. M., Dale, P., and Davy, J. (2007). Conversation with Mr Peter Dale and Assoc. Prof. John Davy, School of Applied Physics, RMIT University.
- Perry, A. and Chong, M. (1987). A description of eddying motions and flow patterns using critical-point concepts. *Annual Reviews in Fluid Mechanics*, 19(1):125–155.
- Quirillo, G. (1999). Flow optimisation of the RMIT Industrial Wind Tunnel.
- Romberg, G. F., Chianese, F., and Lajoie, R. G. (1971). Aerodynamics of race cars in drafting and passing situations. Technical Report 710213, Society of Automotive Engineers, Warrendale, PA.
- Roshko, A. (1954). On the development of turbulent wakes from vortex streets. *NACA Rep*, 1191:1–23.
- Sakamoto, H. and Haniu, H. (1988). Aerodynamic forces acting on two square prisms placed vertically in a turbulent boundary layer. *Journal of Wind Engineering and Industrial Aerodynamics*, 31(1):41–66.

- Saunders, J. W., Watkins, S., and Cassar, R. J. (1993). Vortex optimisation of slotted tops and cavities of two different open rail wagons. *Journal of Wind Engineering & Industrial Aerodynamics*, 49:421–430.
- Schlichting, H. (2000). *Grenzschicht-Theorie (Boundary Layer Theory)*. Springer, 8th edition and English version edition.
- Shiraishi, N., Matsumoto, M., and Shirato, H. (1986). On aerodynamic instabilities of tandem structures. *J. Wind Eng. Ind. Aerodyn*, 23:437–447.
- Shladover, S. E. (1978). Longitudinal control of automated guideway transit vehicles within platoons. *ASME J. Dyn. Sys. Meas. Contr.*, 100:302–310.
- Sims-Williams, D. and Dominy, R. (1999). The reconstruction of periodic pressure fields from point measurements. Technical Report 1999-01-0809, Society of Automotive Engineers, Warrendale, PA.
- Sims-Williams, D. B. and Dominy, R. G. (1998). Experimental investigation into unsteadiness and instability in passenger car aerodynamics. Technical Report 980391, Society of Automotive Engineers, Warrendale, PA.
- Sims-Williams, D. B., Dominy, R. G., and Howell, J. P. (2001). An investigation into large scale unsteady structures in the wake of real and idealized hatchback car models. Technical Report 2001-01-1041, Society of Automotive Engineers, Warrendale, PA.
- Sims-Williams, D. B. and Duncan, B. D. (2002). The Ahmed model unsteady wake: Experimental and computational analysis. Technical Report 2002-01-1315, Society of Automotive Engineers, Warrendale, PA.
- Smith, J. O. (2002). *Mathematics of the Discrete Fourier Transform (DFT) with audio applications*. Center for Computer Research in Music and Acoustics (CCRMA), Stanford University, 2nd edition.
- Spohn, A. and Gillieron, P. (2002). Flow separations generated by a simplified geometry of an automotive vehicle. *IUTAM Symposium: Unsteady Separated Flows*, pages 8–12.
- Steven, W. S. (1999). *The Scientist and Engineer’s Guide to Digital Signal Processing*. California Technical Publishing.
- Strachan, R., Knowles, K., and Lawson, N. (2004). A CFD and Experimental Study of An Ahmed Reference Model. Technical Report 2004-01-0442, Society of Automotive Engineers, Warrendale, PA.
- Strachan, R. K., Knowles, K., and Lawson, N. J. (2007). The vortex structure behind an Ahmed reference model in the presence of a moving ground plane. *Experiments in Fluids*, 42(5):659–669.
- Sun, Y. and Ioannou, P. (1995). A handbook for inter-vehicle spacing in vehicle following. Technical Report UCB-ITS-PRR-95-1, Institute of Transportation Studies, California PATH, Berkeley CA.

- Takeuchi, T. and Matsumoto, M. (1992). Aerodynamic response characteristics of rectangular cylinders in tandem arrangement. *Journal of Wind Engineering and Industrial Aerodynamics*, 41:565–576.
- Tombazis, N. and Bearman, P. (1997). A study of three-dimensional aspects of vortex shedding from a bluff body with a mild geometric disturbance. *Journal of Fluid Mechanics*, 330:85–112.
- Tsuei, L. and Savaş, Ö. (2000). A wind tunnel investigation of the transient aerodynamic effects on a four-car platoon during passing maneuvers. Technical Report 2000-01-0875, Society of Automotive Engineers, Warrendale, PA.
- Tsuei, L. and Savaş, Ö. (2001). Transient aerodynamics of vehicle platoons during in-line oscillations. *Journal of Wind Engineering & Industrial Aerodynamics*, 89(13):1085–1111.
- Unger, R., Kuhn, A., Buchheim, R., Carr, G. W., Cogotti, A., Garrone, A., and Nilsson, L. (1980). Comparison tests between major European automotive wind tunnels. Technical Report 800140, Society of Automotive Engineers, Warrendale, PA.
- Vino, G. (2005). *An experimental investigation into the time-averaged and unsteady aerodynamics of the simplified passenger vehicle in isolation and in convoys*. PhD thesis, RMIT University.
- Vino, G., Watkins, S., and Mousley, P. (2003). The passenger vehicle wake under the influence of upstream turbulence. Technical Report 2003-01-0650, Society of Automotive Engineers, Warrendale, PA.
- Vino, G., Watkins, S., Mousley, P. D., Watmuff, J., and S., P. (2005). Flow structures in the near-wake of the Ahmed model. *Journal of Fluids and Structures*, 20(5):673–695.
- Walter, T., Gossweiler, C., and Willson, B. (2007). Application of an improved model for the determination of acoustic resonances in indicator passages for combustion pressure measurements in large bore gas engines. Technical Report (Kistler special print) 920-352e-02.07, Kistler Instruments AG, Winterthur, Switzerland.
- Washburn, A. E. (1992). Effects of external influences on subsonic delta wing vortices. In *Proceedings of 17th the Aerospace Ground Testing Conference*, number AIAA-1992-4033. American Institute of Aeronautics and Astronautics, Inc.
- Watkins, S. (1984). Calibration of the Industrial Wind Tunnel. Technical Report WTP1026, Royal Melbourne Institute of Technology.
- Watkins, S. (1990). *Wind-tunnel modelling of vehicle aerodynamics: with emphasis on turbulent wind effects on commercial vehicle drag*. PhD thesis, Victorian University of Technology, R.M.I.T. Campus.
- Watkins, S. and Cooper, K. R. (2007). The unsteady wind environment of road vehicles, part two: Effects on vehicle development and simulation of turbulence. In *SAE 2007 Transactions Journal of Passenger Cars: Mechanical Systems*, number 2007-01-1237 in SAE special paper collections. Society of Automotive Engineers, Warrendale, PA.



- Watkins, S., Mousley, P. D., and Vino, G. (2004). The development and use of dynamic pressure probes with extended cones of acceptance. In *15th Australasian Fluid Mechanics Conference*.
- Watkins, S. and Saunders, J. (1998). A review of the wind conditions experienced by a moving vehicle. Technical Report 981182, Society of Automotive Engineers, Warrendale, PA.
- Watmuff, J., Vino, G., Watkins, S., and Hill, B. (2004). Dynamic measurement of differential buffet pressure. In *15th Australasian Fluid Mechanics Conference*.
- Whitmore, S. (2006). Frequency response model for branched pneumatic sensing systems. *Journal of Aircraft*, 43(6):1845–1854.
- Wiedemann, J. and Potthoff, J. (2003). The new 5-belt road simulation system of the IVK wind tunnels-design and first results-design and first results. Technical Report 2003-01-0429, Society of Automotive Engineers, Warrendale, PA.
- Williams, J., Barlow, J. B., and Ranzenbach, R. (1999). Experimental study of  $C_d$  variation with aspect ratio. Technical Report 1999-01-0649, Society of Automotive Engineers, Warrendale, PA.
- Wimer, J. (2003). A digital particle image velocimetry investigation of delta wing vortex flow and vortex breakdown. Master’s thesis, University of Washington Graduate School.
- Wing, W. (1981). Ground simulation in automotive wind tunnel - a survey. Technical Report WTP 1005, Department of Mechanical and Production Engineering, Royal Melbourne Institute of Technology.
- Yang, H., Sims-Williams, D. B., and He, L. (2006). Unsteady pressure measurement with correction on tubing distortion. In Hall, K. C., Kielb, R. E., and Thomas, J. P., editors, *Unsteady Aerodynamics, Aeroacoustics and Aeroelasticity of Turbomachines*, pages 521–529. Springer.
- Zabat, M., Frascaroli, S., and Browand, F. (1993). Drag measurements on a platoon of vehicles. Technical Report PATH research report UCB-ITS-PRR-93-27, Institute of Transportation Studies, California PATH, Berkeley CA.
- Zabat, M., Frascaroli, S., and Browand, F. (1994). Drag measurements on 2, 3 & 4 car platoons. Technical Report 940421, Society of Automotive Engineers, Warrendale, PA.
- Zdravkovich, M. (1987). The effects of interference between circular cylinders in cross flow. *Journal of Fluids and Structures*, 1(2):239–261.
- Zhang, H. and Melbourne, W. H. (1992). Interference between two circular cylinders in tandem in turbulent flow. *J. Wind Eng. Ind. Aerodyn*, 41:44.